Structures and properties of alkali metal hybrid halide perovskites containing dabconium or piperazinium

by

Hendrik J. van der Poll

Submitted in fulfilment of the requirements for the degree:
Master of Science (MSc)
Chemistry

In the Faculty of Natural and Agricultural Sciences
University of Pretoria
Pretoria
September 2021

Supervisor: Prof. Melanie Rademeyer

DECLARATION

I, Hendrik Johannes van der Poll, Student Number: 16012594, declare that this dissertation, which I hereby submit for the degree Master of Science in Chemistry at the University of Pretoria, is my work and has not previously been submitted by me for a degree at this or any other tertiary institution.

I am aware of the University of Pretoria's plagiarism policy, and I understand what plagiarism is. I declare that this dissertation is my own original work, and where the work of other's has been used, it has been acknowledged and referenced as per the university regulations. I have not utilised previous work completed by another student or by any other person and represented it here or elsewhere as my own work. I have not allowed anyone to copy my work with the intention of passing it down as their own work.

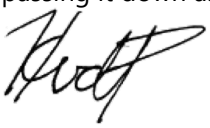

Signed by Hendrik Johannes van der Poll **November 2021**

ACKNOWLEDGEMENTS

With any project of this size and ambition, there are many role players. The first person who needs to be thanked and acknowledged is Prof. Melanie Rademeyer. Without her dedication, effort, and undying interest in the field of crystallography, this study would not have been possible. Her knowledge and passion for her field inspired me to further my understanding of each aspect of the study in the same depth. Her willingness to assist her students and extend herself remains one of the core pillars of this study's success. Knowing she was always just a phone call, email, or WhatsApp away, gave me the best support structure an MSc student could have asked for.

To my mother and father (Breggie van der Poll and André van der Poll), who introduced me to academia from as early as the age of three. Ever since I have aspired to complete a masters degree and subsequent doctorate one day. Without their emotional and financial support over my several years of study and degrees, this study would never have seen the light of day.

Without the assistance of Dr Frederick Malan from UP and Dr Rudolph Erasmus from Wits, the single-crystal X-ray diffraction and Diffuse Reflectance Spectroscopy data would not have been recorded, and most of this study would not have been possible. Their friendliness and helpful nature made this study a pure pleasure to complete. Furthermore, thank you to Dr Praveen Beebeejaun-Boodoo for her assistance with recording the solid-state fluorescence spectra and for always being willing to help, even during the time of the Great Rayleigh Scattering Depression.

My gratitude to Adri Moolman, who assisted me in drawing detailed schematics of instrumentation, choosing colour pallets, and general aspects of the dissertation's presentability from a digital design perspective. Her input helped to make this dissertation a work of art.

Finally, my gratitude to every teacher, lecturer, colleague, friend, choir conductor and person, who have formed part of my life and have taught me the necessary life philosophies that have carried me through all my studies and, specifically, this dissertation.

SUMMARY

Hybrid halide perovskites have received much attention over the past two decades due to their realisation in optoelectronic applications. In this study, hybrid halide alkali metal perovskites that contained either piperazinium (piperazine-1,4-diium) or dabconium (1,4-diazabicyclo[2.2.2]octane-1,4-diium) were studied crystallographically and subsequently, their optical band gaps and solid-state fluorescence properties were measured. Specifically, the alkali metal halides NaCl, NaBr, NaI, KCl, KBr, KI, CsCl, CsBr and CsI were employed in combination with the aforementioned organic dications. Moreover, diffuse reflectance spectroscopy was used to measure the optical band gaps of the materials.

Sixteen perovskite structures were determined, nine of which are novel. Eight novel dabconium-containing perovskite structures and one piperazinium-containing structure were obtained. The dabconium-series exhibited one of two structural dimensionalities, either a 3D perovskite structure (six in total) or a 1D ABX_3-type perovskite structure (five in total). Similarly, the piperazinium-series also exhibited either a 3D structure (four in total) or a 1D ⟨100⟩-type perovskite structure (one structure). In addition, the piperazinium-series was found to generally crystallise with water molecules included in the crystal structure, whereas the dabconium-series did not. The dabconium-containing structures crystallised in a wide range of phases, including monoclinic, orthorhombic, trigonal, and hexagonal phases, while the piperazinium-containing structures were obtained in one of two phases (3D structures in the orthorhombic phase and the 1D structure in the monoclinic phase). Structural trends were identified in both families.

The band gaps of the materials from both series were determined to exceed 3.00 eV and hence the materials are unsuited for application as sensitisers in perovskite solar cells. The materials could be classified as either semi-conductors (band gap below 5.0 eV) or insulators (band gap exceeding 5.0 eV). Subsequently, their solid-state fluorescence spectra were measured, and it was determined that none of the perovskite materials obtained in this study exhibited fluorescence at room temperature. However, because of their wide band gap, they may find application in white-light emission devices, such as perovskite light-emitting diodes.

Furthermore, though the materials were not suitable as sensitisers in perovskite solar cells, they show promise for application as electron transmitting materials and hence may still be considered in the domain of perovskite solar cells.

Notably, structural and property tuneability was illustrated for a specific example of the dabconium-series. It was shown that the material's structure and band gap could be engineered by careful consideration of the precursor constituents, based on the structural trends identified. This tuneability of materials is much desired in the field of materials science.

Finally, several avenues for future work, including synthetic extensions, additional property measurements and other potential optoelectronic applications, were identified form the results of this study and show that the perovskite family tree is still revealing new blossoms each day.

TABLE OF CONTENTS

COLOUR KEY

Here a key to the colours used to represent the elements present in crystal structures is given. Only those elements that are frequently encountered in the study are listed. This colour key is no longer valid in Figures or Schemes where "general" structures are given. In addition, where slight deviations from the key are made for clarity, it will be emphasised.

Metal Element	Colour	Non-Metal Element	Colour
Sodium (Na)		Hydrogen (H)	
Potassium (K)		Carbon (C)	
Rubidium (Rb)		Nitrogen (N)	
Caesium (Cs)		Oxygen (O)	
Tin (Sn)		Chloride (Cl)	
Lead (Pb)		Bromide (Br)	
		Iodide (I)	

SUMMARY OF STRUCTURES

The line structure and name of the structures obtained in this study are given below. Solid lines indicate bonds that appear in the asymmetric unit of the structure, and wavy bonds indicate additional bonds added for a more detailed description. In each case, the complete organic cation is shown. However, in most cases, only a partial moiety is present in the asymmetric unit. This was done for clarity. Note that D is for "dabconium" and P is for "piperazinium".

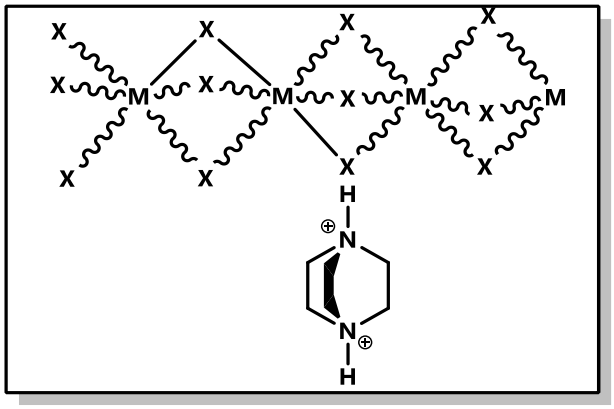

D-NaCl$_3$, D-NaBr$_3$, D-KCl$_3$ and **D-KBr$_3$(1)**

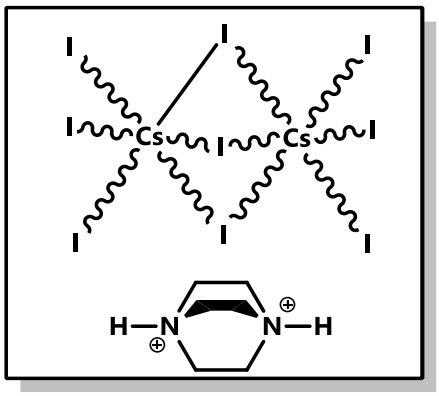

D-CsI$_3$

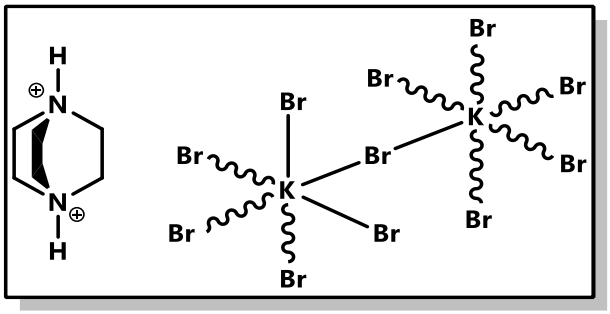

D-KBr$_3$(2)

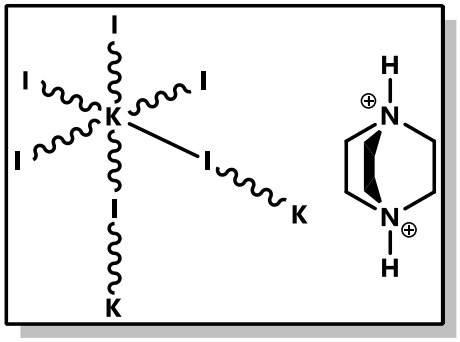

D-KI$_3$

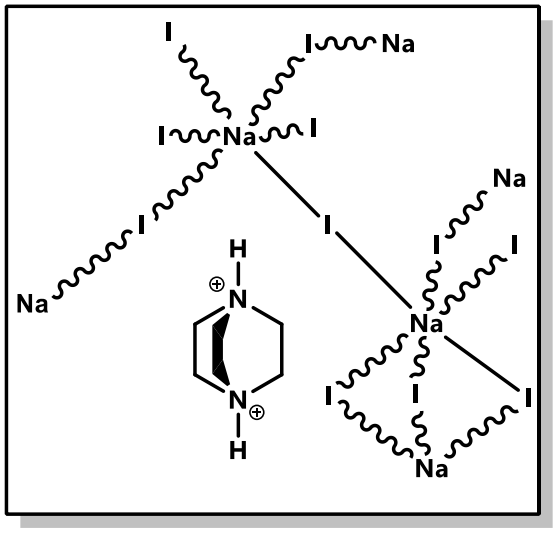

D-NaI$_3$

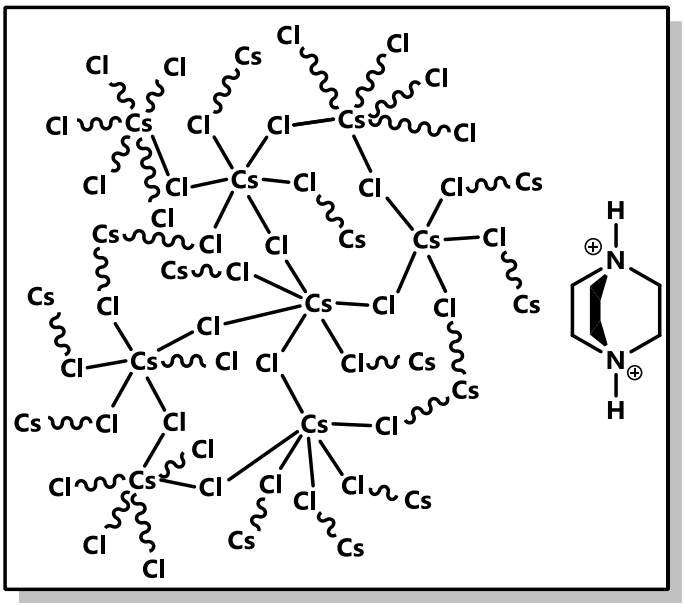

D-CsCl$_3$

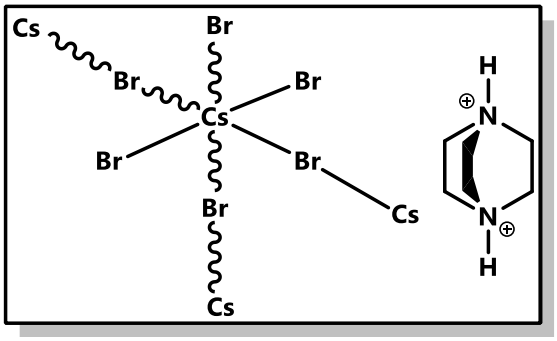

D-$CsBr_3$

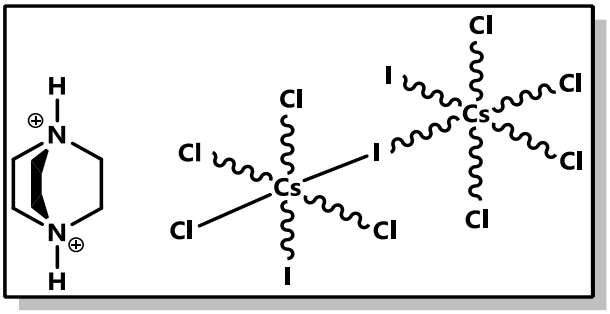

D-$CsCl_2I$

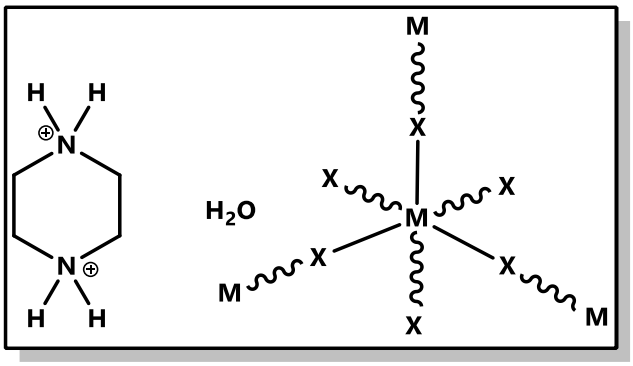

P-KCl_3, P-KBr_3, P-KI_3 and **P-$CsCl_3$**

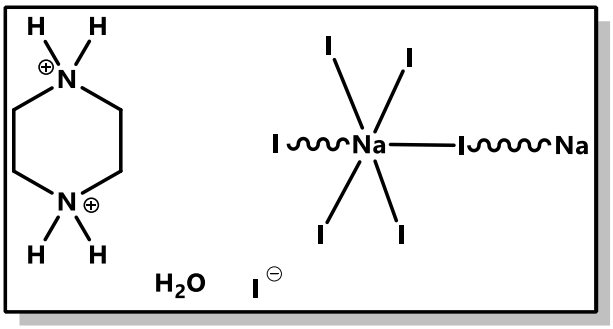

P_3-NaI_5

LIST OF FIGURES

LIST OF SCHEMES

LIST OF TABLES

LIST OF ABBREVIATIONS AND SYMBOLS

%	Percentage
□	Vacancy
°C	Degree Celsius
2-NAM	N-Acetylmuramic Acid
4AMP	1-(4-piperidinyl)methanamine
5-AVA	5-ammoniumvaleric acid
a.u.	Atomic Units
AA^+	Azetamidinium
ACA^+	Acetamidinium
ACI	Alternating Cation in the Interlayer Space
AE2T	Bis-aminoethyl Bithiophene
AM 1.5G	Reference Air Mass 1.5 Spectra
a-Si:H	Amorphous Silicon
AZ^+	Azetidinium
BA^+	*n*-Butylammonium
BCP	Bathocuproine (2,9-Dimethyl-4,7-diphenyl-1,10-phenanthroline)
BPhen	4,7-diphenyl-1,10-phenanthroline
CBM	Conduction Band Minimum
CDTA	2-cyano-3-[5-[4-(diphenylamine) phenyl]-2-thienyl]-propanoic acid
Ch	Chalcogen
CPS	Counts Per Second
CSD	Cambridge Structural Database
c-Si	Crystalline Silicon
c-TiO_2	Compact TiO_2
CTL(s)	Charge Transfer Layer(s)
CVD	Chemical Vapour Deposition
c-γ-TiO_2	Compact Brookite TiO_2
D	Dabconium
Dabconium	1,4-diazabicyclo[2.2.2]octane-1,4-diium
DCM	Dichloromethane
DFT	Density Functional Theory
$DiEA^+$	Diethylammonium
$DiMA^+$	Dimethylammonium
DJ	Dion–Jacobson
DMF	*N*,*N*'-dimethylformamide
DMSO	Dimethylsulfoxide
DRS	Diffuse Reflectance Spectroscopy
DSC	Differential Scanning Calorimetry
DSSC(s)	Dye Sensitised Solar Cell(s)
e^-	Electron
EA^+	Ethylammonium
EDEA	2,2'-(ethylenedioxy)bis(ethylammonium)
E_g	Optical Band Gap
EMIC·PEDOT:PSS	1-ethyl-3-methylimidazolium chloride·Poly(3,4-ethylenedioxythiophene)-poly(styrenesulfonate)
en	Ethylenediamine
EPBT	Energy Payback Time
EtA	Ethylammonium
ETL	Electron Transmitting Layer
ETM	Electron Transmitting Material
eV	Electron Volt
$F(hkl)$	Atomic Scattering Factor
$F(R_\infty)$	Kubelka-Munk Remission Function
FA^+	Formamidinium
FAX	Formamidinium Halide
FF	Fill Factor
FTO	Fluorine Doped Tin Oxide
FTO	Fluorine Doped Tin Oxide
GBL	γ-butyrolactone
GGA	Generalised Gradient Approximation
GUA^+	Gaudinium
GW	Green-Wannier Approximation
$h^\bullet$ or h^+	Hole

HA^+	Hydroxylammonium
HAP	Hydroxyapatite
HEA^+	2-hydroxyethylammonium
HPA	Hypophosphorous Acid
HPSC(s)	Hybrid Perovskite Solar Cell(s)
HTL	Hole Transmitting Layer
HTM	Hole Transmitting Material
HY^+	Hydrazinium
I	Current
***i*-BuA^+**	Isobutylammonium
ICBA	Indene-C_{60} bisadduct
IEP	Intramolecular Exchange Process
IM^+	Imidazolium
IPA	Isopropyl Alcohol
***i*-PA^+**	Isopropylammonium
ITC	Inverse Temperature Crystallisation
ITO	Indium Doped Tin Oxide
IUPAC	International Union of Pure and Applied Chemistry
IV	Current-Voltage
J	Current Density
JDOS	Joint Density of States
K	Kelvin
K	DRS Absorption Factor
LC	Lethal Concentration
LCA(s)	Life Cycle Assessment(s)
LCI	Life Cycle Impact
LD	Lethal Dose
LED(s)	Light Emitting Diode(s)
LiTFSI	Lithium bis(trifluoromethanesulfonyl)imide
MA^+	Methylammonium
MASP	Meniscus-Assisted Solution Printing
MAX	Methylammonium Halide
***m*-MTDATA**	4,4′,4″-tris(3-methylphenylphenylamino)triphenylamine
MP	Maximum Power
mp-Al_2O_3	Mesoporous Al_2O_3
mp-TiO_2	Mesoporous TiO_2
N719 Dye	Di-tetrabutylammonium cis-bis(isothiocyanate) bis (2,2′ -bipyridyl-4,4′ dicarboxylate) ruthenium(II)
***n*D**	*n* Dimensional (*n* = 0, 1, 2 or 3)
***N*-DPBI**	4-(1,3-dimethyl-2,3-dihydro-1H-benzoimidazol-2-yl)-*N*,*N*'-diphenylaniline
NH_4^+	Ammonium
NMP	*N*-methyl-2-pyrrolidone
NREL	National Renewable Energy Laboratory
OC	Open Circuit
P	Power
P	Piperazinium
P3HT	Poly(3-hexylthiophene-2,5-diyl)
PCBM	Methanofullerene phenyl-C_{61}-butyric-acid-methyl-ester
PCDPTBT	Poly[2,6-(4,4-bis-(2-ethylhexyl)-4H-cyclopenta[2,1-b;3,4-b']dithiophene)-alt-4,7-(2,1,3-benzothiadiazole)]
PCE	Power Conversion Efficiency
PDA	Polydiacetylenes
PDBD-T	Poly[(2,6-(4,8-bis(5-(2-ethylhexyl)thiophen-2-yl)-benzo[1,2-b:4,5-b']dithiophene))-alt-(5,5-(1',3'-di-2-thienyl-5',7'-bis(2-ethylhexyl)benzo[1',2'-c:4',5'-c']dithiophene-4,8-dione)]
PEA^+	Phenylethylammonium
PEDOT:PSS	Poly(3,4-ethylenedioxythiophene) polystyrene sulfonate
PEDOT:PSS(PEG)	PEDOT:PSS + Polyethylene glycol
PEIE	Polyethyleneimine
PeLED(s)	Perovskite Light Emitting Diode(s)
PhA^+	Phenylammonium
PIF8-TAA	Poly[[(2,4-dimethylphenyl)imino]-1,4-phenylene(6,12-dihydro-6,6,12,12-tetraoctylindeno[1,2-b]fluorene-2,8-diyl)-1,4-phenylene
Piperazine	1,4-Diazacyclohexane
Piperazinium	Piperazine-1,4-diium
PL	Photoluminescence

PLD	Pulsed Laser Deposition
PMMA	Poly(methyl methacrylate)
PN$^+$	Propylenediammonium
Poly-TPD	Poly(*N*,*N*'-bis-4-butylphenyl-*N*,*N*'-bisphenyl)benzidine
PSC(s)	Perovskite Solar Cell(s)
PTAA	Poly(bis(4-phenyl)(2,4,6-trimethylphenyl)amine)
PV	Photovoltaic
PXRD	Powder X-Ray Diffraction
PY$^+$	Pyrrolidinium
R	Alkyl Group
r	Radius
RH	Relative Humidity
RIP-MAPLE	Resonant-Infrared Matrix-Assisted Pulsed Laser Evaporation
RP	Ruddlesden–Popper
S	DRS Scattering Factor
SC	Short Circuit
SCXRD	Single-Crystal X-Ray Diffraction
SOC	Spin-Orbit Coupling
Spiro-OMeTAD	2,2',7,7'-tetrakis-9,9'-spirobifluorene
t	Goldschmidt Tolerance Factor
TetraMA$^+$	Tetramethylammonium
TFEA$^+$	Trifluoroethyl Ammonium
TGA	Thermogravimetric Analysis
TN$^+$	Trimethylenediammonium
TNRA	TiO_2 Nanorod Array
TPD	Triphenylamine Dimer
TPE	Tetraphenylethylene
TriMA$^+$	Trimethylammonium
UV	Ultraviolet
UV-Vis	Ultraviolet-Visible Light Spectroscopy
V	Voltage
VASP	Vapour-Assisted Solution Processing
VBM	Valence Band Maximum
V_E	Electric Field
WHO	World Health Organisation
X	Halide Ion (Cl^-, Br^- or I^-)
XRD	X-Ray Diffraction
μ	Octahedral Factor
τ	Bartel's Tolerance Factor
Φ	Fitness Factor
Γ	Denotes the centre of the Wigner-Seitz cell

LAYOUT OF THIS DISSERTATION

This dissertation has been written in a *publication format*, with each result chapter (Chapters 4, 5, and 6) presented in the layout of a publication. As a result, a degree of duplication in different chapters is inevitable. A summary of the content of the main chapters of the dissertation is given below.

Chapter 1 introduces the reader first to the different perovskite structure types and the synthetic methods employed to obtain perovskite single crystals. The discussion then shifts to the concept of perovskite solar cells, how they work, how they are characterised, and how they are fabricated. Finally, the Chapter points towards the future of these solar cells and sets the stage for Chapter 2.

Chapter 2 entails a detailed literature study focussing on the current knowledge and trends in the field of perovskite solar cells (lead-containing, lead-free and lead-less perovskites). In the final section of the chapter, the structures containing alkali metal ions and dabconium or piperazinium dications reported in the literature are highlighted. This last section in Chapter 2 also motivates the study and summarises the details of the study.

Chapter 3 focuses on the experimental methods and techniques employed in the current study. First the synthetic methods used in this study are described. Secondly, the theoretical background is provided for the primary methods and instrumentation used (X-ray diffraction techniques and Diffuse Reflectance Spectroscopy). The secondary property measurement method, solid-state fluorescence, is also briefly described.

Chapter 4 is the first of three Results Chapters. Experimental results regarding alkali metal halide perovskites containing the dabconium dication are presented in Chapter 4. These results include the structural characteristics of the compounds, structural trends, band gap measurement results and solid-state fluorescence studies.

Chapter 5 (the second Results Chapter) focuses on the experimental results obtained for piperazinium-containing alkali metal halide compounds and include structural characteristics, the identification of structural trends, band gap measurement results and solid-state fluorescence studies.

Chapter 6 is the final Results Chapter and describes the application of some of the compounds obtained in this study to perovskite solar cells. The chapter also describes a general method for the fabrication of perovskite solar cells.

Chapter 7 summarises the findings of the study and suggests possible avenues for future work.

Several Appendices may be found at the end of the study. Each of these provides essential supporting information, explanations, or applicable additional content for the main chapters. Of special importance is a link to a Google Drive Folder® that contains the .cif, .hkl and .res files of the respective structures, along with the subsequent CheckCIF reports in PDF format for all the crystal structures discussed in this dissertation. Structures are sorted by Chapter and subsequently dimensionality, 1D or 3D:

H.J. van der Poll - MSc Dissertation - Crystallographic Information Files and CheckCIF Reports

CHAPTER 1

Introduction

Chapter 1 serves as an introduction to the perovskite structure and its subsequent application in optoelectronics. A general discussion of the perovskite structure, its application in solar cell technology and outlook follows.

1.1 Hope for a Greener Future

In recent years, terms such as "**Global Warming**", "**The Green House Effect**", "**Carbon Footprint**", and the like have become part of the everyday conversations of ordinary people. However, at the forefront of addressing these environmental challenges are scientists working to resolve these threats to human existence. The current dependence on fossil fuels to fulfil the world's energy needs drives global warming towards a point of no return. Therefore, an alternative to fossil fuels *is* required. One weapon at the disposal of humans is that of renewable energy sources. By increasing the use of renewable energy sources, to fulfil the energy requirements of the people of planet earth, global warming can hopefully be halted and eventually reversed.

This study focuses on developing materials for application as renewable energy sources, with a specific focus on solar cell technology. **Solar cells** harness the sun's natural, free energy and convert this energy into a more useful form of *electrical energy*. Furthermore, in the South African context, where most days are unclouded, solar technology could only be benefitted from since about 88% of the energy in South Africa is provided by non-renewable sources, such as coal and natural gas.[1]

Where solar cells are concerned, the most common commercial technology used is silicon solar cells. Improving the efficiency of photovoltaic devices is an obvious goal and can be done by investigating new photovoltaic technologies. Perovskite solar cells (PSCs) represent such a new technology and have shown an exponential increase in their power conversion efficiency in recent years.[2] With the field of PSCs being relatively new, some challenges still need to be overcome, however, that said, PSCs may offer a unique opportunity to discover the proverbial *holy grail* of solar cell technology.

1.2 The Perovskite Structure

Materials with the same crystal structure as calcium titanate ($CaTiO_3$) are named perovskite materials and have a 3D cubic perovskite structure. Gustav Rose first discovered the mineral $CaTiO_3$ in the Ural mountains (1839) and called it "perovskite" in honour of the Russian Mineralogist Lev Perovski.[3] Later, in 1892, crystals of perovskites were fabricated by Wells[4] based on the mixture of caesium and lead halides, before the perovskite structure (specifically that of $BaTiO_3$) was resolved in 1945 by Helen Megaw,[5] an Irish crystallographer. Subsequently, the photoconductivity of perovskites was recognised by Møller in 1958.[6]

The general formula of a perovskite structure is ABX_3, where both A and B are cations, and X is an anion. For example, in $CaTiO_3$, both Ca^{2+} and Ti^{4+} are cations and O^{2-} is the anion. Furthermore, the size difference between Ca^{2+} and Ti^{4+} ions should be noted, which is typical in a perovskite structure formed between the A- and the B-cations. The structure of $CaTiO_3$ is shown in Figure 1.1,[7] where the cationic species (blue Ca^{2+}-ion) are surrounded by eight BX_6 (TiO_6) octahedra (illustrated as a grey polyhedron) and AX_{12} cuboctahedra formed *via* oxygen coordination, are displayed as light blue polyhedra.

The general perovskite structure has the A-cation in a body centred position in a BX-framework, where the BX-framework consists of corner-sharing octahedra, building a three-dimensional cubic (or distorted cubic) framework in which the A-cation

can *fit*. Therefore, the perovskite structure is regarded as a framework structure with corner-sharing BX_6 octahedra and A-cations in 12-coordinate interstices.[8] This structure is known as a three-dimensional (3D) perovskite structure due to its framework nature. $CaTiO_3$ is an example of a purely all-inorganic oxide perovskite, known as the oxide perovskite structure.

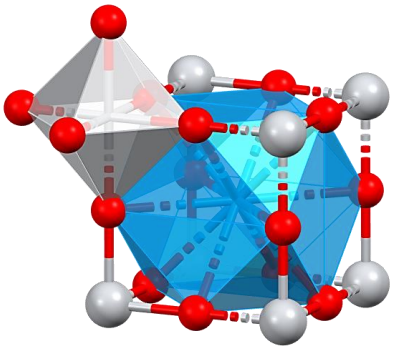

Figure 1.1 Crystal structure of $CaTiO_3$, showing the Ca-cation "caged" by the TiO_6 octahedra framework, representing the general perovskite structure. Ions are displayed as A = Ca^{2+} (blue), B = Ti^{4+} (silver), and X = O^{2-} (red).

However, since the initial discovery of the perovskite structure, many other combinations of A, B and X have been shown to exhibit the perovskite structure. The A-cation may be organic or inorganic, and the X-anion may be varied between oxides, halides, sulphides, phosphides, tetragonal anions, and many other inorganic anions.[7]

The combination of interest in this study is metal halides and organic cations, specifically organic cations containing amine functional groups. In general, the combination of these components in the presence of acid results in what is called organic-inorganic hybrid materials.

Organic-inorganic hybrids may exhibit the 3D perovskite structure in many instances, depending on the relative sizes of the metal cation and the organic cation, as discussed later. When an organic-inorganic hybrid compound exhibits a 3D dimensionality, the compound is called a hybrid organic-inorganic metal halide 3D perovskite (hybrid halide 3D perovskite for short).

Here the A-cation is an organic cation, that is, some organic molecule with a net positive charge due to protonation of an electronegative atom (for example, nitrogen), the B-cation a metal cation (often denoted M-cation when B is a metal ion), and the X-anion is a halide (F^-, Cl^-, Br^- or I^-). Notably, fluoride analogues remain scarce in literature due to the requirement to use HF to prepare these materials.

The corner-sharing of octahedra results in an anionic, inorganic framework formed by B-cations and X-anions. Figure 1.2 (a) shows a polyhedral representation of the framework, while Figure 1.2 (b) shows a ball and stick representation of the framework. Corner-sharing of the octahedra creates cavities in the inorganic framework that can accommodate the A-cation. Important structural parameters include the B–X bond lengths and X–B–X angles since these parameters determine the size and the shape of the cavity in which the A-cation sits.

An ideal cubic 3D perovskite structure crystallises in the space group $Pm\bar{3}m$ and has X–B–X angles of 90° or 180°, as illustrated in Figure 1.2. However, depending on the A-cation size, distortion of this framework can occur to accommodate a smaller cation, resulting in X–B–X angles deviating from the ideal values, as discussed later.

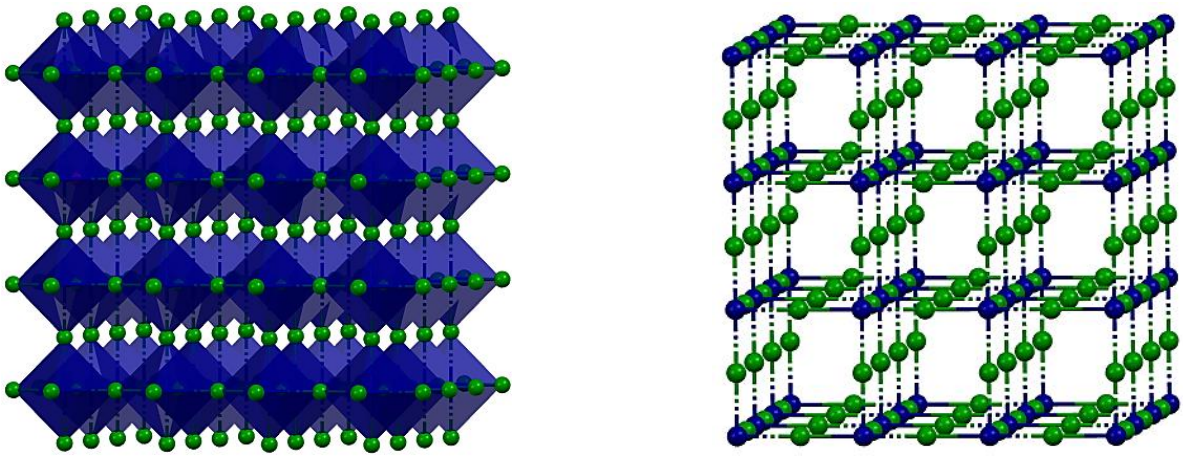

(a) **(b)**

Figure 1.2 The anionic, inorganic framework formed in the ideal 3D cubic perovskite structure. B-cations are shown in dark blue and X-anions in dark green. **(a)** Polyhedral representation and **(b)** ball-and-stick representation.

The 3D cubic perovskite phase is one of several different phases the 3D perovskite structure may adopt, with the different phases crystallising in different space groups. Reported phases (crystal systems) include cubic, hexagonal, trigonal, tetragonal, orthorhombic, rhombohedral, monoclinic and triclinic.[9,10]

The 3D cubic perovskite structure discussed in the previous section is known as the parent perovskite structure. However, other structural subclasses are also classified as perovskites.[10] Perovskite structures may be either 3D, two-dimensional (2D), one-dimensional (1D) or zero-dimensional (0D). The A-cation connects to the anionic portions *via* hydrogen bonding and van der Waals interactions in all four dimensionalities, forming a crystalline structure. This flexibility in structural dimensionality and composition allows for a vast potential range of material applications, including optoelectronics (solar cells and LEDs), lasers, detectors (X-ray- and photodetectors), storage devices etc.[11]

The BX_6 octahedra in the perovskite structure form an inorganic sub-structure. This sub-structure can have various modes of connectivity between the individual octahedra. Three basic modes of connectivity of octahedra are possible, and these include **corner-sharing** (Figure 1.3 (a)), **edge-sharing** (Figure 1.3 (b)) and **face-sharing** (Figure 1.3 (c)). All perovskite structures contain either one or a combination of these types of octahedral-connectivities in their structures.

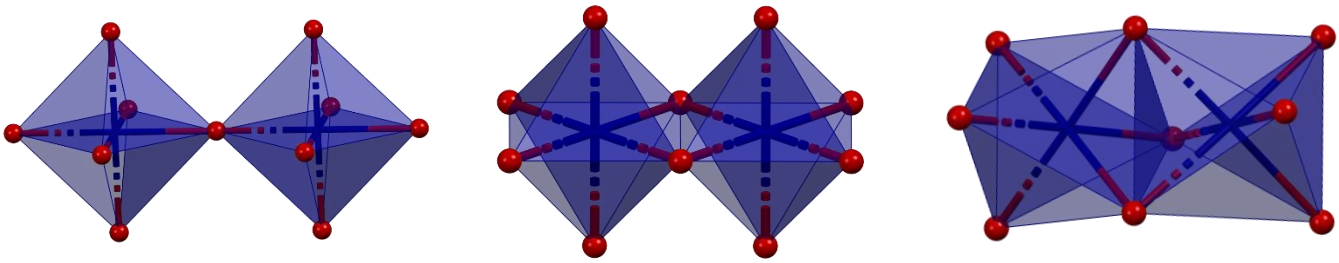

Figure 1.3 Possible different connectivities of BX_6 octahedra encountered in perovskite structures. **(a)** Corner-sharing, **(b)** edge-sharing and **(c)** face-sharing. B-cations are shown as blue octahedra and X-anions as red spheres.

The corner-sharing octahedra BX_6 only have one bridging X-anion between two different octahedra. In contrast, the edge-sharing type has two bridging X-anions, and the face-sharing have three bridging X-anions. These various types of connections in the octahedra allow for the different dimensionalities observed in the perovskite structure. The perovskite structures with dimensionalities lower than 3D are referred to as lower-dimensional perovskites.

Furthermore, certain lower-dimensional perovskite structures can be obtained from the dimensional reduction or "slicing" of the 3D cubic perovskite parent structure along different crystallographic planes. These different dimensionalities are made possible by the stabilisation effect of the organic cation (in hybrid structures) or the inorganic sublattice (the inorganic A-cations) on the metal-anion (metal halide or metal oxide) framework.[12] Figure 1.4 illustrates the different types of perovskite dimensionalities, including corner-sharing perovskites (Figure 1.4 (a)), face-sharing polytypes (Figure 1.4 (b)), dimensionally reduced perovskites (Figure 1.4 (c)), and the hexagonal perovskite polytypes (Figure 1.4 (d)).

Several examples of how the most general forms of these lower-dimensional hybrid perovskites are obtained from the 3D cubic perovskite (ABX_3) structure are shown in Scheme 1.1. The scheme is equally applicable to the pure inorganic perovskite dimensionalities. It is important to note that the lower dimensional perovskite structures shown in Scheme 1.1 are *by no means a comprehensive list* since the schematic serves only to illustrate how specific lower-dimensional perovskite structures are obtained from the 3D parent dimensionality.

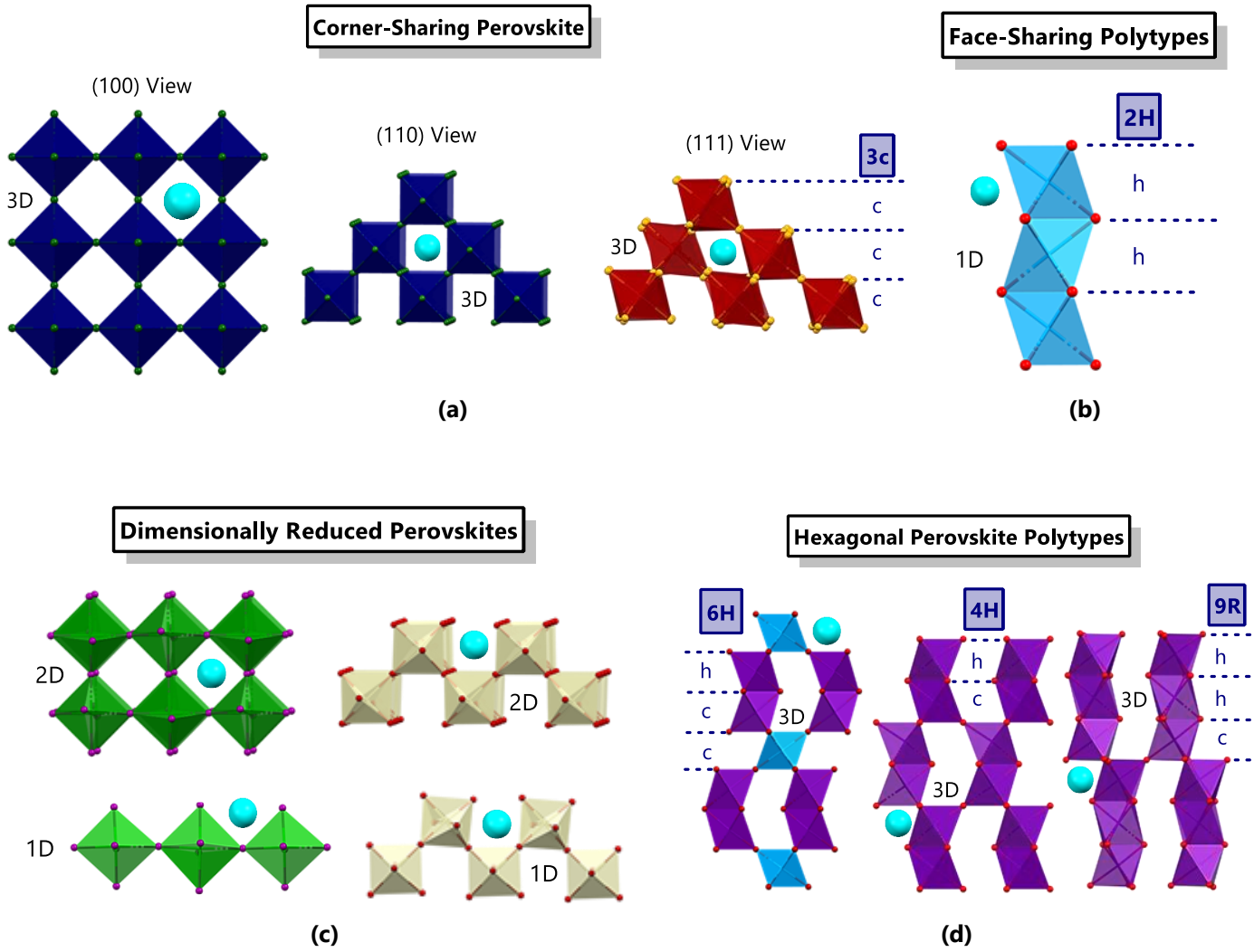

Figure 1.4 Different types of perovskite structures. **(a)** The 3D perovskite structure viewed perpendicular to the Miller planes specified in the Figure. **(b)** Face-sharing perovskite polytype, exhibiting the 1D perovskite dimensionality. **(c)** 2D and 1D perovskite dimensionalities obtained by the dimensional reduction of the 3D parent perovskite structure in the ⟨100⟩ or the ⟨110⟩ directions. **(d)** 3D hexagonal perovskite polytypes, which may be obtained by combining corner-sharing octahedra in the ⟨111⟩ direction and the face-sharing 1D polytypes. The symbols "c" and "h" specify cubic or hexagonal layers, respectively. Copyright American Chemical Society 2017. Adapted from Stoumpos *et al.*[10]

It should also be mentioned that not all of the lower dimensional perovskite structures can be obtained *via* dimensional reduction of the parent 3D cubic perovskite structure. For example, the 1D perovskite with molecular formula ABX_3 (also called hexagonal perovskites in the literature) exhibit face-sharing of octahedra and cannot be obtained by dimensional reduction of the 3D cubic perovskite structure, which displays corner-sharing octahedra.

The first possible lower dimensional perovskite structure that can be derived from the 3D parent structure entails a combination of the 3D and 2D structures (referred to as a **quasi-2D structure** shown in Scheme 1.1 (c)) and secondly a purely **2D structure** (Scheme 1.1 (d)) can be obtained. Furthermore, the sheets of the 2D perovskite structure consisting of corner-sharing octahedra can be disconnected along the (010) set of planes to form a **1D perovskite structure** (formula A_3BX_5, shown in Scheme 1.1 (e)), consisting of cations combined with an anion comprised of corner-sharing octahedra.

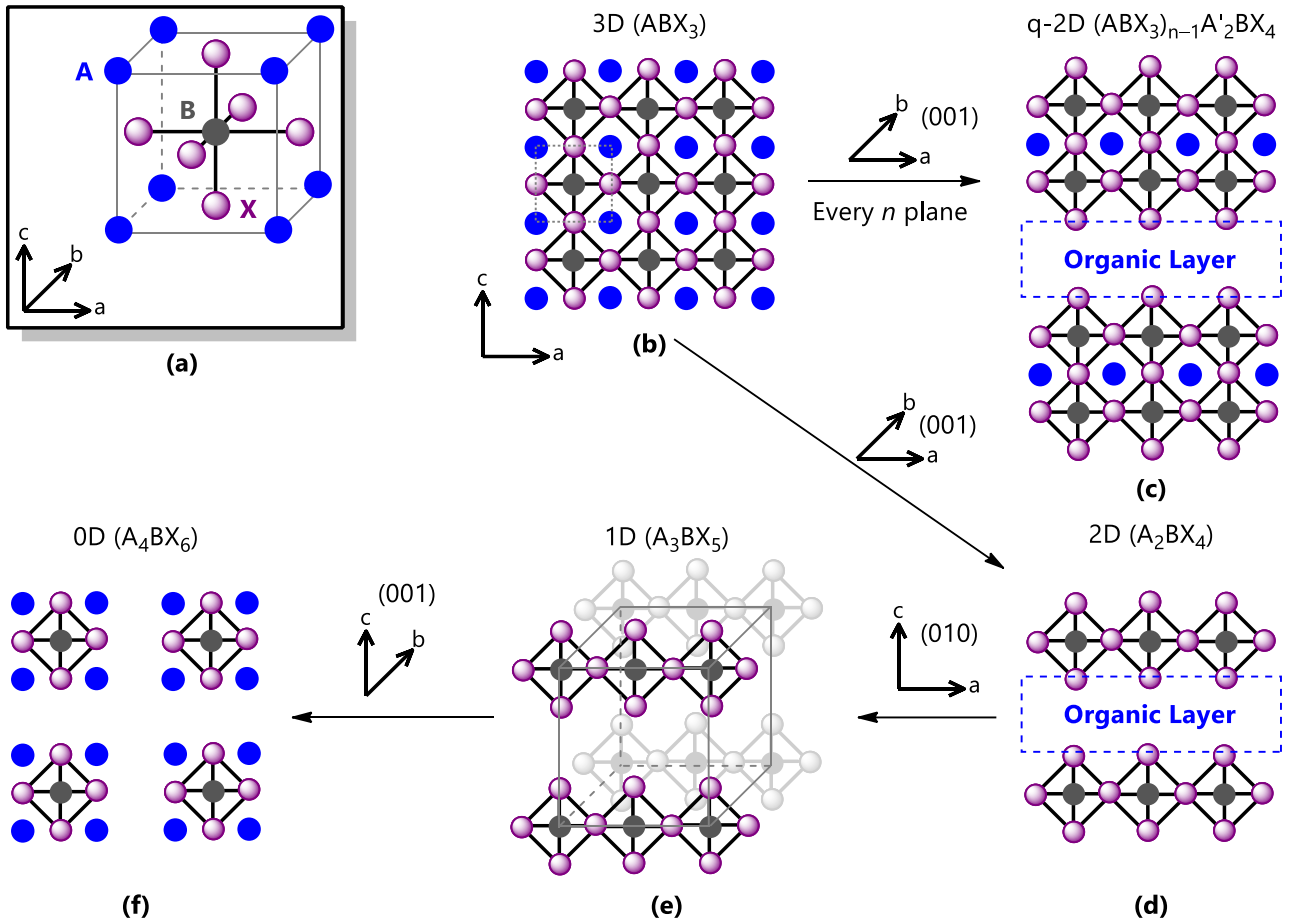

Scheme 1.1 A schematic representation of how the disconnection of BX_6 octahedra in the 3D perovskite structure, along specific crystallographic planes, forms lower-dimensional perovskite structures. **(a)** The unit cell of a 3D perovskite structure, **(b)** the structure of 3D perovskites projected in the (010) plane, characterised by corner-sharing octahedra when viewed down all three axes, **(c)** the 3D structure disconnected along every *n*-th plane of the (100) planes to form a quasi-2D perovskite structure; **(d)** the 3D structure disconnected along the (100) plane to form a single inorganic layer 2D perovskite, characterised by edge-sharing octahedra when viewed down two axes, **(e)** the single inorganic layer 2D perovskite structure sliced along the (010) plane to form a 1D perovskite, characterised by corner-sharing octahedra down one axis, **(f)** the 1D structure disconnected along the (001) set of planes to form a 0D perovskite, characterised by isolated octahedra. (Adapted from Makhsud I. Saidaminov *et al.*[12])

Finally, the **0D perovskite structure** can be derived from the 1D structure by disconnecting along the final plane of octahedral connectivity, the (001) set of planes, as indicated in Scheme 1.1 (f). In the 0D structure, the BX_6 octahedra are isolated or can form octahedral clusters. Furthermore, each of the different perovskite dimensionalities will be discussed in the sections to follow, however, only structures classified in the literature as perovskites are discussed here.

1.2.1 3D Perovskite Structures

The 3D cubic perovskite structure, as discussed previously, consists of corner-sharing BX_6 octahedra, forming a 3D *cage framework*. The A-cation sits in the voids of the framework, as shown in Figure 1.4 (a). This description of the octahedra remains valid for all other phases of the 3D dimensionality (orthorhombic, tetragonal, or monoclinic), except for the hexagonal phase, which will be discussed in the following section.

The ideal phase of the 3D perovskite structure is the cubic phase (see Figure 1.5 (a)), which crystallises in the space group $Pm\bar{3}m$.[13] This phase is seen as the "ideal" phase since the BX_6 octahedra are perfectly octahedral, meaning that X–B–

X bonds are 180° or 90°. However, the cubic phase is the *least common* structure encountered where 3D perovskite structures are concerned. Instead, more distorted versions, such as the orthorhombic, trigonal, rhombohedral, tetragonal and monoclinic phases of the structure, are typically encountered, exhibiting a range of different space groups.[13] Figure 1.5 (b) shows an example of a distorted 3D perovskite structure.

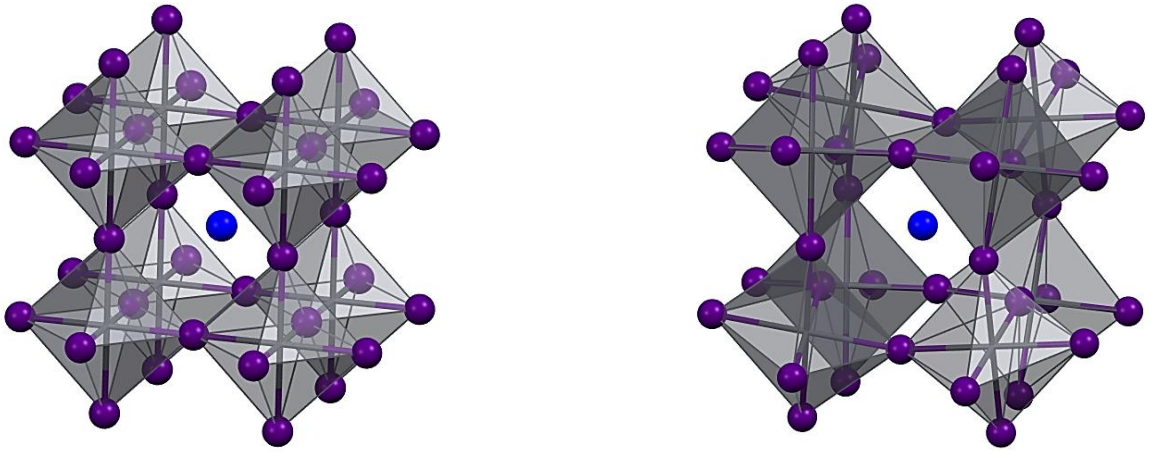

(a) **(b)**

Figure 1.5 (a) The ideal 3D cubic perovskite structure and **(b)** a distorted 3D perovskite structure. The BX_6 octahedra are shown as transparent black polyhedra where the black centra are the metal ions, and the violet spheres represent the X-anions. Additionally, the A-cation is shown as a blue sphere in the centre of the cavity of the inorganic BX cage.

3D Hexagonal Perovskite Structures

3D hexagonal perovskite structures of formula ABX_3 were first reported by Stoumpos *et al*. in 2017.[10] These structures exhibit corner- and face-sharing of octahedra, with different structures showing different corner- and face-sharing ratios of the octahedra. These structures can be considered a combination of the 3D corner-sharing cubic perovskite structure and the face-sharing 2H 1D hexagonal perovskite structure, which is discussed later. The 3D hexagonal perovskite structures cannot be obtained through dimensional reduction of the corner-sharing 3D cubic perovskite structure.

In these structures, different combinations of face-sharing and corner-sharing of octahedra is possible. The nomenclature employed to distinguish between the structures indicates the repeat number of face-sharing (h – for hexagonal) or corner-sharing (c – for cubic) octahedra along the ⟨001⟩ direction, as illustrated in Figure 1.4 (d).[10]

By definition, the 4H polytype exhibits the sequence hchchchc…, the 6H polytype has the sequence hcchcchcc…, while the 9R polytype displays the sequence hhchhchhc..., as illustrated in Figure 1.4 (d).[14] The anionic metal halide framework forms supercavities containing the cations, with the shape of the cavity depending on the structural polytype.[10]

Examples of structures from the literature for each hexagonal polytype, 4H, 6H and 9R, are shown in Figure 1.6, emphasising their characteristic face- and corner-sharing octahedra. Figure 1.6 (a) and (b) illustrate the SnI_6 octahedra of a 4H hexagonal polytype (CSD Refcode: JANPIA03,[10] $GUASnI_3$, with GUA^+ = guanidinium; space group $P6_3mc$).

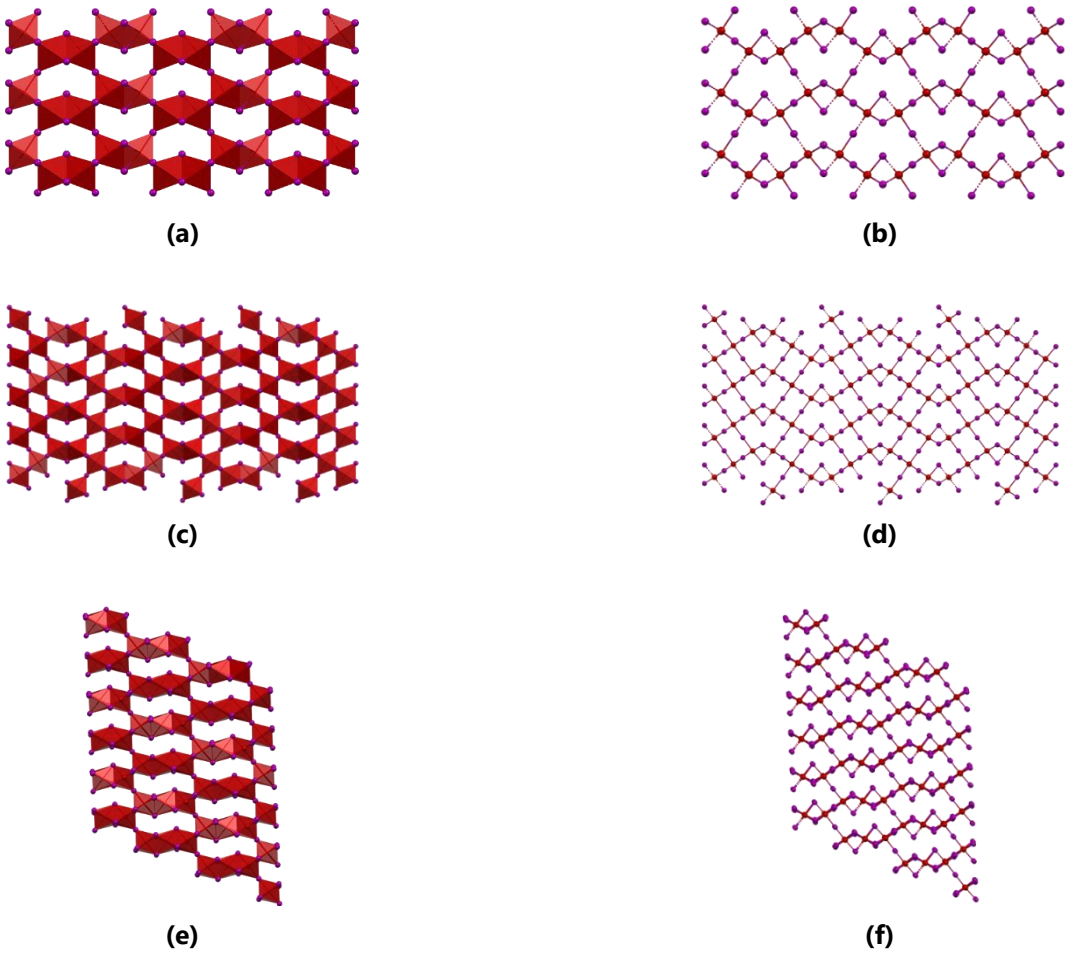

Figure 1.6 3×3 expansion of **(a)** polyhedral and **(b)** ball and stick structures of $GUASnI_3$ (4H polytype),[10] **(c)** polyhedral and **(d)** ball and stick structures of $EtASnI_3$ (6H polytype)[10] and **(e)** polyhedral and **(f)** ball and stick structures of $ImSnI_3$ (9R polytype)[10]. Only the inorganic substructure is shown.

In addition, Figure 1.6 (c) and (d) shows the SnI_6 octahedra of a 6H hexagonal polytype (CSD Refcode: JAMXIH01,[10] $EtASnI_3$, with EtA^+ = ethylammonium; space group $P6_3mc$), while Figure 1.6 (e) and (f) illustrates the SnI_6 octahedra of a 9R hexagonal polytype (CSD Refcode: JANRIC,[10] $IMSnI_3$, with IM^+ = imidazolium; space group Pc). It must be noted that the structure of $ImSnI_3$ crystallises in the monoclinic phase. That said, it is still referred to in the literature as a 3D hexagonal perovskite.[10]

1.2.2 2D Perovskite Structures

Two types of 2D perovskite structures are typically encountered,[15] with the first type obtained from cutting the 3D cubic perovskite structure along the ⟨100⟩ directions, as illustrated in Scheme 1.2 with this type containing BX_6 octahedra sharing corners in two-dimensions (see Scheme 1.2). The second type of 2D perovskite is obtained when cutting the 3D cubic perovskite structure along the ⟨110⟩ directions, as shown in Scheme 1.2. This second type involves edge-sharing BX_6 octahedra forming a two-dimensional anionic sheet, however other 2D types have also been reported in the literature.[15]

The thickness of the 2D layers may vary for both types of 2D perovskite structures, giving structures that are richer in metal halide content than the single inorganic layer structures.[15] In both types of 2D perovskite structures, the cations are sandwiched between the perovskite sheets. The two most common 2D perovskite structures are discussed in more detail below.

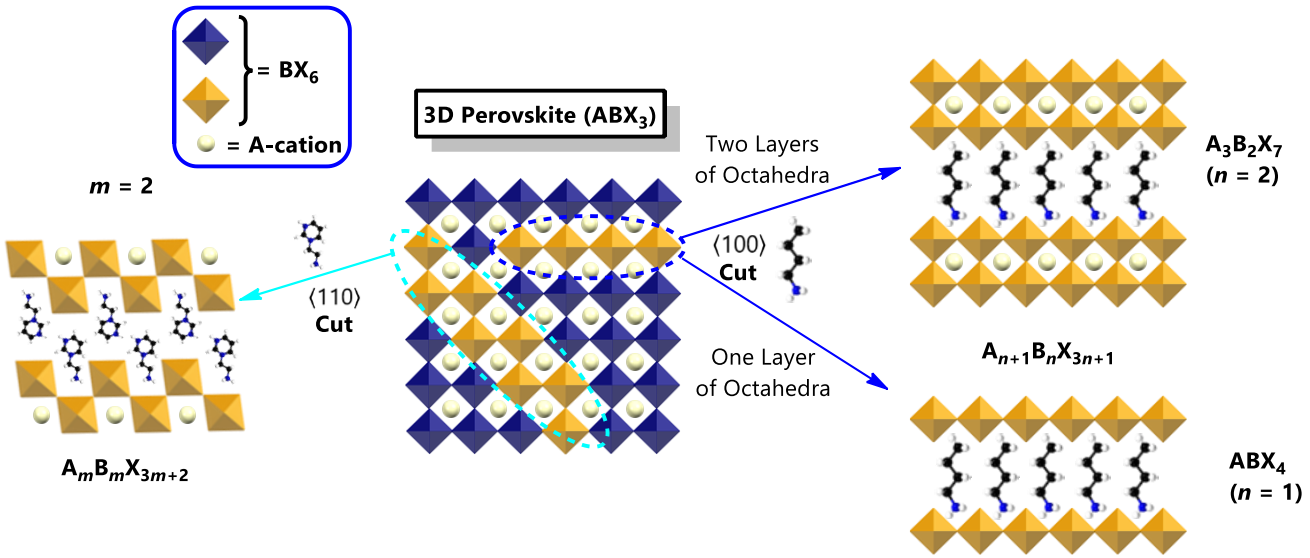

Scheme 1.2 Schematic illustration of how the $A_mB_mX_{3m+2}$ and $A_{n+1}B_nX_{3n+1}$ 2D perovskites can be formed from cutting the 3D parent perovskite along different crystallographic directions.

⟨100⟩ 2D Perovskites

The ⟨100⟩-type 2D perovskite is obtained by cutting layers of a 3D perovskite along any of the planes contained in the ⟨100⟩ set of directions. Thus, they are called ⟨100⟩ 2D perovskites in the literature.[10,12] These are the most commonly encountered 2D perovskites. By disconnecting the corner-sharing octahedra in the 3D structure at set intervals, along the {100} set of planes and at every *n*-th plane in the set, a quasi-2D structure is obtained when *n* is larger than 1, and a 2D perovskite with a single inorganic layer is obtained when *n* = 1. As *n* increases, the structure and stoichiometry approach the 3D perovskite structure. In the quasi-2D structure, which is essentially a combination of 2D and 3D perovskite structures, the thicker 3D perovskite portions are separated by an organic layer (layer of A-cations) to form a layered structure, similar to the single inorganic layer 2D perovskite structure shown in Scheme 1.1 (d). In the single organic layer 2D case, with *n* = 1, edge-sharing BX_6 octahedra are connected in sheets and alternate with A-cation sheets (referred to as the organic layer in Scheme 1.1) to form the 2D perovskite structure.

For example, the combination of $CuCl_2$ and methylammonium (MA^+) leads to a 2D perovskite of the ⟨100⟩ type (*n* = 1) in the monoclinic phase (at 100 K) with molecular formula MA_2CuCl_4 (CSD Refcode: ZZZPMY14[16], space group $P2_1/a$). The crystal structure of MA_2CuCl_4 is shown in Figure 1.7. The 2D structural motif is seen with the organic cations packing in a layer between the separated corner-sharing $CuCl_6$ octahedral sheets in Figure 1.7 (a), whereas the corner-sharing motif is seen in Figure 1.7 (b).

(a) **(b)**

Figure 1.7 The crystal structure of MA_2CuCl_4 (2D perovskite, *n* = 1) as viewed down **(a)** the *a*- and **(b)** the *c*-axis, respectively.

In addition, the ⟨100⟩ 2D perovskites may also form Ruddlesden–Popper (RP)-type, Dion–Jacobson (DJ)-type or Alternating Cation in the Interlayer space (ACI) perovskites.[17] The schematic structures of RP, DJ and ACI 2D perovskites are shown in Figure 1.8. RP perovskites contain two different types of cations, a smaller and a larger one. In this structure, portions of 3D perovskites containing the smaller cation are separated by layers of the larger cation, giving a 2D structure. DJ perovskites are similar to RP structures. However, where the metal ions of consecutive layers in RP structures are staggered, they are eclipsed in DJ perovskites, as shown schematically in Figure 1.8 (a) and (b). Finally, in 2D ACI perovskites, the organic layer contains alternating organic cations, illustrated in Figure 1.8 (c).

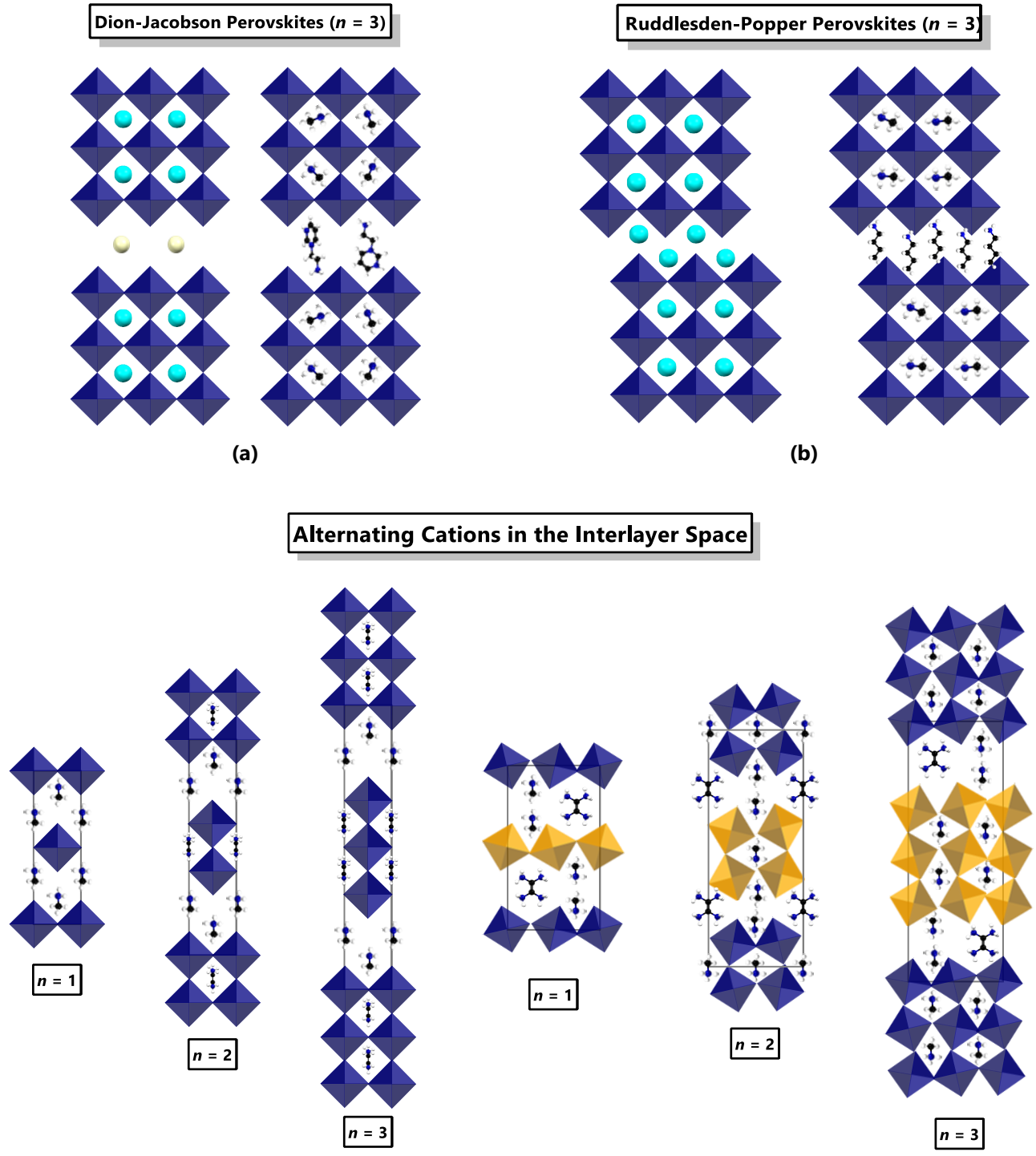

Figure 1.8 Schematic illustrations of ⟨100⟩ type 2D perovskites, specifically **(a)** the 2D Dion-Jacobson type perovskites, **(b)** the 2D Ruddlesden-Popper type perovskites and **(c)** the 2D Alternating Cation in the Interlayer Space type perovskites. Metal octahedra are shown in blue or yellow, while A-cations were chosen randomly as either organic or inorganic (coloured spheres).

Lead halide layered perovskites were first studied in the 1990s by Thorn and Ishihara.[18,19] The generic formula for ⟨100⟩ 2D perovskites are $A'_2A_{n-1}B_nX_{3n+1}$, or $A'A_{n-1}B_nX_{3n+1}$, where A′ has a charge of either +1 or +2 and A has a charge of +1, B is a divalent cation (for example Pb^{2+}, Sn^{2+} etc.) and X = Cl^-, Br^-, or I^-. Ruddlesden–Popper 2D perovskites have a structure as shown in Figure 1.9.[20]

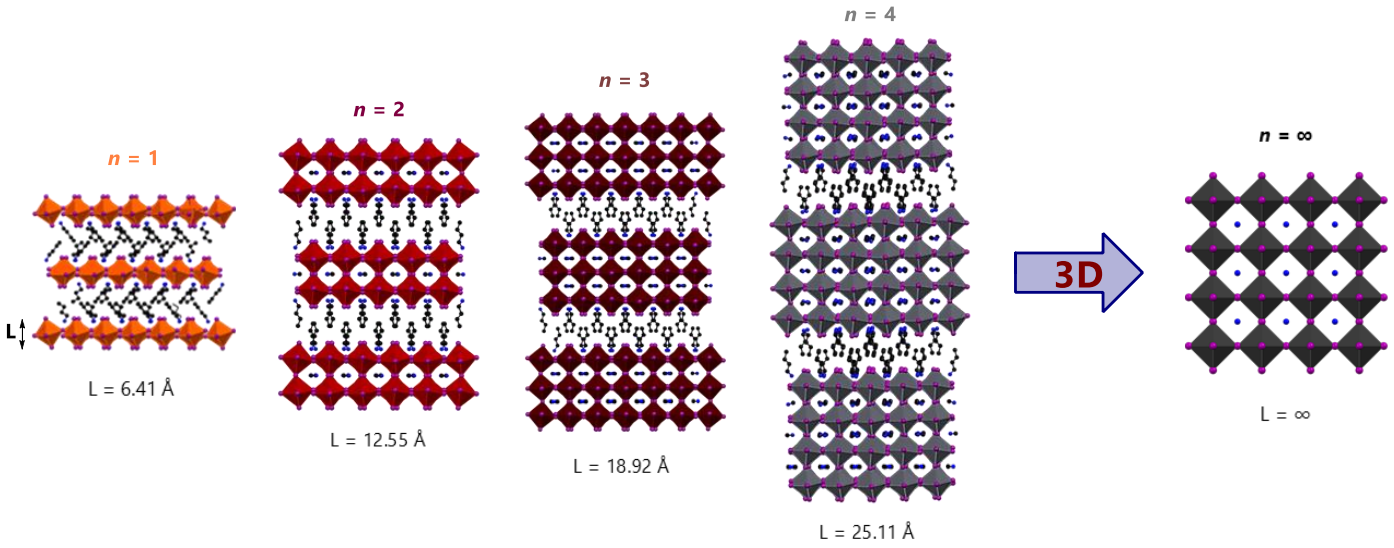

Figure 1.9 2D lead halide perovskite crystal structures of $(BA)_2(MA)_{n-1}Pb_nI_{3n+1}$, for n = 1 tending towards n = ∞ (lead octahedra coloured as per the colour of the actual crystals), adapted from Stoumpos *et al.*[20] BA^+ = *n*-Butylammonium and MA^+ = Methylammonium.

The RNH_3 group in RP perovskites is either an aromatic or primary aliphatic alkylammonium cation, which fulfils the role of a "spacer cation" between the perovskite layers, formed by the A-, B- and X-ions. The 2D network contains $[BX_6]^{4-}$ octahedra, connected in a corner-sharing fashion, separated by bilayers of the RNH_3^+-cations. Hydrophobic and Coulomb forces and hydrogen bonding are responsible for structural stability.[18,20]

⟨110⟩ 2D Perovskites

The second type of 2D perovskite is obtained by cutting the 3D perovskite along the ⟨110⟩ direction, giving the so-called ⟨110⟩ 2D perovskites, which are less common than the ⟨100⟩ 2D perovskites.[17] Additionally, for the ⟨110⟩ 2D perovskites, the general formula is $A'_{n+1}B_nX_{3n+3}$ (where n > 1), and B has a valence of +3, or a mixed-valence averaging +3, or is heterometallic (like for example, Cu^{2+} and Sb^{3+}).

These ⟨110⟩ 2D perovskites are often formed when the cation is too large to fit into the cavity of the 3D perovskite but still narrow enough so that the integrity of the 2D perovskite sheet can be maintained. An example of this type of 2D structure (Figure 1.10) is the structure that forms from the combination of the dication 2,2'-(ethylenedioxy)bis(ethylammonium) (abbreviated $EDEA^{2+}$, see Figure 1.10 (a)) and PbI_2 (CSD Refcode: BOQVUA[21]), which crystallises in the monoclinic phase (space group $P2_1/a$) at 100 K. This structure has the molecular formula $EDEAPbI_4$, and the ⟨110⟩ 2D perovskite crystal structure is shown in Figure 1.10 (b) and (c).

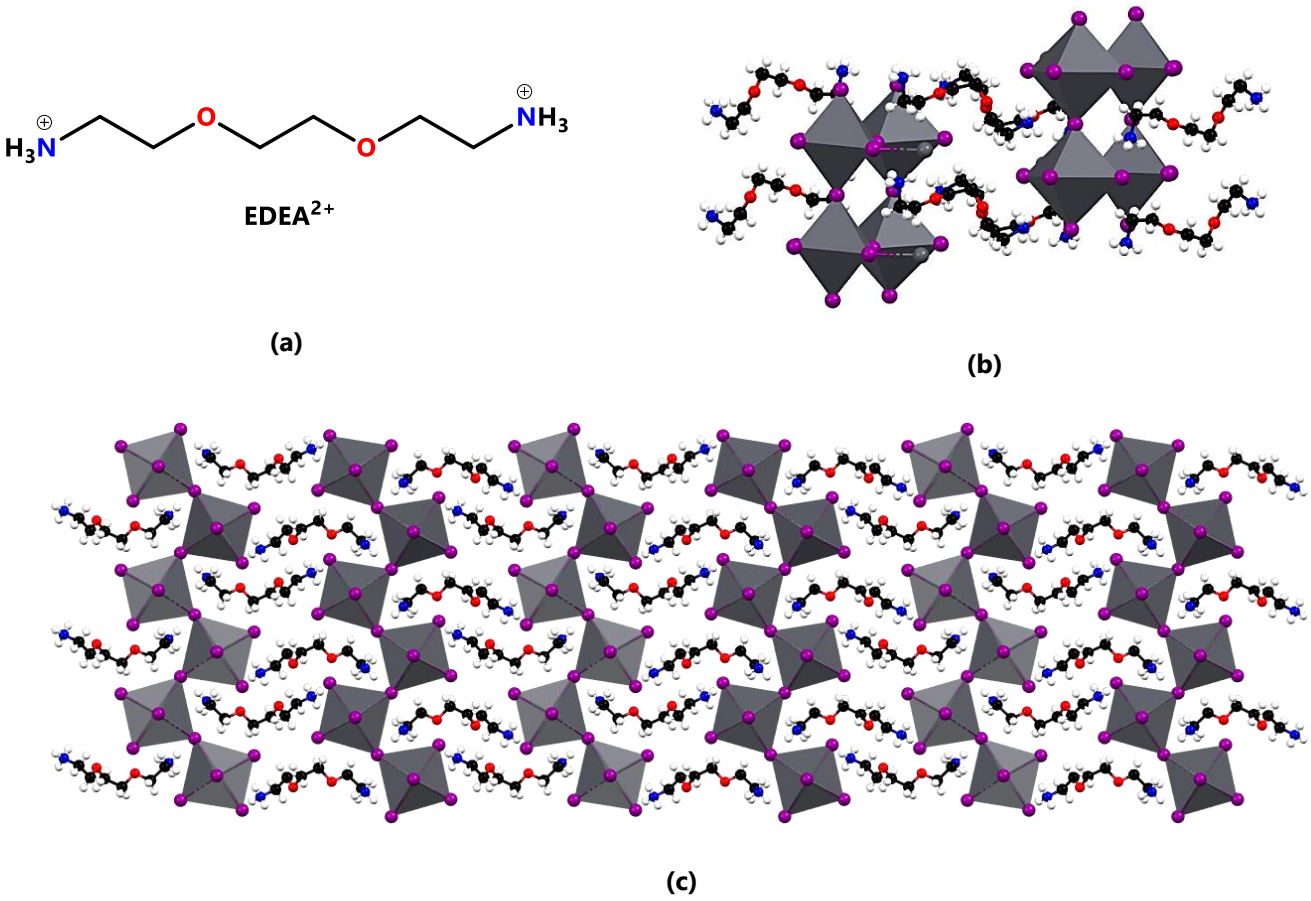

Figure 1.10 (a) The line drawing of 2,2'-(ethylenedioxy)bis(ethylammonium), **(b)** two connected octahedral portions of the structure $EDEAPbI_4$ and **(c)** the 3×3 packing of structure $EDEAPbI_4$ as viewed down the *a*-axis.

1.2.3 1D Perovskite Structures

1D perovskite structures contain 1D inorganic anions surrounded by cations. The inorganic anions consist of metal-halide octahedra, either face-sharing, corner-sharing, or edge-sharing. These anions can also consist of any combination of these modes of sharing. Examples of the three different types are shown in Figure 1.11. Figure 1.11 (a) shows an example of the face-sharing octahedra of the 1D ABX_3-type perovskite, while (b) and (c) illustrate the edge- and corner-sharing octahedra of the 1D ⟨011⟩- and the 1D ⟨100⟩-type perovskite structures, respectively.

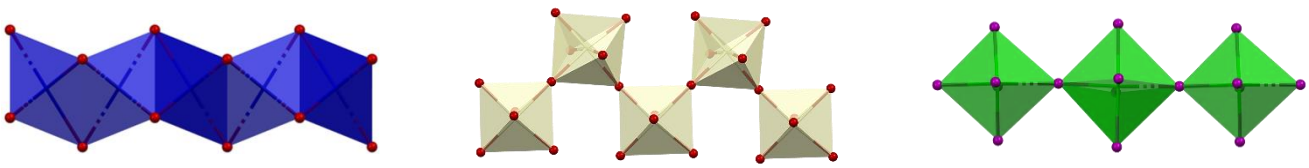

Figure 1.11 The inorganic portions of different types of 1D perovskite structures. **(a)** The ABX_3-type, **(b)** the ⟨011⟩-type and **(c)** the ⟨100⟩-type perovskite.

Both the 1D ⟨100⟩- and the 1D ⟨011⟩-type perovskite structures can be derived from the 3D parent structure. However, the 1D ABX_3-type cannot. These three types of 1D perovskites are discussed in the following sections.

1D ABX_3-Type Perovskite Structures

One specific 1D perovskite structure type relevant to this study is the **1D ABX_3-type perovskite structure** (shown in Figure 1.11 (a) and (b)), often referred to as 1D *hexagonal perovskite structures* in the literature.[9] However, this terminology can be confusing since the structure can crystallise in a crystal system different to that of hexagonal, which leads to unnecessary misperception.[22] Therefore, in this study, they will be referred to as **1D ABX_3-type perovskite structures**.

This structure has the same formula as the 3D perovskite, namely ABX_3, but cannot be obtained through dimensional reduction of the 3D perovskite structure. A 1D ABX_3-type perovskite structure may be formed when the A-cation is larger than what can be accommodated in the 3D framework created by B- and X-ions of the 3D cubic perovskite structure. These 1D ABX_3-type perovskites contain 1D halide-bridged polymers (linked inorganic polyhedra) that typically exhibit face-sharing octahedra or a mixture of face-sharing and corner-sharing octahedra (Figure 1.11 (a)). Isolated cations surround the 1D polymers in the structure.

Since different types of ABX_3-type perovskite structures may form, depending on the octahedral connection, a specific nomenclature has been developed to distinguish between the various structures. The structures are named using an alpha-numeric naming scheme, αH, where α is an integer number indicating the number of repeat units in the 1D inorganic chain. For example, the 4H-perovskite structure contains both face- and corner-sharing of octahedra, as illustrated in Figure 1.12 (a), with the number 4 indicating the number of repeat units in the 1D polymer. The halide-bridged polymer chain in the 2H-perovskite exhibits two repeating units in the polymer, as shown in Figure 1.12 (b), and so on.

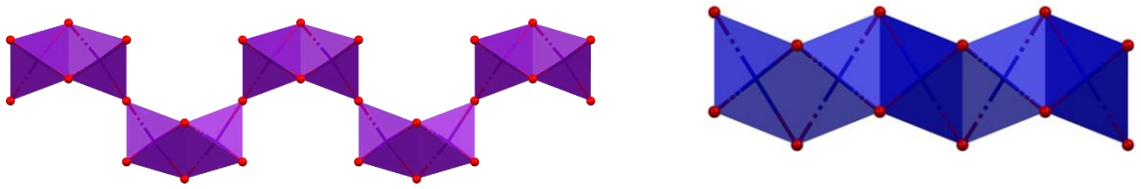

(a) **(b)**

Figure 1.12 1D inorganic chains of **(a)** a 4H-1D-ABX_3-type perovskite (corner- and face-sharing octahedra) and **(b)** a 2H-1D-ABX_3-type perovskite (only face-sharing octahedra).

1D ⟨100⟩-Type Perovskite Structures

The sheets of the 2D ⟨100⟩-type perovskite structure (derived from the 3D parent structure in Scheme 1.1) consisting of corner-sharing octahedra can be disconnected along the {100} set of planes, to form a **1D perovskite structure** (molecular formula A_3BX_5, shown in Scheme 1.1 (e) and Figure 1.11 (c)), consisting of cations combined with an anion comprised of corner-sharing octahedra.[12] This type of structure is referred to as a 1D ⟨100⟩-type perovskite structure.

1D ⟨011⟩-Type Perovskite Structures

Cutting of sheets of the 2D ⟨100⟩-type perovskite structure along the {011} set of planes yields the 1D ⟨011⟩-type perovskite structure, with the anion illustrated in Figure 1.11 (c).[12] In this structure, A-cations surround the 1D anions.

1.2.4 0D Perovskite Structures

Finally, in the 0D case, *non-connected* (isolated) BX_6 octahedra are arranged between the A-cations, as was shown in Scheme 1.1. As an example, the inorganic portion of the structure dabconium-$PbBr_6$ ($DPbBr_6$, CSD Refcode: AFEROV[23]), is shown

in Figure 1.13. This 0D perovskite structure is formed by the combination of isolated $PbBr_6$ octahedra and the dabconium-cation.

(a) **(b)**

Figure 1.13 (a) Isolated $PbBr_6$ octahedron and **(b)** the isolated $PbBr_6$ octahedra as viewed down the *c*-axis of the structure $DPbBr_6$. Cations are omitted for clarity.

Figure 1.13 (a) and (b) show the isolated octahedra of structure $DPbBr_6$, illustrating the trademark of what defines the 0D perovskite structure.[23] The 0D perovskite structure has been obtained in several phases, with the specific example shown in Figure 1.13, crystallising in the hexagonal crystal system.

1.2.5 Halide Double Perovskites

When considering the ABX_3 structure composition, if A is a monovalent cation (A^+), then B must be a divalent cation (M^{2+}) to maintain charge neutrality in the structure for a monovalent X-anion. However, two divalent B cations can be replaced with a combination of a monovalent and a trivalent cation to form the structure $A_2BB'X_6$ (where B = M^+ and B' = M^{3+}) or B could be a single tetravalent cation so that the formula becomes A_2BX_6 (B = M^{4+}) as shown in Figure 1.14. Both these variations are called **halide double perovskites** (when X is a halide), with the latter being called a *vacancy-ordered halide double perovskite*. The vacancy-ordered terminology stems from the fact that one tetravalent B-cation replaces two divalent B-cations, and hence there is a *vacancy* in the perovskite lattice.

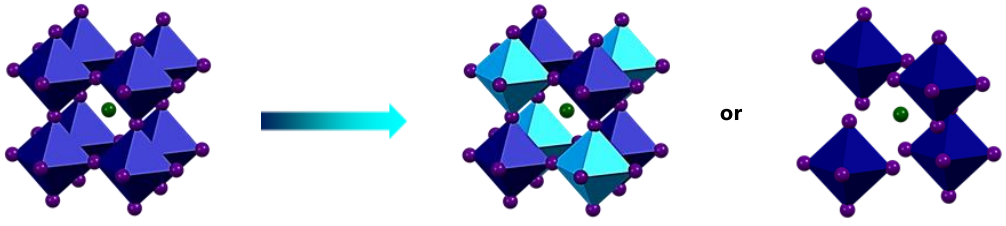

Figure 1.14 Structural comparison of the 3D ABX_3 perovskite, the 3D $A_2BB'X_6$ halide double perovskite and the A_2BX_6 vacancy-ordered halide double perovskite, illustrating the main structural features.

3D Halide Double Perovskites

The 3D perovskite structure (ABX_3) is synonymous with continuous corner-sharing BX_6 octahedra, while the A-cation occupies the centre position in the cavity created by the octahedra. The 3D halide double perovskite does not differ in this respect. Halide double perovskites reported to date generally crystallise in the cubic phase with space group $Fm\bar{3}m$.[24] A 50:50 mixture of alternating $(B^+)X_6$ and $(B^{3+})X_6$ octahedra (or $(B^{4+})X_6$ and vacancies) from the inorganic framework of the halide double perovskite structure.

Several elements have been suggested to *fit the bill* of requirements for halide double perovskite structures.[25] Double perovskites are also known as **elpasolites**, such as the mineral K_2NaAlF_6. Elpasolites have been extensively studied due to the rich chemistry surrounding their possible elemental combinations.[26] These combinations will be further considered in Chapter 2.

Lower Dimensional Halide Double Perovskites

When spacer cations are introduced into the 3D halide double perovskite structure, a 2D halide double perovskite is obtained, in the same vein as for the ABX_3 3D perovskite. The resultant 2D structure can be classified as either the Ruddlesden-Popper or Dion-Jacobson type 2D perovskite.[27] Figure 1.15 shows schematically how the 2D halide double perovskite structure is obtained from the 3D structure.

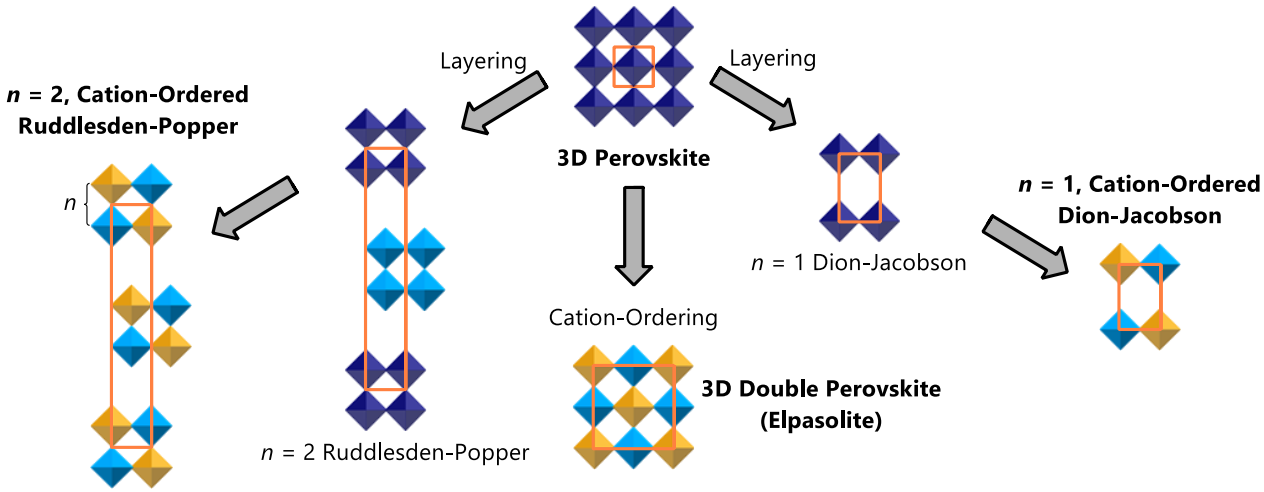

Figure 1.15 A schematic illustration of the systematic transformation of a 3D ABX_3 perovskite structure to the different 2D halide double perovskite structures by introducing spacer cations. Both the Ruddlesden-Popper and Dion-Jacobson types are illustrated. Copyright Journal of the American Chemical Society 2019. Adapted from Mao *et al.*[27]

A few 1D halide double perovskites have been reported in the literature. For example, a 1D chain, consisting of face-sharing octahedra, of the type $A_2BB'X_6$ is shown in Figure 1.16, and forms part of the structure obtained from the combination of MA-cations, KCl and $RuCl_3$ (CSD Refcode: BURMOT[28]). In this chain face-sharing octahedra of metal ions K^+ and Ru^{3+} alternate.

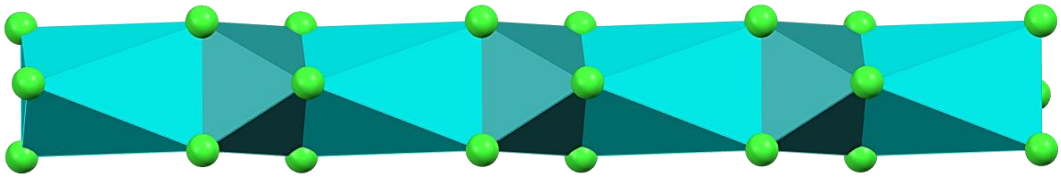

Figure 1.16 The face-sharing octahedra of a 1D halide double perovskite structure. The metal ions are K^+ and $Ru^{3+,}$ and the halide anion is Cl^-. The A-cation is the methylammonium cation.[28]

Technically, the halide vacancy ordered double perovskites is a 0D perovskite structure, and hence it could be argued that 3D, 2D, 1D, and 0D halide double perovskite have been reported in the literature.

1.2.6 Predicting the Dimensionality of Perovskites

For each of the three dimensionalities, specific *geometric limitations* play an essential role. For example, the A-cation *cannot* exceed the size of the void in the framework in the 3D cubic perovskite case. **Victor Goldschmidt** was the first to derive a quantitative relationship for the maximum radius of the A-cation (r_A) that can fit into the 3D perovskite framework, relative to the radii of the B-cation (r_B) and X-anion (r_X).[29] Goldschmidt assumed that each unit comprising the structure (A-, B- and X-cations) are hard spheres with specific radii. Using this information, it can be determined if a cation of a particular size can be expected to fit into the cavity of a 3D perovskite structure. The **Goldschmidt tolerance factor** (t) can be calculated as per Equation (1.1):

$$t = \frac{r_A + r_B}{\sqrt{2}\,(r_B + r_X)} \tag{1.1}$$

When the tolerance factor lies in the range $0.71 < t < 1.05$, a 3D (3D implies dimensionality) perovskite structure is expected. It should be noted that this is by no means an absolute rule. If the tolerance factor lies in the range $0.89 < t < 1$, the cubic 3D (also called the α-phase) phase is expected, whereas when $0.78 \leq t \leq 0.89$, the more distorted phases such as orthorhombic, rhombohedral or trigonal phases are expected.[30,31] Finally, when $0.71 < t \leq 0.78$ or $1.00 < t \leq 1.05$, then the tetragonal, hexagonal, or A_4BX_3-type perovskites are expected.[32]

However, *lower dimensionality* (2D, 1D or 0D) perovskites (or other) structures are expected to occur for values outside this range. The assumption that A, B and X are hard spheres proved to be, as expected in most cases, inaccurate, and another parameter was suggested for the prediction of dimensionalities. A second parameter was introduced to assist in predicting the formation of a 3D perovskite structure, called the **octahedral factor**, and assigned the symbol μ.[30] This factor uses the ratio of the B-cation radius to X-anion radius, as given in Equation (1.2), to infer the compatibility of the constituents of the 3D perovskite framework (hence if the B-cation prefers an octahedral arrangement with the suggested X-anion):

$$\mu = \frac{r_B}{r_X} \tag{1.2}$$

The 3D perovskite structure (octahedral coordination of B and X, to give BX_6 octahedra) is predicted to be stable in a range of $0.442 \leq \mu \leq 0.895$. Therefore, should a given combination of A, B and X comply with $0.78 < t < 1.05$ and $0.442 \leq \mu \leq 0.895$, then a 3D dimensionality is predicted.

The Tolerance Factor for Halide Double Perovskite

For a double perovskite of general formula $A_2BB'X_6$, the effective radius of the B-cation is taken as the average of the two B-cations, determined as follows

$$r_{B_{eff}} = \frac{r_B + r_{B'}}{2} \tag{1.3}$$

The Goldschmidt tolerance factor and the octahedral factor are then calculated in the same manner as for the ABX_3 combination, but with $r_{B_{eff}}$ as defined in Equation (1.3).

In addition to the tolerance factor (t), a so-called **fitness factor (Φ)** has been developed for halide double perovskites, and is given in Equation (1.4)[33]

$$\Phi = \sqrt{2}\frac{r_A}{r_{B_{eff}} + r_X} \tag{1.4}$$

When $\Phi > 1$, a 3D cubic phase is expected, while a tetragonal phase is expected when $0.93 < \Phi < 1$; $0.90 < \Phi < 0.93$ predicts an orthorhombic phase and finally when $\Phi < 0.90$ then a monoclinic phase is expected.[33]

Improvements to the Goldschmidt Tolerance Factor and Octahedral Factor

However, the Goldschmidt tolerance factor (t) only accurately distinguishes between combinations that lead to 3D perovskites and non-3D-perovskites 74% of the time and this level of accuracy is often insufficient.[13] Hence, Bartel *et al*. proposed a new tolerance factor (given the symbol τ, see Equation (1.5)), which has been shown to correctly predict 92% of 576 materials of the halide and oxide perovskite-type.[34] In addition, it has predicted the existence of 23 314 stable double perovskites and 1034 experimentally verified perovskite materials. Equation (1.5) gives the tolerance factor as derived by Bartel *et al.*,

$$\tau = \frac{r_X}{r_B} - n_A\left[n_A - \frac{\left(\frac{r_A}{r_B}\right)}{\ln\left(\frac{r_A}{r_B}\right)}\right] \tag{1.5}$$

where n_A is the oxidation state of the A-site organic cation, and r_i is the radius of the ion i. By definition $r_A > r_B$, so when $\tau < 4.18$, a 3D perovskite structure is predicted. This tolerance factor (Bartel's Tolerance Factor) will be used with the Goldschmidt Tolerance Factor and Octahedral factor to predict structural dimensionalities in this study. In later Chapters, the predictive success of each of the factors will also be evaluated.

1.2.7 The Hybrid Halide Perovskite Structure

When the constituents of the perovskite structure are an organic cation (A-cation), a metal ion (B-cation) and a halide anion (X-anion), the resultant perovskite structure is known as an organic-inorganic hybrid metal halide perovskite structure (hybrid halide perovskite). Figure 1.17 shows the difference in structure between a typical 3D inorganic perovskite structure (halide, oxide or other) and a 3D hybrid halide (or oxide) perovskite structure. The first organic-inorganic perovskite material reported was synthesised by Weber and was the methylammonium lead and tin halide compounds ($MAPbX_3$, $MASnX_3$, $MAPbI_xBr_{3-x}$, $MAPbBr_xCl_{3-x}$ and $MASnBr_xI_{3-x}$ $(0 \leq x \leq 3)$).[35,36] These compounds form the 3D cubic perovskite structure. Furthermore, organic-inorganic halide perovskites, especially those exhibiting the 3D cubic perovskite structure, are relevant for their application in solar cell technology, most notably the methylammonium lead iodide structure; more on this will follow later.

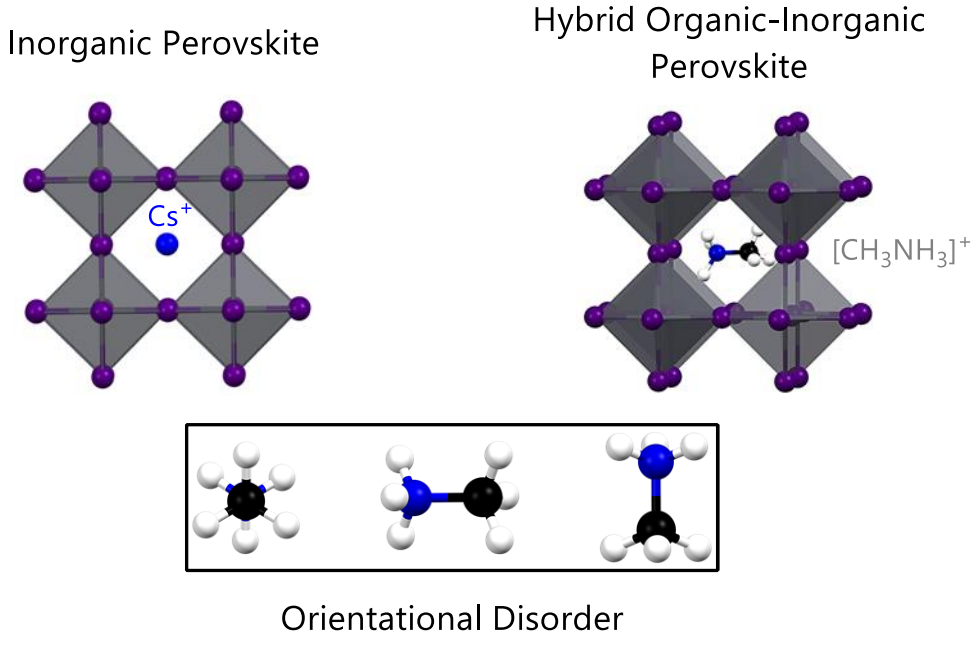

Figure 1.17 Comparison of a purely inorganic perovskite structure with a hybrid perovskite structure. Additionally, a few of the possible orientations of the organic cation (methylammonium cation) in the hybrid structure are shown explicitly to emphasise a further difference between the two structure types (adapted from Chen *et al.*[37]).

When using an organic cation as the A-cation, a new world of possibilities is opened in terms of structural design. The most notable change in going from an inorganic to organic A-cation is the added stability provided by *hydrogen bonding* from the organic cation to the metal-halide framework.[13] Fine-tuning of the compatibility between the A-cation and the BX-framework is typically achieved by carefully considering the cation's size and hydrogen bonding capability. Furthermore, the packing of the cation, in different orientations in the crystal structure (for example packing in a helix), may allow for *chirality* in the structure, which, of course, brings with it a whole host of new properties.[38,39] Even more exciting is that millions of organic molecules can be tested in the hybrid structure. Hence, the enormous scope of this type of structure still open for discovery.

1.2.8 Octahedral Tilt in 3D Perovskites: Glazer Notation

Consider the general 3D cubic perovskite structure with corner-sharing octahedra. To accommodate different sized A-cations, the BX_6 octahedra may be perpendicular relative to each other or may *tilt* or *rotate* cooperatively to change the size of the cavity in the inorganic framework site, which the A-cation occupies. Viewing the structure from a close packing point of view, the A-site coordination number can be reduced from 12 for the perfect 3D cubic perovskite structure to 10, 8 or 6, for the more distorted structures.[7] This allows for an A-cation, which is at first glance too small to fill the vacancy, to still do so, however, at the *cost of distorting the BX-framework*.

Since the octahedra are connected directly, changes in one dimension will result in changes in the other. Therefore, the tilting or rotation of the octahedra along one axis will affect the octahedra along the other axes. Glazer and Alexandrov determined that theoretically, there are 15 *unique* tilt systems possible in a 3D cubic perovskite structure.[40,41] The **Glazer notation** was developed to describe the relative tilts of the octahedra of 3D cubic perovskite structures.[40,41] The notation is summarised below.

1. Consider an ideal 3D cubic perovskite structure. The possible rotation (tilt) of octahedra along the crystallographic axes are labelled *a*, *b*, and *c*. If the degree of rotation about each axis is equal, the notation reads *aaa*. However, should the rotation along one axis differ from the other two, the notation changes to *aac*, and for all three axes having a different degree of rotation, it reads *abc*.

2. Next, the direction of rotation is indicated using a superscript +, – or 0. When there is no rotation along a specific axis, the symbol "0" is used. When the rotation in adjacent planes of octahedra are in-phase (all clockwise or counter-clockwise), the symbol "+" is used, and when they are out-of-phase (alternating between clockwise and counter-clockwise), the symbol "–"is used.

As an illustration of the Glazer Notation, consider the octahedra shown in Figure 1.18. In Figure 1.18, the perfect octahedral arrangement is shown, and then two different tilts (+ and –) along the *c*-direction of the lattice. This example illustrates that the tilting of one octahedron will have repercussions on the tilt of any octahedra connected to it, hence tilting is a *cooperative* movement.

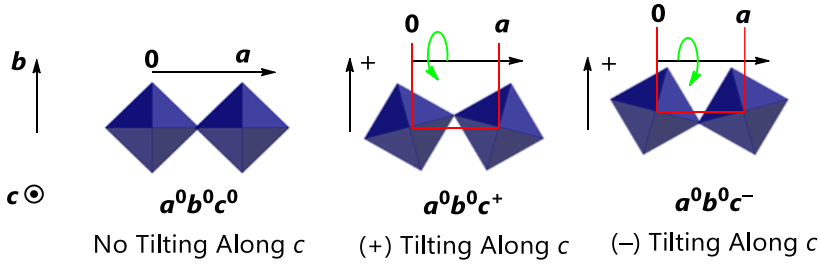

Figure 1.18 Schematic illustration of two tilting modes (+ and –) for a linear chain of octahedra along the *c*-direction. Adapted from Crystal Chemistry by Férey.[42]

Extending the example to three dimensions, as shown in Figure 1.19, the periodicity of the tilting is seen. In addition, the unit cell parameters of a perfectly cubic arrangement (Figure 1.19 (a), and unit cell parameter a_p) are increased when the octahedra are tilted.

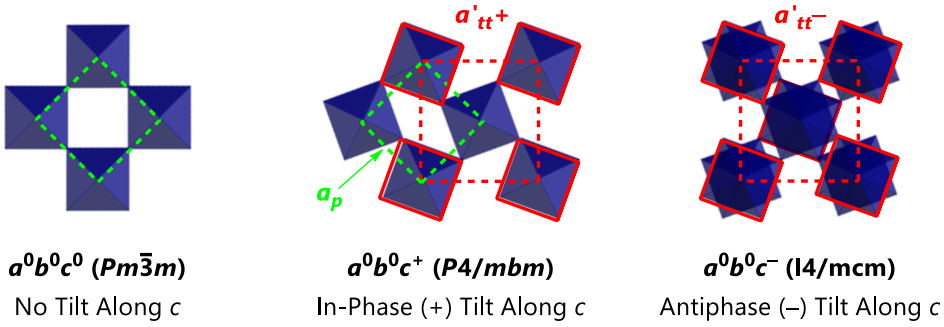

Figure 1.19 (a) The ideal perovskite structure, **(b)** in-phase octahedral chain tilting along the *c*-direction and **(c)** out-of-phase octahedral chain tilting along the *c*-direction. The symbol a_p indicates the cell parameter for the ideal perovskite and $a'_{tt}+$ and $a'_{tt}-$ the expanded cell parameters caused by the tilting of the octahedra. Adapted from Crystal Chemistry by Férey.[42]

When the octahedra of the 3D cubic perovskite are tilted in-phase along the *c*-direction (i.e., + as shown in Figure 1.19 (b)), all the octahedra in the *c*-direction have the same orientation. However, if the octahedra are tilted in an out-of-phase manner (i.e., – as shown in Figure 1.19 (c)), alternating layers of octahedra are rotated in the opposite direction along the *c*-axis. Thus, when either in-phase or out-of-phase rotation occurs, the unit cell is larger than that of the perfect cubic arrangement, due to the rotation of the octahedra. Furthermore, this tilting has the crystallographic consequence of an alteration of the X–B–X angles. These alterations result in changes in the material's physical properties, including magnetic, optic, and electric properties

1.3 Synthesis of Perovskites

In addition to traditional crystallisation methods (slow evaporation), several other synthetic methods have been developed for the preparation of hybrid halide perovskite materials over the past 12 years. These utilise the thermodynamic stability, temperature-dependent solubility, and self-assembly nature of perovskites to their advantage. This section provides an overview of these methods. Here X is always Cl^-, Br^- or I^-, B is a divalent metal cation, and A is a monovalent organic cation. Of course, the charges of A and B may vary in the synthesis of other perovskite materials, which alters the precursor constitution accordingly.

1.3.1 Slow Evaporation

The process of slow evaporation is the most straightforward technique of crystal growth since it only involves the precursors to the perovskite crystal and a solvent. The BX_2 (metal salt) and AX (organic salt) precursors are dissolved in the same or different solvent(s) and then mixed, whereafter, the mixture is left to crystallise through the slow evaporation of the solvent, as shown in Figure 1.20. The formation of the perovskite occurs *via* self-assembly.

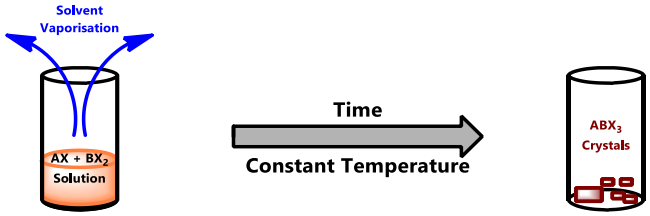

Figure 1.20 A schematic illustration of the slow evaporation method for perovskite single-crystal growth. Blue arrows indicate the evaporation of the solvent.

Alternatively, the evaporation of the solvent can be done at an elevated temperature. However, this may be detrimental to the growth of single crystals and could lead to microcrystalline material formation rather than single crystals. Also, the formation of AX (thus the halide salt A^+X^-) may be done *in situ* if the solvent used allows for the protonation of the organic molecule, like, for example, water.

1.3.2 Inverse Temperature Crystallisation

The process of inverse temperature crystallisation (ITC) was pioneered by Saidaminov *et al*. in 2015.[43] ITC is a commonly used technique for the synthesis of hybrid perovskite materials. The method is popular since it only requires a couple of hours and leads to large single crystals in bulk, as illustrated in Figure 1.21 (a) and (b).

The ITC method starts with an equimolar ratio of precursors (AX and BX_2) dissolved in a solvent. The solvent of choice depends on what the target hybrid perovskite is since the perovskite should be insoluble in the solvent. So, as an example, dimethylformamide (DMF) is used to crystallise $MAPbBr_3$ and γ-butyrolactone (GBL) for $MAPbI_3$.[44] Other restrictions on the solvent used is that it should have a Gutman's Donor Number less than 18 kcal·mol^{-1} and a dielectric constant of below 30. However, there are exceptions to these two restrictions.[45] Different solvents will aid in the acceleration or deceleration of crystallisation times, although, in turn, might have detrimental effects on the crystal quality.

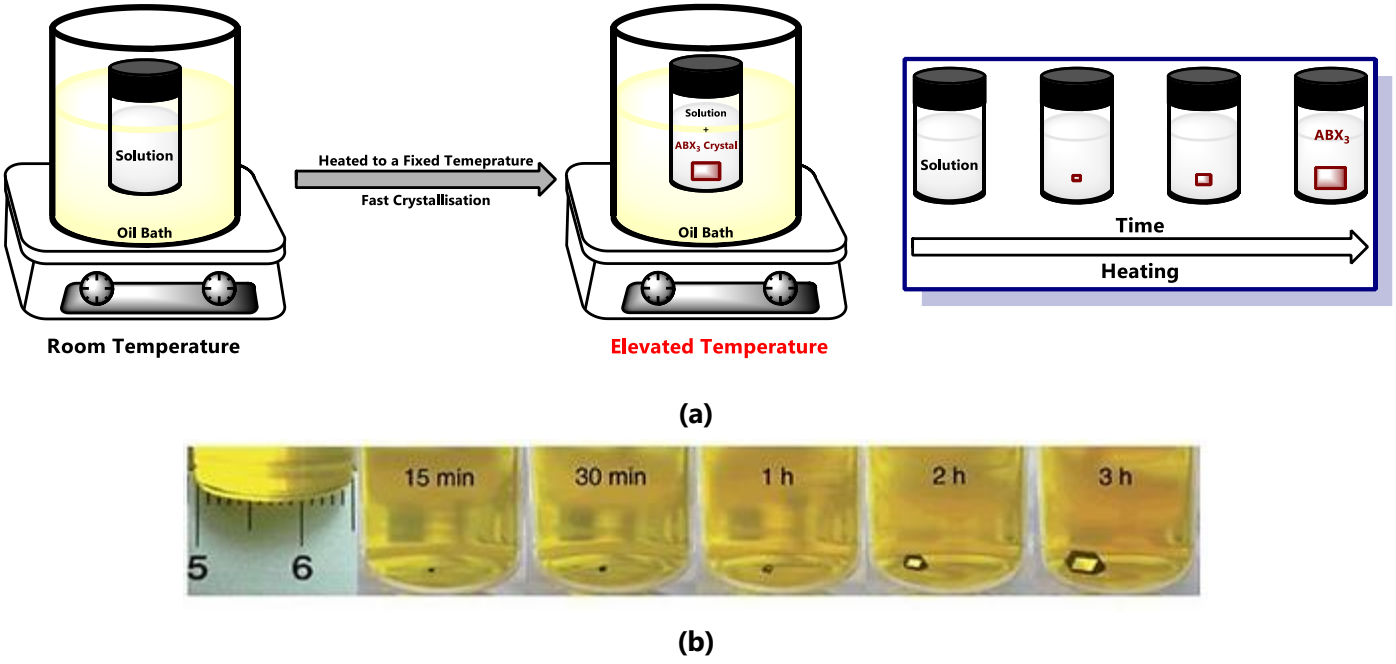

Figure 1.21 (a) A schematic illustration of the ITC method, forming a perovskite single-crystal (adapted from Saidaminov *et al*.) and **(b)** a time-lapse of the ITC method producing a $MAPbI_3$ single-crystal. (b) reproduced with permission.[43] Copyright 2015 Springer Nature.

Additionally, to aid in the dissolving of the solids, rigorous stirring of the mixture of precursors in the solvent takes place for 2 to 3 hours, and subsequent filtration is done to remove any impurities before the ITC process is initiated. The vial with precursor solution is sealed and is usually heated to between 80 °C and 100 °C, where a higher temperature allows for faster crystal growth, however, typically inferior crystal quality. The perovskite material is insoluble in the chosen solvent, hence by heating the solution energy for the nucleation reaction is provided and so the perovskite material is formed.[46]

The ITC method is useful because it provides a way to obtain good quality single crystals in bulk in a relatively short amount of time. Moreover, the process allows for control of the shape of crystals while improving material properties such as carrier lifetimes, carrier mobilities, diffusion lengths and low-trap density, which are all properties relevant to the use of these materials in optoelectronics.[43]

Modified Inversion Temperature Crystallisation Method

With the modified ITC method, even larger single crystals can be obtained. Proposed by Liu *et al.*, this method still starts with dissolving AX and BX_2 in an appropriate solvent and heating the sealed vial as per the traditional ITC method.[47,48] Then, after several hours, when seed crystals are formed, the seed crystal of the highest quality is removed from this vial and placed into a newly prepared vial with the same precursor solution, as schematically illustrated in Figure 1.22. After that, the ITC method is followed again, and once this crystal has grown, the process is repeated, ultimately leading to exceedingly large single-crystal perovskites.

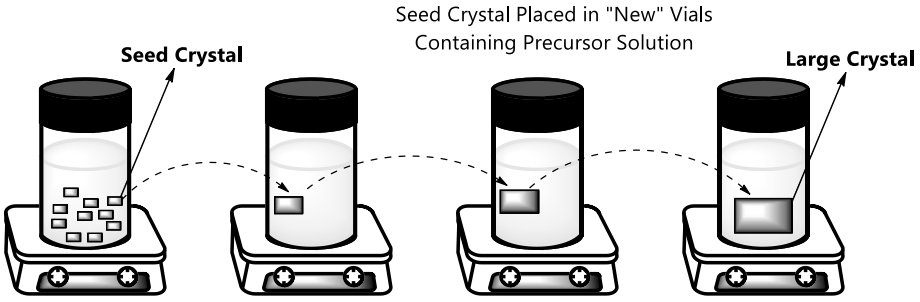

Figure 1.22 Schematic diagram of the modified ITC method, where a seed crystal is moved to a fresh vial after its formation and subsequently removed again as it grows. Adapted from Liu *et al.*[47]

With the modified ITC method, Liu *et al.* obtained crystals with lower trap densities, higher carrier concentrations, and comparatively large carrier mobilities than those obtained using the traditional ITC method.[48]

1.3.3 Anti-Solvent Vapour-Assisted Method

Using ideas from the preparation of thin-film hybrid perovskite films as inspiration (this will be covered later), Bark *et al.* proposed the anti-solvent vapour-assisted method to grow large single crystals of perovskites.[49,50] The technique uses two solvents (one volatile and the other less so), as shown in Figure 1.23. The perovskite precursors (equimolar ratio of AX and BX_2) are dissolved in the less volatile solvent and placed in an open vial (called the solvent solution). This open vial is then placed in a larger, sealed vial that contains the anti-solvent (the more volatile solvent), with enough anti-solvent to reach halfway up around the solvent solution vial. The system is then left so that the more volatile solvent can diffuse into the precursor solution over time, forcing crystallisation at the bottom of the open vial. This happens because the perovskite material is insoluble (anti-soluble, hence anti-solvent) in the more volatile solvent, and with an increase of the amount of the anti-solvent in the precursor solution forcing it to precipitate out of the precursor solution.[49,50]

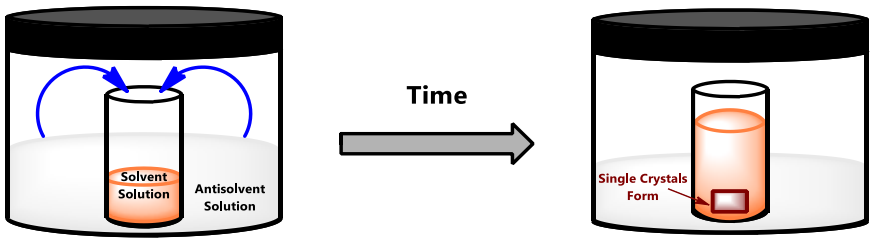

Figure 1.23 Schematic representation of the anti-solvent diffusion method. Blue arrows represent the diffusion of the anti-solvent into the solvent solution. Typically, after a few days, single crystals form at the bottom of the smaller vial.

For example, when growing $MAPbI_3$ and $MAPbBr_3$ single crystals, GBL and DMF are used as solvents and dichloromethane (DCM) as the anti-solvent. This method leads to crystals with minimal gap defects, a lower trap density, larger carrier mobility and a longer charge carrier lifetime.[50]

1.3.4 Top-Seeded Solution Crystal Growth Method

In 2015, Huang and co-workers developed the top-seeded solution crystal growth method for the preparation of crystals of $MAPbI_3$. The technique involves fixing a single $MAPbI_3$ seed crystal at the end of a substrate (usually silicon) at the top of a vial on a hot plate, as shown in Figure 1.24.[48,51] Smaller $MAPbI_3$ seed crystals are then placed at the bottom of the vial (closest to the hot plate), where they dissipate. The temperature is maintained at 75 °C with the help of an oil bath.

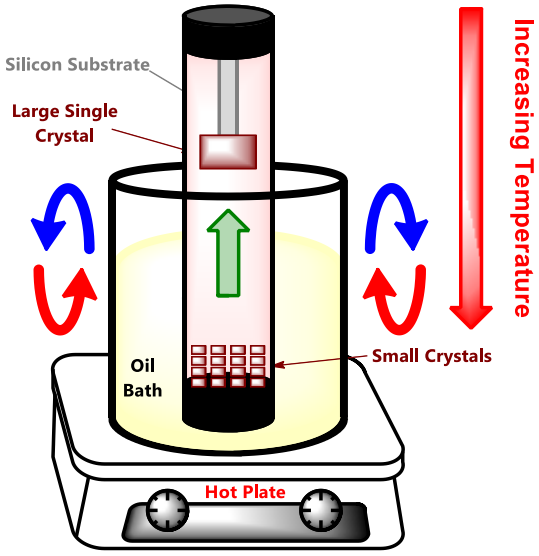

Figure 1.24 A schematic diagram of the top-seeded solution crystal growth method. A light red fade represents the solution; the blue and red arrows indicate the convection of heat, and the green arrow indicates the main flow direction of the A-, B- and X-cations. Supersaturation occurs at the top crystal growth site, allowing for a sizeable single-crystal perovskite formation. Hence, the oil bath is used to regulate the temperature to prevent temperature fluctuations around the tiny crystals. Small crystals may also form at the bottom. Adapted from Maggiora *et al.*[44]

Due to the temperature difference in the vial (top versus bottom temperatures), with the lower temperature at the top where the single-crystal $MAPbI_3$ is located, supersaturation occurs at the top, which forces $MAPbI_3$ out of solution and results in growth of the single-crystal at the top.[52] The temperature and concentration gradient ensure convection of the $MAPbI_3$ in solution and lead to the growth of single crystals at the centimetre scale without compromising carrier lifetime, carrier mobility, trap density, and crystallinity.[49,53]

This top-seeded solution method has since been extended to synthesise a wide range of hybrid perovskites, including $MAPbBr_3$, $MAPbCl_3$, $MASnI_3$, and $FASnI_3$, with FA^+ = formamidinium. However, the procedure is not suitable for materials with low solubility.[47,52]

1.3.5 Bottom Seeded Solution Crystal Growth Method

Poglitsch and Weber pioneered the bottom seeded solution crystal growth method before Lian *et al*. successfully obtained bulk single crystals of $MAPbI_3$ using it in 2015.[47,54,55] The method uses a seed crystal of $MAPbI_3$ in a precursor solution of methylamine and lead (II) acetate trihydrate dissolved in hydroiodic acid (see Figure 1.25). The seed crystal is hung from a platinum wire, and over about 15 days, the temperature is lowered from 100 °C to 57 °C at a rate of 5 °C·h^{-1} to produce a large single-crystal of $MAPbI_3$.[47,52,54]

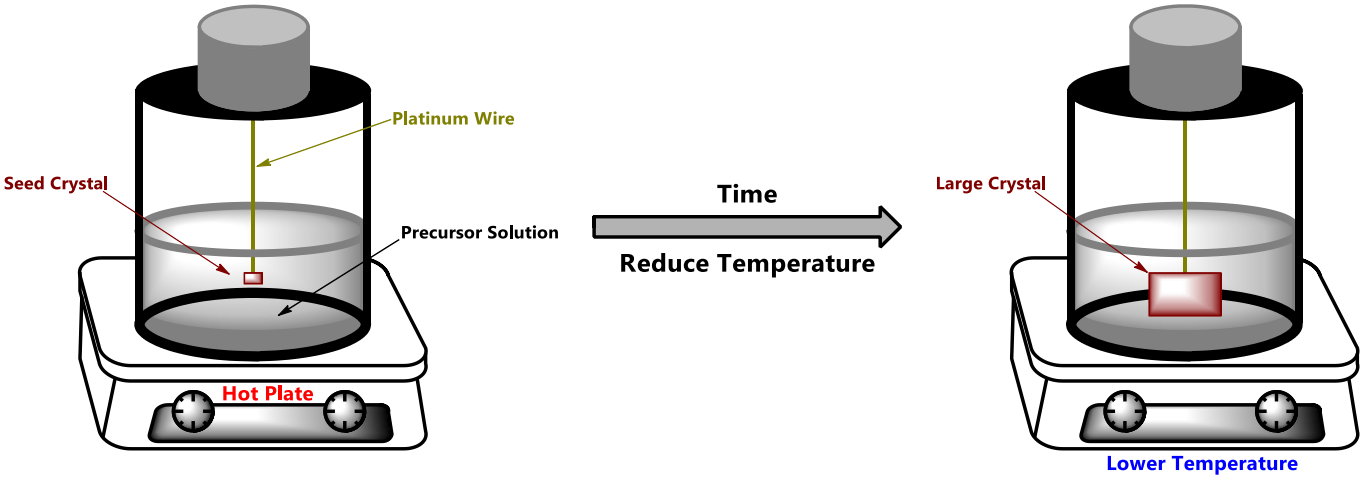

Figure 1.25 A schematic illustration of the bottom seeded solution crystal growth method utilising a $MAPbI_3$ seed crystal. Adapted from Babu *et al.*[47]

The single crystals obtained using this technique are of high quality and their quality can be further improved by adjusting the temperature reduction rate. By slowing the rate, even better-quality crystals can be obtained.

1.3.6 Temperature Lowering Method

Another method used in the synthesis of hybrid halide single crystals is a temperature lowering method proposed by Dang *et al*.[56] They synthesised high-quality $MAPbI_3$ single crystals starting with a solution obtained from the dissolution of $Pb(CH_3COO)_2{\cdot}3H_2O$ and CH_3NH_3I in a hydrogen iodide solution, stirred at a constant temperature of 65 °C. Thereafter, the temperature of the solution was abruptly lowered to 40 °C, and the stirring is halted to allow for saturation of the precursor solution. After a few days, crystals of $MAPbI_3$ were obtained. However, this technique has been primarily surpassed by the ITC method.

1.3.7 Slow Cooling

The slow cooling method utilises the increasing solubility of precipitates in solvents at higher temperatures compared to room temperature and was first employed by Lemmerer.[57] The experimental setup of the slow cooling method is shown schematically in Figure 1.26 (a) and a schematic illustration of the technique in Figure 1.26 (b).

In the slow cooling method, stoichiometric amounts of the organic species and metal halide components are mixed with excess concentrated acid in a vial. However, the amount of solid reagents added is such that the solution is saturated at room temperature. The vial is sealed with a lid and placed in an oil bath and heated to between 80 °C and 100 °C. The vial must be only immersed in oil up to the level of the solution in the vial to allow the vapour in the top part of the vial to condense. Furthermore, the excess powder reagent should be fully dissolved at the elevated temperature. The hot plate is then switched off, and the whole system is left to cool back down to room temperature, as illustrated in Figure 1.26 (a), with crystals forming on cooling due to the saturation of the solution.

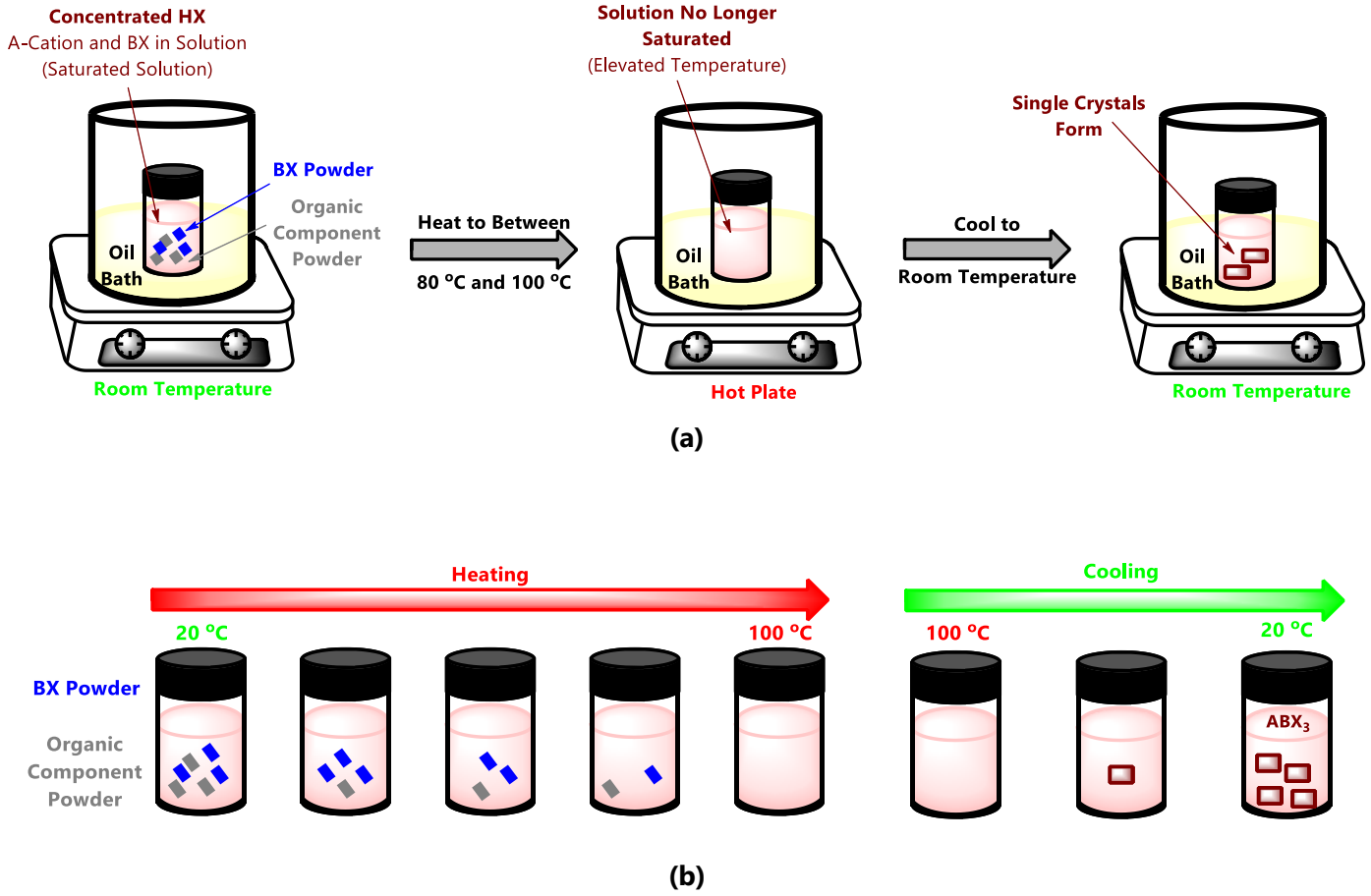

Figure 1.26 The slow cooling method. **(a)** A schematic representation of the dissolution of the reagents in the heating step of the slow cooling method and **(b)** a pictorial illustration of crystal formation in the slow cooling method during the cooling step.

The difference in solubility at higher and room temperatures provides excellent conditions for crystal growth, as schematically shown in Figure 1.26 (b).

1.4 Perovskite Solar Cells (PSCs)

Significant focus has been placed on renewable sources of energy, of which solar cell technology is at the forefront.[58] Recently, in as little as 15 years (between 2005 and 2021), an increasing interest in **hybrid perovskite solar cells** (HPSCs, which falls under the broad term PSCs) has developed. This interest was sparked by the remarkable climb in PSCs efficiency compared to alternative solar cell technology, from initially 3% to specific tandem devices (perovskite-silicon devices), achieving nearly 30% efficiency.[58]

PSCs fall into the category of *thin-film optoelectronic devices*, where a thin-film of perovskite material is used as an absorbing layer (sensitiser) in the solar cell device architecture. Therefore, the perovskite sensitiser needs to be fine-tuned to harvest the

solar spectrum optimally. Furthermore, an electron transport layer (ETL or ETM – electron transport material), a hole transport layer (HTL or HTM – hole transport material) and circuit contacts are required to complete the device.[59] Numerous studies have been carried out on the different layers and how each layer can be optimised.[60]

1.4.1 A Brief History of HPSCs

The first instance where a perovskite structure was mentioned in the context of a solar cell device dates back to work done by Miyasaka and Teshima in 2005, and they continued to focus on this topic until 2009.[59,61,62] The first use of a perovskite material in solar cells involved methylammonium lead iodide ($MAPbI_3$) as a nanocrystalline perovskite absorbing layer, and the device itself was based upon the architecture of a dye sensitised solar cell (DSSC or DSSCs for plural).[59] The device achieved close to 3.8% efficiency, as reported in the first peer-reviewed publication on perovskite solar cells.[59,61,62] This achievement was enough to inspire further research into the use of hybrid perovskite materials for solar cell applications.

The solar device initially reported by Miyasaka *et al.*[59] used a small amount of perovskite material, which later on turned out to be the limiting factor in the device performance. It was later shown by Nam Gyu Park *et al.* that by increasing the perovskite load (even in the dye sensitised architecture), a *higher* power conversion efficiency (PCE) was achievable.[63]

Following on from the initial architecture, the idea of a solid-state DSSC (thin-films later on) employing a perovskite material, using an HTM like spiro-OMeTAD (see later), was investigated.[58] However, some difficulty with stabilising the perovskite material on the HTM was encountered. This problem was resolved by introducing **mixed halide perovskite materials** ($ABX_{3-x}Y_x$ where X, Y = I^-, Br^-, Cl^-) as sensitisers, specifically $MAPbI_{3-x}Br_x$. The mixed halide form of the perovskite was found to be more stable and achieved a PCE of 10.9%.[64,65]

The PCE of PSCs has kept rising and has reached beyond 23%, which places it in competition with the best photovoltaic silicon technologies (crystalline and amorphous) available today that can achieve efficiencies of 25.8%.[66] Recently, in a literal sense of *"if you can't beat them, join them"*, a tandem solar cell device that combines a $MAPbI_3$ thin-film and traditional silicon thin-film was constructed by the venture company Oxford PV™ and achieved a record certified efficiency of 27.3% under laboratory conditions.[67] The focus has shifted to tandem cells because there is a *theoretical performance limit* for a single layer device, as described by the **Shockley−Queisser limit**, which is around 33%, assuming a PCE of 30% should be achievable experimentally.[68] The difference between the theoretical and experimental values are due to unavoidable radiative losses.[68]

However, one primary concern that has always been raised with using $MAPbI_3$ as sensitiser is that it contains *lead* (in the form of Pb^{2+}) which is harmful to human life and the environment. This concern led to research focussing on the substitution of lead by other closely related metal ions. The alternatives include Group 14 elements like Sn^{2+} and Ge^{2+}, alkaline earth metals, transition metals, lanthanides, and even other *p*-block elements like In^{2+} and Ga^{2+}.[58] A detailed literature survey of lead-free perovskites forms part of Chapter 2. Additionally, alternatives to the methylammonium cation have also been investigated. As mentioned before, mixed halide systems (for example, $MAPbI_{3-x}Cl_x$) have been investigated. Each of the chemical *tweaks* to the initial structure of $MAPbI_3$ has led to differences in solar cell efficiencies, stability, charge carrier abilities and more.

On a final note, the $MAPbI_3$ structure is a 3D perovskite. This dimensionality has always been the *preferred* dimensionality for solar cell applications of perovskite materials – the reasons for this preference are discussed later. However, recent results have been reported in the literature that shows that lower dimensionalities (especially 2D perovskite structures) also have photovoltaic applications.[17] That said, the following discussion will focus on the 3D perovskite structure and its application to photovoltaics.

1.4.2 Working Principle of PSCs

All semiconducting devices work on the principle of a p-n junction.[8] Simply put, a p-n junction is a junction that forms when a material with positive (p) charge and a material of negative (n) charge are in contact in either an electric field or when thermal excitation of electrons takes place, as schematically illustrated in Figure 1.27 (a). Hence the separation of charge causes a potential junction, while carriers on either side (positive charge on the p-side and negative charge on the n-side) can diffuse across the barrier to combine with carriers of opposite polarity (Figure 1.27 (b)). The positive charges are called **holes** (**h**$^{\bullet}$ or **h**$^{+}$), and the negative charges are, of course, **electrons** (**e**$^{-}$). These electron-hole pairs give rise to *minority carriers* (electrons on the p-side and holes on the n-side, Figure 1.27 (b)). They are pulled across the junction because of the potential gradient created by the separation of charge. Then if the *minority drift* does not cancel the majority diffusion, a current is developed (like in solar cells). Alternatively, once an equilibrium is reached (meaning *no nett current* possible), a semiconducting diode results.

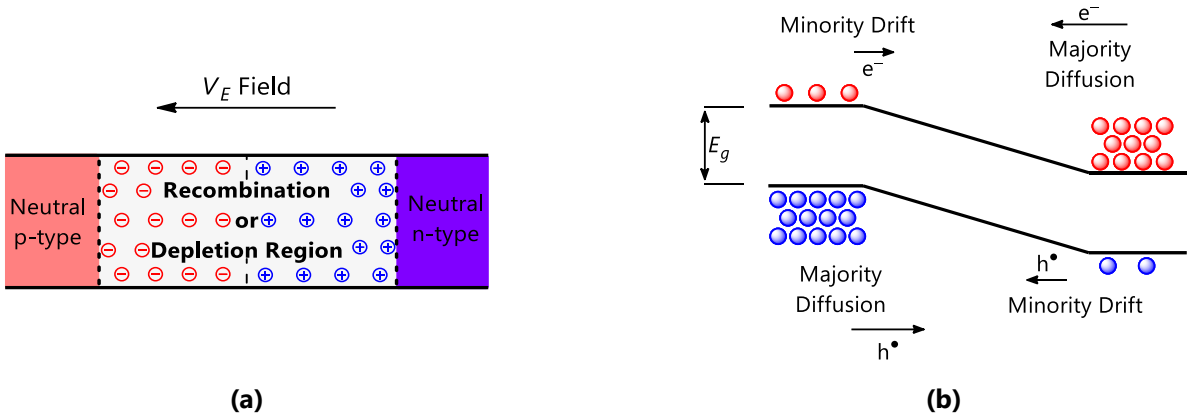

Figure 1.27 (a) A p-n junction in an electric field and **(b)** an illustration of the diffusion or drift of charge carriers (electrons in red and holes in blue) across the depletion region in a p-n junction.

Hybrid halide perovskite crystals that absorb visible light are known to produce Wannier-Mott excitons.[47,69] These excitons are a type of bound electron-hole pair, which acts as a quasiparticle capable of transferring energy while remaining electronically neutral ($e^- + h^+$ = no nett charge). This process of excitation and quasiparticle formation is illustrated in Figure 1.28.

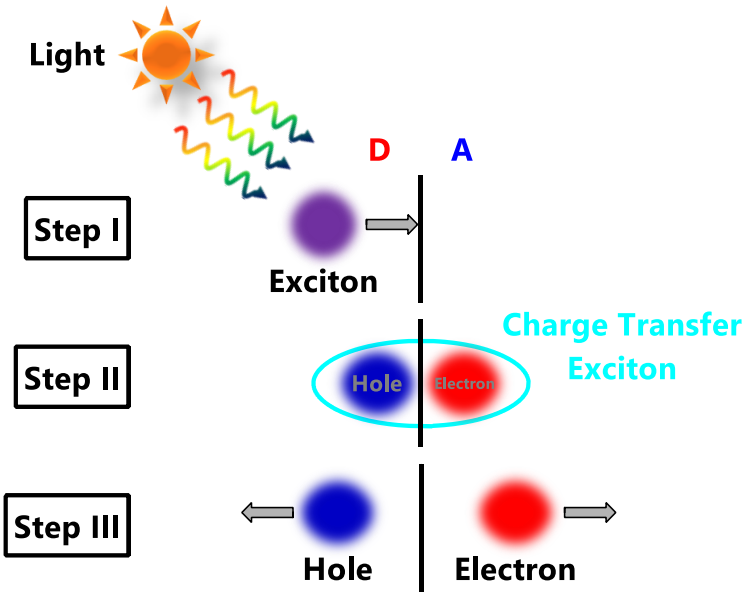

Figure 1.28 Schematic illustration of a Wannier-Mott exciton dissociation process in a thin-film solar cell, where **D** indicates the donor region and **A** indicates the acceptor region.

The charge transport properties of a given semiconductor are mainly determined by the carrier density[70], trap density[71], and the carrier lifetime.[72] Hybrid halide perovskite possesses all these favourable properties. In addition, hybrid halide perovskites are also known to exhibit various unusual optical properties. These include Rashba spin-orbit coupling, nonlinear optical properties, and spectral narrowing effects.[44] All these properties combine to make hybrid perovskite excellent semiconductors.

As stated before, the first application of perovskite materials in photovoltaics was as the dye in a dye sensitised solar cell (DSSC). The perovskite material was coated on a mesoporous TiO_2 photoanode.[59] To clarify, according to the IUPAC nomenclature, the term *mesoporous* refers to any material that contains pores of between 2 and 50 nm in diameter.[73] Therefore, the electronic excitation took place in the perovskite absorber, after which these excited electrons were injected into the TiO_2 layer and eventually reached a fluorine or indium doped tin oxide (FTO or ITO) substrate. However, it was later realised that the perovskite solar cell would still work if the TiO_2 layer were replaced with an insulating material such as mesoporous Al_2O_3, or even *without* any mesoporous layer.[74] This meant that the perovskite absorber could transport electrons and holes by itself without any other semiconducting scaffolding. Therefore, PSCs function more like solid-state p-n junction solar cells than sensitising solar cells. Currently, PSCs are accepted to work as **p-i-n** or **n-i-p** solar cells, where the perovskite layer acts as an *intrinsic* (the i-part) absorber, in-between two contacts (n- and p-layers).[58]

In the n-i-p type cell, TiO_2 is used either as a *compacted* or *mesoporous* layer and acts as the n-type electron transport material/layer (ETM or ETL).[58] Furthermore, the perovskite material plays the role of the intrinsic absorber. The hole transport material (HTM) is an organic molecule, such as Spiro-OMeTAD (2,2',7,7'-Tetrakis-9,9'-spirobifluorene, $C_{81}H_{68}N_4O_8$, Figure 1.29 (a)), which is used as the p-type contact.[75] All that is left to complete the circuit are the metal contact and FTO or ITO contacts. Hence, the complete composition of the solar cell is (FTO or ITO)/TiO_2/perovskite/spiro-OMeTAD/metal-contact, from top to bottom. Here top implies the side of the solar cell which is exposed to solar radiation.

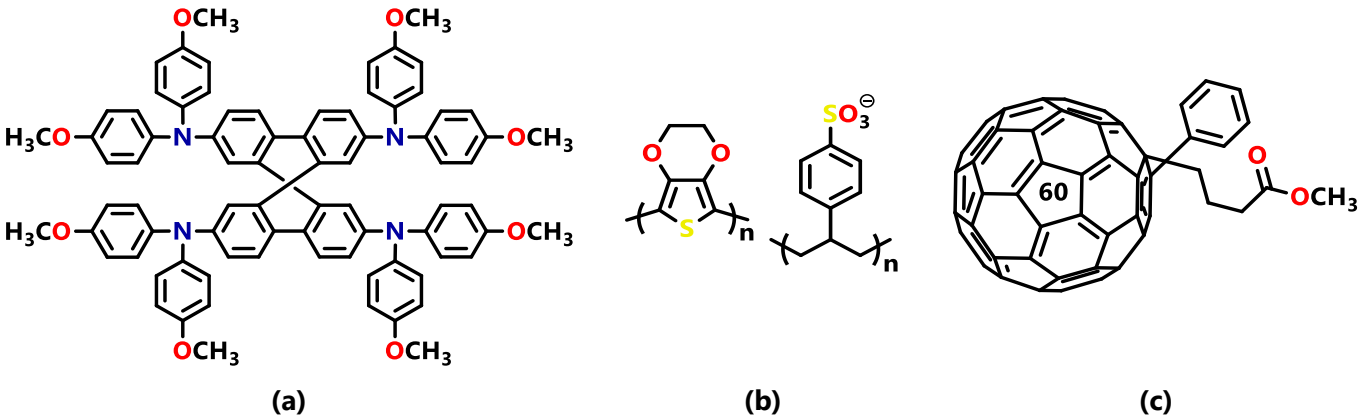

Figure 1.29 The line structures of **(a)** Spiro-OMeTAD (2,2',7,7'-Tetrakis-9,9'-spirobifluorene), **(b)** PEDOT:PSS (poly(3,4-ethylenedioxythiophene) polystyrene sulfonate) and **(c)** PCBM (methanofullerene phenyl-C_{61}-butyric-acid-methyl-ester).

Alternatively, the p-i-n type cell, known as the *inverted architecture*, has the perovskite absorber (i), sandwiched between a p-type material such as PEDOT-PSS (poly(3,4-ethylenedioxythiophene) polystyrene sulfonate, Figure 1.29 (b)) and an n-type material like PCBM (methanofullerene phenyl-C_{61}-butyric-acid-methyl-ester, Figure 1.29 (c)).[58,60] Hence, the complete composition of the solar cell reads (FTO or TiO_2)/PEDOT:PSS/perovskite/PCBM/metal-contact, from top to bottom. Several typical architectures of PSCs reported in the literature are shown in Figure 1.30 (a) through (g).[58] In these examples, specifically in Figure 1.30 (g), it can be seen that the so-called *metal contact* need not be metal as such. It may also be carbon. The architecture in Figure 1.30 (g) is the device architecture employed in this study.

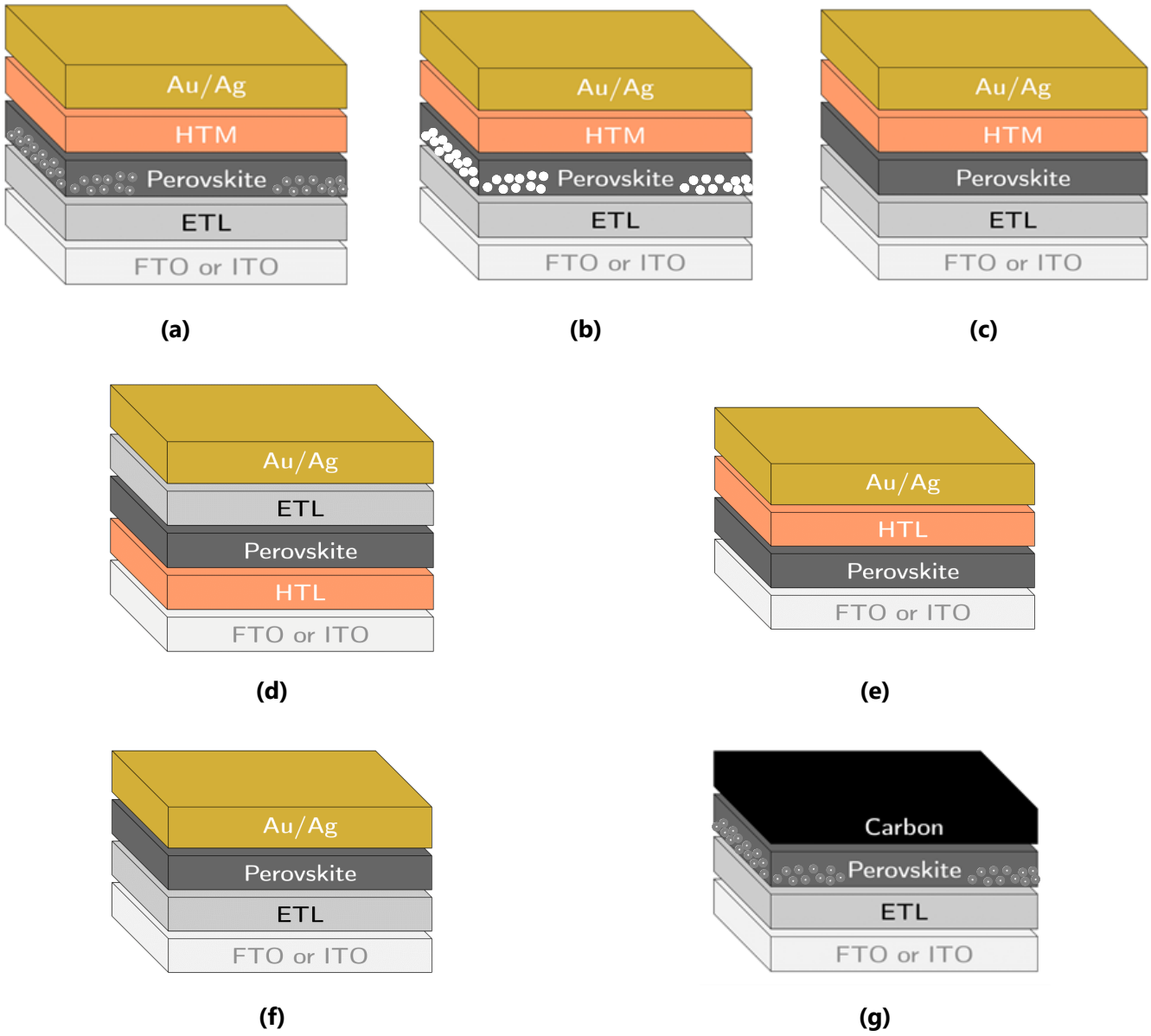

Figure 1.30 A schematic depiction of a variety of perovskite device architectures: **(a)** a mesoscopic n-i-p device with a semiconductor metal oxide layer, **(b)** a mesoscopic (nanoscale) n-i-p device with an insulating metal oxide scaffold, **(c)** a planar n-i-p device, **(d)** a planar p-i-n (inverted) device, **(e)** an ETL-free device, **(f)** an HTM-free device, **(g)** an HTM-free device with a carbon electrode. Perovskite structures containing white dots indicate a mesoporous ETL.

Once photoexcitation has occurred in the perovskite layer, the electrons are selectively carried by the n-type ETL and the holes by the p-type HTM. As a result, the excited electrons move through the external wiring of the device and *recombine* with the holes at the metal contact, hence forming a circuit.

Figure 1.31 shows the band structure of a typical metal oxide ETL-based PSC,[58] and arrows indicate the movement of electrons and holes after photoexcitation. In the example, $MAPbI_3$ is used as the intrinsic absorber, with the ETL, HTM and circuit contacts (FTO and Au) as shown in the figure. Figure 1.31 also shows the importance of the overlap of the band structure of the materials involved since if there is no overlap present, the device *will not* function. The electron is excited from the valence band to the conduction band by absorbing a photon. This photoabsorption creates an electron-hole pair. The ETL layer extracts the electron, and the HTL extracts the hole (technically, an electron from the HTL fills the gap left by the photoelectron, and it creates the illusion of the hole *moving*). The hole and electron inevitably combine at the metal contact

(Au), which is the driving force behind the process. The movement of the charge carriers generate a photocurrent and hence a working PSC device.

It is important to note that the illustrated process of excitation, transportation and recombination of electrons and holes (shown in Figure 1.31(a) and (b)) is an idealised simplification of the process. This simplification is currently accepted as the working model of PSCs. Still, much speculation arises due to the high open-circuit voltages (V_{OC}) observed in PSCs versus amorphous silicon p-i-n solar cells.[58] On the point of clarity, the open-circuit voltage of a solar cell device can be thought of as the voltage that needs to be applied to the device to measure a current of zero.[76] Alternatively, it is the voltage that is measured when the device is disconnected from the external circuit. Returning to the V_{OC} of PSCs, the work functions of the ETL and the HTM have a negligible effect on the obtained V_{OC}. This is due to the unusual behaviour of carriers in the perovskite layer, and therefore the role of the perovskite absorber V_{OC} is still not fully understood.

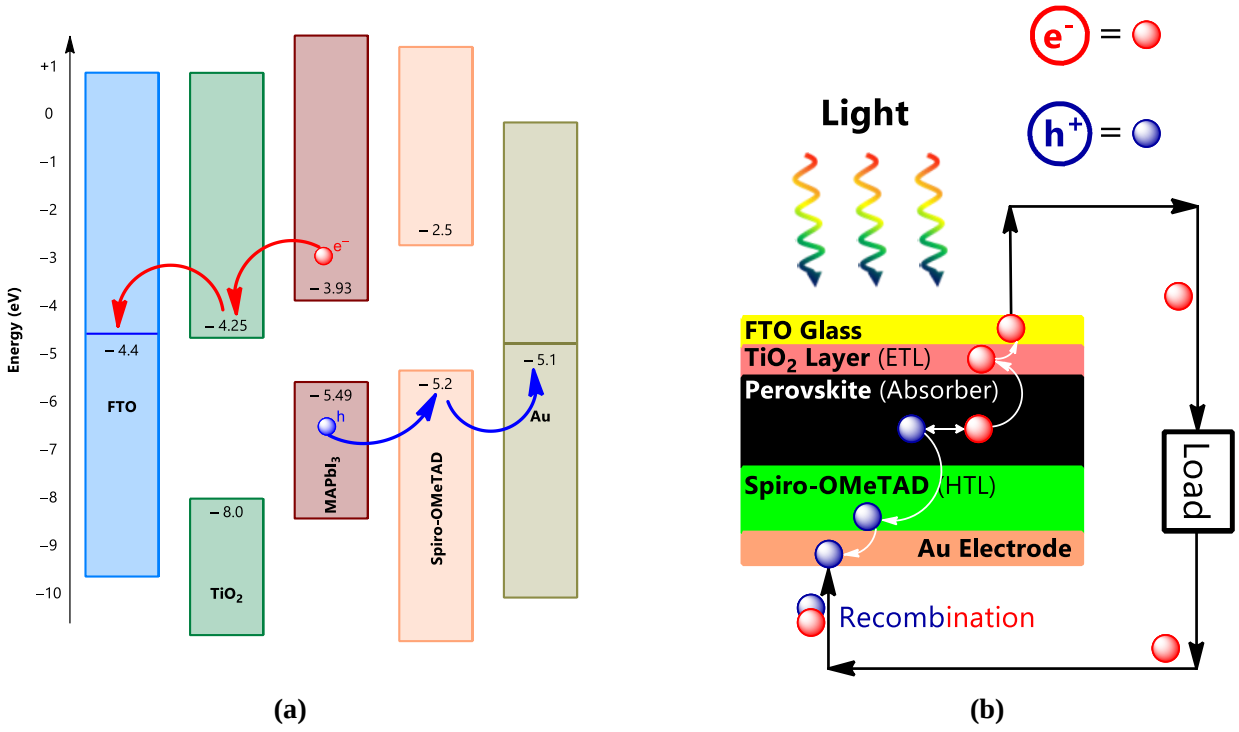

Figure 1.31 (a) The energy levels present in a PSC device through which the electron (e^-) and hole (h^+) movement after photoexcitation in shown by differently coloured arrows, with $MAPbI_3$ being the absorber layer, TiO_2 the ETL and spiro-OMeTAD the HTL. FTO is the so-called "front contact", and Au as the "back contact" (adapted from Jena *et al.*[58]). **(b)** The working principle of a PSC shown as part of an electric circuit.

1.4.3 Why PSCs?

The major drawback of traditional silicon solar cells is the *scarcity* of silicon, and therefore, the cost of production.[77] The production of PSCs is, in comparison, exteremely inexpensive. Non-scarce elements are used in combination with simple solution chemistry. Therefore, no specialised crystal growing equipment is required to synthesise *highly efficient solar cell materials*. Hence, from an economic point of view, PSCs are more alluring than their silicon counterparts.

Additionally, as mentioned in the previous section, unusually high V_{OC}'s are measured in PSCs. The reasons for the high-power conversion efficiencies and hence high V_{OC}'s of PSCs are six-fold. The perovskite material's high absorption coefficient ($\alpha > 105$ cm^{-1}),[58] long carrier diffusion length,[78,79] moderate carrier mobility,[82–84] long carrier lifetime,[80,81] high defect tolerance,[58] and slow carrier recombination[83] are all suspected to increase the PCE and V_{OC}. However, no detailed, systematic study has been completed to investigate the exact effect of each of these contributing factors. Therefore, the

investigation of these variables also falls outside of the scope of this study. That said, the perovskite remains a promising *material*, even though a full understanding of the working mechanism is lacking.

1.4.4 Single Layer versus Tandem Device Architectures

The absorber layer or sensitiser of any solar cell has a specific **band gap**, which allows for the absorption of the solar spectrum. However, a single type of material (a sensitiser/absorber layer made from one kind of material) will only be able to absorb *one specific region* of the entire solar spectrum. This would not be detrimental to solar cell performance if 100% absorbance efficiency were possible. However, a *theoretical maximum limit* for the absorption of solar radiation exists and is described by the **Shockley-Quesser Limit**.[68] This limit gives the ideal band gap of a single layer device and the maximum efficiency of the device at that specific band gap. Therefore, a new solution was proposed to address this issue which limits single-layer devices' performance, and that is using multiple layers of different absorber materials in the so-called tandem device architecture.[85] Using absorber materials with different band gap values allows the solar cell to harvest the solar spectrum more optimally and with higher theoretical efficiency. Note that this study will focus on the single-layer device architecture. Tandem devices are discussed here to inform the reader of possible improvements for future work.

1.4.5 Single Layer Solar Devices

For a solar cell having a single p-n junction architecture, the maximum theoretical efficiency of the cell is given by the **Shockley–Queisser limit** (also called the detailed balance limit).[68] The model assumes that the only mechanism by which power is lost in the cell is *radiative recombination* (the combination of electrons and holes). The limit was first calculated by William Shockley and Hans J. Queisser for a material with an optical band gap of 1.1 eV. They found that a theoretical maximum efficiency of 30% was attainable for a single layer device assumed to be an ideal black body of temperature 300 K and the sun, also an ideal black body, at a temperature of 6000 K, as shown in Figure 1.32 as the blue curve.[68] More recently, Sven Rühle recalculated the efficiency limit using the AM 1.5G spectrum (modern solar spectrum equivalent model), which is the new standard spectrum of use.[86] Additional improvements to the model include using a theoretical back-mirror to ensure the only loss mechanism is radiative recombination (therefore, initial non-interacting radiation is reflected into the material for excitation). Calculated using the modern method (using the back mirror and AM 1.5G spectrum) the theoretical efficiency of a single layer solar device with an optical band gap of 1.34 eV is increased to 33.7%.[86] The red curve in Figure 1.32. shows the theoretical efficiency calculated using the improved model proposed by Rühle.[86] For both calculations, the concentration of sunlight was taken as **one sun**. Thus, a band gap of between 1.1 and 1.3 eV is ideal for maximum solar absorption as determined by the Shockley-Quessier limit.

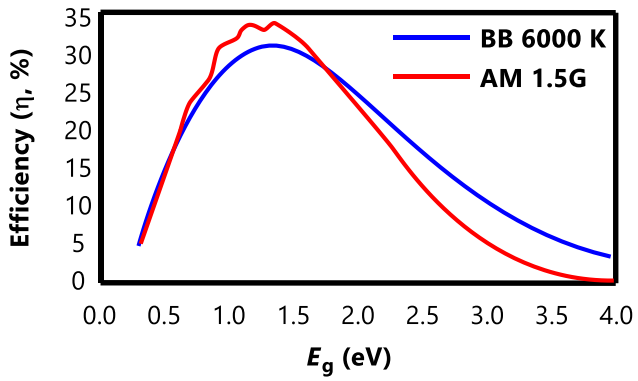

Figure 1.32 Graph showing the calculated percentage efficiency *versus* band gap of the absorber material for solar energy equal to one sun, as per the Shockley-Queisser limit (in blue) and as per the AM 1.5G spectrum (in red). (Adapted from the paper of Sven Rühle[86]).

1.4.6 Tandem Solar Devices

The Shockley-Queisser limit and the recalculation of the maximum theoretical efficiency by Sven Rühle were based on a single layer device. However, recently several tandem solar devices (especially tandem devices based on a perovskite and a silicon layer) have been investigated. The work done by de Vos in 1980 showed how the Shockley-Queisser limit could be applied to tandem devices.[85]

de Vos found that the efficiency of the device *increases* with the addition of another layer to the device. For example, two layers have a theoretical maximum efficiency of 42%, and three layers have a maximum efficiency of 49%, etc. Theoretically, for an infinite number of layers, a maximum efficiency of 68% under one sun of radiation was predicted. Additionally, for concentrated radiation (radiation of strength larger than one sun) and an infinite layered cell, a maximum efficiency of 86% is expected. This provides a promising avenue for future research in solar cell technology, in which the perovskite materials may be employed.

1.4.7 Characterisation of Solar Cells

When comparing different solar cells, be it from different generations or similar cells with different compositions, specific **solar cell parameters** can be used to characterise the solar cell device and allow for comparisons. Some of these parameters are discussed below.

The IV-Curve

The IV-curve is a plot of the current and voltage measurements of a solar cell diode.[87] A solar cell is seen as a diode because when there is no light shone on the cell, there will be no current produced, and hence the device operates as a p-n junction diode.[88] Figure 1.33 (a) shows the ideal IV-curve for a solar cell in the dark (no light) and illuminated modes.

In general, the IV-curve is "flipped" around the *V*-axis as shown in Figure 1.33 (b), and the intercepts are labelled I_{SC} and V_{OC}, which are coined the short-circuit current and the open-circuit voltage. The product of the current (*I*) and voltage (*V*) measurements is then also plotted to give the **power output of the solar cell**, with the maximum power output point labelled P_{MP} as shown in Figure 1.33 (c).

To elaborate on the definitions, the **short-circuit current** is the maximum current the solar cell can produce when the voltage across the cell is zero. The parameter often used is the **short-circuit current density**, which is the short-circuit current divided by the area (*A*) of the device, as shown in Equation (1.6):

$$J_{SC} = \frac{I_{SC}}{A} \ \text{mA}\cdot\text{cm}^{-2} \tag{1.6}$$

The **open-circuit voltage** is the maximum voltage a cell can produce when the net current flowing through the cell is zero. This means the minimum applied voltage necessary to measure a current response from the device. This is not simply zero because there is a so-called leakage current in all semiconductor devices, which is always "lost". Hence, this value must first be overcome before a net current measurement will be registered.[88]

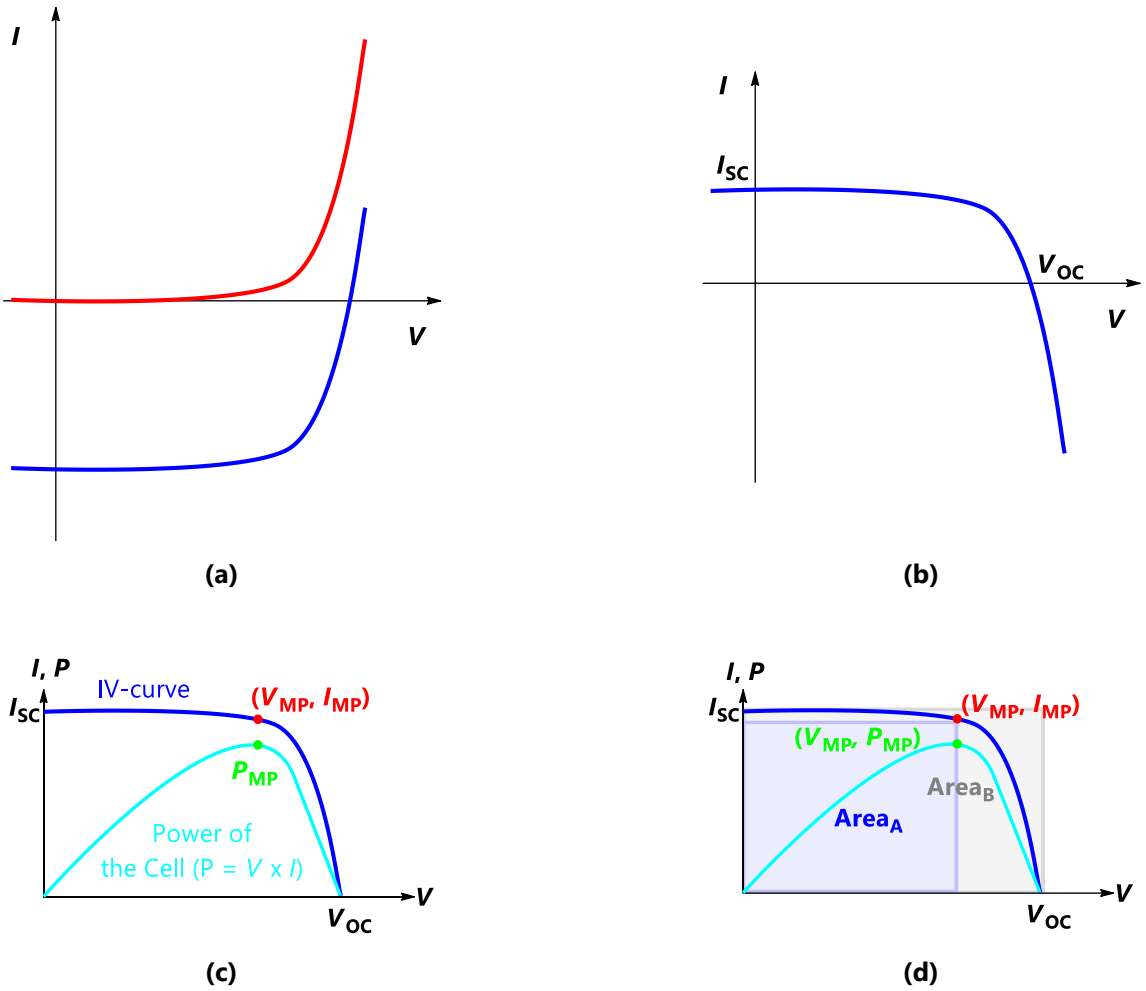

Figure 1.33 (a) The IV-curve of a solar cell device. The red curve is the cell's response to an applied potential bias under no-illumination. The blue curve is the measured IV-characteristics of the solar cell device under a specific intensity of light. **(b)** The flipped convention of the IV-curve. **(c)** The IV-curve and the power output curve of a solar cell, with the maximum voltage (V_{MP}), maximum current (I_{MP}) and maximum power (P_{MP}) points all shown in the figure. **(d)** Visual illustration of the fill factor ($Area_A = V_{MP} \times I_{MP}$, $Area_B = V_{OC} \times I_{SC}$).

The Fill Factor (FF)

The highest possible current and voltage measurements that can be achieved in a solar cell are the short circuit current and the open-circuit voltage. However, as illustrated in Figure 1.33 (c), the cell's power output is zero at both these points. Therefore, another parameter called the **fill factor** (FF) is used along with the I_{SC} and V_{OC} measurements to determine the maximum power output of the solar cell. The fill factor can be calculated as shown in Equation (1.7).[88]

$$FF = \frac{P_{MP}}{I_{SC} V_{OC}} = \frac{I_{MP} V_{MP}}{I_{SC} V_{OC}} \tag{1.7}$$

Put into words, Equation (1.7) defines the fill factor as the ratio of the actual maximum power output (P_{MP}) to the "theoretical maximum power" ($I_{SC} \times V_{OC}$). This becomes more evident when P_{MP} is written as the product of I_{MP} and V_{MP} as in the second part of Equation (1.7). Figure 1.33 (d) visually shows that the fill factor is the ratio of the two areas ($FF = Area_A/Area_B$). $Area_A$ is contained in $Area_B$; the fill factor can only ever be less than or equal to 1.[88] Therefore, a consequence of this is that a solar cell with a higher voltage will have a higher fill factor since this will force the IV-curve to become rectangularly shaped, so smaller power losses are seen.

The Efficiency of Solar Cells (PCE)

Now that all the other parameters needed are defined, the **efficiency of a solar cell** (the PCE, sometimes given the symbol η) may be calculated.[87] The efficiency of a solar cell is defined as the output obtained from the cell from a given input from the sun (radiation source), as shown in Equation (1.8). For comparability between different solar cells, all cells are measured with 1.5 AM radiation and at 25 °C.[89]

$$\eta = \frac{P_{MP}}{P_{Input}} = \frac{FF I_{SC} V_{OC}}{P_{Input}} \tag{1.8}$$

This concludes the discussion of the basic parameters needed to characterise and evaluate the performance of solar cells. Several other factors need to be considered when describing solar cells, however, this falls outside of the scope of this study. Nevertheless, the parameters discussed here are sufficient to provide a basic understanding of solar cells and their performance and to compare to one another.

1.4.8 Factors that Govern the Band Gap of Perovskites

Hybrid halide perovskite materials are well known for their compositional versatility, and hence, tunability of their physical and optical properties. Therefore, understanding the factors that play a role in reducing or increasing the optical band gap of a hybrid halide perovskite material is invaluable in deciding exactly how to go about the *fine-tuning* of the band gap.

The first factor that governs the optical absorption wavelength (and hence the optical band gap), and probably the easiest parameter to alter in a single halide perovskite, is the halide ion (Cl^-, Br^- or I^-), or the molar ratios of the halides in mixed perovskites.[58,90,91] The fact that there are substantial differences in the optical properties of perovskites with different molar ratios of halides indicate that mixed halide perovskites can form solid solutions as ionic crystals. An added improvement gained from using mixed halide systems, in addition to the tunability of the optical band gap, is stability. Mixed halide perovskites are more stable than single halide perovskites in terms of exposure to moisture and sunlight.[78]

Furthermore, the mixing of halides in the metal halide perovskite structure allows for altering the X–B–X angles in the metal halide framework due to the shortening or lengthening of the B–X bonds, which, in turn, influences the band gap. In the 3D perovskite cubic structure, X–B–X angles of 90° and 180° are sought after, since in this ideal case, the orbital overlap between the metal and halide species is maximised. Therefore, the 3D cubic perovskite phase is *preferred* for solar cell applications since the ideal angles are achievable in the cubic arrangement. That said, these desired properties can also be obtained in the quasi-2D and 2D perovskites.[92] However, the preference for a 3D structure is due to the fact that a 3D crystallographic structure (3D connectivity) allows for a 3D electronic dimensionality, which is beneficial for optoelectronic applications. This is further explained in Chapter 2.

Angles close to the ideal values, in a 3D perovskite structure, allow for a reduction in the optical band gap (reduced toward the ideal band gap of between 1.1 and 1.3 eV for maximum solar absorption as determined by the Shockley-Quessier limit) compared to a 3D perovskite structure that does not have these ideal angles. The factor that primarily governs these angles and hence orbital overlap is the A-cation.[93–95] If the A-cation is too small to be accommodated in the cavities formed by the metal halide framework in the 3D cubic perovskite structure, deviations in the X–B–X angles of the inorganic framework from the ideal values occur to accommodate the smaller cation. Therefore, the better the "fit" of the A-cation in the cavity, the closer the angles will be to the ideal values since less octahedral tilting will be observed.[96] As a result, a smaller band gap will be observed.

However, it is still unclear if the only influence of the A-cation (specifically in organic-inorganic halide perovskites) is on the angles in the inorganic framework. Some theoretical calculations have suggested that the orbitals of the A-cation form part of the valence and conduction bands, where it was previously assumed that only the metal and halide orbitals contribute to these bands.[93,97] That said, one fact that has been established is the effect of the A-cation on the X–B–X angles, which directly

affects the optical band gap. Hence, a suitable A-cation is required for an optimal band gap. A volumetric decrease in A-cation size leads to an *increase* in the optical band gap of the 3 D perovskite material. For example, with $MAPbI_3$ $E_g^{MA} \sim 1.6$ eV and for $CsPbI_3$ $E_g^{Cs} \sim 1.7$ eV, due to the Cs^+-ion being much smaller than the MA^+-ion.[98–100] The difference in band gap is observed since, in the Cs^+-case, the lead-iodide orbital overlap is less than in the MA^+-case due to the X–B–X angles deviating from the ideal values since the 3D cubic perovskite framework has to distort to accommodate the smaller Cs^+ cation. However, the difference in band gap is small, suggesting that the A-cation's role is not as significant as that of the metal ion or the halide ion.

From a theoretical perspective, it has been suggested that the metal ion must have accessible *s*-orbital electrons.[93,94,97] These electrons are easily accessible, polarisable and contribute to the conduction electrons of the semiconductor due to the substantial overlap with the *p*-orbitals of the halide ion. Building on this point, a reduction in band gap is seen when using Cl^- versus Br^- versus I^-. For example, in the $MAPbX_3$ series of compounds, where X = Cl^-, Br^- or I^-, the band gap variation with halide ion is as follows: $E_g^I \sim 1.6$ eV, $E_g^{Br} \sim 2.2$ eV and $E_g^{Cl} \sim 2.9$ eV.[50,101,102] This variation is due to the higher binding energies associated with valence electrons from I (5*p*) to Br (4*p*) to Cl (3*p*).[96] Furthermore, spin-orbit coupling effects associated with heavier metals, such as Pb (Z = 82) versus Sn (Z = 50), lead to an increase in the optical band gap, as seen in $MABI_3$, B = Pb^{2+} or Sn^{2+}, with $E_g^{Pb} \sim 1.6$ eV versus $E_g^{Sn} \sim 1.2$ eV.[100,103,104] The heavier lead ion-containing analogue has a higher band gap than its tin counterpart.

Hence, one might say that the ideal PSC would have a perovskite layer with a *light* metal ion, with the significant halide component being iodide, mixed with some bromide ions to stabilise the structure and a perfectly fitting A-cation. This should theoretically lead to the *ideal band gap structure*.

1.5 Methods of PSC Device Fabrication

The preparation of large-area perovskite films is necessary for their practical use in solar cells. Due to the large area of the solar cell device, the preparation of these films requires a high efficiency, and should result in films of a high quality with a high degree of stability. This section presents methods to prepare large-area perovskite films with high PCE and stable crystals. General considerations that aid in the improvement of device efficiency include fine-tuning of the chemical composition of the perovskite, improving the grain sizes, and hence lowering the defects in the perovskite film and interface engineering.[105]

In this section, the techniques reported in the literature for the deposition of the perovskite layer will be discussed. Of course, a PSC device contains several layers, all of which have their optimal deposition methods. That said, this study will focus on the perovskite layer as a sensitiser in the PSC device, and hence the deposition of the "other" layers in the device are of little interest for the moment.

1.5.1 One-Step Deposition Methods

One-step deposition methods are commercially favourable since they are easily implemented and are less complex than two-step deposition methods, which will be described later. The focus will be given to the so-called *general* methods, only implying that these techniques are widely used. However, certain one-step or two-step methods are specialised and will only be described in a later section.

One-Step Spin Coating

Spin coating requires the substrate to rotate (at a specified rate) and a perovskite precursor solution to be sprayed onto the substrate. Usually, the substrate is the ETL of the PSC device. Two spin coating methods are widely used, namely the **one-**

step spin coating method and the **two-step spin coating method**. The one-step spin coating technique is shown schematically in Figure 1.34. In the one-step method, a solution of the metal salt (e.g., PbI_2) and the organic salt (e.g., MAI) are dissolved in a solvent of choice (e.g., DMF or mixtures of solvents are also used).[59] This solution is coined the precursor solution. The precursor solution is then sprayed onto the rotating substrate and annealed to allow for thin-film formation.

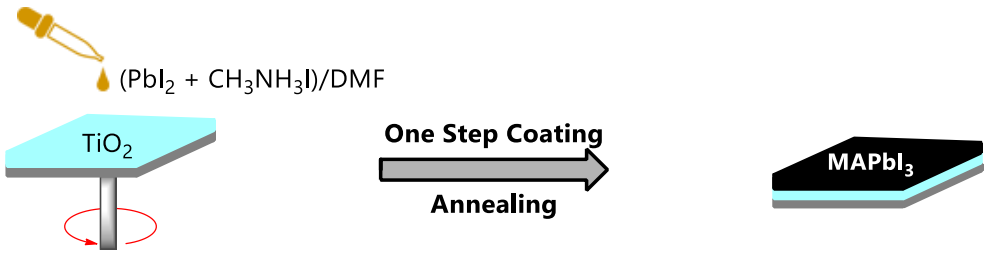

Figure 1.34 A schematic representation of the one-step deposition method, to fabricate a $MAPbI_3$ layer in a PSC device. Adapted from Kojima *et al.*[59]

As the substrate spins, the solvent is initially removed by the centrifugal force and later *via* evaporation due to the annealing. As the solvent is removed, the solution slowly reaches the *supersaturation* point, and hence the perovskite film starts to crystallise. The annealing step contributes three important aspects. Firstly, it removes any excess solvent. Secondly, it assists the growth of the perovskite film through promoting nucleation and thirdly, it thickens the grains.[105]

Due to its simplicity and ease of application, the one-step spin coating method is one of, if not the most utilised techniques for perovskite thin-film deposition.

Solvent Engineering

The **solvent engineering** process is also referred to as **anti-solvent washing**. This method is a slight variation of the one-step spin coating method. Typically, the precursor solution is spin-coated, as described before. Whilst the spinning continues, a nonpolar anti-solvent is dripped onto the spinning substrate, as shown in Figure 1.35.[106]

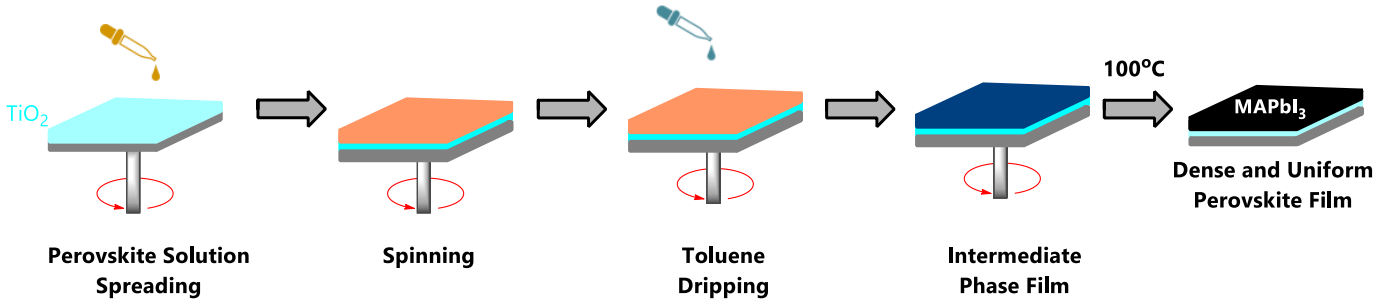

Figure 1.35 A schematic diagram of the solvent engineering or anti-solvent washing method for the formation of a $MAPbI_3$ film. Adapted from Im *et al.*[106]

The beauty of this technique is that the anti-solvent accelerates the point of supersaturation in two ways. The first is by driving out the solvent quicker than it would be typically, and the second is by reducing the perovskite material's solubility in the solvent.[105] This allows for rapid nucleation, leading to larger grains in the perovskite film and subsequently better-performing PSC devices. Furthermore, the anti-solvent can be heated to further improve and speed up the crystallisation process.[107]

Gas-Quenching

The anti-solvent washing technique inspires the **gas-quenching** method. The only difference is that the anti-solvent is "replaced" by an inert gas, such as nitrogen or argon.[108] The coated substrate is blasted with a burst of gas, leading to quick supersaturation due to the enhanced evaporation of the solvent.

Anti-Solvent or Solvent Extraction

The **anti-solvent**, also known as the **solvent extraction** method, uses an anti-solvent just like the solvent engineering process, however, not in the deposition step, instead, by immersing the perovskite film in a bath of anti-solvent after formation *via* spin coating (see Figure 1.36).

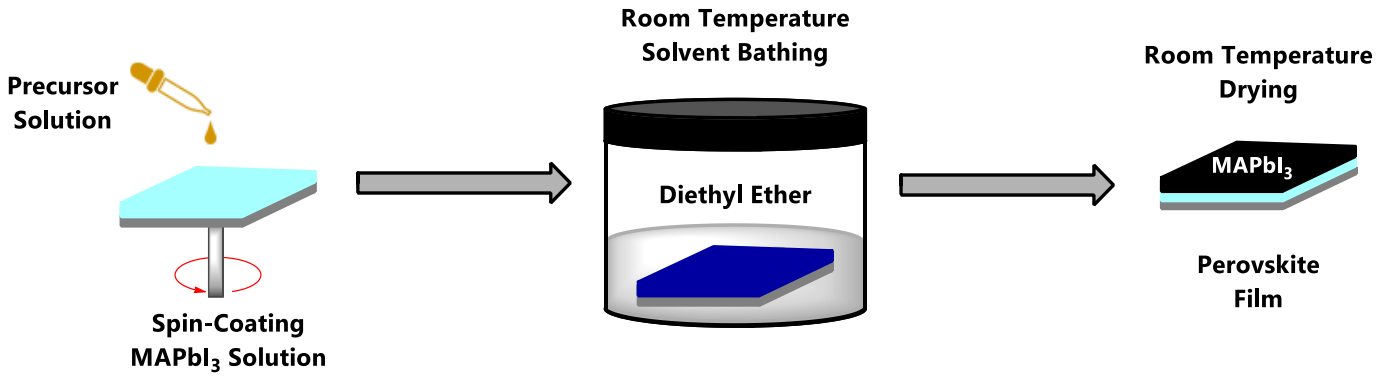

Figure 1.36 A schematic illustration of the anti-solvent (also called the solvent extraction) technique where first the perovskite precursor solution is deposited onto the substrate *via* spin-coating and then placed in an anti-solvent bath, followed by drying at room temperature. Adapted from Zhou *et al.*[109]

This method provides several advantages over the solvent engineering method. Firstly, it avoids the problem of correctly timing the addition of the anti-solvent. Secondly, the possibility of damaging the film by the impact of the solvent on the film is eliminated. Thirdly, the whole process is a low-temperature process, and finally, the process is easily scalable.[105]

Drop-Casting

Perhaps the most intuitive and simplistic manner of depositing the perovskite film is by dropping the precursor solution onto the substrate (could also be spread over the substrate) and allowing the solvent to evaporate at room temperature or at a slightly elevated temperature.[110] This method is called **drop-casting** and is the method that will be employed in this study. Albeit the least technical of all the approaches, PSC devices with PCEs of 16% have been achieved with this straightforward technique.[111]

Dual-Source and Single-Source Evaporation

Several early reports detailed the deposition of the perovskite film by **vapour deposition** rather than solution-based processing.[112] In the vapour deposition method, the perovskite precursors are evaporated or sublimed from crucibles using elevated temperatures, under vacuum and then are directed to collect on a substrate (see Figure 1.37).

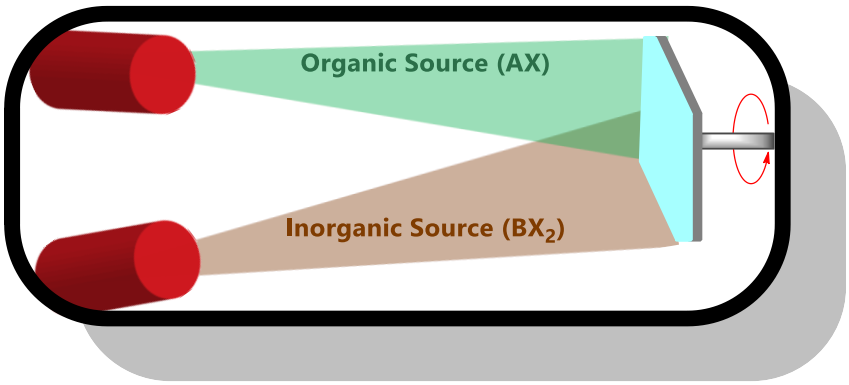

Figure 1.37 A schematic representation of the vapour deposition process. The precursor salts (AX and BX_2) are placed in crucibles, heated until they are evaporated. The vapourised reagents then travel to a spinning substrate on which a perovskite film is formed. Adapted from Liu *et al.*[112]

The organic source (AX) and the inorganic source (BX_2) are placed in crucibles and evaporated under a strong vacuum (10^{-10} torr) or under thermal heating, towards a spinning substrate. The nucleation and film formation then takes place on the substrate.[112] That said, the film growth mechanics are difficult to control in this method and sometimes leads to undesired film properties, however, on average, the technique delivers high-quality films.

Capillary Thin-Film Growth

Encapsulation of the perovskite film can lead to higher device stability, hence a method of *self-encapsulation* called **capillary thin-film growth** is of great use. During this process, two half-cells (one containing the anode/ETL and another containing the cathode/HTL) are stacked like a sandwich, and then the perovskite precursor infiltrates the two layers. The solvent is then driven out by a combination of mechanical pressure, heating, and a vacuum.[113] This ingenious method is yet to set the world alight, however, much promise has been shown.[105]

Melt-Processing

In the **melt-processing** processes, the precursors are melted together and pressed onto a substrate. A material such as glass or polyimide is used as the substrate, as illustrated in Figure 1.38.

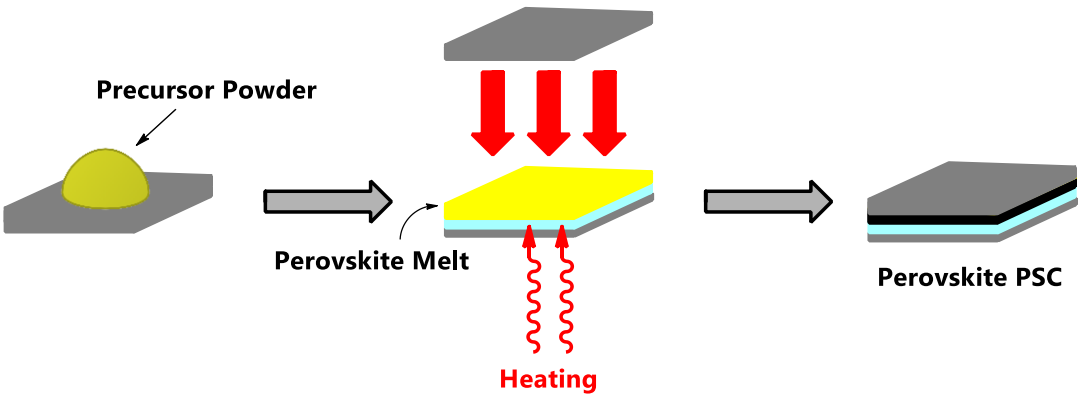

Figure 1.38 A schematic illustration of the melt-processing method used in the formation of a perovskite film in a PSC device. Adapted from Li *et al.*[114]

The melt contains precursors in a 100% weight concentration, and so the formation of pinholes or voids are avoided, which is an added benefit in contrast to solution processing techniques.[105,115] A pinhole (shown in Figure 1.39) is exactly as the name suggests, a small gap between the grains that form the perovskite thin-film in a PSC. This is unfavourable for thin-film devices.

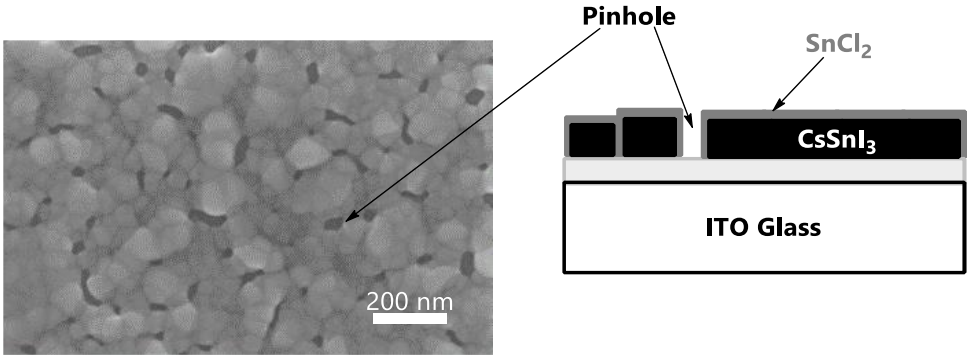

Figure 1.39 A "pinhole" is shown in a SEM image and schematically. Copyright Wiley-VCH 2017. Adapted from Marshall *et al.*[116]

Before moving on to the *two-step* methods, two more one-step methods of note include **pulsed laser deposition (PLD)**[117] and **resonant-infrared matrix-assisted pulsed laser evaporation (RIR-MAPLE)**[118]. Both these techniques require highly specialised equipment and hence are not discussed here. However, they are mentioned for the sake of completeness.

1.5.2 Two-Step Methods

Often, challenges in solubility are encountered in one-step methods, in that the metal and organic salts are not soluble in the same solvent. Hence, a two-step method is used in these cases in that the metal halide is dissolved in one solvent and the organic halide in another, and then they are subsequently deposited.

Two-Step Spin Coating

The one-step spin-coating method often leads to non-uniform and irregular films with small grain sizes. Specifically, the formation of pinholes is of great concern. The **two-step method** (shown in Figure 1.40) uses the same idea as the one-step spin coating method, however, the precursor solution is "split in two". Thus, the two-step method involves the deposition of the metal salt followed by a coating of the organic salt, followed by annealing.

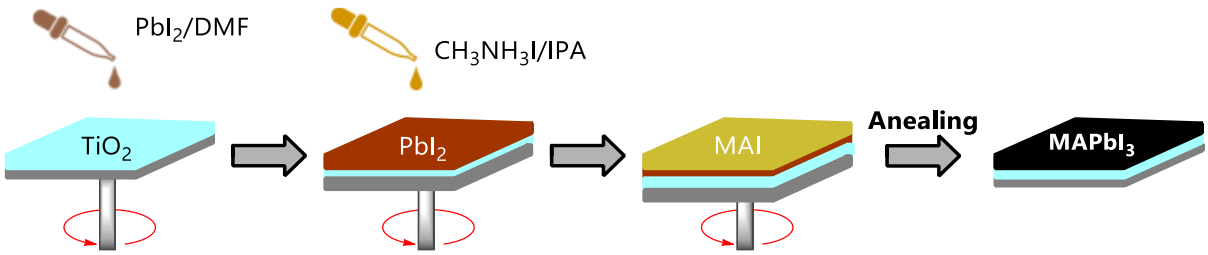

Figure 1.40 A diagrammatic illustration of the two-step deposition method where the precursor solutions are added sequentially to form a perovskite thin-film in a PSC device.

Different rates of rotation lead to varying levels of uniformity in thin-film coverage and grain size. Other techniques, discussed next, offer a solution to this and other challenges faced by spin coating. That said, spin coating is the most commonly used technique due to its ease of application and low cost compared to the other methods discussed here.[119] In addition, the spin

coating technique can be improved by using the anti-solvent spin coating method, where the perovskite precursor is deposited by spin coating (either one- or two-step). Then an anti-solvent is added to aid in the rapid formation of the perovskite film as discussed in the one-step methods.

Vapour-Assisted Solution Processing (VASP)

In the VASP method, the BX_2 film is deposited by spin-coating and is immersed in an organic halide vapour.[120] The organic vapour is prepared in a capped Petri dish by sprinkling the organic salt at the bottom and heating the chamber to 150 °C, as shown in Figure 1.41.[105]

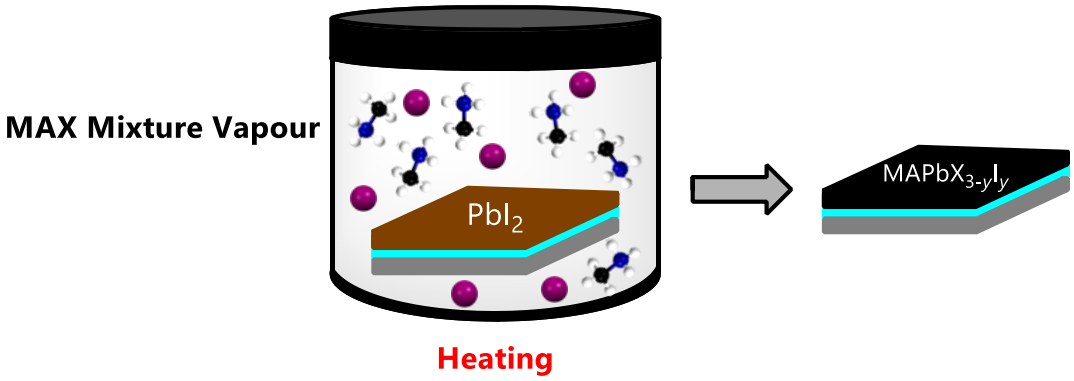

Figure 1.41 A schematic illustration of the vapour-assisted solution processing method used to form a $MAPbX_{3-y}I_y$ film. Adapted from Xiao *et al.*[120]

The VASP method utilises a solid-vapour interface between the precursors where the formation of the perovskite film occurs. This allows for the growth of perovskite films with the original smooth morphology of the BX_2 film. The only drawback is that this process requires an extended fabrication period for optimal film formation (over four hours).[105]

Sequential Vapour Deposition

The vapour deposition process has been discussed earlier. The **sequential vapour deposition** method is similar, except it first deposits one of the precursors as a thin-film and then the other.[121] This method has the advantage that the perovskite film is templated on a near-perfect precursor film, however, this does increase the time needed for fabrication.[121]

Possible Methods for Commercial Use

Of course, developing PSC devices in a commercial sense must form part of the end goal. Hence, the techniques used need to be scalable to produce large-area modules and to be executed in a minimal amount of time. These methods used for commercialisation are far beyond the scope of this study, however, they are briefly described here for completeness.

Doctor-Blading

Doctor-blading is also called blade-coating and is similar to the one-step spin-coating method. The notable difference between the two methods is that instead of a *spinning* motion to remove the solvent, a blade sweeps across the substrate at a fixed height and removes the excess solvent.[105]

The doctor-blading method has shown improvement in film quality compared to many spin-coating techniques, however, it is still under development.

Slot-Die Coating

Slot-die coating (slit-casting or slot-casting) has strong ties to the doctor-blading method, except, in this method, the precursor solution is distributed by a die, the rate of which may be controlled.[122] The die is essentially a print head, which replaces the functionality of a blade in the doctor-blading method. The method allows for superior quality films to the doctor-blading process since the deposition rate can be finely controlled, thus the evaporation of the solvent, and film formation can be governed to near perfection.[123] The slot-die method can also take place in either a one-step or two-step fashion.

Meniscus-Assisted Solution Printing (MASP)

The MASP method was defined as such by Dunlap-Shohl *et al*.,[105] and pioneered by He *et al*.[124] The method of MASP combines blade-coating and slot-die-coating. The precursor solution is dispensed by a fine print head over the substrate surface, while a meniscus forms between the substrate and the print head, allowing for a *conductive* flow of the solvent, ideally leading to large grain boundaries.[124] That said, the speed at which the "printing" takes place needs to be optimised since too slow a speed will lead to the film crystallising and connecting the print head with the substrate. In contrast, completing the process too quickly, will result in the film forming similarly to if the doctor-blading approach were used.[124] However, if the optimal speed is used, then superior film quality compared to the doctor-blading and slot-die-coating methods is achievable.[105] In conclusion, it should be noted that this method is most effective as a one-step processing method.

Soft-Cover Coating

In the soft-cover coating technique the precursor solution is dropped onto a heated substrate (the temperature of which is determined by the solvent used). Thereafter the solution is *covered* with a *flexible* sheet (for example, polyimide), which spreads the solution over the whole substrate.[125] The sheet is then removed ("peeled off"), and the heating allows the *accelerated* vaporisation of the solvent, leading to films with larger grain boundaries.[125]

Spray-Coating

The spray-coating method is similar to the slot-die-coating in minimising waste and loss of material while allowing for high-quality film formation.[126] In this method, a precursor solution (also referred to as a perovskite ink) is ejected through a nozzle, aerolising the solution. The travel process allows for the solvent to evaporate and the subsequent deposition of the perovskite. The film is then annealed to ensure good quality film deposition. The finer the *mist* of the precursor solution, the better the quality of the film formed through annealing.[126]

Inkjet Printing

Inkjet printing is closely related to the process of spray-coating.[105] The precursor solution is still sprayed onto the substrate, however, the nozzle is systematically and precisely moved, sometimes depositing as little as one drop at a time, delivering predetermined patterns. This technique is yet to be widely used, however, it has shown promise in both all-inorganic and hybrid halide perovskite deposition.[105]

1.6 The Future – Towards Lead-Free PSCs

Most research on PSCs has focussed on the benchmark perovskite structure, namely $MAPbI_3$, and its mixed halide derivatives. However, one of the major criticisms of these specific perovskite solar cell sensitisers is that they contain lead. Lead has a negative environmental impact and also negatively affects human health. Human exposure to lead negatively impacts most systems in the human body, including the central nervous, hematopoietic, hepatic, and renal systems.[127] Impairments of these systems can cause severe disorders.

Lead is viewed by the **World Health Organisation (WHO)** as one of the ten most toxic metals, and hence, the use of lead in any industrial process is frowned upon.[128] Furthermore, the maximum amount of lead deemed safe for humans to be exposed to is 15 $\mu g \cdot L^{-1}$ in water and 0.15 $\mu g \cdot L^{-1}$ in air.[129] This is much less than the 0.4 g estimated lead content of a 300 nm thick, 1 m^2 lead-containing PSC.[130]

Hybrid halide perovskite materials are notorious for their moisture sensitivity and instability in direct sunlight. Hence, the possibility that using a lead-containing solar cell device may lead to the introduction of lead into the environment is a risk that cannot be ignored.[17] Even though there have been suggestions of limiting the contamination of soil, water, and air (such as using membrane on the earth of solar farms etc.) by PSCs, the problem could be eliminated in the first place.[58] Therefore, much research has moved towards *lead-free* perovskite materials for use in solar cell devices. Alternative metals include, but are by no means limited to, Group 14 elements such as Sn^{2+} and Ge^{2+}, alkaline earth metals such as Be^{2+}, Mg^{2+}, Ca^{2+}, Sr^{2+}, and Ba^{2+}, transition metals such as V^{2+}, Mn^{2+}, Fe^{2+}, Co^{2+}, Ni^{2+}, Pd^{2+}, Cu^{2+}, Zn^{2+}, Cd^{2+}, and Hg^{2+}, lanthanides such as Eu^{2+}, Tm^{2+}, and Yb^{2+}, and *p*-block elements such as Ga^{2+} and In^{2+}.[131] All these alternatives combine a divalent metal ion (M^{2+}) and a monovalent organic cation (A^+, like MA^+). However, the possibility of *switching* these valences exist (using M^+ and A^{2+}). Therefore, using Group I metals (the alkali metals, including Li^+, Na^+, K^+, Rb^+ and Cs^+), with a divalent organic cation, is a new and unexplored option for PSC technology.

This concludes Chapter 1. The following chapter will provide a literature survey on hybrid halide metal perovskites and their application to PSCs and other optoelectronic technologies. All the theory discussed in Chapter 1 applies to the research discussed in Chapter 2.

1.7 References for Chapter 1

1. Department of Energy of South Africa http://www.energy.gov.za/files/coal_frame.html (accessed Jan 15, 2020).
2. National Renewable Energy Laboratory: Best Research-Cell Efficiency Chart https://www.nrel.gov/pv/cell-efficiency.html (accessed Feb 20, 2021).
3. Webminiral. Perovskite Mineral Data http://webmineral.com/data/Perovskite.shtml#.X9ENF9hLiMo (accessed Jul 20, 2020).
4. Wells, H. L. *Zeitschrift für anorganische Chemie* **1893**, *3* (1), 195–210. https://doi.org/https://doi.org/10.1002/zaac.18930030124.
5. Megaw, H. *Nature* **1945**, *155* (3938), 484–485. https://doi.org/10.1038/155484b0.
6. Møller, C. *Nature* **1957**, *180* (4593), 981–982. https://doi.org/10.1038/180981a0.
7. Gebhardt, J.; Rappe, A. M. *Advanced Materials* **2019**, *31* (47), 1–15. https://doi.org/10.1002/adma.201802697.
8. West, A. R. *Solid State Chemistry and Its Application*, Second Ed.; Wiley, 2014.
9. Boix, P. P.; Agarwala, S.; Koh, T. M.; Mathews, N.; Mhaisalkar, S. G. *Journal of Physical Chemistry Letters* **2015**, *6* (5), 898–907. https://doi.org/10.1021/jz502547f.
10. Stoumpos, C. C.; Mao, L.; Malliakas, C. D.; Kanatzidis, M. G. *Inorganic Chemistry* **2017**, *56* (1), 56–73. https://doi.org/10.1021/acs.inorgchem.6b02764.
11. Zhao, X. G.; Yang, D.; Ren, J. C.; Sun, Y.; Xiao, Z.; Zhang, L. *Joule* **2018**, *2* (9), 1662–1673. https://doi.org/10.1016/j.joule.2018.06.017.
12. Saidaminov, M. I.; Mohammed, O. F.; Bakr, O. M. *ACS Energy Letters* **2017**, *2* (4), 889–896. https://doi.org/10.1021/acsenergylett.6b00705.
13. Li, W.; Wang, Z.; Deschler, F.; Gao, S.; Friend, R. H.; Cheetham, A. K. *Nature Reviews Materials* **2017**, *2* (3), 1–18. https://doi.org/10.1038/natrevmats.2016.99.
14. Katz, L.; Ward, R. *Inorganic Chemistry* **1964**, *3* (2), 205–211. https://doi.org/10.1021/ic50012a013.
15. Mao, L.; Stoumpos, C. C.; Kanatzidis, M. G. *Journal of the American Chemical Society* **2019**, *141* (3), 1171–1190. https://doi.org/10.1021/jacs.8b10851.
16. Pabst, I.; Fuess, H.; Bats, J. W. *Acta Crystallographica Section C Crystal Structure Communications* **1987**, *43* (3), 413–416. https://doi.org/10.1107/s0108270187095568.
17. Ortiz-Cervantes, C.; Carmona-Monroy, P.; Solis-Ibarra, D. *ChemSusChem* **2019**, *12* (8), 1560–1575. https://doi.org/10.1002/cssc.201802992.
18. Calabrese, J.; Jones, N. L.; Harlow, R. L.; Herron, N.; Thorn, D. L.; Wang, Y. *Journal of the American Chemical Society* **1991**, *113* (6), 2328–2330. https://doi.org/https://doi.org/10.1021/ja00006a076.
19. Ishihara, T.; Takahashi, J.; Goto, T. *Physical Review B* **1990**, *42* (17), 11099–11107. https://doi.org/10.1103/PhysRevB.42.11099.
20. Stoumpos, C. C.; Cao, D. H.; Clark, D. J.; Young, J.; Rondinelli, J. M.; Jang, J. I.; Hupp, J. T.; Kanatzidis, M. G. *Chemistry of Materials* **2016**, *28* (8), 2852–2867. https://doi.org/10.1021/acs.chemmater.6b00847.
21. Dohner, E. R.; Jaffe, A.; Bradshaw, L. R.; Karunadasa, H. I. *Journal of the American Chemical Society* **2014**, *136* (38), 13154–13157. https://doi.org/10.1021/ja507086b.
22. Akkerman, Q. A.; Manna, L. *ACS Energy Letters* **2020**, *5* (2), 604–610. https://doi.org/10.1021/acsenergylett.0c00039.
23. Song, J.-L.; Chen, W.-J.; Chu, K.-B.; Zhou, Y.-H. *Dalton Transactions* **2018**, *47* (41), 14497–14502. https://doi.org/10.1039/C8DT03047B.
24. Usman, M.; Yan, Q. *Crystals* **2020**, *10* (2), 62. https://doi.org/10.3390/cryst10020062.
25. Giustino, F.; Snaith, H. J. *ACS Energy Letters* **2016**, *1* (6), 1233–1240. https://doi.org/10.1021/acsenergylett.6b00499.
26. Meyer, G. *Progress in Solid State Chemistry* **1982**, *14* (3), 141–219. https://doi.org/10.1016/0079-6786(82)90005-X.
27. Mao, L.; Teicher, S. M. L.; Stoumpos, C. C.; Kennard, R. M.; DeCrescent, R. A.; Wu, G.; Schuller, J. A.; Chabinyc, M. L.; Cheetham, A. K.; Seshadri, R. *Journal of the American Chemical Society* **2019**, *141* (48), 19099–19109. https://doi.org/10.1021/jacs.9b09945.
28. Vishnoi, P.; Zuo, J. L.; Strom, T. A.; Wu, G.; Wilson, S. D.; Seshadri, R.; Cheetham, A. K. *Angewandte Chemie International Edition* **2020**, *59* (23), 8974–8981. https://doi.org/https://doi.org/10.1002/anie.202003095.
29. Goldschmidt, V. M. *Naturwissenschaften* **1926**, *14* (May), 477–485. https://doi.org/10.1007/BF01507527.
30. Chonghea Li, X. L.; Weizhong Ding, L. F.; Yonghui Gao, Z. G. *Acta Crystallographica Section B* **2008**, *64* (6), 702–707. https://doi.org/10.1107/S0108768108032734.
31. Ava, T. T.; Al Mamun, A.; Marsillac, S.; Namkoong, G. *Applied Sciences (Switzerland)* **2019**, *9* (1), 188. https://doi.org/10.3390/app9010188.
32. Yang, W. F.; Igbari, F.; Lou, Y. H.; Wang, Z. K.; Liao, L. S. *Advanced Energy Materials* **2020**, *10* (13), 1–30. https://doi.org/10.1002/aenm.201902584.
33. Teraoka, Y.; Wei, M.-D.; Kagawa, S. *Journal of Materials Chemistry* **1998**, *8* (11), 2323–2325. https://doi.org/10.1039/A806442C.
34. Bartel, C. J.; Sutton, C.; Goldsmith, B. R.; Ouyang, R.; Musgrave, C. B.; Ghiringhelli, L. M.; Scheffler, M. *Science Advances* **2018**, *2* (5), 1–10. https://doi.org/DOI: 10.1126/sciadv.aav0693.
35. Weber, D. *Zeitschrift für Naturforschung B* **1978**, *33* (Ii), 862–865. https://doi.org/https://doi.org/10.1515/znb-1978-0809.
36. Weber, D. *Zeitschrift für Naturforschung B* **1978**, *33* (12), 1443–1445. https://doi.org/https://doi.org/10.1515/znb-1978-1214.
37. Chen, Q.; De Marco, N.; Yang, Y.; Song, T. Bin; Chen, C. C.; Zhao, H.; Hong, Z.; Zhou, H.; Yang, Y. *Nano Today* **2015**, *10* (3), 355–396. https://doi.org/10.1016/j.nantod.2015.04.009.
38. Xu, W. J.; Kopyl, S.; Kholkin, A.; Rocha, J. *Coordination Chemistry Reviews* **2019**, *387* (May), 398–414. https://doi.org/10.1016/j.ccr.2019.02.012.
39. Zhang, W. Y.; Tang, Y. Y.; Li, P. F.; Shi, P. P.; Liao, W. Q.; Fu, D. W.; Ye, H. Y.; Zhang, Y.; Xiong, R. G. *Journal of the American Chemical Society* **2017**, *139* (31), 10897–10902. https://doi.org/10.1021/jacs.7b06013.

40. Glazer, A. M. *Acta Crystallographica Section A* **1975**, *31* (6), 756–762. https://doi.org/10.1107/S0567739475001635.

41. Glazer, A. M. *Acta Crystallographica Section B* **1972**, *28* (11), 3384–3392. https://doi.org/10.1107/s0567740872007976.

42. Ferey, G. *Crystal Chemistry*, First Ed.; Scientific, World: Versailles, 2017.

43. Saidaminov, M. I.; Abdelhady, A. L.; Murali, B.; Alarousu, E.; Burlakov, V. M.; Peng, W.; Dursun, I.; Wang, L.; He, Y.; MacUlan, G.; Goriely, A.; Wu, T.; Mohammed, O. F.; Bakr, O. M. *Nature Communications* **2015**, *6* (May), 1–6. https://doi.org/10.1038/ncomms8586.

44. Maggiora, J.; Li, F.; Zheng, R. *Physica Status Solidi - Rapid Research Letters* **2021**, *15* (1), 1–22. https://doi.org/10.1002/pssr.202000410.

45. Hamill, J. C.; Schwartz, J.; Loo, Y. L. *ACS Energy Letters* **2018**, *3* (1), 92–97. https://doi.org/10.1021/acsenergylett.7b01057.

46. Kadro, J. M.; Nonomura, K.; Gachet, D.; Grätzel, M.; Hagfeldt, A. *Scientific Reports* **2015**, *5* (1), 1–7. https://doi.org/10.1038/srep11654.

47. Babu, R.; Giribabu, L.; Singh, S. P. *Crystal Growth and Design* **2018**, *18* (4), 2645–2664. https://doi.org/10.1021/acs.cgd.7b01767.

48. Liu, Y.; Yang, Z.; Cui, D.; Ren, X.; Sun, J.; Liu, X.; Zhang, J.; Wei, Q.; Fan, H.; Yu, F.; Zhang, X.; Zhao, C.; Liu, S. *Advanced Materials* **2015**, *27* (35), 5176–5183. https://doi.org/10.1002/adma.201502597.

49. Liu, Y.; Yang, Z.; Liu, S. F. *Advanced Science* **2018**, *5* (1), 1700471. https://doi.org/10.1002/advs.201700471.

50. Shi, D.; Adinolfi, V.; Comin, R.; Yuan, M.; Alarousu, E.; Buin, A.; Chen, Y.; Hoogland, S.; Rothenberger, A.; Katsiev, K.; Losovyj, Y.; Zhang, X.; Dowben, P. A.; Mohammed, O. F.; Sargent, E. H.; Bakr, O. M. *Science* **2015**, *347* (6221), 519–522. https://doi.org/10.1126/science.aaa2725.

51. Dong, Q.; Fang, Y.; Shao, Y.; Mulligan, P.; Qiu, J.; Cao, L.; Huang, J. *Science* **2015**, *347* (6225), 967–970. https://doi.org/10.1126/science.aaa5760.

52. Dang, Y.; Ju, D.; Wang, L.; Tao, X. *CrystEngComm* **2016**, *18* (24), 4476–4484. https://doi.org/10.1039/c6ce00655h.

53. Lian, Z.; Yan, Q.; Gao, T.; Ding, J.; Lv, Q.; Ning, C.; Li, Q.; Sun, J. L. *Journal of the American Chemical Society* **2016**, *138* (30), 9409–9412. https://doi.org/10.1021/jacs.6b05683.

54. Lian, Z.; Yan, Q.; Lv, Q.; Wang, Y.; Liu, L.; Zhang, L.; Pan, S.; Li, Q.; Wang, L.; Sun, J. L. *Scientific Reports* **2015**, *5* (May), 1–11. https://doi.org/10.1038/srep16563.

55. Yang, B.; Keum, J.; Ovchinnikova, O. S.; Belianinov, A.; Chen, S.; Du, M. H.; Ivanov, I. N.; Rouleau, C. M.; Geohegan, D. B.; Xiao, K. *Journal of the American Chemical Society* **2016**, *138* (15), 5028–5035. https://doi.org/10.1021/jacs.5b13254.

56. Dang, Y.; Liu, Y.; Sun, Y.; Yuan, D.; Liu, X.; Lu, W.; Liu, G.; Xia, H.; Tao, X. *CrystEngComm* **2015**, *17* (3), 665–670. https://doi.org/10.1039/c4ce02106a.

57. Lemmerer, A. PhD Thesis, Phase transitions and structural motifs of inorganic-organic lead halide hybrids, University of the Witwatersrand, 2007.

58. Jena, A. K.; Kulkarni, A.; Miyasaka, T. *Chemical Reviews* **2019**, *119* (5), 3036–3103. https://doi.org/10.1021/acs.chemrev.8b00539.

59. Kojima, A.; Teshima, K.; Shirai, Y.; Miyasaka, T. *Journal of the American Chemical Society* **2009**, *131* (17), 6050–6051. https://doi.org/10.1021/ja809598r.

60. Miyasaka, T.; Kulkarni, A.; Kim, G. M.; Öz, S.; Jena, A. K. *Advanced Energy Materials* **2020**, *10* (13), 1–20. https://doi.org/10.1002/aenm.201902500.

61. Ikeda, N.; Teshima, K.; Miyasaka, T. *Chemical Communications* **2006**, *1* (16), 1733–1735. https://doi.org/10.1039/b516417f.

62. Kojima, A. *ECS Meeting Abstracts* **2008**, *MA2008-02* (2), 27. https://doi.org/10.1149/ma2008-02/1/27.

63. Im, J. H.; Lee, C. R.; Lee, J. W.; Park, S. W.; Park, N. G. *Nanoscale* **2011**, *3* (10), 4088–4093. https://doi.org/10.1039/c1nr10867k.

64. Snaith, H. J.; Humphry-Baker, R.; Chen, P., Cesar, I.; Zakeeruddin, S. M.; Grätzel, M. *Nanotechnology* **2008**, *19* (42), 424003. https://doi.org/https://doi.org/10.1088/0957-4484/19/42/424003.

65. Snaith, H. J.; Petrozza, A.; Ito, S.; Miura, H.; Graätzel, M. *Advanced Functional Materials* **2009**, *19* (11), 1810–1818. https://doi.org/10.1002/adfm.200801751.

66. Jeon, N. J.; Na, H.; Jung, E. H.; Yang, T. Y.; Lee, Y. G.; Kim, G.; Shin, H. W.; Il Seok, S.; Lee, J.; Seo, J. *Nature Energy* **2018**, *3* (8), 682–689. https://doi.org/10.1038/s41560-018-0200-6.

67. Cousins, S. Solar eclipse: Oxford firm develops world's most efficient PV cell https://www.ribaj.com/products/oxford-firm-develops-world-s-most-efficient-solar-cell (accessed Jun 11, 2021).

68. Shockley, W.; Queisser, H. J. *Journal of Applied Physics* **1961**, *32* (3), 510–519. https://doi.org/10.1063/1.1736034.

69. Huang, J.; Yuan, Y.; Shao, Y.; Yan, Y. *Nature Reviews Materials* **2017**, *2* (7), 17042. https://doi.org/10.1038/natrevmats.2017.42.

70. Ding, J.; Jing, L.; Cheng, X.; Zhao, Y.; Du, S.; Zhan, X.; Cui, H. *Journal of Physical Chemistry Letters* **2018**, *9* (1), 216–221. https://doi.org/10.1021/acs.jpclett.7b03020.

71. Zhang, L.; Liu, Y.; Ye, X.; Han, Q.; Ge, C.; Cui, S.; Guo, Q.; Zheng, X.; Zhai, Z.; Tao, X. *Crystal Growth and Design* **2018**, *18* (11), 6652–6660. https://doi.org/10.1021/acs.cgd.8b00896.

72. Cho, N.; Li, F.; Turedi, B.; Sinatra, L.; Sarmah, S. P.; Parida, M. R.; Saidaminov, M. I.; Murali, B.; Burlakov, V. M.; Goriely, A.; Mohammed, O. F.; Wu, T.; Bakr, O. M. *Nature Communications* **2016**, *7* (May), 1–11. https://doi.org/10.1038/ncomms13407.

73. Rouquerol, J.; Avnir, D.; Fairbridge, C. W.; Everett, D. H.; Haynes, J. M.; Pernicone, N.; Ramsay, J. D. F.; Sing, K. S. W.; Unger, K. K. *Pure and Applied Chemistry* **1994**, *66* (8), 1739–1758. https://doi.org/doi:10.1351/pac199466081739.

74. Kojima, A.; Ikegami, M.; Teshima, K.; Miyasaka, T. *Chemistry Letters* **2012**, *41* (4), 397–399. https://doi.org/10.1246/cl.2012.397.

75. Lee, M. M.; Teuscher, J.; Miyasaka, T.; Murakami, T. N.; Snaith, H. J. *Science* **2012**, *338* (6107), 643–647. https://doi.org/10.1126/science.1228604.

76. Hook, R. J.; Hall, H. E. *Solid State Physics*, Second Ed.; John Wiley & Sons Ltd., 1991.

77. Lewis, L. *Financial Times*. Tokyo November 20, 2006.

78. Green, M. A.; Ho-Baillie, A.; Snaith, H. J. *Nature Photonics* **2014**, *8* (7), 506–514. https://doi.org/10.1038/nphoton.2014.134.

79. Stranks, S. D.; Eperon, G. E.; Grancini, G.; Menelaou, C.; Alcocer, M. J. P.; Leijtens, T.; Herz, L. M.; Petrozza, A.; Snaith, H. J. *Science* **2013**, *342* (6156), 341–344. https://doi.org/10.1126/science.1243982.

80. Bi, Y.; Hutter, E. M.; Fang, Y.; Dong, Q.; Huang, J.; Savenije, T. J. *Journal of Physical Chemistry Letters* **2016**, *7* (5), 923–928. https://doi.org/10.1021/acs.jpclett.6b00269.

81. Chouhan, A. S.; Jasti, N. P.; Hadke, S.; Raghavan, S.; Avasthi, S. *Current Applied Physics* **2017**, *17* (10), 1335–1340. https://doi.org/10.1016/j.cap.2017.07.005.

82. Wehrenfennig, C.; Eperon, G. E.; Johnston, M. B.; Snaith, H. J.; Herz, L. M. *Advanced Materials* **2014**, *26* (10), 1584–1589. https://doi.org/10.1002/adma.201305172.

83. Ponseca, C. S.; Savenije, T. J.; Abdellah, M.; Zheng, K.; Yartsev, A.; Pascher, T.; Harlang, T.; Chabera, P.; Pullerits, T.; Stepanov, A.; Wolf, J. P.; Sundström, V. *Journal of the American Chemical Society* **2014**, *136* (14), 5189–5192. https://doi.org/10.1021/ja412583t.

84. Johnston, M. B.; Herz, L. M. *Accounts of Chemical Research* **2016**, *49* (1), 146–154. https://doi.org/10.1021/acs.accounts.5b00411.

85. De Vos, A. *Journal of Physics D: Applied Physics* **1980**, *13* (5), 839–846. https://doi.org/10.1088/0022-3727/13/5/018.

86. Rühle, S. *Solar Energy* **2016**, *130* (June), 139–147. https://doi.org/10.1016/j.solener.2016.02.015.

87. Reinders, A.; Verlinden, P.; Van Sark, W.; Freundlich, A. *Photovoltaic Solar Energy: From Fundamentals to Applications*, First Ed.; John Wiley & Sons, 2017.

88. Smets, A. H. M.; Jäger, K.; Isabella, O.; Swaaij, R. A.; Zeman, M. *Solar Energy: The Physics and Engineering of Photovoltaic Conversion, Technologies and Systems*, First Ed.; UIT Cambridge, 2015.

89. Jain, A. *Solar Energy Materials and Solar Cells* **2004**, *81* (2), 269–277. https://doi.org/https://doi.org/10.1016/j.solmat.2003.11.018.

90. Suarez, B.; Gonzalez-Pedro, V.; Ripolles, T. S.; Sanchez, R. S.; Otero, L.; Mora-Sero, I. *J. Phys. Chem. Lett.* **2014**, *5* (10), 1628–1635. https://doi.org/10.1021/jz5006797.

91. Eperon, G. E.; Stranks, S. D.; Menelaou, C.; Johnston, M. B.; Herz, L. M.; Snaith, H. J. *Energy and Environmental Science* **2014**, *7* (3), 982–988. https://doi.org/10.1039/c3ee43822h.

92. Hanmandlu, C.; Singh, A.; Boopathi, K. M.; Lai, C.-S.; Chu, C.-W. *Reports on Progress in Physics* **2020**, *83* (8), 86502. https://doi.org/10.1088/1361-6633/ab9f88.

93. Lee, J. H.; Bristowe, N. C.; Lee, J. H.; Lee, S. H.; Bristowe, P. D.; Cheetham, A. K.; Jang, H. M. *Chemistry of Materials* **2016**, *28* (12), 4259–4266. https://doi.org/10.1021/acs.chemmater.6b00968.

94. Lang, L.; Yang, J. H.; Liu, H. R.; Xiang, H. J.; Gong, X. G. *Physics Letters, Section A: General, Atomic and Solid State Physics* **2014**, *378* (3), 290–293. https://doi.org/10.1016/j.physleta.2013.11.018.

95. Meng, X.; Zhang, R.; Fu, Z.; Zhang, Q. *Physical Chemistry Chemical Physics* **2016**, *18* (39), 27358–27365. https://doi.org/10.1039/c6cp03377f.

96. Wilson, J. N.; Frost, J. M.; Wallace, S. K.; Walsh, A. *APL Materials* **2019**, *7* (1), 1811.01832. https://doi.org/10.1063/1.5079633.

97. Becker, M.; Klüner, T.; Wark, M. *Dalton Transactions* **2017**, *46* (11), 3500–3509. https://doi.org/10.1039/c6dt04796c.

98. Eperon, G. E.; Paternò, G. M.; Sutton, R. J.; Zampetti, A.; Haghighirad, A. A.; Cacialli, F.; Snaith, H. J. *Journal of Materials Chemistry A* **2015**, *3* (39), 19688–19695. https://doi.org/10.1039/c5ta06398a.

99. Leguy, A. M. A.; Azarhoosh, P.; Alonso, M. I.; Campoy-Quiles, M.; Weber, O. J.; Yao, J.; Bryant, D.; Weller, M. T.; Nelson, J.; Walsh, A.; Van Schilfgaarde, M.; Barnes, P. R. F. *Nanoscale* **2016**, *8* (12), 6317–6327. https://doi.org/10.1039/c5nr05435d.

100. Stoumpos, C. C.; Malliakas, C. D.; Kanatzidis, M. G. *Inorganic Chemistry* **2013**, *52* (15), 9019–9038. https://doi.org/10.1021/ic401215x.

101. Maculan, G.; Sheikh, A. D.; Abdelhady, A. L.; Saidaminov, M. I.; Haque, M. A.; Murali, B.; Alarousu, E.; Mohammed, O. F.; Wu, T.; Bakr, O. M. *Journal of Physical Chemistry Letters* **2015**, *6* (19), 3781–3786. https://doi.org/10.1021/acs.jpclett.5b01666.

102. Bokdam, M.; Sander, T.; Stroppa, A.; Picozzi, S.; Sarma, D. D.; Franchini, C.; Kresse, G. *Scientific Reports* **2016**, *6* (1), 1–9. https://doi.org/10.1038/srep28618.

103. Whalley, L. D.; Frost, J. M.; Jung, Y. K.; Walsh, A. *Journal of Chemical Physics* **2017**, *146* (22), 220901. https://doi.org/10.1063/1.4984964.

104. Umari, P.; Mosconi, E.; De Angelis, F. *Scientific Reports* **2014**, *4* (1), 1–7. https://doi.org/10.1038/srep04467.

105. Dunlap-Shohl, W. A.; Zhou, Y.; Padture, N. P.; Mitzi, D. B. *Chemical Reviews* **2019**, *119* (5), 3193–3295. https://doi.org/10.1021/acs.chemrev.8b00318.

106. Im, J.-H.; Kim, H.-S.; Park, N.-G. *APL Materials* **2014**, *2* (8), 81510. https://doi.org/10.1063/1.4891275.

107. Liu, J.; Ozaki, M.; Yakumaru, S.; Handa, T.; Nishikubo, R.; Kanemitsu, Y.; Saeki, A.; Murata, Y.; Murdey, R.; Wakamiya, A. *Angewandte Chemie International Edition* **2018**, *57* (40), 13221–13225. https://doi.org/https://doi.org/10.1002/anie.201808385.

108. Huang, F.; Dkhissi, Y.; Huang, W.; Xiao, M.; Benesperi, I.; Rubanov, S.; Zhu, Y.; Lin, X.; Jiang, L.; Zhou, Y.; Gray-Weale, A.; Etheridge, J.; McNeill, C. R.; Caruso, R. A.; Bach, U.; Spiccia, L.; Cheng, Y.-B. *Nano Energy* **2014**, *10* (November), 10–18. https://doi.org/https://doi.org/10.1016/j.nanoen.2014.08.015.

109. Zhou, Y.; Yang, M.; Wu, W.; Vasiliev, A. L.; Zhu, K.; Padture, N. P. *Journal of Materials Chemistry A* **2015**, *3* (15), 8178–8184. https://doi.org/10.1039/C5TA00477B.

110. Mei, A.; Li, X.; Liu, L.; Ku, Z.; Liu, T.; Rong, Y.; Xu, M.; Hu, M.; Chen, J.; Yang, Y.; Grätzel, M.; Han, H. *Science* **2014**, *345* (6194), 295–298. https://doi.org/10.1126/science.1254763.

111. Rong, Y.; Hou, X.; Hu, Y.; Mei, A.; Liu, L.; Wang, P.; Han, H. *Nature Communications* **2017**, *8* (1), 14555. https://doi.org/10.1038/ncomms14555.

112. Liu, M.; Johnston, M. B.; Snaith, H. J. *Nature* **2013**, *501* (7467), 395–398. https://doi.org/10.1038/nature12509.

113. Xiao, Y.; Han, G.; Zhou, H.; Wu, J. *RSC Advances* **2016**, *6* (4), 2778–2784. https://doi.org/10.1039/C5RA23430A.

114. Li, T.; Dunlap-Shohl, W. A.; Han, Q.; Mitzi, D. B. *Chemistry of Materials* **2017**, *29* (15), 6200–6204. https://doi.org/10.1021/acs.chemmater.7b02363.

115. Mitzi, D. B.; Medeiros, D. R.; DeHaven, P. W. *Chemistry of Materials* **2002**, *14* (7), 2839–2841. https://doi.org/10.1021/cm020264f.

116. Marshall, K. P.; Walker, M.; Walton, R. I.; Hatton, R. A. *Nature Energy* **2016**, *1* (12), 16178. https://doi.org/10.1038/nenergy.2016.178.

117. Bansode, U.; Naphade, R.; Game, O.; Agarkar, S.; Ogale, S. *The Journal of Physical Chemistry C* **2015**, *119* (17), 9177–9185. https://doi.org/10.1021/acs.jpcc.5b02561.

118. Pate, R.; Stiff-Roberts, A. D. *Chemical Physics Letters* **2009**, *477* (4), 406–410. https://doi.org/https://doi.org/10.1016/j.cplett.2009.07.038.

119. Laalioui, S.; Alaoui, K. B.; Dads, H. A.; Assali, K. El; Ikken, B.; Outzourhit, A. *Reviews on Advanced Materials Science* **2020**, *59* (1), 10–25. https://doi.org/10.1515/rams-2020-0017.

120. Xiao, L.; Xu, J.; Luan, J.; Zhang, B.; Tan, Z.; Yao, J.; Dai, S. *Organic Electronics* **2017**, *50* (November), 33–42. https://doi.org/10.1016/j.orgel.2017.07.020.

121. Chen, C.-W.; Kang, H.-W.; Hsiao, S.-Y.; Yang, P.-F.; Chiang, K.-M.; Lin, H.-W. *Advanced Materials* **2014**, *26* (38), 6647–6652. https://doi.org/https://doi.org/10.1002/adma.201402461.

122. Vak, D.; Hwang, K.; Faulks, A.; Jung, Y.-S.; Clark, N.; Kim, D.-Y.; Wilson, G. J.; Watkins, S. E. *Advanced Energy Materials* **2015**, *5* (4), 1401539. https://doi.org/https://doi.org/10.1002/aenm.201401539.

123. Hwang, K.; Jung, Y.-S.; Heo, Y.-J.; Scholes, F. H.; Watkins, S. E.; Subbiah, J.; Jones, D. J.; Kim, D.-Y.; Vak, D. *Advanced Materials* **2015**, *27* (7), 1241–1247. https://doi.org/https://doi.org/10.1002/adma.201404598.

124. He, M.; Li, B.; Cui, X.; Jiang, B.; He, Y.; Chen, Y.; O'Neil, D.; Szymanski, P.; EI-Sayed, M. A.; Huang, J.; Lin, Z. *Nature Communications* **2017**, *8* (1), 16045. https://doi.org/10.1038/ncomms16045.

125. Ye, F.; Chen, H.; Xie, F.; Tang, W.; Yin, M.; He, J.; Bi, E.; Wang, Y.; Yang, X.; Han, L. *Energy & Environmental Science* **2016**, *9* (7), 2295–2301. https://doi.org/10.1039/C6EE01411A.

126. Barrows, A. T.; Pearson, A. J.; Kwak, C. K.; Dunbar, A. D. F.; Buckley, A. R.; Lidzey, D. G. *Energy and Environmental Science* **2014**, *7* (9), 2944–2950. https://doi.org/10.1039/c4ee01546k.

127. Assi, M. A.; Hezmee, M. N. M.; Haron, A. W.; Sabri, M. Y. M.; Rajion, M. A. *Veterinary World* **2016**, *9* (6), 660–671. https://doi.org/10.14202/vetworld.2016.660-671.

128. WHO. World Health Organisation https://www.who.int/news-room/fact-sheets/detail/lead-poisoning-and-health.

129. Babayigit, A.; Ethirajan, A.; Muller, M.; Conings, B. *Nature Materials* **2016**, *15* (3), 247–251. https://doi.org/10.1038/nmat4572.

130. Turkevych, I.; Kazaoui, S.; Ito, E.; Urano, T.; Yamada, K.; Tomiyasu, H.; Yamagishi, H.; Kondo, M.; Aramaki, S. *ChemSusChem* **2017**, *10* (19), 3754–3759. https://doi.org/10.1002/cssc.201700980.

131. Hoefler, S. F.; Trimmel, G.; Rath, T. *Monatshefte fur Chemie* **2017**, *148* (5), 795–826. https://doi.org/10.1007/s00706-017-1933-9.

CHAPTER 2

Literature Survey

Chapter 2 provides a literature survey of organic-inorganic metal halide perovskites and their use in solar cells. First, the structural family of $MAPbX_3$ is discussed, and it will be highlighted how the discoveries of Weber lead to hybrid perovskites becoming a field of interest. This leads to the next section, where an overview of the development of PSCs is given. The final section focuses on perovskite materials comprised of alkali metal ions, halide ions and dabconium or piperazinium cations, and literature reports of structures of these compounds since these structures are central to the current investigation.

2.1 Hybrid Lead Halide Perovskites

Most research in hybrid halide perovskites' application as sensitisers in solar cells has focused on using methylammonium with lead and either chloride, bromide, or iodide since these compounds show a tendency to form 3D perovskite structures. This section will provide a brief overview of the highlights of this research, starting with a description of the different phases of the $MAPbX_3$ family and then focussing on how their properties are *fine-tuned* by mixing the halide constituents. Finally, a glimpse into replacing methylammonium with other cations will conclude the section.

2.1.1 The Phases of Single Halide $MAPbX_3$

The first known report of the synthesis of the $MAPbX_3$ perovskite compound was published in 1978 by Weber, who prepared $MAPbI_3$, $MAPbBr_3$ and $MAPbCl_3$.[1] Initially, $MAPbI_3$ was synthesised at a high temperature of 300 °C by melting the components (MAI and PbI_2), thus yielding the cubic phase. The unit cell parameters were determined from the X-ray powder diffraction pattern measured at room temperature, and it was found to crystallise in a cubic phase in space group $Pm\bar{3}m$. However, the first complete structure elucidation of the cubic phase of $MAPbI_3$ only came in 2016, from Luan *et al.*[2]

Further to the work of Weber and Luan *et al.*, two other phases of $MAPbI_3$ have been reported. These include a tetragonal phase, crystallising in space groups *I*4*cm* or *I*4/*mcm*, stable between 160 K and 330 K, and an orthorhombic phase, crystallising in the space group *Pnma* which exists below 160 K.[3,4] Several structural features of the PbI-framework of the different phases of $MAPbI_3$ are shown in Figure 2.1.

The unit cell of each of these phases is illustrated in Figure 2.1 (a), (b) and (c). The specific transition temperatures between the phases are as follows: orthorhombic → tetragonal at 161.4 K and tetragonal → cubic at 330.4 K.[5] These transitions were observed to be first-order transitions and irreversible.[5]

In the cubic phase of $MAPbI_3$, a high disorder has been reported in the organic cation (MA^+), with 24 distinct possible orientations, to satisfy the cubic symmetry.[6] In this phase, the Pb–I–Pb angles are close to 90° or 180°, as illustrated in Figure 2.1 (d) and (g).[2] In its cubic phase, $MAPbI_3$ crystals have facets along the (110), (111), and (100) Miller planes, which are the same for crystals of $MAPbBr_3$ and $MAPbCl_3$.[7,8]

The disorder of the organic cation is decreased in the tetragonal phase (eight disordered MA^+ positions) and decreases further in the orthorhombic phase, where no disorder is observed.[3] The degree of disorder of the organic cation is reported to influence the dielectric permittivity, which affects the material's photovoltaic prospects.[9,10]

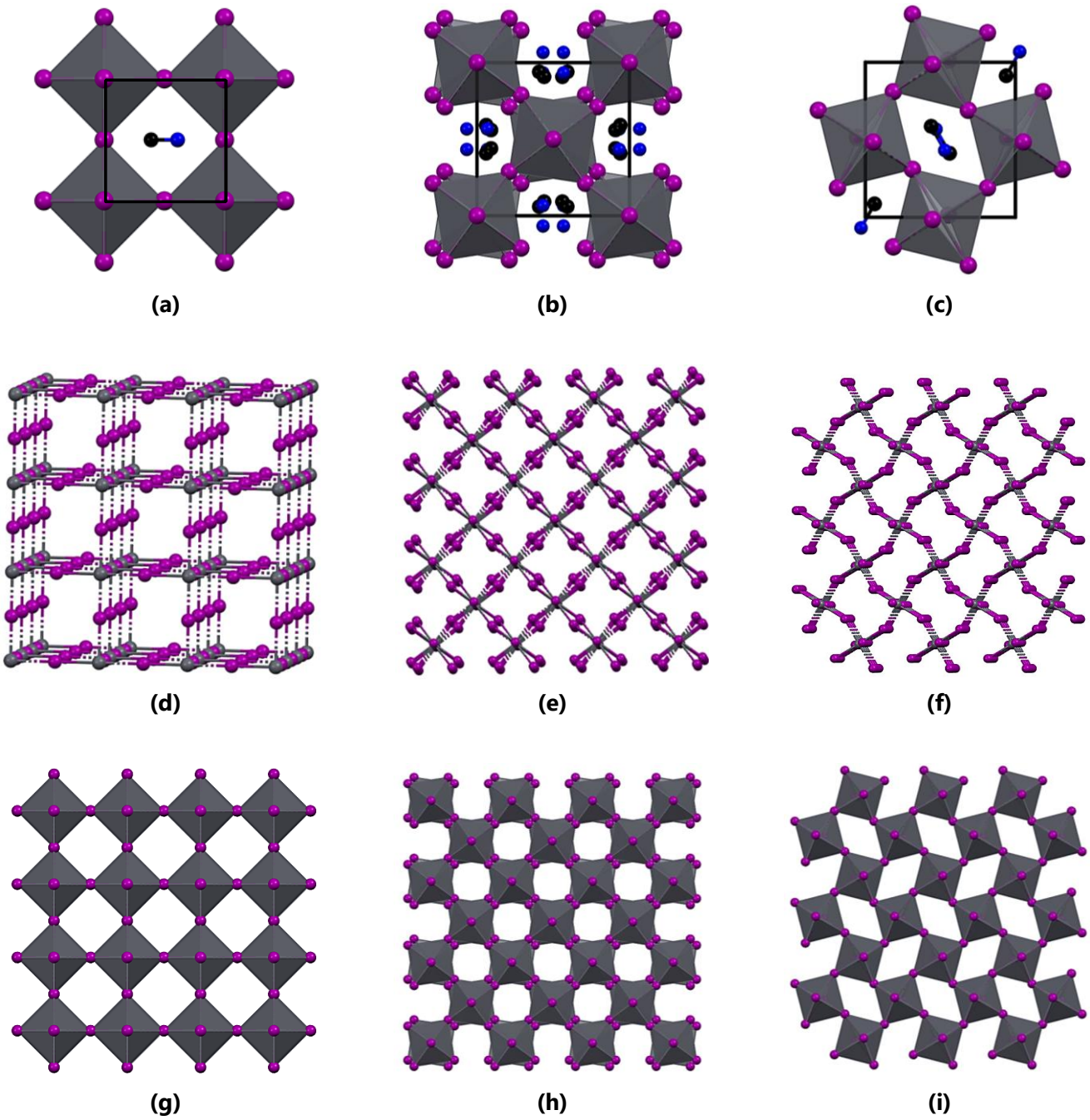

Figure 2.1 The unit cells (shown in black) of $MAPbI_3$ in three different phases. Figure **(a)** shows the cubic phase[2] viewed down the *a*-axis, Figure **(b)** the tetragonal phase[11] viewed down the *c*-axis and Figure **(c)** the orthorhombic phase[12] viewed down the *b*-axis. Hydrogen atoms were omitted for clarity. Figures **(d)**, **(e)** and **(f)** show the ball and stick illustrations of the PbI-frameworks of the cubic, tetragonal, and orthorhombic phases, respectively. Figures **(g)**, **(h)** and **(i)** show the octahedral tilting in the PbI-frameworks of the cubic, tetragonal, and orthorhombic phases, respectively.

The tetragonal phase of $MAPbI_3$ is the most common phase reported in the literature since this is the room temperature phase of the material. Crystals of this phase display natural facets along the (100), (220), and (112) Miller planes.[13] In this structure, the Pb–I–Pb angles in one direction are close to linear, while these angles in the two other directions deviate from linearity. This results in a small degree of octahedral tilting, as illustrated in Figure 2.1 (e) and (h).

In the orthorhombic phase, all the Pb–I–Pb angles deviate from linearity, resulting in significant distortion of the inorganic framework compared to the cubic phase. The large degree of octahedral tilting present in the structure is illustrated in Figure 2.1 (f) and (i).

The powder pattern of the high-temperature phase of $MAPbCl_3$ was first determined by Weber. The chloride analogue has been found in subsequent research to exist in the same phases as $MAPbI_3$. $MAPbCl_3$ has three reported phases, the first of which, a cubic phase[1,14], crystallising in the space group $Pm\bar{3}m$ and stable above 178.8 K. Secondly, a tetragonal phase crystallising in the *P*4/*mmm* space group and stable in the temperature range 172.9 – 178.8 K has been reported.[15,16] Finally, an orthorhombic phase with the space group *Pnma*, stable below 172.9 K is known to exist.[17]

Furthermore, the compound $MAPbBr_3$ displays similar phases as $MAPbI_3$, however, this compound exhibits several phase transitions between cubic[1,18,19] (space groups include $Pm\bar{3}m$, $P\bar{4}3m$ and $Im\bar{3}m$), orthorhombic[20] (space group *Pnma*) and tetragonal[20] (space group *I*4/*mmc*) phases over the temperature range 95 K to 303 K. Importantly, to the knowledge of the author, no literature regarding the temperatures of transitions *between* the cubic phase of $MAPbBr_3$ has been reported.

Table 2.1 summarises the phase transition temperatures and structural data of the three methylammonium lead trihalides, $MAPbCl_3$, $MAPbBr_3$ and $MAPbI_3$. The space groups reported are those most commonly encountered since, for example, the $MAPbBr_3$ cubic phase has been reported in three space groups, however, only one (the most common) is reported in the table.

Table 2.1 Structural data and phase transition temperatures of single halide methylammonium lead trihalides. Taken and adapted from Leijtens *et al.* and Leijtens *et al.*[15,16]

Halide (X)	Temperature (K)	Crystal Phase	Space Group	Lattice Parameters (Å)		
				a	b	c
Cl^-	>178.8	Cubic	$Pm\bar{3}m$	5.675		
	172.9 – 178.8	Tetragonal	*P*4/*mmm*	5.656		5.630
	<172.9	Orthorhombic	$P222_1$	5.673	5.628	11.182
Br^-	>236.9	Cubic	$Pm\bar{3}m$	5.901		
	155.1 – 236.9	Tetragonal	*I*4/*mcm*	8.322		11.832
	149.5 – 155.1	Tetragonal	*P*4/*mmm*	5.894		5.861
	<144.5	Orthorhombic	$Pna2_1$	7.979	8.580	11.849
I^-	>327.4	Cubic	$Pm\bar{3}m$	6.329		
	162.2 – 327.4	Tetragonal	*I*4/*mcm*	8.855		12.659
	<162.2	Orthorhombic	$Pna2_1$	8.861	8.581	12.620

Additionally, no structures with the molecular formula $MAPbF_3$ have been elucidated, at the time of this study. So, to conclude, this section has covered aspects of all the single halide derivatives of $MAPbX_3$. The following sections will focus on analogues containing mixtures of the halide anions Cl^-, Br^- or I^- in combination with the Pb^{2+}-ion and the MA^+-ion. However, first a comment on the cubic phase and its role in perovskite solar cells.

Ideal Phase for Solar Cell Application

The desired phase of $MAPbI_3$ in solar cell applications is the cubic phase due to the almost linear Pb–I–Pb angles (close to 180°) in this phase resulting in optimal orbital overlap, which leads to an important point. A 3D cubic structural dimensionality of a perovskite does not guarantee a so-called **3D electronic dimensionality**.[21]

The electronic dimensionality of a material or structure relates to how the constituents (the ions) of a crystal lattice interact with one another or the lack thereof. For solar cell applications, a 3D electronic dimensionality is required. Firstly, this means that in the BX-framework, the B- and X-ions have good orbital overlap (mostly ensured by a 3D structural dimensionality, typically in the cubic phase). Secondly, both the B- and X-ions atomic orbitals contribute to the valence and conduction bands of the material.[22] This implies that when an electron is excited from the valence band to the conduction band, it does not

have to change its momentum in the process (direct band gap versus indirect band gap), and hence less energy required. Furthermore, since the atomic orbitals of the B- and X-ions contribute to the valence and conduction bands of the structure, the band gap is narrower than it would be for a material in a lower electronic dimensionality.[21]

Hence a 3D structural dimensionality is a prerequisite for a 3D electronic dimensionality allowing for favourable orbital overlap, however, it does not guarantee it. The constituents of the structure still dictate the band gap. A 3D structure is still sought after since the favourable orbital overlap does allow for interesting optoelectronic properties of the material. Therefore, as an initial step, researchers need to find 3D perovskite structures. Once the 3D structure has been obtained, the constituents can be changed, optimised, and the properties further manipulated since perovskite illustrate this remarkable tunability.

2.1.2 Mixed Halide Structures of the $MAPbX_3$ Family

Thus far, only *single halide* $MAPbX_3$ structures and phases have been considered, however, there are three general possibilities for mixed halide structures within the $MAPbX_3$ family. These mixed structures include $MAPbBr_xCl_{3-x}$, $MAPbI_xCl_{3-x}$ and $MAPbI_xBr_{3-x}$, with $0 \leq x \leq 3$. In addition, ternary mixed halide materials containing all three halide ions may be prepared. In Weber's first publication on the $MAPbX_3$ family, three *mixed halide* species were reported, as studied by powder X-ray diffraction, and these included $MAPbBr_{2.3}Cl_{0.7}$, $MAPbI_{0.93}Br_{2.07}$ and $MAPbI_{2.55}Br_{0.45}$.[1] The importance of the ability of the $MAPbX_3$ family to form the mixed halide structure was only realised much later when tuning of the optical band gap and improvement of stability was shown to be possible through the formation of mixed halides of $MAPbX_3$ compared to the single halide compounds.[23]

$MAPbI_xBr_{3-x}$: Mixtures of Iodide and Bromide

By tuning the halide precursors, bromide ions can replace iodide ions in the $MAPbI_3$ lattice to form structures of the form $MAPbI_{3-x}Br_x$, over the complete range of $0 \leq x \leq 3$.[24–27] However, with the ionic radius of the bromide ion (196 pm) smaller than that of iodide (220 pm), bromide has a higher diffusivity in solution and thus dominates the growth kinetics of the crystal.[28,29] Hence, it is expected that if the bromide and iodide precursors are mixed in a 1:1 ratio, the crystal structure will not contain a 1:1 ratio of bromine and iodine ions.[30] Furthermore, when using a mixture of bromide and iodide halides, the complexation of bromide anions with Pb^{2+} is seven (7) times stronger than that of iodide with Pb^{2+}.[31] Hence, careful tuning of the bromide to iodide ratio in precursors is required to ensure that the crystal composition reflects the desired halide ratio.[30] In general, the halides mainly influence the crystal growth rate, where smaller halide ions form stronger coordination bonds thus retarding the crystal growth.[32]

Another factor to consider in the synthesis and crystallisation of Pb^{2+} hybrid perovskites is that the lead ions form complexes with electron-donating solvents and halide ions called halide-plumbate complexes (2-fold or 3-fold coordination). These complexes then react with MA^+-cations, and during solvent evaporation, the larger $MAPbX_3$ unit crystallises.

Overall, to address the aforementioned challenges, one-step solution spin casting allows for the deposition of the perovskite from a mixture of MAX and PbX_2 (X may be either I^- or Br^-) using *N*,*N*'-dimethylformamide (DMF) as the solvent, and has been shown to produce the desired composition.[33,34]

Finally, $MAPbI_{3-x}Br_x$ shows improved thermal and moisture stability compared to pure $MAPbI_3$ at room temperature.[30] The available literature suggests that this is because of the smaller ionic radius of Br^- as compared to I^-. The smaller radius allows the tetragonal phase of $MAPbI_3$ (space group $I4/mcm$) to become cubic (space group $Pm\bar{3}m$) in the $MAPbI_{3-x}Br_x$ structure, improving its stability by allowing for better bonding overlap between metal and halide constituents.[24,33,35,36]

$MAPbI_xCl_{3-x}$: Mixtures of Iodide and Chloride

Similar to the inclusion of bromide ions in the $MAPbI_3$ lattice, replacing a portion of the iodide ions with chloride ions has also received some interest since it aids in tuning the optical band gap of the perovskite material. The substitution of iodide in $MAPbI_3$ by chloride to form $MAPb(I_{1-x}Cl_x)_3$ is achievable by spin-casting a 1:3 molar mixture (at different rates) of $PbCl_2$ and MAI and using DMF as the solvent. Thereafter, the solution is annealed, which produces the mixed halide perovskite film.[37–40]

A treasure chest of properties of $MAPb(I_{1-x}Cl_x)_3$ films may be obtained using different manufacturing processes. For example, in PSCs, a pin-hole free film with a large grain size can be obtained using a heated airflow during spin casting. Moreover, as will be discussed later, solar cell efficiencies of 17.6% are achievable using this film in a PSC device. In addition, several other fabrication techniques have been developed to produce good thin-films for PSCs and include dual-source thermal evaporation,[41] blade coating,[42,43] and spray deposition[44,45], as will be discussed in later sections.

Multi-Halide Mixtures

Ternary mixed halide perovskites, obtained through the introduction of both chloride and bromide into $MAPbI_3$, have not been widely studied, however, these materials do possess 3D perovskite crystal structures, promising broadband light absorption, a wide range of band gaps, increased stability compared to the pure analogues, and improved carrier mobility.[46,47]

In terms of applications to PSCs, Suarez *et al*. tested a $MAPb(Br_xI_{1-x})_{3y}Cl_y$ containing PSC device, which utilised both planar (compact TiO_2) and mesoscopic (Al_2O_3 and TiO_2) architectures.[48] In its synthesis, $PbCl_2$ was mixed with either MAI or MABr in a 1:3 molar ratio followed by stoichiometric mixing of I- and Br-based binary precursor solutions. This lead to PSC devices with efficiencies reaching 12.5%, suggesting the viability of using ternary mixed halide MA perovskites in devices for further investigation.[48]

2.1.3 Replacing Methylammonium in $MAPbX_3$

In Chapter 1, the Goldschmidt tolerance factor[49], octahedral factor[50] and improved version of the tolerance factor[51] were introduced to predict the compatibility of the A-, B- and X-ions to produce a 3D perovskite structure. It turns out that methylammonium is not *the most suitable* A-cation for the combination $APbX_3$, but an alternative, formamidinium (FA^+), is more suited. Table 2.2 lists the Goldschmidt tolerance factor (t), the octahedral factor (μ) and the improved tolerance factor suggested by Bartel *et al*. (τ) for the combinations of $MAPbX_3$ and $FAPbX_3$. From the listed values, it is evident that the FA^+-cation is more suited in all three cases (its t-values are closer than one and τ-values are further away from the boundary edge allowed for 3D perovskite ($\tau < 4.18$)) than the MA^+-cation in combination with PbX, where X = Cl^-, Br^- or I^-.

Table 2.2 The Goldschmidt tolerance factors (t), octahedral factors (μ) and the improved tolerance factors (τ) for the perovskite of combination $APbX_3$, where A and X are listed in the table. Shannon crystal radii were used.[52]

	Cl^-			Br^-			I^-		
	t	τ	μ	t	τ	μ	t	τ	μ
MA^+	0.82	3.6	0.80	0.79	3.7	0.73	0.73	3.9	0.65
FA^+	0.91	3.2		0.87	3.3		0.81	3.5	

Of course, other organic cations may also potentially fit into the cavity created by the 3D cubic PbX-framework. Theoretically, several organic cations are suitable to replace MA^+ in the $MAPbX_3$ structural family.[53] These A-site cations include ammonium, hydrazinium, hydroxylammonium, formamidinium, guanidinium, azetidinium, dimethylammonium,

ethylammonium, azetamidinium, tetramethylammonium, imidazolium, trimethylammonium, isopropylammonium, pyrrolidinium, isobutylammonium, diethylammonium and phenylammonium. Figure 2.2 shows the ball and stick representation of the structures of these potential A-site cations, with methylammonium included to allow for the comparison of the shapes and sizes of the cations.

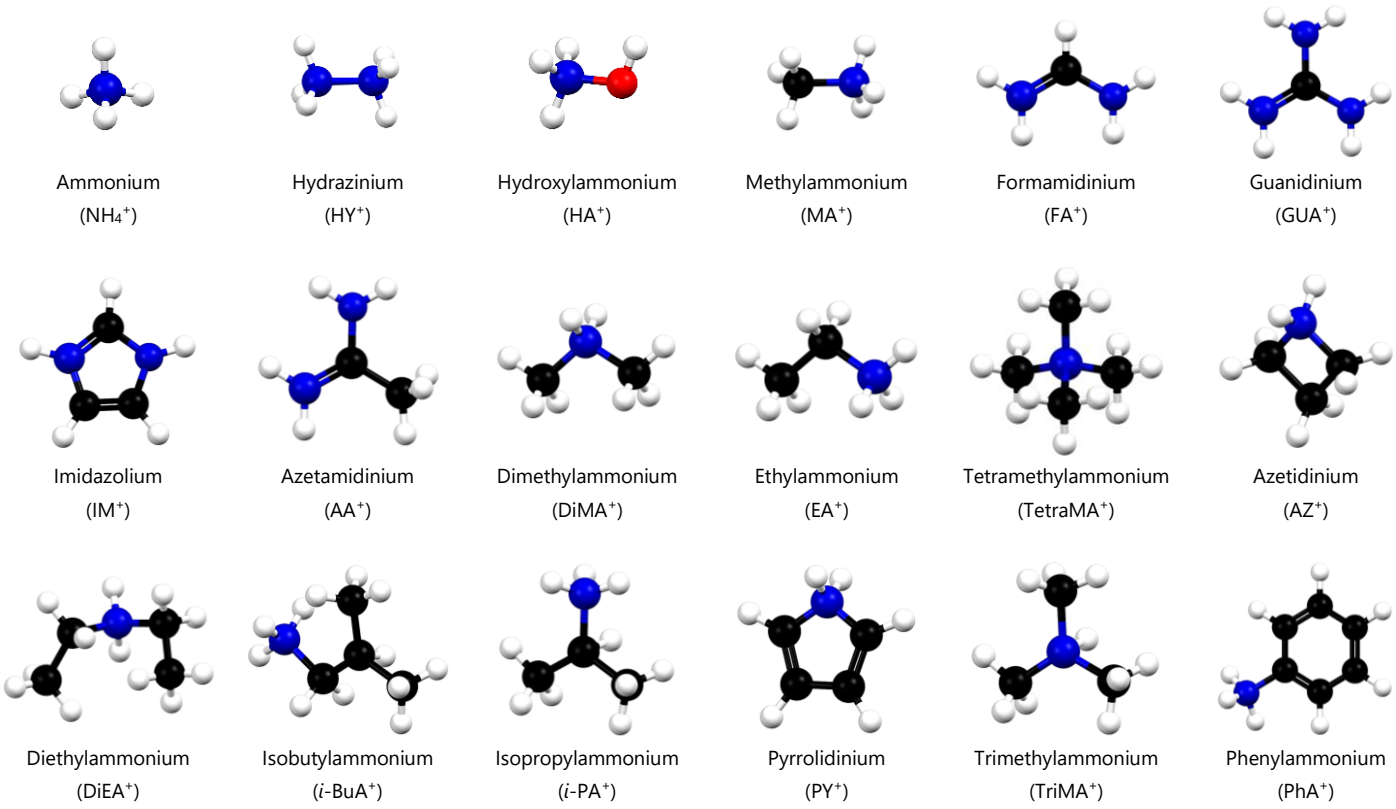

Figure 2.2 Ball and stick representations of different options of organic cations (A-site cations), which could theoretically be combined with PbX_3 to form 3D cubic perovskites of the form $APbX_3$. Methylammonium is shown for size comparison. Nitrogen atoms are shown in dark blue, oxygen in red, carbon in black and hydrogen in white.

Much focus has been placed on the use of $FAPbI_3$-type perovskites in PSCs, and hence a better understanding of the structure and properties of these perovskites is relevant. Therefore, this is the next topic of discussion.

2.1.4 Formamidinium Lead Trihalides

The compounds $FAPbI_3$, $FAPbBr_3$ and $FAPbCl_3$, have all been successfully synthesised and their structures determined. The $FAPbI_3$ compound can crystallise in two structure types, both with the same chemical formula, hence the structures are polymorphs. The two structure types have different crystal systems and dimensionalities. The first is a 1D ABX_3-type structure[54] in the hexagonal phase (space group $P6_3/mmc$) and the second structure type is a 3D perovskite, of which several phases have been reported. The cubic phases include two room-temperature cubic phases[55,56] (space groups $Pm\bar{3}m$ and $P\bar{4}3m$), two trigonal phases[54], one formed at room temperature (space group $P3m1$) and another formed at 150 K (space group $P3$). Figure 2.3 illustrates the trigonal, cubic, and hexagonal phases in (a) and (b), (c) and (d) and (e) and (f), respectively.

Furthermore, the $FAPbBr_3$ compound has been found to crystallise in four different phases, all of the 3D cubic perovskite structure type, namely a room temperature cubic phase[57] (space group $Pm\bar{3}m$), a tetragonal phase[58] stable at 175 K (space group $P4/mbm$), and two phases at 100 K, which include a trigonal phase[59] (space group $R\bar{3}$) and an orthorhombic phase[58]

(space group *Pnma*). Lastly, the $FAPbCl_3$ compound has two known 3D phases, which include a room temperature cubic phase (space group $Pm\bar{3}m$) and an orthorhombic (space group *Cmcm*) phase stable at 200 K.[59]

The compound $FAPbI_3$ can be crystallised in one of two phases *via* solution assisted methods. The 3D cubic α-phase (or so-called black phase, space group *P*3*m*1) is photochemically active and ideal for PV application, however, the 1D hexagonal perovskite phase (yellow phase or δ-phase, space group $P6_3/mmc$) is not due to its much wider band gap (> 2 eV).[60] The structures of the 3D cubic and 1D hexagonal phases are shown in Figure 2.3. The 3D cubic phase could degrade into the 1D hexagonal phase, which is the primary concern in $FAPbI_3$ PSCs.[61] That said, options on how to address this inherent instability will be discussed later.

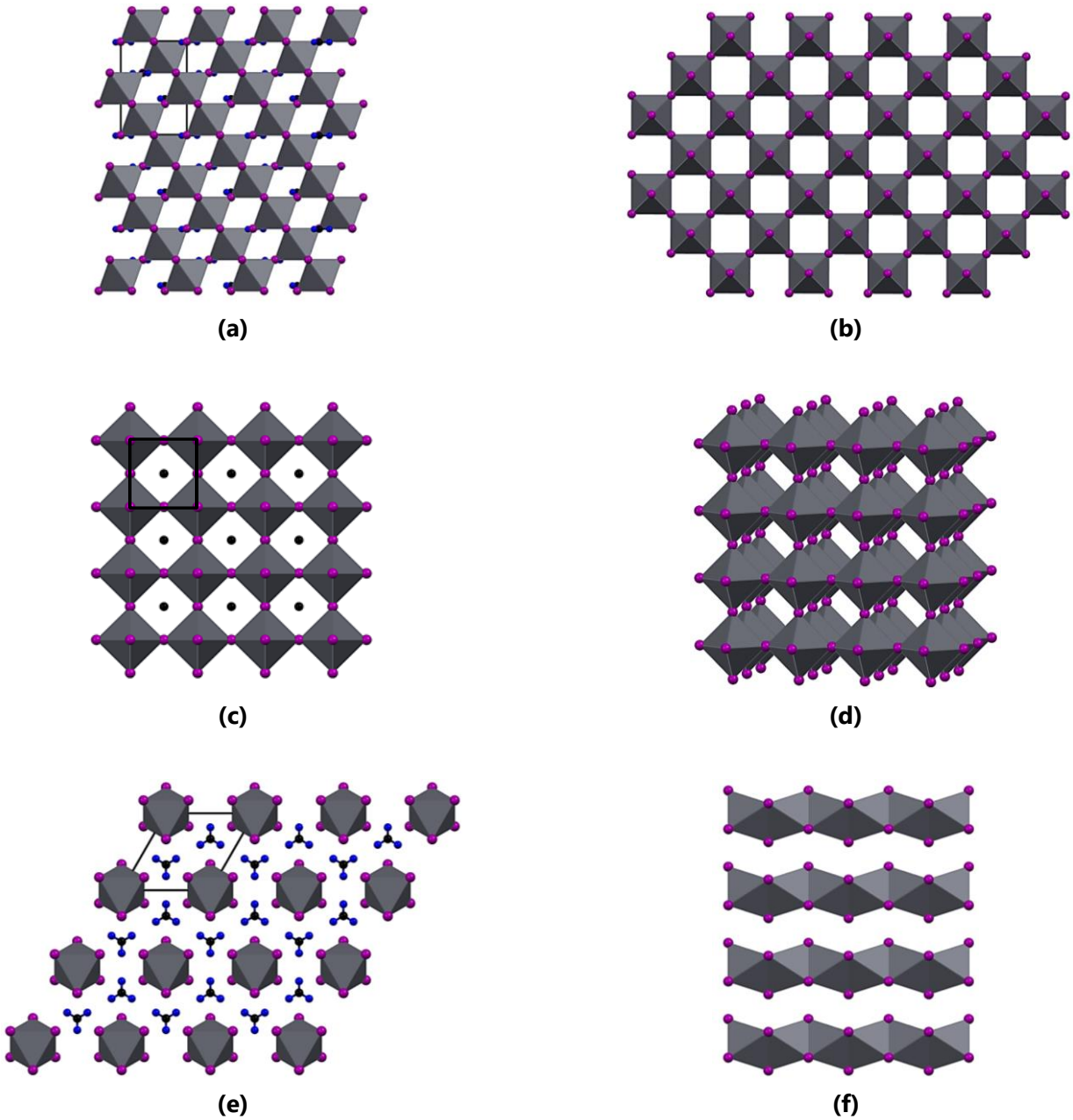

Figure 2.3 The 3×3 expansion of the 3D α-phase (trigonal space group *P*3*m*1)[54] unit cell of $FAPbI_3$. Figure **(a)** $FAPbI_3$ as viewed down the *a*-axis and Figure **(b)** only the PbI_6 octahedra of cubic $FAPbI_3$. Figure **(c)** and **(d)** shows the 3×3 expansion of the 3D α-phase (cubic space group $Pm\bar{3}m$)[62] with (viewed down the *a*-axis) and without the organic cation (FA^+), respectively. The 3×3 expansion of the unit cell of the 1D ABX_3-type perovskite (hexagonal δ-phase)[54] of $FAPbI_3$ as viewed down **(e)** the *c*-axis (disorder in the FA^+-cations make them appear as GUA^+) and **(f)** the *b*-axis (only the PbI_6 octahedra shown). Hydrogen atoms are omitted for clarity. The unit cells are shown in black.

Much debate surrounds the space group of the cubic $FAPbI_3$ phase. The space group *P*3*m*1, as determined by SCXRD, suggests a trigonal phase for the 3D structure, however, neutron diffraction indicates a cubic phase with $Pm\bar{3}m$ symmetry and a lattice constant of 6.3620(8) Å for 3D $FAPbI_3$, hence the cubic nomenclature.[55] Accordingly, at room temperature, the black 3D cubic phase consists of a $[PbI_6]^{4-}$ perovskite framework with disordered FA^+-cations occupying the cavities in the framework, as shown in Figure 2.3 (c) and (d).[62]

Furthermore, the 3D cubic phase is the structure with the higher electronic conductivity of the two (versus the 1D hexagonal phase) due to the higher degree of orbital overlap between Pb^{2+} and I^- in the framework, therefore, making it the *superior* candidate for PV applications.[54] The structures of $FAPbBr_3$ and $FAPbCl_3$ are also 3D cubic perovskites and hence also may have applications in PSCs.

2.1.5 Decomposition of Perovskites

Perovskite structures are known for their instability towards moisture and heat, and hence degradation of the perovskite structure will play a significant role in their application to PV technology.[6] Therefore, this section considers the possible degradation pathways and effects of degradation on the perovskite material.

Thermal Degradation

$MAPbI_3$ has been determined to decompose into two products, namely MAI and PbI_2, when exposed to thermal stress.[6] That said, the specific degradation pathway of $MAPbI_3$ ($CH_3NH_3PbI_3$) is still a topic of discussion, however, what is clear is that the loss of MAI (CH_3NH_3I) is followed by the formation of PbI_2, as stated before. This degradation could occur either *via* sublimation into gases or *via* a chemical reaction. The currently accepted model, suggested by Juarez-Perez *et al.*, argues that the initial step in the thermal degradation (under an inert atmosphere) proceeds as shown in Equations (2.1) and (2.2)[63]

$$CH_3NH_3PbI_3 \xrightarrow{\Delta} NH_3 + CH_3I + PbI_2 \tag{2.1}$$

$$CH_3NH_3I \xrightarrow{\Delta} NH_3 + CH_3I \tag{2.2}$$

Equation (2.1) shows the degradation of $MAPbI_3$, and Equation (2.2) shows the degradation of MAI, neither of which are desirable since they affect the performance of the PSC and lead to environmentally hazardous products.[64]

In addition, $FAPbI_3$ has been shown to degrade at a similar rate in moisture as $MAPbI_3$, however, it is more stable towards thermal stress.[65,66] Furthermore, $FAPbI_3$ exhibits better photostability than $MAPbI_3$.[54,60] That said, claims to the opposite can also be found in the literature.[60,62] These contradictory reports on stability might stem from the deposition methods and conditions used since the crystal structure of perovskite is *extremely* sensitive to its synthetic conditions.[67] The morphology, grain size, crystallisation, optical and electronic properties, and stability can all be affected by synthetic conditions.

Moisture Degradation

Perovskites readily degrade in the presence of moisture since water molecules can bind *via* hydrogen bonding to the perovskite constituents to form hydrated compounds. The degradation is initially contained *locally*, shown in Equation (2.3), and as such, the perovskite can regenerate since the process is reversible.[68]

$$4\ CH_3NH_3PbI_3 + 4\ H_2O \rightleftharpoons 4\ [CH_3NH_3PbI_3 \cdot H_2O] \rightleftharpoons (CH_3NH_3)_4PbI_6 \cdot 2H_2O + 3PbI_2 + 2\ H_2O \tag{2.3}$$

However, further ingression of water causes irreversible degradation of the perovskite to PbI_2 and other compounds, as shown in Equation (2.4)

$$(CH_3NH_3)_4PbI_6{\cdot}2H_2O \longrightarrow 4\ CH_3NH_3I + PbI_2 + 2\ H_2O \tag{2.4}$$

Fortunately, the perovskite can be protected from moisture through encapsulation or the use of non-hygroscopic layers between the perovskite and HTL in PSC devices.[21]

Encapsulation entails placing the device in a glass box (or equivalent methods of protection) and controlling the conditions inside the box, protecting the device from moisture and specific molecules.[21] Thermal stress can also be limited to a certain degree with encapsulation.

Other Degradation Pathways

A degradation pathway that is of more concern than thermal and moisture degradation is the degradation of perovskite in a combination of *air* (the presence of O_2) and visible light. The suggested degradation mechanism is through a so-called superoxide radical ($O_2^{\bullet-}$), whereby a photoexcited perovskite material (indicated by *) transfers an electron to molecular oxygen on the surface of the material.[21] The superoxide radical then deprotonates the organic cation (for example, MA^+). The full mechanism is given in Equations (2.5) through (2.7)[69]

$$CH_3NH_3PbI_3 \xrightarrow{\text{Light, no moisture}} [CH_3NH_3PbI_3]^* \tag{2.5}$$

$$O_2 \xrightarrow{[CH_3NH_3PbI_3]^*} O_2^{\bullet-} \tag{2.6}$$

$$CH_3NH_3PbI_3 + O_2^{\bullet-} \longrightarrow CH_3NH_2 + PbI_2 + \frac{1}{2}I_2 + H_2O \tag{2.7}$$

Therefore, less acidic A-cations could lead to enhanced stability, since then, the final step of the mechanism will be rate determining and lead to extended periods of stability.[21] Additionally, the use of encapsulation of the PSC device under an inert atmosphere (preferably argon since N_2 does also cause degradation similarly to O_2) could also enhance the stability of the perovskite layer. The instability towards light can only be addressed intrinsically by optimising the perovskite components, however, encapsulation will already minimise the degradation of the perovskite layer.[21]

Degradation Consequences on Optical Properties

The response of the optical band gap, and hence energy levels of $MAPbI_3$, to temperature variations, has been studied with photoluminescence (PL) spectroscopy.[70] With an increase in temperature (from 25 °C to 85 °C), the valence band maximum (VBM) and conduction band minimum (CBM) levels were both reduced, by 110×10^{-3} eV and 77×10^{-3}eV, respectively. Hence, the band gap of $MAPbI_3$ increased by 33×10^{-3} eV with the studied temperature increase. This also shows that with an increase in lattice volume, a widening of the band gap is expected. Hence, the efficiency of solar cell devices would be influenced by temperature since devices often operate above room temperature conditions.

In fact, by using temperature-dependent steady-state PL spectroscopy and time-resolved lifetime decay measurements, a study done on $MAPbI_{3-x}Cl_x$ perovskite solar cells showed an electrical and optical degradation beyond temperatures of 70 °C. When the devices were cooled back down, their efficiency was lower than before heating occurred.[71] This suggests that an irreversible optical degradation took place, which is not ideal for PV technology.

In general, as expected, any form of degradation of the perovskite layer leads to an increase in the optical band gap of perovskite materials.[21]

2.2 Lead-Based Perovskite Solar Cells

Up to now, the perovskite structure as a pure crystallographic entity has been discussed, and its application to optoelectronics has been suggested. The following section forms the first of two sections that will cover perovskites' application in photovoltaic technology.

Solar technology is one of the most important technologies humankind has to generate energy with. It is predicted that a 400 km by 400 km solar farm, with only 25% efficiency, in the Sahara Desert, could satisfy the world's energy demands.[72] Table 2.3 lists the advantages and disadvantages of different photovoltaic technologies, which shows a strong indication that the third generation of PV technology (specifically PSCs) represents an improvement on the current technology (first- and second-generation).

Table 2.3 The advantages and disadvantages of the different generations of photovoltaic technologies. Adapted from Ng *et al*.[73] Primary authors are acknowledged and referenced in the Author column (*et al*. is implied).

Generation	Examples	Advantages	Disadvantages	Author
First	Crystalline Silicon (c-Si) Multi-crystalline Silicon	High efficiency Abundant raw materials Ruggedness Non-toxic	Opacity Long energy payback time High cost Low working capability in shaded areas	Fakharuddin[72]
Second	Cadmium-Telluride (CdTe) Copper-Indium-Gallium-Selenide (CIGS) Amorphous Silicon (a-Si:H)	Abundant raw materials Rigid or flexible	Lower efficiency (7 – 10% for commercial modules versus 15 – 21% for crystalline silicon modules)	Meillaud[74]
Third	Dye Sensitised Solar Cells (DSSC) Perovskite Solar Cells (PSCs)	Workable under low light conditions Transparent Flexible Low-cost fabrication	Short term outdoor stability Thermal stability issues and instability towards illumination	Fakharuddin[72]

In Figure 2.4, a chart of the National Renewable Energy Laboratory's highest certified solar cell efficiencies from 1976 to 2021 is shown.[75] The PSC curve is to the far right of the chart, in red circles, filled in yellow. This illustrates the sudden and sharp rise in PCE for PSCs and why it is deemed the future's PV technology.

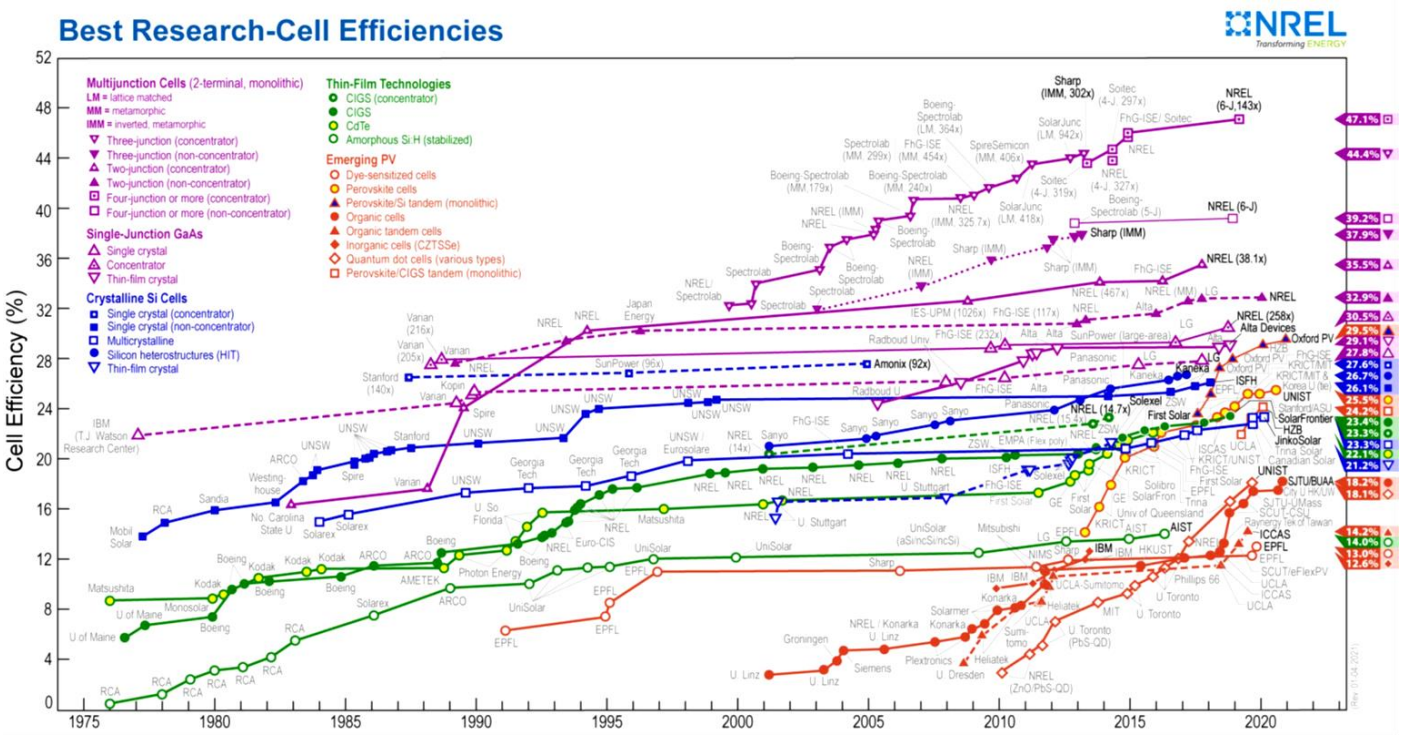

Figure 2.4 National Renewable Energy Laboratory's Official 2021 chart of the highest confirmed conversion efficiencies for solar cell research from 1976 to the present. Reproduced with permission.[75] Copyright 2021, National Renewable Energy Laboratory, Golden, CO, USA.

Furthermore, the comparatively simple fabrication methods of perovskite materials, at relatively low temperatures, compared to those of standard industrial processes, combined with their Energy Payback Time (EPBT) of a few months[76] (compared to the 1.5 to 4.4 years for crystalline silicon solar panels[77]), have placed them firmly as one of the leading materials of importance in the fourth industrial revolution (so-called "Green Revolution") and also for potential use in other optoelectronic applications including lasers, LEDs and photodetectors.[78]

Currently, the device architecture of choice for PSCs is a planar heterojunction (devised by Snaith *et al.*[79]), which employs a solid perovskite absorber layer in conjunction with electron and hole transport contacts on either side (see Chapter 1). The preference of the planar heterojunction over the mesoporous TiO_2 device architecture is due to the fact that the heterojunction can be fabricated at much lower temperatures (<150 °C versus 400 °C) and hence holds certain manufacturing cost benefits.[80]

The fabrication of high-quality perovskite films is achieved *via* film deposition techniques, such as one-step spin coating[81,82] or two-step sequential solution deposition[83,84] and even modern techniques such as inkjet printing fabrication,[85,86] as discussed in Chapter 1. A high-quality film is paramount for high-efficiency devices. Several factors may be varied in obtaining good film morphology, including the optimisation of solvents used for processing[87], optimising the annealing temperature,[88] using certain additives,[89] employing solvent engineering systems[90,91], and the annealing of any solvent used[92,93].

This section will be divided into four different subsections. The first two focus on methylammonium and formamidinium lead trihalide PSCs, followed by a third covering other potential lead-based PSCs and a preceding section on the stability issues encountered with PSCs. The final subsection suggests methods for further stability enhancements. The A-cations MA^+ and FA^+ have formed the basis for $APbX_3$ PSCs. All subsequent research on the topic uses them either in combination with other cations and anions or with each other, giving rise to the layout employed here. But first, a justification in terms of sustainability for perovskite solar cell technology is made.

2.2.1 Sustainability in PSCs

The entire life cycle of any device in commercial use needs to be sustainable for it to be viable to be used on a global scale. Hence, a thorough understanding of how the raw materials are obtained or synthesised, how the device is manufactured, how the device is disassembled after use and what materials are left behind after breakdown is required to determine whether a product is sustainable.[94] Figure 2.5 (a) provides a schematic illustration of the life cycle of a photovoltaic device.

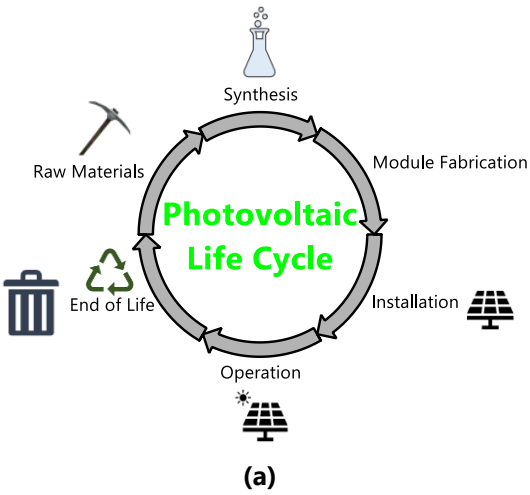

(a)

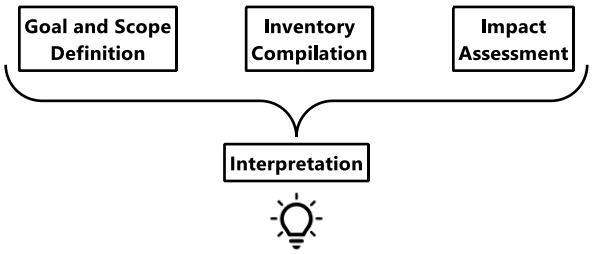

(b)

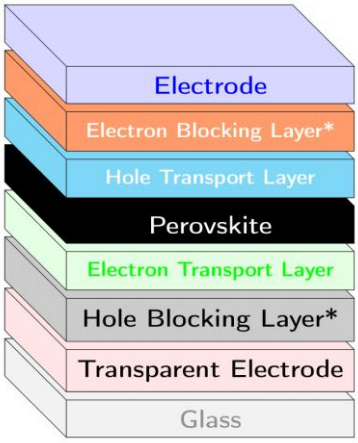

(c)

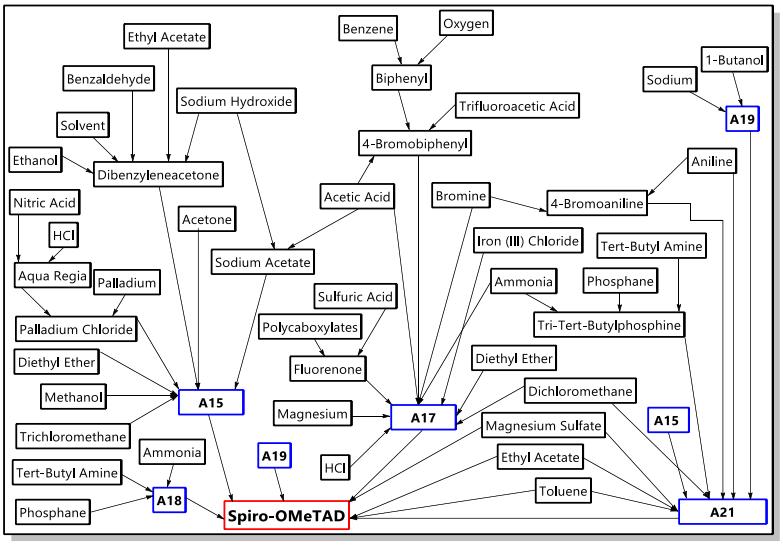

(d)

Figure 2.5 (a) The life cycle of a photovoltaic device, from synthesis to end-of-life recycling. Adapted from Goetz *et al.*[94] **(b)** Schematic representation of a general life cycle assessment workflow, **(c)** a generic PSC module, layers indicated with an asterisk (*) are frequently omitted, and **(d)** the synthetic pathway of the HTM Spiro-OMeTAD, illustrating the large number of materials required for its synthesis. Adapted from Espinosa *et al.*[95]

Sustainability is difficult to quantise hence tools such as life cycle assessments (LCAs) may provide insight into the impact of potential devices, in conjunction with experiments, which studies the direct potential benefit of the device in question. These studies can then compare an emerging device type (like PSCs) to the current industry leaders in PV technology, the silicon solar cell. Figure 2.5 (b) provides a schematic of how an LCA assessment is conducted, and Figure 2.5 (c) provides a schematic of the typical layers of a PSC as considered in most of the literature. Finally, Figure 2.5 (d) provides, as an example, the life cycle impact (LCI) of Spiro-OMeTAD, used in certain PSCs as the HTL and what raw materials are required for its synthesis. The LCI is then considered in the LCA of the device in question.[95]

Due to the short life span of PSCs, even though their efficiencies match or even exceed those of current commercial devices, their LCAs, even with a generous lifespan of five years, are not competitive with other, more established PV technologies, which could have a lifespan of up to 30 years.[96]

Recycling Perovskite Modules

How electronic devices are disposed of or recycled serves as an indicator of their impact on the environment. Moreover, the disposal of electronic devices is not as *everyday* as the disposal or recycling of household items. The subject was considered by Kadro and Hagfeldt, who investigated what the 30-year lifespan of current PV technology could mean for the future.[94] Their research estimates that 10% of all global e-waste (60 000 000 tons) will consist of PV modules by the end of 2050.[97] Hence, the use of recyclable materials in PSCs is still an open topic of discussion.

Though recycling is helpful in that there is a waste reduction, the recycling process itself may be contributing to the problem. One example of this is the recycling of PSCs through the use of organic solvents, and unfortunately, these solvents do contribute to the depletion of the ozone layer.[94] Hence, the process of recycling also needs to be considered in the LCA.

Poll *et al*. suggested using deep eutectic solvents to recycle PSC cells instead of commonly used organic solvents, such as DMF.[98] Several other studies have begun to look at other green alternatives[99–101]. Furthermore, for the case where organic solvents must be used, the environmentally friendly lead absorber, Fe-decorated hydroxyapatite (HAP, $Ca_{10}(PO_4)_6(OH)_2$), has been proposed for the removal of lead from non-aqueous solvents such as DMF.[102] This latter method can reduce lead traces to 15 parts per billion and aid in recycling PSCs. Specifically, the removal of PbI_2 has a reported yield of 99.97%, which bodes well for the commercialisation of PSCs.

Therefore, the literature suggests that valuable raw materials can be recycled from PSC devices. Hence, *new* electronic devices can again be constructed from the recycled material, using relatively simple solution chemistry to do so while having a low environmental impact. However, the economic viability of these recycling methods still needs to be investigated, and subsequent improvement will be required before PSCs can become commercially available. That said, these questions should not stand in the way of furthering the work done on PSCs.

2.2.2 Lead-Halide PSCs

Methylammonium lead iodide ($MAPbI_3$) was the first perovskite compound used in solar cell technology, as described in the work done by Miyasaka and Teshima.[103] The device used a nanocrystalline absorbent perovskite layer, and the device itself had an architecture based on that of a dye sensitised solar cell (DSSC).[103–105] Initial efficiencies reached 3.8%, which allowed for the field of PSCs to be further developed. The best efficiency obtained to date for a single halide $MAPbI_3$ solar cell device is in excess of 20%.[106]

$MAPbI_3$ possesses a direct band gap and allows for *p*-to-*p* transitions between the conduction and valence bands of the material. The lone pair of electrons is located in the *s*-orbital of the lead ion, allowing high optical absorption coefficients in the region 10^5 cm^{-1}.[107] These favourable properties prompted the enthusiasm surrounding the use of lead halide perovskites as solar cell absorber materials.

Later, variations on $MAPbI_3$ were also employed in solar cell technology. For example, the methylammonium ion was replaced with other similar cations, lead ions would ultimately be replaced, and mixed halide compositions were investigated. These modifications are the subject of discussion in the following sections.

Pure Methylammonium Lead Trihalide PSCs

In this section, an overview of the use of $MAPbX_3$ compounds, where X is *only* one of Cl^-, Br^- or I^-, in PSCs. All three compounds $MAPbI_3$, $MAPbBr_3$ and $MAPbCl_3$, are regarded as intrinsic semiconductor materials, meaning that the material's properties are determined by the number of charge carriers (electrons and holes).[108] Therefore, the carrier mobility of the entire material is similar to that of the holes and the electrons, classifying these materials as ambipolar semiconductors.[109–111]

They all possess direct optical band gaps of approximately 1.48 eV to 1.6 eV for $MAPbI_3$, 2.14 eV to 2.26 eV for $MAPbBr_3$ and 2.76 eV to 2.94 eV for $MAPbCl_3$.[112,113] Hence, a direct correlation exists between the specific halide anion employed and the optical band gap. On switching between different halide compositions with methylammonium and lead, a definite correlation is observed between the constituents' low band gap and size compatibility. Additionally, higher binding energies of valence electrons are observed in Cl (4*p*) versus Br (5*p*) versus I (6*p*), which leads to the following trend observed for the band gap[112,113]

$$E_g^{I} \sim 1.6 \text{ eV} < E_g^{Br} \sim 2.2 \text{ eV} < E_g^{Cl} \sim 2.9 \text{ eV},$$

with the more favourable band gap being that of $MAPbI_3$, since it is closest to the ideal band gap of 1.1 eV, suggested by the Shockley–Queisser theory.[114] As discussed earlier, the major benefit of using these materials for optoelectronic applications is that their base materials are cost-effective and abundant. A specific and interesting example (not to be considered in any detail here) is the use of hybrid trihalide perovskites in window glass, where a semi-transparent PV technology is used to generate power, showing the wide scope for PSC technology.[115,116]

Structure defects and ion migration in perovskite materials have been studied theoretically.[117] These studies suggest that MA^+ should be substituted with less-mobile, less-polar, and less-acidic cations (FA^+ or Cs^+ for example). By doing so, slower ion migration and, therefore, more stable PSCs would potentially be obtained.[117] However, ion migration is an unavoidable consequence of placing a PSC under illumination or a voltage bias. Only the extent of the migration can be altered, and this is done by reducing defects in the grain boundaries of the perovskite layer.[118]

Mixed Methylammonium Lead Trihalide PSCs

One of the main concerns with perovskite materials and their application to solar cells is their instability towards thermal stress and moisture. One method of addressing this concern is by adopting a mixed compositional approach to synthesise the perovskite material. Mixtures of A-cation, B-cation and X-anion, and all subsequent permutations improve stability compared to pure perovskite materials. In this section, A-cation and X-anion mixtures will be considered. The topic of mixed B-site materials, or so-called "Lead-Less Perovskite", is discussed in Section 2.4.

Table 2.4 provides the experimentally measured band gap values for $MAPb(I_{1-x}Br_x)_3$ materials as determined by Tu *et al*.[119] They found that the band gap of $MAPb(I_{1-x}Br_x)_3$ materials can be calculated using the empirical relationship shown in Equation (2.8)

$$E_g(x) = E_g(MAPbI_3) + [E_g(MAPbBr_3) - E_g(MAPbI_3) - b]x + bx^2 \quad (2.8)$$

where x is the Br^- composition and b is the bowing parameter.[46,120] Typically, b is small, ranging between 0.30 and 0.34, indicating the immiscibility observed between Br^- and I^- in the perovskite lattice.[27,46] In contrast, when chloride is used, the band gap tunability is quite limited, and the band gap varies between 1.54 eV and 1.59 eV, whereas when bromide is used (see Table 2.4), the band gap varies between 1.57 to 1.73 eV.[121] From Table 2.4, it can be concluded that the optimal concentration of bromide in $MAPbI_{3-x}Br_x$ is 4.67%, which can deliver a PCE value of 18.02%. The lowest PCE value is obtained for $MAPbI_2Br$ (3.83%), however, in work done by Cao *et al*. on $MAPbI_2Br$, this value was improved to 11.03% using a dropping method for fabrication and no HTM.[122]

Table 2.4 Band gap and photovoltaic parameters of PSC devices, using $MAPbI_{3-x}Br_x$ as the absorber layer and spiro-OMeTAD as the HTM, fabricated through spin coating. Adapted from Tu *et al.*[119]

$MAPbI_{3-x}Br_x$	Band gap (eV)	V_{OC} (V)	J_{SC} (mA·cm^{-2})	FF	PCE (%)
x = 0	1.565	1.016	22.92	0.67	15.60
x = 0.09	1.579	1.026	23.04	0.69	16.31
x = 0.11	1.585	1.052	23.08	0.69	16.75
x = 0.14	1.591	1.064	23.52	0.72	18.02
x = 0.20	1.597	1.065	22.95	0.70	17.11
x = 1	1.725	0.827	7.72	0.60	3.83

Several other studies have been conducted on the mixed halide perovskite $MAPbX_{3-x}Y_x$ in PSCs, of which the results of a select few are given in Table 2.5. These studies show that in general, using bromide, as opposed to chloride, in combination with iodide, provides a PCE with a value of 18.02% (Table 2.4), compared to 8.30% for chloride (Table 2.5), suggesting the match between iodide and bromide is better in the $MAPbX_{3-x}Y_x$ structure than that of iodide and chloride.

That said, optimally matching the perovskite layer's band gap with the band gap of the other materials in the PSC device also contributes to higher PCE values, as can be inferred from Table 2.5. Several PCE values for devices employing $MAPbI_3$ have been reported depending on the device architecture. For example, a value of 15.83% is attainable for combining $MAPbI_3$/$MAPbI_2Br$, where $MAPbI_2Br$ acts as the HTM, showing the best PCE for any of the combinations listed in Table 2.5. Other notable architectures listed in Table 2.5 are TiO_2/$MAPbI_3$/CuI/Au and TiO_2/$MAPbI_3$/Au, delivering a PCE of 13.53% and 11.94%, respectively. Here, an HTM (CuI) addition gives an improved PCE value, showing the importance of this layer in a PSC.

Table 2.5 Photovoltaic performances of single and mixed halide MA-lead-based PSCs, prepared using different materials, conditions and device architectures. Adapted from Ng *et al.*[73] Either FTO or ITO was used as the glass substrates. Primary authors are acknowledged in the Author column (*et al.* implied).[a]

Perovskite Material	Device Architecture	HTM	PCE (%)	Author
$MAPbI_3$/$MAPbI_2Br$	TiO_2/$MAPbI_3$/$MAPbI_2Br$/Au	$MAPbI_2Br$	15.83	Zhang[123]
$MAPbI_3$/$CsPbI_{3-x}Br_x$	TiO_2/$MAPbI_3$/$CsPbI_{3-x}Br_x$/MoO_3/Au	$CsPbI_{3-x}Br_x$	11.33	Li[124]
$MAPbI_2Br$	TiO_2/Al_2O_3/$MAPbI_2Br$/carbon	N/A	11.03	Cao[122]
$MAPbI_3$	TiO_2/$MAPbI_3$/Au	N/A	11.94	Zhang[123]
$MAPbI_3$	TiO_2/$MAPbI_3$/CuI/Au	CuI	13.53	Zhang[123]
$MAPbI_3$	TiO_2/$MAPbI_3$/CuI/graphite	CuI	7.5	Sepalage[125]
$MAPbI_3$	Cu_2O/$MAPbI_3$/PCBM	Cu_2O	8.23	Chatterjee[126]
$MAPbI_{3-x}Cl_x$	Cu_2O/$MAPbI_{3-x}Cl_x$/PCBM/Al	Cu_2O	8.30	Chatterjee[126]
$MAPbI_3$	TiO_2/$MAPbI_3$/Au	N/A	10.49	Shi[127]
$MAPbI_3$	TiO_2/$MAPbI_3$/Au	N/A	8.0	Laban[128]

[a] **FTO** = Fluorine-Doped Tin Oxide, **ITO** = Indium Tin Oxide, **PCBM** = Phenyl-C_{61}-butyric acid methyl ester

Other possibilities for using mixed halide $MAPbX_{3-x}Y_x$ compounds exist and have been extensively studied, as listed in Table 2.6.

Table 2.6 Summary of the photovoltaic properties of methylammonium-lead-mixed-halide PSCs, with the device architecture and the deposition method employed indicated. Taken and adapted from Zarick *et al.*[30] Primary authors are acknowledged in the Author column (*et al.* implied).[a]

Perovskite (P)		Device Architecture	Technique	J_{SC} (mA·cm^{-2})	V_{OC} (V)	FF	PCE (%)	Author
$MAPb(I_{0.94}Br_{0.06})_3$		FTO/c-TiO_2/mp-TiO_2/**P**/PTAA/Au	Spin deposition	19.3	0.91	0.70	12.3	Noh[24]
$MAPb(I_{0.89}Br_{0.11})_3$		FTO/c-TiO_2/**P**/spiro-OMeTAD/Au		22.62	1.02	0.73	16.9	Zhou[129]
$MAPb(I_{0.88}Br_{0.12})_3$		FTO/c-TiO_2/**P**/spiro-OMeTAD/Au		13.89	0.89	0.65	8.13	Kulkarni[130]
$MAPbI_{2.86}Br_{0.14}$		FTO/c-TiO_2/mp-TiO_2/**P**/spiro-OMeTAD/Au		23.52	1.06	0.72	18.02	Tu[119]
$MAPb(I_{1-x}Br_x)_3$	x = 0	FTO/c-TiO_2/Al_2O_3/**P**/carbon	Dripping of PbI_2 and dipping in MAI and MABr	18.52	0.92	0.70	11.94	Cao[131]
	x = 0.1			18.98	1.01	0.71	13.49	
	x = 0.2			16.56	1.02	0.70	11.83	
$MAPbI_{2.4}Br_{0.6}$		FTO/c-TiO_2/**P**/spiro-OMeTAD/Au	Spin deposition	18.26	1.09	0.61	12.10	He[35]
		FTO/c-TiO_2/mp-TiO_2/**P**/spiro-OMeTAD/Au		22.92	1.11	0.74	18.94	Kim[132]
		ITO/PEDOT:PSS/**P**/PCBM/C_{60}/BCP/Al		17.5	1.02	0.74	13.1	Bi[25]
$MAPbI_2Br$		FTO/c-TiO_2/mp-TiO_2/Al_2O_3/**P**/carbon	Dripping of PbI_2 and dipping in MABr	15.37	1.04	0.69	11.03	Cao[122]
		FTO/c-TiO_2/**P**/spiro-OMeTAD/Au	Spin deposition	12.12	0.96	0.59	6.84	Cui[26]
$MAPbI_{3-x}Br_x$	x = 0.5	ITO/PTAA/**P**/PBCM/C_{60}/BCP/Al		18.3	1.16	0.78	16.6	Hu[133]
	x = 0.8			15.8	1.21	0.78	14.9	
$MAPb(I_{1-x}Br_x)_3$		FTO/PEDOT:PSS/**P**/PBCM/BCP/Al		20.8	0.87	0.74	13.35	Chai[134]
		FTO/c-TiO_2/mp-TiO_2/**P**/PTAA/Au		19.5	1.09	0.76	16.2	Jeon[91]
		FTO/NiO/**P**/PCBM/bis-C_{60}/Ag		21.67	1.10	0.74	17.64	Xiao[135]
$MAPbI_{3-x-y}Br_yCl_x$	y = 0	FTO/PEDOT:PSS/**P**/PCBM/Al	1-Step deposition of MAI, $PbCl_2$ and $PbBr_2$	19.84	0.87	0.70	12.11	Jeong[136]
	y = 0.05			20.38	0.96	0.70	13.7	
	y = 0.1			21.72	1.01	0.73	16.04	
	y = 0.15			19.77	0.98	0.71	13.8	

Table 2.6 (Continued) Summary of the photovoltaic properties of methylammonium-lead-mixed-halide PSCs, with the device architecture and the deposition method employed indicated. Taken and adapted from Zarick *et al.*[30] Primary authors are acknowledged in the Author column (*et al.* implied).[a]

Perovskite (P)		Device Architecture	Technique	J_{SC} (mA·cm^{-2})	V_{OC} (V)	FF	PCE (%)	Author
$MAPbI_{3-x-y}Br_xCl_y$	x = 0, y = 0.072	FTO/c-TiO_2/mp-TiO_2/**P**/spiro-OMeTAD/Au	1-Step deposition	18.2	0.73	0.46	6.17	Suzuki[47]
	x = 0.090, y = 0			15.5	0.74	0.49	5.56	
	x = 0.091, y = 0.078			16.2	0.74	0.58	7.00	
$MAPbX_{3-y}Cl_y$	X = I	FTO/c-TiO_2/mp-TiO_2/**P**/spiro-OMeTAD/Au	1-Step deposition	15.78	0.97	0.71	10.9	Suarez[48]
	$X = I_{0.75}Br_{0.25}$		Spin deposition	12.97	1.09	0.68	9.1	
$MAPbX_{3-y}Cl_y$	X = I	FTO/c-TiO_2/Al_2O_3/**P**/spiro-OMeTAD/Au		19.63	1.02	0.63	12.5	
	$X = I_{0.5}Br_{0.5}$		1-Step deposition	10.23	1.08	0.40	4.5	
$MAPbI_{2.7}Br_{0.3}Cl_x$		FTO/c-TiO_2/Al_2O_3/**P**/spiro-OMeTAD/Au	1-Step deposition	20.8	1.02	0.67	14.2	Park[137]
$MAPb(Br_{1-x}Cl_x)_3$		FTO/c-TiO_2/**P**/CBP/Au	Spin deposition	7.8	1.24	0.56	5.4	Tidhar[138]
$MAPb(I_{1-x}Cl_x)_3$		FTO/c-TiO_2/C_{60}/**P**/spiro-OMeTAD/Au		22.0	0.98	0.75	16.3	Xioa[139]
$MAPb(I_{1-x}Br_x)_3$		FTO/c-TiO_2/C_{60}/**P**/spiro-OMeTAD/Au	Spin coating	21.6	0.95	0.67	13.7	
$MAPb(I_{1-x}Cl_x)_3$	Without Cl	ITO/PEDOT:PSS/**P**/PCBM/rhodamine/Ag	1-Step deposition	19.79	0.84	0.73	12.23	Khatiwada[140]
	With Cl			15.46	0.92	0.61	8.97	
$MAPb(I_{1-x}Cl_x)_3$		FTO/PEDOT:PSS/**P**/PCBM/Al	1-Step hot casting	22.4	0.94	0.83	18.0	Nie[141]
		ITO/PEDOT:PSS/**P**/C_{60}/BCP/Ag	2-Step deposition	17.8	1.11	0.73	14.5	Li[121]
		ITO/PEDOT:PSS/**P**/PCBM/bis-C_{60}/Ag	Blade coating	15.4	0.92	0.66	9.29	Kim[42]
		FTO/PEDOT:PSS/**P**/PCBM/bis-C_{60}/Ag	1-Step deposition	17.5	0.92	0.73	11.8	Liang[142]
		ITO/PEDOT:PSS/**P**/PCBM/Ag		19.33	0.92	0.75	13.2	Xie[143]
				12.43	0.57	0.81	5.74	Cronin[144]
		ITO/PEDOT:PSS/**P**/PCBM/Ca/Al	Blade coating	16.91	0.87	0.69	10.15	Back[43]
				16.8	0.92	0.72	11.1	Barrows[45]
				19.58	0.99	0.78	15.12	Chen[37]
		ITO/PEDOT:PSS/**P**/PCBM/C_{60}/BCP/Al	Spin coating	20.71	0.97	0.80	16.01	Dong[145]
		FTO/NiO_x/**P**/PCBM/PEI/Ag	Hot casting spin coating	21.2	1.09	0.79	18.2	Liao[146]

Table 2.6 (Continued) Summary of the photovoltaic properties of methylammonium-lead-mixed-halide PSCs, with the device architecture and the deposition method employed indicated. Taken and adapted from Zarick *et al.*[30] Primary authors are acknowledged in the Author column (*et al.* implied).[a]

Perovskite (P)	Device Architecture	Technique	J_{SC} (mA·cm^{-2})	V_{OC} (V)	FF	PCE (%)	Author
$MAPb(I_{1-x}Cl_x)_3$	ITO/PEDOT:PSS/**P**/PCBMZnO/Al	1-Step deposition	22.0	1.03	0.74	16.8	Zhang[147]
			17.07	0.94	0.67	10.59	McLeod[148]
	FTO/c-TiO_2/**P**/PTAA/Au	Spin deposition	20.1	1.05	0.74	15.6	Song[149]
	FTO/c-TiO_2/mp-TiO_2/**P**/P3HT/Au		23.79	0.99	0.58	13.73	Rapsomanikis[150]
	ITO/**P**/C_{60}/BPhen/Al	Co-evaporation	12.5	0.82	0.60	6.1	Ng[151]
	ITO/TiO_2/**P**/spiro-OMeTAD/Ag	Spin deposition	21.45	1.08	0.78	17.91	Chen[152]
	FTO/c-TiO_2/mp-TiO_2/**P**/spiro-OMeTAD/Ag		20.41	0.88	0.68	12.27	Wang[153]
	FTO/c-TiO_2/mp-TiO_2/**P**/spiro-OMeTAD		18.37	0.94	0.68	11.66	Dualeh[154]
	FTO/c-TiO_2mp-TiO_2/**P**/spiro-OMeTAD/PEDOT:PSS		19.48	1.13	0.69	15.2	Jiang[155]
	FTO/c-TiO_2/**P**/spiro-OMeTAD/Au		N/A	N/A	N/A	10.3	Grill[156]
			17.9	0.97	0.70	12.2	Stranks[157]
			20.3	0.89	0.64	11.4	Eperon[88]
			22.58	0.91	0.51	10.49	Jiang[158]
			22.9	0.98	0.69	14.82	Docampo[159]
	ITO/PEIE/c-Y-TiO_2/**P**/spiro-OMeTAD/Au		22.80	1.07	0.67	16.5	Zhou[160]
	FTO/c-TiO_2/**P**/spiro-OMeTAD/Ag	Dual-source vapour deposition	21.5	1.07	0.68	15.4	Liu[41]
		Spin deposition	20.36	1.02	0.58	12.10	Zhao[161]
			23.7	1.08	0.74	19.0	Song[162]

[a] **FTO** = Fluorine-Doped Tin Oxide, **ITO** = Indium Tin Oxide, **c-TiO_2** = Compact TiO_2, **mp-TiO_2** = Mesoporous TiO_2, **PTAA** = Poly(bis(4-phenyl)(2,4,6-trimethylphenyl)amine), **spiro-OMeTAD** = 2,2′,7,7′-tetrakis(*N*,*N*′-di-p-methoxyphenyl-amine)9,9′-spirobifluorene, **PEDOT:PSS** = Poly(3,4-ethylenedioxythiophene)-poly(styrenesulfonate), **PCBM** = Phenyl-C_{61}-butyric acid methyl ester, **BCP** = Bathocuproine (2,9-Dimethyl-4,7-diphenyl-1,10-phenanthroline), **PTAA** = Poly (triaryl amine) (Poly[bis(4-phenyl)(2,4,6-trimethylphenyl)amine]), **P3HT** = poly(3-hexylthiophene-2,5-diyl), **BPhen** = 4,7-Diphenyl-1,10-phenanthroline, **PEIE** = Polyethyleneimine, **c-*y*-TiO_2** = Compact Brookite TiO_2

2.2.3 Formamidinium Lead Trihalide PSCs

The size advantage of the FA^+-ion compared to the MA^+-ion allows for a tolerance factor closer to 1 when used in combination with lead iodide, and hence higher symmetry, since the dual-ammonia groups in the FA^+-cation ensures that the A-cation is less mobile due to more hydrogen bonding interactions and subsequently the structure is more stable. This means that $FAPbI_3$ has a lower band gap value than $MAPbI_3$.[163] Moreover, the band gap of $FAPbI_3$ lies between 1.43–1.47 eV compared to a value of between 1.48 eV and 1.60 eV for $MAPbI_3$.[54,163–165] Experimentally, single crystals of $FAPbI_3$ illustrate a band gap of 1.4 eV, which is slightly lower than that of thin-films of the same compound.[166] This suggests it is better practice to measure optical band gaps of perovskites in the form they will be used in PSCs rather than as they are used for XRD analysis. Whereas $MAPbI_3$ decomposes into VOCs (volatile organic compounds) and PbI_2, $FAPbI_3$ undergoes an unfavourable phase transition from the α- or 3D cubic perovskite phase to the δ- or 1D hexagonal perovskite phase. The δ-phase has a significantly wider band gap than the α-phase and inferior charge-transport properties since it possesses face-sharing PbI_6 octahedra, which results in reduced orbital overlap compared to the 3D cubic perovskite phase.[167] This makes the δ-phase undesirable for PV applications. However, when considering light-emitting applications (like LEDs), the δ-phase is the desired phase.[168]

With research indicating $MAPbI_3$ as being the so-called "best option" in the series of $MAPbI_3$, $MAPbBr_3$ and $MAPbI_3$, most research on formamidinium-lead-based PSCs considered $FAPbI_3$ and how to improve its stability and band gap by enhancing the stability of the perovskite layer in PSCs, and when this is done higher PCE values are automatically obtained. Therefore, this section on FA-lead-based PSCs is split into two sections, both focussing on stability enhancement, namely "Stability Improvement through A-cation and X-Halide Mixtures" and "Stability Improvement through Device Fabrication". In the first section, general and specific examples are discussed, and in the latter, devices reported to date which employs both stabilisation strategies are summarised in Table 2.7 through Table 2.12.

Stability Improvement through A-cation and X-Halide Mixtures

Early reports of FA-based lead PSCs showed low PCEs, mainly because the optically active 3D cubic perovskite phase of $FAPbI_3$ degrades to the inactive 1D hexagonal perovskite phase during use. Since the tolerance factor of $FAPbI_3$ is so close to 1, the initial strategies to stabilise the 3D cubic perovskite phase included the incorporation of Cs^+-ions into the A-site or Br^--ions into the X-site.[169] This strategy of using A- and X-site mixtures has been successfully employed for both single crystals and thin-films.[169–171] In fact, improved stability at ambient conditions have been observed for the partial substitution of FA^+-ions with MA^+-ions[172] and Cs^+-ions.[173]

A-Site Mixtures. A-site mixtures have received much attention in FA-lead-based PSCs. Binary (MAFA, CsFA), ternary (CsFAMA, RbFAMA), and quaternary (RbCsFAMA) cation-containing perovskites have been synthesised thus far.[61] These strategies based on using mixtures attempt to achieve phase stability, wide-ranged spectral absorption, optimised film morphology, low defect density with high charge mobilities, and low recombination losses.[61]

As a specific example, a stable cubic phase is observed for $FA_xMA_{1-x}PbI_3$, with $0.2 \leq x \leq 0.9$, while a tetragonal phase is observed when $x < 0.2$, meaning low MA^+-ion content.[174] In addition, longer carrier lifetimes than for $FAPbI_3$ was observed for $FA_xMA_{1-x}PbI_3$.[175] Additionally, in $FA_xMA_{1-x}PbI_{3-3x}Br_{3x}$ single crystals, the charge carrier lifetime is nearly 20 times that of pure $FAPbI_3$ single crystals.[176] Improved phase stability is possible using ternary A-site mixtures, which are mixtures of Cs^+-, FA^+-, and MA^+-ions, opening the door to a multitude of new possibilities.[177] Furthermore, for the perovskite, $FA_{0.7}MA_{0.3}PbI_3$, PSCs fabricated using it as the absorber layer showed improved stability compared to both $FAPbI_3$ and $MAPbI_3$. These stability tests were conducted at ambient conditions (50–60% humidity) and without encapsulation.[178]

Another possible A-site cation component showing potential for improved stability, though larger than MA^+ or Cs^+ with FA^+, is phenylethylammonium (PEA^+). In pure combination with lead iodide, thus as the compound PEA_2PbI_4, a 2D perovskite

with superior moisture stability compared to $FAPbI_3$ is formed.[179] In combination with FA-lead-based perovskites, the PEA^+ cation results in a quasi-3D structure, where the hydrophobic PEA^+ crystallises on or near the grain boundaries and thereby improves the ambient stability of the perovskite.[179] Furthermore, by adding PEA^+, improved phase stability is observed for 3D $FAPbI_3$.[179] Lastly, the addition of PEA^+ cations ($FA_xPEA_{1-x}PbI_3$) leads to additional stabilisation of device performance (90% initial PCE after 16 days at 40% RH (relative humidity)), compared to pure $FAPbI_3$, which under the same conditions degrades to a PCE of zero.[179] Similar to the enhanced stability seen when using PEA^+, MA–FA–Cs perovskites have increased stability when trifluoroethyl ammonium ($TFEA^+$) cations are incorporated.[180]

X-Site Mixtures. Considering X-site mixtures, one specific example focusses on the mobility of $FAPbI_{3-x}Br_x$, which was found to be lower than that of both $FAPbI_3$ and $FAPbBr_3$, which is in contrast to what is seen for A-site mixtures.[181] However, the introduction of Br does improve the phase stability upon moisture exposure, whereas the benefits seen with Cs are dependent on the amount of Cs introduced.[182] Therefore, a mixture of both A- and X-sites might have a synergic effect. Unfortunately, film compositions of $Cs_xFA_{1-x}PbI_{3-y}Br_y$ do not show good phase stability at high humidity (77%), and they are not inert towards moisture.[182] This is supported by studies on $FAPbI_3$(Cl)-based devices showing that they also undergo a colour change and hence a phase change under ambient conditions within 30 hours, while $FA_{0.9}Cs_{0.1}PbI_3$(Cl)-based devices remain dark, however, they also exhibit a decline in the efficiency of 45% under the same conditions.[183] This does vote well for compositional engineering to aid in increasing the stability of PSCs, however, it does not yet compare to the general benefits seen with encapsulation.[61]

That said, the mixed composition perovskites do show additional stability towards thermal stress and continuous illumination.[184,185] The perovskite $FA_{0.83}Cs_{0.17}Pb(I_{0.6}Br_{0.4})_3$ is stable for nearly 600 hours under constant illumination, without being encapsulated.[185] When the device was encapsulated, however, stability of over 3400 hours was obtained.[185] In further scrutinisation of mixed FA-lead-based PSCs, studies have been completed on their outdoor stability and performance.[186] PSCs with an active layer composed of $(FAPbI_3)_{0.85}(MAPbBr_3)_{0.15}$ showed outdoor stability for over 1000 hours (in Spain, Barcelona during their winter months).[186] In the autumn/winter months in Turin, Italy, further positive results were obtained for $FA_xMA_{1-x}PbI_{3-y}Br_y$ devices, when the PSC was encapsulated with a photocurable fluoropolymer device stability was achieved for 90 days, thus roughly 2100 hours.[187] Table 2.7 gives a summary of the most notable FA-lead-based PSCs fabricated to date. Other FA-lead-based PSCs are discussed in the following section.

Stability Improvement through Device Fabrication

The phase transition (α-phase to δ-phase) of $FAPbI_3$ is retarded when a mesoporous device architecture is used, like mp-TiO_2, compared to when a planar option is utilised, for example, c-TiO_2, with mp indicating mesoporous and c indicating compact. Currently, the accepted explanation for this observation is the rise in activation energy for phase transitioning in the mesoporous device, due to the increased interfacial area with TiO_2 in a mesoporous structure, along with the partial encapsulation of $FAPbI_3$ by TiO_2.[188] This explains the observed stability of $FAPbI_3$ mesoporous devices [65] in contrast to the lower stability observed in $MAPbI_3$ planar devices[60]. As mentioned before in the discussion of perovskite stability, high-quality perovskite films enable high efficiencies in PSCs. The most common methods to obtain perovskite films will be discussed next.[61]

Solution Processing. Solution processing can be executed in both a one-step[189] or two-step[178,190,191] process. In the one-step method, spin coating of a mixture of organic halide (FAI) and metal salt (BI_2) in a solvent (pure solvent or solvent mixture) takes place.[192] The initial step may be followed by an anti-solvent method as well. In the two-step method, the metal salt (BI_2) is placed on the rest of the device architecture, and then an organic halide, in solution, is dropped onto the metal salt layer, followed by drying and annealing.[192] For a mixed composition system (FA-MA), variations of the two-step method are employed. A mixture of the organic precursors follows the coating of the inorganic precursor.[178] Alternatively, one organic precursor can be applied (FA-perovskite first) and then the second organic precursor (MA-perovskite) to form the mixed FA–MA perovskite.[191]

Table 2.7 Summary of the photovoltaic properties of mixed A-cation site lead-based PSCs manufactured using spin deposition, with their device architecture. Taken and adapted from Zarick *et al.*[30] Primary authors are acknowledged in the Author column (*et al.* is implied). [a]

Perovskite (P)	Device Architecture	J_{SC} (mA·cm^{-2})	V_{OC} (V)	FF	PCE (%)	Author
$FA_xPEA_{1-x}PbI_3$	ITO/NiO_x/**P**/PCBM/bis-C_{60}/Ag	22.08	1.04	0.771	17.71	Li[179]
$FA_{0.75}MA_{0.25}PbI_3$	FTO/c-TiO_2/mp-TiO_2/**P**/spiro-OMeTAD/Ag	21.10	1.03	0.714	15.51	Ji[193]
$FA_{0.83}Cs_{0.17}Pb(I_{0.6}Br_{0.4})_3$	FTO/PCBM/**P**/spiro-OMeTAD/Ag	19.4	1.2	0.751	17.1	McKeekin[170]
$MA_{0.80}FA_{0.20}PbI_{3-y}Cl_y$	ITO/PEDOT:PSS/**P**/PCBM/C_{60}/LiF/Ag	21.55	1.10	0.75	17.45	Isikgor[194]
$K_xCs_{0.05}(FA_{0.85}MA_{0.15})_{0.95}Pb(I_{0.85}Br_{0.15})_3$	FTO/SnO_2/**P**/spiro-OMeTAD/Al	22.57	1.13	0.78	19.86	Yang[195]
$Cs_{0.10}FA_{0.90}Pb(I_{0.83}Br_{0.17})_3$	FTO/c-TiO_2/mp-TiO_2/**P**/spiro-OMeTAD/Au	22.69	1.13	0.748	19.20	Saliba[177]
$Cs_{0.20}FA_{0.80}PbI_{2.84}Br_{0.16}$		21.9	1.07	0.742	17.35	Yi[173]
$(MAPbI_3)_{0.9}(CsPbBr_3)_{0.1}$		20.9	1.07	0.71	15.9	Niu[196]
$FA_{2/3}MA_{1/3}PbI_{2.5}Br_{0.5}$		23.7	1.14	0.76	20.7	Jesper[197]
$(FAPbI_3)_{0.85}(MAPbBr_3)_{0.15}$		21	1.01	0.69	14.5	Reyna[186]
$MA_xFA_{1-x}PbI_3$		23.9	0.99	0.66	15.6	Thakur[198]
$MA_xFA_{1-x}Pb(I_{1-y}Br_y)_3$		24.6	1.16	0.73	20.8	Rong[199]

[a] **FTO** = Fluorine-Doped Tin Oxide, **ITO** = Indium Tin Oxide, **c-TiO_2** = Compact TiO_2, **mp-TiO_2** = Mesoporous TiO_2, **spiro-OMeTAD** = 2,2′,7,7′-tetrakis(*N*,*N*′-di-p-methoxyphenyl-amine)9,9′-spirobifluorene, **PEDOT:PSS** = Poly(3,4-ethylenedioxythiophene)-poly(styrenesulfonate), **PCBM** = Phenyl-C_{61}-butyric acid methyl ester

Of course, the main challenge with any processing method is to obtain smooth, continuous, and pinhole-free perovskite films for use in the PSC. In addition, with any FA-based PSCs, the added challenge of removing the δ-phase by-products also exists. Several approaches (using additives or different precursors) have been devised to address this challenge (see Table 2.8). These additives or other precursors are used to aid in selectively forming a specific phase of the FA-based perovskite by changing the solubility of particular species or promoting crystallisation *via* molecular exchange reactions.[61]

Table 2.8 Efficiencies of FA-lead-based PSCs fabricated using additives, precursors, and solvent engineering. Taken and adapted from Li *et al.*[61] Primary authors are acknowledged in the Author column (*et al.* is implied). [a]

Perovskite	Additives or Precursor	PCE (%)	Author
$FAPbI_3$	HI	14.2	Eperon[65]
	Cl^-	12.7	Xu[200]
	FACl	13.7	Wang[201]
	CN^-	16.53	Wei[189]
	SCN^-	11.44	Yang[202]
	Thiourea	19.7	Lee[203]
$FA_{0.8}Cs_{0.2}PbI_3$	$Pb(SCN)_2$	19.57	Yu[204]
$FA_{0.7}MA_{0.2}Cs_{0.1}Pb(I_{5/6}Br_{1/6})_{3-x}(SCN)_x$	$Pb(SCN)_2$	14.09	Sun[205]
$Rb_x(MA_{0.17}FA_{0.83})_{100-x}Pb(I_{0.83}Br_{0.17})_3$	RbI	20.3	Cruz[206]
$FA_xPEA_{1-x}PbI_3$	PEAI	17.7	Li[179]
$Rb_{0.05}(Cs_{0.05}(MA_{0.17}FA_{0.83})_{0.95}Pb(I_{0.83}Br_{0.17})_3$	RbI	19.53	Albadri[207]
$MA_{0.5}FA_{0.5}Pb_{0.5}Sn_{0.5}I_3$	Ascorbic Acid	14.01	Xu[208]
$FA_xMA_{1-x}PbI_{2.55}Br_{0.45}$	DMF	20.1	Wu[209]
$Cs_{0.05}(MA_{0.15}FA_{0.85})_{0.95}Pb(I_{0.85}Br_{0.15})_3$	Fluorinated Salt	16.3	Salado[210]
$FA_{0.83}MA_{0.17}PbI_{2.51}Br_{0.49}$	2-NAM	20.0	Wu[211]
$FA_{0.85}MA_{0.15}Pb(I_{0.85}Br_{0.15})_3$	Potassium	20.32	Tang[212]
$(CF_3CH_3NH_2)_2(FA_{0.825}MA_{0.15}Cs_{0.025})_{29}Pb_{30}(I_{0.85}Br_{0.15})_{91}$	TFEA	18.17	Ye[180]
$Cs_{0.15}FA_{0.85}PbI_3$	*N*-methylimidazole (NMI)	15.38	Huang[213]
$(FAPbI_3)_{0.85}(MAPbBr_3)_{0.15}$	MACl	16.8	Li[214]

[a] **FACl** = Formamidinium chloride, **PEAI** = Phenyl ethylammonium iodide, **2-NAM** = *N*-Acetylmuramic acid, **TFEA** = 2,2,2-Trifluoroethyl ammonium, **MACl** = Methylammonium chloride

Intramolecular Exchange. The intramolecular exchange process (IEP) forms a perovskite structure from an intermediate complex. For example, consider Scheme 2.1. The $FAPbI_3$ perovskite structure is crystallised from the intramolecular exchange with DMSO molecules intercalated in PbI_2 layers with FAI.

A summary of the intermediate complexes used successfully in FA-lead-based PSC fabrication is given in Table 2.9. The IEP has been utilised to provide PSCs with efficiencies above 20%. That said, there exist several other methods that also provide highly efficient solar cells.[61]

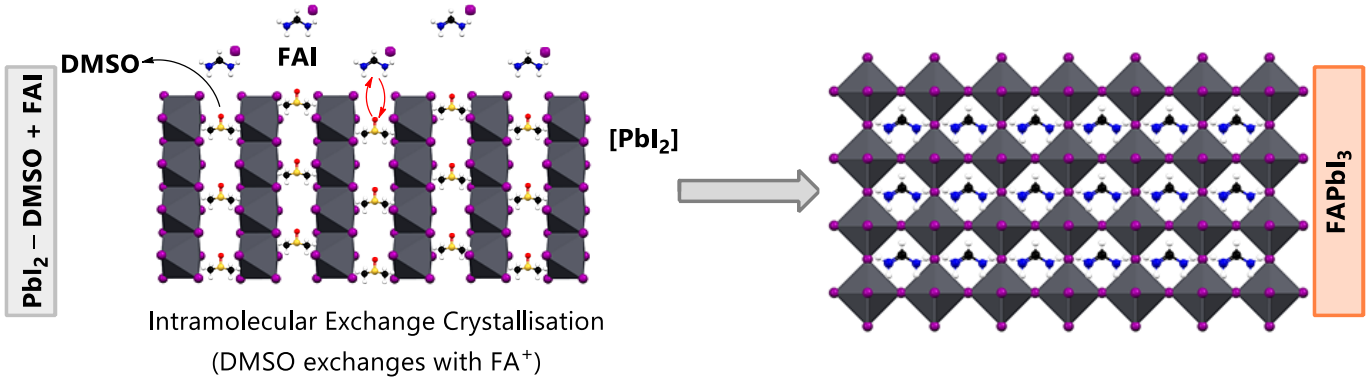

Scheme 2.1 A schematic illustration of direct intramolecular exchange of DMSO with formamidinium iodide (FAI) between PbI_2 layers, forming a 3D $FAPbI_3$ perovskite structure. PbI_2 is dissolved in DMSO, and FAI is added.

Interfacial Engineering. The interfaces of PSCs play a crucial role in the charge collection and recombination mechanism. The photocurrent is dependent on the charge collection and the photovoltage on the charge recombination, hence by improving any of these factors, a higher PCE is obtainable.[61] Therefore, the interfaces between the perovskite absorber layer and the charge transport layers (ETL and HTM) need to be optimally paired for highly efficient devices.

Table 2.9 Efficiencies of FA-lead-based PSCs fabricated using the intramolecular exchange process, with literature references. Taken and adapted from Li *et al.*[61] Primary authors are acknowledged in the Author column (*et al.* is implied).[a]

Perovskite	Additive	Intermediate Complex	PCE (%)	Author
$FAPbI_3$	$HPbI_3$	$HPbI_3$/FAI	17.50	Wang[215]
	N/A	N/A	18.10	Zhou[216]
	N/A	PbI_2–DMSO	14.26	Li[217]
$FAPbI_3$-based	NMP	PbI_2–NMP	17.60	Jo[218]
$FA_{0.85}MA_{0.15}PbI_{0.85}Br_{0.15}$	PbI_2	PbI_2–DMSO–FAI	20.80	Bi[219]
$(FAPbI)_x(MAPbBr)_{1-x}$	I_3^-	PbI_2–DMSO	22.1[b]	Yang[220]
$FA_{0.81}MA_{0.15}PbI_{2.51}Br_{0.45}$	N/A	DMSO–$PbI_{1.7}Br_{0.3}$–$(FAI)_{0.85}(MABr)_{0.15}$	19.6[b]	Li[221]
$FAPbI_{3-x}Br_x$	$HPbI_2Br$ + 1.3FAI	N/A	19.20	Long[222]
$MA_{0.6}FA_{0.4}PbI_3$	N/A	$(FAI)_{0.4}$–PbI_2	13.10	Liu[223]
$FAPbI_{3-x}Cl_x$	FACl	$MAPbI_{3-x}Cl_x$–FACl	17.00	Mu[224]
$(FA_{0.5}MA)PbI_3$	N/A	N/A	16.50	Zhang[225]
$HC(NH_2)_2PbI_3$	MACl, MABr	PbI_2–DMSO	19.16, 15.87	Li[226]
$FA_xMA_{1-x}PbI_{2.55}Br_{0.45}$	DMF	PbX_2–DAI–DMSO–DMF	20.10	Wu[209]
$(FAPbI_3)_{1-x}(MAPbBr_3)_x$	MABr	MABr–FAI	18.10	Zhang[222]

[a] **NMP** = *N*-methyl-2-pyrrolidone , **FAX (X = I^- or Cl^-)** = Formamidinium iodide or chloride, **MAX (X = Br^- or Cl^-)** = Methylammonium chloride or bromide

[b] Certified PCE.

Specifically, in $FAPbI_3$ solar cells, the TiO_2/$FAPbI_3$ (ETL/perovskite) interface influences the photocurrent, while the $FAPbI_3$/spiro-OMeTAD (perovskite/HTM) interface affects the photovoltage.[227] That said, photovoltage is the *limiting factor* when it comes to device efficiency. Therefore, it may be assumed that improving the perovskite/HTM interface interaction will lead to higher efficiencies (above 20%). Several interfaces have been suggested and tested with varying success in studies reported in the literature, as listed in Table 2.10.

Table 2.10 Efficiencies of FA-lead-based PSCs with different interfacial engineering methodologies and literature references. Taken and adapted from Li *et al.*[61] Primary authors are acknowledged in the Author column (*et al.* is implied).[a]

Perovskite	Interfacial Engineering Method	PCE (%)	Author
$FAPbI_3$	Addition of a $MAPbI_3$ layer	16.01	Lee[60]
	Using an mp-TiO_2 film	14.20	Zhou[188]
$(FAPbI_3)_{0.85}(MAPbBr_3)_{0.15}$	Addition of an $FAPbBr_{3-x}I_x$ layer	21.30	Cho[228]
$FAPbBr_3$	Using a Li-doped TiO_2 film	>8%	Arora[229]
$Cs_{0.05}FA_{0.81}MA_{0.14}PbI_{2.55}Br_{0.45}$	Using a chloride capped TiO_2 film	20.30	Tan[230]
$FAPbI_3$·HCl	$FAPbI_3$·sealed with HCl and by PMMA annealing	17.36	Li[231]
$MA_{0.6}FA_{0.4}PbI_3$	Employing restricted volume solvent annealing	16.5	Mahmud[232]
$Cs_x(FA_{0.81}MA_{0.15})_{100-x}Pb(I_{0.836}Br_{0.15})_3$	Modified with Cs_2CO_3	20.6	Ye[233]
Cs/FA/MA Triple Cation Perovskite	Modified with CsBr and using an mp-TiO_2 film	21	Seo[234]
	Using mixed cations to change the compound	18.6	Hu[235]
	Using Ta·WO_x monolayers	21.2	Hou[236]
$(HC(NH_2)_2)_{0.83}Cs_{0.17}Pb(I_{0.6}Br_{0.4})_3$	Using *N*-DPBI doped C_{60} as the ETL	18.3	Wang[237]
Rb/FA/MA Triple Cation Perovskite	Using Li-doped ZnO as the ETL	16.14	Mahmud[238]
$(Cs_{0.2}FA_{0.8})Pb(I_{0.95}Br_{0.05})_3$	Using PTAA as the interlayer	20.05	Wu[239]
$(FAI)_{0.81}(PbI_2)_{0.85}(MABr)_{0.15}(PbBr_2)_{0.15}$	Using α-bis-PCBM	20.8	Zhang[240]

[a] **PMMA** = Poly(methyl methacrylate), ***N*-DPBI** = 4-(1,3-Dimethyl-2,3-dihydro-1*H*-benzoimidazol-2-yl)-*N*,*N*'-diphenylaniline, **PTAA** = Poly (triaryl amine) (Poly[bis(4-phenyl)(2,4,6-trimethylphenyl)amine]), **PCBM** = Phenyl-C61-butyric acid methyl ester

Chemical Vapour Deposition (CVD). CVD allows for batch processing and the production of larger film areas of perovskite thin-films, reducing production costs. Moreover, both $MAPbI_3$ and $FAPbI_3$ cells and modules have been fabricated using CVD.[241] Furthermore, the CVD approach has the added advantage of producing more uniform films over large areas, leading to higher obtainable PCE values than other methods.[242] Consequently, several large-area cells and modules (a combination of several cells) have been produced, as listed in Table 2.11.

Table 2.11 Efficiencies of FA-lead-based PSCs fabricated using CVD and literature references. Taken and adapted from Li *et al.*[61] Primary authors are acknowledged in the Author column (*et al.* is implied).

Perovskite	PCE (%)	Working Area (cm^2)	Author
$FAPbI_3$	10.4	2	Leyden[241]
	9.5	8.8	
	9.0	12	
	12.4	0.09	Zhou[243]
	14.2	0.04 – 0.169	Leyden[66]
$FAPbCl_3$	7.7	1	Leyden[66]
$Cs_{0.07}FA_{0.93}PbI_3$	14.6	12	Jiang[242]

In summary, the literature results indicate that the improvement of FA-lead-based PSCs and any PSCs is best achieved by involving various research groups, each investigating different parameters and sets of conditions to be varied and optimised, all contributing to the development of PSCs. Also, it suggests that the next step is to further improve and optimise the light-harvesting ability of the devices by optimising the film thickness and light trapping properties of the film. Although high efficiencies have been obtained to date, these accomplishments were all achieved using laboratory-based prototype PSCs.

Hence, more work needs to be completed to improve the stability of charge-transport layers and the perovskite layer to ensure optimal outdoor working devices.[61] Finally, any prospective PSC devices need to be tested in different climates (high temperatures, high humidity and so on) before commercialisation can be considered.

2.2.4 Other Methods to Improve Stability

2D perovskite structures have shown superior moisture stability[244–248] compared to their 3D counterparts, and hence, constructing 2D/3D stacking structures (2D layer stacked on top of a 3D layer),[249] significantly improves the stability of a PSC. This raises the question: "Why not simply use only 2D structures?" Unfortunately, the efficiency of pure 2D perovskites in PSCs is much lower than that of their 3D counterparts because of their inferior electrical properties (purely corner-sharing octahedra in 3D materials versus different types of octahedra in 2D materials).[250] Therefore, better use of a 2D perovskite is as a thin layer to cover the surface and grain boundaries of the 3D perovskite, which then *protects* the 3D material.[251] Most of the degradation and defects of 3D perovskites occur at their grain boundaries. Hence, by *covering* the crystal boundaries, the overall device stability is improved, and high efficiency is maintained.

Employing purely 2D perovskites in PSCs has only started to show viable and competitive results as recently as 2018. Stoumpos *et al*.[252] has reported a 2D Dion–Jacobson (2DDJ) structure, which is generally more stable than a 2D Ruddlesden-Popper (2DRP) perovskite structure. In the DJ structure, no van der Waals gap exists between the organic and perovskite layers. The organic layers connect to the perovskite layers *via* strong hydrogen bonds, which increases its stability compared to the 2DRP perovskite structure.

In addition, Guo *et al*.[253] reported a PSC based on a 1,3-propanediamine-based DJ phase perovskite with a maximum PCE of 13.3%. Furthermore, even without encapsulation, the devices can maintain 95% of their initial PCE when exposed to ambient air, continuous illumination, and damp heat (85 °C at 85% RH) for 4000, 3000 and 168 hours, respectively.

Lastly, after the initial focus on 3D perovskites, it has become apparent that the additional benefits of 2D or 2D/3D perovskites, including moisture-resistance, larger compositional freedom and larger formational energy compared to 3D materials promise more stable PSC devices.[247,254] Table 2.12 list a few comparative devices, with their perovskite layer being either purely 3D, purely 2D or a combination of 2D and 3D. In comparison, it is seen that the pure 2D devices are more stable than the pure 3D devices, however, they cannot compete in terms of PCE. On the other hand, the mixture of 2D/3D devices has similar PCE and comparatively better stability than pure 3D devices.

Table 2.12 Stability of selected recently reported PSCs that employ either 3D or 2D perovskites or a combination of the two. Taken and adapted from Dai *et al*.[255] Primary authors are acknowledged in the Author column (*et al.* is implied).[a]

Perovskite	Dimensionality	PCE (%)	Stability	Author
$(FAPbI_3)_{0.85}(MAPbBr_3)_{0.15}$	3D	19.17	600 hours at 40% RH	Jeong[256]
$(FAPbI_3)_{0.95}(MAPbBr_3)_{0.05}$	3D	21.7	95% left after 500 hours	Bella[187]
MA_2PbI_4	2DRP	16.6	97.8% left after 1512 hours at 55% RH	Zhu[257]
$(PDA)(MA)_3Pb_4I_{13}$	2DDJ	13.3	Over 95% for 4000 hours at 40–70 RH	Ahmad[253]
$(Cs_{0.1}FA_{0.9})Pb(I_{0.9}Br_{0.1})_3$	2D/3D	20.08	92% left after 2400 hours at 55% RH	Qiu[258]
$Cs_{0.05}(FA_{0.83}MA_{0.17})_{0.95}Pb(I_{0.83}Br_{0.17})_3$	2D/3D	21.06	90% left after 300 hours in air	Mao[252]

[a] **RH** = Relative humidity, **PDA** = Polydiacetylenes

To conclude this section, it can be summarised that the quality of perovskite crystals, hence their thin-films, depends on synthetic conditions. Therefore identification of the "correct" synthetic method plays just as an essential role in the stability of the perovskite as the composition of the material. Hence, incorrect fabrication methods can leave even the Holy Grail of PV materials as a matter of academic interest.

2.3 Lead-Free Perovskite Solar Cells

The unique optical and electrical properties of organic-inorganic halide perovskites have made them the subject of extensive research and investigation. As described in the previous sections, significant focus has been placed on investigating lead-based organic-inorganic perovskites for applications in optoelectronics, specifically, PSCs. However, due to the toxicity of their main component, lead, and of its organic parts, tremendous efforts have been made in the search for lead-alternative, or so-called lead-free perovskites, in the hope of finding a competitive alternative for commercialisation. This section serves as an introduction to the issue of lead toxicity, proposed methods to substitute lead in the perovskite lattice, the effects of this substitution on structure and properties and the results reported in this literature thus far. Specific focus is placed on lead-free perovskites in PSC technology.

2.3.1 Introduction – Lead Toxicity and its Substitution

The poor stability of lead-based devices is a significant concern when it comes to the commercialisation of lead-based PSC devices. At elevated temperatures and even in semi-humid conditions, the hybrid perovskite structure degrades into its organic and inorganic constituents,[63] potentially leading to severe environmental and human health hazards, as illustrated in Figure 2.6. Even the interlayer diffusion that occurs between the device layers promotes instability and hence accelerates degradation.[259] These aspects are obstacles in commercialising lead-based PSCs and therefore hinder their progress to becoming silicon solar cells' most promising competitors.

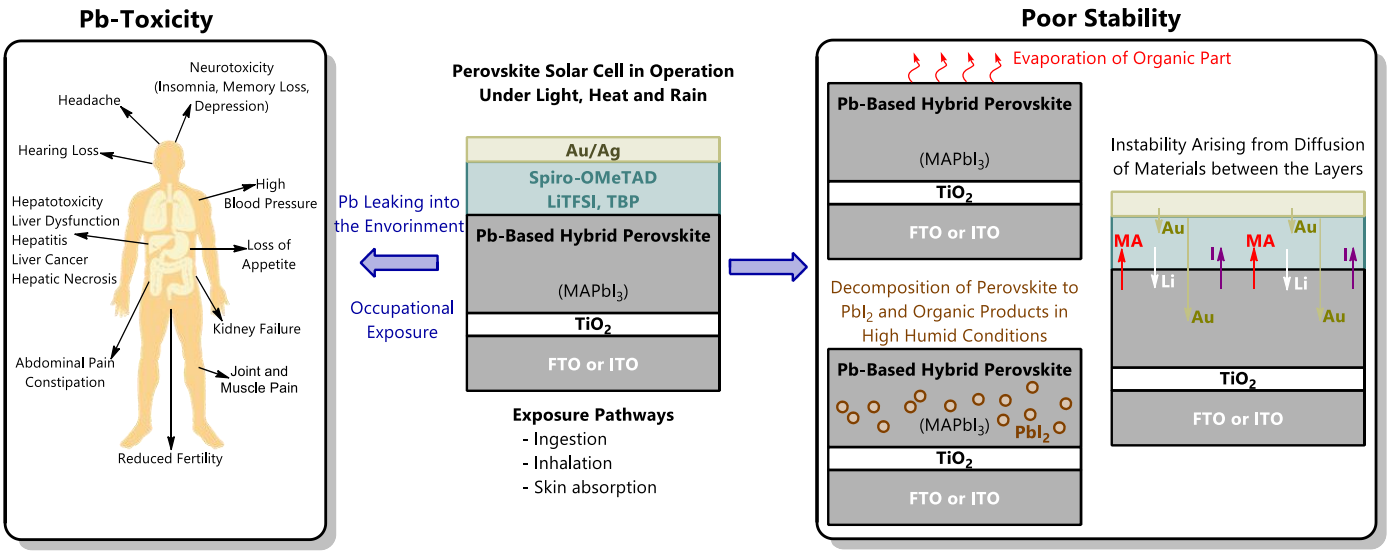

Figure 2.6 Schematic illustration of the effect of exposure to lead on human life (left) and the factors responsible for perovskite degradation in a PSC device (right). Adapted from Miyasaka *et al.*[259]

Lead is a divalent cation, and hence a divalent B^{2+}-cation is needed to replace it in any of the established lead-containing PSCs (this is not *strictly* true, however, this is generally the case). Apparent alternatives include Sn^{2+} and Ge^{2+} since they are isoelectronic to Pb^{2+}. The most promising of these two is Sn^{2+}, with the compound $MASnX_3$ having a theoretical band gap of 1.2–1.4 eV for MASnX3, which is quite close to the ideal value of ~1.1 eV suggested by the Shockley-Quessier limit.[260] However, in the substitution of lead with other divalent metal ions, new challenges appear. In addition, several other suggestions of metal ions that can replace Pb^{2+} have also been made and reviewed extensively.[5,261–263] Figure 2.7 shows an abridged periodic table, highlighting the promising candidates that may or have been shown to replace lead in the perovskite lattice.

The use of lead in solar cell technology has raised many concerns. Therefore, a search for less toxic metals to be used in perovskites was launched soon after the usefulness of hybrid perovskites in solar technology was realised. In this section, an overview of the lead alternatives reported to date is given. In addition, their properties and relevant PV details are provided where possible.

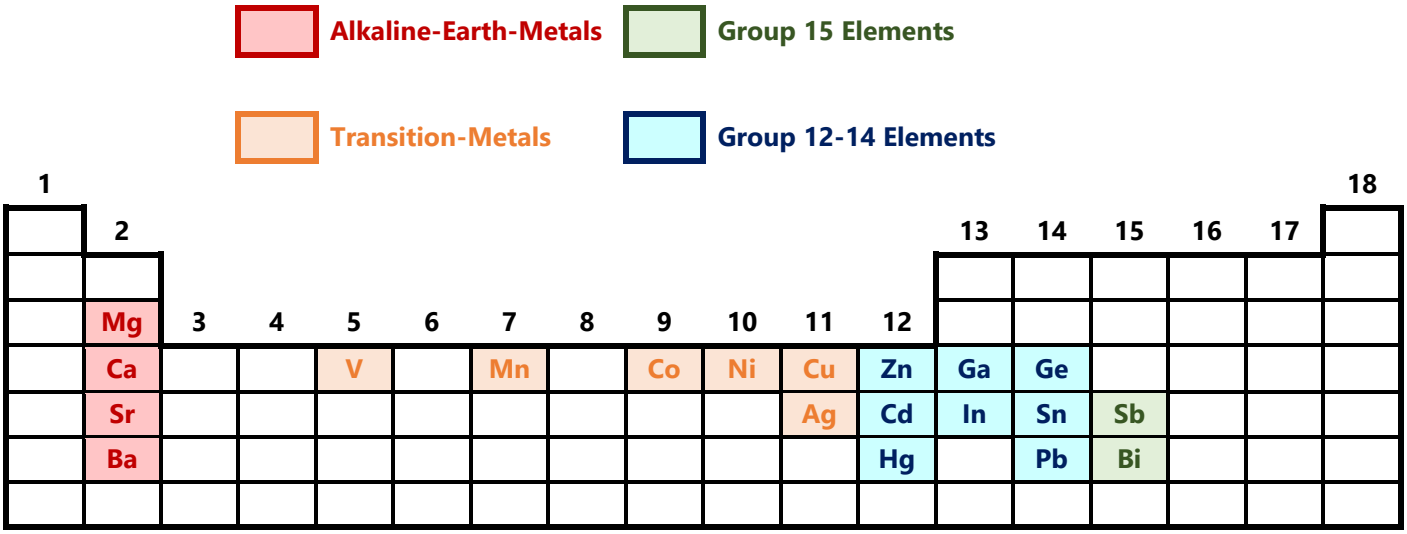

Figure 2.7 An overview of the possible elements which may be used to replace lead in 3D ABX_3 perovskites for application in perovskite solar cell structures.

The substitution of the lead ion in the 3D perovskite lattice leads to different kinds of perovskite or non-perovskite structures, depending on the nature of the substituent metal ion. The following section briefly discusses the viable strategies for lead replacement and its effect on the structures and subsequent properties obtained.

2.3.2 Approaches and Consequences of Lead Substitution

In general, there are two approaches to replacing lead in the 3D $APbX_3$ lattice, namely *homovalent substitution* and *heterovalent substitution*, as illustrated in Figure 2.8. The homovalent route uses B-site cations with a 2+ charge, for example, Sn^{2+}, Ge^{2+}, Mg^{2+}, Mn^{2+} etc., whereas the heterovalent substitution option uses cations with charges different from 2+, for example, Bi^{3+} or Sb^{3+}. In the latter substitution route, vacancies are created (called ordered vacancies), or mixtures of constituents are used (called ion-splitting) to ensure charge balance in the structure. In the heterovalent case, a loss of 3D dimensionality is often encountered.

The ion-splitting method can be subdivided into *mixed anion compounds* (where chalcogen-halogen mixtures are used in the X-site) and *double perovskite compounds* (where a combination of B^{+}- and B^{3+}-cations are used in the B-site). The vacancy ordered category is also subdivided into B^{4+}- and B^{3+}-cation vacancy structures, resulting in $A_2\square BX_6$ and $A_3\square BX_9$ structures, respectively, with the latter being of lower dimension, and where $\square$ indicates a vacancy.

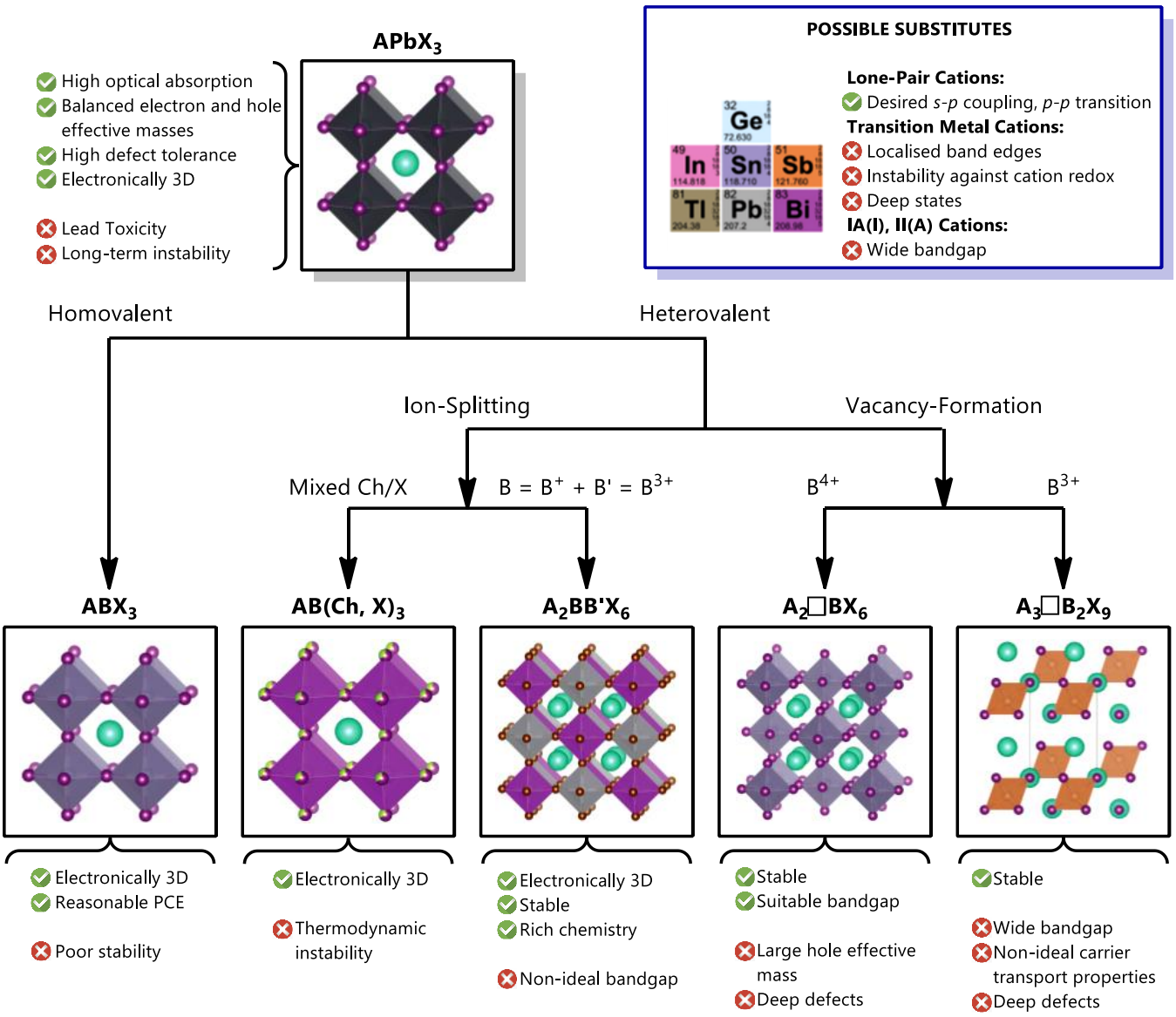

Figure 2.8 The five possible pathways of substituting lead in ABX_3 perovskites and the structural consequences thereof. Ch = chalcogen and □ = vacancy. Adapted from Xiao *et al.*[21]

Figure 2.8 also provides a list of the electronic properties, hence the consequences of lead-replacement in the 3D perovskite lattice on properties. With homovalent replacement, a lack of structural stability is encountered, however, with improved electronic properties. That said, with heterovalent strategies, better stability is obtained, however, at the cost of lower electronic dimensionality (in some cases lower structural dimensionality as well) and hence, inferior electronic properties. As a result, at the moment, all lead-free PSC devices reported in the literature battle to compete with their lead counterparts. Nevertheless, that has not deterred research in the field of lead-free perovskites and their investigation for use in solar cell technology or other optoelectronic technologies.

2.3.3 Tin-Based PSCs

Metal ions with outer ns^2 electrons, with low ionisation energies, result in good optical and transport properties in AMX_3 perovskites.[264] When substituting lead ions, naturally, the first step would be to substitute it with another, and therefore similar, Group 14 element complying to this ns^2 "rule". The metal ions Sn^{2+} and Ge^{2+} both fulfil this requirement. The focus of this section will be on tin ions as a replacement for lead ions.

3D Perovskite Tin-Based PSCs

Tin-based perovskites are certainly viable because of the similar ionic radii of tin and lead, with a value of 118 pm for Sn^{2+} versus that of Pb^{2+} at 119 pm. Moreover, tin-based perovskites have been shown to possess higher charge carrier mobilities than their lead counterparts, which votes positively for their application to PSCs.[54]

In 1974 the first tin-based perovskite compound, $CsSnX_3$, with X = Cl^-, Br^- or I^-, was synthesised and structurally characterised by Fischer *et al.*[265] Thereafter, Weber again synthesised the first organic-inorganic tin-based hybrid perovskites, namely $MASnBr_3$ and $MASnI_3$.[266] In addition to the single halide forms, Weber also synthesised the first mixed halide structure, $MASnIBr_2$. These materials were shown to possess similar 3D structures to their lead analogues. Years later, Stoumpos *et al.* determined that both $MASnI_3$ and $FASnI_3$ perovskites are excellent light absorbers due to their electronic and optical properties (including high carrier mobilities, tuneable direct-band gap and strong photoluminescence), which were similar to their lead analogues.[54]

Further theoretical investigation into the electronic properties of specifically $MASnI_3$ showed that it has a similar band structure to $MAPbI_3$ and exhibits a theoretical direct optical band gap of 1.1 eV (ca. 1.25 eV experimentally), which inspired great hope in tin-halide perovskites for PSC applications.[267,268] Additionally, the $MASnI_3$ perovskite material shows a higher absorption coefficient than $MAPbI_3$.[269] However, high-energy $5s^2$-states do not allow for strong Sn–I bond formation, leading to easy bond breakages and tin vacancies (V_{Sn}) in the crystal structure or thin-films. These vacancies predominately cause transition levels below the valence band minimum (VBM), leading to excessive hole density in SnI_2-based PSCs, making $MASnI_3$ less than ideal as an absorber layer in PSCs.[269]

Another consequence of the high-energy $5s^2$-states is that Sn^{2+} can readily and easily be oxidised to Sn^{4+}. With the oxidisation of tin from Sn^{2+} to Sn^{4+} in the perovskite layer, the Sn^{4+}-ions will act as a source of holes in the solar cell (acts as a p-type dopant). Hence, recombination of excited electrons with holes will occur in the perovskite layer, leading to a loss in device efficiency (PCE). To address the oxidisation and V_{Sn} issues in tin-based perovskites, several solutions have been proposed. The most successful of these was using Sn^{2+}-based additives, such as SnI_2, SnF_2 or SnF_2 with N_2H_4, to increase the Sn^{2+} concentration.[270] Other possible additives include hypophosphorous acid (HPA), ethylenediammonium diiodide ($EDAI_2$) and Lewis bases. By addressing the oxidation issue through additives, increased charge carrier lifetimes and increased charge carrier diffusion lengths have been observed (10-fold improvement compared to when not using additives), ultimately leading to higher device performance.[271] Nevertheless, these potential challenges did not deter research in the field of tin-based PSCs.

Chen *et al.* first reported using an all-inorganic $CsSnI_{3-x}Br_x$-based PSC in 2012, with a low, close to ideal band gap (~1.3 eV) that reached an initial efficiency of 0.9%, showing the viability of tin-based PSCs.[272] Later the use of MA^+ instead of Cs^+ was investigated, with a $MASnI_3$- and $MASnI_{3-x}Br_x$-based PSC delivering efficiencies of 6.4%[267] and 5.2%[268], respectively, on a mesoporous TiO_2 architecture. These early examples further sparked interest in the field of tin-based PSCs, and many of the possible combinations between mixed halide, mixed A-site cation, mixed metal etc., have been investigated. The use of 3D tin-based perovskites in PSCs can be divided into four main categories, namely $CsSn(I, Br)_3$, $MASn(I, Br)_3$, $FASn(I, Br)_3$ and mixed A-cation tin-based perovskites. Examples of these will be discussed separately, and a summary of tin-based PSCs can be found in Table 2.13 through Table 2.15. The chlorine versions have band gaps too wide for PSC application and are, therefore, not discussed in detail here, however, reference will be made to their use where relevant.

$CsSn(I, Br)_3$-Based PSCs. The all-inorganic version of $CsSn(I, Br)_3$ is much more stable in moisture and heat than its hybrid counterparts, $MASn(I, Br)_3$ and $FASn(I, Br)_3$, but it possesses similar electronic and optical properties as the others.[54,269,273] $CsSnI_3$ exhibits four polymorphs, which are listed below:[269]

- A yellow (Y) 1D double-chain structure;
- A black 3D orthorhombic perovskite structure (B-γ, direct band gap);
- A black cubic perovskite phase (B-α), obtained when the Y phase heated above 425 K, and
- A black tetragonal phase (B-β), formed when the B-β phase is cooled to 351 K.

At room temperature $CsSnI_3$ adopts a distorted 3D perovskite structure in the orthorhombic phase (space group: *Pnma*) as shown in Figure 2.9 (a) and Figure 2.9 (b) illustrates why it is called the black-γ phase (B-γ phase). Its intrinsic p-type nature is confirmed by electric conductivity, Hall effect and thermopower measurements.[269]

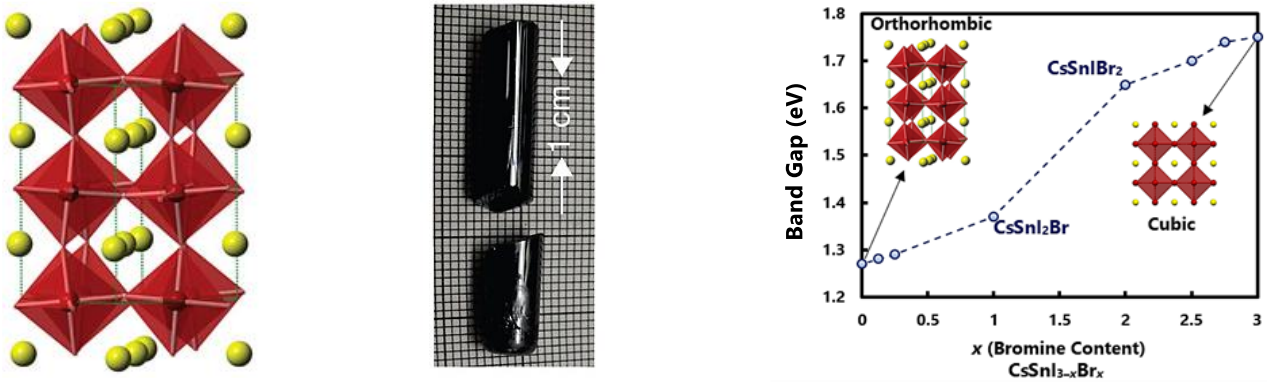

(a) **(b)** **(c)**

Figure 2.9 (a) Orthorhombic phase crystal structure of $CsSnI_3$, **(b)** a picture of a typical ingot of $CsSnI_3$ grown in a Bridgman furnace and **(c)** the experimental band gap of $CsSnI_{3-x}Br_x$ ($0 \leq x \leq 3$) plotted as a function of composition, with the additive SnF_2 (20 mol%). Copyright 2015, American Chemical Society. Reproduced and adapted with permission.[274]

With a band gap of 1.3 eV for $CsSnI_3$, photovoltaic applications are begging to be explored. Furthermore, the band gap of $CsSnX_3$ can be tuned between 1.3 eV for $CsSnI_3$ to 1.7 eV of $CsSnBr_3$, and while the 3D perovskite structure remains intact, the crystal phase changes from orthorhombic to cubic between these compositions (see Figure 2.9 (c)).[273,274] Any of these structures, $CsSnI_{3-x}Br_x$, where $0 \leq x \leq 3$, can be applied to solar cells since they exhibit close to ideal band gaps and possess good thermal and moisture stability, as shown in the summary tables.

Initially, Chen *et al.* used $CsSnI_3$ in a Schottky solar cell which consisted of ITO/$CsSnI_3$/Au/Ti on a glass substrate, using $SnCl_2$ and CsI as precursors. The black film was used as an absorber in the PSC device and yielded a PCE of 0.9%.[272] Thereafter, Kumar *et al*. realised that an additive (SnF_2) would benefit growing perfect films, so $CsSnI_3$ PSCs with 20% SnF_2 achieved a PCE of 2.02%.[275] However, Sabba *et al*. theoretically determined the tendency of tin oxidation in this inorganic perovskite. They found it to be less than with the hybrid tin-based halide perovskites, but still possible.[274] This is the biggest hindrance in $CsSnI_3$'s quest to dethrone $MAPbI_3$ as the perovskite of choice in PSC devices. The so-called orthorhombic black phase of $CsSnI_3$ is ideal for PSC applications in terms of band gap, exciton binding energy and optical absorption coefficient, however, it readily decomposes to the so-called yellow phase in the atmosphere, and as with the yellow phase of $FAPbI_3$, it is no longer useful in PSC applications.[269,276]

Additives such as SnI_2 were proposed to address this instability. For example, Marshall *et al.* used the PSC device ITO/CuI/$CsSnI_3$/fullerene/bathocuproine (BCP)/Al and obtained a PCE of 0.75% without any additives, but this same cell has an improved PCE of 1.5% when 10 mol% SnI_2 is added.[277] After that, different tin-additives were studied systematically to improve device PCE, including SnF_2, $SnCl_2$, SnI_2, and $SnBr_2$, but mixed results were obtained. Only $SnCl_2$ was shown to improve the PCE initially. However, it caused a severe loss in V_{OC} and J_{SC} due to the formation of hole-conducting layers in the ETL layer, leading to charge recombination and eventual loss in PCE.

One fascinating property of the pure inorganic $CsSnX_3$ ($X = Cl^-$, Br^- or I^-) perovskites is their ability to form quantum rods when prepared *via* a solvothermal method.[278] These rods can absorb the entire visible range of the solar spectrum. Moreover, devices based on the rods of $CsSnCl_3$, $CsSnBr_3$ and $CsSnI_3$ have shown PCEs of 12.96%, 10.46% and 9.66% respectively. This field is a new and exciting avenue for investigation in tin-based PSCs.

To conclude the discussion on $CsSn(I, Br)_3$ materials, it is important to mention that they also have other potential optoelectronic applications. For example, Hong *et al*. showed the viability of $CsSnI_3$ in LEDs[279] and Xing *et al*. their applicability in near-infrared lasers[280].

MASn(I, Br)$_3$-Based PSCs. $MASnI_3$ adopts a 3D perovskite structure in the cubic phase (space group $Pm\bar{3}m$) at room temperature as shown in Figure 2.10 (a) and (b). The cubic structure ($Pm\bar{3}m$) was determined by SCXRD, however, several researchers prefer using the pseudocubic structure (space group *P*4*mm*) since it is the more chemically intuitive form.[54,281] since this form contains the complete polar molecule, $CH_3NH_3^+$.[54,281] The room temperature cubic structure is referred to as the α-phase. $MASnI_3$ exhibits phase transitions at ca. 275 K to a tetragonal phase (called the β-phase, space groups *I*4*cm* or *I*4/*mcm*) and at ca. 110 K to an orthorhombic phase (called the γ-phase, space groups $Pbn2_1$ or *Pbnm*).[54,282]

(a) **(b)**

Figure 2.10 (a) A perovskite building block and **(b)** the unit cell (shown in black) of the cubic phase of $MASnI_3$ viewed down the *b*-axis. Hydrogen atoms were omitted for clarity.[54]

$MASnI_3$ is a direct band gap material with an optical band gap of 1.25 eV, which is much lower than that of its lead counterpart $MAPbI_3$, which has a band gap in the region of 1.5 eV, making it more alluring for solar cell applications. By changing the halide and halide concentrations of $MASnX_3$, the band gap can be tuned between 2.15 eV for $MASnBr_3$ to 1.25 eV for $MASnI_3$.[268] Moreover, by the incorporation (doping) of lead (Pb^{2+}) or bismuth (Bi^{3+}) into the $MASnI_3$ material, the band gap of $MASnI_3$ can be altered to 1.1 eV[283] and 0.8 eV,[284] respectively. Furthermore, $MASnI_3$ should have better electron transport abilities than $MAPbI_3$ due to the smaller effective masses of its charge carriers, even though $MAPbI_3$ and $MASnI_3$ have similar band structures, as shown in Figure 2.11 (a) and (b).[281] Lastly, Roknuzzaman *et al*. suggested that since $MASnI_3$ has a lower charge recombination rate than the lead alternative (due to its higher dielectric constant of 6.69), it should have the ability to outperform lead-based PSCs in terms of PCE.[285] However, this performance is inhibited due to the oxidation of Sn^{2+} to Sn^{4+}, as discussed previously. Therefore, if the oxidation challenge can be addressed, tin-based PSCs could easily outperform their lead competitors.

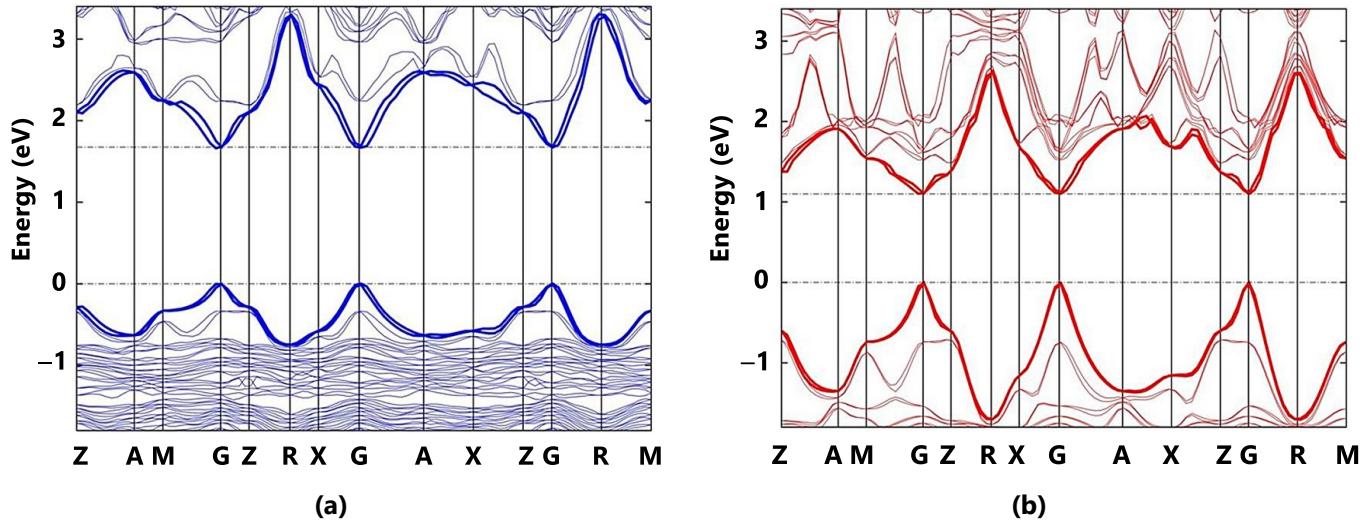

Figure 2.11 The calculated band structures of **(a)** $MAPbI_3$ and **(b)** $MASnI_3$. The conduction and valence bands are shown as thick lines. Adapted from Umari *et al*.[281]

$MASnIBr_2$ was first used as the absorber layer in PSCs in 2014 (architecture FTO/TiO_2/$MASnIBr_2$/Spiro-OMeTAD/Au) and delivered a PCE of 5.73%,[268] thereafter, in the same year, Noel *et al*. were able to increase the PCE of that device architecture to 6.4% by using $MASnI_3$[275]. The initial low PCE values were the result of poor homogeneity and low coverage with/of other layers in the device.[24] Initially, the film formation methods were designed for lead-containing perovskite films and proved inefficient for tin-based perovskite films since the tin-variation crystallises more rapidly than any lead-containing films.[286,287] Hao *et al*. studied the effect of using different solvents in the crystallisation process.[287] They showed that using DMSO instead of DMF results in smoother films (pin-hole free films) on mesoporous TiO_2.[287] Further investigation determined that the solvent *N*-methyl-2-pyrrolidone (NMP) delivers better film quality than the previously mentioned solvents and hence is the current solvent of choice.[286,287]

Other methods to improve the film quality and the PCE of tin-based PSCs are through multi-step film formation methods. Noel *et al*. suggested that the combination of thermal evaporation and solution processing is required to fabricate high-quality $MASnI_3$ films.[267] Depositing SnI_2 precursors *via* vapour thermal deposition, followed by spin coating of a concentrated MAI solution (higher concentration gives larger grain sizes), results in good quality $MASnI_3$ films. In addition, Jung *et al*. fabricated $MASnBr_3$ films using a co-evaporation process of $SnBr_2$ and MABr precursors.[288] However, a maximum PCE of 0.35% was achieved with this film as the absorber since the Sn^{2+} oxidised to Sn^{4+} during the fabrication method. The group then used the sequential deposition method to reduce the oxidation and obtained an increased PCE of 1.12%, implying that sequential deposition is the fabrication method that should be used for tin-based PSCs.

The final method of improving PCEs is to ensure that the band gaps of the respective layers of the device match well. For $MASn(I, Br)_3$, it has been suggested that $Cd_{1-x}Zn_xS$[289] or anatase TiO_2 (the metastable mineral form of TiO_2)[290] might be the best options for the ETL layer of the PSC device, based on the results of theoretical studies. With the use of $Cd_{1-x}Zn_xS$ as ETL, Baig *et al*. obtained a theoretical PCE of 18.71% for an FTO/$Cd_{1-x}Zn_xS$/$MASnI_3$/$MASnBr_3$/Metal Contact device, suggesting a possible new direction for experimental research.[289]

$FASn(I, Br)_3$-Based PSCs. When MA^+ is substituted for FA^+ as the A-cation, the result is improved film morphology and electrical properties, which has made $FASnX_3$ perovskites the more popular choice in terms of photovoltaic applications. $FASnI_3$ also crystallises in the same 3D cubic phase (space group $Pm\bar{3}m$) as $MASnI_3$, however, its more chemically intuitive pseudo cubic form is orthorhombic (polar space group *Amm*2), as shown in Figure 2.12 (a) and (b).[54] However, one important difference compared to $FAPbI_3$ is that $FASnI_3$ has a stable cubic room temperature phase and no yellow δ-phase, making it more suitable for photovoltaic applications. $FASnI_3$ has an experimental band gap of about 1.41 eV, thus higher than that of the MA^+ analogue but lower than that of the lead counterpart.[260] Furthermore, the band gap can be tuned by changing the halide type and content, for example, $FASnI_2Br$ and $FASnBr_3$ have band gaps of 1.68 and 2.4 eV, respectively.[291,292]

Lee *et al*. determined that the introduction of bromide ions into the $FASnI_3$ lattice decreases the carrier density in the film since the tin vacancies are less, allowing for a reduction in current leakage, higher recombination lifetime and more stable PSC devices.[293]

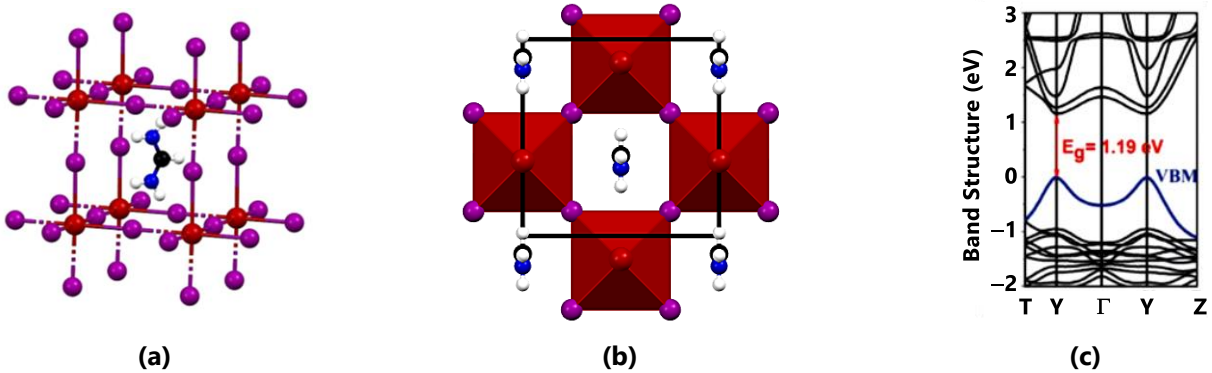

Figure 2.12 (a) A perovskite building block and **(b)** the unit cell of the cubic phase of $FASnI_3$ viewed down the *a*-axis.[54] **(c)** Band structure of $FASnI_3$. (c) reproduced with permission.[294] Copyright 2017, The Royal Society of Chemistry.

Furthermore, $FASnI_3$ has better moisture and O_2 stability than $MASnI_3$ since the FA^+-cation reduces the tendency of Sn^{2+} to oxidise to Sn^{4+}.[295,296] To further understand the role of the A-site cation, Shi *et al*. used DFT (density functional theory) studies to examine the effects of MA^+ and FA^+ on the $ASnI_3$ lattice.[294] It is well-known that the A-site cation only affects the orbital overlap of the M–X bond and plays no direct role in the electronic properties of the materials. Therefore, since FA^+ is a larger cation than MA^+, they found that in the former case, the overlap between the antibonding orbitals of Sn 5*s* and I 5*p* was less than the latter, leading to a higher V_{Sn} formation energy, and of course, less oxidation of tin (Figure 2.12 (c)).

One of the first reports of $FASnI_3$-based PSCs utilised a mesoporous TiO_2 ETL and pyrazine as an additive to achieve a PCE of 4.8%.[297] By careful tuning of the deposition technique, different PCE values could be obtained for the same cell. For example, Liao *et al*.[298] used solvent engineering to deliver a PCE of 6.22%, and Zhu *et al*.[299] used sequential deposition to obtain a PCE of 7%. Other additives, such as ammonium hypophosphite, have been utilised by Cao *et al*. in $FASnI_3$, which improved the grain size, limited the tin oxidation, and led to better film quality and a device PCE 7.3%.[300] Moreover, after 500 hours of storage in the air, the device maintained 50% of its original PCE.

Wu *et al*. proposed the use of the π-conjugated Lewis base molecule 2-cyano-3-[5-[4-(diphenylamine) phenyl]-2-thienyl]-propanoic acid (CDTA) as an additive to control the crystallisation of $FASnI_3$ and used it with great success.[301] Improved film morphology, charge carrier lifetimes and air stability were some of the benefits. A PCE of 10.1% was achieved, and a loss of only 10% in the PCE was seen after 1000 hours of continuous use under illumination and in the air (therefore certified as 9.2%). Further work conducted by Wu's group (Meng *et al*.) used liquid formic acid as a reducing solvent in the $FASnI_3$-based device, and they achieved a PCE of 10.37%.[302]

Instead of using additives, anti-solvents (solvent engineering) such as chlorobenzene (CB), toluene (TL), diethyl ether (DE), and other aprotic nonpolar solvents that are not miscible with DMSO could also prove a helpful strategy.[303] Most importantly, the perovskite material must not be soluble in the anti-solvent. As mentioned before, Liao *et al*. employed solvent engineering methods to obtain high-quality $FASnI_3$ films, which exhibited PCEs of 6.22%.[298] Furthermore, Huang *et al*. have shown that by using chlorobenzene as an anti-solvent on $FASnI_3$ films, PCEs of as high as 9.06% could be obtained.[304] In addition to the Huang group's initial work, they also showed that when $FASnI_3$-based PSC devices were encapsulated, a PCE of 11.4% was attainable for 110 days under the inert encapsulated atmosphere.[305]

Finally, in addition to PSCs, Milot *et al*. showed that $FASnI_3$ is also viable as a light-emitting device, however, this application will not be covered here.[306]

Mixed A-Cation Tin-Based PSCs. The perovskite structure can be further stabilised by employing a mixture of A-site cations, as discussed for lead-containing perovskites. The A-site mixtures in lead-based PSCs are responsible for achieving record efficiencies, and hence is a vital strategy to explore for tin-based PSCs[172]

Zhao *et al*. studied the mixtures of FA^+ and MA^+ in tin iodide perovskites.[307] They showed that the band gaps of $(FA)_x(MA)_{1-x}SnI_3$ range from 1.26 eV for $MASnI_3$ to 1.36 eV for $FASnI_3$. Moreover, the mixture of FA^+- and MA^+-cations results in better film morphology and reduced charge carrier recombination. When they employed the absorber $FA_{0.75}MA_{0.25}SnI_3$ in an inverted planar cell, with 10% SnF_2 as an additive, the resultant PCE was 8.12% with an average value of 7.48% ± 0.52%.[307]

Further research in this field delves into so-called *hollow perovskites* (a complete description of these types of perovskites is given in Section 2.4). The introduction of *medium-sized* cations like ethylenediamine (en) leads to this type of structure. The dication is too large to fit in the A-site and substitutes an inorganic moiety. For example, the structure {en}$FASnI_3$ retains the 3D structure (see Figure 2.13), leading to favourable optical and electric properties.[308] With these larger cations, the band gap can be tuned between 1.3 eV to 1.9 eV, whereas with typical A-site mixtures, the band gap tuning rage is relatively small. This introduction of en leads to better film morphology and overall increased carrier lifetime. PCEs of 7.14% have been reported for {en}$FASnI_3$.

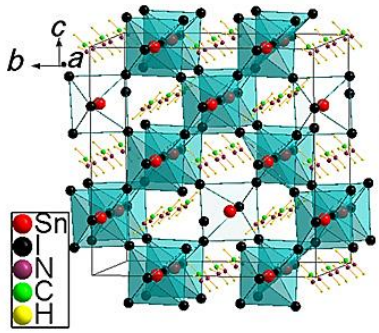

Figure 2.13 The structure of $(FA)_2Sn_2I_6$, a hollow perovskite, which contains two SnI_2 vacancies $[(FA)_{16}Sn_{14}I_{44}]$, where a suitable dication may be placed. Reproduced with permission.[308] Copyright American Association for the Advancement of Science.

The same can be achieved with $MASnI_3$ and $CsSnI_3$ perovskites.[309] In addition, two other dications, namely propylenediammonium (PN) and trimethylenediammonium (TN), can be used to form hollow perovskites of the form $\{TN\}FASnI_3$ and $\{PN\}FASnI_3$.[310] With 10% present, PCEs of 5.85% and 5.53%, were achieved for $\{TN\}FASnI_3$ and $\{PN\}FASnI_3$, respectively. In conclusion, tin-containing perovskites compete with their lead counterparts when it comes to aspects such as the band gap value, being less toxic and theoretical PCE, however, a lot of research and development is still required to address all the problems tin-based PSCs have in obtaining higher PCEs. Therefore, one final strategy to consider is using lower-dimensional perovskites for PSC application, which is the next topic of discussion.

Low Dimensional Perovskite Tin-Based PSCs

As discussed previously, lower-dimensional perovskites, specifically 2D perovskites, are more hydrophobic due to the organic chain linkages in their structure, making them less susceptible to moisture decomposition. The organic *spacer* cations can include propylenediammonium (PN^+), 2-hydroxyethylammonium (HEA^+), guanidinium (GUA^+), *n*-butylammonium (BA^+), the polyethylenimine cation, cyclopropylammonium (CPA^+), phenylethylammonium (PEA^+) and 1-(4-piperidinyl)methanamine ($4AMP^+$).[303]

In Ruddlesden–Popper 2D perovskites, the RNH_3 group is either an aromatic or primary aliphatic alkylammonium cation, acting as a spacer molecule between perovskite layers, formed by the A-, B- and X-ions.[311] The 2D network consists of corner-sharing $[BX_6]^{4-}$ octahedra between bilayers of the RNH_3-cations. Hydrophobic and Coulomb forces are then responsible for structural stability, in addition to hydrogen bonding.[311,312]

With encouraging results obtained with 2D layered lead perovskite in PSCs, researchers soon turned to tin to investigate its viability in 2D perovskites. One of the initial reports by Cao *et al*. focussed on 2D perovskites of the formula $(BA)_2(MA)_{n-1}Sn_nI_{3n+1}$.[313] They found that these perovskites could obtain enhanced PCEs, and stability compared to the lead counterparts. The thin-films of the 2D perovskite's $[BA_{n-1}Sn_nI_{3n+1}]^{2-}$ slabs orientate themselves either parallel or perpendicular to the substrate the film it is deposited onto, depending on the solvent used (DMSO versus DMF), as shown in Figure 2.14 (a), (b) and (c). The perpendicular growth allows for the best charge transport along the I–Sn–I bonds to the adjacent substrates. A maximum PCE of 2.5% was obtained using $(BA)_2(MA)_3Sn_4I_{13}$ as the absorber.[313] More interestingly, the band gaps of the 2D tin-based perovskites could be tuned between 1.83 eV to 1.20 eV by increasing the layer number from $n = 1$ to $n = \infty$.

The PEA^+-cation has also been used in 2D tin-based PSCs. Liao *et al*. used FA^+- and PEA^+-cations to form $(PEA)_2FA_nSnI_{3n+1}$, where the PEA^+-cation acts as the organic spacer cation (see Figure 2.15) to form a 2D layered perovskite.[314] The protection of the perovskite layers by the organic spacer cations significantly improved device stability compared to $FASnI_3$. Moreover, by adjusting the PEA^+-ratio, they found that at 20% PEA, a highly ordered film crystallises perpendicular to the substrate, allowing for improved charge transport. This allowed for a PCE of 5.94% and a more stable device.

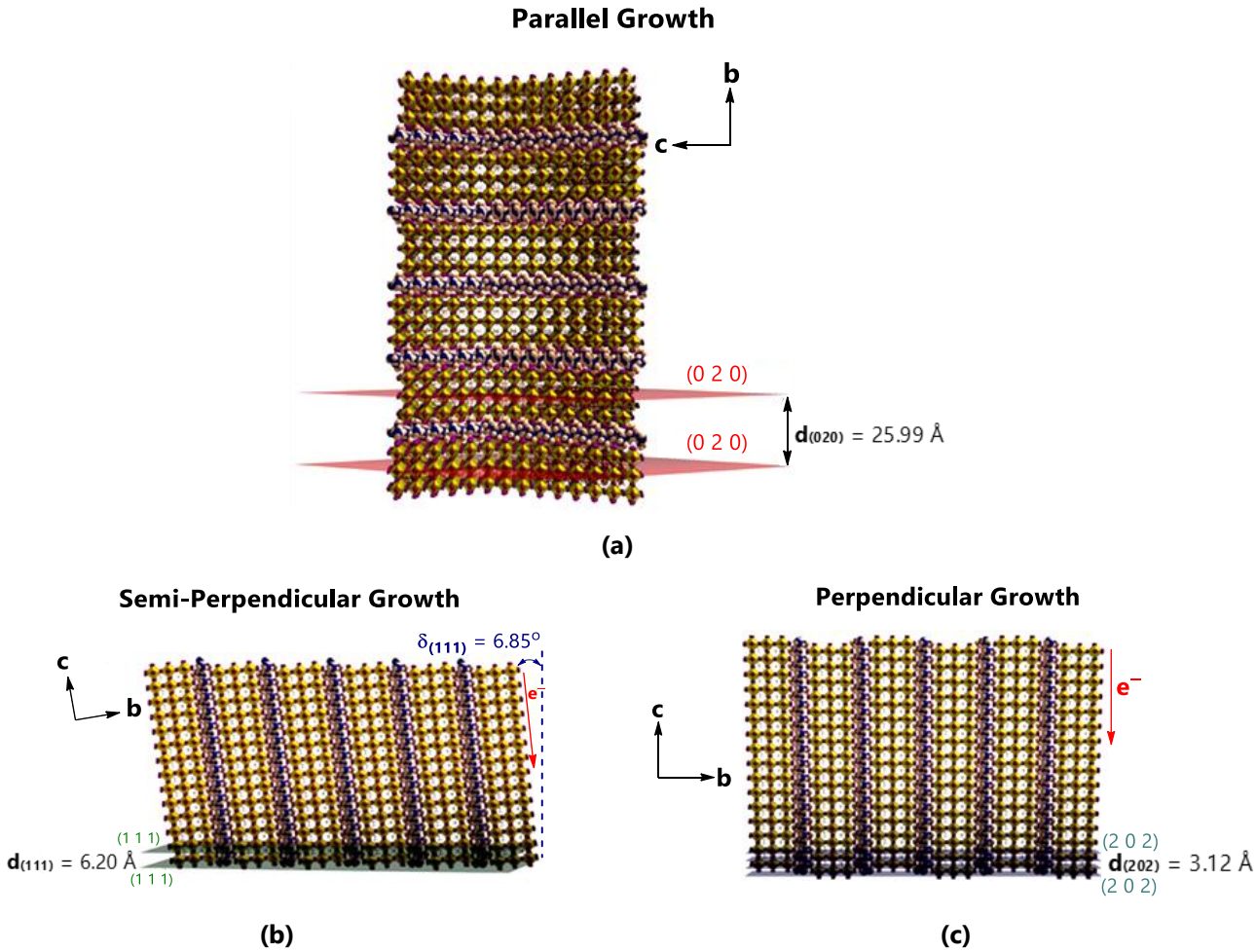

Figure 2.14 The growth of a thin-film of the 2D perovskite material $(BA)_2(MA)_2Sn_3I_{10}$ on a substrate: **(a)** a perfectly parallel film growth on the (0*k*0) plane, **(b)** nearly perpendicular film growth on the (111) plane, and **(c)** purely perpendicular film growth on the (202) plane, adapted from Hao *et al.*[313]

Qui *et al*. proposed using both BA^+ and PEA^+, which resulted in the formation of vertically oriented $(BA_{0.5}PEA_{0.5})_2FA_3Sn_4I_{13}$ 2D RP giving a maximum perovskites PCE of 8.82%.[315] Furthermore, Xu *et al*. have prepared the cation: 5-ammoniumvaleric acid (5-AVA^+), which has been included in an $AVA_2FA_{n-1}Sn_nI_{3n+1}$ film. When $n = 5$, a quasi-2D perovskite is formed with (NH_4Cl) as an additive. They obtained highly (singly) orientated films on the substrate, allowing for superior charge transport properties.[316] The device architecture of ITO/PEDOT:PSS/$AVA_2FA_{n-1}Sn_nI_{3n+1}$/PCBM/BCP/Ag delivered a maximum PCE of 4.19%, however, the device showed better stability in the air compared to standard 3D tin-based devices.

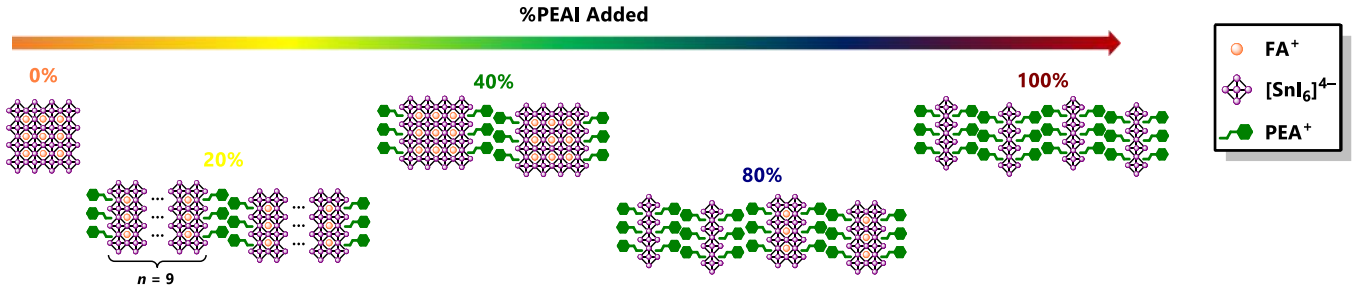

Figure 2.15 A compositional plot of the effect of adding and increasing PEA^+ concentration on the perovskite layers of the structure $FASnI_3$, leading to mixed FA-PEA perovskite and finally $(PEA)_2FASnI_4$. Adapted from Liao *et al.*[314]

The Dion-Jacobson type of 2D perovskite has also been used in PSCs, as recently shown by Chen *et al.*[317] They constructed a device with the absorber layer $(4AMP)(FA)_{n-1}Sn_nI_{3n+1}$, however, a maximum PCE of only 2.15% could be obtained for the device. That said, the 2D RP perovskites have a van der Waals gap between adjacent unit cells. In contrast, in the 2D DJ

perovskites, the layers are more closely packed and uniform, allowing for better optoelectronic properties since charges have less of a barrier to overcome during transport.[318] Moreover, the orientation of 2D DJ perovskite can be altered by using different diammonium salts. Hence, these materials can be altered to *fit* better with the substrate they are being deposited onto, leading to better charge transport properties.[319,320] This makes 2D DJ perovskite an alluring prospect for layered tin-based PSC applications.

Other low dimensional structures of tin, called *hexagonal polytypes*, are formed with the use of cations such as acetamidinium (ACA^+), guanidinium (GUA^+), ethylammonium (EA^+), trimethylammonium (TMA^+), isopropylamine (IPA^+) and imidazolium (IM^+).[260] These cations form structures exhibiting a range of corner (perovskite) and face-sharing (perovskitoid) octahedra in $ASnX_3$ polytypes. However, these structures are not extensively used in PSCs since they have wide band gaps and low electronic dimensionality.[321]

2D/3D Mixed Tin-Based PSCs. The low structural dimensionality of 2D RP or DJ perovskites do not allow for high electronic dimensionality and hence slows down the charge transfer process and limits the solar-to-electric conversion efficiency. A more prudent solution to this is using a combination of 2D/3D perovskites (similar to those proposed for lead-based PSCs). This method still allows for perpendicular growth of the film onto the substrate (see Figure 2.16) while allowing for better charge transfer. Initial PCEs of 5.94% were achieved with this method.[314] Furthermore, Shao. *et al*. utilised a p–i–n planar 2D/3D device to achieve a PCE of 9%.[322] Finally, the use of a PEA^+/NH_4SCN-tailored 2D/3D $PEA_xFA_{1-x}SnI_3$ perovskite led to a champion PSC device (only for lower dimensional tin-based PSCs) ITO/PEDOT/$PEA_{0.15}FA_{0.85}SnI_3$/ICBA/BCP/Ag, which achieved a PCE of 12.4%, by utilising indene-C_{60} bisadduct (ICBA) as ETL, phenylethylamine (PEA^+) insertion, and NH_4SCN doping in the device.[323]

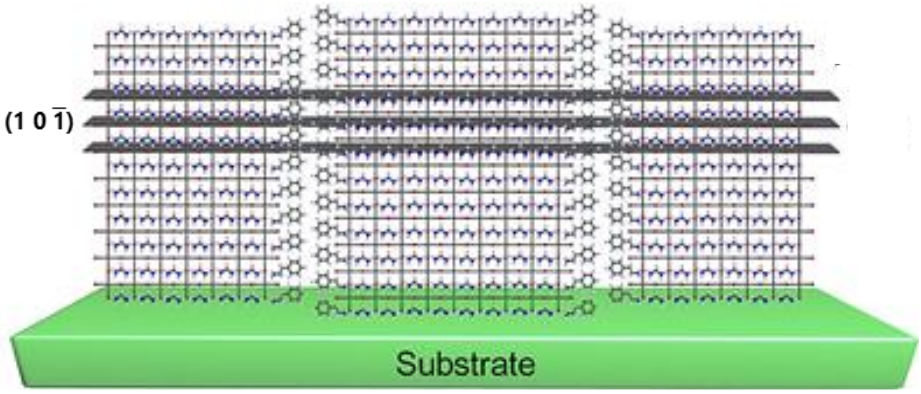

Figure 2.16 The growth of the 2D perovskite $(PEA)_2(FA)_8Sn_9I_{28}$ (n = 9) on a substrate material, showing the perpendicular growth of the perovskite film in the ⟨10$\bar{1}$⟩ direction. Reproduced with permission.[314] Copyright American Chemical Society, 2017.

The final barriers to highly efficient PSCs using tin include the rapid crystallisation of tin-based perovskites, leading to inhomogeneous film layers and inadequate coverage of the electron transport layer in the PSC. This can be addressed by using vapour deposition techniques and different solvents or combinations of solvents.[324] However, tin-based PSCs, employing either 3D or lower dimensional perovskites, are yet to compete with lead-based perovskites, except for the obvious benefit of being less toxic. Therefore, much work still needs to be done on tin-based PSCs before they will rival their lead analogues.

Table 2.13 Photovoltaic parameters and device architectures of various tin-based PSCs prepared through a one-step method. Taken and adapted from Li *et al.*,[325] Jena *et al.*[78] and Wang *et al.*[303] Either ITO or FTO was used as the glass substrate. Primary authors are acknowledged in the Author column (*et al.* is implied).[a]

Perovskite (P)	Device Architecture	V_{OC} (V)	J_{SC} (mA·cm^{-2})	FF	PCE (%)	Author
$MASnI_3$	c-TiO_2/mp-TiO_2/**P**/spiro-OMeTAD/Au	0.68	16.30	0.48	5.23	Hao[268]
$MASnI_2Br$		0.77	14.38	0.50	5.48	
$MASnIBr_2$		0.82	12.30	0.57	5.73	
$MASnBr_3$		0.88	8.26	0.59	4.27	
$MASnI_3$		0.716	15.18	0.50	5.44	Jiang[323]
$MASnI_3$		0.88	16.8	0.42	6.4	Dharani[326]
$MASnI_3$		0.79	13.40	0.52	5.49	Zhang[319]
$CsSnI_3$ + 20% SnF_2		0.201	27.67	0.29	1.66	Zhang[291]
$CsSnI_2Br$ + 20% SnF_2		0.289	15.06	0.38	1.67	
$CsSnIBr_2$ + 20% SnF_2		0.311	11.57	0.43	1.56	
$CsSnI_{2.9}Br_{0.1}$ + 20% SnF_2		0.222	24.16	0.33	1.76	
$FASnI_3$ + 20% SnF_2		0.238	24.45	0.36	2.10	Koh[327]
$CsSnBr_3$ + 20% SnF_2		0.42	9.1	0.57	2.17	Ke[308]
$MASnIBr_2$		0.69	15.9	0.49	5.36	Kieslich[321]
$MASnI_3$ + 20% SnF_2	c-TiO_2/mp-TiO_2/**P**/PTAA/Au	0.25	26.1	0.30	1.94	Hao[283]
{en}$FASnI_3$ + 15% SnF_2		0.48	22.54	0.66	7.14	Zhou[328]
{en}$FASnI_3$ + 15% SnF_2		0.46	22.54	0.70	7.23	Kim[329]
{PN}$FASnI_3$ + 15% SnF_2	c-TiO_2/mp-TiO_2/**P**/TPE/Au	0.44	22.15	0.61	5.85	Ke[310]
{TN}$FASnI_3$ + 15% SnF_2	c-TiO_2/mp-TiO_2/**P**/PTAA/Au	0.40	22.72	0.61	5.53	
{en}$MASnI_3$ + 15% SnF_2		0.43	24.28	0.64	6.63	Ke[309]
$MASnBr_3$		0.307	1.22	0.37	0.14	Handa[330]
$CsSnI_3$ + 20% SnF_2	c-TiO_2/mp-TiO_2/**P**/*m*-MTDATA/Au	0.24	22.70	0.55	2.02	Zhao[307]
$MASnCl_3$	c-TiO_2/**P**/CuSCN/Ag	0.576	12.89	0.63	3.41	Ke[331]
$CsSnI_3$	NiO/**P**/PCBM/Al	0.52	10.21	0.20	3.31	Yokoyama[332]
$CsSnI_3$	c-TiO_2/**P**/spiro-OMeTAD/Au	0.48	8.11	0.56	0.77	

Table 2.13 (Continued) Photovoltaic parameters and device architectures of various tin-based PSCs prepared through a one-step method. Taken and adapted from Li *et al.*,[325] Li *et al.*, Jena *et al.*[78] and Wang *et al.*[303] Either ITO or FTO was used as the glass substrate. Primary authors are acknowledged in the Author column (*et al.* is implied).[a]

Perovskite (P)	Device Architecture	V_{OC} (V)	J_{SC} (mA·cm^{-2})	FF	PCE (%)	Author
$HEA_{0.4}FA_{0.6}SnI_3$	c-TiO_2/mp-TiO_2/**P**/Al_2O_3C	0.37	18.52	0.72	3.9	Tsai[333]
$GA_{0.22}FA_{0.78}SnI_3$ + 1% $EDAI_2$	PEDOT:PSS/**P**/C_{60}/BCP/Ag	0.61	21.2	0.65	9.6	Jokar[334]
$FASnI_3$	PEDOT:PSS/**P**/PCBM/BCP/Ag	0.49	22.24	0.65	7.15	Lin[335]
$FASnI_3$	SnO_2/**P**/PCBM/BCP/Ag	0.55	19.39	0.69	7.34	Cao[300]
$FASnI_3$	PEDOT:PSS/**P**/C_{60}/BCP/Ag	0.63	21.6	0.75	10.17	Wu[301]
$FASnI_3$		0.628	22.25	0.74	10.37	Meng[302]
$PEA_xFA_{1-x}SnI_3$ + NH_4SCN	PEDOT:PSS/**P**/ICBA/BCP/Ag	0.94	17.4	0.75	12.4	Jiang[323]
$FASnI_3$ + 5% PHCl	PEDOT:PSS/**P**/C_{60}/BCP/Ag	0.76	23.5	0.64	11.4	Wang[305]

[a] **FTO** = Fluorine-Doped Tin Oxide, **ITO** = Indium Tin Oxide, **c-TiO_2** = Compact TiO_2, **mp-TiO_2** = Mesoporous TiO_2, **spiro-OMeTAD** = 2,2′,7,7′-tetrakis(*N*,*N*′-di-p-methoxyphenyl-amine)9,9′-spirobifluorene, **PTAA** = Poly(bis(4-phenyl)(2,4,6-trimethylphenyl)amine), **TPE** = Tetraphenylethylene , ***m*-MTDATA** = 4,4′,4″-tris(3-methylphenylphenylamino)triphenylamine, **PEDOT:PSS** = Poly(3,4-ethylenedioxythiophene)-poly(styrenesulfonate), **BCP** = Bathocuproine (2,9-Dimethyl-4,7-diphenyl-1,10-phenanthroline), **PCBM** = Phenyl-C_{61}-butyric acid methyl ester, **ICBA** = Indene-C_{60} bisadduct

Table 2.14 Photovoltaic parameters and device architectures of various tin-based PSCs prepared through solvent-engineering. Taken and adapted from Li *et al.*,[325] Jena *et al.*[78] and Wang *et al.*[303] Either ITO or FTO was used as the glass substrate. Primary authors are acknowledged in the Author column (*et al.* is implied).[a]

Perovskite (P)	Device Architecture	V_{OC} (V)	J_{SC} (mA·cm^{-2})	FF	PCE (%)	Author
$FASnI_3$ + 10% SnF_2 + pyrazine	c-TiO_2/mp-TiO_2/**P**/spiro-OMeTAD/Au	0.32	23.7	0.63	4.80	Kumar[275]
$FASnI_3$ + 20% SnF_2		0.38	23.1	0.60	5.27	Ke[336]
$MASnI_3$ + 20% SnF_2		0.232	26.0	0.39	2.33	Kieslich[321]
$FASnI_3$ + 10% SnF_2	PEDOT:PSS/**P**/C_{60}/BCP/Ag	0.47	22.1	0.61	6.22	Liao[298]
$FASnI_3$ + 20% PEAI + 10% SnF_2	NiO/**P**/PCBM/Al	0.59	14.4	0.69	5.94	Liao[314]
$FA_{0.75}MA_{0.25}SnI_3$ + 10% SnF_2	PEDOT:PSS/**P**/C_{60}/BCP/Ag	0.61	21.2	0.63	8.12	Sabba[274]
$FA_{0.5}MA_{0.5}SnI_3$ + 10% SnF_2		0.53	21.3	0.52	5.92	
$FA_{0.25}MA_{0.75}SnI_3$ + 10% SnF_2		0.48	20.7	0.45	4.49	
$FASnI_3$ + 10% SnF_2		0.48	21.3	0.65	6.60	
$MASnI_3$ + 10% SnF_2		0.46	21.4	0.43	4.29	
$(FASnI_3)_{0.92}(PEAI)_{0.08}$ + 10% SnF_2		0.53	24.1	0.71	9.00	Song[270]

Table 2.14 (Continued) Photovoltaic parameters and device architectures of various tin-based PSCs prepared through solvent-engineering. Taken and adapted from Li *et al.*,[325] Li *et al.*, Jena *et al.*[78] and Wang *et al.*[303] Either ITO or FTO was used as the glass substrate. Primary authors are acknowledged in the Author column (*et al.* is implied).[a]

Perovskite (P)	Device Architecture	V_{OC} (V)	J_{SC} (mA·cm^{-2})	FF	PCE (%)	Author
$FASnI_2Br$	PEDOT:PSS/**P**/C_{60}/Ca/Ag	0.47	6.82	0.54	1.72	Ke[308]
$MA_{0.9}Cs_{0.1}SnI_3$	PEDOT:PSS/**P**/PCBM/bis-C_{60}/Ag	0.20	4.53	0.36	0.33	Liu[337]
$FA_{0.8}Cs_{0.2}SnI_3$		0.24	16.1	0.36	1.38	
$FASnI_3$		0.04	11.7	0.23	0.11	
PEA_2SnI_4	NiO_x/**P**/PCBM/BCP/Ag	0.61	22.0	0.70	9.41	Wang[338]
$(BA_{0.5}PEA_{0.5})_2FA_3Sn_4I_{13}$	PEDOT:PSS/**P**/C_{60}/LiF/Al	0.60	21.8	0.67	8.82	Qiu[315]
$AVA_2FA_{n-1}Sn_nI_{3n+1}$	PEDOT:PSS/**P**/PCBM/BCP/Ag	0.61	21.0	0.68	8.71	Xu[316]
$AMP_4FA_3Sn_4I_{13}$	c-TiO_2/ZrO_2/**P**/carbon	0.64	14.9	0.44	4.42	Cohen[318]
$FASnI_3$ + PEABr + 10% SnF_2	PEDOT:PSS/**P**/C_{60}/BCP/Cu	0.45	24.87	0.63	7.05	Tsai[339]
$FASnI_3$ + 2.5% N_2H_5Cl + 10% SnF_2	EDOT:PSS/**P**/C_{60}/PCBM/BCP/Ag	0.46	17.64	0.67	5.40	Li[340]
$FASnI_3$ + 12% SnF_2	PEDOT:PSS(PEG)/**P**/PCBM/BCP/Ag	0.46	17.64	0.67	5.40	
$MASnI_3$ + 20% SnF_2	PEDOT:PSS/**P**/C_{60}/BCP/Ag	0.45	11.82	0.40	2.14	Chen[341]
$FASnI_3$ + 1% $EDAI_2$		0.58	21.3	0.72	8.9	Jokar[342]
$FASnI_3$		0.64	21.95	0.73	10.16	Meng[343]

[a] **FTO** = Fluorine-Doped Tin Oxide, **ITO** = Indium Tin Oxide, **c-TiO_2** = Compact TiO_2, **mp-TiO_2** = Mesoporous TiO_2, **spiro-OMeTAD** = 2,2′,7,7′-tetrakis(*N*,*N*′-di-p-methoxyphenyl-amine)9,9′-spirobifluorene, **PCBM** = Phenyl-C_{61}-butyric acid methyl ester, **BCP** = Bathocuproine (2,9-Dimethyl-4,7-diphenyl-1,10-phenanthroline), **PEDOT:PSS** = Poly(3,4-ethylenedioxythiophene)-poly(styrenesulfonate), **PEDOT:PSS(PEG)** = PEDOT:PSS + Polyethylene glycol

Table 2.15 Photovoltaic parameters and device architectures of various tin-based PSCs prepared through various methods. Taken and adapted from Li *et al.*,[325] Jena *et al.*[78] and Wang *et al.*[303] Either ITO or FTO was used as the glass substrate. Primary authors are acknowledged in the Author column (*et al.* is implied).[a]

Preparation Method	Perovskite (P)	Device Architecture	V_{OC} (V)	J_{SC} (mA·cm^{-2})	FF	PCE (%)	Author
Hot-casting	$BA_2MA_3Sn_4I_{13}$ + 100% SnF_2	c-TiO_2/mp-TiO_2/**P**/PTAA/Au	0.229	24.1	0.46	2.53	Cao[313]
	$MASnI_3$ + 20% SnF_2/hydrazine		0.378	19.92	0.52	3.89	Moyez[344]
	$CsSnI_3$ + 20 SnF_2/hydrazine		0.170	30.75	0.35	1.83	
	$CsSnBr_3$ + 20% SnF_2		0.367	13.96	0.59	3.04	
	$MASnI_3$	PEDOT/**P**/PCBM/Al	0.595	17.8	0.30	3.2	Wang[345]

Table 2.15 (Continued) Photovoltaic parameters and device architectures of various tin-based PSCs prepared through various methods. Taken and adapted from Li *et al.*,[325] Li *et al.*, Jena *et al.*[78] and Wang *et al.*[303] Either ITO or FTO was used as the glass substrate. Primary authors are acknowledged in the Author column (*et al.* is implied).[a]

Vapour-assisted	$MASnI_3$	c-TiO_2/mp-TiO_2/**P**/PTAA/Au	0.273	17.36	0.39	1.86	
	$MASnI_{3-x}Br_x$		0.452	5.02	0.48	1.10	Handa[330]
Quantum rods	$CsSnI_3$	c-TiO_2/**P**/spiro-OMeTAD/Au	0.86	23.2	0.65	12.96	Zhao[346]
	$CsSnBr_3$		0.85	21.23	0.58	10.46	
	$CsSnCl_3$		0.87	19.82	0.56	6.66	
Sequential deposition	$FASnI_3$ + 10% SnF_2 + TMA	SnO_2/C_{60}/**P**/spiro-OMeTAD/Ag	0.31	21.65	0.65	4.34	Shum[347]
	$FASnI_3$ + 10% SnF_2 + TMA	PEDOT:PSS/**P**/C_{60}/bis-$C_{60/Ag}$	0.47	22.45	0.68	7.09	
	$FASnI_3$	PEDOT:PSS/**P**/C_{60}/BCP/Ag	0.33	17.78	0.68	3.98	Shao[322]
Thermal evaporation	$MASnBr_3$	c-TiO_2/**P**/P3HT/Au	0.50	4.27	0.49	1.12	Jung[288]
	$CsSnBr_3$ + 2.5% SnF_2	MoO_3/**P**/C_{60}/BCP/Ag	0.40	2.4	0.55	0.55	Chen[278]
	(PEA, FA)SnI_3	LiF/PEDOT:PSS/**P**/C_{60}/BCP/Ag	0.47	20.07	0.74	6.98	Xi[348]
	$MASnI_3$	PEDOT:PSS/TPD/**P**/C_{60}/BCP/Ag	0.38	12.1	0.37	1.7	Moghe[349]
	$CsCSnI_3$	ITO/**P**/Au/Ti	0.42	4.80	0.22	0.88	Lee[297]
Direct dropping	$MASnIBr_{1.8}Cl_{0.2}$ + 20% SnF_2	c-TiO_2/mp-TiO_2/mp-Al_2O_3/**P**/carbon	0.38	13.99	0.57	3.11	Ran[350]
Hot-dropping	$CsSnIBr_2$ + 60% SnF_2 + H_3PO_2		0.31	17.4	0.56	3.2	Yu[351]

[a] **FTO** = Fluorine-Doped Tin Oxide, **ITO** = Indium Tin Oxide, **c-TiO_2** = Compact TiO_2, **mp-TiO_2** = Mesoporous TiO_2, **PTAA** = Poly(bis(4-phenyl)(2,4,6-trimethylphenyl)amine), **PEDOT:PSS** = Poly(3,4-ethylenedioxythiophene)-poly(styrenesulfonate), **PCBM** = Phenyl-C_{61}-butyric acid methyl ester, **spiro-OMeTAD** = 2,2′,7,7′-tetrakis(*N*,*N*'-di-p-methoxyphenyl-amine)9,9′-spirobifluorene, **BCP** = Bathocuproine (2,9-Dimethyl-4,7-diphenyl-1,10-phenanthroline), **P3HT** = poly(3-hexylthiophene-2,5-diyl), **TPD** = triphenylamine dimer: *N*,*N*′-diphenyl-bis(4-methylphenyl)-biphenyl-4,4′-diamine polymer, **mp-Al_2O_3** = Mesoporous Al_2O_3

2.3.4 Germanium-Based PSCs

Like both tin and lead, germanium-analogues have been observed to have similar optoelectronic properties in perovskites as its two counterparts.[352] With the ionic radius of Ge^{2+} being the smallest of the divalent ions of germanium, tin and lead, the optimal combinations of cations and halides to form the $AGeX_3$ 3D cubic perovskite structure differs from its tin and lead analogues. For example, in contrast to lead- and tin-based perovskites, increasing A-site cation radii increases the band gap observed in germanium-based perovskites.[353] Moreover, certain cations that are "larger" than MA^+, for example, GUA^+, $TriMA^+$ etc., lead to a change of the 3D dimensionality of the $AGeX_3$ perovskite to a 1D structure. This loss in dimensionality leads to higher band gaps, and the band gaps changing from direct to indirect, resulting in poor absorption. Hence, the lower dimensionality structures will not be discussed here.[354] For example, the structures $GUAGeI_3$, $IPAGeI_3$, and $TMAGeI_3$ all exhibit 1D chain-like structures, with band gaps of 2.7 eV, 2.5 eV, and 2.8 eV, respectively, making them unsuited for PSC applications.[354] Furthermore, an increase in band gap is seen when the ionic radius of the halide anion used decreases, so for the compound $CsGeX_3$, the band gaps for the X = I^--, Br^-- or Cl^--analogues are 1.6 eV, 2.3 eV and 3.2 eV respectively.[355–357]

Ge-based PSCs have not proved useful yet, since several issues still need to be addressed, such as severe moisture sensitivity.[353] That said, Ge-based PSCs (specifically $MAGeI_3$) do show tremendous theoretical potential in the conduction of holes and electrons.[358]

In 2015, Stoumpos *et al*. synthesised a range of germanium-based halide perovskites, $AGeI_3$, using different A-site cations, such as Cs^+, MA^+, FA^+ and others, with the compounds exhibiting a range of optical band gaps between 1.6 eV and 2.8 eV, with the band gap strongly dependent on the A-site cation used.[354] In general, $AGeI_3$ has been experimentally found to exhibit wider band gaps than the corresponding tin and lead analogues, which differs from the expected trend. In theory, germanium-containing analogues should have the narrowest band gaps of all lead-, tin- and germanium-based perovskites. This is because it becomes progressively easier (less energy is required) to excite the ns^2 electrons in lead ($6s^2$) versus tin ($5s^2$) versus germanium ($4s^2$), leading to a narrower band gap.[354]

Two reasons are suggested for the unexpectedly wide band gap of $AGeI_3$ perovskites.[21] The first is that the germanium 4*s* electrons are lower in energy than the 5*s*-states of tin and the 6*s*-states of lead. This translates into weaker halogen *p*-state hybridisation, lowering the valence band maximum energy. The second is the distortion seen in the GeI_6 octahedra, where three long (3.26–3.58 Å) Ge–I and three shorter (2.73–2.77 Å) Ge–I bond lengths are observed (see Figure 2.17 (a) and (b)). This distortion of the octahedra negatively affects the electronic properties of the perovskite.

Nevertheless, germanium-based perovskites show potential as absorbers in PSCs since they are stable above 150 °C.[264] Specifically, the 3D perovskites $CsGeI_3$, $MAGeI_3$, and $FAGeI_3$ with band gaps of 1.63 eV, 2.0 eV and 2.35 eV, and all being in the rhombohedral phase at room temperature, are of interest.[359] The most promising of these is $CsGeI_3$ since it has the highest optical absorption coefficient of the three.[354] Additionally, $MAGeI_3$ and $CsGeI_3$ show nearly complete film coverage morphology, whereas $FAGeI_3$ delivers poor film quality.[359] However, their application has been limited due to the same oxidation problem encountered with their tin analogues. A few of the most notable applications are discussed next.

Krishnamoorthy *et al.* developed two germanium iodide PSCs, utilising TiO_2 as the ETL and spiro-OMeTAD as the HTM.[359] $CsGeI_3$ and $MAGeI_3$ exhibited PCEs of 0.11% and 0.20%, respectively, whereas the $FAGeI_3$ film failed to deliver a photocurrent. Low values for the open circuit voltage, short circuit current, and fill factor were obtained. Kopacic *et al*. built on this initial work and substituted 10% of the iodide ions in the $MAGeI_3$ structure with bromide ions to form $MAGeI_{2.7}Br_{0.3}$, which, in the same device architecture as Krishnamoorthy *et al.* employed, delivered a PCE of 0.57%.[360] However, this was a significant improvement from the first report, even though it was still not comparable to the efficiencies of either tin- or lead-based PSCs.

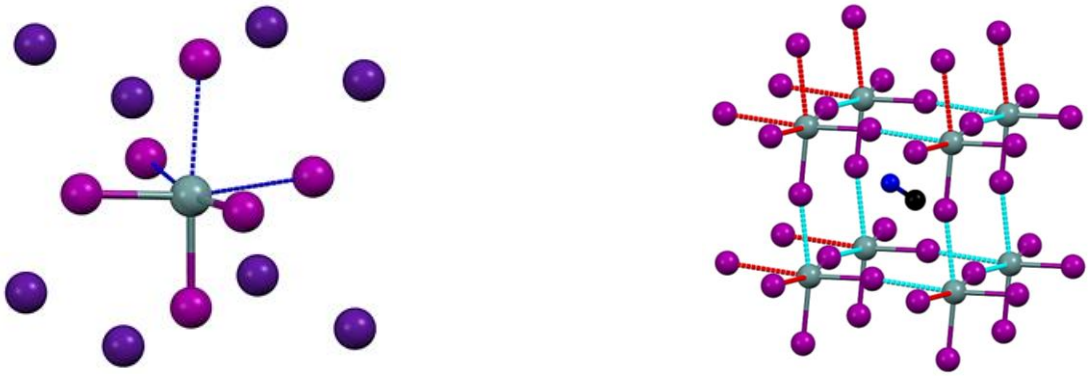

(a) **(b)**

Figure 2.17 (a) A $[GeI_6]^{4-}$-ion surrounded by eight Cs^+-ions, illustrating the two different bond lengths in the Ge–I octahedra (solid bonds are shorter than the bonds shown as dashed lines) and **(b)** a perovskite building block of $MAGeI_3$.

Tin-Germanium Mixtures

Improved stability has been shown in theoretical and experimental studies when germanium is substituted with tin in germanium-based PSCs. To this end, Zeng *et al.* theoretically considered 17 different combinations of $AB_{0.5}B'_{0.5}X_3$ and $A_{0.5}A'_{0.5}B_{0.5}B'_{0.5}X_3$ for PSC applications (see Figure 2.18).[361] These combinations gave varying theoretical band gap values, ranging between 0.9 eV and 3.15 eV. The most promising of these combinations was $RbSn_{0.5}Ge_{0.5}I_3$, with a direct band gap of 1.6 eV and a promising maximum Shockley–Queisser efficiency of 25% for a single-junction PSC device. In addition, Nagane *et al.* synthesised a range of $MASn_{1-x}Ge_xI_3$ perovskites with band gap values between 1.3 eV and 2.0 eV, making them prime candidates for applications in both single-junction and tandem PSCs.[362] Germanium has also been used as a dopant (5%) in tin-based PSCs (specifically with $FA_{0.75}MA_{0.25}SnI_3$ as the sensitiser) to improve efficiency.[363] The suggested reason for the improved efficiency is that the germanium dopant fills the tin-vacancies, allowing for better charge carrier abilities.[259] To date, the maximum efficiency for a tin-germanium mixed PSC device is 7.9%, utilising an FTO/PEDOT:PSS/$FA_{0.75}MA_{0.25}Sn_{x-1}Ge_xI_3$/PCBM/$C_{60}$/BCP/Ag/Au device architecture and SnF_2 as an additive.[364] Moreover, the device showed improved stability and reproducibility compared to the device based on mono-metal structures. This family of materials are yet to be as extensively investigated as other lead-free alternatives, and hence a lot of scope remains for further research.

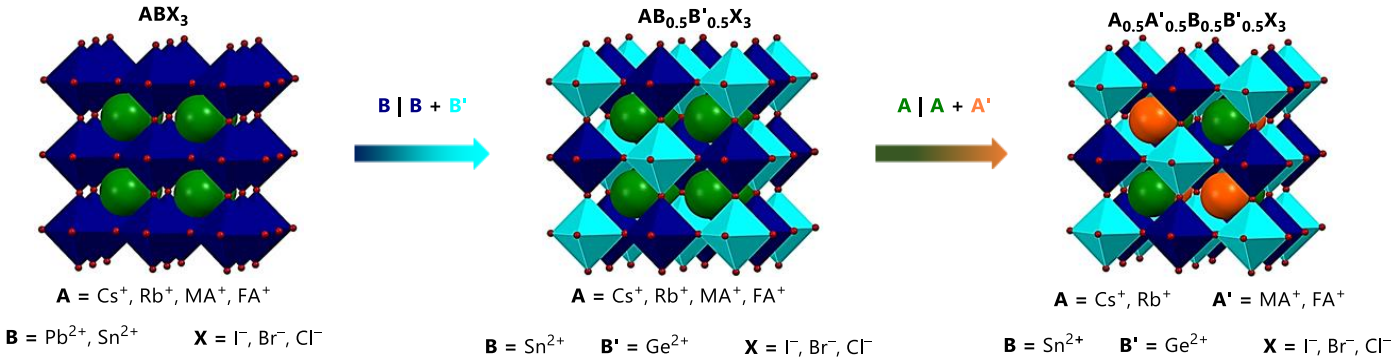

Figure 2.18 A schematic illustration, with examples, of how the partial replacement of A- and B-cations, by A'- and B'-cations, in the ABX_3 perovskite lattice leads to double perovskite of the form $AB_{0.5}B'_{0.5}X_3$ and $A_{0.5}A'_{0.5}B_{0.5}B'_{0.5}X_3$ perovskites. Adapted from Li *et al.*[325]

2.3.5 Transition Metal-Based PSCs

The natural abundance and rich chemistry surrounding transition metals make them attractive substitutes for lead in lead-free PSCs. Most transition metals have a stable 2+ oxidation state and hence are prime candidates to replace Pb^{2+}. However, their multitude of oxidation states makes them susceptible to easy oxidation or reduction, leading to stability issues (such as for tin- and germanium-based PSCs) and the appearance of trap states in the perovskite lattice.[21]

Moreover, transition metal ions usually have smaller ionic radii than Pb^{2+} (73 pm, 78 pm, and 86 pm for Cu^{2+}, Fe^{2+}, and Pd^{2+}, respectively versus 119 pm for Pb^{2+}), which causes sterically hindered perovskites with cations such as MA^+, leading to lower-dimensional structures than the desired 3D perovskite structures. The general structure of transition metal perovskites are that of the 2D perovskites $(RNH_3)_2M(II)X_4$, for example, $MA_2CuCl_xBr_{4-x}$,[365] MA_2FeCl_4,[366] and MA_2PdCl_4.[367]

Of these examples listed, only the copper-based perovskites have been applied to PSCs. The optical properties of $MA_2CuCl_xBr_{4-x}$ have been studied theoretically and experimentally by Cortecchia *et al*.[365] They mixed MABr, MACl, $CuCl_2$ and $CuBr_2$ in DMSO as the precursor solution to obtain materials with tuneable band gaps between 2.48 eV to 1.80 eV, proportional to the bromide content. Figure 2.19 (a) shows the structure of $MACuCl_2Br_2$, which is representative of the entire $MA_2CuCl_xBr_{4-x}$ family and (b) an isolated $[CuX_6]^{4-}$ octahedra, with alternating bond lengths in three directions, due to Jahn-Teller distortion. The study concluded that large effective masses of charge carriers, a low absorption coefficient and high trap state density could place major limitations on the efficiencies of copper-based PSCs. Hence, the efficiencies obtained for FTO/c-TiO_2/mp-TiO_2/$MA_2CuCl_xBr_{4-x}$/spiro-OMeTAD/Au devices were rather low (< 0.2%).

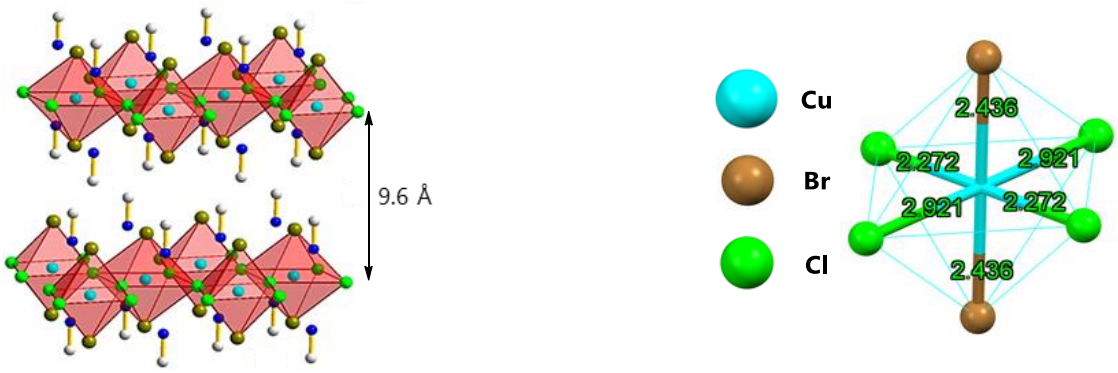

Figure 2.19 (a) The $MA_2CuCl_2Br_2$ crystal structure, showing the layered characteristics of a 2D perovskite structure and **(b)** the three distinct sets of Cu–X bond lengths (X = Cl^- and Br^-). Bond lengths are given in units of Å. (a) reproduced with permission.[365] Copyright American Chemical Society 2016.

These initial reports on the *failure* of copper-based PSCs did not prevent more research on using these materials in PSCs. Cui *et al*. showed that (p-F-$C_6H_5C_2H_4$-NH_3)$_2CuBr_4$- and $(CH_3(CH_2)_3NH_3)_2CuBr_4$-based PSCs could obtain PCEs of 0.51 and 0.63%, respectively.[356] Work done by Li *et al*. showed that a PCE of 0.2% could be obtained for $(C_6H_5CH_2NH_3)_2CuBr_4$-based PSCs.[357] Overall, though they lack high PCE, the copper-based PSCs are much more stable than other PSC devices. Hence, once their charge carrier abilities have been improved, they might become some of the most promising replacements for lead perovskites in PSC technology.

2.3.6 Alkaline Earth Metal-Based PSCs

The divalent alkaline-earth metals have been studied theoretically in the perovskite structure with MA^+ as the A-site cation.[368,369] However, they possess wide band gaps due to the high ionicity of the metal cations, making them unfavourable for photovoltaic applications. Moreover, the calculations were carried out using standard DFT methods, which means that the calculated band gap values underestimated the true values. The studied materials included $MACaI_3$, $MASrI_3$ and $MBaI_3$,

having band gap values of 2.95 eV, 3.6 eV and 3.3 eV, respectively. One of the only experimental studies completed on this type of material was conducted by Uribe *et al.*[370] They synthesised $MACaI_3$ and confirmed the wide band gap value. This wide band gap was confirmed by the white colour of the $MACaI_3$ sample.

That said, alkaline-earth metals are not entirely without use in PSCs. For example, they find applications in so-called lead-less PSCs, which are discussed in Section 2.4.

2.3.7 Low-Dimensional Structure PSCs

Although the ideal perovskite absorber structure would have a 3D structural dimensionality to allow for a high electronic dimensionality, many lower dimensional structures have been considered for application in PSCs. This section covers the most prominent of the lower dimensional structures used in PSCs to date.

0D A_2BX_6 Perovskite Variants

When using a tetravalent B-cation (B^{4+}) to substitute a divalent B-cation such as lead in ABX_3, the result is that half of the B-sites become vacant to achieve charge neutrality. Hence, the notation of $A_2\square BX_6$ is often used, where □ indicates the presence of a B-site vacancy. These structures have attracted attention for PSC application due to their black appearance (therefore, high absorption of light), as shown in Figure 2.20 (a) for a sample of Cs_2PdBr_6.[371] The B^{4+}-ions adopt rock salt-like arrangements (alternating ordered vacancy and octahedra in three dimensions, see Figure 2.20 (b)). Due to the ordered nature of the B^{4+}-cations and the B-site vacancies, these perovskites are often referred to as vacancy-ordered double perovskites. In this section, specific focus is placed on the structures where the $[BX_6]^{2-}$ octahedra are not connected, and hence a 0D structure dimensionality is observed. This means that their optoelectronic properties differ quite drastically from the properties of 3D compounds employed in PSCs. These materials show intrinsic n-type conductivity.

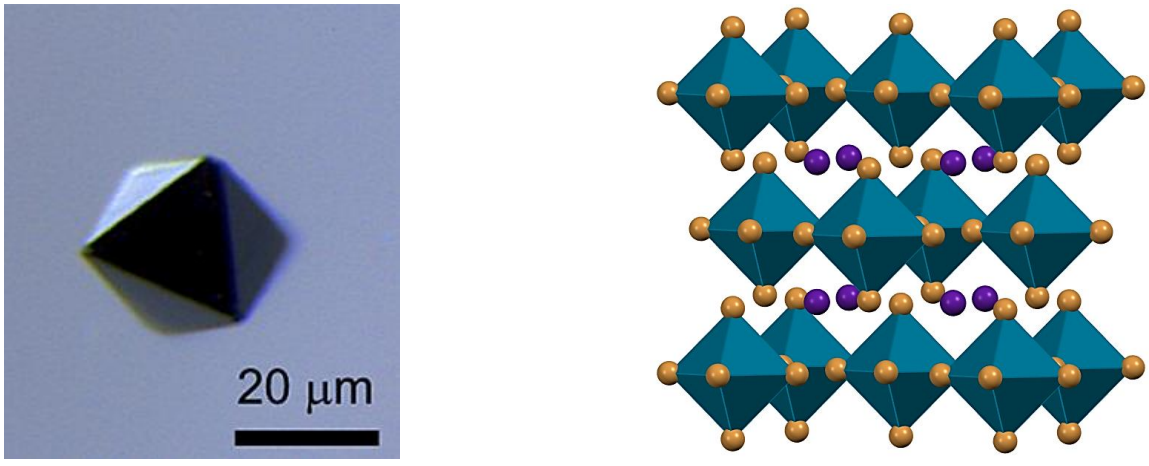

(a) **(b)**

Figure 2.20 (a) A microscope image of a Cs_2PdBr_6 single-crystal. Reproduced with permission. Copyright American Chemical Society 2017.[371] **(b)** The 0D crystal structure of Cs_2PdBr_6 showing the cubic unit cell with isolated $[PdBr_6]^{2-}$ octahedra.[371]

The compounds of Cs_2SnI_6,[372] Cs_2PdBr_6,[371] and Cs_2TiBr_6,[373] have band gap values of 1.5 eV, 1.6 eV and 1.8 eV respectively, making them prime candidates for PSC applications. However, only a few reports on their application have been published. Qiu *et al.* employed the perovskite Cs_2SnI_6 and achieved a PCE of 0.96%.[372,374] Later, Lee *et al.* considered $Cs_2SnI_{6-x}Br_x$ films, which had varying band gaps between 1.3 eV and 2.9 eV for $x = 0$ to $x = 6$.[375] A champion PCE of 2.1%

for the perovskite absorber $Cs_2SnI_4Br_2$ was obtained. Most notably, Chen *et al*. obtained a PCE of 3.3% utilising a Cs_2TiBr_6-based (band gap of 1.8 eV) device.[373]

Though there are few reports on this type of material, it does provide one potential avenue to utilise the tendency of Sn^{2+} and like-metals to oxidise as an advantage. Since they naturally form their B^{4+} oxidation state, the 0D vacancy ordered structure can be formed. Furthermore, the A_2BX_6 materials can be used as hole transport materials in DSSCs. For example, Cs_2SnI_6 has been shown to allow for a PCE of 8% when used as an HTL in the device FTO/TiO_2/Cs_2SnI_6/Pt/FTO.[376]

Other low toxicity options for Cs_2BX_6 compounds include B = Ti^{4+}, Pd^{4+}, Pt^{4+} or Nb^{4+}. Of these, Cs_2TiBr_6 and Cs_2PtI_6 show the most promise, with band gaps of 1.8 eV and 1.4 eV, respectively.[373,377] Moreover, the Cs_2PtI_6 material has been used in the device FTO/CdS/Cs_2PtI_6/carbon/Cu to deliver a PCE of 13.88%, indicating great promise in this field, since this PCE is comparable to that of lead-containing PSCs.[377]

0D $A_3B_2X_9$ Non-Perovskites (Dimer Phases)

In venturing around the periodic table in the lead region, two elements with similar electronic configurations and ionic radii to lead are antimony and bismuth. Their similarity allows for substitution into the same perovskite lattice types as those containing lead. Sb and Bi form perovskites, perovskite-like and non-perovskite materials of the form $A_3M_3X_9$ or $A_3M_2X_9$, where A includes Cs^+, Rb^+ and MA^+ and X is either Cl^- or I^-.[378–381] These structures have enjoyed attention due to their high moisture stability and non-toxicity.

By removing one-third of the B-sites in the ABX_3 parent structure, trivalent B-cations can be used to form the structure $A_3B_2X_9$ (see, for example, Figure 2.21 (a) for $Cs_3Bi_2I_9$). This structure typically has two polymorphs, one being a dimer phase (0D non-perovskite isolated face-shared $[B_2X_9]^{3-}$ bi-octahedra) and the second a 2D layered modification of a vacancy-ordered perovskite.[382]

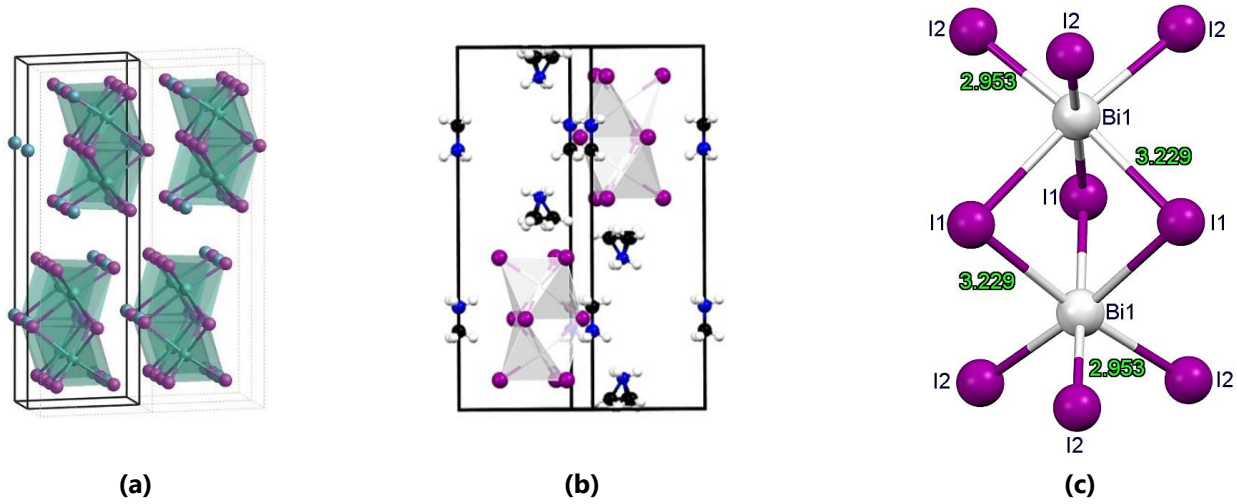

Figure 2.21 (a) Two neighbouring unit cells of $Cs_3Bi_2I_9$ consisting of isolated $[Bi_2I_9]^{3-}$ bioctahedra. Reproduced with permission.[383] Copyright 2015, Wiley-VCH. **(b)** The unit cell of the crystal structure of $MA_3Bi_2I_9$ also consisting of isolated $[Bi_2I_9]^{3-}$ bioctahedra and **(c)** the structure of a $[Bi_2I_9]^{3-}$ anion in the $MA_3Bi_2I_9$ structure. Bond lengths are given in units of Å. Adapted from Eckhardt *et al*.[384]

The 0D structures have the lowest possible structural dimensionality and low electronic dimensionality, making them less suited for photovoltaic applications. For example, the material $Cs_3Bi_2I_9$ has a calculated indirect band gap of 2.10 eV.[385] In addition, due to the isolated nature of the $[Bi_2I_9]^{3-}$ octahedra, the effective charge carrier masses are large, which negatively impacts charge carrier mobilities, exciton binding energies and absorption.[386,387] Furthermore, the low formation energy of defect states causes a high concentration of deep states, which causes intrinsic charge recombination.[386] These unfavourable

properties have also been reported for other 0D structures[388] and hence these materials have no positive outcome when testing them for photovoltaic applications[389,390] as well. Table 2.16 provides an overview of the work completed on these types of materials in PSCs, and it is evident that there is not much potential.

Bismuth-Based Devices. Eckhardt *et al.*[384] and Park *et al.*[383] investigated the structure of $MA_3Bi_2I_9$, while Hoye *et al.*[388] focussed on its photovoltaic applications. The crystal structure of $MA_3Bi_2I_9$ differs markedly from that of $MAPbI_3$ in that $Bi_2I_9^{3-}$ ions are surrounded by three MA^+-ions rather than a 3D BX-framework surrounding MA^+-ions as in the case of $MAPbI_3$. However, the $MAPbI_3$ structure has a direct band gap of ~1.6 eV, whereas $MA_3Bi_2I_9$ has an indirect band gap of ~2.4 eV. This does imply that the lead counterparts of bismuth-based PSCs will have higher efficiencies. That said, the moisture stability of $MA_3Bi_2I_9$ is much better than that of $MAPbI_3$, with it taking, on average, nearly five times as long to degrade in 61% moisture conditions.

Park *et al*. also considered both $Cs_3Bi_2I_9$ and $MA_3Bi_2I_9$ in a mesoporous device, using a spin coating method of deposition, achieving PCEs of 1.09% and 0.12%, respectively.[383] However, Shin *et al*. then used the same $MA_3Bi_2I_9$ film with a vapour assisted process to achieve a PCE of 3.17%.[391] Furthermore, Bai *et al*. used the inorganic film $Cs_3Bi_2I_9$ and further improved the PCE to 3.20% while using a dissolution-recrystallisation process.[392] Figure 2.22 provides a schematic illustration of the fabrication of a $MA_3Bi_2I_9$ film through a process of dropping and spin coating of precursors, followed by an annealing process.

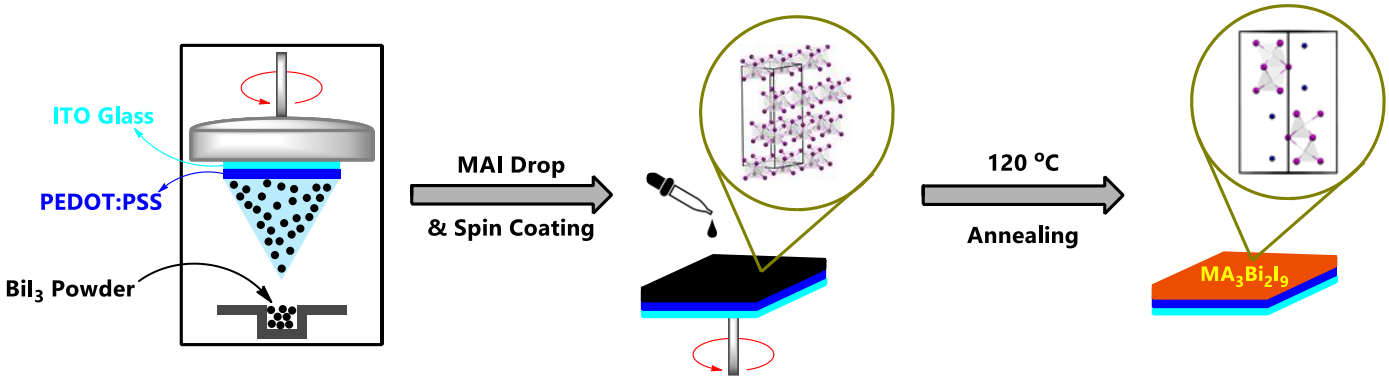

Figure 2.22 The fabrication procedure of $MA_3Bi_2I_9$ film through drop and spin coating of precursors followed by an annealing step. Adapted from Ran *et al.*[393]

The rapid crystallisation of the non-perovskite film ($Cs_3Bi_2I_9$ and $MA_3Bi_2I_9$) has been suggested to cause poor film morphology, leading to lower PCEs due to insufficient charge transport.[394] To address this issue, one possible solution is the use of additives to slow film crystallisation. The additive *N*-methyl-2-pyrrolidone (NMP) was used by Miyasaka *et al*. to good effect, which improved the PCE to 0.31% for $MA_3Bi_2I_9$.

Moreover, it can be seen from the works highlighted here and those listed in the summary table (Table 2.16) that bismuth-based devices are yet to achieve a level of PCE that is competitive compared to other lead-free PSCs. This is mainly attributed to their large band gaps, high effective masses of charge carriers, internal defects, low defect tolerance and large exciton binding energies. Even though much improvement of PCE has been achieved (0.12% to 3.2%) through film deposition engineering and the use of additives, it is improbable that this avenue of research will become competitive as a lead substitute. Unless these structures' structural and electronic dimensionality is increased, no significant improvement in PCE can be expected. One method to increase the structural dimensionality is discussed later under the topic of so-called silver-bismuth like structures.

Antimony-Based Devices. Although antimony is a heavy metal, it can also be employed in these 0D structures the same way bismuth is, but with lower exciton binding energies.[391,395] The reason antimony excites researchers is that it possesses

the same ns^2 electron lone pair as lead does. Table 2.17 provides a summary of the antimony-based PSCs reported in the literature. Some of the most important results are discussed here.

Initial success was achieved by Mitzi *et al.* by fabricating $Cs_3Sb_2I_9$ films for PSC applications through a two-step deposition method.[396] The inorganic species $Cs_3Sb_2I_9$ has a nearly direct band gap of 2.05 eV and showed the same absorption intensity as $MAPbI_3$. However, the PSC fabricated using this as the absorber layer showed a PCE of < 1%, however, with better air stability compared to $MAPbI_3$. Further investigation was conducted by Kirchartz *et al.*, who used $MA_3Sb_2I_9$ in a planar heterojunction solar cell.[397] They also only obtained PCE values of about 0.5%.

One route to address these low efficiencies, is to use HI as an additive in the precursor step. Boopathi *et al.* and Ahmad *et al.* utilised this strategy in devices based on $A_3Sb_2I_9$ (A = MA^+, Cs^+). The device architecture used was ITO/PEDOT:PSS/$A_3Sb_2I_9$/$PC_{71}BM$/C_{60}/BCP/Al, which delivered a PCE of 2.04% for A = MA^+ and 0.84% for A = Cs^+, with minimal hysteresis, which is a considerable improvement on the previously reported values.[398,399] Figure 1.22 (a) shows the crystal structure of $A_3Sb_2I_9$, and in (b), a schematic illustration of the photovoltaic device used is shown.

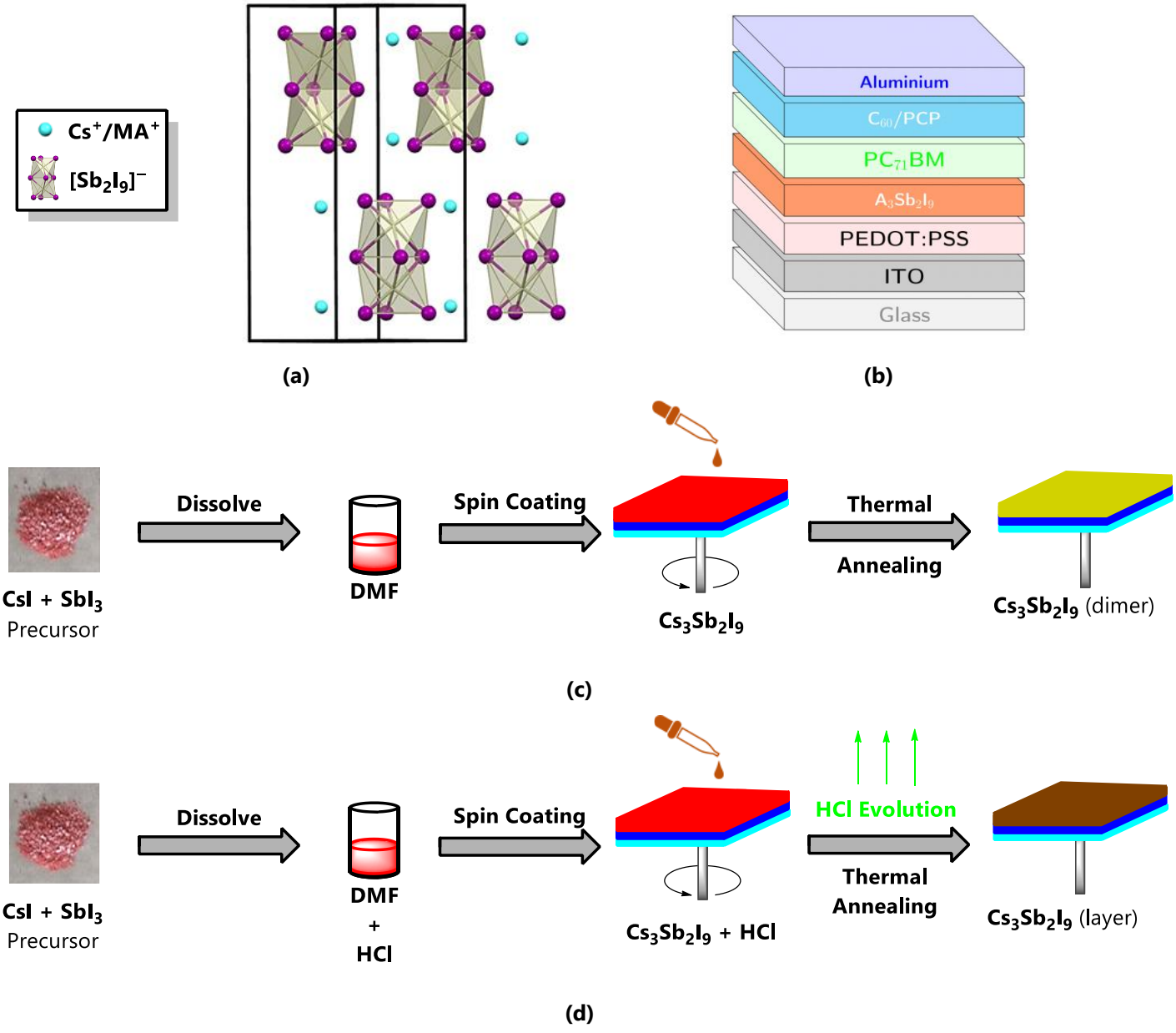

Figure 2.23 (a) The unit cell and crystal structure of the $A_3Sb_2I_9$ perovskite materials, where A = MA^+ or Cs^+ and **(b)** a schematic representation of a planar PSC. Adapted from Boopathi *et al.*[398] The fabrication processes of **(c)** a $Cs_3Sb_2I_9$-dimer film and **(d)** a $Cs_3Sb_2I_9$-layered film. Adapted from Umar *et al.*[400]

The suggested reason for these low PCE values is that the 0D dimer antimony layer suffers from a low symmetry band gap, quantum confinement effects and poor carrier mobility.[397] To a certain extent, if the 0D structure can be converted to a 2D structure, most of these effects can be evaded. One method to control the formation of the 0D polymorph versus the 2D polymorph has been suggested by Umar *et al.*[400] The use of HCl as an additive helps in the formation of the 2D layered structure, rather than the 0D dimer (see Figure 2.23 (c) and (d)). This topic is the focus of the following section.

2D $A_3B_2X_9$ Layered Perovskites (Layer Phases)

The second polymorph, in addition to the 0D phase, of the $A_3B_2X_9$ structure is a vacancy-ordered layered perovskite, with the general formula of $A_3(B_{2/3}\square_{1/3})_3X_9$ or $A(B_{2/3}\square_{1/3})X_3$ as shown in Figure 2.24 (a). This structure can be derived from the 3D ABX_3 structure by removing every third layer of B-site cations along the ⟨111⟩ direction. It is expected that the 2D layered phase should have a more direct, narrower band gap and better in-layer transport properties than the 0D dimer polymorph discussed previously.[303]

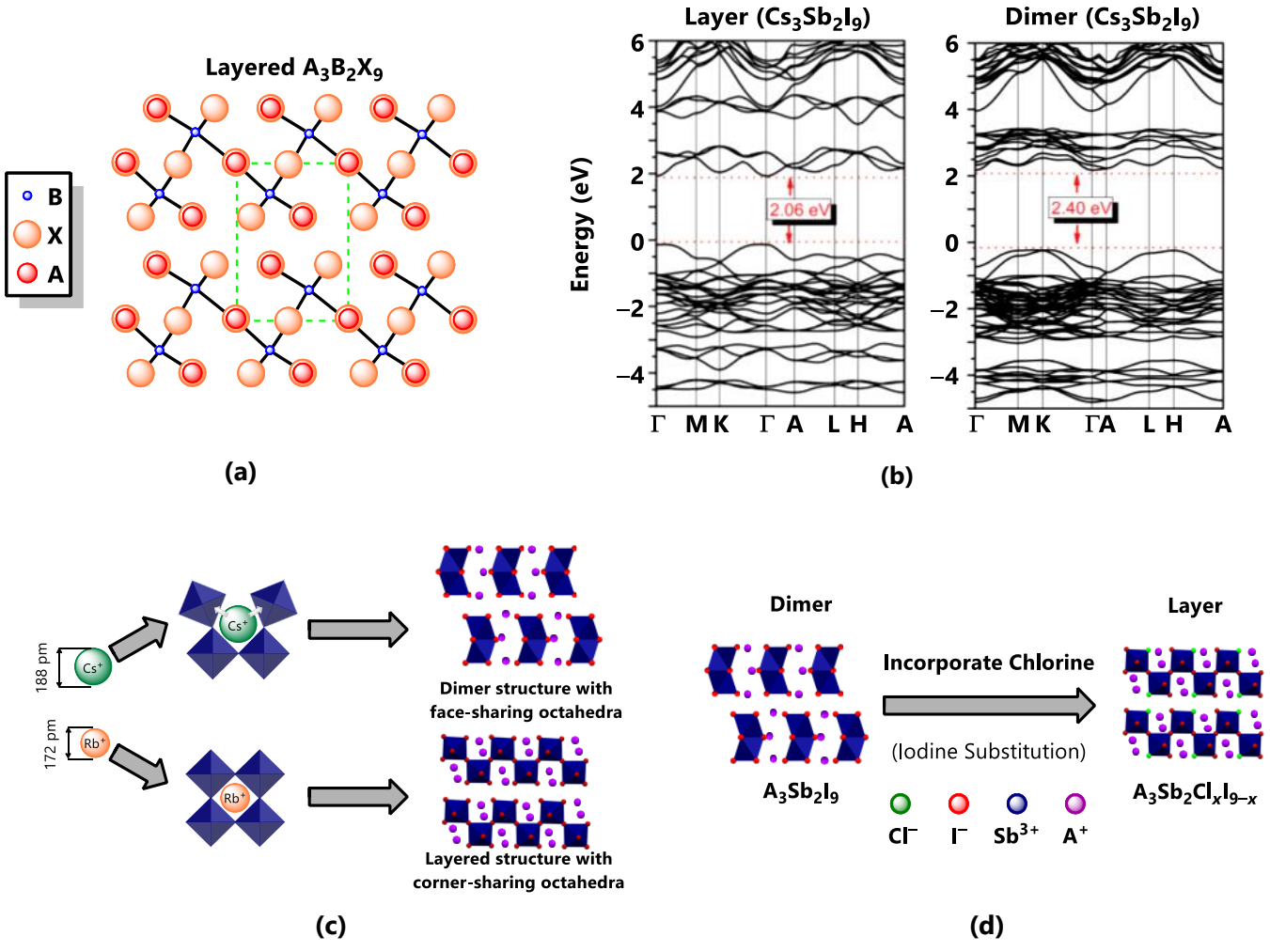

Figure 2.24 (a) The layered perovskite $A_3B_2X_9$'s crystal structure (unit cell shown in green) viewed down the *c*-axis and **(b)** the band structures of the layered and dimer polymorphs of $Cs_3Sb_2I_9$. (a) and (b) adapted and reproduced with permission.[396] Copyright 2015, American Chemical Society. **(c)** A schematic illustration showing how the size of the A-cation influences the polymorphism of the structure $A_3Sb_2I_9$. Adapted from Harikesh *et al.*[401] **(d)** A schematic illustration of crystal engineering through the substitution of iodide for chloride in the structure of $A_3Sb_2I_9$ allows for the formation of the 2D layered phase $A_3Sb_2Cl_xI_{9-x}$. Adapted from Jian *et al.*[402]

The added structural dimension allows for a higher electronic dimension than that of the dimer polymorph discussed earlier, inferring that this polymorph should have better success in photovoltaic applications. For example, Saparov *et al.* theoretically studied the dimer and layer polymorphs of $Cs_3Sb_2I_9$ and determined from their band diagrams (see Figure 2.24 (b)) that the layered polymorph has a nearly direct band gap of 2.06 eV. In contrast, the dimer polymorph has an indirect one of 2.40 eV, demonstrating the higher electronic dimensionality of the former.[396] The calculations further showed deep defect states in the layered phase, leading to non-radiative recombination and an overall loss of device efficiency when used in photovoltaic applications.

Therefore, the layered polymorph is more sought after than the dimer polymorph. However, by employing simple solution techniques, the dimer polymorph is more readily obtained, and much effort has been put into developing strategies to synthesise the layered polymorph. In the same paper reporting the theoretical study conducted by Saparov *et al.*, the synthesis of $Cs_3Sb_2I_9$ was also reported.[396] CsI and SbI_3 precursors were co-evaporated and thereafter annealed to deliver $Cs_3Sb_2I_9$ films. These films showed a band gap of 2.05 eV and superior stability compared to traditional lead-based PSCs. That said, initial PCEs were below 1%.

Thereafter, Harikesh *et al*. showed that when the A-site cation is changed to a smaller cation like Rb^+ or NH_4^+, the layered polymorph is obtained in a solution process, as schematically illustrated in Figure 2.24 (c).[401] However, the PCE of the Rb^+-cation device was still only 0.66%. Other attempts using the small cation NH_4^+ in the compound $NH_4Sb_2I_9$ also delivered a low PCE of 0.51%.[403] Later, Jiang *et al*. showed that the introduction of chloride ions to form $MA_3Sb_2Cl_xI_{9-x}$ resulted in the stabilisation of the layered phase (Figure 2.24 (d)). These chloride-stabilised films could reach an experimental PCE of 2.19% when used in a PSC device.[402]

Though the 2D polymorph is yet to set the world alight in terms of PCE values, it is the better choice between the two polymorphs. This is because its direct band gap votes well for PSC applications. Hence, once the band gap value can be fine-tuned closer to the optimal value of 1.1 eV (for example, by doping), its non-toxicity and air/heat-stability could potentially result in it outshining its lead alternatives.

Table 2.16 Photovoltaic parameters and device architectures of various bismuth-based PSCs prepared through various methods. Taken and adapted from Li *et al.*,[325] Jena *et al.*[78] and Wang *et al.*[303] Primary authors are acknowledged in the Author column (*et al.* is implied).[a]

Preparation Method	Perovskite (P)	Device Architecture	V_{OC} (V)	J_{SC} (mA·cm^{-2})	FF	PCE (%)	Author
One-step spin coating	$Cs_3Bi_2I_9$	c-TiO_2/mp-TiO_2/**P**/P3HT/Ag	0.31	0.34	0.38	0.40	Zhang[404]
		c-TiO_2/mp-TiO_2/**P**/spiro-OMeTAD/Ag	0.85	2.15	0.60	1.09	Park[383]
		c-TiO_2/**P**/spiro-OMeTAD/Au	0.79	4.45	0.50	1.77	Shin[391]
		c-TiO_2/**P**/CuI/Au	0.86	5.78	0.64	3.20	
		c-TiO_2/**P**/PTAA/Au	0.83	4.82	0.58	2.30	
	$MA_3Bi_2I_9$	c-TiO_2/**P**/spiro-OMeTAD/Au	0.72	0.49	0.32	0.11	Cui[356]
		c-TiO_2/mp-TiO_2/**P**/spiro-OMeTAD/Au	0.68	0.38	0.88	0.22	Ran[393]
		c-TiO_2/mp-TiO_2/**P**/spiro-OMeTAD/Ag	0.68	0.52	0.33	0.12	Park[383]
		c-TiO_2/mp-TiO_2/**P**/P3HT/Au	0.35	1.16	0.46	0.19	Johansson[405]
		c-TiO_2/mp-TiO_2/**P**/PIF8-TAA/Au	0.85	1.22	0.73	0.71	Baranwal[406]
		ITO/c-TiO_2/mp-TiO_2/**P**/spiro-OMeTAD/MoO_3/Ag	0.67	1.00	0.63	0.42	Zhang[407]
	$MA_3Bi_2I_9Cl_x$	c-TiO_2/mp-TiO_2/**P**/spiro-OMeTAD/Ag	0.04	0.18	0.38	0.03	Park[383]
Two-step evaporation spin coating	$MA_3Bi_2I_9$	PEDOT:PSS/**P**/C_{60}/BCP/Ag	0.83	1.39	0.37	0.39	Hoye[388]
Two-step thermal evaporation	$MA_3Bi_2I_9$	c-TiO_2/mp-TiO_2/**P**/spiro-OMeTAD/Au	0.83	3.00	0.79	1.64	Abulikemu[408]
Vapour-assisted solution process	$MA_3Bi_2I_9$	c-TiO_2/mp-TiO_2/**P**/P3HT/Au	1.01	4.02	0.78	3.17	Lyu[409]

Table 2.16 (Continued) Photovoltaic parameters and device architectures of various bismuth-based PSCs prepared through various methods. Taken and adapted from Li *et al.*,[325] Li *et al.*, Jena *et al.*[78] and Wang *et al.*[303] Primary authors are acknowledged in the Author column (*et al.* is implied).[a]

Preparation Method	Perovskite (P)	Device Architecture	V_{OC} (V)	J_{SC} (mA·cm^{-2})	FF	PCE (%)	Author
Vapour-assisted	$MA_3Bi_2I_9$	FTO/c-TiO_2/mp-TiO_2/**P**/P3HT/Au	1.01	4.02	0.78	3.17	Jain[395]
Vapour deposition	$MA_3Bi_2I_9$	FTO/c-TiO_2/mp-TiO_2/**P**/spiro-OMeTAD/Au	0.81	2.95	0.69	1.64	Zhang[404]
Gas-assisted deposition	$MA_3Bi_2I_9$	ITO/PEDOT:PSS/**P**/C_{60}/BCP/Ag	0.83	1.39	0.34	0.39	Okano[410]
Recrystallisation	$CsBi_3I_{10}$	FTO/c-TiO_2/mp-TiO_2/**P**/TQ1/Au	0.62	2.38	0.52	0.77	Zhu[411]
Spin coating	$CsBi_3I_{10}$	FTO/c-TiO_2/mp-TiO_2/**P**/P3HT/Ag	0.31	3.40	0.38	0.40	Johansson[405]
Recrystallisation	$Cs_3Bi_2I_9$	FTO/c-TiO_2/mp-TiO_2/**P**/CuI/Au	0.68	5.39	0.52	1.09	Ahmad[412]
Anti-solvent	$Cs_3Bi_2I_9$	ITO/NiO_x/**P**/PCBM/C_{60}/BCP/Ag	0.75	0.51	0.59	0.23	Yu[413]
Spin coating	$Cs_3Bi_2I_9$-$Ag_3Bi_2I_9$	FTO/c-TiO_2/mp-TiO_2/**P**/BHJ/PDBD-T/Au	0.78	7.65	0.60	3.59	Hu[414]
One-step spin coating	$CsBi_3I_{10}$	FTO/c-TiO_2/mp-TiO_2/**P**/spiro-OMeTAD/Au	0.53	4.31	0.46	1.05	Liang[415]
Dynamic hot casting	Ag_2BiI_5	FTO/c-TiO_2/mp-TiO_2/**P**/PTAA/Au	0.69	6.04	0.62	2.60	Ghosh[416]
Spin coating	$AgBi_2I_7$	FTO/c-TiO_2/mp-TiO_2/**P**/P3HT/Ag	0.56	3.30	0.67	1.22	Kim[417]
	$AgBi_2I_7$	FTO/c-TiO_2/**P**/spiro-OMeTAD/Au	0.69	2.76	0.44	0.83	Shao[418]
One-step crystallisation	$AgBi_2I_7$	FTO/c-TiO_2/mp-TiO_2/**P**/P3HT/Ag	0.62	4.83	0.70	2.12	Kulkarni[419]
Two-step co-evaporation	$AgBiI_4$	FTO/c-TiO_2/**P**/P3HT/Ag	0.84	2.37	0.44	0.49	Khazanee[420]
Dynamic hot casting	$AgBiI_4$	FTO/c-TiO_2/mp-TiO_2/**P**/PTAA/Au	0.67	5.24	0.62	2.20	Ghosh[416]
One-step spin coating	$(C_5H_6N)BiI_4$	FTO/c-TiO_2/mp-TiO_2/ZrO_2/carbon/**P**	0.62	2.71	0.54	0.90	Li[421]

[a] **FTO** = Fluorine-Doped Tin Oxide, **ITO** = Indium Tin Oxide, **c-TiO_2** = Compact TiO_2, **mp-TiO_2** = Mesoporous TiO_2, **P3HT** = poly(3-hexylthiophene-2,5-diyl), **spiro-OMeTAD** = 2,2′,7,7′-tetrakis(*N*,*N*′-di-p-methoxyphenyl-amine)9,9′-spirobifluorene, **PTAA** = Poly(bis(4-phenyl)(2,4,6-trimethylphenyl)amine), **PIF8-TAA** = Poly[[(2,4-dimethylphenyl)imino]-1,4-phenylene(6,12-dihydro-6,6,12,12-tetraoctylindeno[1,2-b]fluorene-2,8-diyl)-1,4-phenylene], **PEDOT:PSS** = Poly(3,4-ethylenedioxythiophene)-poly(styrenesulfonate), **BCP** = Bathocuproine (2,9-Dimethyl-4,7-diphenyl-1,10-phenanthroline), **TQ1** = Poly[[2,3-bis(3-octyloxyphenyl)-5,8-quinoxalinediyl]-2,5-thiophenediyl], **PCBM** = Phenyl-C_{61}-butyric acid methyl ester, **PDBD-T** = Poly[(2,6-(4,8-bis(5-(2-ethylhexyl)thiophen-2-yl)-benzo[1,2-b:4,5-b']dithiophene))-alt-(5,5-(1',3'-di-2-thienyl-5',7'-bis(2-ethylhexyl)benzo[1',2'-c:4',5'-c']dithiophene-4,8-dione)]

Table 2.17 Photovoltaic parameters and device architectures of various antimony-based PSCs prepared through various methods. Taken and adapted from Li *et al.*,[325] Jena *et al.*[78] and Wang *et al.*[303] Primary authors are acknowledged in the Author column (*et al.* is implied).[a]

Preparation Method	Perovskite (P)	Device Architecture	V_{OC} (V)	J_{SC} (mA·cm^{-2})	FF	PCE (%)	Author
Two-step deposition	$MA_3Sb_2I_9$	FTO/c-TiO_2/mp-TiO_2/**P**/spiro-OMeTAD/Au	0.74	1.40	0.47	0.54	Ahmad[399]
Solution process	$MA_3Sb_2I_9$	ITO/PEDOT:PSS/**P**/$PC_{61}BM$/CO_{60}/BCP/Al	0.62	5.41	0.60	2.04	Boopathi[398]
	$Cs_3Sb_2I_9$	ITO/PEDOT:PSS/**P**/$PC_{60}BM$/CO_{60}/BCP/Al	0.60	2.91	0.48	0.84	
Spin coating	$(NH_4)_3Sb_2I_9$	ITO/PEDOT:PSS/**P**/$PC_{61}BM$/Al	1.03	1.15	0.43	0.51	Zuo[403]
	$MA_3Sb_2Cl_xI_{9-x}$	FTO/c-TiO_2/mp-TiO_2/**P**/spiro-OMeTAD/Au	0.69	5.04	0.63	2.19	Jiang[402]
	(N-EtPY)$SbBr_6$	ITO/c-TiO_2/**P**/P3HT/Au	1.29	5.10	0.58	3.80	Adonin[422]
	$MASbSI_2$	FTO/BL/mp-TiO_2/**P**/PCDP/TBT/PEDOT:PSS/Au	0.65	8.12	0.58	3.08	Nie[423]
	$Rb_3Sb_2I_9$	FTO/c-TiO_2/mp-TiO_2/**P**/Poly-TPD/Au	0.55	2.11	0.57	0.66	Harikesh[401]
Recrystallisation	$Cs_3Sb_2I_9$	FTO/c-TiO_2/mp-TiO_2/**P**/CuI/Au	0.55	3.50	0.28	0.68	Ahmad[412]
Anti-solvent engineering	$Cs_3Sb_2I_9$	FTO/c-TiO_2/**P**/Au	0.61	3.55	0.56	1.21	Umar[400]

[a] **FTO** = Fluorine-Doped Tin Oxide, **ITO** = Indium Tin Oxide, **c-TiO_2** = Compact TiO_2, **mp-TiO_2** = Mesoporous TiO_2, **spiro-OMeTAD** = 2,2′,7,7′-tetrakis(*N*,*N*′-di-p-methoxyphenyl-amine)9,9′-spirobifluorene, **PEDOT:PSS** = Poly(3,4-ethylenedioxythiophene)-poly(styrenesulfonate), **$PC_{61}BM$** = [6,6]-Phenyl-C_{61}-butyric acid methyl ester, **BCP** = Bathocuproine (2,9-Dimethyl-4,7-diphenyl-1,10-phenanthroline), **P3HT** = poly(3-hexylthiophene-2,5-diyl), **BL** = Bulk layer , **PCDPTBT** = poly[2,6-(4,4-bis-(2-ethylhexyl)-4H-cyclopenta[2,1-b;3,4-b′]dithiophene)-alt-4,7-(2,1,3-benzothiadiazole)], **Poly-TPD** = Poly(*N*,*N*′-bis-4-butylphenyl-*N*,*N*′-bisphenyl)benzidine

Table 2.18 Photovoltaic parameters and device architecture of various double perovskite-based PSCs prepared through various methods. Adapted from Li *et al.*,[325] Jena *et al.*[78] and Wang *et al.*[303] Either ITO or FTO was used as the glass substrate. Primary authors are acknowledged in the Author column (*et al.* is implied).[a]

Perovskite (P)	Preparation Method	Device Architecture	V_{OC} (V)	J_{SC} (mA·cm^{-2})	FF	PCE (%)	Author
$Cs_2AgBiBr_6$	Spin coating	c-TiO_2/mp-TiO_2/**P**/spiro-OMeTAD/Au	0.98	3.93	0.63	2.43	Greul[424]
	Low pressure solution processing	SnO_2/**P**/P3HT/Au	1.04	1.78	0.78	1.44	Wu[425]
	Anti-solvent dropping	Cu-NiO/**P**/C_{60}/BCP/Ag	1.00	3.23	0.68	2.21	Gao[426]
	Vapour deposition	c-TiO_2/**P**/P3HT/Au	N/A	N/A	N/A	1.37	Wang[427]
	Spin coating and annealing at high temperatures	c-TiO_2/mp-TiO_2/**P**/PTAA/Au	1.02	1.84	0.67	1.26	Pantaler[428]
		c-TiO_2/mp-TiO_2/**P**/PCDPTBT/Au	0.71	1.67	0.57	0.68	
		c-TiO_2/mp-TiO_2/**P**/spiro-OMeTAD/Au	0.64	2.45	0.57	0.90	
Cs_2NaBiI_6	Spin coating	c-TiO_2/mp-TiO_2/**P**/spiro-OMeTAD/Au	0.47	1.99	0.44	0.42	Chen[429]

[a] **FTO** = Fluorine-Doped Tin Oxide, **ITO** = Indium Tin Oxide, **c-TiO_2** = Compact TiO_2, **mp-TiO_2** = Mesoporous TiO_2, **spiro-OMeTAD** = 2,2′,7,7′-tetrakis(*N*,*N*′-di-p-methoxyphenyl-amine)9,9′-spirobifluorene, **P3HT** = poly(3-hexylthiophene-2,5-diyl) **BCP** = Bathocuproine (2,9-Dimethyl-4,7-diphenyl-1,10-phenanthroline), **PTAA** = Poly(bis(4-phenyl)(2,4,6-trimethylphenyl)amine), **PCDPTBT** = poly[2,6-(4,4-bis-(2-ethylhexyl)-4H-cyclopenta[2,1-b;3,4-b′]dithiophene)-alt-4,7-(2,1,3-benzothiadiazole)]

2.3.8 3D Structures Using Heterovalent Elements

When lead is replaced by non-isovalent elements, like Bi^{3+} and the like, certain vacancies form in the ABX_3 structure to ensure charge neutrality. This leads to lower-dimensional structures, as discussed before. However, ideally, a 3D structure is pursued for photovoltaic applications since this inevitably leads to high electronic dimensionality. Therefore, when replacing lead in the 3D ABX_3 cubic perovskite, the structure should preferably remain 3D. To this end, two ion-splitting methods have been proposed for the heterovalent replacement of lead so that the 3D dimensionality and charge neutrality may be maintained. The first is called anion splitting. Two anions are utilised to ensure charge neutrality and 3D dimensionality. The other method is to replace two Pb^{2+} ions with one monovalent ion (B^+) and one trivalent ion (B^{3+}). These two methods will be discussed in this order in this section, with a preceding section dealing with *other 3D bismuth structures* alluded to earlier.

3D Perovskite Derivatives Silver-Bismuth-Based Solar Cells

Several bismuth-based compounds with reduced band gaps and 3D cubic perovskite-like structures have been synthesised. These structures include $CsBi_3I_{10}$ and $Ag_xBi_yI_{x+3y}$ ($1 \leq x \leq 3$ and $1 \leq y \leq 2$).[419,430–432] A list of the most notable structures that have been determined to date and used in solar cells is given in Table 2.16.

For comparative purposes, Khazaee *et al*. fabricated films using a two-step deposition process with 0D $Cs_3Bi_2I_9$, 2D $Rb_3Bi_2I_9$ and 3D $AgBi_2I_7$. The films had band gap values of 2.16 eV, 2.10 eV, and 1.83 eV, respectively, showing potential as absorbers in solar cells.[433] Then in 2017, Zhu *et al*. fabricated $AgBi_2I_7$ (cubic phase, space group $Fd\bar{3}m$, Figure 2.25 (a)) and Ag_2BiI_5 films (trigonal phase, space group $R\bar{3}m$, Figure 2.25 (b)), which delivered PCEs of 0.4% and 2.1%.[434] After that, Simonov *et al*. conducted a systematic study of the effect of anionic sulphide substitution ($Ag_3BiI_{6-2x}S_x$) on these silver-bismuth halide structures.[432] They studied 0% to 6% sulphide content and achieved a maximum PCE of 5.44% for 6% content.

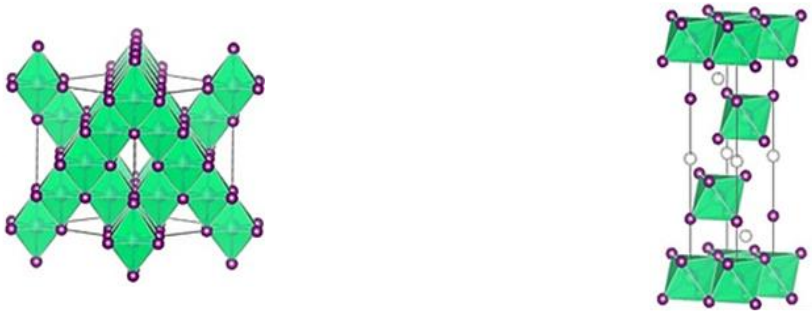

(a) **(b)**

Figure 2.25 The unit cells of the crystal structures of **(a)** $AgBi_2I_7$ (in the cubic space group $Fd\bar{3}m$) and **(b)** Ag_2BiI_5 (in the trigonal space group $R\bar{3}m$), illustrating the cubic and trigonal phases of the two structures. Reproduced and adapted with permission. Copyright Elsevier 2017.[434]

3D $AB(Ch, X)_3$ Mixed-Anion Perovskites

The so-called *mixed anion approach* was proposed by Sun *et al*., where two different X-anions (for example, a chalcogen and a halide) are introduced into the same structure. At the same time, lead is substituted by a heterovalent element to ensure charge neutrality and a 3D perovskite structure.[435] This process is illustrated in Figure 2.26 (a).

The initial study used bismuth to obtain structures of the proposed structural form $MABiChX_2$, where the chalcogen was either sulfur, selenium, or tellurium and the halide either chloride, bromide, or iodide. The most promising compounds for

photovoltaic applications were $MABiSI_2$ and $MABiSeI_2$ since they possess band gaps in the region of 1.3 – 1.4 eV, which is in the optimal range as suggested by the Shockley–Queisser theory.[114]

Figure 2.26 (b) shows the calculated band structures of $MAPbI_3$ and $MABiSI_2$.[435] The valence band minimum consists mainly of the bismuth 6*s*-, iodine 5*p*- and sulfur 3*p*-orbitals, while the conduction band maximum consists primarily of the bismuth's 6*p*-states, which is similar to the case of $MAPbI_3$, where the lead 6*p*-states dominate. In addition, both compounds have similar relative charge carrier masses for electrons and holes. $MABiSI_2$ also has a higher absorption coefficient than $MAPbI_3$. Hence, this new family of structures are promising sensitisers for use in PSCs.

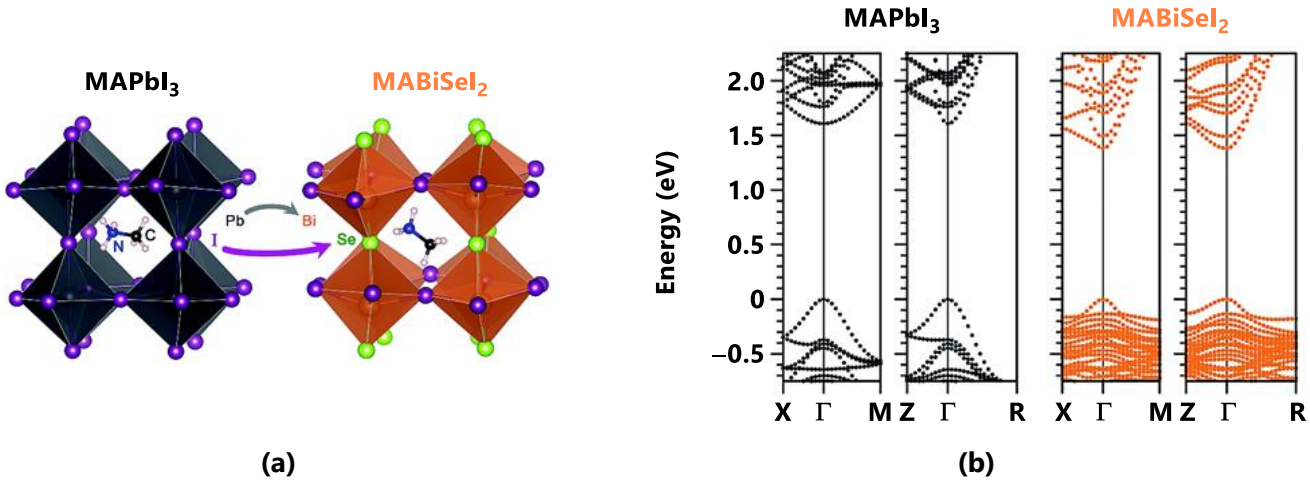

Figure 2.26 (a) A schematic representation of the split-anion approach to replace Pb^{2+} in $MAPbI_3$ to form the mixed-anion $MABiSeI_2$ perovskite. **(b)** Band structures of $MAPbI_3$ and $MABiSeI_2$. Adapted with permission. [435] Copyright 2016, The Royal Society of Chemistry.

However, Hong *et al*. showed by DFT calculations that the $AB(Ch, X)_3$ perovskites are unstable and that they decompose *via* solid-state reactions into ternary, binary or non-perovskite phases.[436] That said, a successful synthesis of $MASbSI_2$ by Nie *et al.* showed photovoltaic promise, [423] however, Li *et al*.[437] later suggested through synthesis and computation that the active constituents are a combination of Sb_2S_3 and $MA_3Sb_2I_9$, rather than the mixed-anion perovskite. Therefore, no conclusive evidence is available to suggest if this is a possible new avenue of PSC research or if it is simply not possible to synthesise these compounds due to their thermodynamic instability.

3D $A_2BB'X_6$ Halide Double Perovskites

In 2016, for the first time, three reports on double perovskites ($A_2BB'X_6$, where B is a monovalent element and B' a trivalent element) were published, showing their application in lead-free PSCs.[438–440] Double perovskites are also known as *elpasolites*, stemming from the mineral K_2NaAlF_6. Elpasolites have been extensively studied due to the rich chemistry surrounding their possible elemental combinations. They mostly crystallise in a cubic or tetragonal phase.[441]

The possible elements that can be utilised in this halide double perovskite structure were extensively surveyed by Giustino *et al*.[442] Figure 2.27 shows a periodic table indicating all the elements and in which category (A, B or X) they can be considered. The possible permutations of these elements lead to 9520 potential halide double perovskites. However, most of them can be ignored for photovoltaic applications by considering the effect of B^+, B^{3+} and X^- on the optical band gap and charge carrier properties of the material.

Firstly, when using the alkali metal cations (and NH_4^+) as B^+-cations, 0D structures are usually obtained.[443–445] The 0D structure dimensionality leads to wide band gaps and is unfavourable as absorbers in PSCs.[303] However, the perovskite Cs_2NaBiI_6 has been shown to possess a direct band gap of 1.66 eV when adopting a 3D structure, suggesting that if a 3D dimensionality is possible for the alkali metal cations, they might still be a viable option.[303]

Furthermore, transition metals with multiple oxidation states and electrons in *d*- and *f*-orbitals introduce deep defect states and localised band edges, making them less desirable for photovoltaic considerations.[21] Finally, only fluoride and chloride seem to be reported in double perovskite structures as halide components, and their use often leads to wide band gaps.[441,446] The use of bromide, iodide or cyanide ions would be more favourable for photovoltaic applications due to narrower band gaps, however, they are not thermodynamically stable in the double perovskite structure.[447,448] That said, some progress has been made in their incorporation in PSCs.[449] Some of the most notable work completed, specifically on silver-bismuth devices, in this field of PSCs will be discussed next.

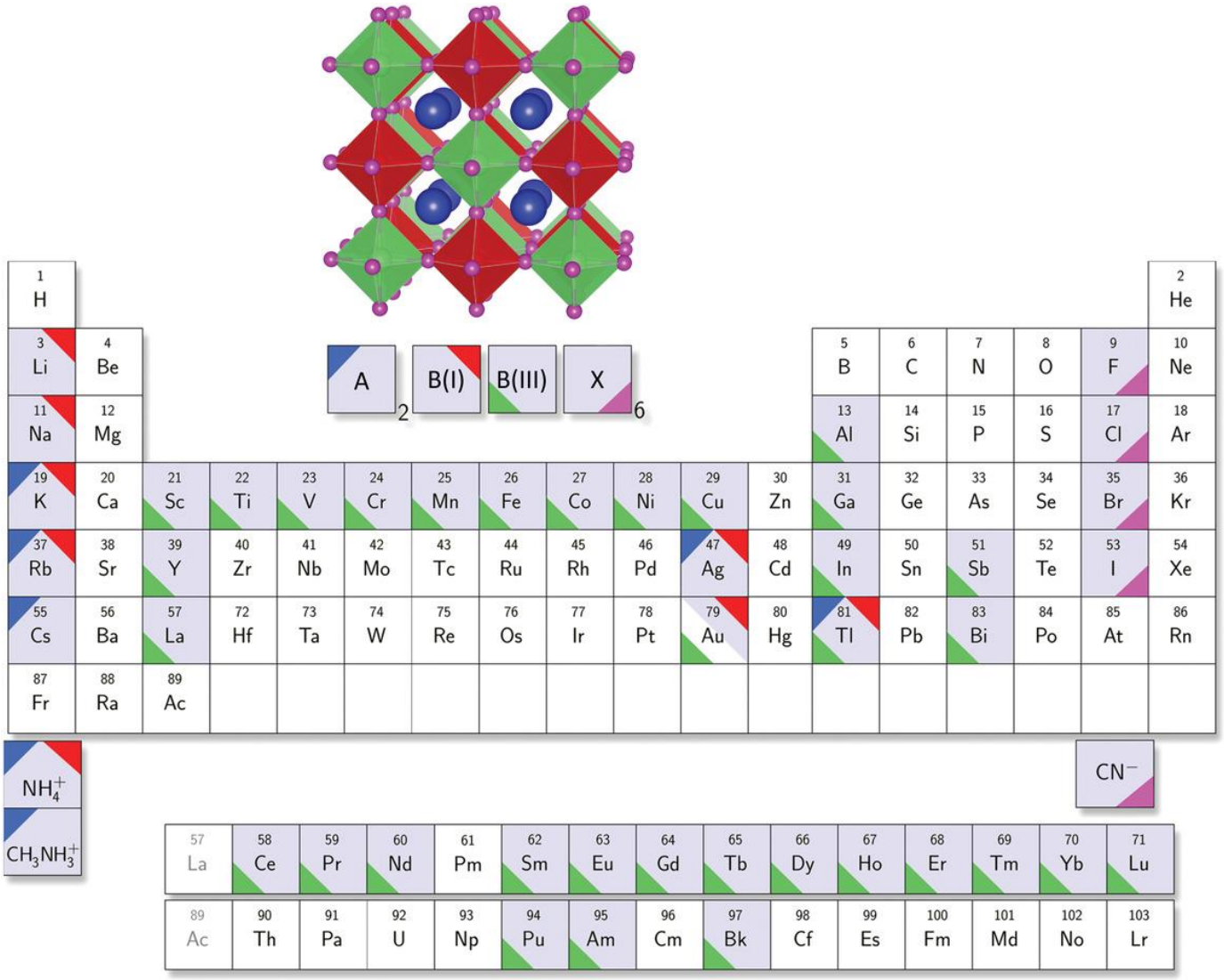

Figure 2.27 A periodic table, showing elements that could potentially form double perovskites with composition $A_2BB'X_6$ ($B = B^+$ and $B' = B^{3+}$). Grey tinting indicates that those elements have been used in at least one successful synthesis of a double perovskite, where only room temperature structures that form the cubic phase (space group $Fm\bar{3}m$) are listed. Triangular tags indicate the possible site an element may occupy as per the key shown at the top. Gold (Au) is only half-coloured since it can only exist in the polymorph $A_2Au_2X_6$ where A is either Rb^+ or Cs^+ and X is Cl^-, Br^- or I^-. The gold-containing structures are double perovskite in that they have alternating elongated and truncated AuX_6 octahedra present, giving rise to the double perovskite motif. Reproduced with permission.[442] Copyright 2016, American Chemical Society.

Among the compounds Cs_2AgBiX_6 (X = Br^-, Cl^-), $Cs_2AgSbCl_6$, $Cs_2AgInCl_6$, $(MA)_2AgBiBr_6$, $(MA)_2KBiCl_6$, and $(MA)_2TlBiBr_6$ that have been synthesised and considered for PSC applications, $Cs_2AgBiBr_6$ seems the most promising, with

the smallest band gap of between 2.05 eV and 2.3 eV, and superior stability towards heat and moisture compared to the others.[438–440] A summary of the PSCs utilising this material is given in Table 2.18.

$Cs_2AgBiBr_6$ has an indirect band gap (Figure 2.28 (a)) due to the mismatch in angular momentum of the bismuth and silver atomic orbitals.[450] In addition, the $Cs_2AgBiBr_6$ electronic dimensionality is less than 3D, causing heavier carrier effective masses and leading to poorer absorption properties than its lead counterparts.[451] This wide indirect band gap hinders the application of $Cs_2AgBiBr_6$ in PSCs. One solution to this is to obtain a direct band gap. For example, the band diagram of $Cs_2AgInCl_6$, shown in Figure 2.28 (b), exhibits a direct band gap at the Γ point.[452] The conduction band maximum (CBM) is composed of the In 5*s*-, Ag 5*s*-, and Cl 3*p*-orbitals. In contrast, the valence band minimum (VBM) consists of the antibonding states of Ag 4*d*- and Cl 3*p*-orbitals (illustrated in Figure 2.28 (c)). That said, the direct transition between the CBM to the VBM is parity forbidden (confirmed experimentally by Luo *et al.*[453]), since double perovskites have an intrinsic centrosymmetry and the CBM containing the unoccupied In 5*s*-states. These results disqualify the structure of $Cs_2AgInCl_6$ for PV applications.

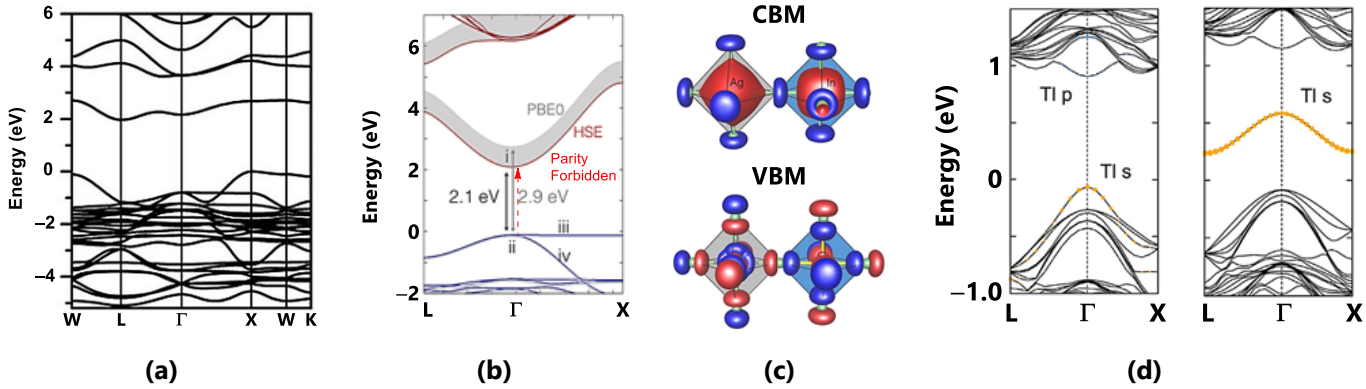

Figure 2.28 (a) $Cs_2AgBiBr_6$ band diagram. Reproduced with permission.[451] Copyright 2016, Wiley-VCH. **(b)** The band diagram of $Cs_2AgInCl_3$ and **(c)** a plot of the CBM and the VBM of $Cs_2AgInCl_3$. Reproduced with permission.[454] Copyright 2017, American Chemical Society. **(d)** The effect of alloying with thallium on the band diagram of $Cs_2AgBiBr_6$. Adapted with permission.[455] Copyright 2017, American Chemical Society.

Further band gap engineering of $Cs_2AgBiBr_6$ is possible through thallium-alloying as proposed by Slavney *et al.*[455] Using dilute Tl-alloying, the band gap is decreased to 1.4 eV, which is close to ideal for single-junction PV applications. The decrease in the band gap is suggested by DFT calculations to occur due to the thallium impurity-induced band edge reconstruction, as illustrated in Figure 2.28 (d). The introduction of thallium also improves the charge carrier lifetimes. However, thallium is exceptionally toxic, and hence this makes for a problematic argument for its inclusion. Similar work has been done with Sb^{3+}-alloying, but with this method, the lowest band gap obtained is for $Cs_2Ag(Bi_{0.625}Sb_{0.375})Br_6$ and is 1.86 eV is still not ideal for PSC applications.[456]

The use of $Cs_2AgBiBr_6$ in PSCs started with Greul *et al.*, who synthesised these double perovskite films (*via* solution methods and solid-state reactions) and used them in a mesoporous structure.[424] This PSC device obtained an optimised PCE of 2.5%, inspiring further investigation into the field. In addition, when used in a planar device, Ning *et al.* showed that an average PCE of above 1% was maintainable.[457] Further work done by Gao *et al.* used the double perovskite in an inverted planar heterojunction to deliver a PCE of 2.23%.[426]

In 2018, Xiao *et al.* fabricated $Cs_2AgBiBr_6$ films using DMSO as a solvent and a low-pressure process (20 Pa), different from the traditional annealing process.[425] This method provides a smoother film compared to the conventional methods used. A planar heterojunction cell with P3HT as the HTL was constructed using the $Cs_2AgBiBr_6$ film and delivered a PCE of 1.44%. Subsequently, Wu *et al.* used an anti-solvent dropping method, shown in Figure 2.29 (a), to achieve smooth $Cs_2AgBiBr_6$ films with micro-sized grains and good crystallinity.[426] An inverted planar heterojunction cell was employed and gave a PCE of 2.23%. However, in both these works, *J*–*V* hysteresis was present due to defects in the perovskite films. Finally, Liu *et al.*

fabricated $Cs_2AgBiBr_6$ films through a sequential vapour deposition procedure (illustrated in Figure 2.29 (b)) to obtain a PCE of 1.37%, and the device remained stable for 240 hours under ambient conditions (90% PCE maintained).[427]

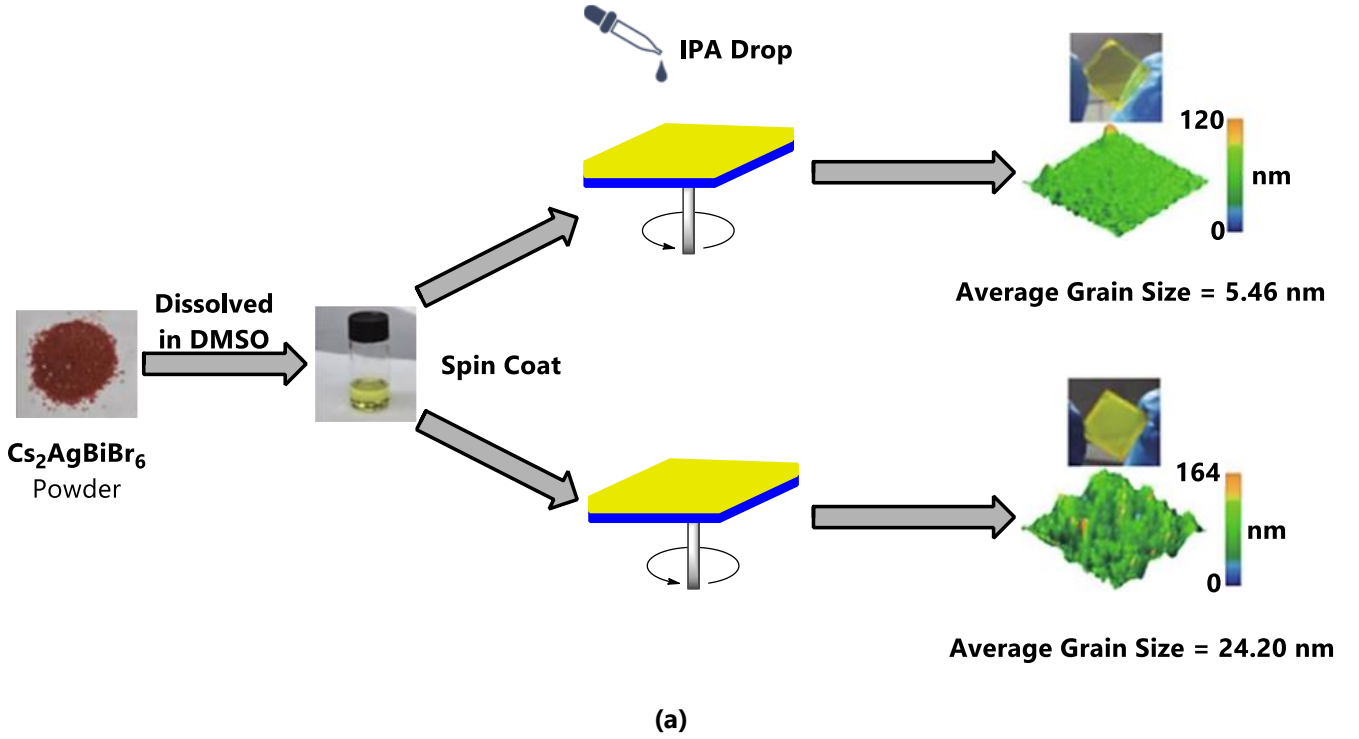

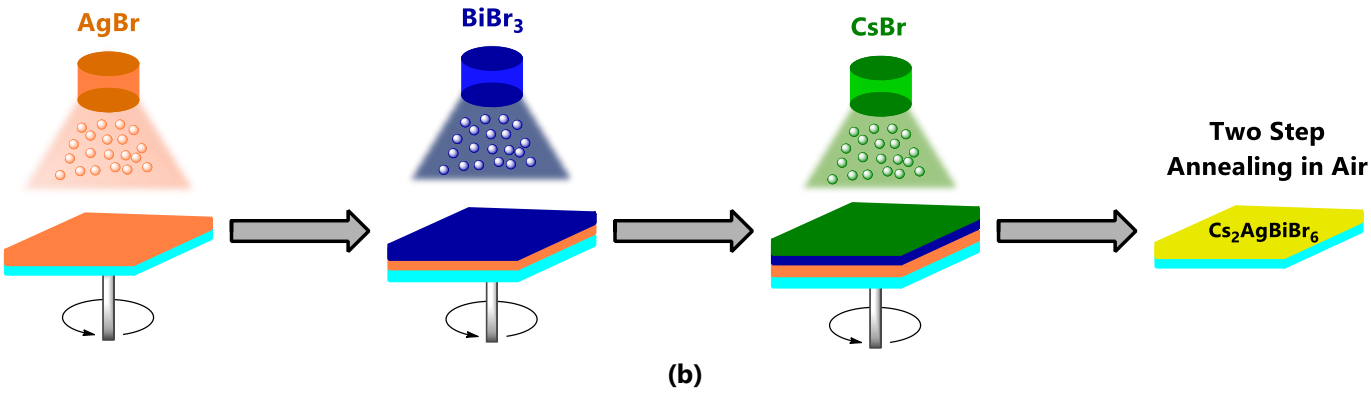

Figure 2.29 (a) A technical drawing, illustrating the formation of $Cs_2AgBiBr_6$ thin-films using a combination of spin coating and anti-solvent dropping or spin coating alone, and the effect of this choice on the resultant film morphology. Adapted and reproduced with permission.[426] Copyright 2018, Wiley-VCH. **(b)** A schematic of the sequential vapour deposition process to form $Cs_2AgBiBr_6$ films. Adapted and reproduced with permission.[427] Copyright 2018, Wiley-VCH.

Ideally, Cs_2AgBiI_6 would be used in PSCs since it has a narrower band gap (*ca.* 1.75 eV) than its bromide counterpart, however, thermodynamically, it is too unstable to be synthesised *via* either solution or solid-state methods. That said, the Cs_2AgBiI_6 form has been synthesised from the $Cs_2AgBiBr_6$ structure using ion-exchange methods, however, it quickly decomposes to the $Cs_3Bi_2I_9$ phase, making it a poor option for PSC application.[458]

With the band gap of $Cs_2AgBiBr_6$ being indirect and too wide for single-junction PSC applications, a concerted effort has been made to obtain a related material with a narrow and direct band gap. Initial theoretical work has shown that by replacing bismuth with indium, the band gap of Cs_2AgInX_6 materials will become direct.[454] Synthetically, only $Cs_2AgInCl_6$ has been successfully synthesised.[459] However, Meng *et al.* determined that the direct transition is parity-forbidden due to the centrosymmetry of the double perovskite structure and the conduction band maximum containing unoccupied orbitals of indium.[452] The parity-forbidden transitions were confirmed experimentally.[453] That said, the large band gap of 3.2 eV makes the successful photovoltaic application highly improbable.

Other band gap engineering methods have been investigated since the suggestion to use indium instead of bismuth. Slavney *et al*. proposed using dilute thallium-alloying, which aided in decreasing the band gap of $Cs_2AgBiBr_6$ to 1.4 eV, making it more viable for single-junction applications. The decrease is suggested to occur due to the impurities of thallium, causing a reduction in band edges.[455] However, the high toxicity of thallium is detrimental to its application in PSCs. Du *et al*. proposed using a mixture of bismuth and antimony. This combination resulted in a reduced band gap of 1.86 eV for the combination of $Cs_2Ag(Bi_{0.625}Sb_{0.375})Br_6$ due to the increased energy of the antimony 5*s*-states, raising the valence band maximum.[456]

Furthermore, the replacement of Ag^+ with Cu^+ has been studied theoretically. However, due to the high energy $3d^{10}$ electrons of copper and the requirement of $[CuX_6]^{5-}$ octahedra in the double perovskite, decomposition occurs to $[CuX_4]^{3-}$ tetrahedra, as a thermodynamically driven process, making this a non-viable route.[448]

Although these double perovskites have 3D structural dimensionalities, they lack electronic dimensionality. This can be ascribed to the high ionicity of the B^+-cations or the overall orbital mismatch between the B^+- and B^{3+}-cations.[21] Hence, improving the match between the orbital properties of the two B-cations should increase the electronic dimensionality of the perovskites. Theoretical studies have identified the type of B-cations that will allow for a higher electronic dimensionality, which are B-cations with lone pair electrons, with the best options being $B^+ = Tl^+$ or In^+ and $B^{3+} = Bi^{3+}$ or Sb^{3+}.[460–462] These studies showed that the band diagrams of $Cs_2TlBiBr_6$ and $Fr_2InBiBr_6$ are quite similar (direct band gaps at the Γ point) to Cs_2PbPbI_6 (or just $CsPbI_3$), as shown in Figure 2.30 (a), and even though francium-containing devices are implausible, the material gave interesting computational results.[462] These similarities vote well for their potential application in PSCs. In addition, the 3D electronic nature of their band diagrams is seen in the dispersive nature of the conduction band minimum and the valence band maximum, as shown in Figure 2.30 (b).[461] However, issues are encountered with In^+ quickly oxidising to In^{3+} and the extreme toxicity of thallium, making them less attractive for PSC application.[450]

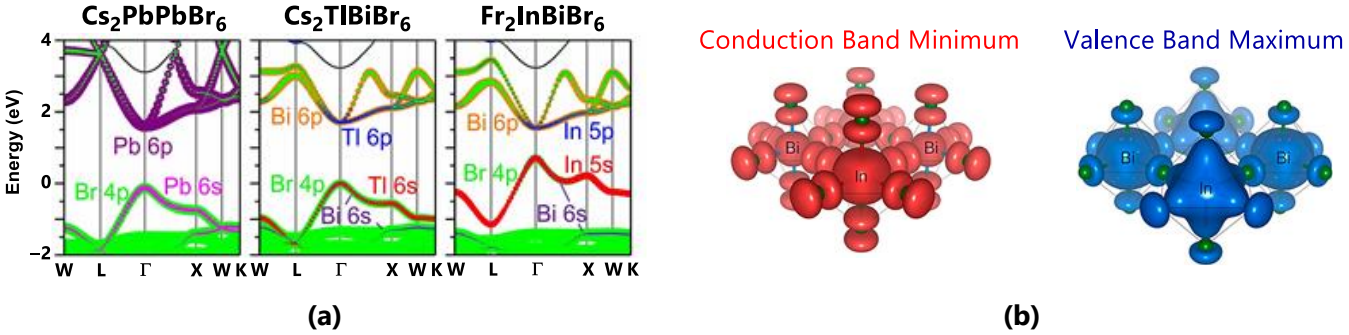

Figure 2.30 (a) The calculated band structures of $CsPbBr_3$, $Cs_2TlBiBr_6$, and $Fr_2InBiBr_6$ as indicated. Reproduced with permission.[462] Copyright 2018, American Chemical Society. **(b)** Typical square modulus of the electronic wave functions at the CBM (red) and at the VBM (blue) of $A_2BB'X_6$ (B = Tl^+ or In^+, and B' = Bi^{3+} or Sb^{3+}), illustrating a 3D electronic dimensionality. Adapted and reproduced with permission.[461] Copyright 2017, American Chemical Society.

One can only improve film quality and, therefore, PCE to a certain extent with fabrication techniques. To obtain further improvements, substitution (structural doping) is considered as the next logical step. Zhang *et al*. reported the substitution of Cs^+ with Rb^+ to form the structure $(Cs_{0.9}Rb_{0.1})_2AgBiBr_6$, which exhibited a lower defect density than the pure caesium-containing film.[463] The resultant cell produced a PCE of 1.52%. Following this idea, Pai *et al*. partially substituted bromide with sulphide (S^{2-}), leading to pin-hole free films and a PCE of 1.9%.[464] Further research on the A-site substitution was done by Li *et al*. with 0.01 mol Li^+ (Na^+, K^+ and Rb^+ were also investigated), with the cell obtaining a PCE of 2.57% in a carbon-based PSC device.[465]

The final method for improving device efficiency is by improving the compatibility of the device layers, specifically the ETL/Perovskite and Perovskite/HTL interfaces. Luo *et al*. proposed a strategy of using C_{60}/TiO_2 as the ETL and PCDPTBT (poly[2,6-(4,4-bis-(2-ethylhexyl)-4H-cyclopenta[2,1-b;3,4-b′]dithiophene)-alt-4,7-(2,1,3-benzothiadiazole)]) as the HTL, with the perovskite $Cs_2AgBiBr_6$, and zinc chlorophyll derivative (Zn-Chl) as an additive.[466] This allowed for an optimised PCE of 2.79% due to the enhanced optical effects of the interfaces and the additive, allowing for better film morphology. Yang *et al*. used an organic additive, N719 dye (di-tetrabutylammonium cis-bis(isothiocyanate) bis (2,2′ -bipyridyl-4,4′

dicarboxylate) ruthenium(II)), on the Perovskite/HTL interface to assemble efficient $Cs_2AgBiBr_6$ PSCs.[467] The N719 dye broadened the light-absorbing range to deliver a PCE of 2.84%.

Further to the use of $Cs_2AgBiBr_6$, Cs_2NaBiI_6 has also been employed in PSCs as the light absorber layer. Though it showed good air stability, a PCE of only 0.42% was obtained. However, with its band gap value of ca. 1.6 eV and stability, further investigation is warranted.[468]

Since the birth of halide double perovskite for solar cell applications stemmed from a thermodynamic stability study of the materials and their structure, excellent stability (and being environmentally friendly) is synonymous with the field, making them one of the most attractive new avenues for lead-free PSC research.

On a final note, the use of large A-site cations can reduce the dimensionality of the double perovskite structure, altering the material's optoelectronic properties. For example, the BA^+-cation ($CH_3(CH_2)_3NH_3^+$) can be introduced instead of caesium to form either a 2D mono-layer structure $(BA)_4AgBiBr_8$ or 2D bilayer structure $(BA)_2CsAgBiBr_7$ (see Figure 2.31 (a) and (b)).[469] The mono-layer compound still has an indirect band gap, whereas the bilayer material has a direct band gap. Unfortunately, with the reduction in dimensionality, an increase in band gap is expected. Interestingly, when the bifunctional spacer cation (bis-aminoethyl) bithiophene ($AE2T^{2+}$) is used to obtain the compound $(AE2T)_2AgBiI_8$, the band gap value is 2.0 eV, a value that is relatively small compared to other 2D perovskites.[470] Since these structures have band gap values too wide for PSC applications, they open the door for other optoelectronic applications, which will be reviewed in the following section.

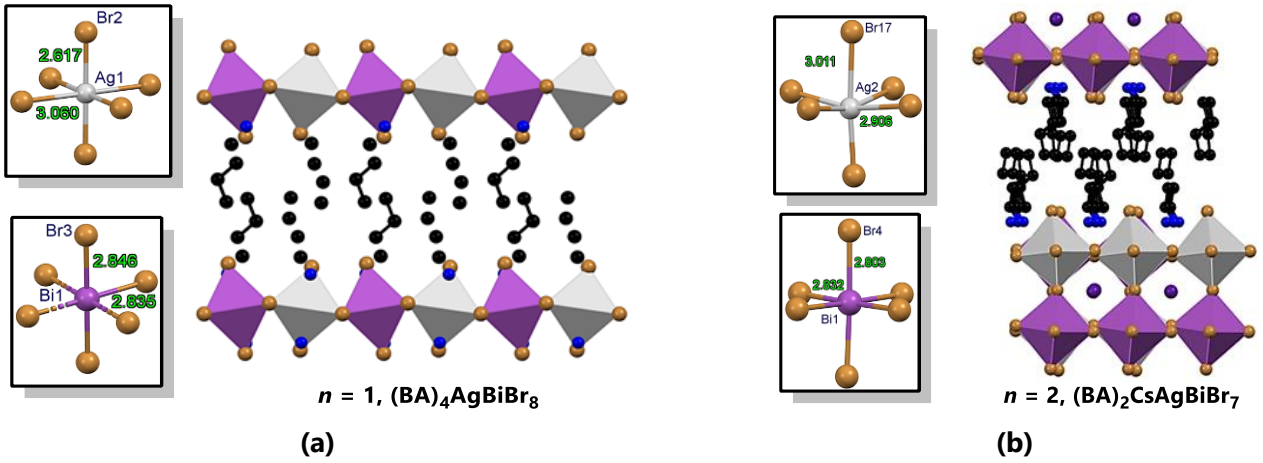

Figure 2.31 The crystal structures of **(a)** $(BA)_4AgBiBr_8$ and **(b)** $(BA)_2CsAgBiBr_7$ viewed down the *b*- and *a*-axis, respectively (hydrogen atoms were omitted for clarity).[469] Bond lengths are given in units of Å.

Other Applications of Halide Double Perovskites. Halide double perovskite (like many other perovskite materials) may also potentially find application a whole host of optoelectronic devices, as illustrated in Figure 2.32. For example, Tang *et al*. fabricated high-performance X-ray and UV detectors using single crystals of $Cs_2AgBiBr_6$ and $Cs_2AgInCl_6$.[453,471] Red- and blue-emissive phosphors have utilised Mn-doped $Cs_2AgInCl_6$,[472] A_2BAlF_6 ($A = Rb^+$, Cs^+; $B = K^+$, Rb^+),[473] and Bi-doped Cs_2SnCl_6,[474] respectively.

In addition, fluoride double perovskites have been applied as hosts to Ge^{3+}-based laser materials[475,476], and Zhou *et al*. has demonstrated the photocatalytic abilities of $Cs_2AgBiBr_6$ nanocrystals in the conversion of CO_2 into solar fuels[477].

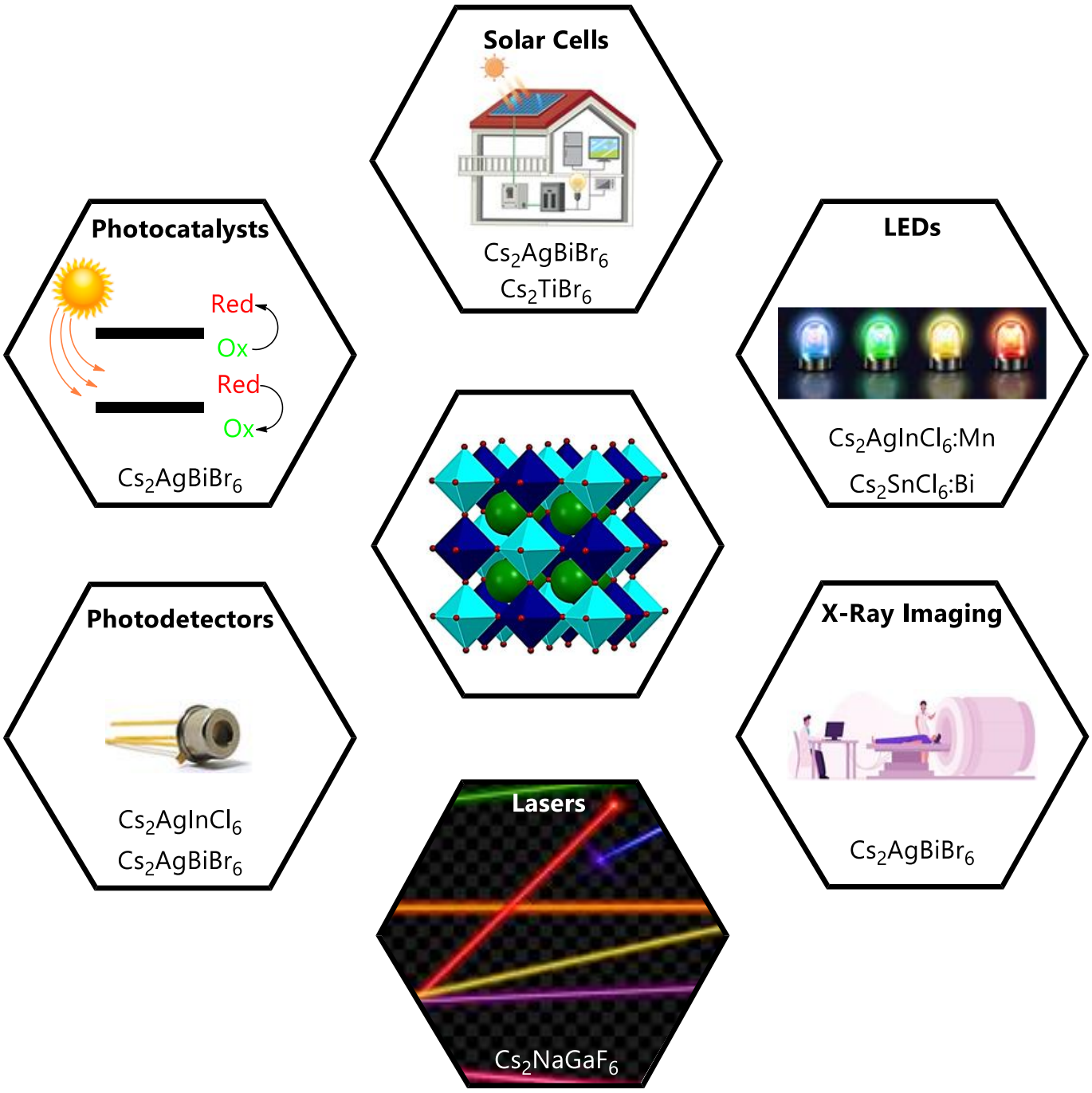

Figure 2.32 A summary of the optoelectronic applications of halide double perovskite, including both reported and potential applications. The molecular formula of the perovskite suitable for each application is also given. Adapted from Zhao *et al.*[449]

Table 2.19 gives an overview of the different double perovskites and their proposed optoelectronic applications. Of course, the band gap of a material dictates what applications it is useful for. Most of the materials listed in the table cannot simply be used in PSCs, however, they can be applied to detectors (UV and X-ray) or LEDs. These materials once more emphasise the flexibility of the perovskite structure in optoelectronic applications.

Table 2.19 Reported or calculated band gap values of lead-free halide double perovskites and their reported or potential applications. Taken and adapted from Li *et al.*[325] Primary authors are acknowledged in the Author column (*et al.* is implied).

Perovskite	Band Gap (eV)	Direct/Indirect	Morphology	Reported/Potential Application	Author
$Cs_2AgBiBr_6$	2.19	Indirect	Powder	Tandem solar cells	McClure[439]
	1.85	Indirect	Nanocrystal	Photovoltaic devices	Bekenstein[478]
	2.12	Indirect	Powder	Photovoltaic devices, detectors	Su[479]
$Cs_2AgBiCl_6$	2.77	Indirect	Powder	Tandem solar cells	McClure[439]
	2.41	Indirect	Powder	UV photodetectors	Wang[480]
Cs_2AgBiI_6	1.75	–	Nanocrystal	–	Creutz[458]
$Cs_2NaBiCl_6$	3.73	Indirect	Single-crystal	X-ray detectors, photocatalyst	Zhao[445]
$Cs_2AgSbBr_6$	1.64	Indirect	Single-crystal	Photovoltaic devices	Wei[481]
$Cs_2AgBiBr_6$	1.72	Indirect	Single-crystal	Photodetectors	Ji[482]
Cs_2NaBiI_6	1.66	–	Microcrystal	LEDs, lasers	Zhang[483]
$MA_2TlBiBr_6$	2.00	–	Single-crystal	Photovoltaic devices	Deng[484]
$Cs_2AgInBr_6$	3.23	Direct	Single-crystal	Detectors, LEDs	Volonakis[454]
$MA_2AgBiBr_6$	2.02	Indirect	Single-crystal	Photovoltaic devices	Wei[485]
$BA_2AgBiBr_7$	2.40	Direct	Single-crystal	Detectors	Connor[469]

In conclusion, even if lead-free perovskite materials are not necessarily valuable for photovoltaic applications, there is a treasure trove of possibilities in terms of their optoelectronic applications. Therefore, whenever a perovskite material is obtained, there is undoubtedly an application for it.

2.4 Lead-Less Perovskite Solar Cells

Now that a full literature review of the pure-lead and lead-free PSC fields has been completed, it is time to evaluate what these studies have shown. The lead-containing perovskite PSCs' PCEs far exceed that of the lead-free options. However, lead does have a considerable drawback due to its toxicity. So, the question remains, are the benefits of using lead in PSCs worth the risk? Perhaps not in a pure sense, but the following section suggests one possible route to keep the benefits of lead while addressing the inherent toxicity. Investigations on how to reduce the lead content of PSCs gave rise to the field of **lead-deficient perovskites**, or **lead-less perovskites** as referred to here. This section will follow the historical development of lead-less perovskites. However, first, an understanding of why lead is *so superior* will lead the discussion.

2.4.1 Superior Properties of Lead Photovoltaics

To fully understand and optimise the replacement of lead in the perovskite lattice ($APbX_3$) for solar cell applications, a thorough understanding of why lead halide perovskites work so well in photovoltaic applications will be beneficial. Broadly speaking, the properties that make these lead-containing perovskite materials exceptional in PSCs include high optical absorption coefficients (ca. 10^5 cm^{-1}), equal electron and hole mobilities, long charge carrier (electrons and holes) lifetimes (a maximum of 1 μs), large diffusion lengths (possibly up to 1 μm), low concentration of trap densities of 10^{15} to 10^{16} cm^{-3}, small exciton binding energies, and Urbach energies as low as 12.6 meV. In addition, the high perovskite symmetry (O_h), high electronic dimensionality, unique electronic properties of lead (lone pair 6*s* electrons, inactive 6*p*-states and strong spin-

orbit coupling (SOC)), polar A-site cations and ionic nature of the halide ions, all combine to make lead-based perovskites optimal absorbers in PSC technology. A selection of these desired properties is discussed below, in the context of lead-containing PSCs.

High Optical Absorption Coefficient

The high optical absorption of thin-films allows for *efficient* and *low-cost* PSC devices. In this category, lead-based perovskites outshines almost all its photovoltaic competitors.[486] Lead-based perovskite absorber layers are optimal when about 500 nm thick, which is much thinner than required for any of the other PV competitors, including GaAs, $Cu(In,Ga)Se_2$ (CIGS), or CdTe, due to their high optical absorption coefficient.[487]

In Figure 2.33 (a), the absorption mechanism for first-generation (silicon), second-generation (GaAs) and perovskite solar cells is illustrated using schematic band structures.[488,489] The optical absorption of a semiconductor is determined by two factors, namely the **joint density of states** (JDOS) and the **transition matrix elements**. Due to its indirect band gap, the silicon-based solar cell has mainly *forbidden transitions* between band edges, leading to a low optical absorption coefficient. In contrast, the GaAs (second-generation) and perovskite (for example, $MAPbI_3$) materials have *allowed transitions* between band edges due to their direct band gaps, leading to higher absorption coefficients.

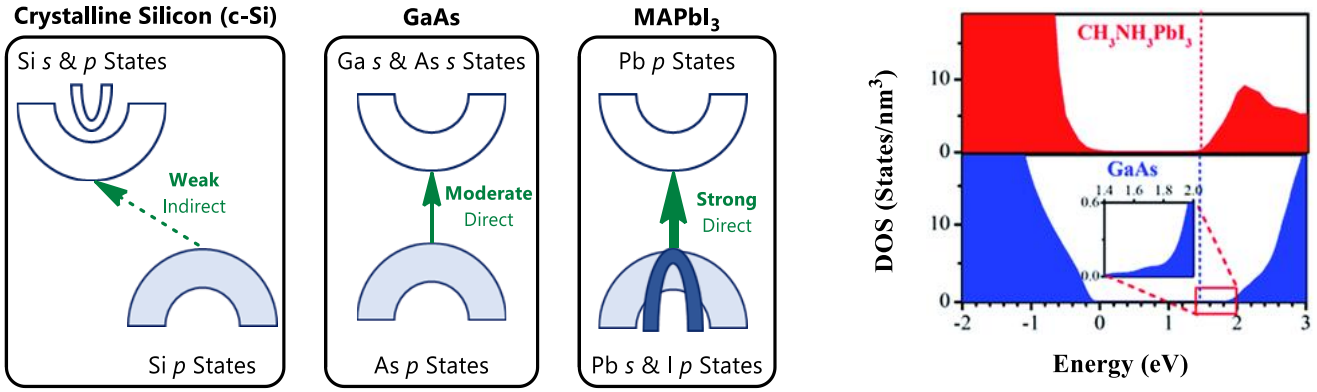

Figure 2.33 (a) The optical absorption of c-Si, GaAs, and $MAPbI_3$ perovskites. Adapted from Yin *et al.*[489] **(b)** Plots of the density of states of $MAPbI_3$ and GaAs. The VBMs represent the zero-energy levels, and dashed lines indicate CBMs. Reproduced with permission.[488] Copyright 2015, Royal Society of Chemistry.

Furthermore, the perovskite materials have a better absorption coefficient than the second-generation materials because the lower part of the conduction band (LCB) is less dispersive (see Figure 2.33 (b)). It is less dispersive because the LCB of GaAs consists of the gallium 4*s*-states, and that of $MAPbI_3$ consists of the lead 6*p*-states, and *p*-states are less dispersive than *s*-states. In addition, $MAPbI_3$ has a higher JDOS than GaAs, allowing for a higher optical absorption coefficient. Specifically, in the visible light range, the absorption coefficient of $MAPbI_3$ is nearly one order of magnitude higher than that of GaAs. This results in a higher calculated maximum PCE for $MAPbI_3$ than for any of the GaAs, $CuInSe_2$ (CIS), or $Cu_2ZnSnSe_4$ (CZTS) based technologies, with PCEs of 21%, 16%, 14%, and 12%, respectively.[490]

Small Carrier Effective Masses

Highly efficient polycrystalline thin-film solar cells require small carrier effective masses. When the effective masses are small, higher carrier mobilities, less nonradiative recombination and longer carrier diffusion lengths result.

Generally, when band edges are derived from *p*-states of materials, the effective masses of the charge carriers are higher than when they are derived from *s*-states (and *p*-states are less than *d*-states and so on). This then intuitively suggests that $APbI_3$ type materials should have large carrier effective masses since its conduction band edge is derived from its 6*p*-state, however, due to the strong SOC seen in these structures, a small effective electron mass is observed.[491–493] This was confirmed by Umari *et al*.[281] They utilised different computational techniques (GGA, GGA + SOC and GW + SOC) to determine the charge carriers' effective masses (m_e and m_h), where the GW + SOC calculations yielded the band structure closest to experimental observations.[281]

Excellent Defect Tolerance

Thin-films inevitability have defects, and these defects subsequently have a detrimental effect on device performance. Therefore, the properties of the defects, including point defects, point defect complexes, surfaces, and grain boundaries (GBs), play a critical role in the performance of any device.[21]

However, not all defects are undesired when it comes to solar cell applications. For example, shallow-level point defects can provide *free charge carriers* allowing for an increased PCE and hence are desirable. In contrast, deep level defects cause nonradiative recombination, which hinders device performance.

The advantage of $APbX_3$-based absorbers is that their device performance shows a unique tolerance towards defects formed in the absorber layer. The reason for this is twofold.[21] Firstly, the vast majority of defects formed are shallow-level point defects, by far outnumbering the deep level defects, to ensure a positive contribution to device PCE rather than a loss. Secondly, the electrons and holes formed become large polarons (a quasi-particle used to illustrate the interaction between atoms and charges in crystals), which means that a large charge screening effect is the result, ensuring that these charge carriers do not easily recombine at deep level defects.

Yin *et al*. considered the reasons behind the defect tolerance from a first-principles perspective (see Figure 2.34 (a)) and determined that the tolerance stems from a combination of the factors of the high crystal symmetry, the inactive lead 6*p*-orbitals, the lead 6*s* lone-pair electrons, the ionic nature of the halides, and large atomic sizes of the ions.[489] Of these factors, the lead 6*s* lone pair and 6*p*-orbital play the most pivotal role. Figure 2.34 (b) shows the formation energy of defects in the $MAPbI_3$ structure. They found that defects with low formation energies included interstitial (I_i), MA-on-Pb anti-site (MA_{Pb}), MA^+-vacancy (V_{MA}), V_{Pb}, MA_i, Pb_{MA}, V_I, and MA_I, due to their shallow transition energy levels. The defects with deep transition energy levels, such as I_{MA}, I_{Pb}, Pb_i, and Pb_I, have higher formation energies (see Figure 2.34 (c)). Therefore, as suggested before, in $MAPbI_3$, only shallow defects form in a meaningful sense. Yin's group further indicated that the lead's strong lone-pair *s*-orbital and iodide *p*-orbital antibonding coupling, along with their high ionicity, contribute to the high defect tolerance.[494]

Moreover, the large polarons formed by charge carriers are formed by the optical phonon modes in the perovskite sublattice. Due to the Coulomb screening, which they experience from charged defect states, they scatter readily, thereby not allowing non-radiative recombination to occur.[494] The formation of these polarons explains the observation of super long charge carrier lifetimes in $MAPbI_3$. Still, the orientational relaxation of surrounding dipoles creates a so-called *dielectric drag* on the charge carriers, leading to low carrier mobility in lead-based PSCs, as schematically shown in Figure 2.34 (d).[495]

This section summarised why the performance of lead-containing PSCs far exceeds that of PSC's that are lead-free. Hence, perhaps the compromise of moving to lead-less perovskites, suggested earlier is not only a "good idea", but it might also allow for a green solution to the world's energy crisis. By partially substituting lead with any B^{2+} alternatives, the excellent performance of lead is retained, however, more importantly, the toxicity threat is minimised or at least reduced. The sections to follow will discuss the partial substitution of lead with various elements in PSCs.

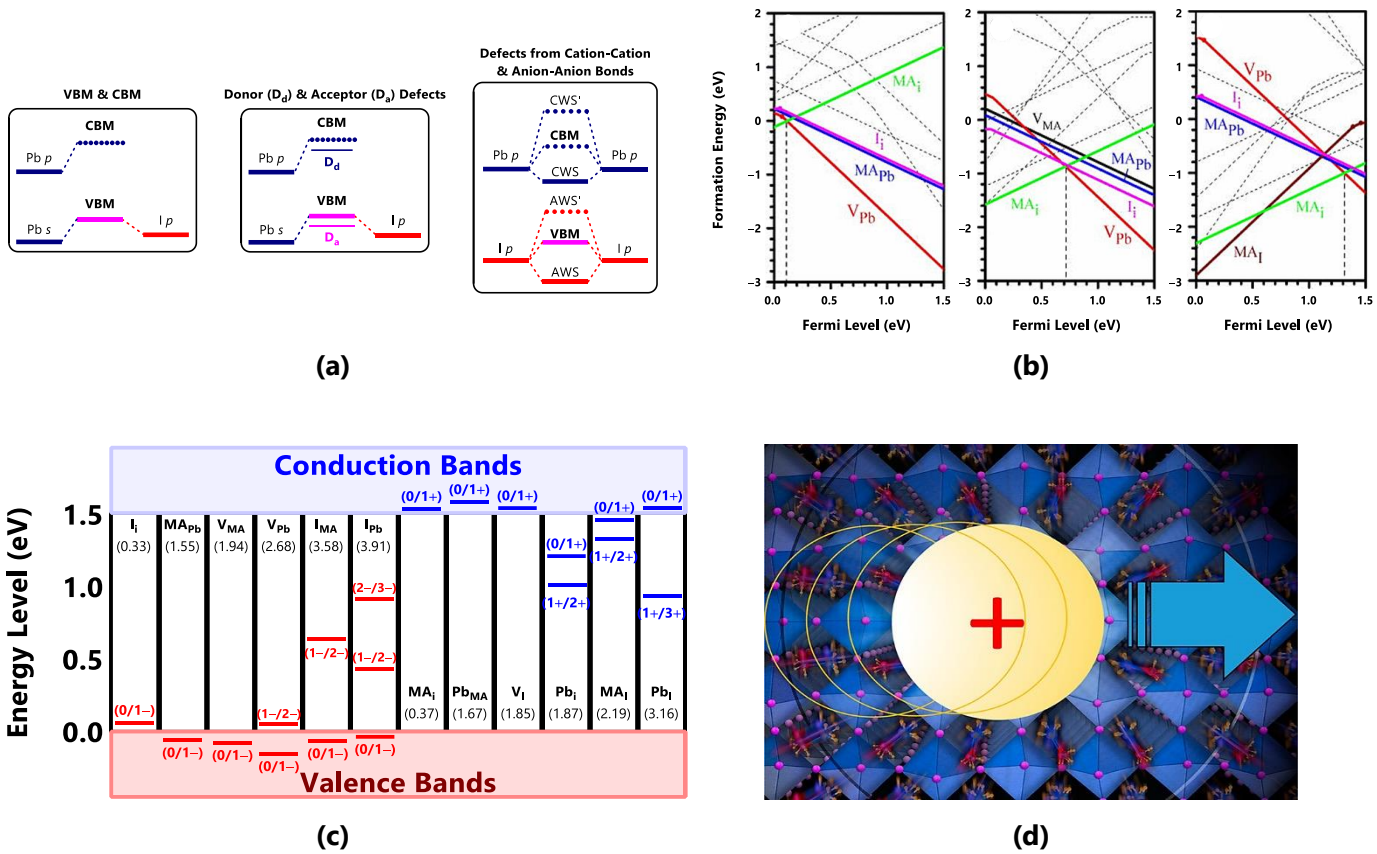

Figure 2.34 (a) Schematic illustrations of the formation of donor-like and acceptor-like defects, and other defects in lead halide perovskites. Adapted from Yin *et al.*[489] **(b)** Calculated the intrinsic formation energy of point defects in $MAPbI_3$ under I-rich/Pb-poor (left), modest (middle), and I-poor/Pb-rich (right) chemical conditions. Defects with larger formation energies are indicated with dashed lines. Adapted and reproduced with permission.[494] Copyright 2014, AIP Publishing LLC. **(c)** Transition energy levels in $MAPbI_3$ for different point defects. Neutral defect formation energies are shown in brackets. Adapted from Yin *et al.*[490] **(d)** A schematic illustration of a large polaron moving through a hybrid lead halide perovskite, showing the dielectric drag. Reproduced with permission.[495] Copyright 2017, American Chemical Society.

2.4.2 Tin-Based Lead-Less PSCs

Tin-based PSCs have been shown to have similar potential as their lead counterparts, however, they are yet to achieve the heights of lead-based PSCs. Hence, it is a *logical* step to partially substitute lead to obtaining the high efficiencies lead-based PSCs have achieved, with the smaller toxicity risk benefits of tin-based devices.

Properties of Tin-Based Lead-Less PSCs

Though lead and tin are in the same group in the periodic table and hence have similar electronic properties, the optoelectronic properties of tin-based lead-less PSCs differ from that of either pure tin or pure lead PSCs. In 2014 an optoelectronic study of tin-based mixed perovskites investigated the influence of the percentage Sn in $MAPb_{1-x}Sn_xI_3$ on the optical properties and performance of the PSC device.[496] With increasing tin content, the optical band gap was determined to decrease (1.51 eV for pure $MAPbI_3$ to 1.1 eV for pure $MASnI_3$), and the absorption onset could reach a maximum of 1060 nm for 70% Sn content, corresponding to a 260 nm red shift for $MAPbI_3$.

Furthermore, the study found that when the concentration of tin was 15%, the crystallinity of the perovskite film increased, which allowed a 97% coverage by the perovskite film, leading to ideal thin-film properties. This translates into good conductivity with the HTM (PEDOT:PSS in this case). Additionally, charge recombination was suppressed, which also improved the charge transport abilities of the device. These improvements lead to the construction of a device with a PCE of 10.1% and a maximum J_{SC} of 19.5 mA·cm^{-2}, showing great promise for the field of lead-less PSCs.

In a theoretical study by Mosconi *et al*., it was shown that with an increase in the tin content, a continuous redshift and increase in optical absorption following Vegard's law results.[497] Furthermore, an increase in energy levels and transport properties is also observed, which have been proven experimentally.[283]

After the effects of the tin concentration were understood, the next step in structural engineering was considering different A-site cations and their mixtures. Prasanna *et al.* showed that it is possible to tune tin-based lead-less hybrid perovskites' band gap through two competing mechanisms *via* A-site engineering.[498] The first mechanism showed (using pure lead perovskites) that when the BX_6 octahedra are *tilted* (for example, by switching from FA^+ to Cs^+), an increase in band gap is observed. The second mechanism (using pure Sn perovskites) linked lattice contraction to a decrease in band gap, facilitated by partial substitution of FA^+ by Cs^+ in the perovskite lattice. Hence, by altering the A-site composition, the band gap of Pb-Sn lead-less PSCs can be tuned.

Moving on to the most recent developments, a DFT study of the effects of halide substitution in $MAPb_{0.5}Sn_{0.5}I_{3-y}X_y$ (X = Br^- or Cl^-) was conducted by Liu *et al*.[499] They found that substituting iodide with either bromide or chloride widens the perovskite material's band gap. In contrast, chloride has a more significant effect in this regard than bromide. Moreover, the substitution decreases the carrier mobility and hence the device performance as well. A blue shift is observed for both chloride and bromide substitution, and an overall decrease of absorption intensity follows with increasing concentration, *y*.

Furthermore, the Liu study investigated the stability of these devices in the presence of O_2 and H_2O, however, the devices showed no gain in their stability with substitution of either bromide or chloride since O_2 preferentially absorbs on tin and H_2O on lead.[499] That said, all the results discussed here indicate that tin-based lead-less PSCs are good candidates to compete with lead-based PSCs while reducing the lead content in devices.

Improving the PCE of Tin-Based Lead-Less PSCs

The most prominent strategies to improve the stability of a PSC device are deposition techniques, the use of additives, or using the correct charge transfer layers (CTLs) in the device. Tin-based lead-less devices are no different in this regard, therefore, this section will cover the literature reports of studies that utilise these strategies. Table 2.20 summarises the available literature on these topics at the time of writing as a function of tin content. Therefore, in the discussion to follow, only selected results from the literature will be highlighted.

Deposition Techniques. The essential deposition techniques used in lead-free and lead-less PSCs include the one-step solution method, the two-step solution method, the dripping or quenching method, and the vapour deposition method. Additionally, solvent-free processes have been reported, however, the efficiencies obtained with their use are relatively low compared to the others listed here.[500] Table 2.20 provides an overview of the tin-based lead-less PSCs reported in the literature, including the deposition method.

The Use of Additives. The additives used in PSC fabrication are elements that are also used for halogen substitutions. For example, the use of $SnCl_2$ in $MAPb_{1-x}Sn_xI_{3-y}Cl_y$-based mesoscopic (grains between 10 nm and 1000 nm) solar cells aids in the crystallisation of the perovskite layer since its co-crystallises in large concentrations with the perovskite film.[501] The additive further decreases the symmetry of the crystal structure, reduces the unit cell dimensions and subsequently is responsible for altering the optical and electronic properties of the perovskite layer. Furthermore, using SnF_2 as an additive, which is a commonly used additive in tin-based PSCs to combat the oxidation of tin,[271,275,297,307,327,340] and after inserting a NiO_x layer between a $MAPb_{0.25}Sn_{0.75}I_{3-x}Cl_x$ film and a carbon electrode, a PCE of 5.13% is achievable.

However, halogen elements are not the only additives used in tin-based lead-less PSCs. Liu *et al*. discovered the use of C_{60} to assist in the crystallisation in perovskite films.[502] This specific study used $MAPb_{0.75}Sn_{0.25}I_3$ as the perovskite layer in the PSC and employed a two-step deposition method. Other non-halogen additives include thiocyanate (SCN), which has been shown to allow for larger grain size and improved film morphology in both lead-less[503] and pure-Pb-based PSCs.[504,505]

To the date of writing, the greatest success story of employing additives in tin-based lead-less PSCs was reported by Zhou *et al*. in 2020.[506] They obtained a record PCE of 20.63% using guanidinium bromide (GUABr) as an additive in the perovskite $FA_{0.7}MA_{0.3}Pb_{0.7}Sn_{0.3}I_3$.[506] The introduction of GUABr into the unit cell leads to an increase in the unit cell volume. This was proven to be the case by using PXRD measurements which showed a shift in the reflection peaks at low angles, with this observation being synonymous with the expansion of unit cell volume.

Matching of CTL Energy Levels. If the CTL energy levels in a PSC device are not matched correctly, this can cause a large V_{OC} deficit and hence a lower efficiency device. That said, the interface between layers is also of significant concern. For example, the charge density at recombination centres, charge transport mobilities and their subsequent extraction, compound crystallisation and thin-film growth are all dependent on the interface. Therefore, a thorough understanding of the materials used as either an HTL or an ETL is required to optimise a PSC device.[507]

As explained in Chapter 1, the ETL forms a crucial part of any PSC device. In the direct architecture, TiO_2[508] or SnO_2[509] is regularly used as ETL, the former more so than the latter. On the other hand, these types of PSCs utilise the inverted device architecture. In this architecture, the ETL is of lesser importance than the perovskite or hole transport layers since it does not impact the growth mechanism of the perovskite. Therefore, by engineering the ETL layer, minimal advantages are obtained in terms of device PCE.

In contrast, the HTL is of extreme importance in PSCs for their hole extraction and transport properties and their ability to block electrons.[510–513] Especially in lead-less PSCs, the HTL has attracted attention since it affects both the crystallisation and the charge extraction of the perovskite layer, which directly influences the optoelectronic properties, as the ETL does in the direct architecture. Currently, the commonly used HTM in the inverted structure, and hence in tin-based lead-less PSCs, is PEDOT:PSS.[514–516] However, due to its acidic nature, it breaks down the anode interface.[517] Furthermore, its work function of 5.1 eV does not match perfectly with the valence band of any tin-based lead-less perovskites, which causes a reduction in V_{OC} in the device. This is one avenue of improvement yet to be considered.

That said, Shao *et al*. reported an alternative HTM to PEDOT:PSS, which is poly[2,6-(4,4-bis-(propane-1-sulfonate sodium)-4H-cyclopenta[2,1-*b*;3,4-*b*']dithiophene)-alt-(4,4'-biphenyl)] or PCP-Na for short.[518] This is a neutral pH anionic conjugated polymer with an alkyl sulfonate side group and can be deposited using spin coating.

To conclude the discussion on tin-based lead-less PSCs, Table 2.20 provides an overview of the work mentioned here and others as a function of the tin content of the perovskite layer. Even though tin-based lead-less PSCs are quite promising in terms of their low environmental impact, the tin component does still cause some challenges with air-stability, which means that these structures degrade too quickly to find application in PSCs. However, good progress has been made, and many avenues of research remain to be explored.

Table 2.20 Photovoltaic parameters, deposition methods and device architecture of organic-inorganic hybrid tin-based based lead-less PSCs. Taken and adapted from Gollino *et al.*[500] Primary authors are acknowledged in the Author column (*et al.* is implied).[a]

Perovskite (P)	Sn (%)	Deposition Method	Architecture	V_{OC} (V)	J_{SC} (mA·cm^{-2})	FF	PCE (%)	Author
$MASn_{0.1}Pb_{0.9}I_3$	10	DMSO vapour-assisted	ITO/PEDOT:PSS/**P**/PCBM/BCP/Al	0.78	19	0.67	9.95	Zhu[519]
$MAPb_{0.85}Sn_{0.15}I_{3-x}Cl_x$	15	One-step	ITO/PEDOT:PSS/**P**/PCBM/bis-C_{60}/Ag	0.77	19.5	0.67	10.1	Zuo[520]
$MAPb_{0.75}Sn_{0.25}I_3$	25	One-step	FTO/c-TiO_2/mp-TiO_2/**P**/spiro-OMeTAD/Au	0.728	15.82	0.64	7.37	Hao[283]
$MAPb_{0.75}Sn_{0.25}I_3$	25	Two-step	FTO/PEDOT:PSS/**P**/PCBM/BCP/Ag	0.745	23.8	0.79	13.93	Liu[521]
$MAPb_{0.75}Sn_{0.25}I_3$ + 0.05 mg·mL^{-1} C_{60}	25	Two-step	FTP/PEDOT:PSS/**P**/PCBM/BCP/Ag	0.736	23.5	0.79	13.7	Liu[502]
$MA_{0.9}Cs_{0.10}Pb_{0.75}Sn_{0.25}I_3$	25	Thermal evaporation	ITO/MoO_3/mp-MTDATA/**P**/C_{60}/BCP/Ag	0.677	25	0.53	8.9	Igual[522]
$FA_{0.7}MA_{0.3}Pb_{0.7}Sn_{0.3}I_3$	30	Two-step	ITO/PTAA/**P**/PCBM/ZnO/Al	0.78	23.6	0.74	13.6	Wang[515]
$FAPb_{0.7}Sn_{0.3}I_3$ + MASCN	30	Two-step	ITO/PEDOT:PSS/**P**/PEAI/PCBM/BCP/Ag	0.78	26.46	0.79	16.26	Lian[523]
$MAPb_{0.7}Sn_{0.3}I_3$	30	Dripping	FTO/c-TiO_2/mp-TiO_2/C_{60}-COOH/**P**/spiro-OMeTAD/Au	0.49	27.06	0.59	7.92	Hamanda[524]
$FA_{0.7}MA_{0.3}Pb_{0.7}Sn_{0.3}I_3$ + 12% GUABr + 0.03 mmol SnF_2	30	Dripping	ITO/EMIC·PEDOT:PSS/**P**/S-acetylthiocholine chloride C_{60}/BCP/Ag	1.02	26.61	0.76	20.63	Zhou[506]
$MAPb_{0.6}Sn_{0.4}I_3$	40	One-step	ITO/PEDOT:PSS/**P**/PCBM/Al	0.767	20.5	0.63	10	Zhao[346]
$MAPb_{0.5}Sn_{0.5}I_3$	50	One-step	FTO/c-TiO_2/mp-TiO_2/**P**/P3HT/Au	0.42	20.04	0.50	4.18	Ogomi[525]
$MAPb_{0.5}Sn_{0.5}I_3$	50	Two-step	ITO/PEDOT:PSS/**P**/C_{60}/BCP/Ag	0.75	24.9	0.69	13.6	Li[514]

Table 2.20 (Continued) Photovoltaic parameters, deposition methods and device architecture of organic-inorganic hybrid tin-based based lead-less PSCs. Taken and adapted from Gollino *et al.*[500] Primary authors are acknowledged in the Author column (*et al.* is implied).[a]

Perovskite (P)	Sn (%)	Deposition Method	Architecture	V_{OC} (V)	J_{SC} (mA·cm^{-2})	FF	PCE (%)	Author
$MAPb_{0.5}Sn_{0.5}I_3$ + 10% ascorbic acid	50	Dripping	ITO/PEDOT:PSS/**P**/PCBM/bis-C_{60}/Ag	0.78	25.69	0.70	14.01	Xu[208]
$FA_{0.5}MA_{0.5}Pb_{0.5}Sn_{0.5}I_3$ + 10 mol% SnF_2			ITO/PEDOT:PSS/**P**/PCBM (5 mg·mL^{-1})/ C_{60}/PCBM/Ag	0.75	30.56	0.76	17.59	Kapil[526]
			ITO/PEDOT:PSS/**P**/PCBM/ZnO/Ag	0.79	28.9	0.79	18.1	Liu[527]
$FAPb_{0.5}Sn_{0.5}I_3$ + 10 mol% SnF_2			ITO/PCP·Na/P/C_{60}/BCP/Al	0.782	28.1	0.73	16.27	Shao[518]
$(FASnI_3)_{0.6}(MAPbI_3)_{0.4}$ + 10 mol% SnF_2	60		ITO/PEDOT:PSS/**P**/C_{60}/BCP/Ag	0.795	26.86	0.71	15.08	Liao[528]
$MA_{0.4}FA_{0.6}Pb_{0.4}Sn_{0.6}I_3$ + 20 mol% SnF_2			ITO/PEDOT:PSS/**P**/C_{60}/BCP/Ag	0.83	27.3	0.80	18.2	Prasanna[498]
$MAPb_{0.4}Sn_{0.6}I_{2.6}Br_{0.4}$ + 10 mol% SnF_2			ITO/PEDOT:PSS/**P**/PCBM/Ag	0.78	20.65	0.75	12.1	Lee[529]
$(FASnI_3)_{0.6}(MAPbI_3)_{0.34}(MAPbBr_3)_{0.06}$ + 10 mol% SnF_2			ITO/PEDOT:PSS/**P**/C_{60}/BCP/Ag	0.888	28.72	0.75	19.03	Li[516]
$(FASnI_3)_{0.6}(MAPbI_3)_{0.4}$ + 7% GUASCN			ITO/PEDOT:PSS/**P**/C_{60}BCP/Ag	0.842	30.5	0.80	20.2	Tong[530]
$(FASnI_3)_{0.6}(MAPbI_3)_{0.4}$ + 10 mol% SnF_2			ITO/CuI (10 mg·mL^{-1}) /PEDOT:PSS/**P**/C_{60} /BCP/Cu	0.75	28.5	0.74	15.75	Song[531]
$MAPb_{0.38}Sn_{0.62}I_3$	62	Thermal evaporation + CVD	ITO/TiO_2/**P**/spiro-OMeTAD/Au	0.796	25.5	0.69	14.04	Tavakoli[532]
$MAPb_{0.25}Sn_{0.75}I_{3-x}Cl_x$ + 30 mol% SnF_2	75	One-step	FTO/c-TiO_2/**P**/Al_2O_3/carbon	0.366	23.01	0.48	4.03	Tsai[533]
$PEA_{0.15}FA_{0.85}SnI_3$ + SnF_2 doping	100	Dripping	ITO/PEDOT:PSS/**P**/ICBA/BCP/Ag	0.94	17.4	0.75	12.4	Jiang[323]

[a] **FTO** = Fluorine-Doped Tin Oxide, **ITO** = Indium Tin Oxide, **c-TiO_2** = Compact TiO_2, **mp-TiO_2** = Mesoporous TiO_2, **PEDOT:PSS** = Poly(3,4-ethylenedioxythiophene)-poly(styrenesulfonate), **PCBM** = [6,6]-Phenyl-C_{61}-butyric acid methyl ester, **BCP** = Bathocuproine (2,9-Dimethyl-4,7-diphenyl-1,10-phenanthroline), **spiro-OMeTAD** = 2,2′,7,7′-tetrakis(*N*,*N*'-di-p-methoxyphenyl-amine)9,9′-spirobifluorene, ***m*-MTDATA** = 4,4′,4″-tris(3-methylphenylphenylamino)triphenylamine, **PTAA** = Poly(bis(4-phenyl)(2,4,6-trimethylphenyl)amine), **EMIC·PEDOT:PSS** = 1-ethyl-3-methylimidazolium chloride·Poly(3,4-ethylenedioxythiophene)-poly(styrenesulfonate), **P3HT** = poly(3-hexylthiophene-2,5-diyl), **PCP·Na** = Phenylcyclohexyl piperidine·Na, **ICBA** = Indene-C_{60} bisadduct

2.4.3 Strontium-Based Lead-Less PSCs

Strontium is an element in group 2 of the periodic table, meaning it has a stable oxidation state of 2+, the same as Pb^{2+}. Furthermore, its ionic radius of 118 pm is, for all practical purposes, the same as that of lead's, which is 119 pm.[534] In addition, its orbital symmetry allows it to coordinate to iodide similarly as lead does.[534]

The tendency of group 2 elements to form the perovskite structure has been the subject of DFT calculations by Pazoki *et al*.[369] That said, the alkaline-earth-metal-based lead-free PSCs, such as $MASrI_3$, have wide band gap values in the region of 3.6 eV, making them poor light-harvesting materials, and implying that they should instead be considered as hole or electron transmitting materials.

On the other hand, using the alkaline-earth metals with lead to form lead-less perovskite materials to be subsequently used in lead-less PSCs is worth exploring. However, most of the literature on this topic is focused on strontium-based based perovskite materials for their use in lead-less PSCs.

In 2015, Kai and Liang *et al*. were the first to explore the possibility of mixing strontium and lead in the perovskite lattice.[535] A $MAPb_{1-x}Sr_xI_3$ film was manufactured using a one-step method and used in an FTO/c-TiO_2/mp-TiO_2/**P**/Spiro-OMeTAD/Ag device architecture (**P** = perovskite). However, when this device contained 90% strontium (10% lead), a loss of 71% in PCE compared to the pure lead version was observed, hence leaving significant room for improvement.

Later, an all-inorganic perovskite, $CsPb_{1-x}Sr_xI_2Br$, was considered to study the effects of varying strontium content. It was found that when the strontium content was kept to less than 5% and a low-temperature deposition method was used, the film morphology of the perovskite changed dramatically.[536] Specifically, when 1% or 2% strontium was incorporated, a better charge carrier lifetime was observed in the perovskite film, leading to more efficient PSCs. The device mp-TiO_2/c-TiO_2/$CsPb_{0.98}Sr_{0.02}I_2Br$/P3HT/Au could deliver a PCE of 11.2% under mild conditions (encapsulation in a dark box and only 50% humidity). After one week of use, the HTM, P3HT had oxidised, which led to higher observed efficiencies, however, under these mild conditions, no "real world" application can be extrapolated.

Other devices, for example, ITO/c-TiO_2/mp-TiO_2/$MASr_{0.05}Pb_{0.95}I_{3-x}Cl_x$/spiro-OMeTAD/Au, using larger quantities of strontium, showed better film morphology than their pure lead counterparts. The smaller grains observed for the perovskite in this device allowed for a more compact morphology, allowing for a PCE of 16.3%.[537] Other studies utilising different quantities of strontium (fraction of Sr^{2+} = 0.01, 0.02, 0.05 or 0.1) was conducted by Wu *et al*.[538] for $MAPb_{1-x}Sr_xI_3$ and Zhang *et al*.[539] using $SrCl_2$ (for better hole extraction and less charge recombination), with the results all summarised in Table 2.21. Using SrX_2 as a precursor and different deposition methods need to be carefully considered, as they may lead to pinhole formation in the perovskite film, which in turn affects the potential efficiency of the device.[500]

The ETL can be optimised using a TNRA (TiO_2 nanorod array), leading to high-efficiency strontium-based -based PSCs as shown by Zhang and Pauporté in 2015 and Li *et al*. in 2020.[540,541] This array allows for the direct transport of electrons into PSCs. By employing this ETL, PCEs of 16.08% and 15.09% were reported for strontium substitution of 5% and 15%, respectively, while improved device stability was observed. Furthermore, even for an unencapsulated device, no loss in PCE was reported after 432 hours at 20 °C in 30% RH. This showed that the introduction of strontium has a positive effect on the stability of PSC devices.

Using SrX_2 as an additive in lead-based PSCs is not considered as constituting a lead-less device since the strontium does not replace lead in the perovskite lattice. That said, a lot of research has focussed on using SrX_2 materials as additives in lead-based PSCs. Using these additives, charge recombination can be suppressed, denser films can be obtained, and the inhibition of defect formation and enhanced optoelectronic performances have been reported.[542–544]

On the face of it, strontium-based based high-efficiency devices seem to be more challenging to fabricate than tin-based devices since when the percentage strontium exceeds 5%-10%, a definite change in film morphology is seen depending on the deposition method and ETL used. That said, there certainly are benefits to substituting lead with strontium for lead-less

PSCs and more research should be done in optimising these materials. Table 2.21 summarises the available literature on strontium-based lead-less PSC devices and others, which will be discussed in the next section.

2.4.4 Other Substitutes for Lead-Less PSCs

In theory, any other metal ion that possesses a 2+ oxidation state is a viable substitute to lead in the perovskite lattice. As a result, several different metals have been considered in the same spirit as tin- and strontium-based lead-less perovskites. This section will provide a brief overview of the literature regarding these *other* options for lead substitution.

Barium and Calcium

Since moderate success has been achieved with substituting lead with strontium in the perovskite lattice, other group 2 divalent metals warrant consideration. Both Ba^{2+} and Ca^{2+} have comparative ionic radii, 135 and 100 pm respectively, with Pb^{2+} (119 pm).

In 2017, Chan *et al.* showed that for varying substitution concentrations (0% to 10%) of lead for Mg^{2+}, Ca^{2+}, Sr^{2+} or Ba^{2+} in $MAPbI_3$, either similar or lower efficiencies were obtained for the resultant devices.[545] Most interestingly, for 3% barium introduction ($MAPb_{0.97}Ba_{0.03}I_3$), improved film coverage and crystallinity was observed. These improvements lead to enhanced absorption and less charge recombination at the ETL (TiO_2) interface. Moreover, the band gap of this material is 1.59 eV versus 1.62 eV for the pure lead-containing alternative. The complete device, FTO/TiO_2/$MAPb_{0.97}Ba_{0.03}I_3$/spiro-OMeTAD/Au, achieved a PCE of 14.9%, which is 3.1% better than the comparative pure lead device. Improved stability was also observed for this device. Of course, barium halide additives have also been a subject of interest in the literature.[546]

When lead is substituted by calcium, reports show that using a low calcium concentration ($\lesssim$5%) is best suited for PSC applications.[500] However, as demonstrated by Uribe *et al*., calcium-based PSCs have low efficiencies due to the wide band gap of the perovskite layer (approximately 3.5 eV).[370] The greatest success of calcium thus far is in its use in $CsPbI_3$ PSCs.[547] The incorporation of calcium stabilised the black phase of $CsPbI_3$. A calcium oxide layer forms on top of the perovskite film allowing for better charge carrier lifetimes and film morphology. Using 5% calcium, the PSC device FTO/c-TiO_2/mp-TiO_2/$CsPb_{0.95}Ca_{0.05}I_3$/P3HT/Au achieved a PCE of 12.6%, and with an ant-reflection MgF_2 coating, this value was pushed up to 13.5%. Even though this example is for a purely inorganic PSC, this does prove viability for the substitution of lead by calcium in other materials.

In summary, the substitution of lead by alkaline-earth-metals mainly improves the film morphology of the perovskite layer. Therefore, it is beneficial for the efficiency of the lead-less PSCs, suggesting further research opportunities in this field. Table 2.21 provides a summary of the materials discussed here and others for completeness.

Transition Metals

Transition metals are some of the most abundant metals found in the earth's crust, and some of them have shown a tendency to form the perovskite structure. In this section, attention will be given to Ni^{2+} (ionic radius of 69 pm), Cu^{2+} (ionic radius of 73 pm), Co^{2+} (ionic radius of 75 pm), Fe^{2+} (ionic radius of 78 pm), Mn^{2+} (ionic radius of 83 pm), and Ag^{2+} (ionic radius of 94 pm) which all have ionic radii smaller than Pb^{2+}, and have been shown to play an interesting role in lead-less perovskites and their applications in PSCs, because they are isovalent to lead and possess extremely stable +2 oxidation states.

The first report of using a transition metal in combination with lead dates back to 2016 when Jahandar *et al.* synthesised the perovskite $MA(PbI_2)_{1-x}(CuBr_2)_x$ employing a dripping method using $CuBr_2$ as a precursor.[548] This lead to larger crystal grains and better film morphology than found in $MAPbI_3$. An optimal amount of 5 mol% $CuBr_2$ used in the PSC device

ITO/PEDOT:PSS/MA(PbI_2)$_{1-x}$($CuBr_2$)$_x$/PCBM/LiF/Al delivered a PCE of 17.09%. Later, Gong *et al*. studied the effect of nickel as a lead substitute in the device FTO/SnO_2/$MAPb_{1-x}Ni_xI_3$/spiro-OMeTAD/Au and found that 3% nickel could yield an efficiency of 20.6%.[549]

Klug *et al*. studied the substitution of lead with cobalt.[550] They found that using PEDOT:PSS as the ETL and employing a Pb:Co ratio of 63:1 gave the most favourable outcome. This ratio also allows for phase control over the perovskite material, with a ratio of 63:1 giving a tetragonal room temperature phase versus a ratio of 127:1, resulting in a cubic phase. When the tetragonal phase was utilised in a PSC device, a PCE of 17.2% was obtained, which is higher than obtained for pure $MAPbI_3$. This was argued to be the result of better band alignment between the ETL and perovskite layers. Another group, Xu *et al*., also utilised cobalt in the $MAPbI_3$ lattice to partially substitute lead and obtain a maximum PCE of 21.43% for the device ITO/PTAA/$MAPb_{0.9}Co_{0.1}I_3$/PCBM/Al.[551]

Turning to iron, Cai *et al*. studied the device FTO/TiO_2/MAI(PbI_2)$_{1-x}$($FeCl_2$)$_x$/spiro-OMeTAD/Au and found that it was able to produce a PCE of 17.31%, for 1.8% iron, making it less attractive than the other transition metals considered.[552]

Furthermore, Chen *et al*. partially substituted lead by silver (Ag^{2+}), which proved to reduce charge recombination and allowed for a PCE of 18.4%, nearly an absolute increase of 2.5% compared to lead-only PSCs.[553]

Manganese was added as a dopant by Liang *et al.* in the all-inorganic $CsPbIBr_2$ perovskite.[554] A decrease in the optical band gap of the compound was observed with an increase in the concentration of manganese dopant (0.5%, 1% and 2% were investigated). However, with an increase in dopant concentration, film morphology started to suffer (the development of pinholes). Hence, even though the band gap of the absorber layer was narrower, a loss in efficiency was observed. The maximum efficiency of 7.36% was obtained for a concentration of 0.5% manganese in the device FTO/TiO_2/$CsPb_{0.995}Mn_{0.005}I_{1.01}Br_{1.99}$/carbon compared to the 6.14% obtained when no manganese was present. In addition, the manganese doped device remained stable in ambient conditions for three times longer than the undoped device.

Further research focussing on manganese as a dopant was recently published by Deng *et al*.[555] They utilised manganese as a dopant in the $MAPbI_3$ lattice to obtain $MAPb_{1-x}Mn_xI_3$ films. A device with architecture ITO/SnO_2/$MAPb_{1-x}Mn_xI_3$/spiro-OMeTAD/Au was employed. The dopant concentrations of 0%, 0.6%, 1.3% and 2.6% manganese yielded maximum PCEs of 18.83%, 20.55%, 19.09% and 16.73%, respectively. The PCE of 20.55% for 0.6% manganese is a significant improvement from 18.83% for 0% doping, illustrating that manganese doping plays a major role in these devices by improving the film morphology, and so an improved PCE is possible. Several other reports also showed the successful incorporation of manganese in $MAPbI_3$, however, the devices were not as successful as those reported by Deng *et al.*[556,557]

In a similar vein to the metal substitutes discussed for group 2, these transition metals exhibit a lot of promise for the replacement of lead, however, much research is still to be done in this field. The structures discussed here, and others available in the literature are listed in Table 2.21.

Group 12–13 Elements

Even though the ionic radii of Zn^{2+} (74 pm) and In^{3+} (80 pm) are much smaller than that of Pb^{2+}, these metal ions are suitable for substituting lead in lead-less perovskite.

Jin *et al*. have successfully substituted lead for zinc in the $MAPbI_3$ perovskite lattice.[558] With an optimised zinc concentration of 3% zinc (determined theoretically to be 3.125%) in the perovskite $MAPb_{1-x}Zn_xI_3$, enhanced absorbance and better film morphology were observed.[559] For the PSC device incorporating the perovskite $MAPb_{0.97}Zn_{0.03}I_3$, a PCE of 18.2% was achieved, markedly more efficient than the pure $MAPbI_3$-containing device with a PCE of 16.4%. When a higher concentration of zinc was used, larger grains were obtained, however, this led to the cracking of the perovskite film and the creation of pinholes.

Indium, being trivalent, seems on the face of it, that it should not work in substituting lead in $MAPbI_3$, however, Wang *et al.* has shown that $MAPb_{1-x}In_xI_{3-x}Cl_x$-based PSCs possess high film quality and multiple crystal orientations, which allowing for extensive charge transport.[560] In addition, the introduction of indium reduces grain size, which lessens the possibility of pinhole formation without the loss of efficiency. When 15% indium was present in the device with the architecture ITO/PEDOT:PSS/$MAPb_{1-x}In_xI_{3-x}Cl_x$/PCBM/Bphen/Ag, a PCE of 17.55% was achieved, significantly outperforming the pure lead device.

Germanium

Germanium's (Ge^{2+}) ionic radius of 73 pm is much smaller than that of lead, but it has been shown to partially substitute lead to form lead-less perovskites. However, in the section on lead-free PSCs, it was seen that when solely germanium was used, wide band gap materials with poor stability were obtained, which left the idea of germanium for a complete replacement for lead in its infancy. That said, certain groups then considered its application in combination with lead.

A theoretical study of $MAPb_{1-x}Ge_xI_3$, for $x = 0$ to $x = 1$ (0% to 100%), showed an increase in absorption with increasing germanium content.[561] Additionally, greater charge transport was also seen with increasing germanium concentration. A maximum theoretical efficiency of 24.24% was calculated for the perovskite $MAGe_{0.75}Pb_{0.25}I_3$, showing great promise in the field of Ge-Pb lead-less PSCs.

To date, the most remarkable success story is that reported by Kim *et al.*, who in 2020 employed a MACl additive to the precursor solution of GeI_2. The device FTO/TiO_2/SnO_2/$FA_{0.87}MA_{0.13}Pb_{1-x}Ge_x(I_{0.9}Br_{0.1})_3$/spiro-OMeTAD/Au showed a PCE of 22.09% and retained 80% of its efficiency after one month without encapsulation, a marked improvement over the pure lead device, which only retains 40% of its initial PCE after the same period.[562] The group also employed this technique to a quadrupole of cations to fabricate a perovskite $K_{0.03}Cs_{0.05}(FA_{0.87}MA_{0.13})_{0.92}Pb_{1-x}Ge_x(I_{0.9}Br_{0.1})_3$, which in the same device as before could deliver a PCE of up to 22.7%.

Group 15 Elements

The group 15 elements that have been considered in lead-free perovskite solar cells have also been considered for lead-less PSCs. Both bismuth (Bi^{3+}) and antimony (Sb^{3+}) have shown promise in both fields, although they are trivalent metal cations.

Antimony has not shown any promise of completely replacing lead anytime soon in lead-free PSCs, however, Zhang *et al.* have shown for $MAPb_{1-x}Sb_{2x/3}I_3$ that this material has a tuneable band gap of 1.55 eV to 2.06 eV for 0% to 100% antimony content.[563] Between 0% and 10%, no notable changes in the lattice size were observed, however an increase in the quasi-Fermi level was noted, which corresponds to improved electron mobility. This allowed for a PSC with a PCE of 15.6%. Contrary to Zhang et al., Oku *et al.* used a one-step method that showed that antimony inclusion does expand the lattice.[564] Furthermore, they found that 3% antimony produces an optimal response from the device FTO/c-TiO_2/mp-TiO_2/$MAPb_{1-x}Sb_xI_3$/spiro-OMeTAD/Au, but only a 9.07% PCE. Other devices (ITO/NiO_x/$MAPb_{0.92}Sb_{0.08}I_3$/PCBM/Al) manufactured by Chatterjee *et al.* have only achieved a PCE of 12.8%.[565] This raises questions regarding the validity of Zhang *et al.*'s work, however, the fact of the matter is, there are examples of where antimony is successfully employed, and hence the foundation for further work have been laid.

Turning to bismuth, only a few reports of its use in lead-less PSCs are available. In all-inorganic PSCs, the material $CsPb_{1-x}Bi_xI_3$ has better stability in its black phase than the pure $CsPbI_3$ material, which naturally ensures a more stable final device.[566] By using 4 mol% bismuth, better electronic properties (absorbance and charge transfer) where obtained. The device FTO/TiO_2/$CsPb_{0.96}Bi_{0.04}I_3$/CuI/Au achieved a PCE of 13.21% and retained 68% of its initial PCE after 168 hours at 55% RH and 25 °C. This is an improvement in both efficiency and stability compared to the pure lead device.

Ternary Systems

Up to now, only lead mixed with one other metal has been considered, and unfortunately, only low concentrations of the non-lead metal show any promise in terms of PSC applications. However, the mixture of three metals, including lead, may allow for further fine-tuning and a further decrease in the lead content while addressing the multiple negative factors discussed before.

One report on ternary systems focussed on work conducted by Li *et al.*, with the study investigating the planar structure PSC FTO/TiO_2/$MAPb_{0.9}Sn_{0.05}Cu_{0.05}I_{2.9}Br_{0.1}$/spiro-OMeTAD/$MoO_3$/Ag.[567] This ternary system allowed for a PCE of 21.08% due to the redshift in absorbance and better film morphology accompanying the substitution with tin and copper.

Furthermore, Liu *et al*. conducted a theoretical study of $MAPb_{1-x-y}Sn_xGe_y$-based PSCs in terms of their structural and optical properties through DFT calculations.[568] The study reports that this perovskite should have better structural stability and a tuneable band gap between 0.91 eV for $MASnI_3$ to 1.77 eV for $MAPb_{0.75}Ge_{0.25}I_3$. The optimal ratio of Pb:Sn:Ge was found to be 50:25:25, which gives a band gap value of 1.37 eV and a maximum theoretical efficiency of 23.65%. However, the device architecture was not indicated, leaving some unanswered questions regarding its viability.

To conclude, Table 2.21 summarises the work discussed in this section, with selected other results from the field of lead-less PSCs for completeness. From all these reports, it seems that the transition metals and germanium are the most promising, and this is perhaps the next central direction in the field of PSC devices since the lead-free PSC revolution.

Table 2.21 Photovoltaic parameters of lead-less PSC devices discussed Sections 2.4.2 and 2.4.3, with their device architecture, deposition methods and perovskite material used listed. Taken and adapted from Gollino *et al.*[500] Primary authors are acknowledged in the Author column (*et al*. is implied).[a]

Perovskite (P)	Substituent (%)	Deposition Method	Architecture	V_{OC} (V)	J_{SC} (mA·cm^{-2})	FF	PCE (%)	Author
$MAPb_{0.995}Ag_{0.005}I_3$	0.5 Ag	Dripping	ITO/NiO_x/**P**/PCBM/Ag	1.1	20.6	0.81	18.4	Chen[553]
$CsPb_{0.995}Mn_{0.005}I_{1.01}Br_{1.99}$	0.5 Mn	Two-step	FTO/TiO_2/**P**/carbon	0.99	13.2	0.57	7.36	Liang[554]
$MAPb_{0.994}Mn_{0.006}I_3$	0.6 Mn	One-step	ITO/SnO_2/**P**/spiro-OMeTAD/Au	1.15	24.5	0.73	20.55	Deng[555]
$MAPb_{0.99}Sb_{0.01}I_3$	1 Sb	Not Reported	FTO/c-TiO_2/mp-TiO_2/**P**/spiro-OMeTAD/Au	0.985	21.8	0.69	15.6	Zhang[563]
$MAPb_{0.99}Ca_{0.01}I_3$	1 Ca	One-step	FTO/TiO_2/**P**/spiro-OMeTAD/Au	0.98	19.1	0.68	12.9	Wu[569]
$MAPbCoI_3$ (Pb:Co, 63:1)	≈1 Co	One-step	ITO/PEDOT:PSS/**P**/Ca-BCP/Al-Ag	1.05	21.1	0.78	17.2	Klug[550]
$MAPb_{0.99}Sr_{0.01}I_3$	1 Sr	Not Reported	FTO/TiO_2/**P**/spiro-OMeTAD/Ag	0.9	18.9	0.63	10.6	Wu[538]
$MAPb_{0.99}Ba_{0.01}I_3$	1 Ba	One-step	FTO/TiO_2/**P**/spiro-OMeTAD/Au	0.98	19.6	0.68	13	Wu[570]
$MAI(PbI_2)_{0.982}(FeCl_2)_{0.018}$	1.8 Fe	One-step	FTO/TiO_2/**P**/spiro-OMeTAD/Au	1.10	22.21	70.9	17.3	Cai[552]
$CsPb_{0.98}Sr_{0.02}I_2Br$	2 Sr	Vapour assisted	FTO/c-TiO_2/mp-TiO_2/**P**/P3HT/Au	1.043	15.3	0.70	11.2	Lau[536]
$MAPb_{0.97}Ni_{0.03}I_3$	3 Ni	Two-step	FTO/SnO_2/**P**/spiro-OMeTAD/Au	1.13	22.6	0.81	20.6	Gong[549]
$MAPb_{0.97}Sb_{0.03}I_3$	3 Sb	One-step	FTO/c-TiO_2/mp-TiO_2/**P**/spiro-OMeTAD/Au	0.843	19.2	0.56	9.07	Oku[564]
$MAPb_{0.97}Ba_{0.03}I_3$	3 Ba	One-step	FTO/TiO_2/**P**/spiro-OMeTAD/Au	0.99	20.4	0.70	14.9	Chan[545]
$MA(PbI_2)_{0.97}(ZnCl_2)_{0.03}$	3 Zn	Dripping	FTO/TiO_2/**P**/spiro-OMeTAD/Au	1.09	22.0	0.76	18.2	Jin[558]
$FA_{0.87}MA_{0.13}Pb_{0.97}Ge_{0.03}(I_{0.9}Br_{0.1})_3$	3 Ge	Dripping	FTO/TiO_2/SnO_2/**P**/spiro-OMeTAD/Au	1.14	25.0	0.77	22.09	Kim[562]
$CsPb_{0.96}Bi_{0.04}I_3$	4 Bi	One-step	FTO/TiO_2/**P**/CuI/Au	0.97	18.76	0.73	13.21	Hu[566]
$MA(PbI_2)_{0.95}(CuBr_2)_{0.05}$	5 Cu	Dripping	ITO/PEDOT:PSS/**P**/PCBM/LiF/Al	0.961	21.51	0.83	17.09	Jahandar[548]
$MAPb_{0.95}Sr_{0.05}I_{2.95}Cl_{0.05}$	5 Sr	Two-step	ITO/c-TiO_2/mp-TiO_2/**P**/spiro-OMeTAD/Au	1.11	21.08	0.71	16.3	Shai[537]
$CsPb_{0.95}Ca_{0.05}I_3$	5 Ca	Vapour-assisted	FTO/c-TiO_2/mp-TiO_2/P3HT/Au/MgF_2	0.95	17.9	0.80	13.5	Lau[547]
$MAPb_{0.95}Sr_{0.05}I_{2.95}Cl_{0.50}$	5 Sr	Two-step	FTO/TNRAs/**P**/spiro-OMeTAD/Au	1.02	19.96	0.75	16.08	Li[540]

Table 2.21 (Continued) Photovoltaic parameters of lead-less PSC devices discussed Sections 2.4.2 and 2.4.3, with their device architecture, deposition methods and perovskite material used listed. Taken and adapted from Gollino *et al.*[500] Primary authors are acknowledged in the Author column (*et al.* is implied).[a]

Perovskite (P)	Substituent (%)	Deposition Method	Architecture	V_{OC} (V)	J_{SC} (mA·cm^{-2})	FF	PCE (%)	Author
$MAPb_{0.92}Sb_{0.08}I_3$	8 Sb	Two-step	ITO/NiO_x/**P**/PCBM/Al	1.13	17.4	0.65	12.8	Chatterjee[565]
$MAPb_{0.9}Co_{0.1}I_3$	10 Co	Two-step	ITO/PTAA/**P**/PCBM/Al	1.07	24.42	0.82	21.43	Xu[551]
$MAPb_{0.9}Sr_{0.1}I_3$	10 Sr	One-step	FTO/c-TiO_2/mp-TiO_2/**P**/spiro-OMeTAD/Ag	0.87	4.32	0.53	1.97	Kai[535]
$MAPb_{0.9}Sr_{0.1}I_{2.9}Cl_{0.1}$	10 Sr	Two-step	FTO/c-TiO_2/mp-TiO_2/**P**/spiro-OMeTAD/Au	1.08	19.45	0.74	15.64	Zhang[539]
$MAPb_{0.9}Sn_{0.1}I_3$	10 Sn	Two-step	FTO/c-TiO_2/mp-TiO_2/spiro-OMeTAD/Au	1.06	20.32	072	15.52	Zhang[571]
$MAPb_{0.9}Sn_{0.05}Cu_{0.05}I_{2.9}Br_{0.1}$	5 Sn & 5 Cu	Dripping	FTO/TiO_2/**P**/MoO_3/Ag	1.08	23.97	0.81	21.08	Li[567]
$MAPb_{0.85}In_{0.15}I_{2.85}Cl_{0.15}$	15 In	One-step	ITO/PEDOT:PSS/**P**/PCBM/Bphen/Ag	1.03	21.9	0.78	17.55	Wang[560]
$CsPb_{0.8}Ge_{0.2}I_2Br$	20 Ge	Dripping	FTO/SnO_2/**P**/P3HT/spiro-OMeTAD/Au	1.27	12.15	0.70	10.8	Yang[572]
$CsPb_{0.8}Ba_{0.2}I_2Br$	20 Ba	One-step	FTO/c-TiO_2/mp-TiO_2/**P**/spiro-OMeTAD/Au	14	1.28	0.78	14	Xiang[573]
$MAPbI_3$:Sr_2 + (2% doping)	–	One-step	FTO/PEDOT:PSS/**P**/IPH/Ba-Ag	0.95	18.5	0.85	15	Pérez-del-Rey[542]
$MAPbI_2Br(SrCl_2)_{0.1}$ (doping)	–	One-step	FTO/c-TiO_2/mp-TiO_2/**P**/mp-Al_2O_3/carbon	1.05	20.2	0.75	15.9	Zhang[543]
$Pb(I_{0.83}Br_{0.17})_3$ (2% Sr doping)	–	Dripping	ITO/PTAA/**P**/C_{60}/BCP/Cu	1.18	23.2	0.74	20.3	Caprioglio[574]

[a] **FTO** = Fluorine-Doped Tin Oxide, **ITO** = Indium Tin Oxide, **c-TiO_2** = Compact TiO_2, **mp-TiO_2** = Mesoporous TiO_2, **PCBM** = [6,6]-Phenyl-C_{61}-butyric acid methyl ester, **PEDOT:PSS** = Poly(3,4-ethylenedioxythiophene)-poly(styrenesulfonate), **BCP** = Bathocuproine (2,9-Dimethyl-4,7-diphenyl-1,10-phenanthroline), **spiro-OMeTAD** = 2,2′,7,7′-tetrakis(*N*,*N*′-di-p-methoxyphenyl-amine)9,9′-spirobifluorene, **P3HT** = poly(3-hexylthiophene-2,5-diyl), **TNRAs** = TiO_2 nanorod array, **PTAA** = Poly(bis(4-phenyl)(2,4,6-trimethylphenyl)amine), **Bphen** = 4,7-Diphenyl-1,10-phenanthroline, **IPH** = Indene-C_{60}-propionicacid hexyl ester

2.4.5 Partial Lead-Halide Substitution by Large Organic Cations

Traditionally, when an organic cation is "too big" to be accommodated in the 3D cubic perovskite lattice of a given metal and halide combination, a lower dimensionality structure is expected, as per the various tolerance factors. However, as recently as 2017, the groups of N. Mercier and M.G. Kanatzidis discovered that certain organic cations that are *too large* as determined by the tolerance factor replace a $(PbI)^+$ entity in the perovskite lattice, while the dimensionality remains 3D, rather than forcing the structure into a lower dimensionality.[575]

Two names emerged for these types of perovskites, namely d-HPs (for lead-iodide deficient halide perovskite, named so by the Mercier group) and "hollow" perovskites (called so by the Kanatzidis group). The term "hollow" is misleading in that it is not a $(PbI)^+$ vacancy that is created but the entity that is replaced by a monovalent organic cation. The reason for the two different names is that they refer to the use of different organic cations. Figure 2.35 shows in (a) a theoretical inorganic framework of a d-HP of $MAPbI_3$ and (b) a schematic of the real crystal structure when HEA^+ is used in d-MAPI. The HEA^+-cation would fit in the vacancy as shown.

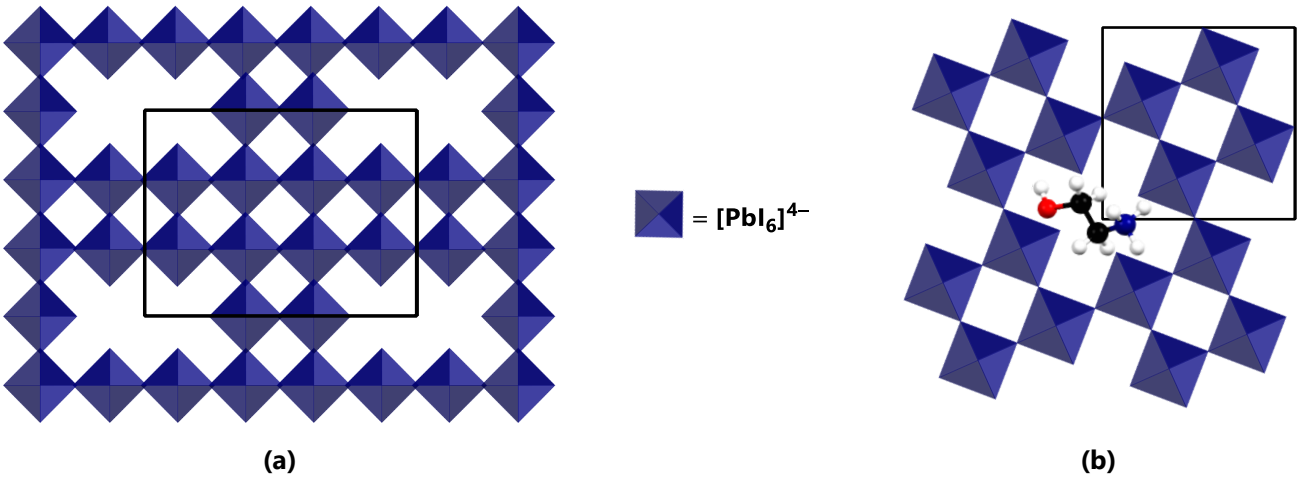

Figure 2.35 (a) The hypothetical d-MAPI network $Pb_{10}I_{34}$ (or $Pb_{0.83}I_{2.83}$) consisting of ⟨100⟩ Pb_2I_7 layers connected by PbI_6 octahedra and **(b)** schematic of the framework of the experimental deficient structure of a d-MAPI $(MA)_{0.55}(HEA)_{0.63}Pb_{0.82}I_{2.82}$ crystal. Adapted from Gollino *et al.*[500]

Hollow perovskites use propylenediammonium (PN), ethylenediammonium ({en}), and trimethylenediammonium (TN), whereas the d-HPs utilise thioethylammonium (TEA^+), hydroxyethylammonium (HEA^+), fluoroethylammonium (FEA^+), and an expanded dication (Dic^{2+}).[500]

In general, the hollow perovskites have higher efficiencies than the d-HPs, but lack in terms of stability and vice versa.[576] Therefore, this is an exciting new avenue of research in lead-less PSCs, and the field still has a large scope since only a few research groups have investigated the possibilities. However, the large deterrent in this field is that the patent rights to these structures are owned by two research groups, hindering others from joining.

This concludes the lead-less perovskite section, and now the focus will move to what can be concluded from the literature survey thus far. The following section will place this study into perspective and provide the rationale behind why it is to be completed.

2.5 Alkali Metals in Hybrid Halide Perovskites

In considering the LCA (Life Cycle Assessment) of lead-based PSCs, several research groups[95,577,578] have deduced that the lead component of lead-based PSCs is not the main culprit when it comes to its environmental impact. Zhang *et al.* determined that in the decomposition and construction of a lead-based PSC, CH_3NH_3I accounts for 62.31% of its human toxicity potential (HTP), whereas PbI_2 contributes a miserly 3.68% to the global HTP.[578]

Lead-based PSCs have achieved PCE values of over 20% for multiple device types,[239,579–581] in contrast to the comparatively low value of about 13% being the highest for lead-free based PSCs, for a perovskite with the composition $GUA_{0.2}FA_{0.8}SnI_3$.[334] This is concerning, seeing that Sn is the champion of lead-free devices, and yet, it cannot compete against Pb for its PSC crown.

Other alternative compounds to lead based perovskites include the likes of $Cs_3Bi_2I_9$, $MA_3Bi_2I_9$ and $MA_3Sb_2I_9$. All these alternatives possess a 0D structure and thus have a large exciton binding energy, a large band gap and deep defect states, making them non-ideal for photovoltaic applications. This means the maximum PCE, as discussed previously, is only 3.20%, which is nowhere near that reported and predicted for lead-based PSCs.[21]

In addition, Pb has one of the lowest GWPs (global warming potentials) of all naturally occurring metals (1.3 kg CO_2-eq per kg).[582] All the other alternatives to lead for PSC applications show higher values (Table 2.22), with the added disadvantage of being scarcer and hence more expensive than lead. Therefore furthering the argument that at the moment, there are no *responsible* alternatives to lead in PSCs.[64]

Table 2.22 Availability, cost and global warming potential of Pb versus Pb alternatives in contention as substitutes for Pb in PSCs.[64,582]

Element	Average Price in 2006-2010 (USD per kg)	Global Production in 2008 (tons)	Main Source	GWP (kg CO_2-eq per kg)
Pb	2.26	8 065 000	Pb Ores	1.3
Sb	6.24	188 000	Sb_2S_3	12.9
Sn	20.6	333 000	SnO_2	17.1
Bi	21.12	16 600	Pb Ores	58.9
Te	150.40	140	Cu Ores	21.9
Ag	481.36	21 350	Cu, Au/Ag and Pb Ores	196
In	692.6	600	Zn Ores	102
Ge	1172	59	Zn Ores	170

Of those listed in Table 2.22 many of the metal alternatives proposed for lead in lead-based PSCs are not mined directly, but rather indirectly from other metals' ores (Bi, Te, Ag, In and Ge). Only Sn, Sb and Pb are mined from a direct source (meaning the source contains the element being mined), however, the GWP of Sb and Sn are 13 and 17 times more than that of lead, which does seem an awful price to pay to go lead-free. Even in terms of *direct costs*, tin is nearly 10 times as expensive as lead, which correlates with the scarcity of tin in the earth's crust.[583]

Sustainability implies that the technology used provides advantages to the current and future generations who use it. For a renewable technology such as solar cells to be sustainable, it should be cheap to manufacture, be composed of abundant and inexpensive materials and, of course, be environmentally friendly. Unfortunately, so far, all the proposed alternatives to lead have failed to meet one or more of these criteria.[64] Only Sn seems to be able to compete with Pb on any level, however, the easy oxidation of Sn^{2+} to Sn^{4+}, as discussed earlier, does pose a significant problem with Sn-based PSCs. Therefore, only by encapsulation under inert atmosphere (N_2 or Ar) are Sn-based PSCs remotely competitive. This additional requirement does not vote well for Sn-based PSC applications, and hence other alternatives should be considered.

While the metallic version of tin is much less toxic than lead[584], in PSCs, the metal-halide constituents (for example, tin iodide (SnI_2) or lead iodide (PbI_2)) are the points of concern. In comparing the toxicity of SnI_2 and PbI_2 through material safety data sheets, both are classified as acutely toxic. The only unknown is the ecotoxicity of SnI_2, otherwise, it is not immediately clear which metal halide is *safer*.

Babayigit *et al*. considered a comparison of LC_{50} and EC_{50} of both PbI_2 and SnI_2 in zebrafish, which concluded that the widespread belief that tin is more environmentally friendly than lead is misplaced.[585] The study went further to show that when SnI_2 is exposed to water and oxygen, several decomposition pathways are possible, all leading to the formation of hazardous hydrogen iodide (HI).

Even though many of the lead alternatives discussed thus far are *much less* toxic than lead, most of them are still harmful to humans and the environment. Alternatives to lead that have not been investigated in detail, are the alkali metal ions, and this option deserves further exploration. Employing a doubly charged A-site cation (A^{2+}) allows for the use of alkali metals in the B-site, hence, removing the toxicity to a large degree and this is where the current study finds its motivation and inspiration.

2.5.1 Alkali Metal Ions in Mixed Metal Perovskites

A CSD (2021, Version 5.42, update May 2021)[586] search was conducted to find structures containing a +1 metal ion, a halide ion, and an H–N–C portion in combination with any other metals. The results were sifted manually, and only those structures that fall within the perovskite category are considered here. Table 2.23 summarises the structures containing alkali metal ions as part of mixed metal halide compounds. The perovskite structures found in this survey will be discussed shortly.

Table 2.23 Summary of the mixed metal perovskite structures containing alkali metal ions reported in the literature, with an array of A-site cations. The A-site cation(s), the dimensionality of the structure, the temperature at which the structure was determined, the structure type, the lattice type and the space group are included.

Metal Ions	Halide Ions	
	Cl^-	Br^-
Na^+ and Ru^{3+}	**BURLIM**[587] (MA^+, 1D ABX_3-type, 299 K, Double Perovskite, Trigonal, $P\bar{3}m1$)	**BURMAF**[587] (MA^+, 1D ABX_3-type, 299 K, Double Perovskite, Trigonal, $P\bar{3}m1$)
K^+ and Ru^{3+}	**BURLUY**[587] (MA^+, 1D ABX_3-type, 293 K, Double Perovskite, Trigonal, $P\bar{3}m1$)	**BURMOT**[587] (MA^+, 1D ABX_3-type, 293 K, Double Perovskite, Trigonal, $P\bar{3}m1$)
K^+ and Bi^{3+}	**EKIVOL**[443] (MA^+, 3D, 298 K, Double Perovskite, Trigonal, $R\bar{3}m$)	N/A
K^+ and Gd^{3+}	**JEHKIT**[444] (MA^+, 3D, 300 K, Double Perovskite, Trigonal, $R\bar{3}m$)	N/A
K^+ and Y^{3+}	**JEHKOZ**[444] (MA^+, 3D, 300 K, Double Perovskite, Trigonal, $R\bar{3}m$)	N/A
Cs^+ and Sn^{2+} [a]	N/A	**EFOLAP**[588] (GUA^+, 2D ACI-type, 250 K, 2D Perovskite, Orthorhombic, *Imma*)
Cs^+ and Pb^{2+} [a]	N/A	**MIXDEF**[589] (*i*Pr-$CH_2NH_3^+$, 2D ACI-type, 360 K, 2D Perovskite, Orthorhombic, *Cmca*) **MIXDEF01**[589] (*i*Pr-$CH_2NH_3^+$, 2D ACI-type, 293 K, 2D Perovskite, Orthorhombic, *Pnmb*) **VEHWEN**[588] (GUA^+, 2D ACI-type, 300 K, 2D Perovskite, Orthorhombic, *Cmmm*) **VEHWIR**[588] (GUA^+, 2D ACI-type, 300 K, 2D Perovskite, Orthorhombic, *Imma*) **VEHWOX**[588] (GUA^+, 2D ACI-type, 250 K, 2D Perovskite, Orthorhombic, *Pnnm*) **VEHWUD**[588] (GUA^+, 2D ACI-type, 300 K, 2D Perovskite, Orthorhombic, *Pnnm*)

[a] Note Cs^+ is an A-site cation in these cases.

The structures with combinations of Cs^+ and Sn^{2+} or Pb^{2+} use Cs^+ as an A-site cation alongside GUA^+ or *i*Pr-$CH_2NH_3^+$, thus they are not of interest because this focus is on the substitution of lead with alkali metal ions in the B-site.

From Table 2.23, it is evident that not much research has been conducted on structures containing alkali metal ions in B-site mixtures with other metals (i.e., in halide double perovskites). However, the seven structures that have been reported suggest that there is a possibility for further investigation.

These seven structures can be divided into two structural categories, namely the 1D ABX_3-type perovskites and 3D perovskites. Since all the structures have a 1:1 ratio of B^+ and B'^{3+} ions in the B-site, all can be classified as halide double perovskites, as defined in Chapter 1.

Four of the structures listed in Table 2.23 are of the 1D ABX_3-type and crystallise in the trigonal $P\bar{3}m1$ space group. Therefore, they are all isostructural (all determined at room temperature) and contain the same A-site cation, MA^+. Figure 2.36 (a) through (d) shows the unit cells and packing diagrams of these structures, emphasising their isostructurality. Furthermore, Figure 2.36 (e) shows the alternating metal ion (K^+ and Ru^{3+}) face-sharing octahedra present in the inorganic 1D chain in the structure BURMOT,[587] which illustrates the double perovskite structural characteristics and the 1D ABX_3-type structural motif.

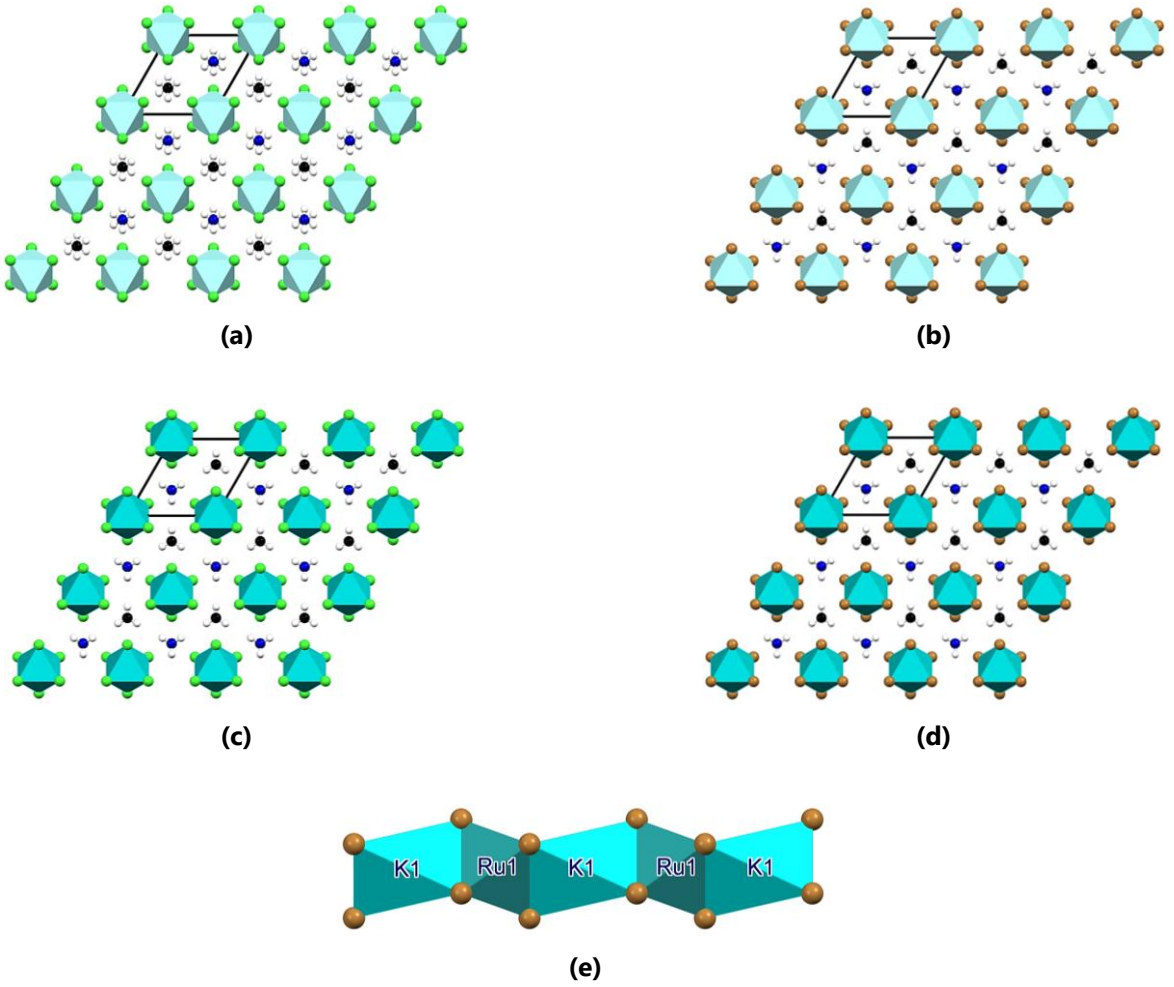

Figure 2.36 The 2×2 expansion of the unit cells (shown in black) of **(a)** BURLIM,[587] **(b)** BURMAF,[587] **(c)** BURLUY[587] and **(d)** BURMOT[587] as viewed down the *c*-axis. **(e)** Polyhedral view of the 1D face-sharing $[KBr_6]$-$[RuBr_6]$ inorganic octahedra in structure BURMOT[587], which is representative of the octahedra in structures BURLIM,[587] BURMAF,[587] and BURLUY[587].

In addition, three of the structures listed in Table 2.23 are 3D double perovskites and crystallise in the trigonal $R\bar{3}m$ space group, therefore, are all isostructural. EKIVOL,[443] JEHKIT,[444] and JEHKOZ[444] are double perovskites containing MA^+ as the A-site cation, Cl^- as the X-site halide and K^+ with either Bi^{3+}, Gd^{3+} or Y^{3+} in a 1:1 ratio in the B-site, respectively. Figure

2.37 (a), (b), (c), (d), (e), (f), (g), (h) and (i) show the inorganic framework of corner-sharing octahedra for the structures EKIVOL,[443] JEHKIT,[444] and JEHKOZ[444], viewed down the *a*-, *b*-, and *c*-directions. This illustrates their isostructurality and 3D nature.

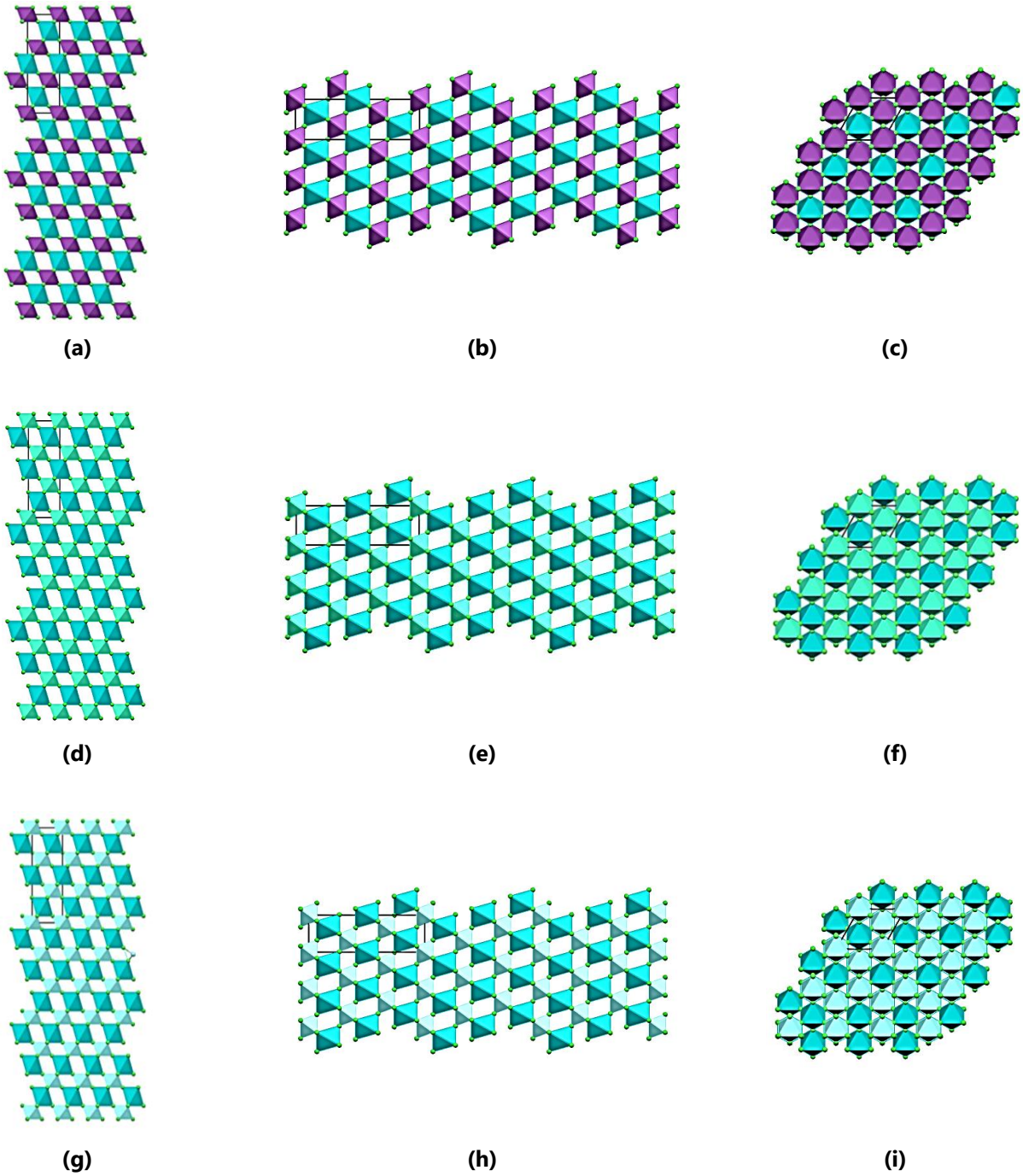

Figure 2.37 3×3 expansions and unit cells (shown in black) of EKIVOL,[443] JEHKIT,[444] and JEHKOZ[444]. Figures **(a)**, **(b)** and **(c)** show the inorganic framework (Bi-octahedra in purple and K-octahedra in sea green) of EKIVOL[443] viewed down the *a*-, *b*- and *c*-axis, respectively. Figures **(d)**, **(e)** and **(f)** shows the inorganic framework (Gd-octahedra in light green and K-octahedra in sea green) of JEHKIT[444] viewed down the *a*-, *b*- and *c*-axis, respectively. Figures **(g)**, **(h)** and **(i)** shows the inorganic framework (Y-octahedra in light blue and K-octahedra in sea green) of JEHKOZ[444] viewed down the *a*-, *b*- and *c*-axis, respectively.

This section has considered mixtures of alkali metals with other known perovskite B-site cations to illustrate the viability of including alkali metal ions in halide perovskites as B-site ions. The next logical step is to see if there are any pure alkali metal hybrid halide perovskites reported in the literature.

2.5.2 Alkali Metal Only Perovskites

A CSD (2021, Version 5.42, update May 2021)[586] search was conducted to find structures containing only an alkali metal ion, halide ion and an H–N–C portion. The structures were sifted manually to find perovskite structures of any dimensionality containing a doubly charged organic cation, an alkali metal ion, and a halide ion. The structures identified in this search were found to contain one of only four organic cations, namely dabconium, 1-methyl dabconium, piperazinium or 1-methyl piperazinium. The line structures of these cations are indicated in Figure 2.38.

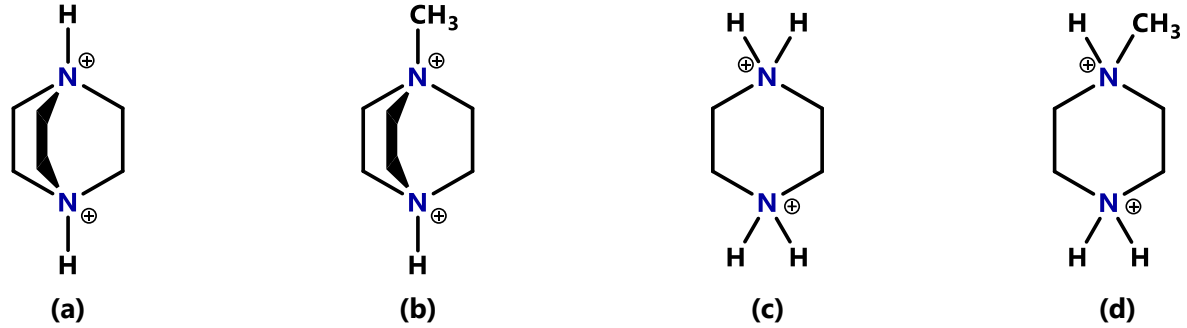

Figure 2.38 The line structures of the organic dications present in the structures reported in the literature **(a)** 1,4-diazabicyclo[2.2.2]octane-1,4-diium (dabconium), **(b)** 1-methyl-1,4-diazabicyclo[2.2.2]octane-1,4-diium (1-methyl dabconium), **(c)** piperazine-1,4-diium (piperazinium) and **(d)** 1-methylpiperazine-1,4-diium (1-methyl piperazinium).

The first report of alkali metals in halide perovskites was published by Paton *et al.*[590] in 2010, and alkali-metal based hybrid perovskites have since received intermittent attention. Therefore, there exists a viable avenue for further investigation of these materials and their potential application in lead-free PSCs.

This section will provide an overview of the alkali metal halide hybrid perovskites reported in the literature, with specific focus on structures containing 1,4-diazabicyclo[2.2.2]octane-1,4-diium, hereafter abbreviated dabconium, or piperazinium as the doubly charged organic cation. Furthermore, no results have been published on the band gaps of these materials or their use in PSC technology, making the current study the first to do so, joining the search for lead-free PSCs.

Dabconium-Containing Perovskites

A search of the Cambridge Structural Database (CSD (2021, Version 5.42, update May 2021)[586]) indicated that 10 structures consisting of dabconium cations and anions comprising monovalent alkali metal ions and halide anions have been reported in the literature.

Two structures falling in the 1D ABX_3-type perovskite category, described in Chapter 1, have been reported. The 1D perovskite structure consisting of dabconium cations and KCl-based anions has been reported with the CSD refcodes DOTHOK[591] and DOTHOK01[590]. The two structures were determined at 100 K and 120 K, respectively, with the structure remaining in its trigonal phase at both temperatures (space group $R\bar{3}c$). The combination of dabconium cations and RbI-based anions also results in the formation of a 1D perovskite structure, with CSD refcode HEJHOW,[592] with the structure determined to be in a hexagonal phase (space group $P\bar{6}2c$) at room temperature (293 K).

3D perovskite structures have been reported in the literature for the combination of dabconium and several monovalent metal alkali ions and halide ions. The perovskite structure obtained from the combination of dabconium and KBr-based anions (CSD refcode: FIZYIZ[593]) was determined at 300 K to be in the trigonal phase (space group $P3_121$). In addition, three different structures have been reported for the combination of dabconium and RbCl-based anions, (CSD refcodes: GUYNEU[590], GUYNEU01[592] and GUYNEU02[592]), with the structures representing two trigonal phases (space groups $P3_221$ and $P3_121$), determined at 120 K and 293 K, and a cubic phase (space group $Pm\bar{3}m$) determined at 458 K. Furthermore, two structures have been reported containing dabconium cations and RbBr-based anions (CSD refcodes: HEJGUB and HEJGUB01),[592] with the structures representing the trigonal (space group $P3_221$) and cubic (space group $Pm\bar{3}m$) phases of the compound determined at 293 K and 353 K, respectively. Lastly, a monoclinic 3D perovskite (space group $C2/c$) structure was reported to form for the combination of dabconium and CsCl-based anions as determined at 120 K (CSD refcode: GUYNIY[590]).

Table 2.24 summarises the structures obtained from the literature search with their CSD[586] reference codes. There remain several structures in the matrix yet to be determined, including the combination of dabconium cations and anions based on LiCl, LiBr, LiI, NaCl, NaBr, NaI, KI, CsBr and CsI, as can be seen from Table 2.24.

Table 2.24 A summary of the results obtained for literature structures reported containing dabconium cations and anions comprising monovalent alkali metal ions and halide anions. The dimensionality of the structure, the temperature at which it was determined, the structure type, the lattice type and the space group are included.

Metal Cation	Halide Anion		
	Cl^-	Br^-	I^-
Li^+	N/A	N/A	N/A
Na^+	N/A	N/A	N/A
K^+	**DOTHOK**[591] (100 K, 1D ABX_3-type perovskite, trigonal, $R\bar{3}c$) **DOTHOK01**[590] (120 K, 1D ABX_3-type perovskite, trigonal, $R\bar{3}c$)	**FIZYIZ**[593] (300 K, 3D perovskite, trigonal, $P3_121$)	N/A
Rb^+	**GUYNEU**[590] (120 K, 3D perovskite, trigonal, $P3_221$) **GUYNEU01**[592] (293 K, 3D perovskite, trigonal, $P3_121$) **GUYNEU02**[592] (458 K, 3D perovskite, cubic, $Pm\bar{3}m$)	**HEJGUB**[592] (293 K, 3D perovskite, trigonal, $P3_221$) **HEJGUB01**[592] (353 K, 3D perovskite, cubic, $Pm\bar{3}m$)	**HEJHOW**[592] (293 K,1D ABX_3-type perovskite, hexagonal, $P\bar{6}2c$)
Cs^+	**GUYNIY**[590] (120 K, 3D perovskite, monoclinic, $C2/c$)	N/A	N/A

From Table 2.24, it can be seen that two structural types are formed when dabconium cations are combined with alkali metal ions. Firstly, a 1D ABX_3-type perovskite structure, as defined in Chapter 1, is formed for the combination of dabconium cations with KCl- and RbI-based anions. A 3D perovskite structure, as defined in Chapter 1, is formed for the combination of dabconium cations with KBr-, RbCl-, RbBr- and CsCl-based anions.

However, it is interesting that two of the compounds were reported to undergo phase transitions from one 3D perovskite phase to another. Firstly, the compound formed from the combination of dabconium cations and RbCl-based anions crystallises in a trigonal, chiral, 3D perovskite phase at both 120 K and room temperature (GUYNEU[590] and GUYNEU01[592]). The source of the chirality of the structure is the helical packing of the dabconium cations. The authors indicated that the crystal was

enantiomerically pure but suggested that the bulk of the sample forms a *conglomerate*, crystallising in space groups $P3_221$ and $P3_121$. However, at a higher temperature (458 K), this compound crystallises in a highly symmetric, centrosymmetric cubic phase (GUYNEU02[592]). The two different phases are illustrated in Figure 2.39 (a) and (b). The phase transition temperature was reported to be around 430 K.[592] It is unclear from the literature whether this transition is irreversible, as is the case for $MAPbI_3$.

In addition, the compound formed from the combination of RbBr-based anions and dabconium cations also shows the same behaviour, with the low-temperature and high-temperature phases crystallising in the same respective space groups as those reported for the dabconium and RbCl-containing compounds. Here, a 3D trigonal perovskite is also formed at room temperature (HEJGUB[592]), while a 3D cubic perovskite structure is present at 353 K (HEJGUB01[592]). The phase transition temperature was reported to be around 340 K.[592] It was not reported if this phase transition is reversible.

(a) **(b)**

Figure 2.39 Structures formed for the combination of dabconium cations and RbCl-based anions. **(a)** Room temperature phase (GUYNEU01[592]). **(b)** High-temperature phase (GUYNEU02[592]).

As can be seen in Figure 2.39 (b), the angles of the anionic metal halide framework are exactly 90° and 180° degrees in the high-temperature phase (GUYNEU02[592]) of the compound formed from the combination of RbCl-based anions and dabconium cations, whereas this is not the case in the room temperature phase GYUNEU01[592]. In addition, the cations are ordered in the room temperature phase, whereas they are disordered in the high-temperature phase. The same applies to the structures formed through the combination of RbBr-based anions and dabconium cations. Another interesting observation is that while the RbCl and RbBr analogues with dabconium cations form 3D perovskite structures, the RbI-analogue reverts to a 1D ABX_3-type perovskite structure (HEJHOW[592]), as observed for the combination of dabconium and the smaller metal and halide ions K^+ and Cl^-.

A meaningful comparison can be made between the structures DOTHOK, DOTHOK01 and BURMOT (and the isostructural double perovskites). These structures illustrate the same 1D ABX_3-type perovskite structures, as illustrated in Figure 2.40 (a) and (b).

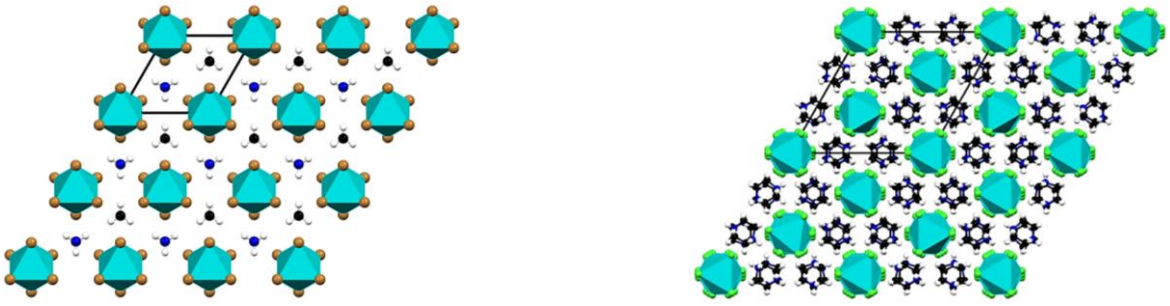

(a) **(b)**

Figure 2.40 The 2×2 expansion of the unit cell (shown in black) of **(a)** the structure BURMOT[587] (representative of BURLIM,[587] BURMAF[587] and BURLUY[587]) and **(b)** the structure of DOTHOK[591] (representative of DOTHOK01[590]), both viewed down the *c*-axis.

The BURMOT isostructural family described earlier showed that K^+ and Ru^{3+} could allow for a halide double perovskite with MA^+, however, structures DOTHOK and DOTHOK01 show that once MA^+ is replaced with dabconium (a dication), then pure K^+ may also be used to form an ABX_3-type 1D perovskite.

Considering the reported literature on dabconium-containing perovskites and the link between these and the halide double perovskites, it does suggest that further work on this system would prove fruitful and could lead to many perovskite possibilities.

1-Methyl Dabconium-Containing Perovskites

A search of the Cambridge Structural Database (CSD (2021, Version 5.42, update May 2021)[586]) indicated that only four structures consisting of 1-methyl dabconium cations and anions comprising monovalent alkali metal ions and halide anions have been reported in the literature.

The combination of K^+, I^- and 1-methyl dabconium lead to two 3D perovskite structures, with CSD refcodes: IPERON[594] and IPERON01[594]. IPERON is a room temperature structure (determined at 293 K), crystallising in the trigonal space group *R*3, whereas IPERON01 is a high-temperature structure (determined at 450 K) crystallising in the cubic phase with space group *P*432.[594] The structures of both these phases are illustrated in Figure 2.41 (a) and (b). The room temperature trigonal phase has more distorted KI_6 octahedra compared to the high-temperature cubic phase, however, in contrast, the trigonal phase has a less disordered organic cation than the cubic phase. The authors showed by DSC (Differential Scanning Calorimetry) studies that the phase transition between the trigonal and cubic phases is reversible, and that the transition occurs around 427.5 K when heating and at about 407.0 K upon cooling the compound.[594]

(a) **(b)**

Figure 2.41 The crystal structures of **(a)** IPERON[594] (representative of HEJGOV01[592]) and **(b)** IPERON01[594] (representative of HEJGOV[592]), illustrating the differences in octahedral distortions and A-site cation disorder between the two structures.

Two other related structures were obtained from the literature search. These resulted from combinations of Rb^+, I^- and 1-methyl dabconium, with CSD refcodes: HEJGOV[592] and HEJGOV01[592]. Both of these form the 3D perovskite structure. HEJGOV is a room temperature structure (determined at 293 K) which crystallises in the cubic phase (space group *P*432), and HEJGOV01 is a lower-temperature structure (determined at 273 K) in the trigonal phase with space group *R*3. HEJGOV is isostructural with IPERON01 and HEJGOV01 with IPERON. Again here, the cubic phase has less distorted octahedra, however, more disordered A-site cations than the trigonal phase. Moreover, no indication of the phase transition temperature was provided.

Piperazinium-Containing Perovskites

As for the combination of dabconium or 1-methyl dabconium cations with monovalent alkali metal ions and halide anions, a search of the Cambridge Structural Database (CSD (2021, Version 5.42, update May 2021)[586]) was carried out to find structures combining singly and doubly protonated piperazine and alkali metal ions.

Seven 3D perovskite structures have been reported for the combination of a piperazinium cation with a monovalent alkali metal ion and halide ion. The combination with NaI results in two monoclinic phases, both recorded at room temperature, with CSD refcodes: MEXMAG[595] (space group $C2/c$, structure determined at 293 K) and MEXNIP[595] (space group $P2_1/c$, structure determined at 293 K), with the latter structure crystallising with isolated iodide ions and water molecules as part of the structure. The MEXMAG[595] structure is of the 3D perovskite-type, while the structure MEXNIP[595] is of the ⟨100⟩-type 1D perovskite-type consisting of corner-sharing octahedra shown in Figure 2.42 (a) and (b). The MEXMAG structure was obtained from a 1:1 molar ratio of piperazine (1,4-diazacyclohexane) and NaI in water, while the MEXNIP structure formed from the reaction of a 3:1 molar ratio of piperazine and NaI in water. It is interesting to note that the MEXMAG 3D perovskite structure does not contain solvent water molecules. In contrast, other structures in this family do, as discussed below, even though all were crystallised from an aqueous solution.

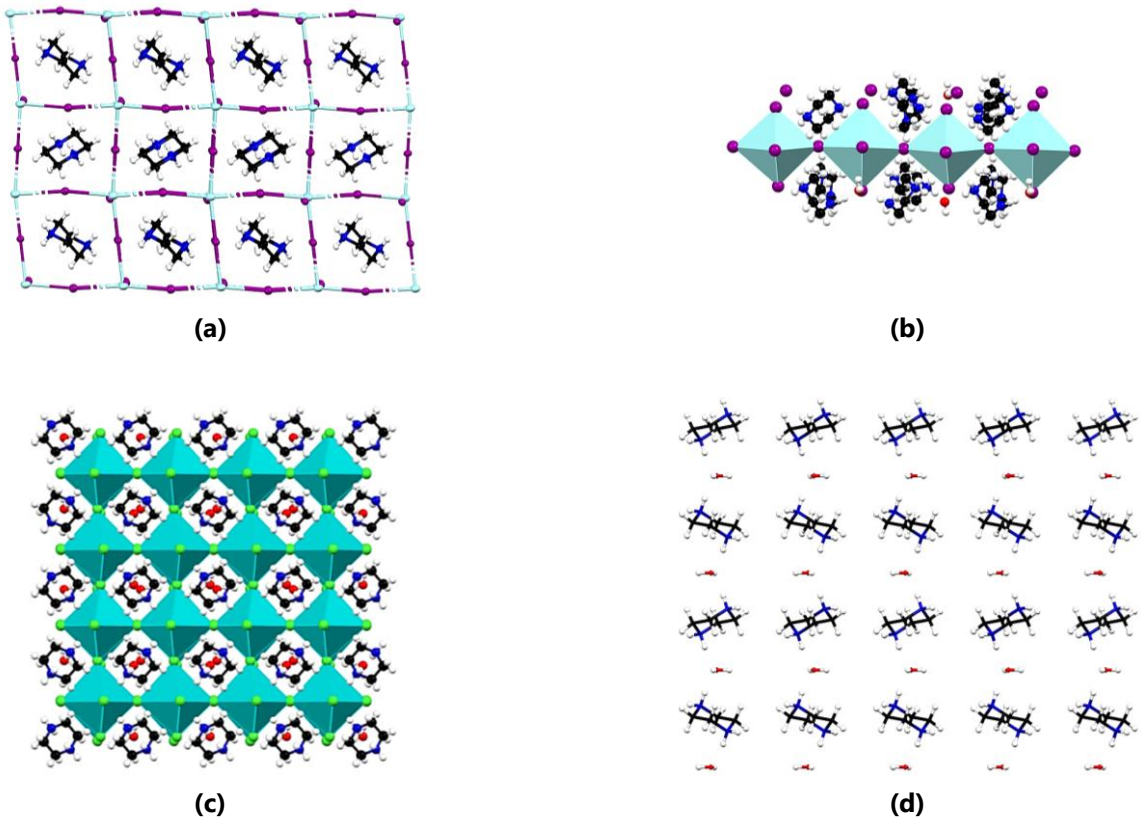

Figure 2.42 The structures of **(a)** MEXMAG,[595] **(b)** MEXNIP[595] and **(c)** GUYMIX[590]. **(d)** The packing of piperazinium cations and water molecules in the structure GUYMIX[590]. The structure of GUYMIX is also representative of the isostructural structures MOMLEI,[596] GUYMOD,[590] MOMSEP[596] and GUYMUJ[590].

Combinations of piperazinium with KCl (refcode: GUYMIX[590], structure determined at 120 K), KBr (refcode: MOMLEI[596] structure determined at 120 K), RbCl (refcode: GUYMOD[590] structure determined at 120K), RbBr (refcode: MOMSEP[596] structure determined at 120 K) and CsCl (refcode: GUYMUJ[590] structure determined at 120 K) all resulted in isostructural orthorhombic 3D perovskite structures (all crystallising in space group *Pbcm*) containing solvent water molecules, with the structure of GUYMIX illustrated in Figure 2.42 (c).

The crystals of MEXMAG,[595] which does not contain water molecules, and the crystals of the structures isostructural to GUYMIX,[590] which contain solvent water molecules, were all obtained from an aqueous solution. The difference between the anhydrous and hydrated structures is illustrated in Figure 2.42. It can be seen that the inorganic framework of the anhydrous MEXMAG structure (Figure 2.42 (a)) is more distorted than that of the water-containing structures (Figure 2.42 (c)). Moreover, each piperazinium cation in the structure GUYMIX crystallises alongside two water molecules as shown in Figure 2.42 (d).

Additionally, two isostructural 2D organic-inorganic hybrid structures, both crystallising in an orthorhombic phase (space group *Pbcm*), were reported for the combination of a singly protonated piperazinium cation with RbBr and CsBr, with refcodes VONDEK[597] and VONDAG[597] (both determined at 93 K) respectively. The two structures do not fall into any of the perovskite structure categories. This means that the combination of RbBr-based anions and piperazine-based cations can result in two different structure types with two different dimensionalities, at approximately the same temperature, since the 3D perovskite structure was determined at 120 K. However, the structures differ with regards to the protonation of the piperazinium cation, since it is only singly protonated in the 2D phase, but doubly protonated in the 3D cubic perovskite phase.

Table 2.25 summarises the piperazinium-containing structures obtained from the literature search with the CSD[586] reference codes indicated. Several structures in this matrix remain to be determined, for example, the structures comprised of the combination of piperazinium cations and LiCl, LiBr, LiI, NaCl, NaBr, KI, RbI and CsI are still outstanding, as can be seen from Table 2.25.

Table 2.25 A summary of the structures reported in the literature for the combination of piperazinium cations and anions comprising monovalent alkali metal ions and halide anions. The dimensionality of the structure, the temperature at which it was determined, the lattice type, the structure type and the space group are also included.

Metal Cation	**Halide Anion**		
	Cl^-	Br^-	I^-
Li^+	N/A	N/A	N/A
Na^+	N/A	N/A	**MEXMAG**[595] (293 K, 3D perovskite, monoclinic, *C*2/*c*) **MEXNIP**[595] (293 K, ⟨100⟩-type 1D perovskite, monoclinic, $P2_1/c$)
K^+	**GUYMIX**[590] (120 K, 3D perovskite, orthorhombic, *Pbcm*)	**MOMLEI**[596] (120 K, 3D perovskite, orthorhombic, *Pbcm*)	N/A
Rb^+	**GUYMOD**[590] (120 K, 3D perovskite, orthorhombic, *Pbcm*)	**MOMSEP**[596] (120 K, 3D perovskite, orthorhombic, *Pbcm*) **VONDEK**[597] (93 K, 2D organic-inorganic hybrid, orthorhombic, *Pbcm*)	N/A
Cs^+	**GUYMUJ**[590] (120 K, 3D perovskite, orthorhombic, *Pbcm*)	**VONDAG**[597] (93 K, 2D organic-inorganic hybrid, orthorhombic, *Pbcm*)	N/A

1-Methyl Piperazinium-Containing Perovskites

Three 3D perovskite structures that contain the methyl piperazinium cation with alkali metal halides (KBr, RbBr and CsBr) were reported previously. All three structures were determined at 93 K and crystallised in the orthorhombic phase with space

group *Amm*2, therefore they are isostructural. Their CSD refcodes and the metal halides they contain are as follows: VONCEJ[598] (KBr), VONCIN[598] (RbBr) and VONCOT[598] (CsBr).

Figure 2.43 (a), (b) and (c) show the structures of VONCEJ, VONCIN and VONCOT, respectively.[598] There are several similarities between these three structures and that of the piperazinium-containing structures (GUYMIX,[590] MOMLEI,[596] GUYMOD,[590] MOMSEP[596] and GUYMUJ[590]).

Like the piperazinium-containing structures, the structures containing methyl piperazinium cations also contain water molecules in the structure, and their cations also exhibit two different orientations in the structure. However, where the piperazinium-containing structures have two water molecules per two cations, the methyl piperazinium-containing structures only have one water molecule per two cations, as can be seen from the comparison of Figure 2.42 (d) and Figure 2.43(d). The fact that the piperazinium- and methyl piperazinium-containing structures tend to contain water molecules is likely due to the shape of the methyl piperazinium and piperazinium cations. Since both these molecules are relatively planar in their geometry, the association of water molecules (one per cation in the case of piperazinium and "half" per cation in the case of methyl piperazinium) effectively increases the "size" of the overall "species" contained in the inorganic framework cavity and assists in "filling the gaps" to allow for the 3D perovskite geometry, so to speak. In the case of the methylammonium-containing structures, effectively only half a water molecule per cation is required, since the methyl group occupies space on the other surface of the "planar" part of the molecule.

The methyl piperazinium-containing structures have more distorted octahedra in one crystallographic direction compared to the piperazinium-containing structures. Hence, since the piperazinium-containing structures have less distorted octahedra, their bond overlap is expected to be better and from the arguments presented earlier, they should have narrower band gaps that their methylated cousins.

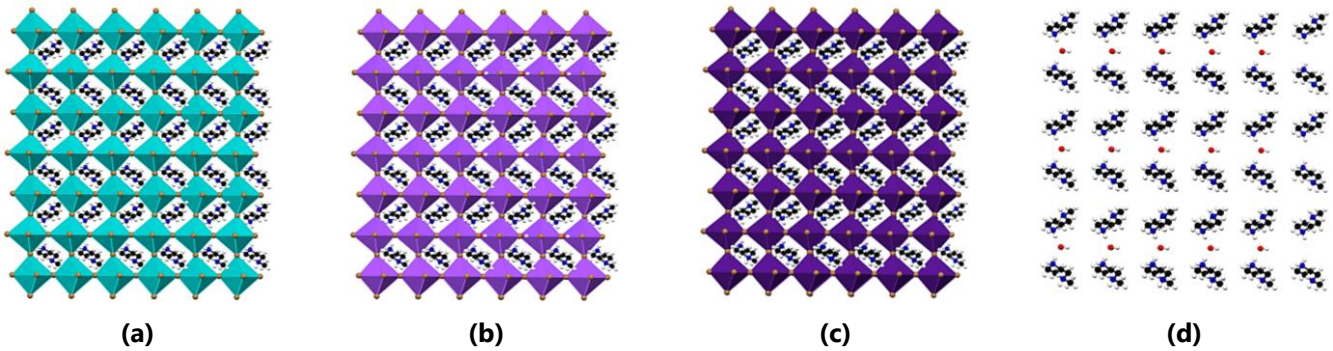

Figure 2.43 The 3×3 expansion of the structures of **(a)** VONCEJ,[598] **(b)** VONCIN,[598] and **(c)** VONCOT,[598] illustrating their structural features, such as their isostructurality and the incorporation of water in the crystal structure. **(d)** The packing of the methyl piperazinium cations and water molecules in the structure VONCEJ, which is representative of VONCIN and VONCOT.

3-Aminopyrrolidinium-Containing Perovskites

During the CSD search, one structure type (two different phases) containing the 3-aminopyrrolidinium cation (see Figure 2.44 (a)) was also found. The two structures, with CSD refcodes GEFLOV[599] and GEFLOV01,[599] are 3D perovskites consisting of $RbBr_6$ octahedra and 3-aminopyrrolidinium cations, as shown in Figure 2.44 (b) and (c).

The room temperature (293 K) structure (GEFLOV) crystallises in the monoclinic phase with space group *Ia*, and undergoes a solid-state phase transition around 440 K, which leads to the high-temperature cubic phase (GEFLOV01, space group $Pm\bar{3}m$), determined at 453 K.[599] The authors suggested that this phase transition is reversible and leads to desirable ferroelectric properties in the high temperature phase.[599]

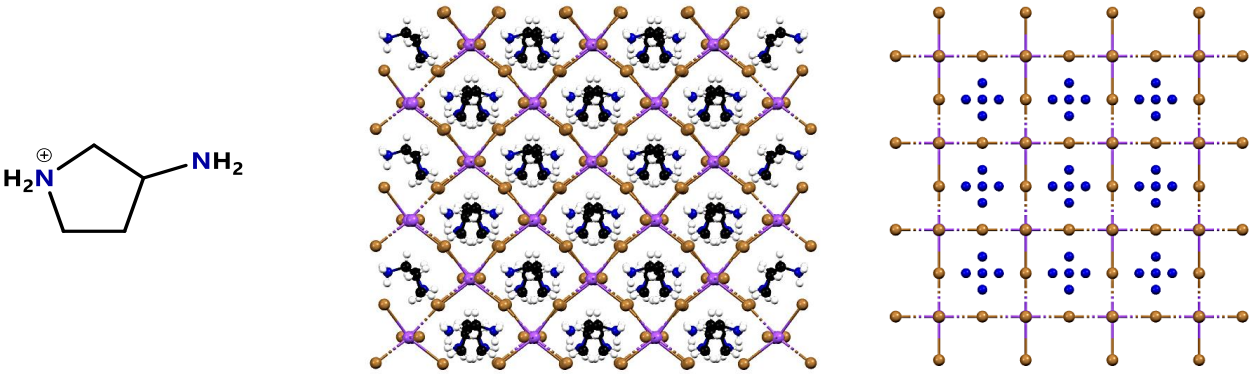

Figure 2.44 (a) The line structure of the 3-aminopyrrolidinium cation. **(b)** The 3×3 expansion of structure GEFLOV[599] and **(c)** the 3×3 expansion of structure GEFLOV01,[599] with both (b) and (c) viewed down the *a*-axis.

This concludes the structural literature review. In the following section, the aspects of this study and how it will aim to fill the gap in the literature identified in the preceding paragraphs, are discussed.

2.5.3 Aspects of This Study

It is clear from the matrix of structures reported in the literature, as listed in Table 2.24 and Table 2.25 that there is a tendency of compounds comprised of either dabconium cations or piperazinium cations and alkali metal ions and halide ions to form 3D hybrid perovskite structures. However, it can also be seen from the tables that a lot of scope still exists for the study of the structural characteristics of these compounds since several permutations have not been investigated structurally, and these may potentially also form 3D cubic perovskite structures.

As indicated in the previous sections of this chapter, the 3D cubic perovskite structure is the sought-after structure for sensitiser materials to be used in PSCs. However, the band gaps of these materials or the potential application of 3D perovskites comprising dabconium or piperazinium cations and alkali metal halides have not been reported or studied previously.

It should be noted that all of the structures reported in the literature, as listed in Table 2.24 and Table 2.25, were determined from crystals that were obtained from water as solvent. This means that these compounds can be prepared without the need for harmful solvents using a green method of synthesis. This, in addition to their non-toxic metal ions, add to their appeal as potential solar cell sensitisers. This apparent gap in the literature will be addressed in the current study, as explained below.

General Aspects

This study will now join the search for lead-free alternative perovskites that match the efficiencies of their lead counterparts in PSCs. The focus of this study is on the use of *alkali metals* in hybrid halide perovskite structures, with the perovskite material containing the organic constituents 1,4-diazabicyclo[2.2.2]octane-1,4-diium (hereafter referred to as dabconium or the dabconium dication) or piperazine-1,4-diium (hereafter referred to as piperazinium or the piperazinium dication) (see Figure 2.45 (a) and (b) respectively) as cationic species. Hence the perovskite sensitiser material contains A^{2+} and B^{+} ions instead of the traditional combination of A^{+} and B^{2+}. The halide species under investigation include Cl^{-}, Br^{-} or I^{-}. Therefore, this study will aim to lower the potentially harmful effects of PSCs on both the environment and human health by replacing toxic lead ions with alkali metal ions.

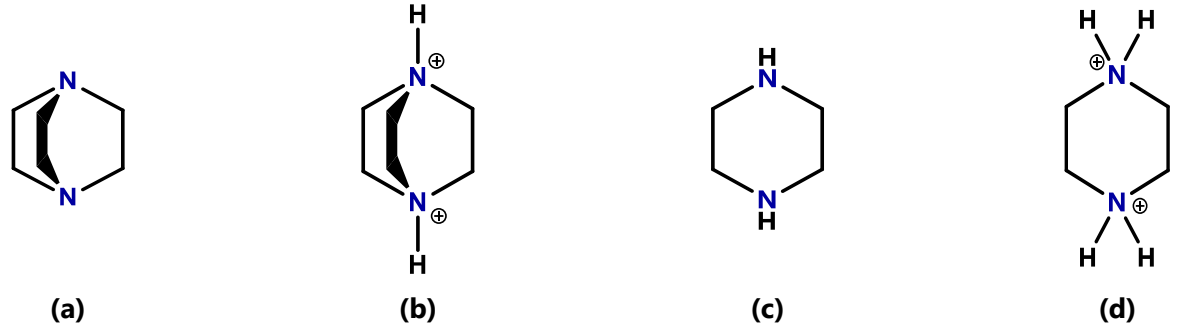

Figure 2.45 The line structures of the unprotonated organic species, and the organic dications used in this study. **(a)** 1,4-diazabicyclo[2.2.2]octane and **(b)** the dabconium dication (1,4-diazabicyclo[2.2.2]octane-1,4-diium). **(c)** 1,4-diazacyclohexane (piperazine) and **(d)** the piperazinium dication (piperazine-1,4-diium).

The piperazinium and dabconium cations contain two nitrogen atoms on the opposite side of the cation, linked by either two or three ethyl linkers. The nitrogen atoms both carry a positive charge of one each, giving the cation an overall charge of +2. However, the cations differ in terms of their hydrogen bonding capability. In the dabconium cation, each nitrogen atom is bonded to one hydrogen atom, acting as a hydrogen bond donor. In contrast, in the piperazinium cation, each nitrogen atom is bonded to two hydrogen atoms, increasing the number of hydrogen bond donors relative to the dabconium cation. Another essential difference between the two cations relevant in the structural context is their approximate shape. The dabconium cation displays a roughly spherical shape, whereas the piperazinium cation typically adopts a chair conformation, giving it an almost planar (disc-like) shape.

Piperazinium may be used medicinally as *anthelmintic drugs*, meaning that it is used to treat cases of parasitic worms, and hence is quite safe for human consumption.[600] Similarly, dabconium is widely used in the chemical industry (as a catalyst, in dyes or for oxygen quenching) and does not pose any hazards or toxicity to the environment, making the use of both dabconium or piperazinium in this study environmentally friendly.[601]

In the current study, the alkali metal ions that will be studied include Na^+, K^+ and Cs^+. Due to the prohibitive costs of most of the halide salts of Rb^+ and Li^+, these alkali metal ions were not included in the study, since their subsequent applications would not be economically viable, and investigating only isolated cases cannot be rationalised.

Importantly, again, none of the alkali metal halides (NaCl, NaBr, NaI, KCl, KBr, KI, CsCl, CsBr or CsI) are environmentally hazardous or pose any threat to human health. In fact, most of these salts are commonly used in everyday life for seasoning, dietary supplements and in pharmaceuticals.[602] This information combined with the safe-nature of the organic cations, makes the proposed study environmentally safe. Furthermore, since all the proposed constituents are water soluble, water may be used as the primary solvent in the study and hence the use of *green solvents* further contribute to the low environmental impact of the study. Moreover, the resultant implications are safe, green materials for optoelectronic use.

The study will focus firstly on the synthesis and crystallisation of materials combining the dabconium or piperazinium cation, an alkali metal ion, and a halide ion according to the reaction $A + BX + 2HX \rightarrow ABX_3$, where A indicates the unprotonated organic component, BX the alkali metal halide salt and HX an acid. Crystal engineering aspects will also be considered.

Secondly, the focus will be on investigating the structural aspects of the alkali metal ion-containing compounds to identify structural trends and classify the structures. Following, the effect of the composition of the material, thus the role of the specific cation, metal ion and halide anion, and their sizes on the structures formed, will be highlighted. Thirdly, the band gaps of the materials will be determined experimentally to identify structure–band gap relationships and subsequently these absorption properties will be used to study the solid-state fluorescence emission spectra of the materials.

Aims

The study's broad aim is to generate knowledge on organic-inorganic hybrid compounds comprised of dabconium or piperazinium dications, alkali metal ions, and halide ions. Specific focus is placed on investigating the structural aspects of these compounds and identifying structural trends.

In addition, the second area of focus is the investigation of the optical properties of the materials, specifically their band gaps, and fluorescence properties, with the aim of the identification of structure-optical property relationships.

Objectives

The objectives of this study include:

- The successful synthesis of the hybrid materials of interest, and obtaining good quality single crystals of each of the compounds;
- The structural characterisation of the synthesised materials by X-ray diffraction techniques;
- Structural analysis, categorisation, and the identification of structural trends;
- Determination of the band gaps of the prepared materials;
- Measurement of the solid-state fluorescence spectra of the prepared materials;
- Identification of structure-property relationships;
- Construction of perovskite solar cells (PSCs) employing hybrid materials of various structure types as different layers of these optoelectronic devices.

This concludes the literature survey chapter. The literature survey has shown the viability of applying hybrid halide perovskite materials to PSCs and the potential of alkali metals to be used as constituents of these materials. The focus will now be shifted towards the experimental procedures used and the results obtained in this study.

2.6 References for Chapter 2

1. Weber, D. *Zeitschrift für Naturforschung B* **1978**, *33* (12), 1443–1445. https://doi.org/https://doi.org/10.1515/znb-1978-1214.
2. Luan, M.; Song, J.; Wei, X.; Chen, F.; Liu, J. *CrystEngComm* **2016**, *18* (28), 5257–5261. https://doi.org/10.1039/C6CE00375C.
3. Baikie, T.; Fang, Y.; Kadro, J. M.; Schreyer, M.; Wei, F.; Mhaisalkar, S. G.; Graetzel, M.; White, T. J. *Journal of Materials Chemistry A* **2013**, *1* (18), 5628–5641. https://doi.org/10.1039/c3ta10518k.
4. Choi, J. J.; Yang, X.; Norman, Z. M.; Billinge, S. J. L.; Owen, J. S. *Nano Letters* **2014**, *14* (1), 127–133. https://doi.org/10.1021/nl403514x.
5. Chen, Q.; De Marco, N.; Yang, Y.; Song, T. Bin; Chen, C. C.; Zhao, H.; Hong, Z.; Zhou, H.; Yang, Y. *Nano Today* **2015**, *10* (3), 355–396. https://doi.org/10.1016/j.nantod.2015.04.009.
6. Ava, T. T.; Al Mamun, A.; Marsillac, S.; Namkoong, G. *Applied Sciences (Switzerland)* **2019**, *9* (1), 188. https://doi.org/10.3390/app9010188.
7. Zhang, Y.; Huang, F.; Mi, Q. *Chemistry Letters* **2016**, *45* (8), 1030–1032. https://doi.org/10.1246/cl.160419.
8. Zhang, L.; Liu, Y.; Ye, X.; Han, Q.; Ge, C.; Cui, S.; Guo, Q.; Zheng, X.; Zhai, Z.; Tao, X. *Crystal Growth and Design* **2018**, *18* (11), 6652–6660. https://doi.org/10.1021/acs.cgd.8b00896.
9. Onoda-Yamamuro, N.; Matsuo, T.; Suga, H. *Journal of Physics and Chemistry of Solids* **1992**, *53* (7), 935–939. https://doi.org/10.1016/0022-3697(92)90121-S.
10. Poglitsch, A.; Weber, D. *The Journal of Chemical Physics* **1987**, *87* (11), 6373–6378. https://doi.org/10.1063/1.453467.
11. Szafrański, M.; Katrusiak, A. *The Journal of Physical Chemistry Letters* **2016**, *7* (17), 3458–3466. https://doi.org/10.1021/acs.jpclett.6b01648.
12. Whitfield, P. S.; Herron, N.; Guise, W. E.; Page, K.; Cheng, Y. Q.; Milas, I.; Crawford, M. K. *Scientific Reports* **2016**, *6* (1), 35685. https://doi.org/10.1038/srep35685.
13. Ding, J.; Jing, L.; Cheng, X.; Zhao, Y.; Du, S.; Zhan, X.; Cui, H. *Journal of Physical Chemistry Letters* **2018**, *9* (1), 216–221. https://doi.org/10.1021/acs.jpclett.7b03020.
14. Knop, O.; Wasylishen, R. E.; White, M. A.; Cameron, T. S.; Oort, M. J. M. Van. *Canadian Journal of Chemistry* **1990**, *68* (3), 412–422. https://doi.org/10.1139/v90-063.
15. Leijtens, T.; Giovenzana, T.; Habisreutinger, S. N.; Tinkham, J. S.; Noel, N. K.; Kamino, B. A.; Sadoughi, G.; Sellinger, A.; Snaith, H. J. *ACS Applied Materials and Interfaces* **2016**, *8* (9), 5981–5989. https://doi.org/10.1021/acsami.5b10093.
16. Leijtens, T.; Eperon, G. E.; Noel, N. K.; Habisreutinger, S. N.; Petrozza, A.; Snaith, H. J. *Advanced Energy Materials* **2015**, *5* (20), 1–23. https://doi.org/10.1002/aenm.201500963.
17. Chen, K.; Deng, X.; Goddard, R.; Tüysüz, H. *Chemistry of Materials* **2016**, *28* (15), 5530–5537. https://doi.org/10.1021/acs.chemmater.6b02233.
18. Chen, L.; Tan, Y. Y.; Chen, Z. X.; Wang, T.; Hu, S.; Nan, Z. A.; Xie, L. Q.; Hui, Y.; Huang, J. X.; Zhan, C.; Wang, S. H.; Zhou, J. Z.; Yan, J. W.; Mao, B. W.; Tian, Z. Q. *Journal of the American Chemical Society* **2019**, *141* (4), 1665–1671. https://doi.org/10.1021/jacs.8b11610.
19. Jaffe, A.; Lin, Y.; Beavers, C. M.; Voss, J.; Mao, W. L.; Karunadasa, H. I. *ACS Central Science* **2016**, *2* (4), 201–209. https://doi.org/10.1021/acscentsci.6b00055.
20. López, C. A.; Martínez-Huerta, M. V.; Alvarez-Galván, M. C.; Kayser, P.; Gant, P.; Castellanos-Gomez, A.; Fernández-Díaz, M. T.; Fauth, F.; Alonso, J. A. *Inorganic Chemistry* **2017**, *56* (22), 14214–14219. https://doi.org/10.1021/acs.inorgchem.7b02344.
21. Xiao, Z.; Song, Z.; Yan, Y. *Advanced Materials* **2019**, *31* (47), 1–22. https://doi.org/10.1002/adma.201803792.
22. Xiao, Z.; Meng, W.; Wang, J.; Mitzi, D. B.; Yan, Y. *Materials Horizons* **2017**, *4* (2), 206–216. https://doi.org/10.1039/c6mh00519e.
23. Maggiora, J.; Li, F.; Zheng, R. *Physica Status Solidi - Rapid Research Letters* **2021**, *15* (1), 1–22. https://doi.org/10.1002/pssr.202000410.
24. Noh, J. H.; Im, S. H.; Heo, J. H.; Mandal, T. N.; Seok, S. Il. *Nano Letters* **2013**, *13* (4), 1764–1769. https://doi.org/10.1021/nl400349b.
25. Bi, C.; Yuan, Y.; Fang, Y.; Huang, J. *Advanced Energy Materials* **2015**, *5* (6), 1614–6832. https://doi.org/10.1002/aenm.201401616.
26. Cui, D.; Yang, Z.; Yang, D.; Ren, X.; Liu, Y.; Wei, Q.; Fan, H.; Zeng, J.; Liu, S. *Journal of Physical Chemistry C* **2016**, *120* (1), 42–47. https://doi.org/10.1021/acs.jpcc.5b09393.
27. Sutter-Fella, C. M.; Li, Y.; Amani, M.; Ager, J. W.; Toma, F. M.; Yablonovitch, E.; Sharp, I. D.; Javey, A. *Nano Letters* **2016**, *16* (1), 800–806. https://doi.org/10.1021/acs.nanolett.5b04884.
28. Kim, T. G.; Seo, S. W.; Kwon, H.; Hahn, J.; Kim, J. W. *Physical Chemistry Chemical Physics* **2015**, *17* (37), 24342–24348. https://doi.org/10.1039/c5cp04207k.
29. Zhou, Y.; Yang, M.; Game, O. S.; Wu, W.; Kwun, J.; Strauss, M. A.; Yan, Y.; Huang, J.; Zhu, K.; Padture, N. P. *ACS Applied Materials and Interfaces* **2016**, *8* (3), 2232–2237. https://doi.org/10.1021/acsami.5b10987.
30. Zarick, H. F.; Soetan, N.; Erwin, W. R.; Bardhan, R. *Journal of Materials Chemistry A* **2018**, *6* (14), 5507–5537. https://doi.org/10.1039/c7ta09122b.
31. Yoon, S. J.; Stamplecoskie, K. G.; Kamat, P. V. *Journal of Physical Chemistry Letters* **2016**, *7* (7), 1368–1373. https://doi.org/10.1021/acs.jpclett.6b00433.
32. Manser, J. S.; Saidaminov, M. I.; Christians, J. A.; Bakr, O. M.; Kamat, P. V. *Accounts of Chemical Research* **2016**, *49* (2), 330–338. https://doi.org/10.1021/acs.accounts.5b00455.
33. Fedeli, P.; Gazza, F.; Calestani, D.; Ferro, P.; Besagni, T.; Zappettini, A.; Calestani, G.; Marchi, E.; Ceroni, P.; Mosca, R. *Journal of Physical Chemistry C* **2015**, *119* (37), 21304–21313. https://doi.org/10.1021/acs.jpcc.5b03923.
34. Kim, G. Y.; Oh, S. H.; Nguyen, B. P.; Jo, W.; Kim, B. J.; Lee, D. G.; Jung, H. S. *Journal of Physical Chemistry Letters* **2015**, *6* (12), 2355–2362. https://doi.org/10.1021/acs.jpclett.5b00967.
35. He, J.; Tao, C. *Journal of Materials Chemistry A* **2015**, *36* (3), 18514–18520. https://doi.org/https://doi.org/10.1039/C5TA05373K.
36. Atourki, L.; Vega, E.; Marí, B.; Mollar, M.; Ait Ahsaine, H.; Bouabid, K.; Ihlal, A. *Applied Surface Science* **2016**, *371* (May), 112–117. https://doi.org/10.1016/j.apsusc.2016.02.207.

37. Yonghua, C.; Tao, C.; Liming, D. *Advanced Materials* **2015**, *27* (6), 1053–1059. https://doi.org/https://doi.org/10.1002/adma.201404147.

38. Liang, P. W.; Chueh, C. C.; Xin, X. K.; Zuo, F.; Williams, S. T.; Liao, C. Y.; Jen, A. K. Y. *Advanced Energy Materials* **2015**, *5* (1), 1400960. https://doi.org/10.1002/aenm.201400960.

39. Pool, V. L.; Gold-Parker, A.; McGehee, M. D.; Toney, M. F. *Chemistry of Materials* **2015**, *27* (21), 7240–7243. https://doi.org/10.1021/acs.chemmater.5b03581.

40. Ralaiarisoa, M.; Busby, Y.; Frisch, J.; Salzmann, I.; Pireaux, J.-J.; Koch, N. *Physical Chemistry Chemical Physics* **2017**, *19* (1), 828–836. https://doi.org/https://doi.org/10.1039/C6CP06347K.

41. Liu, M.; Johnston, M. B.; Snaith, H. J. *Nature* **2013**, *501* (7467), 395–398. https://doi.org/10.1038/nature12509.

42. Kim, J. H.; Williams, S. T.; Cho, N.; Chueh, C. C.; Jen, A. K. Y. *Advanced Energy Materials* **2015**, *5* (4), 1401229. https://doi.org/10.1002/aenm.201401229.

43. Back, H.; Kim, J.; Kim, G.; Kyun Kim, T.; Kang, H.; Kong, J.; Ho Lee, S.; Lee, K. *Solar Energy Materials and Solar Cells* **2016**, *144* (January), 309–315. https://doi.org/10.1016/j.solmat.2015.09.018.

44. Habibi, M.; Rahimzadeh, A.; Bennouna, I.; Eslamian, M. *Coatings* **2017**, *7* (3), 42. https://doi.org/10.3390/coatings7030042.

45. Barrows, A. T.; Pearson, A. J.; Kwak, C. K.; Dunbar, A. D. F.; Buckley, A. R.; Lidzey, D. G. *Energy and Environmental Science* **2014**, *7* (9), 2944–2950. https://doi.org/10.1039/c4ee01546k.

46. Jang, D. M.; Park, K.; Kim, D. H.; Park, J.; Shojaei, F.; Kang, H. S.; Ahn, J. P.; Lee, J. W.; Song, J. K. *Nano Letters* **2015**, *15* (8), 5191–5199. https://doi.org/10.1021/acs.nanolett.5b01430.

47. Suzuki, A.; Okada, H.; Oku, T. *Energies* **2016**, *9* (5), 376. https://doi.org/10.3390/en9050376.

48. Suarez, B.; Gonzalez-Pedro, V.; Ripolles, T. S.; Sanchez, R. S.; Otero, L.; Mora-Sero, I. *J. Phys. Chem. Lett.* **2014**, *5* (10), 1628–1635. https://doi.org/10.1021/jz5006797.

49. Goldschmidt, V. M. *Naturwissenschaften* **1926**, *14* (May), 477–485. https://doi.org/10.1007/BF01507527.

50. Chonghea Li, X. L.; Weizhong Ding, L. F.; Yonghui Gao, Z. G. *Acta Crystallographica Section B* **2008**, *64* (6), 702–707. https://doi.org/10.1107/S0108768108032734.

51. Bartel, C. J.; Sutton, C.; Goldsmith, B. R.; Ouyang, R.; Musgrave, C. B.; Ghiringhelli, L. M.; Scheffler, M. *Science Advances* **2018**, *2* (5), 1–10. https://doi.org/DOI: 10.1126/sciadv.aav0693.

52. Shannon, R. D. *Acta Crystallographica Section A* **1976**, *32* (1), 751–767. https://doi.org/10.1023/A:1018927109487.

53. Becker, M.; Klüner, T.; Wark, M. *Dalton Transactions* **2017**, *46* (11), 3500–3509. https://doi.org/10.1039/c6dt04796c.

54. Stoumpos, C. C.; Malliakas, C. D.; Kanatzidis, M. G. *Inorganic Chemistry* **2013**, *52* (15), 9019–9038. https://doi.org/10.1021/ic401215x.

55. Wang, H.; Wu, H.; Xian, Y.; Niu, G.; Yuan, W.; Li, H.; Yin, H.; Liu, P.; Long, Y.; Li, W.; Fan, J. *ACS Applied Materials and Interfaces* **2019**, *11* (14), 13812–13821. https://doi.org/10.1021/acsami.9b02840.

56. Huang, Y.; Li, L.; Liu, Z.; Jiao, H.; He, Y.; Wang, X.; Zhu, R.; Wang, D.; Sun, J.; Chen, Q.; Zhou, H. *Journal of Materials Chemistry A* **2017**, *5* (18), 8537–8544. https://doi.org/10.1039/c7ta01441d.

57. Elbaz, G. A.; Straus, D. B.; Semonin, O. E.; Hull, T. D.; Paley, D. W.; Kim, P.; Owen, J. S.; Kagan, C. R.; Roy, X. *Nano Letters* **2017**, *17* (3), 1727–1732. https://doi.org/10.1021/acs.nanolett.6b05022.

58. Schueller, E. C.; Laurita, G.; Fabini, D. H.; Stoumpos, C. C.; Kanatzidis, M. G.; Seshadri, R. *Inorganic Chemistry* **2018**, *57* (2), 695–701. https://doi.org/10.1021/acs.inorgchem.7b02576.

59. Govinda, S.; Kore, B. P.; Swain, D.; Hossain, A.; De, C.; Guru Row, T. N.; Sarma, D. D. *Journal of Physical Chemistry C* **2018**, *122* (25), 13758–13766. https://doi.org/10.1021/acs.jpcc.8b00602.

60. Lee, J. W.; Seol, D. J.; Cho, A. N.; Park, N. G. *Advanced Materials* **2014**, *26* (29), 4991–4998. https://doi.org/10.1002/adma.201401137.

61. Li, Y.; Liu, F. Z.; Waqas, M.; Leung, T. L.; Tam, H. W.; Lan, X. Q.; Tu, B.; Chen, W.; Djurišić, A. B.; He, Z. B. *Small Methods* **2018**, *2* (7), 1700387. https://doi.org/10.1002/smtd.201700387.

62. Weller, M. T.; Weber, O. J.; Frost, J. M.; Walsh, A. *Journal of Physical Chemistry Letters* **2015**, *6* (16), 3209–3212. https://doi.org/10.1021/acs.jpclett.5b01432.

63. Juarez-Perez, E. J.; Hawash, Z.; Raga, S. R.; Ono, L. K.; Qi, Y. *Energy and Environmental Science* **2016**, *9* (11), 3406–3410. https://doi.org/10.1039/c6ee02016j.

64. Schileo, G.; Grancini, G. *Journal of Materials Chemistry C* **2021**, *9* (1), 67–76. https://doi.org/10.1039/d0tc04552g.

65. Eperon, G. E.; Stranks, S. D.; Menelaou, C.; Johnston, M. B.; Herz, L. M.; Snaith, H. J. *Energy and Environmental Science* **2014**, *7* (3), 982–988. https://doi.org/10.1039/c3ee43822h.

66. Leyden, M. R.; Lee, M. V.; Raga, S. R.; Qi, Y. *Journal of Materials Chemistry A* **2015**, *3* (31), 16097–16103. https://doi.org/10.1039/c5ta03577e.

67. Liu, F.; Dong, Q.; Wong, M. K.; Djurišić, A. B.; Ng, A.; Ren, Z.; Shen, Q.; Surya, C.; Chan, W. K.; Wang, J.; Ng, A. M. C.; Liao, C.; Li, H.; Shih, K.; Wei, C.; Su, H.; Dai, J. *Advanced Energy Materials* **2016**, *6* (7), 1–9. https://doi.org/10.1002/aenm.201502206.

68. Leguy, A. M. A.; Hu, Y.; Campoy-Quiles, M.; Alonso, M. I.; Weber, O. J.; Azarhoosh, P.; van Schilfgaarde, M.; Weller, M. T.; Bein, T.; Nelson, J.; Docampo, P.; Barnes, P. R. F. *Chemistry of Materials* **2015**, *27* (9), 3397–3407. https://doi.org/10.1021/acs.chemmater.5b00660.

69. Aristidou, N.; Sanchez-Molina, I.; Chotchuangchutchaval, T.; Brown, M.; Martinez, L.; Rath, T.; Haque, S. A. *Angewandte Chemie International Edition* **2015**, *54* (28), 8208–8212. https://doi.org/https://doi.org/10.1002/anie.201503153.

70. Foley, B. J.; Marlowe, D. L.; Sun, K.; Saidi, W. A.; Scudiero, L.; Gupta, M. C.; Choi, J. J. *Materials Engineering and Sciences Division 2015 - Core Programming Area at the 2015 AIChE Annual Meeting* **2015**, *106* (24), 581–586. https://doi.org/10.1063/1.4922804.

71. Mamun, A. Al; Ava, T. T.; Byun, H. R.; Jeong, H. J.; Jeong, M. S.; Nguyen, L.; Gausin, C.; Namkoong, G. *Physical Chemistry Chemical Physics* **2017**, *19* (29), 19487–19495. https://doi.org/10.1039/c7cp03106h.

72. Fakharuddin, A.; Jose, R.; Brown, T. M.; Fabregat-Santiago, F.; Bisquert, J. *Energy and Environmental Science* **2014**, *7* (12), 3952–3981. https://doi.org/10.1039/c4ee01724b.

73. Ng, C. H.; Lim, H. N.; Hayase, S.; Zainal, Z.; Huang, N. M. *Renewable and Sustainable Energy Reviews* **2018**, *90* (April), 248–274. https://doi.org/10.1016/j.rser.2018.03.030.

74. Meillaud, F.; Boccard, M.; Bugnon, G.; Despeisse, M.; Hänni, S.; Haug, F. J.; Persoz, J.; Schüttauf, J. W.; Stuckelberger, M.; Ballif, C. *Materials Today* **2015**, *18* (7), 378–384. https://doi.org/10.1016/j.mattod.2015.03.002.

75. National Renewable Energy Laboratory: Best Research-Cell Efficiency Chart https://www.nrel.gov/pv/cell-efficiency.html (accessed Feb 20, 2021).

76. Kim, B. J.; Kim, D. H.; Kwon, S. L.; Park, S. Y.; Li, Z.; Zhu, K.; Jung, H. S. *Nature Communications* **2016**, *7* (1), 1–9. https://doi.org/10.1038/ncomms11735.

77. Zuser, A.; Rechberger, H. *Resources, Conservation and Recycling* **2011**, *56* (1), 56–65. https://doi.org/10.1016/j.resconrec.2011.09.004.

78. Jena, A. K.; Kulkarni, A.; Miyasaka, T. *Chemical Reviews* **2019**, *119* (5), 3036–3103. https://doi.org/10.1021/acs.chemrev.8b00539.

79. Lee, M. M.; Teuscher, J.; Miyasaka, T.; Murakami, T. N.; Snaith, H. J. *Science* **2012**, *338* (6107), 643–647. https://doi.org/10.1126/science.1228604.

80. Wojciechowski, K.; Saliba, M.; Leijtens, T.; Abate, A.; Snaith, H. J. *Energy and Environmental Science* **2014**, *7* (3), 1142–1147. https://doi.org/10.1039/c3ee43707h.

81. Wang, L. Y.; Deng, L. L.; Wang, X.; Wang, T.; Liu, H. R.; Dai, S. M.; Xing, Z.; Xie, S. Y.; Huang, R. Bin; Zheng, L. S. *Nanoscale* **2017**, *9* (45), 17893–17901. https://doi.org/10.1039/c7nr06410a.

82. Gao, L. L.; Liang, L. S.; Song, X. X.; Ding, B.; Yang, G. J.; Fan, B.; Li, C. X.; Li, C. J. *Journal of Materials Chemistry A* **2016**, *4* (10), 3704–3710. https://doi.org/10.1039/c6ta00230g.

83. Fan, L.; Ding, Y.; Luo, J.; Shi, B.; Yao, X.; Wei, C.; Zhang, D.; Wang, G.; Sheng, Y.; Chen, Y.; Hagfeldt, A.; Zhao, Y.; Zhang, X. *Journal of Materials Chemistry A* **2017**, *5* (16), 7423–7432. https://doi.org/10.1039/c7ta00973a.

84. Xiao, Z.; Bi, C.; Shao, Y.; Dong, Q.; Wang, Q.; Yuan, Y.; Wang, C.; Gao, Y.; Huang, J. *Energy and Environmental Science* **2014**, *7* (8), 2619–2623. https://doi.org/10.1039/c4ee01138d.

85. Mathies, F.; Abzieher, T.; Hochstuhl, A.; Glaser, K.; Colsmann, A.; Paetzold, U. W.; Hernandez-Sosa, G.; Lemmer, U.; Quintilla, A. *Journal of Materials Chemistry A* **2016**, *4* (48), 19207–19213. https://doi.org/10.1039/c6ta07972e.

86. Grancini, G.; Roldán-Carmona, C.; Zimmermann, I.; Mosconi, E.; Lee, X.; Martineau, D.; Narbey, S.; Oswald, F.; De Angelis, F.; Graetzel, M.; Nazeeruddin, M. K. *Nature Communications* **2017**, *8* (1), 1–9. https://doi.org/10.1038/ncomms15684.

87. Conings, B.; Baeten, L.; De Dobbelaere, C.; D'Haen, J.; Manca, J.; Boyen, H. G. *Advanced Materials* **2014**, *26* (13), 2041–2046. https://doi.org/10.1002/adma.201304803.

88. Eperon, G. E.; Burlakov, V. M.; Docampo, P.; Goriely, A.; Snaith, H. J. *Advanced Functional Materials* **2014**, *24* (1), 151–157. https://doi.org/10.1002/adfm.201302090.

89. Gao, C.; Dong, H.; Bao, X.; Zhang, Y.; Saparbaev, A.; Yu, L.; Wen, S.; Yang, R.; Dong, L. *Journal of Materials Chemistry C* **2018**, *6* (30), 8234–8241. https://doi.org/10.1039/c8tc02507j.

90. Chang, C. W.; Kwang, Z. W.; Hsieh, T. Y.; Wei, T. C.; Lu, S. Y. *Electrochimica Acta* **2018**, *292* (December), 399–406. https://doi.org/10.1016/j.electacta.2018.09.161.

91. Jeon, N. J.; Noh, J. H.; Kim, Y. C.; Yang, W. S.; Ryu, S.; Seok, S. Il. *Nature Materials* **2014**, *13* (9), 897–903. https://doi.org/10.1038/nmat4014.

92. Li, S.; Zhang, P.; Chen, H.; Wang, Y.; Liu, D.; Wu, J.; Sarvari, H.; Chen, Z. D. *Journal of Power Sources* **2017**, *342* (February), 990–997. https://doi.org/10.1016/j.jpowsour.2017.01.024.

93. Wang, B.; Zhang, Z. G.; Ye, S.; Rao, H.; Bian, Z.; Huang, C.; Li, Y. *Journal of Materials Chemistry A* **2016**, *4* (44), 17267–17273. https://doi.org/10.1039/c6ta08655a.

94. Goetz, K. P.; Taylor, A. D.; Hofstetter, Y. J.; Vaynzof, Y. *ACS Applied Materials and Interfaces* **2021**, *13* (1), 1–17. https://doi.org/10.1021/acsami.0c17269.

95. Espinosa, N.; Serrano-Luján, L.; Urbina, A.; Krebs, F. C. *Solar Energy Materials and Solar Cells* **2015**, *137* (June), 303–310. https://doi.org/10.1016/j.solmat.2015.02.013.

96. Rashedi, A.; Khanam, T. *Environmental Science and Pollution Research* **2020**, *27* (23), 29075–29090. https://doi.org/10.1007/s11356-020-09194-1.

97. Kadro, J. M.; Hagfeldt, A. *Joule* **2017**, *1* (1), 29–46. https://doi.org/10.1016/j.joule.2017.07.013.

98. Poll, C. G.; Nelson, G. W.; Pickup, D. M.; Chadwick, A. V.; Riley, D. J.; Payne, D. J. *Green Chemistry* **2016**, *18* (10), 2946–2955. https://doi.org/10.1039/c5gc02734a.

99. Capello, C.; Fischer, U.; Hungerbühler, K. *Green Chemistry* **2007**, *9* (9), 927–993. https://doi.org/10.1039/b617536h.

100. Gardner, K. L.; Tait, J. G.; Merckx, T.; Qiu, W.; Paetzold, U. W.; Kootstra, L.; Jaysankar, M.; Gehlhaar, R.; Cheyns, D.; Heremans, P.; Poortmans, J. *Advanced Energy Materials* **2016**, *6* (14), 1–8. https://doi.org/10.1002/aenm.201600386.

101. Clarke, C. J.; Tu, W. C.; Levers, O.; Bröhl, A.; Hallett, J. P. *Chemical Reviews* **2018**, *118* (2), 747–800. https://doi.org/10.1021/acs.chemrev.7b00571.

102. Park, S. Y.; Park, J. S.; Kim, B. J.; Lee, H.; Walsh, A.; Zhu, K.; Kim, D. H.; Jung, H. S. *Nature Sustainability* **2020**, *3* (12), 1044–1051. https://doi.org/10.1038/s41893-020-0586-6.

103. Kojima, A.; Teshima, K.; Shirai, Y.; Miyasaka, T. *Journal of the American Chemical Society* **2009**, *131* (17), 6050–6051. https://doi.org/10.1021/ja809598r.

104. Ikeda, N.; Teshima, K.; Miyasaka, T. *Chemical Communications* **2006**, *1* (16), 1733–1735. https://doi.org/10.1039/b516417f.

105. Kojima, A. *ECS Meeting Abstracts* **2008**, *MA2008-02* (2), 27. https://doi.org/10.1149/ma2008-02/1/27.

106. Wu, Y.; Xie, F.; Chen, H.; Yang, X.; Su, H.; Cai, M.; Zhou, Z.; Noda, T.; Han, L. *Advanced Materials* **2017**, *29* (28), 1–8. https://doi.org/10.1002/adma.201701073.

107. Green, M. A.; Ho-Baillie, A.; Snaith, H. J. *Nature Photonics* **2014**, *8* (7), 506–514. https://doi.org/10.1038/nphoton.2014.134.

108. Saidaminov, M. I.; Abdelhady, A. L.; Murali, B.; Alarousu, E.; Burlakov, V. M.; Peng, W.; Dursun, I.; Wang, L.; He, Y.; MacUlan, G.; Goriely, A.; Wu, T.; Mohammed, O. F.; Bakr, O. M. *Nature Communications* **2015**, *6* (May), 1–6. https://doi.org/10.1038/ncomms8586.

109. Cho, N.; Li, F.; Turedi, B.; Sinatra, L.; Sarmah, S. P.; Parida, M. R.; Saidaminov, M. I.; Murali, B.; Burlakov, V. M.; Goriely, A.; Mohammed, O. F.; Wu, T.; Bakr, O. M. *Nature Communications* **2016**, *7* (May), 1–11. https://doi.org/10.1038/ncomms13407.

110. Abdelhady, A. L.; Saidaminov, M. I.; Murali, B.; Adinolfi, V.; Voznyy, O.; Katsiev, K.; Alarousu, E.; Comin, R.; Dursun, I.; Sinatra, L.; Sargent, E. H.; Mohammed, O. F.; Bakr, O. M. *Journal of Physical Chemistry Letters* **2016**, *7* (2), 295–301. https://doi.org/10.1021/acs.jpclett.5b02681.

111. Musiienko, A.; Moravec, P.; Grill, R.; Praus, P.; Vasylchenko, I.; Pekarek, J.; Tisdale, J.; Ridzonova, K.; Belas, E.; Landová, L.; Hu, B.; Lukosi, E.; Ahmadi, M. *Energy and Environmental Science* **2019**, *12* (4), 1413–1425. https://doi.org/10.1039/c9ee00311h.

112. Maculan, G.; Sheikh, A. D.; Abdelhady, A. L.; Saidaminov, M. I.; Haque, M. A.; Murali, B.; Alarousu, E.; Mohammed, O. F.; Wu, T.; Bakr, O. M. *Journal of Physical Chemistry Letters* **2015**, *6* (19), 3781–3786. https://doi.org/10.1021/acs.jpclett.5b01666.

113. Bokdam, M.; Sander, T.; Stroppa, A.; Picozzi, S.; Sarma, D. D.; Franchini, C.; Kresse, G. *Scientific Reports* **2016**, *6* (1), 1–9. https://doi.org/10.1038/srep28618.

114. Shockley, W.; Queisser, H. J. *Journal of Applied Physics* **1961**, *32* (3), 510–519. https://doi.org/10.1063/1.1736034.

115. Kim, G. M.; Tatsuma, T. *Scientific Reports* **2017**, *7* (1), 4–6. https://doi.org/10.1038/s41598-017-11193-1.

116. Xue, Q.; Xia, R.; Brabec, C. J.; Yip, H. L. *Energy and Environmental Science* **2018**, *11* (7), 1688–1709. https://doi.org/10.1039/c8ee00154e.

117. Mosconi, E.; De Angelis, F. *ACS Energy Letters* **2016**, *1* (1), 182–188. https://doi.org/10.1021/acsenergylett.6b00108.

118. Yun, J. S.; Seidel, J.; Kim, J.; Soufiani, A. M.; Huang, S.; Lau, J.; Jeon, N. J.; Seok, S. Il; Green, M. A.; Ho-Baillie, A. *Advanced Energy Materials* **2016**, *6* (13), 1–8. https://doi.org/10.1002/aenm.201600330.

119. Tu, Y.; Wu, J.; Lan, Z.; He, X.; Dong, J.; Jia, J.; Guo, P.; Lin, J.; Huang, M.; Huang, Y. *Scientific Reports* **2017**, *7* (February), 1–9. https://doi.org/10.1038/srep44603.

120. Jong, U. G.; Yu, C. J.; Ri, J. S.; Kim, N. H.; Ri, G. C. *Physical Review B* **2016**, *94* (12), 125139. https://doi.org/10.1103/PhysRevB.94.125139.

121. Li, Y.; Sun, W.; Yan, W.; Ye, S.; Peng, H.; Liu, Z.; Bian, Z.; Huang, C. *Advanced Functional Materials* **2015**, *25* (30), 4867–4873. https://doi.org/10.1002/adfm.201501289.

122. Cao, K.; Cui, J.; Zhang, H.; Li, H.; Song, J.; Shen, Y.; Cheng, Y.; Wang, M. *Journal of Materials Chemistry A* **2015**, *3* (17), 9116–9122. https://doi.org/10.1039/c5ta01129a.

123. Zhang, S.; Zhang, C.; Bi, E.; Miao, X.; Zeng, H.; Han, L. *Journal of Power Sources* **2017**, *339* (January), 61–67. https://doi.org/10.1016/j.jpowsour.2016.11.030.

124. Li, B.; Zhang, Y.; Zhang, L.; Yin, L. *Advanced Materials* **2017**, *29* (39), 1701221. https://doi.org/10.1002/adma.201701221.

125. Sepalage, G. A.; Meyer, S.; Pascoe, A.; Scully, A. D.; Huang, F.; Bach, U.; Cheng, Y.-B.; Spiccia, L. *Advanced Functional Materials* **2015**, *25* (35), 5650–5661. https://doi.org/https://doi.org/10.1002/adfm.201502541.

126. Chatterjee, S.; Pal, A. J. *Journal of Physical Chemistry C* **2016**, *120* (3), 1428–1437. https://doi.org/10.1021/acs.jpcc.5b11540.

127. Shi, J.; Dong, J.; Lv, S.; Xu, Y.; Zhu, L.; Xiao, J.; Xu, X.; Wu, H.; Li, D.; Luo, Y.; Meng, Q. *Applied Physics Letters* **2014**, *104* (6), 063901. https://doi.org/10.1063/1.4864638.

128. Laban, W. A.; Etgar, L. *Energy and Environmental Science* **2013**, *6* (11), 3249–3253. https://doi.org/10.1039/c3ee42282h.

129. Zhou, Y.; Wang, F.; Fang, H. H.; Loi, M. A.; Xie, F. Y.; Zhao, N.; Wong, C. P. *Journal of Materials Chemistry A* **2016**, *4* (41), 16191–16197. https://doi.org/10.1039/c6ta07647e.

130. Kulkarni, S. A.; Baikie, T.; Boix, P. P.; Yantara, N.; Mathews, N.; Mhaisalkar, S. *Journal of Materials Chemistry A* **2014**, *2* (24), 9221–9225. https://doi.org/10.1039/c4ta00435c.

131. Cao, K.; Li, H.; Liu, S.; Cui, J.; Shen, Y.; Wang, M. *Nanoscale* **2016**, *8* (16), 8839–8846. https://doi.org/https://doi.org/10.1039/C6NR01043A.

132. Kim, M. C.; Kim, B. J.; Son, D. Y.; Park, N. G.; Jung, H. S.; Choi, M. *Nano Letters* **2016**, *16* (9), 5756–5763. https://doi.org/10.1021/acs.nanolett.6b02473.

133. Hu, M.; Bi, C.; Yuan, Y.; Bai, Y.; Huang, J. *Advanced Science* **2015**, *3* (6), 1–7. https://doi.org/10.1002/advs.201500301.

134. Chai, G.; Luo, S.; Zhou, H.; Daoud, W. A. *Materials and Design* **2017**, *125* (July), 222–229. https://doi.org/10.1016/j.matdes.2017.04.010.

135. Xiao, S.; Bai, Y.; Meng, X.; Zhang, T.; Chen, H.; Zheng, X.; Hu, C.; Qu, Y.; Yang, S. *Advanced Functional Materials* **2017**, *27* (12), 1–7. https://doi.org/10.1002/adfm.201604944.

136. Jeong, J.; Kim, H. B.; Kim, H.; Walker, B.; Song, S.; Heo, J.; Yoon, Y. J.; Jo, Y.; Choi, H.; Kim, G. H.; Kim, D. S.; Kim, J. Y. *ACS Energy Letters* **2016**, *1* (4), 712–718. https://doi.org/10.1021/acsenergylett.6b00281.

137. Park, B. W.; Philippe, B.; Jain, S. M.; Zhang, X.; Edvinsson, T.; Rensmo, H.; Zietz, B.; Boschloo, G. *Journal of Materials Chemistry A* **2015**, *3* (43), 21760–21771. https://doi.org/10.1039/c5ta05470b.

138. Tidhar, Y.; Edri, E.; Weissman, H.; Zohar, D.; Hodes, G.; Cahen, D.; Rybtchinski, B.; Kirmayer, S. *Journal of the American Chemical Society* **2014**, *136* (38), 13249–13256. https://doi.org/10.1021/ja505556s.

139. Xiao, L.; Xu, J.; Luan, J.; Zhang, B.; Tan, Z.; Yao, J.; Dai, S. *Organic Electronics* **2017**, *50* (November), 33–42. https://doi.org/10.1016/j.orgel.2017.07.020.

140. Khatiwada, D.; Venkatesan, S.; Adhikari, N.; Dubey, A.; Mitul, A. F.; Mohammad, L.; Iefanova, A.; Darling, S. B.; Qiao, Q. *Journal of Physical Chemistry C* **2015**, *119* (46), 25747–25753. https://doi.org/10.1021/acs.jpcc.5b08294.

141. Nie, W.; Tsai, H.; Asadpour, R.; Neukirch, A. J.; Gupta, G.; Crochet, J. J.; Chhowalla, M.; Tretiak, S.; Alam, M. A.; Wang, H. *Science* **2015**, *347* (6221), 522–525. https://doi.org/10.1126/science.aaa0472.

142. Liang, P. W.; Liao, C. Y.; Chueh, C. C.; Zuo, F.; Williams, S. T.; Xin, X. K.; Lin, J.; Jen, A. K. Y. *Advanced Materials* **2014**, *26* (22), 3748–3754. https://doi.org/10.1002/adma.201400231.

143. Xie, F. X.; Su, H.; Mao, J.; Wong, K. S.; Choy, W. C. H. *Journal of Physical Chemistry C* **2016**, *120* (38), 21248–21253. https://doi.org/10.1021/acs.jpcc.6b06914.

144. Cronin, H. M.; Jayawardena, K. D. G. I.; Stoeva, Z.; Shkunov, M.; Silva, S. R. P. *Nanotechnology* **2017**, *28* (11), 114004. https://doi.org/10.1088/1361-6528/aa5bec.

145. Dong, Q.; Yuan, Y.; Shao, Y.; Fang, Y.; Wang, Q.; Huang, J. *Energy and Environmental Science* **2015**, *8* (8), 2464–2470. https://doi.org/10.1039/C5EE01179E.

146. Liao, H. C.; Guo, P.; Hsu, C. P.; Lin, M.; Wang, B.; Zeng, L.; Huang, W.; Soe, C. M. M.; Su, W. F.; Bedzyk, M. J.; Wasielewski, M. R.; Facchetti, A.; Chang, R. P. H.; Kanatzidis, M. G.; Marks, T. J. *Advanced Energy Materials* **2017**, *7* (8), 1601660. https://doi.org/10.1002/aenm.201601660.

147. Zhang, L. Q.; Zhang, X. W.; Yin, Z. G.; Jiang, Q.; Liu, X.; Meng, J. H.; Zhao, Y. J.; Wang, H. L. *Journal of Materials Chemistry A* **2015**, *3* (23), 12133–12138. https://doi.org/10.1039/c5ta01898f.

148. McLeod, J. A.; Wu, Z.; Sun, B.; Liu, L. *Nanoscale* **2016**, *8* (12), 6361–6368. https://doi.org/10.1039/c5nr06217a.

149. Song, D.; Heo, J. H.; Han, H. J.; You, M. S.; Im, S. H. *Journal of Power Sources* **2016**, *310* (April), 130–136. https://doi.org/10.1016/j.jpowsour.2016.02.010.

150. Rapsomanikis, A.; Karageorgopoulos, D.; Lianos, P.; Stathatos, E. *Solar Energy Materials and Solar Cells* **2016**, *151* (July), 36–43. https://doi.org/10.1016/j.solmat.2016.03.001.

151. Ng, T. W.; Chan, C. Y.; Lo, M. F.; Guan, Z. Q.; Lee, C. S. *Journal of Materials Chemistry A* **2015**, *3* (17), 9081–9085. https://doi.org/10.1039/c4ta05819d.

152. Chen, Q.; Zhou, H.; Fang, Y.; Stieg, A. Z.; Song, T. Bin; Wang, H. H.; Xu, X.; Liu, Y.; Lu, S.; You, J.; Sun, P.; McKay, J.; Goorsky, M. S.; Yang, Y. *Nature Communications* **2015**, *6* (1), 1–9. https://doi.org/10.1038/ncomms8269.

153. Wang, W.; Zhang, Z.; Cai, Y.; Chen, J.; Wang, J.; Huang, R.; Lu, X.; Gao, X.; Shui, L.; Wu, S.; Liu, J. M. *Nanoscale Research Letters* **2016**, *11* (1), 1–9. https://doi.org/10.1186/s11671-016-1540-4.

154. Dualeh, A.; Tétreault, N.; Moehl, T.; Gao, P.; Nazeeruddin, M. K.; Grätzel, M. *Advanced Functional Materials* **2014**, *24* (21), 3250–3258. https://doi.org/10.1002/adfm.201304022.

155. Jiang, F.; Rong, Y.; Liu, H.; Liu, T.; Mao, L.; Meng, W.; Qin, F.; Jiang, Y.; Luo, B.; Xiong, S.; Tong, J.; Liu, Y.; Li, Z.; Han, H.; Zhou, Y. *Advanced Functional Materials* **2016**, *26* (44), 8119–8127. https://doi.org/10.1002/adfm.201603968.

156. Grill, I.; Handloser, K.; Hanusch, F. C.; Giesbrecht, N.; Bein, T.; Docampo, P.; Handloser, M.; Hartschuh, A. *Solar Energy Materials and Solar Cells* **2017**, *166* (November), 269–275. https://doi.org/10.1016/j.solmat.2016.11.021.

157. Stranks, S. D.; Eperon, G. E.; Grancini, G.; Menelaou, C.; Alcocer, M. J. P.; Leijtens, T.; Herz, L. M.; Petrozza, A.; Snaith, H. J. *Science* **2013**, *342* (6156), 341–344. https://doi.org/10.1126/science.1243982.

158. Jiang, M.; Wu, J.; Lan, F.; Tao, Q.; Gao, D.; Li, G. *Journal of Materials Chemistry A* **2015**, *3* (3), 963–967. https://doi.org/10.1039/c4ta05373g.

159. Docampo, P.; Hanusch, F. C.; Stranks, S. D.; Döblinger, M.; Feckl, J. M.; Ehrensperger, M.; Minar, N. K.; Johnston, M. B.; Snaith, H. J.; Bein, T. *Advanced Energy Materials* **2014**, *4* (14), 1400355. https://doi.org/10.1002/aenm.201400355.

160. Zhou, H.; Chen, Q.; Li, G.; Luo, S.; Song, T.; Duan, H.-S.; Hong, Z.; You, J.; Liu, Y.; Yang, Y. *Photovoltaics* **2014**, *345* (6196), 542–546. https://doi.org/10.1126/science.1254050.

161. Zhao, Y.; Zhu, K. *Journal of Physical Chemistry C* **2014**, *118* (18), 9412–9418. https://doi.org/10.1021/jp502696w.

162. Song, S.; Hörantner, M. T.; Choi, K.; Snaith, H. J.; Park, T. *Journal of Materials Chemistry A* **2017**, *5* (8), 3812–3818. https://doi.org/10.1039/c6ta09020f.

163. Koh, T. M.; Fu, K.; Fang, Y.; Chen, S.; Sum, T. C.; Mathews, N.; Mhaisalkar, S. G.; Boix, P. P.; Baikie, T. *Journal of Physical Chemistry C* **2014**, *118* (30), 16458–16462. https://doi.org/10.1021/jp411112k.

164. Pang, S.; Hu, H.; Zhang, J.; Lv, S.; Yu, Y.; Wei, F.; Qin, T.; Xu, H.; Liu, Z.; Cui, G. *Chemistry of Materials* **2014**, *26* (3), 1485–1491. https://doi.org/10.1021/cm404006p.

165. Xie, Z.; Sun, S.; Yan, Y.; Zhang, L.; Hou, R.; Tian, F.; Qin, G. G. *Journal of Physics Condensed Matter* **2017**, *29* (24), 245702. https://doi.org/10.1088/1361-648X/aa6e6c.

166. Saidaminov, M. I.; Abdelhady, A. L.; Maculan, G.; Bakr, O. M. *Chemical Communications* **2015**, *51* (100), 17658–17661. https://doi.org/10.1039/c5cc06916e.

167. Yang, W. S.; Noh, J. H.; Jeon, N. J.; Kim, Y. C.; Ryu, S.; Seo, J.; Seok, S. Il. *Science* **2015**, *348* (6240), 1234–1237. https://doi.org/10.1126/science.aaa9272.

168. Liang, B.; Wang, S.; Kuang, D.; Hou, L.; Yu, B.; Lin, L.; Deng, L.; Huang, H.; He, J. *Nanotechnology* **2018**, *29* (8), 085604. https://doi.org/10.1088/1361-6528/aaa52f.

169. Nazarenko, O.; Yakunin, S.; Morad, V.; Cherniukh, I.; Kovalenko, M. V. *NPG Asia Materials* **2017**, *9* (4), 373–378. https://doi.org/10.1038/am.2017.45.

170. McMeekin, D. P.; Sadoughi, G.; Rehman, W.; Eperon, G. E.; Saliba, M.; Hörantner, M. T.; Haghighirad, A.; Sakai, N.; Korte, L.; Rech, B.; Johnston, M. B.; Herz, L. M.; Snaith, H. J. *Science* **2016**, *351* (6269), 151–155. https://doi.org/10.1126/science.aad5845.

171. Lee, J. W.; Kim, D. H.; Kim, H. S.; Seo, S. W.; Cho, S. M.; Park, N. G. *Advanced Energy Materials* **2015**, *5* (20), 1501310. https://doi.org/10.1002/aenm.201501310.

172. Pellet, N.; Gao, P.; Gregori, G.; Yang, T.-Y.; Nazeeruddin, M. K.; Maier, J.; Grätzel, M. *Angewandte Chemie* **2014**, *126* (12), 3215–3221. https://doi.org/10.1002/ange.201309361.

173. Yi, C.; Luo, J.; Meloni, S.; Boziki, A.; Ashari-Astani, N.; Grätzel, C.; Zakeeruddin, S. M.; Röthlisberger, U.; Grätzel, M. *Energy and Environmental Science* **2016**, *9* (2), 656–662. https://doi.org/10.1039/c5ee03255e.

174. Weber, O. J.; Charles, B.; Weller, M. T. *Journal of Materials Chemistry A* **2016**, *4* (40), 15375–15382. https://doi.org/10.1039/c6ta06607k.

175. Chen, J.; Xu, J.; Xiao, L.; Zhang, B.; Dai, S.; Yao, J. *ACS Applied Materials and Interfaces* **2017**, *9* (3), 2449–2458. https://doi.org/10.1021/acsami.6b13410.

176. Xie, L. Q.; Chen, L.; Nan, Z. A.; Lin, H. X.; Wang, T.; Zhan, D. P.; Yan, J. W.; Mao, B. W.; Tian, Z. Q. *Journal of the American Chemical Society* **2017**, *139* (9), 3320–3323. https://doi.org/10.1021/jacs.6b12432.

177. Saliba, M.; Matsui, T.; Seo, J. Y.; Domanski, K.; Correa-Baena, J. P.; Nazeeruddin, M. K.; Zakeeruddin, S. M.; Tress, W.; Abate, A.; Hagfeldt, A.; Grätzel, M. *Energy and Environmental Science* **2016**, *9* (6), 1989–1997. https://doi.org/10.1039/c5ee03874j.

178. Li, X.; Yang, J.; Jiang, Q.; Chu, W.; Zhang, D.; Zhou, Z.; Xin, J. *ACS Applied Materials and Interfaces* **2017**, *9* (47), 41354–41362. https://doi.org/10.1021/acsami.7b14926.

179. Li, N.; Zhu, Z.; Chueh, C. C.; Liu, H.; Peng, B.; Petrone, A.; Li, X.; Wang, L.; Jen, A. K. Y. *Advanced Energy Materials* **2017**, *7* (1), 1601307. https://doi.org/10.1002/aenm.201601307.

180. Ye, J.; Zheng, H.; Zhu, L.; Liu, G.; Zhang, X.; Hayat, T.; Pan, X.; Dai, S. *Solar RRL* **2017**, *1* (11), 1700125. https://doi.org/10.1002/solr.201700125.

181. Rehman, W.; Milot, R. L.; Eperon, G. E.; Wehrenfennig, C.; Boland, J. L.; Snaith, H. J.; Johnston, M. B.; Herz, L. M. *Advanced Materials* **2015**, *27* (48), 7938–7944. https://doi.org/10.1002/adma.201502969.

182. Yan, J.; Qiu, W.; Wu, G.; Heremans, P.; Chen, H. *Journal of Materials Chemistry A* **2018**, *6* (24), 11063–11077. https://doi.org/10.1039/c8ta02288g.

183. Ning, Z.; Yiheng, S.; Yu, Z.; Ziqi, X.; Guanhaojie, Z.; Liang, L.; Qi, C.; Huanping, Z. *Advanced Energy Materials* **2017**, *1* (13), 1700484. https://doi.org/10.1002/smll.201700484.

184. He, W.; Hu, J.; Chen, C.; Chen, Y.; Zeng, L.; Zhang, X.; Cai, B.; Mai, Y.; Guo, F. *ACS Applied Materials and Interfaces* **2020**, *12* (50), 55830–55837. https://doi.org/10.1021/acsami.0c15733.

185. Yu, G.; Feng, L.; Meng, L.; Ye, Z.; Lu, J. *Surface Review and Letters* **2018**, *25* (2), 1–5. https://doi.org/10.1142/S0218625X18500579.

186. Reyna, Y.; Salado, M.; Kazim, S.; Pérez-Tomas, A.; Ahmad, S.; Lira-Cantu, M. *Nano Energy* **2016**, *30* (August), 570–579. https://doi.org/10.1016/j.nanoen.2016.10.053.

187. Bella, F.; Griffini, G.; Correa-Baena, J. P.; Saracco, G.; Grätzel, M.; Hagfeldt, A.; Turri, S.; Gerbaldi, C. *Science* **2016**, *354* (6309), 203–206. https://doi.org/10.1126/science.aah4046.

188. Zhou, Y.; Kwun, J.; Garces, H. F.; Pang, S.; Padture, N. P. *Chemical Communications* **2016**, *52* (45), 7273–7275. https://doi.org/10.1039/c6cc02086k.

189. Wei, Q.; Yang, D.; Yang, Z.; Ren, X.; Liu, Y.; Feng, J.; Zhu, X.; Liu, S. *RSC Advances* **2016**, *6* (62), 56807–56811. https://doi.org/10.1039/c6ra10007d.

190. Hu, M.; Liu, L.; Mei, A.; Yang, Y.; Liu, T.; Han, H. *Journal of Materials Chemistry A* **2014**, *2* (40), 17115–17121. https://doi.org/10.1039/c4ta03741c.

191. He, X.; Guo, P.; Wu, J.; Tu, Y.; Lan, Z.; Lin, J.; Huang, M. *Solar Energy* **2017**, *157* (September), 853–859. https://doi.org/10.1016/j.solener.2017.09.014.

192. Szostak, R.; Castro, J. A. P.; Marques, A. S.; Nogueira, A. F. *Journal of Photonics for Energy* **2017**, *7* (2), 022002. https://doi.org/10.1117/1.jpe.7.022002.

193. Ji, F.; Wang, L.; Pang, S.; Gao, P.; Xu, H. *Journal of Materials Chemistry A* **2016**, *4* (37), 14437–14443. https://doi.org/10.1039/C6TA05727F.

194. Isikgor, F. H.; Li, B.; Zhu, H.; Xu, Q.; Ouyang, J. *Journal of Materials Chemistry A* **2016**, *4* (32), 12543–12553. https://doi.org/10.1039/c6ta03381d.

195. Yang, Y.; Feng, S.; Xu, W.; Li, M.; Li, L.; Zhang, X.; Ji, G.; Zhang, X.; Wang, Z.; Xiong, Y.; Cao, L.; Sun, B.; Gao, X. *ACS Applied Materials and Interfaces* **2017**, *9* (27), 23141–23151. https://doi.org/10.1021/acsami.7b03941.

196. Niu, G.; Yu, H.; Li, J.; Wang, D.; Wang, L. *Nano Energy* **2016**, *27* (September), 87–94. https://doi.org/10.1016/j.nanoen.2016.06.053.

197. Jesper Jacobsson, T.; Correa-Baena, J. P.; Pazoki, M.; Saliba, M.; Schenk, K.; Grätzel, M.; Hagfeldt, A. *Energy and Environmental Science* **2016**, *9* (5), 1706–1724. https://doi.org/10.1039/c6ee00030d.

198. Thakur, U.; Kwon, U.; Hasan, M. M.; Yin, W.; Kim, D.; Ha, N. Y.; Lee, S.; Ahn, T. K.; Park, H. J. *Scientific reports* **2017**, *7* (1), 43979. https://doi.org/10.1038/srep43979.

199. Rong, Y.; Liu, L.; Mei, A.; Li, X.; Han, H. *Advanced Energy Materials* **2015**, *5* (20), 1–16. https://doi.org/10.1002/aenm.201501066.

200. Xu, X.; Chen, Q.; Hong, Z.; Zhou, H.; Liu, Z.; Chang, W. H.; Sun, P.; Chen, H.; Marco, N. De; Wang, M.; Yang, Y. *Nano Letters* **2015**, *15* (10), 6514–6520. https://doi.org/10.1021/acs.nanolett.5b02126.

201. Wang, Z.; Zhou, Y.; Pang, S.; Xiao, Z.; Zhang, J.; Chai, W.; Xu, H.; Liu, Z.; Padture, N. P.; Cui, G. *Chemistry of Materials* **2015**, *27* (20), 7149–7155. https://doi.org/10.1021/acs.chemmater.5b03169.

202. Yang, S.; Liu, W.; Zuo, L.; Zhang, X.; Ye, T.; Chen, J.; Li, C. Z.; Wu, G.; Chen, H. *Journal of Materials Chemistry A* **2016**, *4* (24), 9430–9436. https://doi.org/10.1039/c6ta02999j.

203. Lee, J. W.; Kim, H. S.; Park, N. G. *Accounts of Chemical Research* **2016**, *49* (2), 311–319. https://doi.org/10.1021/acs.accounts.5b00440.

204. Yu, Y.; Wang, C.; Grice, C. R.; Shrestha, N.; Chen, J.; Zhao, D.; Liao, W.; Cimaroli, A. J.; Roland, P. J.; Ellingson, R. J.; Yan, Y. *ChemSusChem* **2016**, *9* (23), 3288–3297. https://doi.org/10.1002/cssc.201601027.

205. Sun, Y.; Peng, J.; Chen, Y.; Yao, Y.; Liang, Z. *Scientific Reports* **2017**, *7* (April), 1–8. https://doi.org/10.1038/srep46193.

206. Turren-Cruz, S. H.; Saliba, M.; Mayer, M. T.; Juárez-Santiesteban, H.; Mathew, X.; Nienhaus, L.; Tress, W.; Erodici, M. P.; Sher, M. J.; Bawendi, M. G.; Grätzel, M.; Abate, A.; Hagfeldt, A.; Correa-Baena, J. P. *Energy and Environmental Science* **2018**, *11* (1), 78–86. https://doi.org/10.1039/c7ee02901b.

207. Albadri, A.; Yadav, P.; Alotaibi, M.; Arora, N.; Alyamani, A.; Albrithen, H.; Dar, M. I.; Zakeeruddin, S. M.; Grätzel, M. *Journal of Physical Chemistry C* **2017**, *121* (45), 24903–24908. https://doi.org/10.1021/acs.jpcc.7b04766.

208. Xu, X.; Chueh, C. C.; Yang, Z.; Rajagopal, A.; Xu, J.; Jo, S. B.; Jen, A. K. Y. *Nano Energy* **2017**, *34* (April), 392–398. https://doi.org/10.1016/j.nanoen.2017.02.040.

209. Wu, J.; Xu, X.; Zhao, Y.; Shi, J.; Xu, Y.; Luo, Y.; Li, D.; Wu, H.; Meng, Q. *ACS Applied Materials and Interfaces* **2017**, *9* (32), 26937–26947. https://doi.org/10.1021/acsami.7b08504.

210. Salado, M.; Fernández, M. A.; Holgado, J. P.; Kazim, S.; Nazeeruddin, M. K.; Dyson, P. J.; Ahmad, S. *ChemSusChem* **2017**, *10* (19), 3846–3853. https://doi.org/10.1002/cssc.201700797.

211. Wu, Z.; Raga, S. R.; Juarez-Perez, E. J.; Yao, X.; Jiang, Y.; Ono, L. K.; Ning, Z.; Tian, H.; Qi, Y. *Advanced Materials* **2018**, *30* (3), 1703670. https://doi.org/10.1002/adma.201703670.

212. Tang, Z.; Bessho, T.; Awai, F.; Kinoshita, T.; Maitani, M. M.; Jono, R.; Murakami, T. N.; Wang, H.; Kubo, T.; Uchida, S.; Segawa, H. *Scientific Reports* **2017**, *7* (1), 1–8. https://doi.org/10.1038/s41598-017-12436-x.

213. Huang, J.; Xu, P.; Liu, J.; You, X. Z. *Small* **2017**, *13* (10), 1603225. https://doi.org/10.1002/smll.201603225.

214. Li, Y.; Zhang, T.; Xu, F.; Wang, Y.; Li, G.; Yang, Y.; Zhao, Y. *Crystals* **2017**, *7* (9), 272. https://doi.org/10.3390/cryst7090272.

215. Wang, F.; Yu, H.; Xu, H.; Zhao, N. *Advanced Functional Materials* **2015**, *25* (7), 1120–1126. https://doi.org/10.1002/adfm.201404007.

216. Zhou, Y.; Yang, M.; Pang, S.; Zhu, K.; Padture, N. P. *Journal of the American Chemical Society* **2016**, *138* (17), 5535–5538. https://doi.org/10.1021/jacs.6b02787.

217. Li, S.; Yang, B.; Wu, R.; Zhang, C.; Zhang, C.; Tang, X. F.; Liu, G.; Liu, P.; Zhou, C.; Gao, Y.; Meng, J. Q.; Yang, J. *Organic Electronics* **2016**, *39* (December), 304–310. https://doi.org/10.1016/j.orgel.2016.10.017.

218. Jo, Y.; Oh, K. S.; Kim, M.; Kim, K. H.; Lee, H.; Lee, C. W.; Kim, D. S. *Advanced Materials Interfaces* **2016**, *3* (10), 1–7. https://doi.org/10.1002/admi.201500768.

219. Bi, D.; Tress, W.; Dar, M. I.; Gao, P.; Luo, J.; Renevier, C.; Schenk, K.; Abate, A.; Giordano, F.; Correa Baena, J. P.; Decoppet, J. D.; Zakeeruddin, S. M.; Nazeeruddin, M. K.; Grätzel, M.; Hagfeldt, A. *Science Advances* **2016**, *2* (1), 1501170. https://doi.org/10.1126/sciadv.1501170.

220. Yang, W. S.; Park, B. W.; Jung, E. H.; Jeon, N. J.; Kim, Y. C.; Lee, D. U.; Shin, S. S.; Seo, J.; Kim, E. K.; Noh, J. H.; Seok, S. Il. *Science* **2017**, *356* (6345), 1376–1379. https://doi.org/10.1126/science.aan2301.

221. Li, X.; Bi, D.; Yi, C.; Décoppet, J. D.; Luo, J.; Zakeeruddin, S. M.; Hagfeldt, A.; Grätzel, M. *Science* **2016**, *353* (6294), 58–62. https://doi.org/10.1126/science.aaf8060.

222. Zhang, T.; Long, M.; Yan, K.; Qin, M.; Lu, X.; Zeng, X.; Cheng, C. M.; Wong, K. S.; Liu, P.; Xie, W.; Xu, J. *Advanced Energy Materials* **2017**, *7* (15), 1–10. https://doi.org/10.1002/aenm.201700118.

223. Liu, J.; Shirai, Y.; Yang, X.; Yue, Y.; Chen, W.; Wu, Y.; Islam, A.; Han, L. *Advanced Materials* **2015**, *27* (33), 4918–4923. https://doi.org/10.1002/adma.201501489.

224. Mu, C.; Pan, J.; Feng, S.; Li, Q.; Xu, D. *Advanced Energy Materials* **2017**, *7* (6), 1614–6832. https://doi.org/10.1002/aenm.201601297.

225. Zhang, H.; Shi, J.; Xu, X.; Zhu, L.; Luo, Y.; Li, D.; Meng, Q. *Journal of Materials Chemistry A* **2016**, *4* (40), 15383–15389. https://doi.org/10.1039/c6ta06879k.

226. Li, C.; Guo, Q.; Zhang, H.; Bai, Y.; Wang, F.; Liu, L.; Hayat, T.; Alsaedi, A.; Tan, Z. *Nano Energy* **2017**, *40* (March), 248–257. https://doi.org/10.1016/j.nanoen.2017.08.009.

227. Seol, D. J.; Lee, J. W.; Park, N. G. *ChemSusChem* **2015**, *8* (14), 2414–2419. https://doi.org/10.1002/cssc.201403442.

228. Cho, K. T.; Paek, S.; Grancini, G.; Roldán-Carmona, C.; Gao, P.; Lee, Y.; Nazeeruddin, M. K. *Energy and Environmental Science* **2017**, *10* (2), 621–627. https://doi.org/10.1039/c6ee03182j.

229. Arora, N.; Dar, M. I.; Abdi-Jalebi, M.; Giordano, F.; Pellet, N.; Jacopin, G.; Friend, R. H.; Zakeeruddin, S. M.; Grätzel, M. *Nano Letters* **2016**, *16* (11), 7155–7162. https://doi.org/10.1021/acs.nanolett.6b03455.

230. Tan, H.; Jain, A.; Voznyy, O.; Lan, X.; De Arquer, F. P. G.; Fan, J. Z.; Quintero-Bermudez, R.; Yuan, M.; Zhang, B.; Zhao, Y.; Fan, F.; Li, P.; Quan, L. N.; Zhao, Y.; Lu, Z. H.; Yang, Z.; Hoogland, S.; Sargent, E. H. *Science* **2017**, *355* (6326), 722–726. https://doi.org/10.1126/science.aai9081.

231. Li, G.; Zhang, T.; Xu, F.; Zhao, Y. *Materials Today Energy* **2017**, *5* (September), 293–298. https://doi.org/10.1016/j.mtener.2017.07.010.

232. Arafat Mahmud, M.; Kumar Elumalai, N.; Baishakhi Upama, M.; Wang, D.; Gonçales, V. R.; Wright, M.; Justin Gooding, J.; Haque, F.; Xu, C.; Uddin, A. *Solar Energy Materials and Solar Cells* **2018**, *174* (1), 172–186. https://doi.org/10.1016/j.solmat.2017.08.032.

233. Ye, T.; Petrovic, M.; Peng, S.; Yoong, J. L. K.; Vijila, C.; Ramakrishna, S. *ACS Applied Materials and Interfaces* **2017**, *9* (3), 2358–2368. https://doi.org/10.1021/acsami.6b12845.

234. Seo, J. Y.; Uchida, R.; Kim, H. S.; Saygili, Y.; Luo, J.; Moore, C.; Kerrod, J.; Wagstaff, A.; Eklund, M.; McIntyre, R.; Pellet, N.; Zakeeruddin, S. M.; Hagfeldt, A.; Grätzel, M. *Advanced Functional Materials* **2018**, *28* (15), 1705763. https://doi.org/10.1002/adfm.201705763.

235. Hu, C.; Bai, Y.; Xiao, S.; Zhang, T.; Meng, X.; Ng, W. K.; Yang, Y.; Wong, K. S.; Chen, H.; Yang, S. *Journal of Materials Chemistry A* **2017**, *5* (41), 21858–21865. https://doi.org/10.1039/c7ta07139f.

236. Hou, Y.; Du, X.; Scheiner, S.; McMeekin, D. P.; Wang, Z.; Li, N.; Killian, M. S.; Chen, H.; Richter, M.; Levchuk, I.; Schrenker, N.; Spiecker, E.; Stubhan, T.; Luechinger, N. A.; Hirsch, A.; Schmuki, P.; Steinrück, H. P.; Fink, R. H.; Halik, M.; Snaith, H. J.; Brabec, C. J. *Science* **2017**, *358* (6367), 1192–1197. https://doi.org/10.1126/science.aao5561.

237. Wang, Z.; McMeekin, D. P.; Sakai, N.; van Reenen, S.; Wojciechowski, K.; Patel, J. B.; Johnston, M. B.; Snaith, H. J. *Advanced Materials* **2017**, *29* (5), 1604186. https://doi.org/10.1002/adma.201604186.

238. Mahmud, M. A.; Elumalai, N. K.; Upama, M. B.; Wang, D.; Soufiani, A. M.; Wright, M.; Xu, C.; Haque, F.; Uddin, A. *ACS Applied Materials and Interfaces* **2017**, *9* (39), 33840–33854. https://doi.org/10.1021/acsami.7b09153.

239. Yang, D.; Yang, R.; Wang, K.; Wu, C.; Zhu, X.; Feng, J.; Ren, X.; Fang, G.; Priya, S.; Liu, S. (Frank). *Nature Communications* **2018**, *9* (1), 3239. https://doi.org/10.1038/s41467-018-05760-x.

240. Zhang, F.; Shi, W.; Luo, J.; Pellet, N.; Yi, C.; Li, X.; Zhao, X.; Dennis, T. J. S.; Li, X.; Wang, S.; Xiao, Y.; Zakeeruddin, S. M.; Bi, D.; Grätzel, M. *Advanced Materials* **2017**, *29* (17), 1606806. https://doi.org/10.1002/adma.201606806.

241. Leyden, M. R.; Jiang, Y.; Qi, Y. *Journal of Materials Chemistry A* **2016**, *4* (34), 13125–13132. https://doi.org/10.1039/c6ta04267h.

242. Jiang, Y.; Leyden, M. R.; Qiu, L.; Wang, S.; Ono, L. K.; Wu, Z.; Juarez-Perez, E. J.; Qi, Y. *Advanced Functional Materials* **2018**, *28* (1), 1870007. https://doi.org/10.1002/adfm.201870007.

243. Zhou, Z.; Pang, S.; Ji, F.; Zhang, B.; Cui, G. *Chemical Communications* **2016**, *52* (19), 3828–3831. https://doi.org/10.1039/c5cc09873d.

244. Smith, I. C.; Hoke, E. T.; Solis-Ibarra, D.; McGehee, M. D.; Karunadasa, H. I. *Angewandte Chemie - International Edition* **2014**, *53* (42), 11232–11235. https://doi.org/10.1002/anie.201406466.

245. Cao, D. H.; Stoumpos, C. C.; Farha, O. K.; Hupp, J. T.; Kanatzidis, M. G. *Journal of the American Chemical Society* **2015**, *137* (24), 7843–7850. https://doi.org/10.1021/jacs.5b03796.

246. Tsai, H.; Nie, W.; Blancon, J. C.; Stoumpos, C. C.; Asadpour, R.; Harutyunyan, B.; Neukirch, A. J.; Verduzco, R.; Crochet, J. J.; Tretiak, S.; Pedesseau, L.; Even, J.; Alam, M. A.; Gupta, G.; Lou, J.; Ajayan, P. M.; Bedzyk, M. J.; Kanatzidis, M. G.; Mohite, A. D. *Nature* **2016**, *536* (7616), 312–317. https://doi.org/10.1038/nature18306.

247. Quan, L. N.; Yuan, M.; Comin, R.; Voznyy, O.; Beauregard, E. M.; Hoogland, S.; Buin, A.; Kirmani, A. R.; Zhao, K.; Amassian, A.; Kim, D. H.; Sargent, E. H. *Journal of the American Chemical Society* **2016**, *138* (8), 2649–2655. https://doi.org/10.1021/jacs.5b11740.

248. Yao, K.; Wang, X.; Xu, Y. X.; Li, F.; Zhou, L. *Chemistry of Materials* **2016**, *28* (9), 3131–3138. https://doi.org/10.1021/acs.chemmater.6b00711.

249. Lin, Y.; Bai, Y.; Fang, Y.; Chen, Z.; Yang, S.; Zheng, X.; Tang, S.; Liu, Y.; Zhao, J.; Huang, J. *Journal of Physical Chemistry Letters* **2018**, *9* (3), 654–658. https://doi.org/10.1021/acs.jpclett.7b02679.

250. Zhang, X.; Ren, X.; Liu, B.; Munir, R.; Zhu, X.; Yang, D.; Li, J.; Liu, Y.; Smilgies, D. M.; Li, R.; Yang, Z.; Niu, T.; Wang, X.; Amassian, A.; Zhao, K.; Liu, S. *Energy and Environmental Science* **2017**, *10* (10), 2095–2102. https://doi.org/10.1039/c7ee01145h.

251. Wang, Q.; Chen, B.; Liu, Y.; Deng, Y.; Bai, Y.; Dong, Q.; Huang, J. *Energy and Environmental Science* **2017**, *10* (2), 516–522. https://doi.org/10.1039/c6ee02941h.

252. Mao, L.; Ke, W.; Pedesseau, L.; Wu, Y.; Katan, C.; Even, J.; Wasielewski, M. R.; Stoumpos, C. C.; Kanatzidis, M. G. *Journal of the American Chemical Society* **2018**, *140* (10), 3775–3783. https://doi.org/10.1021/jacs.8b00542.

253. Ahmad, S.; Fu, P.; Yu, S.; Yang, Q.; Liu, X.; Wang, X.; Wang, X.; Guo, X.; Li, C. *Joule* **2019**, *3* (3), 794–806. https://doi.org/10.1016/j.joule.2018.11.026.

254. Koh, T. M.; Shanmugam, V.; Schlipf, J.; Oesinghaus, L.; Müller-Buschbaum, P.; Ramakrishnan, N.; Swamy, V.; Mathews, N.; Boix, P. P.; Mhaisalkar, S. G. *Advanced Materials* **2016**, *28* (19), 3653–3661. https://doi.org/10.1002/adma.201506141.

255. Dai, X.; Xu, K.; Wei, F. *Beilstein Journal of Nanotechnology* **2020**, *11* (1), 51–60. https://doi.org/10.3762/bjnano.11.5.

256. Jeong, D. N.; Lee, D. K.; Seo, S.; Lim, S. Y.; Zhang, Y.; Shin, H.; Cheong, H.; Park, N. G. *ACS Energy Letters* **2019**, *4* (5), 1189–1195. https://doi.org/10.1021/acsenergylett.9b00042.

257. Zhu, X.; Xu, Z.; Zuo, S.; Feng, J.; Wang, Z.; Zhang, X.; Zhao, K.; Zhang, J.; Liu, H.; Priya, S.; Liu, S. F.; Yang, D. *Energy and Environmental Science* **2018**, *11* (12), 3349–3357. https://doi.org/10.1039/c8ee02284d.

258. Qiu, J.; Zheng, Y.; Xia, Y.; Chao, L.; Chen, Y.; Huang, W. *Advanced Functional Materials* **2019**, *29* (47), 1–7. https://doi.org/10.1002/adfm.201806831.

259. Miyasaka, T.; Kulkarni, A.; Kim, G. M.; Öz, S.; Jena, A. K. *Advanced Energy Materials* **2020**, *10* (13), 1–20. https://doi.org/10.1002/aenm.201902500.

260. Ke, W.; Stoumpos, C. C.; Kanatzidis, M. G. *Advanced Materials* **2019**, *31* (47), 1803230. https://doi.org/10.1002/adma.201803230.

261. Babayigit, A.; Duy Thanh, D.; Ethirajan, A.; Manca, J.; Muller, M.; Boyen, H. G.; Conings, B. *Scientific Reports* **2016**, *6* (1), 1–11. https://doi.org/10.1038/srep18721.

262. Stroyuk, O. *Beilstein Journal of Nanotechnology* **2018**, *9* (1), 2209–2235. https://doi.org/10.3762/bjnano.9.207.

263. Kour, R.; Arya, S.; Verma, S.; Gupta, J.; Bandhoria, P.; Bharti, V.; Datt, R.; Gupta, V. *Global Challenges* **2019**, *3* (11), 1900050. https://doi.org/10.1002/gch2.201900050.

264. Giorgi, G.; Fujisawa, J. I.; Segawa, H.; Yamashita, K. *Journal of Physical Chemistry Letters* **2013**, *4* (24), 4213–4216. https://doi.org/10.1021/jz4023865.

265. Scaife, D. E.; Weller, P. F.; Fisher, W. G. *Journal of Solid State Chemistry* **1974**, *9* (3), 308–314. https://doi.org/10.1016/0022-4596(74)90088-7.

266. Weber, D. *Zeitschrift für Naturforschung B* **1978**, *33* (Ii), 862–865. https://doi.org/https://doi.org/10.1515/znb-1978-0809.

267. Noel, N. K.; Stranks, S. D.; Abate, A.; Wehrenfennig, C.; Guarnera, S.; Haghighirad, A. A.; Sadhanala, A.; Eperon, G. E.; Pathak, S. K.; Johnston, M. B.; Petrozza, A. M.; Herz, L. M.; Snaith, H. J.; Samuel D. Stranks, A. A.; Wehrenfennig, C.; Guarnera, S.; Amir Abbas Haghighirad, A. S.; E.; Eperon, G. E.; Johnston, M. B.; Petrozza, A. M.; Herz, L. M.; J., H. S. *Energy & Environmental Science* **2014**, *7* (9), 3061-3068. https://doi.org/10.1039/c4ee01076k.

268. Hao, F.; Stoumpos, C. C.; Cao, D. H.; Chang, R. P. H.; Kanatzidis, M. G. *Nature Photonics* **2014**, *8* (6), 489–494. https://doi.org/10.1038/nphoton.2014.82.

269. Chung, I.; Song, J. H.; Im, J.; Androulakis, J.; Malliakas, C. D.; Li, H.; Freeman, A. J.; Kenney, J. T.; Kanatzidis, M. G. *Journal of the American Chemical Society* **2012**, *134* (20), 8579–8587. https://doi.org/10.1021/ja301539s.

270. Song, T. Bin; Yokoyama, T.; Stoumpos, C. C.; Logsdon, J.; Cao, D. H.; Wasielewski, M. R.; Aramaki, S.; Kanatzidis, M. G. *Journal of the American Chemical Society* **2017**, *139* (2), 836–842. https://doi.org/10.1021/jacs.6b10734.

271. Ma, L.; Hao, F.; Stoumpos, C. C.; Phelan, B. T.; Wasielewski, M. R.; Kanatzidis, M. G. *Journal of the American Chemical Society* **2016**, *138* (44), 14750–14755. https://doi.org/10.1021/jacs.6b09257.

272. Chen, Z.; Wang, J. J.; Ren, Y.; Yu, C.; Shum, K. *Applied Physics Letters* **2012**, *101* (9), 093901. https://doi.org/10.1063/1.4748888.

273. Chung, I.; Lee, B.; He, J.; Chang, R. P. H.; Kanatzidis, M. G. *Nature* **2012**, *485* (7399), 486–489. https://doi.org/10.1038/nature11067.

274. Sabba, D.; Mulmudi, H. K.; Prabhakar, R. R.; Krishnamoorthy, T.; Baikie, T.; Boix, P. P.; Mhaisalkar, S.; Mathews, N. *Journal of Physical Chemistry C* **2015**, *119* (4), 1763–1767. https://doi.org/10.1021/jp5126624.

275. Kumar, M. H.; Dharani, S.; Leong, W. L.; Boix, P. P.; Prabhakar, R. R.; Baikie, T.; Shi, C.; Ding, H.; Ramesh, R.; Asta, M.; Graetzel, M.; Mhaisalkar, S. G.; Mathews, N. *Advanced Materials* **2014**, *26* (41), 7122–7127. https://doi.org/10.1002/adma.201401991.

276. Li, F.; Zhang, C.; Huang, J. H.; Fan, H.; Wang, H.; Wang, P.; Zhan, C.; Liu, C. M.; Li, X.; Yang, L. M.; Song, Y.; Jiang, K. J. *Angewandte Chemie - International Edition* **2019**, *58* (20), 6688–6692. https://doi.org/10.1002/anie.201902418.

277. Marshall, K. P.; Walton, R. I.; Hatton, R. A. *Journal of Materials Chemistry A* **2015**, *3* (21), 11631–11640. https://doi.org/10.1039/c5ta02950c.

278. Chen, L. J.; Lee, C. R.; Chuang, Y. J.; Wu, Z. H.; Chen, C. *Journal of Physical Chemistry Letters* **2016**, *7* (24), 5028–5035. https://doi.org/10.1021/acs.jpclett.6b02344.

279. Hong, W. L.; Huang, Y. C.; Chang, C. Y.; Zhang, Z. C.; Tsai, H. R.; Chang, N. Y.; Chao, Y. C. *Advanced Materials* **2016**, *28* (36), 8029–8036. https://doi.org/10.1002/adma.201601024.

280. Xing, G.; Kumar, M. H.; Chong, W. K.; Liu, X.; Cai, Y. *Advanced Materials* **2016**, *28* (37), 8191–8196. https://doi.org/10.1002/adma.201601418.

281. Umari, P.; Mosconi, E.; De Angelis, F. *Scientific Reports* **2014**, *4* (1), 1–7. https://doi.org/10.1038/srep04467.

282. Parrott, E. S.; Milot, R. L.; Stergiopoulos, T.; Snaith, H. J.; Johnston, M. B.; Herz, L. M. *Journal of Physical Chemistry Letters* **2016**, *7* (7), 1321–1326. https://doi.org/10.1021/acs.jpclett.6b00322.

283. Hao, F.; Stoumpos, C. C.; Chang, R. P. H.; Kanatzidis, M. G. *Journal of the American Chemical Society* **2014**, *136* (22), 8094–8099. https://doi.org/10.1021/ja5033259.

284. Hasegawa, H.; Kobayashi, K.; Takahashi, Y.; Harada, J.; Inabe, T. *Journal of Materials Chemistry C* **2017**, *5* (16), 4048–4052. https://doi.org/10.1039/c7tc00446j.

285. Roknuzzaman, M.; Ostrikov, K. (Ken); Chandula Wasalathilake, K.; Yan, C.; Wang, H.; Tesfamichael, T. *Organic Electronics* **2018**, *59* (February), 99–106. https://doi.org/10.1016/j.orgel.2018.04.051.

286. Yokoyama, T.; Cao, D. H.; Stoumpos, C. C.; Song, T. Bin; Sato, Y.; Aramaki, S.; Kanatzidis, M. G. *Journal of Physical Chemistry Letters* **2016**, *7* (5), 776–782. https://doi.org/10.1021/acs.jpclett.6b00118.

287. Hao, F.; Stoumpos, C. C.; Guo, P.; Zhou, N.; Marks, T. J.; Chang, R. P. H.; Kanatzidis, M. G. *Journal of the American Chemical Society* **2015**, *137* (35), 11445–11452. https://doi.org/10.1021/jacs.5b06658.

288. Jung, M. C.; Raga, S. R.; Qi, Y. *RSC Advances* **2016**, *6* (4), 2819–2825. https://doi.org/10.1039/c5ra21291j.

289. Baig, F.; Khattak, Y. H.; Marí, B.; Beg, S.; Ahmed, A.; Khan, K. *Journal of Electronic Materials* **2018**, *47* (9), 5275–5282. https://doi.org/10.1007/s11664-018-6406-3.

290. Yang, Z.; Wang, Y.; Liu, Y. *Applied Surface Science* **2018**, *441* (May), 394–400. https://doi.org/10.1016/j.apsusc.2018.02.038.

291. Zhang, M.; Lyu, M.; Yun, J. H.; Noori, M.; Zhou, X.; Cooling, N. A.; Wang, Q.; Yu, H.; Dastoor, P. C.; Wang, L. *Nano Research* **2016**, *9* (6), 1570–1577. https://doi.org/10.1007/s12274-016-1051-8.

292. Ferrara, C.; Patrini, M.; Pisanu, A.; Quadrelli, P.; Milanese, C.; Tealdia, C.; Malavasi, L. *Journal of Materials Chemistry* **2017**, *5* (19), 9391–9395. https://doi.org/10.1039/C7TA01668A.

293. Lee, S. J.; Shin, S. S.; Im, J.; Ahn, T. K.; Noh, J. H.; Jeon, N. J.; Seok, S. Il; Seo, J. *ACS Energy Letters* **2018**, *3* (1), 46–53. https://doi.org/10.1021/acsenergylett.7b00976.

294. Shi, T.; Zhang, H. S.; Meng, W.; Teng, Q.; Liu, M.; Yang, X.; Yan, Y.; Yip, H. L.; Zhao, Y. J. *Journal of Materials Chemistry A* **2017**, *5* (29), 15124–15129. https://doi.org/10.1039/c7ta02662e.

295. Dang, Y.; Zhou, Y.; Liu, X.; Ju, D.; Xia, S.; Xia, H.; Tao, X. *Angewandte Chemie - International Edition* **2016**, *55* (10), 3447–3450. https://doi.org/10.1002/anie.201511792.

296. Wang, F.; Ma, J.; Xie, F.; Li, L.; Chen, J.; Fan, J.; Zhao, N. *Advanced Functional Materials* **2016**, *26* (20), 3417–3423. https://doi.org/10.1002/adfm.201505127.

297. Lee, S. J.; Shin, S. S.; Kim, Y. C.; Kim, D.; Ahn, T. K.; Noh, J. H.; Seo, J.; Seok, S. Il. *Journal of the American Chemical Society* **2016**, *138* (12), 3974–3977. https://doi.org/10.1021/jacs.6b00142.

298. Liao, W.; Zhao, D.; Yu, Y.; Grice, C. R.; Wang, C.; Cimaroli, A. J.; Schulz, P.; Meng, W.; Zhu, K.; Xiong, R. G.; Yan, Y. *Advanced Materials* **2016**, *28* (42), 9333–9340. https://doi.org/10.1002/adma.201602992.

299. Zhu, Z.; Chueh, C. C.; Li, N.; Mao, C.; Jen, A. K. Y. *Advanced Materials* **2018**, *30* (6), 1703800. https://doi.org/10.1002/adma.201703800.

300. Cao, J.; Tai, Q.; You, P.; Tang, G.; Wang, T.; Wang, N.; Yan, F. *Journal of Materials Chemistry A* **2019**, *7* (46), 26580–26585. https://doi.org/10.1039/c9ta08679j.

301. Wu, T.; Liu, X.; He, X.; Wang, Y.; Meng, X.; Noda, T.; Yang, X.; Han, L. *Science China Chemistry* **2020**, *63* (1), 107–115. https://doi.org/10.1007/s11426-019-9653-8.

302. Meng, X.; Wu, T.; Liu, X.; He, X.; Noda, T.; Wang, Y.; Segawa, H.; Han, L. *Journal of Physical Chemistry Letters* **2020**, *11* (8), 2965–2971. https://doi.org/10.1021/acs.jpclett.0c00923.

303. Wang, M.; Wang, W.; Ma, B.; Shen, W.; Liu, L.; Cao, K.; Chen, S.; Huang, W. *Nano-Micro Letters* **2021**, *62* (13), 1–36. https://doi.org/https://doi.org/10.1007/s40820-020-00578-z.

304. Liu, X.; Yan, K.; Tan, D.; Liang, X.; Zhang, H.; Huang, W. *ACS Energy Letters* **2018**, *3* (11), 2701–2707. https://doi.org/10.1021/acsenergylett.8b01588.

305. Wang, C.; Gu, F.; Zhao, Z.; Rao, H.; Qiu, Y.; Cai, Z.; Zhan, G.; Li, X.; Sun, B.; Yu, X.; Zhao, B.; Liu, Z.; Bian, Z.; Huang, C. *Advanced Materials* **2020**, *32* (31), 1907623. https://doi.org/10.1002/adma.201907623.

306. Milot, R. L.; Eperon, G. E.; Green, T.; Snaith, H. J.; Johnston, M. B.; Herz, L. M. *Journal of Physical Chemistry Letters* **2016**, *7* (20), 4178–4184. https://doi.org/10.1021/acs.jpclett.6b02030.

307. Zhao, Z.; Gu, F.; Li, Y.; Sun, W.; Ye, S.; Rao, H.; Liu, Z.; Bian, Z.; Huang, C. *Advanced Science* **2017**, *4* (11), 1700204. https://doi.org/10.1002/advs.201700204.

308. Ke, W.; Stoumpos, C. C.; Zhu, M.; Mao, L.; Spanopoulos, I.; Liu, J.; Kontsevoi, O. Y.; Chen, M.; Sarma, D.; Zhang, Y.; Wasielewski, M. R.; Kanatzidis, M. G. *Science Advances* **2017**, *3* (8), 1–10. https://doi.org/10.1126/sciadv.1701293.

309. Ke, W.; Stoumpos, C. C.; Spanopoulos, I.; Mao, L.; Chen, M.; Wasielewski, M. R.; Kanatzidis, M. G. *Journal of the American Chemical Society* **2017**, *139* (41), 14800–14806. https://doi.org/10.1021/jacs.7b09018.

310. Ke, W.; Stoumpos, C. C.; Spanopoulos, I.; Chen, M.; Wasielewski, M. R.; Kanatzidis, M. G. *ACS Energy Letters* **2018**, *3* (7), 1470–1476. https://doi.org/10.1021/acsenergylett.8b00687.

311. Stoumpos, C. C.; Cao, D. H.; Clark, D. J.; Young, J.; Rondinelli, J. M.; Jang, J. I.; Hupp, J. T.; Kanatzidis, M. G. *Chemistry of Materials* **2016**, *28* (8), 2852–2867. https://doi.org/10.1021/acs.chemmater.6b00847.

312. Calabrese, J.; Jones, N. L.; Harlow, R. L.; Herron, N.; Thorn, D. L.; Wang, Y. *Journal of the American Chemical Society* **1991**, *113* (6), 2328–2330. https://doi.org/https://doi.org/10.1021/ja00006a076.

313. Cao, D. H.; Stoumpos, C. C.; Yokoyama, T.; Logsdon, J. L.; Song, T.-B.; Farha, O. K.; Wasielewski, M. R.; Hupp, J. T.; Kanatzidis, M. G. *ACS Energy Letters* **2017**, *2* (5), 982–990. https://doi.org/10.1021/acsenergylett.7b00202.

314. Liao, Y.; Liu, H.; Zhou, W.; Yang, D.; Shang, Y.; Shi, Z.; Li, B.; Jiang, X.; Zhang, L.; Quan, L. N.; Quintero-Bermudez, R.; Sutherland, B. R.; Mi, Q.; Sargent, E. H.; Ning, Z. *Journal of the American Chemical Society* **2017**, *139* (19), 6693–6699. https://doi.org/10.1021/jacs.7b01815.

315. Qiu, J.; Xia, Y.; Zheng, Y.; Hui, W.; Gu, H.; Yuan, W.; Yu, H.; Chao, L.; Niu, T.; Yang, Y.; Gao, X.; Chen, Y.; Huang, W. *ACS Energy Letters* **2019**, *4* (7), 1513–1520. https://doi.org/10.1021/acsenergylett.9b00954.

316. Xu, H.; Jiang, Y.; He, T.; Li, S.; Wang, H.; Chen, Y.; Yuan, M.; Chen, J. *Advanced Functional Materials* **2019**, *29* (47), 1807696. https://doi.org/10.1002/adfm.201807696.

317. Chen, M.; Ju, M. G.; Hu, M.; Dai, Z.; Hu, Y.; Rong, Y.; Han, H.; Zeng, X. C.; Zhou, Y.; Padture, N. P. *ACS Energy Letters* **2019**, *4* (1), 276–277. https://doi.org/10.1021/acsenergylett.8b02051.

318. Cohen, B. El; Li, Y.; Meng, Q.; Etgar, L. *Nano Letters* **2019**, *19* (4), 2588–2597. https://doi.org/10.1021/acs.nanolett.9b00387.

319. Zhang, X.; Wu, G.; Fu, W.; Qin, M.; Yang, W.; Yan, J.; Zhang, Z.; Lu, X.; Chen, H. *Advanced Energy Materials* **2018**, *8* (14), 1–9. https://doi.org/10.1002/aenm.201702498.

320. Ma, C.; Shen, D.; Ng, T. W.; Lo, M. F.; Lee, C. S. *Advanced Materials* **2018**, *30* (22), 1800710. https://doi.org/10.1002/adma.201800710.

321. Kieslich, G.; Sun, S.; Cheetham, A. K. *Chemical Science* **2014**, *5* (12), 4712–4715. https://doi.org/10.1039/c4sc02211d.

322. Shao, S.; Liu, J.; Portale, G.; Fang, H. H.; Blake, G. R.; ten Brink, G. H.; Koster, L. J. A.; Loi, M. A. *Advanced Energy Materials* **2018**, *8* (4), 1702019. https://doi.org/10.1002/aenm.201702019.

323. Jiang, X.; Wang, F.; Wang, C.; Cheng, P.; Chen, Q.; Chen, L. *Nature Communications* **2020**, *11* (1), 1–7. https://doi.org/10.1038/s41467-020-15078-2.

324. Song, T. Bin; Yokoyama, T.; Aramaki, S.; Kanatzidis, M. G. *ACS Energy Letters* **2017**, *2* (4), 897–903. https://doi.org/10.1021/acsenergylett.7b00171.

325. Li, J.; Duan, J.; Yang, X.; Duan, Y.; Yang, P.; Tang, Q. *Nano Energy* **2021**, *80* (October), 105526. https://doi.org/10.1016/j.nanoen.2020.105526.

326. Dharani, S.; Mulmudi, H. K.; Yantara, N.; Thu Trang, P. T.; Park, N. G.; Graetzel, M.; Mhaisalkar, S.; Mathews, N.; Boix, P. P. *Nanoscale* **2014**, *6* (3), 1675–1679. https://doi.org/10.1039/c3nr04857h.

327. Koh, T. M.; Krishnamoorthy, T.; Yantara, N.; Shi, C.; Leong, W. L.; Boix, P. P.; Grimsdale, A. C.; Mhaisalkar, S. G.; Mathews, N. *Journal of Materials Chemistry A* **2015**, *3* (29), 14996–15000. https://doi.org/10.1039/c5ta00190k.

328. Zhou, Y.; Garces, H. F.; Senturk, B. S.; Ortiz, A. L.; Padture, N. P. *Materials Letters* **2013**, *110* (November), 127–129. https://doi.org/10.1016/j.matlet.2013.08.011.

329. Kim, H. Do; Miyamoto, Y.; Kubota, H.; Yamanari, T.; Ohkita, H. *Chemistry Letters* **2017**, *46* (2), 253–256. https://doi.org/10.1246/cl.160994.

330. Handa, T.; Yamada, T.; Kubota, H.; Ise, S.; Miyamoto, Y.; Kanemitsu, Y. *Journal of Physical Chemistry C* **2017**, *121* (30), 16158–16165. https://doi.org/10.1021/acs.jpcc.7b06199.

331. Ke, W.; Priyanka, P.; Vegiraju, S.; Stoumpos, C. C.; Spanopoulos, I.; Soe, C. M. M.; Marks, T. J.; Chen, M. C.; Kanatzidis, M. G. *Journal of the American Chemical Society* **2018**, *140* (1), 388–393. https://doi.org/10.1021/jacs.7b10898.

332. Yokoyama, T.; Song, T. Bin; Cao, D. H.; Stoumpos, C. C.; Aramaki, S.; Kanatzidis, M. G. *ACS Energy Letters* **2017**, *2* (1), 22–28. https://doi.org/10.1021/acsenergylett.6b00513.

333. Tsai, C. M.; Lin, Y. P.; Pola, M. K.; Narra, S.; Jokar, E.; Yang, Y. W.; Diau, E. W. G. *ACS Energy Letters* **2018**, *3* (9), 2077–2085. https://doi.org/10.1021/acsenergylett.8b01046.

334. Jokar, E.; Chien, C. H.; Tsai, C. M.; Fathi, A.; Diau, E. W. G. *Advanced Materials* **2019**, *31* (2), 1–7. https://doi.org/10.1002/adma.201804835.

335. Lin, Z.; Liu, C.; Liu, G.; Yang, J.; Duan, X.; Tan, L.; Chen, Y. *Chemical Communications* **2020**, *56* (28), 4007–4010. https://doi.org/10.1039/d0cc01106a.

336. Ke, W.; Stoumpos, C. C.; Logsdon, J. L.; Wasielewski, M. R.; Yan, Y.; Fang, G.; Kanatzidis, M. G. *Journal of the American Chemical Society* **2016**, *138* (45), 14998–15003. https://doi.org/10.1021/jacs.6b08790.

337. Liu, X.; Yang, Z.; Chueh, C. C.; Rajagopal, A.; Williams, S. T.; Sun, Y.; Jen, A. K. Y. *Journal of Materials Chemistry A* **2016**, *4* (46), 17939–17945. https://doi.org/10.1039/c6ta07712a.

338. Wang, F.; Jiang, X.; Chen, H.; Shang, Y.; Liu, H.; Wei, J.; Zhou, W.; He, H.; Liu, W.; Ning, Z. *Joule* **2018**, *2* (12), 2732–2743. https://doi.org/10.1016/j.joule.2018.09.012.

339. Tsai, C. M.; Mohanta, N.; Wang, C. Y.; Lin, Y. P.; Yang, Y. W.; Wang, C. L.; Hung, C. H.; Diau, E. W. G. *Angewandte Chemie - International Edition* **2017**, *56* (44), 13819–13823. https://doi.org/10.1002/anie.201707037.

340. Li, W.; Li, J.; Li, J.; Fan, J.; Mai, Y.; Wang, L. *Journal of Materials Chemistry A* **2016**, *4* (43), 17104–17110. https://doi.org/10.1039/c6ta08332c.

341. Chen, K.; Wu, P.; Yang, W.; Su, R.; Luo, D.; Yang, X.; Tu, Y.; Zhu, R.; Gong, Q. *Nano Energy* **2018**, *49* (March), 411–418. https://doi.org/10.1016/j.nanoen.2018.05.006.

342. Jokar, E.; Chien, C. H.; Fathi, A.; Rameez, M.; Chang, Y. H.; Diau, E. W. G. *Energy and Environmental Science* **2018**, *11* (9), 2353–2362. https://doi.org/10.1039/c8ee00956b.

343. Meng, X.; Wang, Y.; Lin, J.; Liu, X.; He, X.; Barbaud, J.; Wu, T.; Noda, T.; Yang, X.; Han, L. *Joule* **2020**, *4* (4), 902–912. https://doi.org/10.1016/j.joule.2020.03.007.

344. Moyez, S. A.; Roy, S. *Journal of Nanoparticle Research* **2018**, *20* (1), 5. https://doi.org/10.1007/s11051-017-4108-z.

345. Wang, N.; Zhou, Y.; Ju, M.-G.; Garces, H. F.; Ding, T.; Pang, S.; Zeng, X. C.; Padture, N. P.; Sun, X. W. *Advanced Energy Materials* **2016**, *6* (24), 1601130. https://doi.org/10.1002/aenm.201601130.

346. Zhao, B.; Abdi-Jalebi, M.; Tabachnyk, M. *Advanced Materials* **2017**, *29* (2), 1604744. https://doi.org/10.1002/adma.201604744.

347. Shum, K.; Chen, Z.; Qureshi, J.; Yu, C.; Wang, J. J.; Pfenninger, W.; Vockic, N.; Midgley, J.; Kenney, J. T. *Applied Physics Letters* **2010**, *96* (22), 1–4. https://doi.org/10.1063/1.3442511.

348. Xi, J.; Wu, Z.; Jiao, B.; Dong, H.; Ran, C.; Piao, C.; Lei, T.; Song, T. Bin; Ke, W.; Yokoyama, T.; Hou, X.; Kanatzidis, M. G. *Advanced Materials* **2017**, *29* (23), 1606964. https://doi.org/10.1002/adma.201606964.

349. Moghe, D.; Wang, L.; Traverse, C. J.; Redoute, A.; Sponseller, M.; Brown, P. R.; Bulović, V.; Lunt, R. R. *Nano Energy* **2016**, *28* (October), 469–474. https://doi.org/10.1016/j.nanoen.2016.09.009.

350. Ran, C.; Xi, J.; Gao, W.; Yuan, F.; Lei, T.; Jiao, B.; Hou, X.; Wu, Z. *ACS Energy Letters* **2018**, *3* (3), 713–721. https://doi.org/10.1021/acsenergylett.8b00085.

351. Yu, Y.; Zhao, D.; Grice, C. R.; Meng, W.; Wang, C.; Liao, W.; Cimaroli, A. J.; Zhang, H.; Zhu, K.; Yan, Y. *RSC Advances* **2016**, *6* (93), 90248–90254. https://doi.org/10.1039/c6ra19476a.

352. Sun, P. P.; Li, Q. S.; Yang, L. N.; Li, Z. S. *Nanoscale* **2016**, *8* (3), 1503–1512. https://doi.org/10.1039/c5nr05337d.

353. Thirumal, K.; Hong, D.; Chen, Y.; Wei, L. L.; Tom, B.; Ziyi, Z.; Matthew, S.; Shuzhou, L.; Mark, A.; Nripan, M.; Subodh G., M. *Journal of Materials Chemistry A* **2013**, *3* (47), 23829–23832. https://doi.org/10.1039/C5TA05741H.

354. Stoumpos, C. C.; Frazer, L.; Clark, D. J.; Kim, Y. S.; Rhim, S. H.; Freeman, A. J.; Ketterson, J. B.; Jang, J. I.; Kanatzidis, M. G. *Journal of the American Chemical Society* **2015**, *137* (21), 6804–6819. https://doi.org/10.1021/jacs.5b01025.

355. Xiao, Z.; Meng, W.; Saparov, B.; Duan, H. S.; Wang, C.; Feng, C.; Liao, W.; Ke, W.; Zhao, D.; Wang, J.; Mitzi, D. B.; Yan, Y. *Journal of Physical Chemistry Letters* **2016**, *7* (7), 1213–1218. https://doi.org/10.1021/acs.jpclett.6b00248.

356. Cui, X. P.; Jiang, K. J.; Huang, J. H.; Zhang, Q. Q.; Su, M. J.; Yang, L. M.; Song, Y. L.; Zhou, X. Q. *Synthetic Metals* **2015**, *209* (November), 247–250. https://doi.org/10.1016/j.synthmet.2015.07.013.

357. Li, X.; Li, B.; Chang, J.; Ding, B.; Zheng, S.; Wu, Y.; Yang, J.; Yang, G.; Zhong, X.; Wang, J. *ACS Applied Energy Materials* **2018**, *1* (6), 2709–2716. https://doi.org/10.1021/acsaem.8b00372.

358. Ming, W.; Shi, H.; Du, M. H. *Journal of Materials Chemistry A* **2016**, *4* (36), 13852–13858. https://doi.org/10.1039/c6ta04685a.

359. Krishnamoorthy, T.; Ding, H.; Yan, C.; Leong, W. L.; Baikie, T.; Zhang, Z.; Sherburne, M.; Li, S.; Asta, M.; Mathews, N.; Mhaisalkar, S. G. *Journal of Materials Chemistry A* **2015**, *3* (47), 23829–23832. https://doi.org/10.1039/c5ta05741h.

360. Kopacic, I.; Friesenbichler, B.; Hoefler, S. F.; Kunert, B.; Plank, H.; Rath, T.; Trimmel, G. *ACS Applied Energy Materials* **2018**, *1* (2), 343–347. https://doi.org/10.1021/acsaem.8b00007.

361. Ju, M. G.; Dai, J.; Ma, L.; Zeng, X. C. *Journal of the American Chemical Society* **2017**, *139* (23), 8038–8043. https://doi.org/10.1021/jacs.7b04219.

362. Nagane, S.; Ghosh, D.; Hoye, R. L. Z.; Zhao, B.; Ahmad, S.; Walker, A. B.; Saiful Islam, M.; Ogale, S.; Sadhanala, A. *Journal of Physical Chemistry C* **2018**, *122* (11), 5940–5947. https://doi.org/10.1021/acs.jpcc.8b00480.

363. Ito, N.; Kamarudin, M. A.; Hirotani, D.; Zhang, Y.; Shen, Q.; Ogomi, Y.; Iikubo, S.; Minemoto, T.; Yoshino, K.; Hayase, S. *Journal of Physical Chemistry Letters* **2018**, *9* (7), 1682–1688. https://doi.org/10.1021/acs.jpclett.8b00275.

364. Ng, C. H.; Nishimura, K.; Ito, N.; Hamada, K.; Hirotani, D.; Wang, Z.; Yang, F.; likubo, S.; Shen, Q.; Yoshino, K.; Minemoto, T.; Hayase, S. *Nano Energy* **2019**, *58* (January), 130–137. https://doi.org/10.1016/j.nanoen.2019.01.026.

365. Cortecchia, D.; Dewi, H. A.; Yin, J.; Bruno, A.; Chen, S.; Baikie, T.; Boix, P. P.; Grätzel, M.; Mhaisalkar, S.; Soci, C.; Mathews, N. *Inorganic Chemistry* **2016**, *55* (3), 1044–1052. https://doi.org/10.1021/acs.inorgchem.5b01896.

366. Mostafa, M. F.; Willett, R. D. *Physical Review B* **1971**, *4* (7), 2213–2215. https://doi.org/10.1103/PhysRevB.4.2213.

367. Huang, T. J.; Thiang, Z. X.; Yin, D. X.; Tang, D. C.; Qi, D. G.; Gong, P. H. *Chemistry - A European Journal* **2016**, *22* (6), 2146–2152. https://doi.org/10.1002/chem.201503680.

368. Filip, M. R.; Giustino, F. *Journal of Physical Chemistry C* **2016**, *120* (1), 166–173. https://doi.org/10.1021/acs.jpcc.5b11845.

369. Pazoki, M.; Jacobsson, T. J.; Hagfeldt, A.; Boschloo, G.; Edvinsson, T. *Physical Review B* **2016**, *93* (14), 1–10. https://doi.org/10.1103/PhysRevB.93.144105.

370. Uribe, J. I.; Ramirez, D.; Osorio-Guillén, J. M.; Osorio, J.; Jaramillo, F. *Journal of Physical Chemistry C* **2016**, *120* (30), 16393–16398. https://doi.org/10.1021/acs.jpcc.6b04207.

371. Sakai, N.; Haghighirad, A. A.; Filip, M. R.; Nayak, P. K.; Nayak, S.; Ramadan, A.; Wang, Z.; Giustino, F.; Snaith, H. J. *Journal of the American Chemical Society* **2017**, *139* (17), 6030–6033. https://doi.org/10.1021/jacs.6b13258.

372. Qiu, X.; Jiang, Y.; Zhang, H.; Qiu, Z.; Yuan, S.; Wang, P.; Cao, B. *Physica Status Solidi - Rapid Research Letters* **2016**, *10* (8), 587–591. https://doi.org/10.1002/pssr.201600166.

373. Chen, M.; Ju, M. G.; Carl, A. D.; Zong, Y.; Grimm, R. L.; Gu, J.; Zeng, X. C.; Zhou, Y.; Padture, N. P. *Joule* **2018**, *2* (3), 558–570. https://doi.org/10.1016/j.joule.2018.01.009.

374. Qiu, X.; Cao, B.; Yuan, S.; Chen, X.; Qiu, Z.; Jiang, Y.; Ye, Q.; Wang, H.; Zeng, H.; Liu, J.; Kanatzidis, M. G. *Solar Energy Materials and Solar Cells* **2017**, *159* (January), 227–234. https://doi.org/10.1016/j.solmat.2016.09.022.

375. Lee, B.; Krenselewski, A.; Baik, S. Il; Seidman, D. N.; Chang, R. P. H. *Sustainable Energy and Fuels* **2017**, *1* (4), 710–724. https://doi.org/10.1039/c7se00100b.

376. Lee, B.; Stoumpos, C. C.; Zhou, N.; Hao, F.; Malliakas, C.; Yeh, C. Y.; Marks, T. J.; Kanatzidis, M. G.; Chang, R. P. H. *Journal of the American Chemical Society* **2014**, *136* (43), 15379–15385. https://doi.org/10.1021/ja508464w.

377. Schwartz, D.; Murshed, R.; Larson, H.; Usprung, B.; Soltanmohamad, S.; Pandey, R.; Barnard, E. S.; Rockett, A.; Hartmann, T.; Castelli, I. E.; Bansal, S. *Physica Status Solidi - Rapid Research Letters* **2020**, *14* (8), 2000182. https://doi.org/10.1002/pssr.202000182.

378. Kawai, T.; Ishii, A.; Kitamuha, T.; Shimanuki, S.; Iwata, M.; Ishibashi, Y. *Journal of the Physical Society of Japan* **1996**, *65* (5), 1464–1468. https://doi.org/10.1143/JPSJ.65.1464.

379. Kawai, T.; Shimanuki, S. *Physica Status Solidi (B)* **1993**, *177* (1), K43–K45. https://doi.org/10.1002/pssb.2221770128.

380. Arakcheeva, A.; Bonin, M.; Chapuis, G.; Zaitsev, A. *Crystalline Materials* **1999**, *214* (5), 279–283. https://doi.org/10.1524/zkri.1999.214.5.279.

381. Szklarz, P.; Pietraszko, A.; Jakubas, R.; Bator, G.; Zieliński, P.; Gałazka, M. *Journal of Physics Condensed Matter* **2008**, *20* (25), 255221. https://doi.org/10.1088/0953-8984/20/25/255221.

382. Chang, J. H.; Doert, T.; Ruck, M. *Zeitschrift fur Anorganische und Allgemeine Chemie* **2016**, *642* (13), 736–748. https://doi.org/10.1002/zaac.201600179.

383. Park, B. W.; Philippe, B.; Zhang, X.; Rensmo, H.; Boschloo, G.; Johansson, E. M. J. *Advanced Materials* **2015**, *27* (43), 6806–6813. https://doi.org/10.1002/adma.201501978.

384. Eckhardt, K.; Bon, V.; Getzschmann, J.; Grothe, J.; Wisser, F. M.; Kaskel, S. *Chemical Communications* **2016**, *52* (14), 3058–3060. https://doi.org/10.1039/c5cc10455f.

385. Zhang, Y.; Yin, J.; Parida, M. R.; Ahmed, G. H.; Pan, J.; Bakr, O. M.; Brédas, J. L.; Mohammed, O. F. *Journal of Physical Chemistry Letters* **2017**, *8* (14), 3173–3177. https://doi.org/10.1021/acs.jpclett.7b01381.

386. Ghosh, B.; Chakraborty, S.; Wei, H.; Guet, C.; Li, S.; Mhaisalkar, S.; Mathews, N. *Journal of Physical Chemistry C* **2017**, *121* (32), 17062–17067. https://doi.org/10.1021/acs.jpcc.7b03501.

387. Pazoki, M.; Johansson, M. B.; Zhu, H.; Broqvist, P.; Edvinsson, T.; Boschloo, G.; Johansson, E. M. J. *Journal of Physical Chemistry C* **2016**, *120* (51), 29039–29046. https://doi.org/10.1021/acs.jpcc.6b11745.

388. Hoye, R. L. Z.; Brandt, R. E.; Osherov, A.; Stevanovic, V.; Stranks, S. D.; Wilson, M. W. B.; Kim, H.; Akey, A. J.; Perkins, J. D.; Kurchin, R. C.; Poindexter, J. R.; Wang, E. N.; Bawendi, M. G.; Bulovic, V.; Buonassisi, T. *Chemistry - A European Journal* **2016**, *22* (8), 2605–2610. https://doi.org/10.1002/chem.201505055.

389. Ghosh, B.; Wu, B.; Mulmudi, H. K.; Guet, C.; Weber, K.; Sum, T. C.; Mhaisalkar, S.; Mathews, N. *ACS Applied Materials and Interfaces* **2018**, *10* (41), 35000–35007. https://doi.org/10.1021/acsami.7b14735.

390. Huang, X.; Huang, S.; Biswas, P.; Mishra, R. *Journal of Physical Chemistry C* **2016**, *120* (51), 28924–28932. https://doi.org/10.1021/acs.jpcc.6b09567.

391. Shin, S. S.; Correa Baena, J. P.; Kurchin, R. C.; Polizzotti, A.; Yoo, J. J.; Wieghold, S.; Bawendi, M. G.; Buonassisi, T. *Chemistry of Materials* **2018**, *30* (2), 336–343. https://doi.org/10.1021/acs.chemmater.7b03227.

392. Bai, F.; Hu, Y.; Hu, Y.; Qiu, T.; Miao, X.; Zhang, S. *Solar Energy Materials and Solar Cells* **2018**, *184* (January), 15–21. https://doi.org/10.1016/j.solmat.2018.04.032.

393. Ran, C.; Wu, Z.; Xi, J.; Yuan, F.; Dong, H.; Lei, T.; He, X.; Hou, X. *Journal of Physical Chemistry Letters* **2017**, *8* (2), 394–400. https://doi.org/10.1021/acs.jpclett.6b02578.

394. Chakraborty, S.; Cameau, M.; Zhu, H.; Ahuja, R.; Boschloo, G. *Inorganic Chemistry* **2019**, *58* (18), 12040–12052. https://doi.org/10.1021/acs.inorgchem.9b01233.

395. Jain, S. M.; Phuyal, D.; Davies, M. L.; Li, M.; Philippe, B.; De Castro, C.; Qiu, Z.; Kim, J.; Watson, T.; Tsoi, W. C.; Karis, O.; Rensmo, H.; Boschloo, G.; Edvinsson, T.; Durrant, J. R. *Nano Energy* **2018**, *49* (May), 614–624. https://doi.org/10.1016/j.nanoen.2018.05.003.

396. Saparov, B.; Hong, F.; Sun, J. P.; Duan, H. S.; Meng, W.; Cameron, S.; Hill, I. G.; Yan, Y.; Mitzi, D. B. *Chemistry of Materials* **2015**, *27* (16), 5622–5632. https://doi.org/10.1021/acs.chemmater.5b01989.

397. Hebig, J. C.; Kühn, I.; Flohre, J.; Kirchartz, T. *ACS Energy Letters* **2016**, *1* (1), 309–314. https://doi.org/10.1021/acsenergylett.6b00170.

398. Boopathi, K. M.; Karuppuswamy, P.; Singh, A.; Hanmandlu, C.; Lin, L.; Abbas, S. A.; Chang, C. C.; Wang, P. C.; Li, G.; Chu, C. W. *Journal of Materials Chemistry A* **2017**, *5* (39), 20843–20850. https://doi.org/10.1039/c7ta06679a.

399. Ahmad, K.; Kumar, P.; Mobin, S. M. *ChemElectroChem* **2020**, *7* (4), 946–950. https://doi.org/10.1002/celc.201902107.

400. Umar, F.; Zhang, J.; Jin, Z.; Muhammad, I.; Yang, X.; Deng, H.; Jahangeer, K.; Hu, Q.; Song, H.; Tang, J. *Advanced Optical Materials* **2019**, *7* (5), 1801368. https://doi.org/10.1002/adom.201801368.

401. Harikesh, P. C.; Mulmudi, H. K.; Ghosh, B.; Goh, T. W.; Teng, Y. T.; Thirumal, K.; Lockrey, M.; Weber, K.; Koh, T. M.; Li, S.; Mhaisalkar, S.; Mathews, N. *Chemistry of Materials* **2016**, *28* (20), 7496–7504. https://doi.org/10.1021/acs.chemmater.6b03310.

402. Jiang, F.; Yang, D.; Jiang, Y.; Liu, T.; Zhao, X.; Ming, Y.; Luo, B.; Qin, F.; Fan, J.; Han, H.; Zhang, L.; Zhou, Y. *Journal of the American Chemical Society* **2018**, *140* (3), 1019–1027. https://doi.org/10.1021/jacs.7b10739.

403. Zuo, C.; Ding, P. L. *Angewandte Chemie* **2017**, *129* (55), 6628–6632. https://doi.org/10.1002/ange.201702265.

404. Zhang, Z.; Li, X.; Xia, X.; Wang, Z.; Huang, Z.; Lei, B.; Gao, Y. *Journal of Physical Chemistry Letters* **2017**, *8* (17), 4300–4307. https://doi.org/10.1021/acs.jpclett.7b01952.

405. Johansson, M. B.; Zhu, H.; Johansson, E. M. J. *Journal of Physical Chemistry Letters* **2016**, *7* (17), 3467–3471. https://doi.org/10.1021/acs.jpclett.6b01452.

406. Baranwal, A. K.; Masutani, H.; Sugita, H.; Kanda, H.; Kanaya, S.; Shibayama, N.; Sanehira, Y.; Ikegami, M.; Numata, Y.; Yamada, K.; Miyasaka, T.; Umeyama, T.; Imahori, H.; Ito, S. *Nano Convergence* **2017**, *4* (1), 26. https://doi.org/10.1186/s40580-017-0120-3.

407. Zhang, X.; Wu, G.; Gu, Z.; Guo, B.; Liu, W.; Yang, S.; Ye, T.; Chen, C.; Tu, W.; Chen, H. *Nano Research* **2016**, *9* (10), 2921–2930. https://doi.org/10.1007/s12274-016-1177-8.

408. Abulikemu, M.; Ould-Chikh, S.; Miao, X.; Alarousu, E.; Murali, B.; Ngongang Ndjawa, G. O.; Barbé, J.; El Labban, A.; Amassian, A.; Del Gobbo, S. *Journal of Materials Chemistry A* **2016**, *4* (32), 12504–12515. https://doi.org/10.1039/c6ta04657f.

409. Lyu, M.; Yun, J. H.; Cai, M.; Jiao, Y.; Bernhardt, P. V.; Zhang, M.; Wang, Q.; Du, A.; Wang, H.; Liu, G.; Wang, L. *Nano Research* **2016**, *9* (3), 692–702. https://doi.org/10.1007/s12274-015-0948-y.

410. Okano, T.; Suzuki, Y. *Materials Letters* **2017**, *191* (March), 77–79. https://doi.org/10.1016/j.matlet.2017.01.047.

411. Zhu, H.; Johansson, M. B.; Johansson, E. M. J. *ChemSusChem* **2018**, *11* (6), 1114–1120. https://doi.org/10.1002/cssc.201702169.

412. Ahmad, K.; Kumar, P.; Mobin, S. M. *Chemistry - An Asian Journal* **2020**, *15* (18), 2859–2863. https://doi.org/10.1002/asia.202000680.

413. Yu, B. Bin; Liao, M.; Yang, J.; Chen, W.; Zhu, Y.; Zhang, X.; Duan, T.; Yao, W.; Wei, S. H.; He, Z. *Journal of Materials Chemistry A* **2019**, *7* (15), 8818–8825. https://doi.org/10.1039/c9ta01978b.

414. Hu, W.; He, X.; Fang, Z.; Lian, W.; Shang, Y.; Li, X.; Zhou, W.; Zhang, M.; Chen, T.; Lu, Y.; Zhang, L.; Ding, L.; Yang, S. *Nano Energy* **2020**, *68* (February), 104362. https://doi.org/10.1016/j.nanoen.2019.104362.

415. Liang, G. X.; Chen, X. Y.; Chen, Z. H.; Lan, H. Bin; Zheng, Z. H.; Fan, P.; Tian, X. Q.; Duan, J. Y.; Wei, Y. D.; Su, Z. H. *Journal of Physical Chemistry C* **2019**, *123* (45), 27423 – 27428. https://doi.org/10.1021/acs.jpcc.9b09617.

416. Ghosh, B.; Wu, B.; Guo, X.; Harikesh, P. C.; John, R. A.; Baikie, T.; Arramel; Wee, A. T. S.; Guet, C.; Sum, T. C.; Mhaisalkar, S.; Mathews, N. *Advanced Energy Materials* **2018**, *8* (33), 1802051. https://doi.org/10.1002/aenm.201802051.

417. Kim, D. Y.; Yang, D. Z.; Jain, D. A.; Voznyy, D. O.; Kim, D. G.; Liu, D. M.; Quan, L. N. Q.; Arquer, D. F. P. G. de S.; James, D. R. C.; Fan, Z.; H., P. D. E. *Angewandte Chemie - International Edition* **2016**, *55* (33), 9586–9590. https://doi.org/10.1002/anie.201603608.

418. Shao, Z.; Le Mercier, T.; Madec, M. B.; Pauporté, T. *Materials Letters* **2018**, *221* (June), 135–138. https://doi.org/10.1016/j.matlet.2018.03.085.

419. Kulkarni, A.; Jena, A. K.; Ikegami, M.; Miyasaka, T. *Chemical Communications* **2019**, *55* (28), 4031–4034. https://doi.org/10.1039/c9cc00733d.

420. Khazaee, M.; Sardashti, K.; Chung, C. C.; Sun, J. P.; Zhou, H.; Bergmann, E.; Dunlap-Shohl, W. A.; Han, Q.; Hill, I. G.; Jones, J. L.; Lupascu, D. C.; Mitzi, D. B. *Journal of Materials Chemistry A* **2019**, *7* (5), 2095–2105. https://doi.org/10.1039/c8ta08679f.

421. Li, T.; Hu, Y.; Morrison, C. A.; Wu, W.; Han, H.; Robertson, N. *Sustainable Energy and Fuels* **2017**, *1* (2), 308–316. https://doi.org/10.1039/c6se00061d.

422. Adonin, S. A.; Frolova, L. A.; Sokolov, M. N.; Shilov, G. V.; Korchagin, D. V.; Fedin, V. P.; Aldoshin, S. M.; Stevenson, K. J.; Troshin, P. A. *Advanced Energy Materials* **2018**, *8* (6), 1701140. https://doi.org/10.1002/aenm.201701140.

423. Nie, R.; Mehta, A.; Park, B. W.; Kwon, H. W.; Im, J.; Seok, S. Il. *Journal of the American Chemical Society* **2018**, *140* (3), 872–875. https://doi.org/10.1021/jacs.7b11332.

424. Greul, E.; Petrus, M. L.; Binek, A.; Docampo, P.; Bein, T. *Journal of Materials Chemistry A* **2017**, *5* (37), 19972–19981. https://doi.org/10.1039/c7ta06816f.

425. Wu, C.; Zhang, Q.; Liu, Y.; Luo, W.; Guo, X.; Huang, Z.; Ting, H.; Sun, W.; Zhong, X.; Wei, S.; Wang, S.; Chen, Z.; Xiao, L. *Advanced Science* **2018**, *5* (3), 1700759. https://doi.org/10.1002/advs.201700759.

426. Gao, W.; Ran, C.; Xi, J.; Jiao, B.; Zhang, W.; Wu, M.; Hou, X.; Wu, Z. *ChemPhysChem* **2018**, *19* (14), 1696–1700. https://doi.org/10.1002/cphc.201800346.

427. Wang, M.; Zeng, P.; Bai, S.; Gu, J.; Li, F.; Yang, Z.; Liu, M. *Solar RRL* **2018**, *2* (12), 1800217. https://doi.org/10.1002/solr.201800217.

428. Pantaler, M.; Cho, K. T.; Queloz, V. I. E.; García Benito, I.; Fettkenhauer, C.; Anusca, I.; Nazeeruddin, M. K.; Lupascu, D. C.; Grancini, G. *ACS Energy Letters* **2018**, *3* (8), 1781–1786. https://doi.org/10.1021/acsenergylett.8b00871.

429. Chen, C.; Han, T. H.; Han, T. H.; Tan, S.; Xue, J.; Zhao, Y.; Liu, Y.; Wang, H.; Hu, W.; Bao, C.; Mazzeo, M.; Wang, R.; Duan, Y.; Duan, Y.; Yang, Y. *Nano Letters* **2020**, *20* (6), 4673–4680. https://doi.org/10.1021/acs.nanolett.0c01550.

430. Zhang, Q.; Wu, C.; Qi, X.; Lv, F.; Zhang, Z.; Liu, Y.; Wang, S.; Qu, B.; Chen, Z.; Xiao, L. *ACS Applied Energy Materials* **2019**, *2* (5), 3651–3656. https://doi.org/10.1021/acsaem.9b00366.

431. Jung, K. W.; Sohn, M. R.; Lee, H. M.; Yang, I. S.; Sung, S. Do; Kim, J.; Wei-Guang Diau, E.; Lee, W. I. *Sustainable Energy and Fuels* **2018**, *2* (1), 294–302. https://doi.org/10.1039/c7se00477j.

432. Pai, N.; Lu, J.; Gengenbach, T. R.; Seeber, A.; Chesman, A. S. R.; Jiang, L.; Senevirathna, D. C.; Andrews, P. C.; Bach, U.; Cheng, Y. B.; Simonov, A. N. *Advanced Energy Materials* **2019**, *9* (5), 1–11. https://doi.org/10.1002/aenm.201803396.

433. Khazaee, M.; Sardashti, K.; Sun, J. P.; Zhou, H.; Clegg, C.; Hill, I. G.; Jones, J. L.; Lupascu, D. C.; Mitzi, D. B. *Chemistry of Materials* **2018**, *30* (10), 3538–3544. https://doi.org/10.1021/acs.chemmater.8b01341.

434. Zhu, H.; Pan, M.; Johansson, M. B.; Johansson, E. M. J. *ChemSusChem* **2017**, *10* (12), 2592–2596. https://doi.org/10.1002/cssc.201700634.

435. Sun, Y. Y.; Shi, J.; Lian, J.; Gao, W.; Agiorgousis, M. L.; Zhang, P.; Zhang, S. *Nanoscale* **2016**, *8* (12), 6284–6289. https://doi.org/10.1039/c5nr04310g.

436. Hong, F.; Saparov, B.; Meng, W.; Xiao, Z.; Mitzi, D. B.; Yan, Y. *Journal of Physical Chemistry C* **2016**, *120* (12), 6435–6441. https://doi.org/10.1021/acs.jpcc.6b00920.

437. Li, T.; Wang, X.; Yan, Y.; Mitzi, D. B. *Journal of Physical Chemistry Letters* **2018**, *9* (14), 3829–3833. https://doi.org/10.1021/acs.jpclett.8b01641.

438. Slavney, A. H.; Hu, T.; Lindenberg, A. M.; Karunadasa, H. I. *Journal of the American Chemical Society* **2016**, *138* (7), 2138–2141. https://doi.org/10.1021/jacs.5b13294.

439. McClure, E. T.; Ball, M. R.; Windl, W.; Woodward, P. M. *Chemistry of Materials* **2016**, *28* (5), 1348–1354. https://doi.org/10.1021/acs.chemmater.5b04231.

440. Volonakis, G.; Filip, M. R.; Haghighirad, A. A.; Sakai, N.; Wenger, B.; Snaith, H. J.; Giustino, F. *Journal of Physical Chemistry Letters* **2016**, *7* (7), 1254–1259. https://doi.org/10.1021/acs.jpclett.6b00376.

441. Meyer, G. *Progress in Solid State Chemistry* **1982**, *14* (3), 141–219. https://doi.org/10.1016/0079-6786(82)90005-X.

442. Giustino, F.; Snaith, H. J. *ACS Energy Letters* **2016**, *1* (6), 1233–1240. https://doi.org/10.1021/acsenergylett.6b00499.

443. Wei, F.; Deng, Z.; Sun, S.; Xie, F.; Kieslich, G.; Evans, D. M.; Carpenter, M. A.; Bristowe, P. D.; Cheetham, A. K. *Materials Horizons* **2016**, *3* (4), 328–332. https://doi.org/10.1039/c6mh00053c.

444. Deng, Z.; Wei, F.; Brivio, F.; Wu, Y.; Sun, S.; Bristowe, P. D.; Cheetham, A. K. *Journal of Physical Chemistry Letters* **2017**, *8* (20), 5015–5020. https://doi.org/10.1021/acs.jpclett.7b02322.

445. Zhao, S.; Yamamoto, K.; Iikubo, S.; Hayase, S.; Ma, T. *Journal of Physics and Chemistry of Solids* **2018**, *117* (June), 117–121. https://doi.org/10.1016/j.jpcs.2018.02.032.

446. Flerov, I. N.; Gorev, M. V.; Aleksandrov, K. S.; Tressaud, A.; Grannec, J.; Couzi, M. *Materials Science and Engineering R: Reports* **1998**, *24* (3), 81–151. https://doi.org/10.1016/S0927-796X(98)00015-1.

447. Filip, M. R.; Liu, X.; Miglio, A.; Hautier, G.; Giustino, F. *Journal of Physical Chemistry C* **2018**, *122* (1), 158–170. https://doi.org/10.1021/acs.jpcc.7b10370.

448. Xiao, D. Z.; Du, D. K.; Meng, W.; Mitzi, P. D. B.; Yan, P. Y.; Xiao, Z.; Du, K.; Meng, W.; Mitzi, D.; Yan, Y. *Angewandte Chemie - International Edition* **2017**, *129* (40), 12275–12279. https://doi.org/10.1002/ange.201705113.

449. Zhao, X. G.; Yang, D.; Ren, J. C.; Sun, Y.; Xiao, Z.; Zhang, L. *Joule* **2018**, *2* (9), 1662–1673. https://doi.org/10.1016/j.joule.2018.06.017.

450. Savory, C. N.; Walsh, A.; Scanlon, D. O. *ACS Energy Letters* **2016**, *1* (5), 949–955. https://doi.org/10.1021/acsenergylett.6b00471.

451. Xiao, Z.; Meng, W.; Wang, J.; Yan, Y. *ChemSusChem* **2016**, *9* (18), 2628–2633. https://doi.org/10.1002/cssc.201600771.

452. Meng, W.; Wang, X.; Xiao, Z.; Wang, J.; Mitzi, D. B.; Yan, Y. *Journal of Physical Chemistry Letters* **2017**, *8* (13), 2999–3007. https://doi.org/10.1021/acs.jpclett.7b01042.

453. Luo, J.; Li, S.; Wu, H.; Zhou, Y.; Li, Y.; Liu, J.; Li, J.; Li, K.; Yi, F.; Niu, G.; Tang, J. *ACS Photonics* **2018**, *5* (2), 398–405. https://doi.org/10.1021/acsphotonics.7b00837.

454. Volonakis, G.; Haghighirad, A. A.; Milot, R. L.; Sio, W. H.; Filip, M. R.; Wenger, B.; Johnston, M. B.; Herz, L. M.; Snaith, H. J.; Giustino, F. *Journal of Physical Chemistry Letters* **2017**, *8* (4), 772–778. https://doi.org/10.1021/acs.jpclett.6b02682.

455. Slavney, A. H.; Leppert, L.; Bartesaghi, D.; Gold-Parker, A.; Toney, M. F.; Savenije, T. J.; Neaton, J. B.; Karunadasa, H. I. *Journal of the American Chemical Society* **2017**, *139* (14), 5015–5018. https://doi.org/10.1021/jacs.7b01629.

456. Du, K. Z.; Meng, W.; Wang, X.; Yan, Y.; Mitzi, D. B. *Angewandte Chemie - International Edition* **2017**, *56* (28), 8158–8162. https://doi.org/10.1002/anie.201703970.

457. Ning, W.; Wang, F.; Wu, B.; Lu, J.; Yan, Z.; Liu, X.; Tao, Y.; Liu, J. M.; Huang, W.; Fahlman, M.; Hultman, L.; Sum, T. C.; Gao, F. *Advanced Materials* **2018**, *30* (20), 1706246. https://doi.org/10.1002/adma.201706246.

458. Creutz, S. E.; Crites, E. N.; De Siena, M. C.; Gamelin, D. R. *Nano Letters* **2018**, *18* (2), 1118–1123. https://doi.org/10.1021/acs.nanolett.7b04659.

459. Zhou, J.; Xia, Z.; Molokeev, M. S.; Zhang, X.; Peng, D.; Liu, Q. *Journal of Materials Chemistry A* **2017**, *5* (29), 15031–15037. https://doi.org/10.1039/c7ta04690a.

460. Xiao, Z.; Du, K. Z.; Meng, W.; Wang, J.; Mitzi, D. B.; Yan, Y. *Journal of the American Chemical Society* **2017**, *139* (17), 6054–6057. https://doi.org/10.1021/jacs.7b02227.

461. Volonakis, G.; Haghighirad, A. A.; Snaith, H. J.; Giustino, F. *Journal of Physical Chemistry Letters* **2017**, *8* (16), 3917–3924. https://doi.org/10.1021/acs.jpclett.7b01584.

462. Xiao, Z.; Yan, Y.; Hosono, H.; Kamiya, T. *Journal of Physical Chemistry Letters* **2018**, *9* (1), 258–262. https://doi.org/10.1021/acs.jpclett.7b02949.

463. Zhang, Z.; Wu, C.; Wang, D.; Liu, G.; Zhang, Q.; Luo, W.; Qi, X.; Guo, X.; Zhang, Y.; Lao, Y.; Qu, B.; Xiao, L.; Chen, Z. *Organic Electronics* **2019**, *74* (June), 204–210. https://doi.org/10.1016/j.orgel.2019.06.037.

464. Pai, N.; Lu, J.; Wang, M.; Chesman, A. S. R.; Seeber, A.; Cherepanov, P. V.; Senevirathna, D. C.; Gengenbach, T. R.; Medhekar, N. V.; Andrews, P. C.; Bach, U.; Simonov, A. N. *Journal of Materials Chemistry A* **2020**, *8* (4), 2008–2020. https://doi.org/10.1039/c9ta10422d.

465. Li, J.; Duan, J.; Du, J.; Yang, X.; Wang, Y.; Yang, P.; Duan, Y.; Tang, Q. *ACS Applied Materials and Interfaces* **2020**, *12* (42), 47408–47415. https://doi.org/10.1021/acsami.0c11770.

466. Wang, B.; Yang, L.; Dall'Agnese, C.; Jena, A. K.; Sasaki, S. ichi; Miyasaka, T.; Tamiaki, H.; Wang, X. F. *Solar RRL* **2020**, *4* (7), 2000166. https://doi.org/10.1002/solr.202000166.

467. Yang, X.; Chen, Y.; Liu, P.; Xiang, H.; Wang, W.; Ran, R.; Zhou, W.; Shao, Z. *Advanced Functional Materials* **2020**, *30* (23), 2001557. https://doi.org/10.1002/adfm.202001557.

468. Li, P.; Gao, W.; Ran, C.; Dong, H.; Hou, X.; Wu, Z. *Physica Status Solidi (A) Applications and Materials Science* **2019**, *216* (23), 1900567. https://doi.org/10.1002/pssa.201900567.

469. Connor, B. A.; Leppert, L.; Smith, M. D.; Neaton, J. B.; Karunadasa, H. I. *Journal of the American Chemical Society* **2018**, *140* (15), 5235–5240. https://doi.org/10.1021/jacs.8b01543.

470. Jana, M. K.; Janke, S. M.; Dirkes, D. J.; Dovletgeldi, S.; Liu, C.; Qin, X.; Gundogdu, K.; You, W.; Blum, V.; Mitzi, D. B. *Journal of the American Chemical Society* **2019**, *141* (19), 7955–7964. https://doi.org/10.1021/jacs.9b02909.

471. Pan, W.; Wu, H.; Luo, J.; Deng, Z.; Ge, C.; Chen, C.; Jiang, X.; Yin, W.; Niu, G.; Zhu, L.; Yin, L.; Zhou, Y.; Xie, Q.; Ke, X. *Nature Photonics* **2017**, *11* (1), 1–8. https://doi.org/10.1038/s41566-017-0012-4.

472. Nila Nandha, K.; Nag, A. *Chemical Communications* **2018**, *54* (41), 5205–5208. https://doi.org/10.1039/c8cc01982g.

473. Deng, T. T.; Song, E. H.; Zhou, Y. Y.; Wang, L. Y.; Zhang, Q. Y. *Journal of Materials Chemistry C* **2017**, *5* (47), 12422–12429. https://doi.org/10.1039/c7tc04411a.

474. Tan, Z.; Li, J.; Zhang, C.; Li, Z.; Hu, Q.; Xiao, Z.; Kamiya, T.; Hosono, H.; Niu, G.; Lifshitz, E.; Cheng, Y.; Tang, J. *Advanced Functional Materials*. 2018, p 1801131. https://doi.org/10.1002/adfm.201801131.

475. Aull, B. F.; Jenssen, H. P. *Physical Review B* **1986**, *34* (10), 6647–6655. https://doi.org/10.1103/PhysRevB.34.6647.

476. Da Fonseca, R. J. M.; Sosman, L. P.; Dias Tavares, A.; Bordallo, H. N. *Journal of Fluorescence* **2000**, *10* (4), 375–381. https://doi.org/10.1023/A:1009430530367.

477. Zhou, L.; Xu, Y. F.; Chen, B. X.; Kuang, D. Bin; Su, C. Y. *Small* **2018**, *14* (11), 1703762. https://doi.org/10.1002/smll.201703762.

478. Bekenstein, Y.; Dahl, J. C.; Huang, J.; Osowiecki, W. T.; Swabeck, J. K.; Chan, E. M.; Yang, P.; Alivisatos, A. P. *Nano Letters* **2018**, *18* (6), 3502–3508. https://doi.org/10.1021/acs.nanolett.8b00560.

479. Su, J.; Huang, Y. qiang; Chen, H.; Huang, J. *Crystal Research and Technology* **2020**, *55* (3), 4–7. https://doi.org/10.1002/crat.201900222.

480. Wang, M.; Zeng, P.; Wang, Z.; Liu, M. *Advanced Science*. 2020, p 1903662. https://doi.org/10.1002/advs.201903662.

481. Wei, F.; Deng, Z.; Sun, S.; Hartono, N. T. P.; Seng, H. L.; Buonassisi, T.; Bristowe, P. D.; Cheetham, A. K. *Chemical Communications* **2019**, *55* (26), 3721–3724. https://doi.org/10.1039/c9cc01134j.

482. Ji, F.; Klarbring, J.; Wang, F.; Ning, W.; Wang, L.; Yin, C.; Figueroa, J. S. M.; Christensen, C. K.; Etter, M.; Ederth, T.; Sun, L.; Simak, S. I.; Abrikosov, I. A.; Gao, F. *Angewandte Chemie - International Edition* **2020**, *59* (35), 15191–15194. https://doi.org/10.1002/anie.202005568.

483. Zhang, C.; Gao, L.; Teo, S.; Guo, Z.; Xu, Z.; Zhao, S.; Ma, T. *Sustainable Energy and Fuels* **2018**, *2* (11), 2419–2428. https://doi.org/10.1039/c8se00154e.

484. Deng, Z.; Wei, F.; Sun, S.; Kieslich, G.; Cheetham, A. K.; Bristowe, P. D. *Journal of Materials Chemistry A* **2016**, *4* (31), 12025–12029. https://doi.org/10.1039/c6ta05817e.

485. Wei, F.; Deng, Z.; Sun, S.; Zhang, F.; Evans, D. M.; Kieslich, G.; Tominaka, S.; Carpenter, M. A.; Zhang, J.; Bristowe, P. D.; Cheetham, A. K. *Chemistry of Materials* **2017**, *29* (3), 1089–1094. https://doi.org/10.1021/acs.chemmater.6b03944.

486. Palik, E. D. *Handbook of Optical Constants of Solids*, Third Ed.; Academic Press: San Diego, 1998.

487. Green, M.; Dunlop, E.; Hohl-Ebinger, J.; Yoshita, M.; Kopidakis, N.; Hao, X. *Progress in Photovoltaics: Research and Applications* **2021**, *29* (1), 3–15. https://doi.org/10.1002/pip.3371.

488. Yin, W. J.; Yang, J. H.; Kang, J.; Yan, Y.; Wei, S. H. *Journal of Materials Chemistry A* **2015**, *3* (17), 8926–8942. https://doi.org/10.1039/c4ta05033a.

489. Yin, W. J.; Shi, T.; Yan, Y. *Journal of Physical Chemistry C* **2015**, *119* (10), 5253–5264. https://doi.org/10.1021/jp512077m.

490. Yin, W. J.; Shi, T.; Yan, Y. *Advanced Materials* **2014**, *26* (27), 4653–4658. https://doi.org/10.1002/adma.201306281.

491. Tanaka, K.; Takahashi, T.; Ban, T.; Kondo, T.; Uchida, K.; Miura, N. *Solid State Communications* **2003**, *127* (9–10), 619–623. https://doi.org/10.1016/S0038-1098(03)00566-0.

492. Jin, H.; Im, J.; Freeman, A. J. *Physical Review B - Condensed Matter and Materials Physics* **2012**, *86* (12), 1–5. https://doi.org/10.1103/PhysRevB.86.121102.

493. Even, J.; Pedesseau, L.; Jancu, J. M.; Katan, C. *Journal of Physical Chemistry Letters* **2013**, *4* (17), 2999–3005. https://doi.org/10.1021/jz401532q.

494. Yin, W. J.; Shi, T.; Yan, Y. *Applied Physics Letters* **2014**, *104* (6), 063903. https://doi.org/10.1063/1.4864778.

495. Bonn, M.; Miyata, K.; Hendry, E.; Zhu, X. Y. *ACS Energy Letters* **2017**, *2* (11), 2555–2562. https://doi.org/10.1021/acsenergylett.7b00717.

496. Ogomi, Y.; Morita, A.; Tsukamoto, S.; Saitho, T.; Fujikawa, N.; Shen, Q.; Toyoda, T.; Yoshino, K.; Pandey, S. S.; Hayase, S. *Journal of Physical Chemistry Letters* **2014**, *5* (6), 1004–1011.

497. Mosconi, E.; Umari, P.; Angelis, F. De. *Journal of Materials Chemistry* **2015**, *3* (17), 9208–9215. https://doi.org/10.1039/c4ta06230b.

498. Prasanna, R.; Gold-parker, A.; Leijtens, T.; Conings, B.; Babayigit, A.; Boyen, H.; Toney, M. F.; Mcgehee, M. D. *Journal of the American Chemical Society* **2017**, *139* (32), 11117–11124. https://doi.org/10.1021/jacs.7b04981.

499. Liu, H.; Li, X.; Zeng, Y.; Meng, L. *Computational Materials Science* **2020**, *177* (November), 109576. https://doi.org/10.1016/j.commatsci.2020.109576.

500. Gollino, L.; Pauporté, T. *Solar Energy* **2021**, *5* (3), 2000616. https://doi.org/10.1002/solr.202000616.

501. Yang, Z.; Rajagopal, A.; Chueh, C. C.; Jo, S. B.; Liu, B.; Zhao, T.; Jen, A. K. Y. *Advanced Materials* **2016**, *28* (40), 8990–8997. https://doi.org/10.1002/adma.201602696.

502. Liu, C.; Li, W.; Li, H.; Zhang, C.; Fan, J.; Mai, Y. *Nanoscale* **2017**, *9* (37), 13967–13975. https://doi.org/10.1039/c7nr03507a.

503. Ke, W.; Xiao, C.; Wang, C.; Saparov, B.; Duan, H. S.; Zhao, D.; Xiao, Z.; Schulz, P.; Harvey, S. P.; Liao, W.; Meng, W.; Yu, Y.; Cimaroli, A. J.; Jiang, C. S.; Zhu, K.; Al-Jassim, M.; Fang, G.; Mitzi, D. B.; Yan, Y. *Advanced Materials* **2016**, *28* (26), 5214–5221. https://doi.org/10.1002/adma.201600594.

504. Zhao, D.; Yu, Y.; Wang, C.; Liao, W.; Shrestha, N.; Grice, C. R.; Cimaroli, A. J.; Guan, L.; Ellingson, R. J.; Zhu, K.; Zhao, X.; Xiong, R. G.; Yan, Y. *Nature Energy* **2017**, *2* (4), 1–8. https://doi.org/10.1038/nenergy.2017.18.

505. Harvey, S. P.; Li, Z.; Christians, J. A.; Zhu, K.; Luther, J. M.; Berry, J. J. *ACS Applied Materials and Interfaces* **2018**, *10* (34), 28541–28552. https://doi.org/10.1021/acsami.8b07937.

506. Zhou, X.; Zhang, L.; Wang, X.; Liu, C.; Chen, S.; Zhang, M.; Li, X.; Yi, W.; Xu, B. *Advanced Materials* **2020**, *32* (14), 1908107. https://doi.org/10.1002/adma.201908107.

507. Wang, P.; Shao, Z.; Ulfa, M.; Pauporté, T. *Journal of Physical Chemistry C* **2017**, *121* (17), 9131–9141. https://doi.org/10.1021/acs.jpcc.7b00979.

508. Wang, P.; Ulfa, M.; Pauporté, T. *Journal of Physical Chemistry C* **2018**, *122* (4), 1973–1981. https://doi.org/10.1021/acs.jpcc.7b11010.

509. Ulfa, M.; Wang, P.; Zhang, J.; Liu, J.; Marcillac, W. D. De; Coolen, L.; Pauporte, T. *ACS Applied Materials and Interfaces* **2018**, *10* (41), 35118–35128. https://doi.org/10.1021/acsami.8b10979.

510. Bui, T.; Ulfa, M.; Maschietto, F.; Ottochian, A.; Nghiêm, M.; Cio, I.; Goubard, F.; Pauporté, T. *Organic Electronics* **2018**, *60* (May), 22–30. https://doi.org/10.1016/j.orgel.2018.05.024.

511. Ulfa, M.; Pauporte, T.; Goubard, F. *Journal of Physical Chemistry C* **2018**, *122* (22), 11651–11658. https://doi.org/10.1021/acs.jpcc.8b02141.

512. Ulfa, M.; Zhu, T.; Goubard, F.; Pauporte, T. *Journal of Materials Chemistry A* **2018**, *6* (27), 13350–13358. https://doi.org/10.1039/c8ta03875a.

513. Magaldi, D.; Ulfa, M.; Nghiêm, M. P.; Sini, G.; Goubard, F.; Pauporté, T.; Bui, T. T. *Journal of Materials Science* **2020**, *55* (11), 4820–4829. https://doi.org/10.1007/s10853-019-04342-6.

514. Li, Y.; Sun, W.; Yan, W.; Ye, S.; Rao, H.; Peng, H.; Zhao, Z.; Bian, Z.; Liu, Z.; Zhou, H.; Huang, C. *Advanced Energy Materials* **2016**, *6* (24), 1601353. https://doi.org/10.1002/aenm.201601353.

515. Wang, Y.; Fu, W.; Yan, J.; Chen, J.; Yang, W.; Chen, H. *Journal of Materials Chemistry A* **2018**, *6* (27), 13090–13095. https://doi.org/10.1039/c8ta03054e.

516. Li, C.; Song, Z.; Zhao, D.; Xiao, C.; Subedi, B.; Shrestha, N.; Junda, M. M.; Wang, C.; Jiang, C. S.; Al-Jassim, M.; Ellingson, R. J.; Podraza, N. J.; Zhu, K.; Yan, Y. *Advanced Energy Materials* **2019**, *9* (3), 1803135. https://doi.org/10.1002/aenm.201803135.

517. Cui, Y.; Xu, B.; Yang, B.; Yao, H.; Li, S.; Hou, J. *Macromolecules* **2016**, *49* (21), 8126–8133. https://doi.org/10.1021/acs.macromol.6b01595.

518. Shao, S.; Cui, Y.; Duim, H.; Qiu, X.; Dong, J.; ten Brink, G. H.; Portale, G.; Chiechi, R. C.; Zhang, S.; Hou, J.; Loi, M. A. *Advanced Materials* **2018**, *30* (35), 1803703. https://doi.org/10.1002/adma.201803703.

519. Zhu, L.; Yuh, B.; Schoen, S.; Li, X.; Aldighaithir, M.; Richardson, B. J.; Alamer, A.; Yu, Q. *Nanoscale* **2016**, *8* (14), 7621–7630. https://doi.org/10.1039/c6nr00301j.

520. Zuo, F.; Williams, S. T.; Liang, P.-W.; Chueh, C.-C.; Liao, C.-Y.; Jen, A. K.-Y. *Advanced Materials* **2014**, *26* (37), 6454–6460. https://doi.org/10.1002/adma.201401641.

521. Liu, C.; Fan, J.; Li, H.; Zhang, C.; Mai, Y. *Scientific Reports* **2016**, *6* (1), 1–8. https://doi.org/10.1038/srep35705.

522. Igual-mun, A. M.; Castillo, A.; Dreessen, C.; Boix, P. P.; Bolink, H. J. *ACS Applied Energy Materials* **2020**, *3* (3), 2755–2761. https://doi.org/10.1021/acsaem.9b02413.

523. Lian, X.; Chen, J.; Zhang, Y.; Qin, M.; Li, J.; Tian, S.; Yang, W.; Lu, X.; Wu, G.; Chen, H. *Advanced Functional Materials* **2019**, *29* (5), 1807024. https://doi.org/10.1002/adfm.201807024.

524. Hamanda, K.; Minemoto, T.; Yoshino, K.; Toyoda, T.; Ma, T.; Kang, D.; Hayase, S. *ACS Applied Materials and Interfaces* **2020**, *12* (15), 17776–17782. https://doi.org/10.1021/acsami.0c01411.

525. Ogomi, Y.; Morita, A.; Tsukamoto, S.; Saitho, T.; Fujikawa, N.; Shen, Q.; Toyoda, T.; Yoshino, K.; Pandey, S. S.; Hayase, S. *Journal of Physical Chemistry Letters* **2014**, *5* (6), 1004–1011. https://doi.org/10.1021/jz5002117.

526. Kapil, G.; Ripolles, T. S.; Hamada, K.; Ogomi, Y.; Bessho, T.; Kinoshita, T.; Chantana, J.; Yoshino, K.; Shen, Q.; Toyoda, T.; Minemoto, T.; Murakami, T. N.; Segawa, H.; Hayase, S. *Nano Letters* **2018**, *18* (6), 3600–3607. https://doi.org/10.1021/acs.nanolett.8b00701.

527. Liu, M.; Chen, Z.; Yang, Y.; Yip, H.; Cao, Y. *Journal of Materials Chemistry* **2019**, *7* (29), 17324–17333. https://doi.org/10.1039/c9ta04366g.

528. Liao, W.; Zhao, D.; Yu, Y.; Shrestha, N.; Ghimire, K.; Grice, C. R.; Wang, C.; Xiao, Y.; Cimaroli, A. J.; Ellingson, R. J.; Podraza, N. J.; Zhu, K.; Xiong, R.; Yan, Y. *Journal of the American Chemical Society* **2016**, *138* (38), 12360–12363. https://doi.org/10.1021/jacs.6b08337.

529. Lee, S.; Kang, D. *ACS Applied Materials and Interfaces* **2017**, *9* (27), 4–11. https://doi.org/10.1021/acsami.7b04011.

530. Tong, J.; Song, Z.; Kim, D. H.; Chen, X.; Chen, C.; Palmstrom, A. F.; Ndione, P. F.; Reese, M. O.; Dunfield, S. P.; Reid, O. G.; Liu, J.; Zhang, F.; Harvey, S. P.; Li, Z.; Christensen, S. T.; Teeter, G.; Zhao, D.; Al-Jassim, M. M.; Hest, M. F. A. M. Van; Beard, M. C. *Science* **2019**, *364* (6439), 475–479. https://doi.org/10.1126/science.aav7911.

531. Song, J.; Hu, W.; Li, Z.; Wang, X.; Tian, W. *Solar Energy Materials and Solar Cells* **2020**, *207* (September), 110351. https://doi.org/10.1016/j.solmat.2019.110351.

532. Tavakoli, M. M.; Zakeeruddin, S. M.; Grätzel, M.; Fan, Z. *Advanced Materials* **2018**, *30* (11), 1705998. https://doi.org/10.1002/adma.201705998.

533. Tsai, C.; Wu, H.; Chang, S.; Huang, C.; Wang, C.; Narra, S.; Yang, Y.; Wang, C.; Hung, C.; Diau, E. W. *ACS Energy Letters* **2016**, *1* (6), 1086–1093. https://doi.org/10.1021/acsenergylett.6b00514.

534. Sri, C. H. N. H.; Jacobsson, T. J.; Pazoki, M.; Hagfeldt, A.; Edvinsson, T. *Journal of Physical Chemistry C* **2015**, *119* (46), 25673–25683. https://doi.org/10.1021/acs.jpcc.5b06436.

535. Kai, W.; Liang, W. *Acta Physico-Chimica Sinica* **2015**, *31* (2), 285–290. https://doi.org/10.3866/PKU.WHXB201412241.

536. Lau, C. F. J.; Zhang, M.; Deng, X.; Zheng, J.; Bing, J.; Ma, Q.; Kim, J.; Hu, L.; Green, M. A.; Huang, S.; Ho-Baillie, A. *ACS Energy Letters* **2017**, *2* (10), 2319–2325. https://doi.org/10.1021/acsenergylett.7b00751.

537. Shai, X.; Zuo, L.; Sun, P.; Liao, P.; Huang, W.; Yao, E. *Nano Energy* **2017**, *36* (April), 213–222. https://doi.org/10.1016/j.nanoen.2017.04.047.

538. Wu, M.; Lin, T.; Chan, S.; Liao, Y.; Chang, Y. *ACS Applied Energy Materials* **2018**, *1* (9), 4849–4859. https://doi.org/10.1021/acsaem.8b00915.

539. Zhang, H.; Liu, W.; Li, R.; Zhang, M.; Guo, M. *Ceramics International* **2018**, *44* (15), 18863–18870. https://doi.org/10.1016/j.ceramint.2018.07.121.

540. Li, R.; Zhang, H.; Han, X.; Huo, X.; Zhang, M.; Guo, M. *ACS Applied Materials and Interfaces* **2020**, *12* (9), 10515–10526. https://doi.org/10.1021/acsami.9b22556.

541. Zhang, J.; Pauporté, T. *ChemPhysChem* **2015**, *16* (13), 2836. https://doi.org/10.1002/cphc.201500456.

542. Pérez-del-Rey, D.; Forgács, D.; Hutter, E. M.; Savenije, T. J.; Nordlund, D.; Schulz, P.; Berry, J. J.; Sessolo, M.; Bolink, H. J. *Advanced Materials* **2016**, *28* (44), 9839. https://doi.org/10.1002/adma.201603016.

543. Zhang, H.; Wang, H.; Williams, S. T.; Xiong, D.; Zhang, W.; Chueh, C.; Chen, W.; Jen, A. K. -Y. *Advanced Materials* **2017**, *29* (15), 1606608. https://doi.org/10.1002/adma.201606608.

544. Kumar, A.; Balasubramaniam, K. R. *Physical Review B* **2016**, *94* (18), 1–5. https://doi.org/10.1103/PhysRevB.94.180105.

545. Chan, S. H.; Wu, M. C.; Lee, K. M.; Chen, W. C.; Lin, T. H.; Su, W. F. *Journal of Materials Chemistry A* **2017**, *5* (34), 18044–18052. https://doi.org/10.1039/c7ta05720b.

546. Zhang, H.; Shang, M. hui; Zheng, X.; Zeng, Z.; Chen, R.; Zhang, Y.; Zhang, J.; Zhu, Y. *Electrochimica Acta* **2017**, *254* (November), 165–171. https://doi.org/10.1016/j.electacta.2017.09.091.

547. Lau, C. F. J.; Deng, X.; Zheng, J.; Kim, J.; Zhang, Z.; Zhang, M.; Bing, J.; Wilkinson, B.; Hu, L.; Patterson, R.; Huang, S.; Ho-Baillie, A. *Journal of Materials Chemistry A* **2018**, *6* (14), 5580–5586. https://doi.org/10.1039/c7ta11154a.

548. Jahandar, M.; Heo, J. H.; Song, C. E.; Kong, K. J.; Shin, W. S.; Lee, J. C.; Im, S. H.; Moon, S. J. *Nano Energy* **2016**, *27* (September), 330–339. https://doi.org/10.1016/j.nanoen.2016.07.022.

549. Gong, X.; Guan, L.; Pan, H.; Sun, Q.; Zhao, X.; Li, H.; Pan, H.; Shen, Y.; Shao, Y.; Sun, L.; Cui, Z.; Ding, L.; Wang, M. *Advanced Functional Materials* **2018**, *28* (50), 1–8. https://doi.org/10.1002/adfm.201804286.

550. Klug, M. T.; Osherov, A.; Haghighirad, A. A.; Stranks, S. D.; Brown, P. R.; Bai, S.; Wang, J. T. W.; Dang, X.; Bulović, V.; Snaith, H. J.; Belcher, A. M. *Energy and Environmental Science* **2017**, *10* (1), 236–246. https://doi.org/10.1039/c6ee03201j.

551. Xu, W.; Zheng, L.; Zhang, X.; Cao, Y.; Meng, T.; Wu, D.; Liu, L.; Hu, W.; Gong, X. *Advanced Energy Materials* **2018**, *8* (14), 1–11. https://doi.org/10.1002/aenm.201703178.

552. Caia, Q.; Li, H.; Jiang, Y.; Tu, L.; Ma, L.; Wu, X.; Yang, S.; Shi, Z.; Zang, J.; Chen, Y. *Solar Energy* **2018**, *159* (January), 786–793. https://doi.org/10.1016/j.solener.2017.11.063.

553. Chen, Q.; Chen, L.; Ye, F.; Zhao, T.; Tang, F.; Rajagopal, A.; Jiang, Z.; Jiang, S.; Jen, A. K. Y.; Xie, Y.; Cai, J.; Chen, L. *Nano Letters* **2017**, *17* (5), 3231–3237. https://doi.org/10.1021/acs.nanolett.7b00847.

554. Liang, J.; Liu, Z.; Qiu, L.; Hawash, Z.; Meng, L.; Wu, Z.; Jiang, Y.; Ono, L. K.; Qi, Y. *Advanced Energy Materials* **2018**, *8* (20), 1800504. https://doi.org/10.1002/aenm.201800504.

555. Deng, L.; Yang, H.; Pan, R.; Yu, H.; Li, J.; Xu, L.; Wang, K. *Journal of Energy Chemistry* **2021**, *60* (September), 376–383. https://doi.org/10.1016/j.jechem.2021.01.028.

556. Ren, L.; Wang, M.; Wang, S.; Yan, H.; Zhang, Z.; Li, M.; Zhang, Z.; Jin, K. *ACS Applied Materials and Interfaces* **2019**, *11* (17), 16174–16180. https://doi.org/10.1021/acsami.9b01506.

557. Wu, Y.; Chen, W.; Wan, Z.; Djurišić, A. B.; Feng, X.; Liu, L.; Chen, G.; Liu, R.; He, Z. *Journal of Power Sources* **2019**, *425* (March), 130–137. https://doi.org/10.1016/j.jpowsour.2019.04.009.

558. Jin, J.; Li, H.; Chen, C.; Zhang, B.; Xu, L.; Dong, B.; Song, H.; Dai, Q. *ACS Applied Materials and Interfaces* **2017**, *9* (49), 42875–42882. https://doi.org/10.1021/acsami.7b15310.

559. Sa, R.; Wang, L.; Wang, J.; Chen, X.; Chen, J. *Applied Physics Letters* **2014**, *12* (8), 37–41. https://doi.org/10.7567/1882-0786/ab32ca.

560. Wang, Z. K.; Li, M.; Yang, Y. G.; Hu, Y.; Ma, H.; Gao, X. Y.; Liao, L. S. *Advanced Materials* **2016**, *28* (31), 6695–6703. https://doi.org/10.1002/adma.201600626.

561. Sun, P. P.; Li, Q. S.; Feng, S.; Li, Z. S. *Physical Chemistry Chemical Physics* **2016**, *18* (21), 14408–14418. https://doi.org/10.1039/c6cp02105k.

562. Kim, G. M.; Ishii, A.; Öz, S.; Miyasaka, T. *Advanced Energy Materials* **2020**, *10* (7), 1903299. https://doi.org/10.1002/aenm.201903299.

563. Zhang, J.; Shang, M. H.; Wang, P.; Huang, X.; Xu, J.; Hu, Z.; Zhu, Y.; Han, L. *ACS Energy Letters* **2016**, *1* (3), 535–541. https://doi.org/10.1021/acsenergylett.6b00241.

564. Oku, T.; Ohishi, Y.; Suzuki, A. *Chemistry Letters* **2016**, *45* (2), 134–136. https://doi.org/10.1246/cl.150984.

565. Chatterjee, S.; Dasgupta, U.; Pal, A. J. *Journal of Physical Chemistry C* **2017**, *121* (37), 20177–20187. https://doi.org/10.1021/acs.jpcc.7b06963.

566. Hu, Y.; Bai, F.; Liu, X.; Ji, Q.; Miao, X.; Qiu, T.; Zhang, S. *ACS Energy Letters* **2017**, *2* (10), 2219–2227. https://doi.org/10.1021/acsenergylett.7b00508.

567. Li, M.; Wang, Z. K.; Zhuo, M. P.; Hu, Y.; Hu, K. H.; Ye, Q. Q.; Jain, S. M.; Yang, Y. G.; Gao, X. Y.; Liao, L. S. *Advanced Materials* **2018**, *30* (20), 1–7. https://doi.org/10.1002/adma.201800258.

568. Liu, D.; Li, Q.; Hu, J.; Sa, R.; Wu, K. *Journal of Physical Chemistry C* **2019**, *123* (20), 12638–12646. https://doi.org/10.1021/acs.jpcc.9b02705.

569. Wu, M. C.; Lin, T. H.; Chan, S. H.; Su, W. F. *Journal of the Taiwan Institute of Chemical Engineers* **2017**, *80* (November), 695–700. https://doi.org/10.1016/j.jtice.2017.09.004.

570. Wu, M. C.; Chen, W. C.; Chan, S. H.; Su, W. F. *Applied Surface Science* **2018**, *429* (January), 9–15. https://doi.org/10.1016/j.apsusc.2017.08.131.

571. Zhang, H.; Li, R.; Zhang, M.; Guo, M. *Inorganic Chemistry Frontiers* **2018**, *5* (6), 1354–1364. https://doi.org/10.1039/c8qi00131f.

572. Yang, F.; Hirotani, D.; Kapil, G.; Kamarudin, M. A.; Ng, C. H.; Zhang, Y.; Shen, Q.; Hayase, S. *Angewandte Chemie - International Edition* **2018**, *57* (39), 12745–12749. https://doi.org/10.1002/anie.201807270.

573. Xiang, W.; Wang, Z.; Kubicki, D. J.; Wang, X.; Tress, W.; Luo, J.; Zhang, J.; Hofstetter, A.; Zhang, L.; Emsley, L.; Grätzel, M.; Hagfeldt, A. *Nature Communications* **2019**, *10* (1), 4686. https://doi.org/10.1038/s41467-019-12678-5.

574. Caprioglio, P.; Zu, F.; Wol, M.; Stolterfoht, M.; Becker, P.; Koch, N.; Unold, T.; Rech, B.; Neher, D. *Sustainable Energy and Fuels* **2019**, *3* (2), 550–563. https://doi.org/10.1039/c8se00509e.

575. Mercier, N. *Angewandte Chemie* **2019**, *131* (50), 18078–18083. https://doi.org/10.1002/ange.201909601.

576. Ke, W.; Spanopoulos, I.; Tu, Q.; Hadar, I.; Li, X.; Shekhawat, G. S.; Dravid, V. P.; Kanatzidis, M. G. *Journal of the American Chemical Society* **2019**, *141* (21), 8627–8637. https://doi.org/10.1021/jacs.9b03662.

577. Celik, I.; Song, Z.; Cimaroli, A. J.; Yan, Y.; Heben, M. J.; Apul, D. *Solar Energy Materials and Solar Cells* **2016**, *156* (November), 157–169. https://doi.org/10.1016/j.solmat.2016.04.037.

578. Zhang, J.; Gao, X.; Deng, Y.; Li, B.; Yuan, C. *ChemSusChem* **2015**, *8* (22), 3882–3891. https://doi.org/10.1002/cssc.201500848.

579. Jung, E. H.; Jeon, N. J.; Park, E. Y.; Moon, C. S.; Shin, T. J.; Yang, T. Y.; Noh, J. H.; Seo, J. *Nature* **2019**, *567* (7749), 511–515. https://doi.org/10.1038/s41586-019-1036-3.

580. Jiang, Q.; Zhao, Y.; Zhang, X.; Yang, X.; Chen, Y.; Chu, Z.; Ye, Q.; Li, X.; Yin, Z.; You, J. *Nature Photonics* **2019**, *13* (7), 460–466. https://doi.org/10.1038/s41566-019-0398-2.

581. Zheng, X.; Hou, Y.; Bao, C.; Yin, J.; Yuan, F.; Huang, Z.; Song, K.; Liu, J.; Troughton, J.; Gasparini, N.; Zhou, C.; Lin, Y.; Xue, D. J.; Chen, B.; Johnston, A. K.; Wei, N.; Hedhili, M. N.; Wei, M.; Alsalloum, A. Y.; Maity, P.; Turedi, B.; Yang, C.; Baran, D.; Anthopoulos, T. D.; Han, Y.; Lu, Z. H.; Mohammed, O. F.; Gao, F.; Sargent, E. H.; Bakr, O. M. *Nature Energy* **2020**, *5* (2), 131–140. https://doi.org/10.1038/s41560-019-0538-4.

582. Nuss, P.; Eckelman, M. J. *PLoS ONE* **2014**, *9* (7), 1–12. https://doi.org/10.1371/journal.pone.0101298.

583. Hu, Z.; Gao, S. *Chemical Geology* **2008**, *253* (3–4), 205–221. https://doi.org/10.1016/j.chemgeo.2008.05.010.

584. Gracia, R. C.; Snodgrass, W. R. *American Journal of Health-System Pharmacy* **2007**, *64* (1), 45–53. https://doi.org/10.2146/ajhp060175.

585. Babayigit, A.; Ethirajan, A.; Muller, M.; Conings, B. *Nature Materials* **2016**, *15* (3), 247–251. https://doi.org/10.1038/nmat4572.

586. Groom, C. R.; Bruno, I. J.; Lightfoot, M. P.; Ward, S. C. The Cambridge Structural Database. https://doi.org/DOI: 10.1107/S2052520616003954.

587. Vishnoi, P.; Zuo, J. L.; Strom, T. A.; Wu, G.; Wilson, S. D.; Seshadri, R.; Cheetham, A. K. *Angewandte Chemie International Edition* **2020**, *59* (23), 8974–8981. https://doi.org/https://doi.org/10.1002/anie.202003095.

588. Nazarenko, O.; Kotyrba, M. R.; Wörle, M.; Cuervo-Reyes, E.; Yakunin, S.; Kovalenko, M. V. *Inorganic Chemistry* **2017**, *56* (19), 11552–11564. https://doi.org/10.1021/acs.inorgchem.7b01204.

589. Wu, Z.; Liu, X.; Ji, C.; Li, L.; Wang, S.; Peng, Y.; Tao, K.; Sun, Z.; Hong, M.; Luo, J. *Journal of the American Chemical Society* **2019**, *141* (9), 3812–3816. https://doi.org/10.1021/jacs.8b13827.

590. Paton, L. A.; Harrison, W. T. A. *Angewandte Chemie* **2010**, *49* (42), 7684–7687. https://doi.org/10.1002/anie.201003541.

591. Thétiot, F.; Sasaki, I.; Duhayon, C.; Sutter, J. P. *Journal of Chemical Crystallography* **2009**, *39* (3), 225–227. https://doi.org/10.1007/s10870-008-9511-y.

592. Zhang, W. Y.; Tang, Y. Y.; Li, P. F.; Shi, P. P.; Liao, W. Q.; Fu, D. W.; Ye, H. Y.; Zhang, Y.; Xiong, R. G. *Journal of the American Chemical Society* **2017**, *139* (31), 10897–10902. https://doi.org/10.1021/jacs.7b06013.

593. Muhammad azeem, Hong Zhang, Li-Jun Ji, Li-Yuan Dong, Pei-Xiang Lu, Wei Li, J. H. *CSD Private Communication* **2020**.

594. An, L.-C.; Li, K.; Li, Z.-G.; Zhu, S.; Li, Q.; Zhang, Z.-Z.; Ji, L.-J.; Li, W.; Bu, X.-H. *Small* **2021**, *17* (22), 2006021. https://doi.org/https://doi.org/10.1002/smll.202006021.

595. Chen, X. G.; Gao, J. X.; Hua, X. N.; Liao, W. Q. *Acta Crystallographica Section C: Structural Chemistry* **2018**, *74* (6), 728–733. https://doi.org/10.1107/S2053229618006885.

596. Harrison, W. T. A. *CSD Private Communication* **2019**.

597. Rickaby, K. A.; Slawin, A. M. Z.; Harrison, W. T. A. *Acta Crystallographica Section E: Crystallographic Communications* **2019**, *75* (8), 1249–1252. https://doi.org/10.1107/S2056989019010375.

598. Ferrandin, S.; Slawin, A. M. Z.; Harrison, W. T. A. *Acta Crystallographica Section E* **2019**, *75* (8), 1243–1248. https://doi.org/https://doi.org/10.1107/S2056989019010338.

599. Pan, Q.; Liu, Z.-B.; Tang, Y.-Y.; Li, P.-F.; Ma, R.-W.; Wei, R.-Y.; Zhang, Y.; You, Y.-M.; Ye, H.-Y.; Xiong, R.-G. *Journal of the American Chemical Society* **2017**, *139* (11), 3954–3957. https://doi.org/10.1021/jacs.7b00492.

600. Mayo Foundation for Medical Education and Research. Piperazine Uses https://www.mayoclinic.org/drugs-supplements/piperazine-oral-route/proper-use/drg-20065522 (accessed Jul 10, 2021).

601. Ouannes, C.; Wilson, T. *Journal of the American Chemical Society* **1968**, *90* (23), 6527–6528. https://doi.org/10.1021/ja01025a059.

602. Murphy, C.; Cardello, A. V; Brand, J. G. *Physiology & Behavior* **1981**, *26* (6), 1083–1095. https://doi.org/https://doi.org/10.1016/0031-9384(81)90213-4.

CHAPTER 3

Experimental Procedures

This chapter provides an overview of the synthetic procedures, structural characterisation methods, property characterisation methods and computer software used in this study.

3.1 Synthetic Procedures Used

In this section, a summary of the different synthetic techniques used in this study to prepare hybrid halide materials *via* self-assembly is given. Three methods, namely **slow evaporation**, **elevated temperature evaporation**, and **slow cooling,** were employed to obtain single crystals suitable for SCXRD. All compounds used as reagents were obtained commercially and used without further purification.

This section gives a general overview of the synthetic procedures used, while specific, detailed procedures employed to obtain the individual compounds, including masses and volumes used, are given in the result chapters, as per the publication format of the result chapters.

Two different organic cations were considered in this study, namely *dabconium* and *piperazinium*. The protonation of both nitrogen atoms of a 1,4-diazabicyclo[2.2.2]octane molecule results in the formation of a **dabconium** (1,4-diazabicyclo[2.2.2]octane-1,4-diium) dication (i.e., +2 charge) as shown in Scheme 3.1 (a). Similarly, the protonation of both nitrogen atoms of a 1,4-diazacyclohexane (piperazine) molecule results in the formation of a **piperazinium** (piperazine-1,4-diium) dication (i.e., +2 charge), which will be referred to as the piperazinium cation, illustrated in Scheme 3.1 (b).

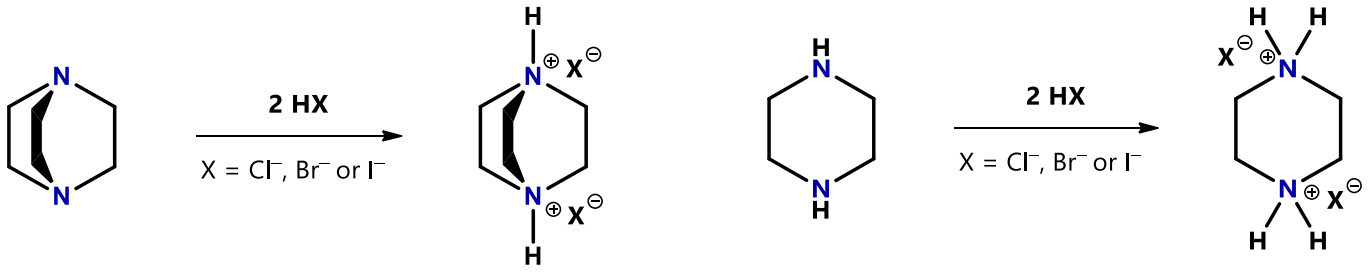

Scheme 3.1 (a) The protonation of 1,4-diazabicyclo[2.2.2]octane using HX (X = Cl^-, Br^- or I^-) to form the diprotonated dabconium cation (1,4-diazabicyclo[2.2.2]octane-1,4-diium) and **(b)** the protonation of piperazine using HX (X = Cl^-, Br^- or I^-) to form the diprotonated piperazinium cation (piperazine-1,4-diium).

Compounds and their structures will be referred to according to the abbreviation of their structural formulas, **A-BX$_n$**, with **A** indicating if the cation is the dabconium dication (**D**) or the piperazinium dication (**P**), **B** indicating the metal ion (Na^+, K^+ or Cs^+), **X** indicating the halide anion (Cl^-, Br^- or I^-), and ***n*** indicating the number of halide ions in the molecular formula. For example, the abbreviation **D-NaCl$_3$** refers to the structure resulting from the combination of dabconium cations and anionic species comprised of Na^+- and Cl^--ions. This naming scheme is further adapted to describe polymorphic structures by the addition of a number contained in brackets, e.g., **D-KBr$_3$(1), D-KBr$_3$(2)** and so on, which indicates two different structure types for the combination of dabconium cations and KBr, while having the same molecular formula, **D-KBr$_3$**.

More than 100 reactions were carried out in attempts to produce crystals or powders of the hybrid products consisting of dabconium- or piperazinium dications, and anions based on alkali metal halides, however, only those that successfully

produced perovskite or organic-inorganic hybrid products are included in the Tables in Sections 3.1.1 to 3.1.3 below. It was found that several reactions did not give the desired products, but instead resulted in the formation of materials consisting of a mixture of the organic halide salt and metal halide salt, instead of the hybrid compound, as illustrated by PXRD in Appendix D.

The separate crystallisation of the organic halide salt and metal salt from a solution containing the reagents for hybrid synthesis is ascribed to the difference in solubility of these two salts in the solvent employed, causing one of the salts to crystallise out first, with the second salt remaining in solution, and then crystallising at a later stage. After the crystallisation of one of the salts occurred, one of the components required for the formation of the hybrid material (perovskite or other) was no longer available in solution, hence the hybrid was not formed. Three different techniques were employed to successfully prepare the hybrid materials, as described below.

3.1.1 Slow Evaporation

The general procedure followed for all of the materials prepared through the slow evaporation method is as follows:

The organic reagent (either 1,4-diazabicyclo[2.2.2]octane or 1,4-diazacyclohexane) is dissolved in an appropriate amount of solvent, to which an excess amount of HX acid (4 to 8 equivalents to the organic reagent) is added. The MX species (1 equivalent to the organic reagent) is dissolved separately in an appropriate amount of solvent and this solution is then added to the solution of the protonated organic component. The resultant solution is left, open to the atmosphere, to air-dry in a well-ventilated area. The air-drying process occurs at room temperature (RT). Crystals are harvested after evaporation of all the solvent and subsequently washed with an appropriate anti-solvent.

Table 3.1 summarises the specific details of each of the experiments carried out using the slow evaporation technique for the preparation of materials containing the dabconium and the piperazinium cations.

Table 3.1 Experimental details for the preparation of dabconium- or piperazinium-containing materials using the slow evaporation technique. [a]

Organic Cation	Metal Halide (MX)	Acid & Equivalence	Solvent Used		Structure or Compound Code
			Organic	MX	
Dabconium	NaCl	HCl (4 eq.)	Water	Water	**D-NaCl$_3$**
	NaBr	HBr (4 eq.)			**D-NaBr$_3$**
	KCl	HCl (4 eq.)			**D-KCl$_3$**
	KBr	HBr (4 eq.)			**D-KBr$_3$**
	CsCl	HCl (4 eq.)			**D-CsCl$_3$**
	CsBr	HBr (4 eq.)			**D-CsBr$_3$**
	CsI	HI (4 eq.)			**D-CsI$_3$**
	CsI	HCl (8 eq.)			**D-CsICl$_2$**
Piperazinium	NaBr	HBr (2 eq.)	Water	Water	**P-NaBr$_2$**
	KCl	HCl (4 eq.)			**P-KCl$_3$**
	KBr	HBr (4 eq.)			**P-KBr$_3$**
	KI	HI (4 eq.)			**P-KI$_3$**
	CsCl	HCl (4 eq.)			**P-CsCl$_3$**

[a] All materials listed in the table are perovskites, aside from **P-NaBr$_2$**, which is an organic-inorganic hybrid material.

3.1.2 Slow Cooling Method

The slow cooling method utilised in this study is the same as reported by Andreas Lemmerer and described in detail in Chapter 1.[1] In general, the **slow cooling method** was performed as follows:

The organic species (either 1,4-diazabicyclo[2.2.2]octane or 1,4-diazacyclohexane) and the metal halide compound (MX) are dissolved in excess concentrated acid (HX) in a vial. However, enough of both of the solid reagents is added so that the solution is saturated at room temperature. The vial is sealed with a lid and placed in an oil bath and heated to between 80 °C and 120 °C, with the vial immersed in the oil to the same level as the solution in the vial. Once all the solid reagents are dissolved, the hot plate is turned off, and the set-up is left to cool back down to room temperature, with crystals forming on cooling due to the solution being saturated at room temperature. The crystals are then carefully harvested from the acidic solution and washed with an anti-solvent.

The details of the experiments carried out to obtain compounds using the slow cooling method are summarised in Table 3.2. The slow cooling method was only utilised for dabconium-containing compounds.

Table 3.2 The details of the syntheses which lead to the formation of perovskite materials containing the dabconium cation, employing the slow cooling method.

Metal Halide (MX)	Acid & Equivalence	Solvent Used		Structure or Compound Code
		Organic	MX	
NaI	Excess HI	Conc. Acid	Conc. Acid	**D-NaI$_3$**
KI	Excess HI	Conc. Acid	Conc. Acid	**D-KI$_3$**

Several miscellaneous dabconium salts were also obtained through the slow cooling method, however, these are outlined in Appendix B.

3.1.3 Elevated Temperature Evaporation Method

The elevated temperature method is unlikely to yield good quality single crystals, hence, the procedure outlined here is generally used to synthesise bulk powders of the desired material. However, in certain cases, crystals were obtained from this method. When a bulk powder is prepared, its experimental PXRD pattern is matched to the calculated powder pattern of a single-crystal structure to determine its purity (see Appendix D) before being used for property measurements. The general procedure followed for all of the materials prepared through the elevated temperature evaporation method is as follows:

The organic reagent (either 1,4-diazabicyclo[2.2.2]octane or 1,4-diazacyclohexane) is dissolved in an appropriate amount of solvent, to which an excess amount of HX acid (4 to 8 equivalents to the organic reagent) is added. The MX species (1 equivalent to the organic reagent) is dissolved separately in an appropriate amount of solvent and this solution is then added to the solution of the protonated organic component. The resultant solution is left, open to the atmosphere and heated to between 60 and 120 °C on a hot plate. Crystals are harvested after evaporation of all the solvent and subsequently washed with an appropriate anti-solvent.

The details of the experiments carried out to obtain compounds using the elevated temperature evaporation method are summarised in Table 3.3.

Table 3.3 The details of the synthetic process which lead to the formation of structures containing the dabconium or piperazinium cation from the elevated temperature evaporation method.

Organic Cation	Metal Halide (MX)	Acid & Equivalence	Solvent Used		Structure or Compound Code
			Organic	MX	
Dabconium	NaCl	HCl (2.2 eq.)	Water	Water	**D-NaCl$_3$**
	NaI	HI (2.2 eq.)			**D-NaI$_3$**
	KBr	HBr (2.2 eq.)			**D-KBr$_3$(2)**
	KI	HI (2.2 eq.)			**D-KI$_3$**
Piperazinium	NaI	HI (2.2 eq.)	Water	Water	**P$_3$-NaI$_5$**[a]
	CsCl	HCl (2.2 eq.)			**P-CsCl$_3$**

[a] The structure **P$_3$-NaI$_5$** is an exception to the naming scheme described earlier, however, P$_3$ only indicates three piperazinium cations present in the molecular formula.

This concludes the synthetic methods section. The following section will focus on the experimental methods used to characterise the materials obtained in this study.

3.2 Characterisation Methods

This section discusses the methods and instrumentation used in structure determination (characterisation) and purity analysis of the prepared compounds. These methods include X-ray diffraction techniques, namely **single-crystal X-ray diffraction (SCXRD)** and **powder X-ray diffraction (PXRD)**.

3.2.1 X-Ray Diffraction (XRD)

The primary structure characterisation method employed in this study is **X-ray diffraction**. Both **single-crystal X-ray diffraction (SCXRD)** and **powder X-ray diffraction (PXRD)** methods were employed. X-ray diffraction is a process where X-ray electromagnetic radiation interacts with the electrons of atoms situated in a crystal lattice. X-rays can be used for this purpose since the spacing between atoms (1–3 Å) is the same order of magnitude as the wavelength of an X-ray (for example 1.54 Å for Cu *Kα* X-rays), which allows for the diffraction of X-rays from the diffraction grid created by the atoms and their electrons.[2] The atoms diffract the X-rays, and only constructively interfering X-rays are detected afterwards. The success of the method lies in the ordered nature of crystal structures, which allow for constructive interference, as described by Bragg[3] and von Laue[4]. The main components of an X-ray diffractometer are shown in Figure 3.1 and include an X-ray source, the sample under investigation (single-crystal or powder) and a detector to detect the diffracted X-rays.

Additionally, the electronic environment of an atom is unique to the type of atom. Hence, the diffraction of different atoms in the crystal lattice can be distinguished from one another, with each atom contributing to the overall diffraction pattern obtained. In general, *heavier* atoms, like lead, diffract X-rays better than *lighter* atoms, like hydrogen, as indicated by the atomic scattering factor of the specific atom. This may cause difficulty in detecting lighter atoms, especially in the presence of heavier atoms.

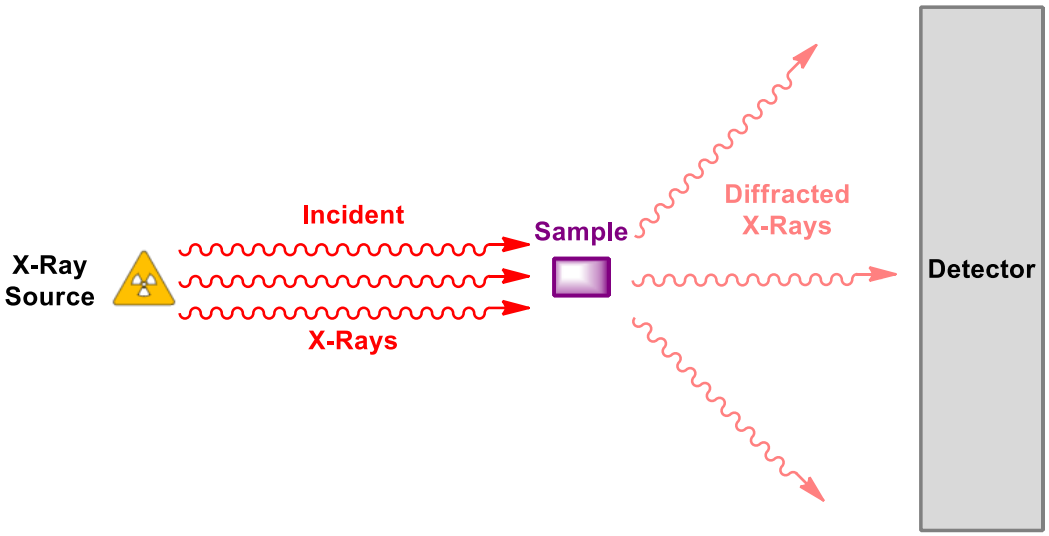

Figure 3.1 A schematic illustration of the typical setup of an X-ray diffractometer. The "sample" may be either a powder or a single-crystal.

Diffraction from an Optical Grating

Similarly to how an optical grating diffracts light, X-rays may be diffracted by the electrons in atoms in a crystal lattice. To this end, consider the 1D diffraction grating shown in Figure 3.2. The 1D case can easily be converted into the 3D case, however, the algebra is much more elegant in the 1D case, and hence it will be considered here. Electromagnetic radiation (visible light, X-rays etc.) is diffracted by the grating (of the correct spacing) and thereafter observed by a detector.

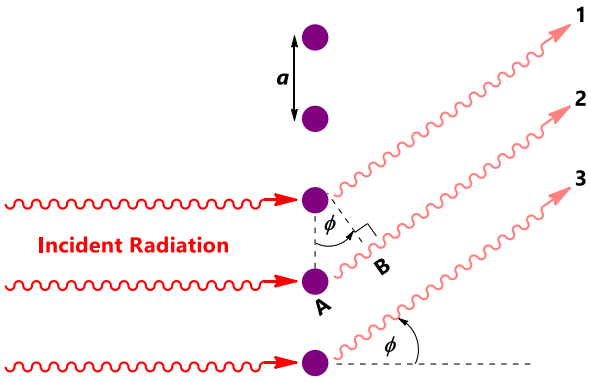

Figure 3.2 Diffraction of electromagnetic radiation by a 1D optical grating. This figure defines the symbols used in the Laue equations.

Then beams labelled 1 and 2 are *in-phase* (i.e., interfere constructively) and diffract at an angle ϕ to the incident beam. For them to be in-phase, the distance AB must be equal to a whole number of the wavelength (λ) of the radiation. Mathematically this implies that Equation (3.1) is valid:[2]

$$\mathrm{AB} = \lambda, 2\lambda, \cdots, n\lambda \tag{3.1}$$

where n is an integer. However, it is also true from the geometry of Figure 3.2 that $\mathrm{AB} = a\sin(\phi)$. Therefore, substituting AB in Equation (3.1) leads to the requirement for constructive interference as given in Equation (3.2)[2]

$$a\sin(\phi) = n\lambda \tag{3.2}$$

Equation (3.2) provides the condition for constructive interference and provides a relationship between the diffraction grating spacing and the wavelength of the incident beam of radiation. Also, depending on the value of $a\sin(\phi)$, different diffraction orders corresponding to $n = 1, 2, 3, \ldots$, may be observed.

Intuitively, the spacing in the diffraction grating must be of the same order of magnitude as the wavelength of the electromagnetic radiation. However, Equation (3.2) implies that the first-order diffracted beam ($n = 1$) occurs when $a\sin(\phi) = \lambda$, and since the maximum value of $\sin(\phi)$ is 1, this means that $\phi = 90°$. Nevertheless, realistically, this is difficult to observe, and so for an observable first-order diffraction beam, $a > \lambda$, which allows for $\phi < 90°$. This explains why the spacing in the diffraction grating must be a bit larger than the wavelength of radiation used. This concept is vital for X-ray diffraction studies on crystals since this allows for the measurement of diffraction patterns of crystals with spacings larger than that of the wavelength of X-rays.

If it were the case that $a \gg \lambda$, then there would be no distinct constructive and destructive interference, and hence a continuum of diffracted beams would be observed. Moreover, the lines of the optical grating need to be parallel to allow for distinct values of ϕ, in which case, if they were not, blurred (poor) diffraction patterns would be observed. These requirements make crystals perfect for use in X-ray diffraction studies, since they have uniform packing of species comprising the structure (hence spacing), they are *ideal optical gratings*.

Therefore, using the same idea as with an optical grating, crystals may be studied by diffraction of electromagnetic radiation, specifically, X-ray radiation, electrons, or neutrons. Though this study will employ X-ray radiation, the theory does not change for other radiation types or particles like electrons or neutrons.

The two mathematical models are used to describe the diffraction of X-rays by crystals, the first by Max von Laue and the second by the Bragg father-son pair. Both models are entirely consistent with one another. Chemists mostly use the Bragg model, and hence it will enjoy greater attention here, that said, the von Laue method will first be described briefly for completeness.

The Laue Equations

As mentioned before, the 1D diffraction grating may be assumed to be a 1D crystal lattice. However, in reality, crystals have a 3D arrangement of atoms, for which the so-called *Laue Equations* (shown in Equations (3.3) through (3.5)) may be written using the same notation as defined in Figure 3.2 and with symbols carrying the same meaning as in Equations (3.1) and (3.2).[5]

$$a_1 \sin(\phi_1) = n\lambda \tag{3.3}$$

$$a_2 \sin(\phi_2) = n\lambda \tag{3.4}$$

$$a_3 \sin(\phi_3) = n\lambda \tag{3.5}$$

Each of these three equations corresponds to one crystallographic direction seen in a real crystal, namely directions 1, 2 and 3, each corresponding to a specific direction in the crystal lattice. Therefore, for a beam to diffract constructively in a 3D arrangement, all three of these equations must hold. They represent a rigorous mathematical way of describing 3D diffraction defined by Max von Laue.[4] However, the alternative theory, called **Bragg's Law**, is much simpler and hence enjoys more use.

The Bragg Equations

According to the Bragg theory, crystals are model as layers (planes) of semi-transparent "mirrors". These planes are known as Miller planes. Some incident X-rays are reflected by these planes, while others pass through certain planes only to be reflected by a subsequent plane. For the derivation of Bragg's Law, consider Figure 3.3.

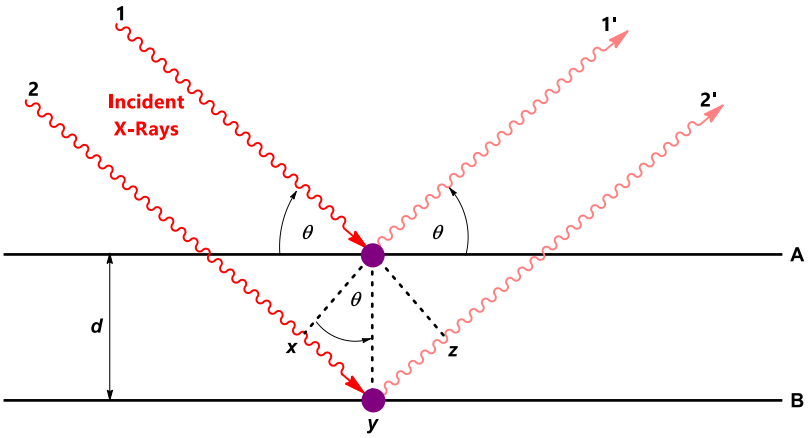

Figure 3.3 Schematic illustration of the reflection of incident X-rays on subsequent semi-transparent planes in a crystal lattice, as used in the derivation of Bragg's Law. All symbols used in the derivation of Bragg's Law are defined in the figure.

In Figure 3.3, two X-ray beams (beams 1 and 2) are reflected from two subsequent planes A and B, and hence, the objective is to know when the reflected beams (beams 1' and 2') are in-phase (constructive interference). The combined beam 2-2' must travel an additional distance *xyz* compared to the combined beam 1-1'. For them to be in-phase, this *additional distance travelled* must equal a whole number of wavelengths ($n\lambda$) of the radiation. Otherwise, the beams will interfere destructively.

Furthermore, the perpendicular distance between the planes A and B, d (called the d-spacing), and the angle of incidence of the radiation (the Bragg angle, θ) can be used to calculate the distances xy and yz as follows:

$$xy = yz = d\sin(\theta)$$

In other words, since $xy = yz$, then the distance $xyz = xy + yz = 2xy$, so that

$$xyz = 2d\sin(\theta)$$

Then adding the requirement for constructive interference, hence that $xyz = n\lambda$, where $n = 1, 2, 3,\ldots$, leads to Equation (3.6), which is known as Bragg's Law[3]

$$2d\sin(\theta) = n\lambda \tag{3.6}$$

Bragg's Law, therefore, gives another mathematical version of the condition for constructive interference. At angles that are not equal to the Bragg angle, diffracted beams are out-of-phase and destructive interference occurs. Hence the beams "cancel" at these angles. In a real crystal, there are many (in theory an infinite number) of these reflection planes, and even in these cases, when the angle of incidence differs a few tenths of a degree with the Bragg angle, the reflectance or diffraction is not observed.

From Equation (3.6), it is evident that there are several solutions for a set of planes due to the allowance of $n = 1, 2, 3,\ldots$ However, usually, n is set to 1. Another important note is on the notion of reflectance or diffraction. In a physical sense, there is no reflection from semi-transparent planes. Physically there is only diffraction observed from the electrons in the atoms in the crystal lattice, however, this model of reflection has been proven to be valid and delivers one of the most beautiful results in crystallography.

Both the Bragg and von Laue set of equations deals with diffraction from a crystal lattice as a physical entity in real 3D space, however, it turns out that it is much more convenient to consider diffraction in something called the *reciprocal space*. The reciprocal lattice is an imaginary inverse of the real physical lattice. Thus, the real lattice can easily be converted into a reciprocal lattice, as suggested by Paul Ewald. It turns out that when the concept of diffraction in reciprocal space is converted back to real space, the Bragg Law is again obtained. This is briefly described in the following section.

The Reciprocal Lattice and the Construction of the Ewald Sphere

To see why the notion of a reciprocal lattice is useful in understanding diffraction, consider Figure 3.4. Here, C represents the planes of a crystal lattice and AC, a beam of X-rays incident on crystal planes at an angle of θ. Next, a sphere of radius $1/\lambda$ is drawn through the crystal, where λ is the wavelength of the incident radiation. This sphere drawn here is known as the *Ewald sphere*.[6] In the figure, a 2D profile of the sphere's construction is illustrated.

The vector $\overrightarrow{CP}$ is perpendicular to the planes of the crystal lattice, C. If the magnitude (length) of $\overrightarrow{CP}$ is $1/d$, then $\overrightarrow{CP}$ is called the reciprocal lattice vector for the set of lattice planes, C. Furthermore, from the triangle ACP, it can be seen that $1/\lambda$ is the magnitude of the vector $\overrightarrow{AC}$, and so

$$\sin(\theta) = \frac{|\overrightarrow{CP}|}{2|\overrightarrow{AC}|} = \frac{\frac{1}{d}}{2\left(\frac{1}{\lambda}\right)} = \frac{\lambda}{2d} \tag{3.7}$$

which is Bragg's Law when $n = 1$. Put into words, this means that if a reciprocal lattice point resides on the surface of the Ewald sphere, then a diffracted beam will be observed in the direction of the vector $\overrightarrow{OP}$. Moreover, if the lattice planes are orientated such that the reciprocal lattice point does not lie on the Ewald sphere, no diffraction will be observed.[6] This allows for a better mathematical model to describe constructive and destructive interference and allows the measurements to be simplified using software.

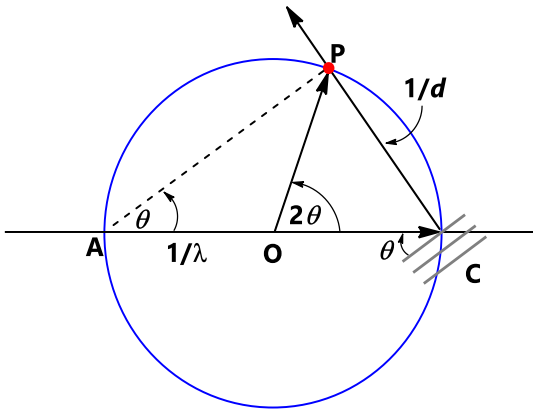

Figure 3.4 Schematic illustration of the construction of the Ewald sphere (shown in blue) for the derivation of Bragg's Law from the reciprocal lattice.

This requirement in reciprocal space also implies that if a monochromatic source of radiation is used, to obtain a complete data collection of all the possible reflections, the crystal must be rotated, otherwise, only those reciprocal lattice points lying on the Ewald sphere for that orientation would be seen. Thus, by rotating the crystal, all the reciprocal lattice points will move through the Ewald Sphere at some point in the data collection, and hence a complete set of reflections can be obtained.

Reflection Intensities and Amplitudes

After reflection (diffraction), the diffracted waves will arrive at a detector, each with its relative phase difference and amplitude. That said, the detector can only record the intensities of the diffracted waves, and from general wave mechanics, the intensity of a wave is proportional to the square of its amplitude. Though, this proportionality to the square of a value means that all information regarding the relative phase of the wave is lost, which is where most of the difficulties in structure determination are found.

A so-called structure factor gives a measure of the amplitude of the diffracted wave, $F(hkl)$, where h, k and l are the Miller indices of the plane from which the diffraction occurred. Therefore, the intensity of the waves and this structure factor are related, as written in Equation (3.8)[2]

$$I(hkl) \propto |F(hkl)|^2 \tag{3.8}$$

Furthermore, if a diffraction pattern is centrosymmetric, in that $I(hkl) = I(\bar{h}\,\bar{k}\,\bar{l})$, this relationship is known as Friedel's Law, however, it assumes no absorption of X-rays by the atoms.[7] Since this section does not aim to be a comprehensive text on the subject of X-ray crystallography, the discussion will now shift its focus to methods of application of the theory of X-ray diffraction. The subsequent theory will be introduced as required.

Powder X-Ray Diffraction (PXRD)

PXRD may be used as a fingerprinting method or a method for determining the purity of a bulk sample, where the latter application was employed in this study (see Appendix D). Firstly, the bulk sample is analysed using PXRD. This experimental powder pattern is then matched to the powder pattern calculated from a known single-crystal structure obtained from the single-crystal X-ray diffraction analysis (using SCXRD, described later). A match between the experimental and calculated powder patterns indicates that the single-crystal structure used in SCXRD analysis is representative of the bulk sample. Thus, that the bulk powder sample is pure, and may be used for property measurements.

The first step in using PXRD is to grind the sample into a fine, polycrystalline powder (a collection of random small crystals) using a mortar and pestle. Thereafter, the sample is sifted over a sample holder (see Figure 3.5 (a)), and only a small amount of the sample is required when a low background silicon sample holder is used. The sample holder containing the sample is placed in the PXRD instrument and scanned over a range of 2θ angles, while irradiating the sample with an X-ray source, as illustrated in Figure 3.5 (b).

The X-ray detector detects the scattered X-rays as rings, known as Debye-Scherrer rings,[8] shown in Figure 3.5 (c), with the diffraction rings resulting from the differently orientated microcrystals in the sample. To explain how these rings are formed and subsequently converted into a so-called powder pattern, consider Figure 3.5 (d) through (i). In Figure 3.5 (d), the diffraction pattern of a single-crystal is shown with the use of blue and green dots, as explained next. The central blue dot illustrates the X-ray beam(s) that pass through the sample without being diffracted, hence it is comparatively larger. The spots have differing intensities and lie on the positions as determined by the reciprocal lattice.

Furthermore, in Figure 3.5 (e) and (f), the effect on the observed diffraction patterns of having two and three slightly differently aligned crystals of the same structure is illustrated. Each crystal that is orientated differently gives rise to slightly shifted diffraction peaks, however, still at the same 2θ value. If an "infinite" number of randomly orientated (differently orientated) crystals are present, the individual spots on the diffraction detector will form a continuum of different intensity rings (Debye-Scherrer rings), as shown in Figure 3.5 (g).

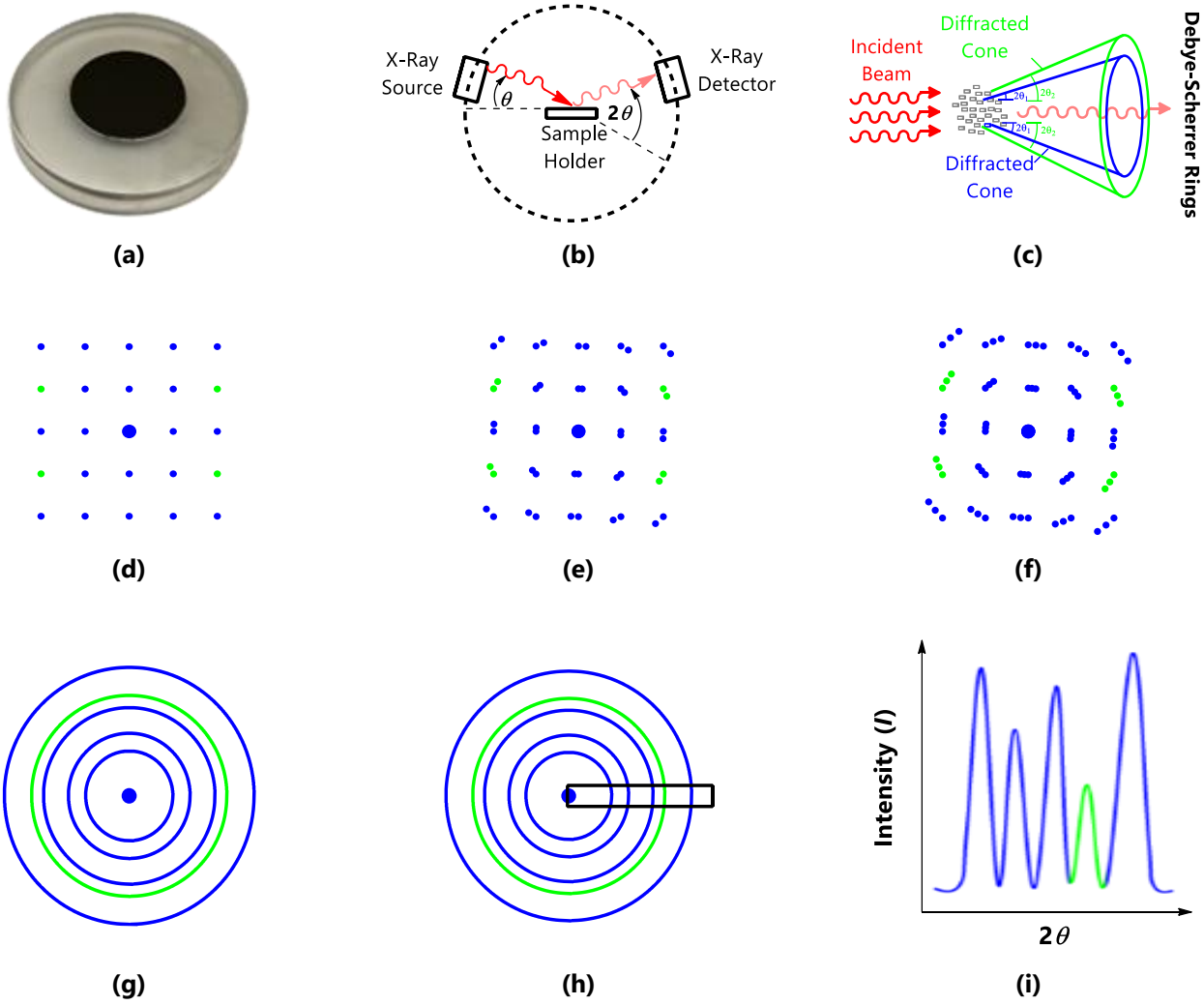

Figure 3.5 (a) A picture of a low background silicon sample holder. **(b)** A schematic representation of the PXRD data collection process and definition of relevant symbols. **(c)** The formation of Debye-Scherrer rings[8] by rotating or moving the X-ray source. **(d)** The diffraction spots from a single-crystal. **(e)** The diffraction pattern of two single-crystals with different alignments. **(f)** The diffraction pattern of three crystals with different alignments. **(g)** The diffraction pattern of many crystals all aligned differently. **(h)** A section of the diffraction pattern scanned by the detector. **(i)** A schematic of the resultant powder pattern from the scan shown in Figure (h). The green and blue colours do not indicate different types of crystals or orientations, the colours are only used to highlight one specific peak in the powder pattern of Figure (i).

In a real PXRD instrument, the detector will only be moved over the sample in a hemisphere (between 0° and 90° in one axis), which leads to it only scanning the parts of the rings highlighted in the black bar in Figure 3.5 (h). Therefore, a 1D PXRD pattern is collected, as illustrated in Figure 3.5 (i), with each of the Debye-Scherrer rings corresponding to a specific peak in the pattern.[2] A typical powder pattern plot will have intensity (in a.u.) on its ordinate axis and 2θ (in degrees) on its abscissa.

Primarily PXRD is used as a fingerprint method to identify materials or for indicating the purity of a powder sample by matching it to other pure powder samples or calculated patterns from single-crystal structures. However, in 1969 Hugo Rietveld[9] showed that it is possible to determine a crystal structure from a PXRD pattern using *Rietveld refinement*, though one still requires a reasonable starting model of the crystal structure to be successful.

PXRD Instrumentation used in this study. In the current study, powder X-ray diffraction patterns were measured using a Bruker D2 Phaser instrument, at room temperature, using Cu radiation (λ = 1.54 Å), and a low background silicon sample holder. Typically, the powder patterns were collected from 5° to 45° 2θ with a step size of 0.05° and a counting time of between 1 and 3 seconds per step. The Bruker D2 Phaser instrument used in this study is shown in Figure 3.6 (a) and (b).

(a) **(b)**

Figure 3.6 The Bruker D2 Phaser powder diffractometer used in this study **(a)** from the outside and **(b)** a photo of the inner workings of the instrument.

PXRD is useful when bulk samples are to be analysed and the structure of the material studied is known. However, even with methods such as Rietveld refinement available,[9] alternatively, X-rays can be used in another way to determine the structure of a crystal. The technique used to do so is called single-crystal X-ray diffraction (SCXRD), and with this technique, one can obtain the structure of a single-crystal. However, before considering how one can obtain a crystal structure, a few theoretical concepts must be addressed, which are important in SCXRD. The first of which is the **phase problem** and is discussed next.

The Phase Problem

When viewing an object using visible light and a lens, all the "information" is perceived by the focal plane simultaneously. Hence, the lens combines all the waves' amplitudes and their phases to form the object so a person may *see* the object. Therefore, if there is no lens, the information of the waves' amplitudes and their phases will not be combined, and only the amplitudes can be observed. This is the *problem* experienced when X-rays diffract off a crystal lattice because there exist no "X-ray lenses" to help focus the information, so the phase information is permanently *lost*.[2]

X-ray crystallography uses the intensities of X-rays diffracted off Miller planes in a crystal lattice. It correlates that to the structure factors, as shown in Equation (3.8). Therefore, a method needs to be obtained to replace the concept of an X-ray lens so that the crystal structure may be determined. This is the objective of solving the **phase problem**, and there are several mathematical approaches to solve it.

The most commonly used method for solving the phase problem is known as **direct methods**, developed by Hauptman and Karle, for which they were awarded the Nobel Prize in 1985.[10]

Direct methods utilise equations to extract the phase information from the intensity of the diffracted beams and subsequently this allows for the assignment of atoms' location, based on the analysis of the intensity of the diffraction spots.[11] Additional methods developed by Patterson (known as Patterson Synthesis[12]) and Charge Flipping (an Ab initio technique developed by Gábor Oszlányi and András Sütő in 2004[13,14]) are also used in modern-day crystallography.

William Bragg suggested the first technique to combine amplitudes and phases in 1915, known as *Fourier Synthesis*.[15] This method uses Fourier transforms to generate the electron density function of the structure from the structure factors and relative phases of the diffraction, which can be obtained using one of methods discussed above. From the electron density map, the atoms may be assigned with prior knowledge or computer software.

The final section on X-ray crystallography will cover the experimental aspects of single-crystal X-ray diffraction since all of the required theory has already been discussed.

Single-Crystal X-Ray Diffraction (SCXRD)

SCXRD is a non-destructive characterisation technique employed to determine the crystal structure of a crystalline compound, using a small crystal, hence the name, *single-crystal X-ray diffraction*. A rotating single-crystal is bombarded with monochromatic X-ray radiation, which is diffracted by the crystal, and the diffracted X-rays are measured by a charged coupled device (CCD) detector as shown in Figure 3.7 (a) and (b).

All the diffraction patterns collected are combined in a single data file, known as the hkl file, and the diffraction data is used to determine the unit cell and space group of the structure. As a first step the crystal structure is "solved", to obtain a starting model of the structure, using the methods to solve the phase problem discussed previously. The starting model is then further improved by refining it using least squares refinement that compares the experimental diffraction data with the data calculated from the model structure. The diffraction data calculated from the structure model is obtained through Fourier synthesis, which also allows for the generation of a three-dimensional electron density map of the crystal structure.

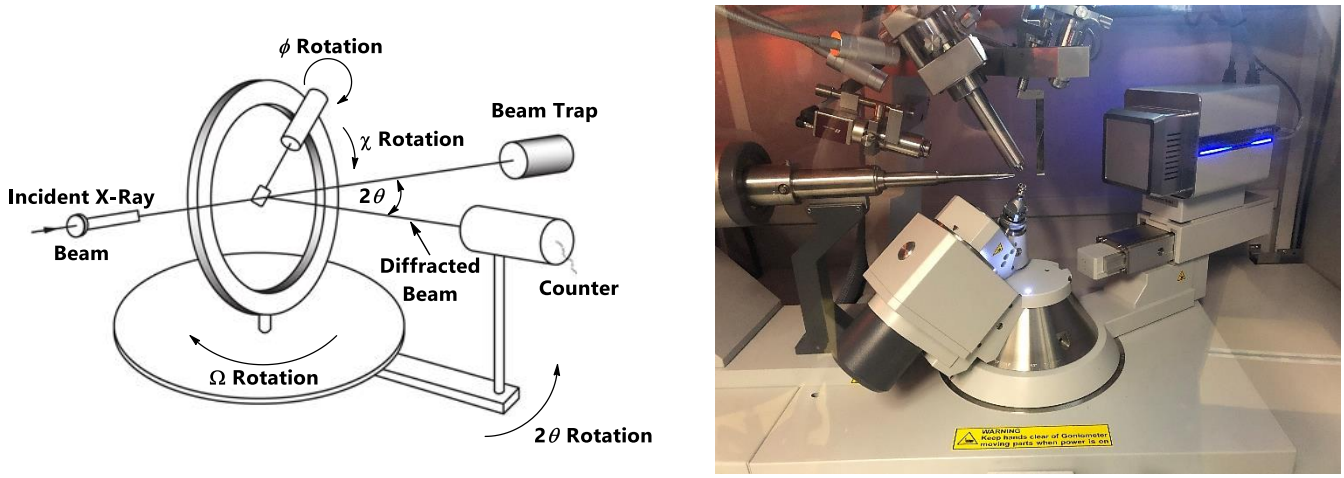

Figure 3.7 (a) A schematic illustration of a so-called 4-circle diffractometer used for SCXRD analysis and **(b)** a photo of one of the 4-circle diffractometers used in this study.

In contrast to PXRD, where a bulk powder sample is used (many microcrystalline particles), SCXRD requires a small, good quality single-crystal (between 50 and 250 microns in size), which is optically clear and ideally should not be *twinned*. These crystals are picked from under a polarised microscope to ensure that an optically clear, unfractured, single-crystal is selected for the analysis. The selected crystal is then mounted on a nylon loop using *N*-Paratone oil. Both nylon and *N*-Paratone oil are inert and do not diffract X-rays, hence they are employed for this purpose. A schematic illustration of a nylon loop and a photo of a mounted crystal on a nylon loop are shown in Figure 3.8 (a) and (b), respectively. The mounted crystal is then placed on the diffractometer, cantered relative to the incident X-ray beam and the analysis is commenced. When data is to be collected at a lower temperature than room temperature, typically liquid nitrogen is blown over the mounted crystal, to *cool down* the single-crystal, using a cryostat system.

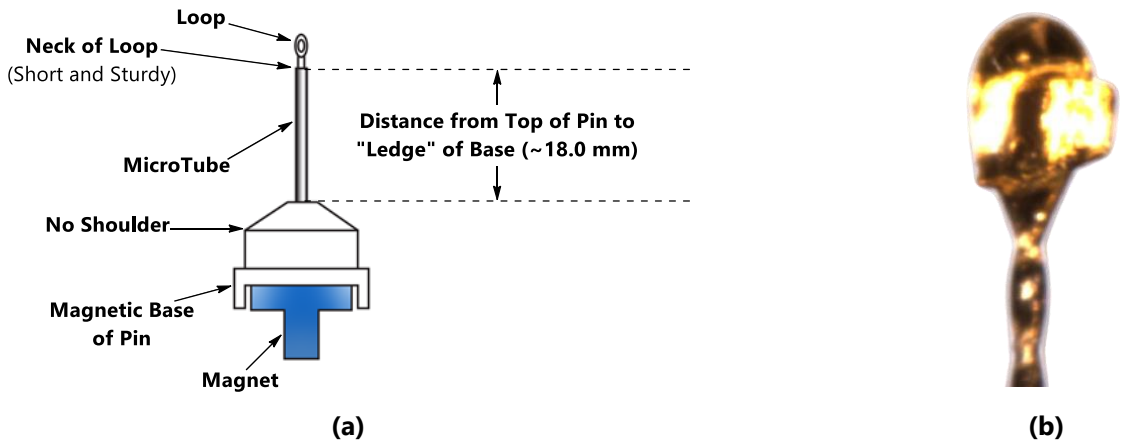

Figure 3.8 (a) A schematic illustration of a nylon crystal mounting loop used for SCXRD analysis and **(b)** a mounted crystal on a nylon loop, covered with *N*-Paratone oil.

Once the analysis begins, the crystal is rotated and *screened* to determine its quality and determine specific parameters used later in the data collection. A preliminary determination of the unit cell can then be done by a collection of several reflections. Furthermore, a sphere or hemisphere of data is collected during an incremental scan of the crystal, depending on the crystal system of the unit cell obtained. Finally, after all the data has been collected, corrections for absorption, background, and certain other corrections (depending on the software used) are applied to the raw diffraction data is completed.

After the diffraction data have been obtained, the phases must be obtained and combined with structure factors to obtain the electron density distribution and hence the crystal structure. To do so, modern software uses, among others, direct methods, charge flipping or the Patterson method to initially assign phases to strong reflections. Once a starting model is obtained, the starting model is subsequently improved using an iteration method to determine an improved fit.[16]

The initial electron density map obtained is combined with the pre-knowledge of which elements are present to obtain the full crystal structure. Other indicators that may be used include distances between intensity centra and assignment based upon chemical intuition (likely coordination, chemical environment, etc.).

The R value is used as a measure of the fit of the calculated data determined from the structural model to the experimental data, and the lower the R value, the superior the match, and the better the structure. Two R values are typically employed, namely R_1 and wR_2. The formula to calculate R_1 is $R_1 = \frac{\sum||F_o|-|F_c||}{\sum|F_o|}$, where F is the structure factor, and o indicates observed, and c calculated structure factors. wR_2 is similar to R_1 but refers to squared F-values. As a result, wR_2 always has a higher value than R_1.

SCXRD Instrumentation used in this study. In the current study, single-crystal X-ray diffraction data were collected employing two different single-crystal X-ray diffractometers. The first is a Rigaku XtaLAB Synergy R diffractometer, with a HyPix detector, equipped with a rotating anode source providing Cu or Mo radiation. Cooling was achieved using an Oxford Cryogenics Cryostat. Secondly, data were collected on a Bruker D8 Venture diffractometer, with a Photon 100 CMOS detector and an Iμs source providing Cu or Mo radiation. Cooling was achieved using an Oxford Cryogenics Cryostat. Moreover, X-ray diffraction data were collected at 150 K, as explained in the result chapters.

Figure 3.9 shows photos of the two instruments used to collect single-crystal X-ray diffraction data in this study, namely (a) Rigaku XtaLAB Synergy R diffractometer and (b) the Bruker D8 Venture diffractometer.

(a) **(b)**

Figure 3.9 Photos of the two single-crystal X-ray diffractometers used in this study. **(a)** The Rigaku XtaLAB Synergy R diffractometer and **(b)** the Bruker D8 Venture diffractometer.

3.3 Material Property Analysis

A selection of properties were measured for the materials synthesised in this study. Two instrumental techniques were employed, namely **diffuse reflectance spectroscopy (DRS)** to determine the optical band gap of the materials and **fluorescence spectroscopy** to determine the emission properties of the materials.

3.3.1 Diffuse Reflectance Spectroscopy (DRS)

Absorption techniques (such as UV-Vis spectroscopy) are usually employed to determine the optical band gaps of materials. However, crystalline materials are typically opaque and *do not* allow light transmission but refract incoming radiation. Therefore, absorption techniques tend to deliver erroneous absorbance data, giving higher absorption maxima than the true values. One proposed solution is to use the refracting and hence reflecting nature of the sample, and therefore to record the reflectance of the material, which forms the basis for **diffuse reflectance spectroscopy** (DRS). Consider Figure 3.10 as illustration of the technique. In DRS, a fine powder sample of the material is irradiated with a broad range of radiation wavelengths, as shown in Figure 3.10 (a), while the scattered radiation is collected with an integration sphere, which collimates the light into a single beam that can be spectrally analysed (see Figure 3.10 (b)). Additionally, Figure 3.10 (c) shows the inner workings of a "Praying Mantis" diffuse reflectance spectrometer, illustrating how the radiation (shown in red) enters the integrating sphere, interacts with the powder sample, after which the integrating sphere collimates the reflected radiation into a single beam (shown in blue), before the radiation moves to the detector.

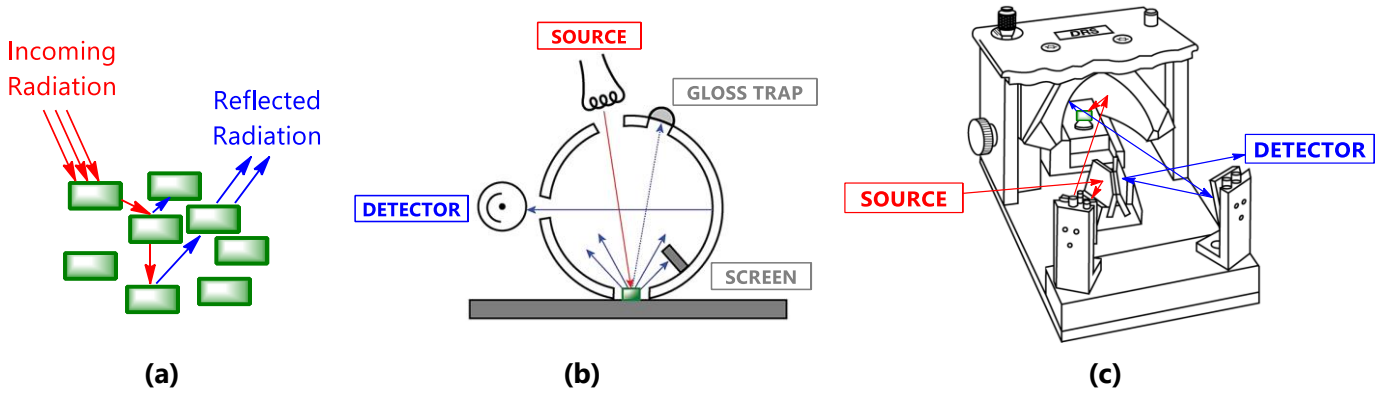

Figure 3.10 (a) A schematic representation of the interaction of radiation with powder crystalline material, **(b)** a schematic representation of the integrating sphere used in DRS and **(c)** a schematic representation of the "Praying Mantis" Diffuse Reflection Spectrometer, with UV radiation shown as arrows, tracing out the path of radiation through the spectrometer (adapted from Harrick Scientific Products[17]).

The resulting raw data set consists of a percentage reflectance (%R) value at each radiation wavelength the sample was subjected to. A typical graph of percentage reflectance versus wavelength can be constructed as shown in Figure 3.11. There are three defined regions in this graph, as explained below.

The first region is in a *low energy* radiation region (long wavelength, region A in Figure 3.11), where a high percentage reflectance plateau is observed. This high reflectance plateau comes about since the radiation in this region has insufficient energy to excite electrons between the valence and conduction bands of the material, meaning that the energy of the radiation is less than the energy of the band gap. Therefore, the radiation is reflected rather than absorbed. As the radiation's energy increases (and the wavelength of the radiation decreases), the second region (region B in Figure 3.11) is entered. Region B is called the *absorption edge*, and here the energy of the radiation is sufficient such that electrons can be excited across the band gap. The absorption increases (and the percentage reflectance decreases) as the radiation reaches the maximum energy value for absorption. Thereafter, in region C in Figure 3.11, the percentage reflectance is nearly zero since almost all of the radiation of energy higher than in region B is absorbed. Therefore, the band gap information lies in region B since this region can be used to determine the lowest energy radiation that the material can absorb. Determining the band gap from this data region is explained next.

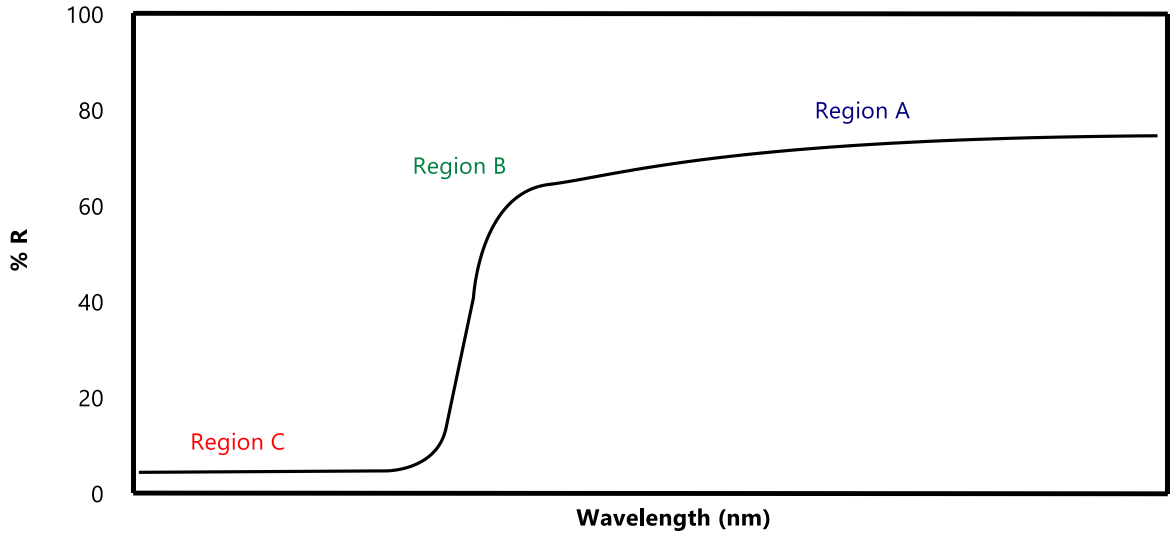

Figure 3.11 A generic plot of percentage reflectance versus wavelength of radiation for the DRS analysis of a semiconducting material.

Determining the Optical Band Gap from DRS

Several methods have been reported in the literature on how to derive the optical band gap for solid materials from a DRS spectrum. The method used in this study is based on the **Kubelka-Munk theory**,[18] which employs the **Tauc method**[19] to analyse the reflectance data. Additionally, a method developed by Davis and Mot is also employed.[20,21]

The fundamental assumption of the Tauc method is that the absorbance, and hence the energy-dependent absorbance coefficient (α) of the crystalline material can be expressed as shown in Equation (3.9)

$$(\alpha \cdot h\nu)^{\frac{1}{\gamma}} = B\left(h\nu - E_g\right) \tag{3.9}$$

where h is the Planck constant, ν is the photon's frequency, E_g is the band gap energy, and B is a constant. The factor γ is dependent on the type of excitation the electrons undergo – if the transition is *direct* $\gamma = 0.5$ and if the transition is *indirect* $\gamma = 2$.[22] The difference between a direct and an indirect transition is illustrated in Figure 3.12. The direct transition, shown in Figure 3.12 (a), is characterised by an electronic transition between the valence and conduction band, w*ithout a change in momentum space* (in other words, the *k*-vector is the same for electrons and holes). In contrast, an indirect transition, as shown in Figure 3.12 (b), means that after the electronic transition, the electrons and holes are in two *different momentum states* (*k*-states, valence band maximum at ⟨000⟩ versus conduction band minimum at ⟨111⟩), and a phonon facilitates the excitation of the electron. Hence, two energy absorption edges will be observed (one at E_g and the other at E_g') versus the one observed for a direct band gap material.[5] Using the DRS technique, a material with an indirect band gap will have a lower first absorption value than the single value for a material with a direct band gap. Additionally, two absorption edges should be observed for an indirect band gap material. However, this is dependent on the radiation range employed.[5]

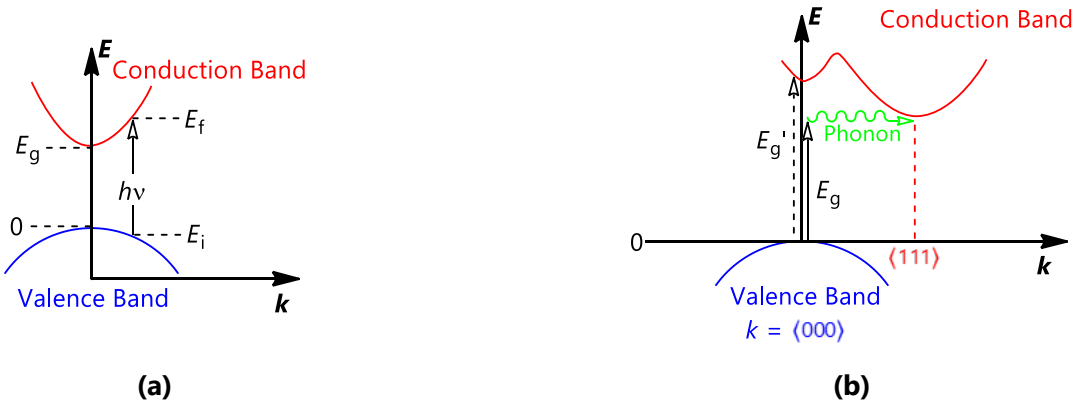

Figure 3.12 A schematic representation of the electronic transitions in a crystalline material, where **(a)** the optical band gap has a direct transition and **(b)** the optical band gap has an indirect transition.

For processing DRS data, the **Kubelka-Munk function** shown in Equation (3.10) is employed.[18,23,24] According to the Kubelka-Munk theory, the reflectance data of an infinitely thick specimen can be converted to absorbance data by use of the Kubelka-Munk remission function $\left(F(R_\infty)\right)$, as follows

$$F(R_\infty) = \frac{K}{S} = \frac{(1 - R_\infty)^2}{2R_\infty} \tag{3.10}$$

where $R_\infty = \frac{R_{sample}}{R_{standard}} = \frac{\%R}{100}$ is related to the percentage reflectance of the material, while K and S are the absorption and scattering coefficients, respectively.[23] Since the theory relates absorbance with reflectance, the α coefficient in Equation (3.9) is replaced by $F(R_\infty)$ from Equation (3.10). Therefore, yielding Equation (3.11)

$$(F(R_\infty) \cdot h\nu)^{\frac{1}{\gamma}} = B\left(h\nu - E_g\right) \tag{3.11}$$

Hence, by plotting $(F(R_\infty)\cdot h\nu)^{1/\gamma}$ against $h\nu$, the band gap (E_g) can be determined by the extrapolation as shown in Figure 3.13. A tangent line (dashed blue line) is extrapolated from the linear part of the Tauc plot. The intersection of this tangent line with the *x*-axis (the energy axis) provides the optical band gap value, and as shown in Figure 3.13, the band gap is 3.22 eV in this example.

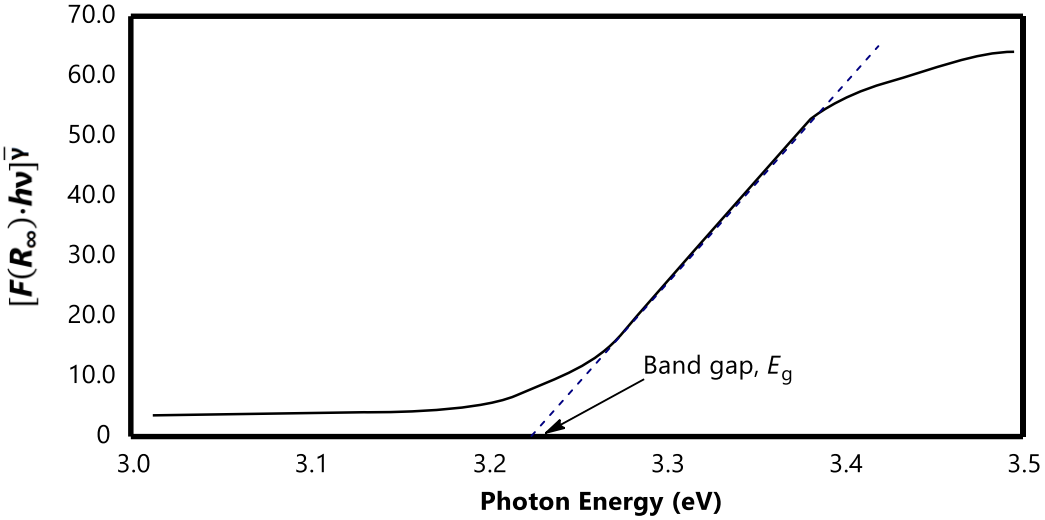

Figure 3.13 An example of how a Tauc plot is employed to determine the optical band gap of a semiconducting solid by using the Kubelka-Munk remission function. An optical band gap of 3.22 eV is shown with the blue tangent line. The value $\gamma = 0.5$ was assumed for this example.

Furthermore, most hybrid halide perovskite materials have been theoretically shown to possess *direct band gaps*.[25–27] Hence, it is generally assumed that $\gamma = 0.5$ unless two absorption edges are seen in the DRS spectrum. Therefore, the optical band gaps of most of the materials of interest in this study are determined by plotting $(F(R_\infty)\cdot h\nu)^2$ against $h\nu$. However, some materials exhibited two absorption edges, and in these cases the indirect band gaps were also determined. An explicit example of how the optical band gap is calculated for one of the materials in this study is included in Appendix A. Also, it should be noted that the DRS technique, when used to obtained the optical band gap of solid materials provides a band gap value with an accuracy of ±0.5 eV.[24]

DRS Instrumentation used in This Study

The DRS spectrophotometer used in this study, a Cary 500 UV-vis-NIR spectrophotometer with praying mantis DRS attachment, is shown in Figure 3.14. Samples are prepared as ground-up powders, using a mortar and pestle. The DRS spectra of the powders were collected in the range of 200 nm to 800 nm at room temperature. However, the instrument has to change its radiation source at 350 nm, which leads to a jump-discontinuity in the recorded spectra.

Figure 3.14 Image of the praying mantis DRS attachment for a Cary 500 UV-vis-NIR spectrophotometer, used to perform the diffuse reflectance spectroscopy measurements. Taken from Harrick Scientific Products.[17]

In addition to the DRS technique, solid-state fluorescence spectroscopy was employed to study the emission properties of the materials synthesised in this study.

3.3.2 Photoluminescence Spectroscopy

Photoluminescence is the phenomenon that occurs when a material absorbs a photon to excite an electron from its ground state to an excited state,[28] and thereafter, luminescence occurs when a photon of lower energy is emitted. Photoluminescence may be split into two categories, namely **fluorescence** and **phosphorescence**.[29] In this study, the former process will be studied for the materials obtained.

When a pair of electrons occupy the same ground state energy, they are said to be of opposite spin and exist in a singlet spin state (Figure 3.15 (a)). Then when the analyte absorbs a photon, and one of the electrons are excited to a higher energy state (called the excited state), the excited electron may be found in one of two spin states in its new excited state. These states are either a singlet excited state (Figure 3.15(b)) where no change in spin momentum occurs or a so-called triplet excited state (Figure 3.15 (c)) where the spin momentum is changed during the transition from the ground to the excited state. Fluorescence is observed when A singlet transition (excited to ground or *vice versa* where the electrons remain paired) occurs. Fluorescence has a very short half-life (10^{-5} to 10^{-8} s) and the excited state decays quickly after the excitation source is removed.[30]

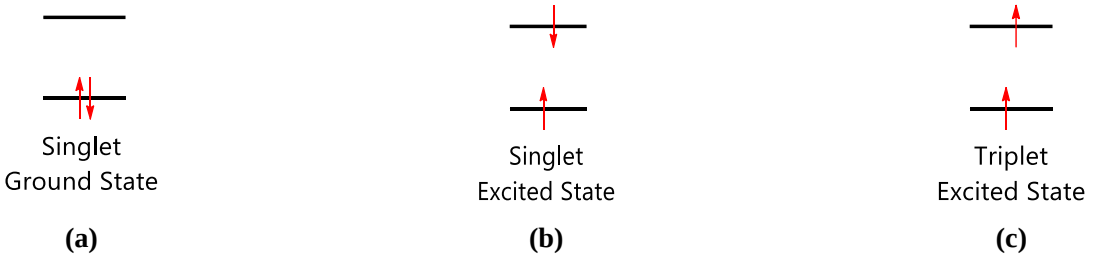

Figure 3.15 The electron configurations for **(a)** a singlet ground state, **(b)** a singlet excited state and **(c)** a triplet excited state.

Transitions from singlet to triplet states or *vice versa*, where the electrons are not paired between the ground and excited state, result in **phosphorescence**. The average lifetime of phosphorescence is 10^{-4} to 10^{4} s.[30] Hence the emission will occur after the excitation source is removed. In addition, fluorescence spectroscopy may be used in quantitative or qualitative modes.

Fluorescence and Phosphorescence Spectra

To explain the process, consider a molecule that absorbs a photon of energy. Firstly, assume that the molecule occupies its lowest vibrational energy state, called a singlet state, labelled S_0. After absorption of the photon, the molecule is excited to a vibrational state in either of its higher excited electronic states, called S_1 or S_2, both singlet states.[31] The relaxation mechanisms then determine whether the process observed is fluorescence or phosphorescence. These pathways are shown in Figure 3.16.[31] The most likely pathway is always the one with the shortest-lived excited state.

The excited electron may relax to a lower electronic, vibrational state or the ground state, without the emission of a photon *via* four pathways, either vibrational relaxation (vr), internal conversion (ic), external conversion (ec) or inter system crossing (isc). These pathways are known as *radiation less deactivation*.

The full process of fluorescence occurs as follows (see Figure 3.16). First, vibrational relaxation occurs, where the molecules lose excess vibrational energy through collisions and move to a lower or the lowest possible vibrational excited state in a specified electronic excited state, S_1 or S_2. Thereafter, molecules in the excited electronic state will undergo internal conversion to a lower excited state, however, of a higher vibrational energy, S_1, hence its energy will remain the same, yet it has undergone a conversion. Subsequently, a vibrational relaxation may occur again, and this process continues until the lowest vibrational state of the *first excited state* is reached (the bottom level of S_1). From this level the molecule may revert to any of the *ground state* vibrational levels (S_0), during which it will emit energy in the form of fluorescence. This implies that the emitted wavelength will always be of lower energy (longer wavelength) than that of the absorbed photon. This *change in wavelength* is known as the Stokes shift.[31]

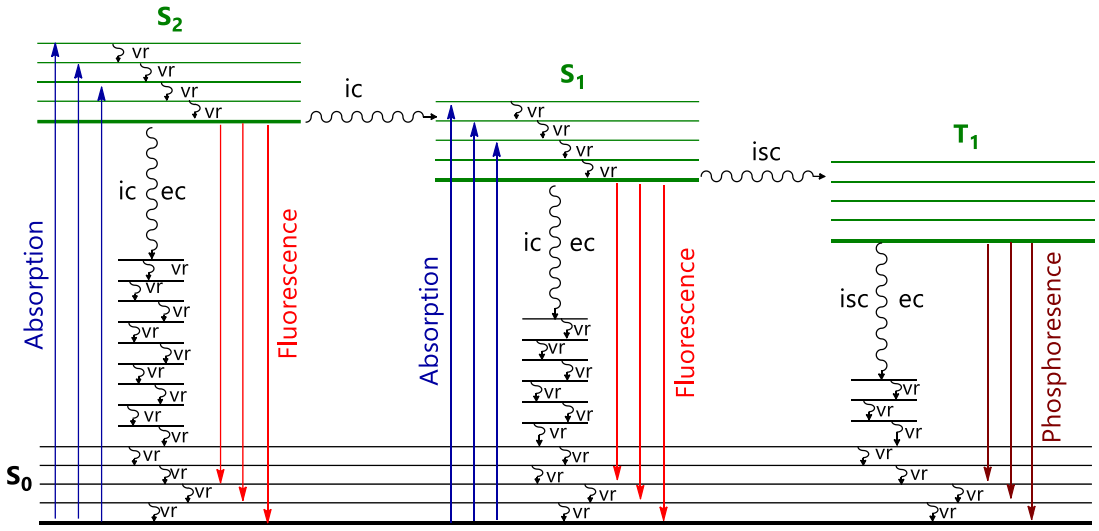

Figure 3.16 The energy level diagram (Jablonski diagram)[31] of a molecule in different vibrational and electronic excited states and the associated possible relaxation pathways. Pathways that lead to the emission or absorption of photons are shown as solid lines and those that do not as wiggly lines.

Since only the solid-state fluorescence will be measured in this study, the discussion will now focus on this aspect of photoluminescence.

Excitation and Emission Spectra in Solid-State Fluorescence

A solid-state fluorescence excitation spectrum is recorded while monitoring a fixed wavelength for emission and varying the excitation wavelength. In contrast, with the emission spectra, a fixed wavelength radiation source excites the sample, and the intensity of the emitted radiation is measured as a function of wavelength. This is illustrated in Figure 3.17.

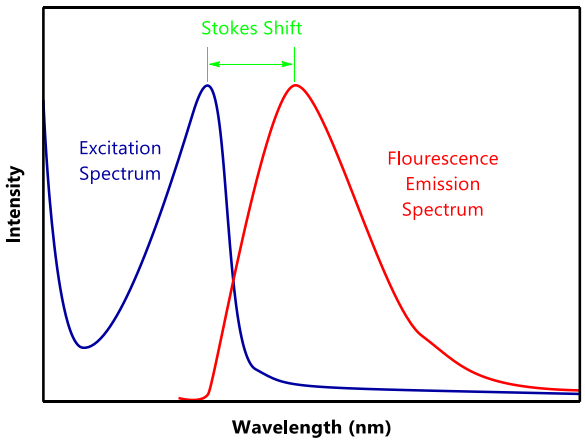

Figure 3.17 Typical excitation and fluorescence emission spectra. The excitation spectrum indicates an excitation peak at a specific wavelength, which is then used to irradiate the sample, and the emission is monitored as a function of wavelength.

Instrumentation used for Solid-State Fluorescence measurements

The basic design of a fluorescence spectrometer is shown in Figure 3.18 (a). Firstly, an excitation wavelength is selected, and secondly, the monitored emission wavelength is selected. In both cases, the wavelengths are *selected* by using an optical filter and aided by a monochromator. When the monochromator is used, the specific spectrometer is called and **spectrofluorometer**.[28] This instrument further uses a xenon lamp since it provides a continuous spectrum of radiation.

Instrumentation Used in This Study. A Horiba Fluoromax-4 spectrofluorometer (shown in Figure 3.18 (b)), fitted with a Xenon lamp light source and a photomultiplier detector, was employed to collect solid-state fluorescence data in the current study. The samples were analysed under ambient conditions and at room temperature. The optical system uses a plane-grating Czery-Turner spectrometer, with excitation wavelengths ranging between 200 nm and 950 nm. A front entrance and exit slit of 5.00 nm bandpass was used for both excitation and emission spectra. Ground samples were sandwiched between two glass microscope slides and measured at a 45° geometry. The band gap, as determined by the DRS studies, provided the excitation wavelengths for the materials.

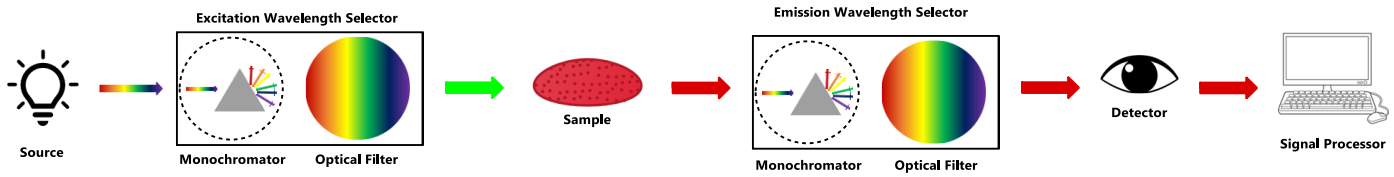

(a)

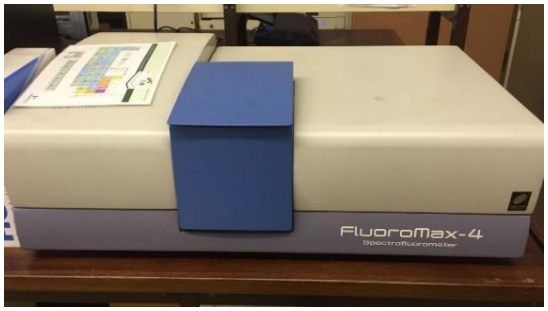

(b)

Figure 3.18 (a) A schematic illustration of how a spectrofluorometer works and **(b)** a photo of the Horiba Fluoromax-4 spectrofluorometer used in this study.

3.4 Computer Software Packages

In this study, several software packages were used to refine structural data, in the processing of data, the plotting of graphs, the preparation of figures and the typesetting of this document. The software packages used and what they were used for are described in Table 3.4.

Table 3.4 A summary of the software packages used in this study and the specific use of each software package.

Software Package	Description of Use
The Cambridge Structural Database (CSD) and ConQuest search engine[32]	The CSD was used for the search of structures described in the literature survey (Chapter 2) and results chapters (Chapters 4 and 5).
ShelXS and ShelXL[33]	Crystal structures obtained in this study were solved by direct methods in ShelXS and refined using ShelXL.
Mercury[34]	The Mercury software package was used to analyse crystal structures and generate graphics.
ChemDraw Pro 12.0[35]	ChemDraw was employed to draw line structures, reaction schemes and in the generation of several other figures.
Origin (8.0)[36]	The OriginPro software package was employed to process the PXRD and DRS data obtained in this study.
Microsoft Excel[37]	Microsoft Excel was employed for the plotting of graphs and calculations of *best-fit* lines.
Microsoft Word[37]	Microsoft Word was used to typeset this dissertation.

This concludes Chapter 3. The discussion will now shift to the results obtained from this study. Chapter 4 is the first of three results chapters (Chapters 4, ,5 and 6).

3.5 References for Chapter 3

1. Lemmerer, A. PhD Thesis, Phase transitions and structural motifs of inorganic-organic lead halide hybrids, University of the Witwatersrand, 2007.
2. West, A. R. *Solid State Chemistry and Its Application*, Second Ed.; Wiley, 2014.
3. Bragg, W. H.; Bragg, W. L. *Proceedings of the Royal Society A* **1913**, *88* (605), 428–438. https://doi.org/http://doi.org/10.1098/rspa.1913.0040.
4. Laue, M. von. *Verlag der Akademie der Wissenschaften* **1912**, *16*, 363–373.
5. Hook, R. J.; Hall, H. E. *Solid State Physics*, Second Ed.; John Wiley & Sons Ltd., 1991.
6. Ewald, P. *Physikalische Zeitschrift* **1913**, *14* (11), 465–472.
7. Friedel, G. *Bulletin de la Société française de Minéralogie* **1913**, *36* (5), 211–252. https://doi.org/10.3406/bulmi.1913.3558.
8. Scherrer, P. In *Colloid Chemistry A Textbook. Chemical technology in single representations*; Springer: Berlin, 1912; pp 387–409. https://doi.org/10.1007/978-3-662-33915-2_7.
9. Rietveld, H. M. *Journal of applied Crystallography* **1969**, *2* (2), 65–71. https://doi.org/10.1107/S0021889869006558.
10. Giacovazzo, C. *Nature* **2011**, *479* (7373), 300. https://doi.org/10.1038/479300a.
11. Hauptman, H. A.; Hauptman, H.; Karle, J. *Solution of the Phase Problem: 1. The Centrosymmetric Crystal, by Herbert Hauptman and Jerome Karle*, First Ed.; American Crystallographic Association, 1953.
12. Patterson, A. L. *Zeitschrift für Kristallographie-Crystalline Materials* **1935**, *90* (1–6), 517–542. https://doi.org/10.1524/zkri.1935.90.1.517.
13. Oszlányi, G.; Sütő, A. *Acta Crystallographica Section A: Foundations of Crystallography* **2004**, *60* (2), 134–141. https://doi.org/10.1107/S0108767303027569.
14. Oszlányi, G.; Sütő, A. *Acta Crystallographica Section A: Foundations of Crystallography* **2005**, *61* (1), 147–152. https://doi.org/10.1107/S0108767304027746.
15. Bragg, W. H. *Nature* **1915**, *95* (2378), 344. https://doi.org/10.1038/095344a0.
16. Müller, P.; Herbst-Irmer, R.; Spek, A. L.; Schneider, T. R.; Sawaya, M. R. *Crystal Structure Refinement: A Crystallographer's Guide to SHELXL*; Oxford University Press: Oxford, 2006. https://doi.org/10.1093/acprof:oso/9780198570769.001.0001.
17. Harrick Scientific Products Inc. http://www.harricksci.com/ftir/accessories/group/Praying-Mantis™-Diffuse-Reflection-Accessory.
18. Kubelka, P.; Franz, M. *Technical Physics* **1931**, *19* (12), 593–601.
19. Tauc, J.; Menth, A. *Journal of Non-Crystalline Solids* **1972**, *8* (10), 569–585. https://doi.org/10.1016/0022-3093(72)90194-9.
20. Davis, E.; Mott, N. *Philosophical Magazine* **1970**, *22* (179), 0903−0922. https://doi.org/https://doi.org/10.1080/14786437008221061.
21. Davis, E.; Mott, N. *Electronic Processes in Non-Crystalline Materials*; Oxford University Press, 2012.
22. Pankove, J. I.; Kiewit, D. A. *Journal of The Electrochemical Society* **1975**, *119* (5), 156. https://doi.org/10.1149/1.2404256.
23. López, R.; Gómez, R. *Journal of Sol-Gel Science and Technology* **2012**, *61* (1), 1–7. https://doi.org/10.1007/s10971-011-2582-9.
24. Nowak, M.; Kauch, B.; Szperlich, P. *Review of Scientific Instruments* **2009**, *80* (4), 21–24. https://doi.org/10.1063/1.3103603.
25. Long, G.; Zhou, Y.; Zhang, M.; Sabatini, R.; Rasmita, A.; Huang, L.; Lakhwani, G.; Gao, W. *Advanced Materials* **2019**, *31* (17), 1–6. https://doi.org/10.1002/adma.201807628.
26. Meng, X.; Zhang, R.; Fu, Z.; Zhang, Q. *Physical Chemistry Chemical Physics* **2016**, *18* (39), 27358–27365. https://doi.org/10.1039/c6cp03377f.
27. Becker, M.; Klüner, T.; Wark, M. *Dalton Transactions* **2017**, *46* (11), 3500–3509. https://doi.org/10.1039/c6dt04796c.
28. Perkowitz, S. *Optical Characterization of Semiconductors: Infrared, Raman, and Photoluminescence Spectroscopy*; Elsevier, 2012.
29. Barr, E. S. *American Journal of Physics* **1970**, *38* (1), 50–58. https://doi.org/10.1119/1.1976227.
30. Hayes, G. R.; Deveaud, B. *physica status solidi (a)* **2002**, *190* (3), 637–640. https://doi.org/10.1002/1521-396X(200204)190:3<637::AID-PSSA637>3.0.CO;2-7.
31. Jabłoński, A. *Zeitschrift für Physik* **1935**, *94* (1–2), 38–46. https://doi.org/10.1007/BF01330795.
32. Groom, C. R.; Bruno, I. J.; Lightfoot, M. P.; Ward, S. C. The Cambridge Structural Database. https://doi.org/DOI: 10.1107/S2052520616003954.
33. Sheldrick, G. *Acta Crystallographica Section C* **2015**, *71* (1), 3–8. https://doi.org/10.1107/S2053229614024218.
34. Macrae, C. F.; Sovago, I.; Cottrell, S. J.; Galek, P. T. A.; McCabe, P.; Pidcock, E.; Platings, M.; Shields, G. P.; Stevens, J. S.; Towler, M.; Wood, P. A. *Journal of Applied Crystallography* **2020**, *53* (1), 226–235. https://doi.org/10.1107/S1600576719014092.
35. PerkinElmer Informatics. PerkinElmer Informatics 2011.
36. OriginLab. Northampton, MA, USA 2009.
37. The Microsoft Corporation. Microsoft 2019.

CHAPTER 4

Results: Dabconium-Containing Hybrid Halide Perovskites

Chapter 4 is the first of three results chapters. Crystal structures resulting from the combination of the dabconium dication (doubly protonated 1,4-diazabicyclo[2.2.2]octane), BX and HX, where B is a monovalent alkali metal ion (Na^+, K^+ or Cs^+), while X is either Cl^-, Br^- or I^-, are discussed here. These combinations lead to the formation of either 1D ABX_3-type perovskite structures or 3D perovskite structures. Single halide and mixed halide systems were investigated. Subsequently, these compounds' band gaps and fluorescence spectra were determined by employing Diffuse Reflectance Spectroscopy and Solid-State Fluorescence Spectroscopy, respectively. Complete structural analyses and comparisons with literature Rb^+-containing structures are also included.

4.1 Introduction

Metal halide perovskites have enjoyed much attention from the scientific community over recent years because of their wide range of applications, specifically also as sensitisers in so-called Perovskite Solar Cells (PSCs).[1] The 3D parent perovskite structure has the general formula ABX_3, where A is either an organic or inorganic cation, B is usually a metal cation, and X is an anion.[2,3] The B-and X-ions form an inorganic BX_6-framework where the A-cation "slots into". A schematic illustration of the building blocks and formation of a perovskite structure is shown in Figure 4.1. If A is an organic cation, B is a metal cation, and X is a halide anion, the resultant structure is called a hybrid metal halide perovskite. In addition, of course, charge neutrality needs to be maintained, so this dictates the nature (oxidation state) of A and B.

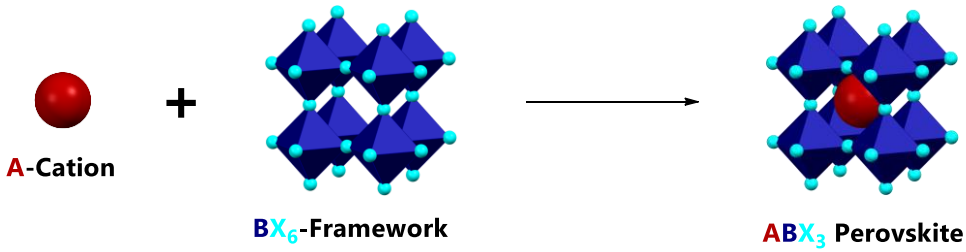

Figure 4.1 A schematic representation of the formation of a 3D parent perovskite structure. The A-cation (shown as a red sphere) is incorporated in the "voids" of the BX_6-framework, forming the 3D perovskite structure ABX_3.

With achieving PSC device efficiencies close to 30% in recent studies, perovskite materials show promise in solving the increasing world energy crisis.[4] Moreover, their applications are not limited to photovoltaics but encompass almost the entire field of optoelectronics, with other reported applications ranging from perovskite LEDs (PeLEDs) to X-ray photodetectors and more.[5] The properties of perovskites are also highly tuneable, with mixtures of different A, B and X constituents leading to various properties, making them a chameleon of materials.

The much-celebrated hybrid halide perovskite $MAPbI_3$ (MA = methylammonium, $CH_3NH_3^+$), originally synthesised by Weber in 1978,[6] was first considered in PSCs by Miyasaka and Teshima.[7–9] Since its initial application in PSC's, $MAPbI_3$ has been modified using other A-cations such as FA (formamidinium, $NH_2CHNH_2^+$) and Cs^+ or even combinations of all

three cations. Furthermore, halide mixtures (X = Cl^-, Br^- or I^-) have also been reported.[10] So have combinations of lead and other divalent metal ions in an attempt to increase the stability and efficiency of these perovskites in PSCs.[11]

The need to reduce the lead content in these structures is crucial since lead is a highly toxic metal, and hence exposing the environment to lead is a risk to avoid. This needs to reduce the lead content of perovskites gave rise to the field of so-called lead-free and lead-less (partial substitution of lead by another metal ion) perovskites and their subsequent applications. A whole host of metal ions (tin, germanium, bismuth, antimony, copper, iron, manganese etc.) have been considered as ions for lead replacement or substitution. However, they all fail to compare favourably to their lead counterparts in terms of performance.[11]

With the perovskite dining table set, this section will aim to provide a short, digestible account of the perovskite structural family, their properties, and possible applications before moving to the literature survey and this study's contributions to the field of lead-free perovskites.

4.1.1 The Perovskite Structure

The technical description of the ABX_3 3D perovskite structure states that the B-cation has 6-fold coordination and is octahedrally surrounded by anions. At the same time, the A-cation lies in a 12-fold cuboctahedral coordination vacancy, as shown schematically in Figure 4.2 (a).[12] The term "3D" is added to the nomenclature because the BX_6-framework forms a 3D network of corner-sharing octahedra extending in all three dimensions (Figure 4.2 (b)).

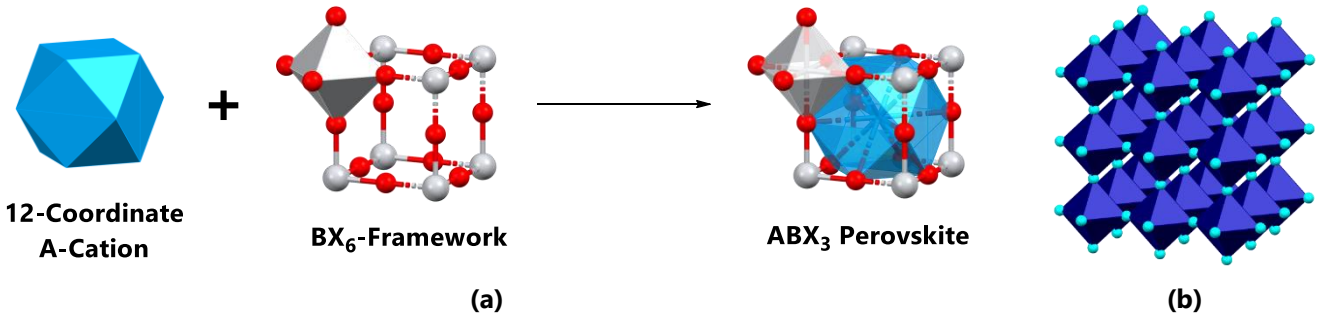

Figure 4.2 (a) Schematic illustration of how the 12-coordinate A-site combines with an inorganic BX_6-framework to form the ABX_3 3D perovskite structure. **(b)** An extended view of the BX_6-framework illustrating the 3D dimensionality (A-cations fill the voids left between the BX_6 octahedra but are omitted for clarity).

In the field of perovskite optoelectronics (specifically PSCs), it is well known that the 3D structural dimensionality is sought after. This is because in the 3D structure, optimal overlap between the B- and X-ion's orbitals are seen, resulting in reduced band gaps.[13] Hence, favourable electronic properties may be maximised when X–B–X angles are close to 90° and 180°.[13] The *ideal form* of the perovskite structure is the cubic phase (see Figure 4.2 (b)), which has the space group $Pm\bar{3}m$, since this phase allows the structure to possess B–X–B and X–B–X angles close to 90° and 180°, respectively.[14] However, the cubic phase is not commonly formed in either inorganic or inorganic-organic hybrid perovskite structures. Instead, the more distorted versions (those of lower symmetry), such as the tetragonal, trigonal, orthorhombic, monoclinic, or triclinic 3D phases, are encountered, associated with a range of different space groups.

In most *non-cubic* phases, as shown in Figure 4.3, distorted octahedra or non-corner-sharing octahedra are present. Even though the 3D *cubic* perovskite structure is the desired phase for optoelectronic applications, this does not imply that the other 3D phases are of *no use*. On the contrary, they are still 3D in character and may find use in the plethora of applications listed earlier for perovskites.

The 3D hexagonal-type perovskites (often referred to as a hexagonal polytype) shown in Figure 4.3 still maintains the ABX_3 structural formula.[15] However, they are better described using the hexagonal close-packing scheme. In this description, the

B-site cations are sandwiched between close-packed hexagonal AX_3 layers along one crystallographic axis, conventionally the *c*-axis.[16] The layers may be stacked in a cubic (c) or hexagonal (h) fashion. When the cubic stacking is observed, the BX_6 octahedra only share their vertices, however, in the hexagonal stacking, they exhibit face-sharing. Different sequences of cubic and hexagonal packing give rise to different 3D ABX_3 hexagonal perovskites.[16] Moreover, there further exists 1D perovskite ABX_3 polytypes for which this description is also relevant, which will be described later.

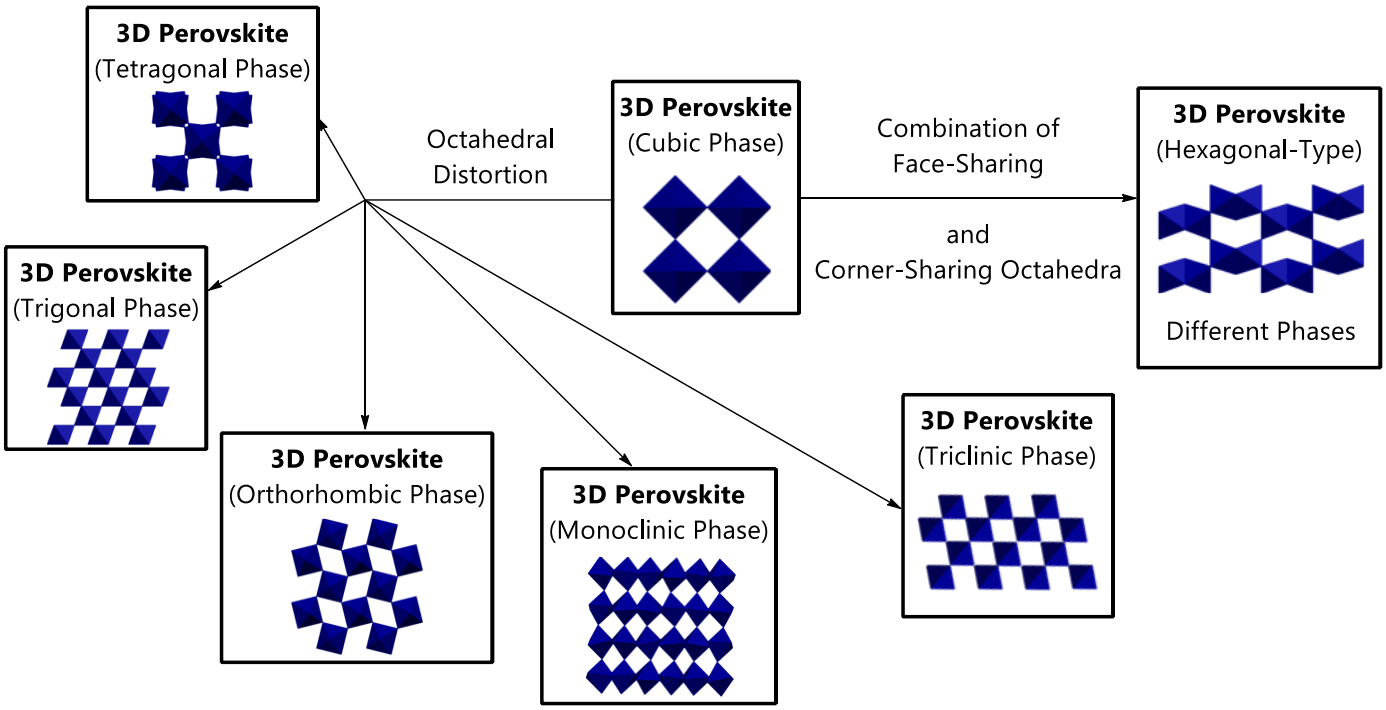

Figure 4.3 A diagram of the sharing of octahedra in different 3D perovskite phases, and how they are related (octahedral distortion or replacement with corner- and face-sharing octahedra) to the 3D cubic parent structure.

These hexagonal polytypes are named using an alpha-numeric naming scheme, αH, where α is an integer number indicating the number of repeat units. By definition, the 4H polytype (Figure 4.4 (a)) exhibits the sequence hchchchc…, the 6H polytype (Figure 4.4 (b)) has the sequence hcchcchcc.., while the 9R polytype displays the sequence hhchhchhc..., as illustrated in Figure 4.4 (c).[16] The anionic metal halide framework forms supercavities containing the cations, with the shape of the cavity depending on the structural polytype.[15]

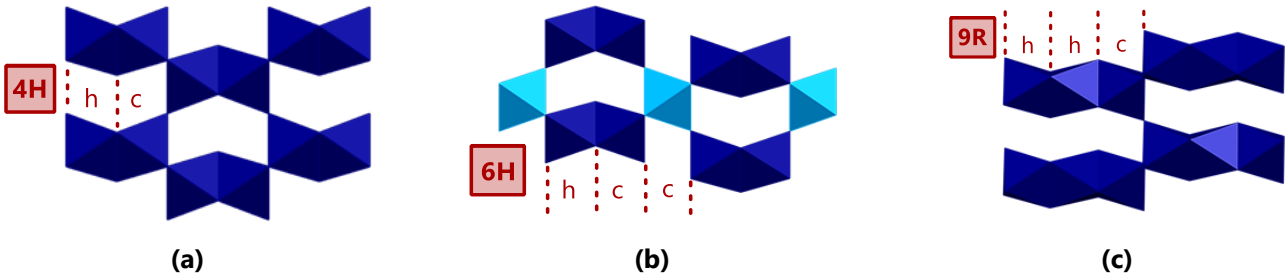

Figure 4.4 Schematic illustrations of the sharing of octahedra in different 3D hexagonal-type perovskite structures. **(a)** The 4H polytype, **(b)** the 6H polytype and **(c)** the 9R polytype. The light blue octahedra do not represent a different type of octahedron, only another type of repeat unit of the structure.

Of course, not all perovskite structures have a 3D structural dimensionality. There exist several lower-dimensional structures as well, including quasi-3D, 2D, 1D and 0D perovskites. All these structural dimensionalities are also defined by mode of sharing of the BX_6 octahedra. The 1D perovskite structure dimensionality is of interest in the current study, hence it will be described here in detail.

4.1.2 1D Perovskite Structures

Specifically relevant to this chapter are the 1D structural types. The 1D perovskite structural types can be identified by their mode of sharing of octahedra, as shown in Figure 1.11.

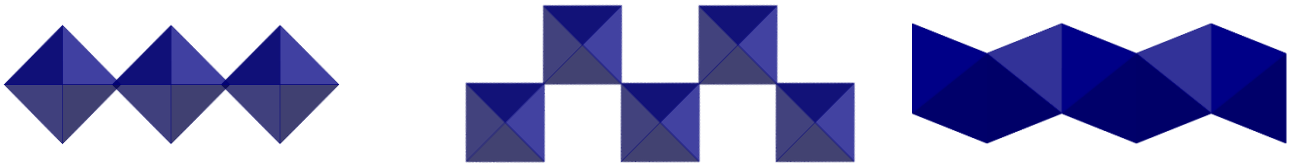

(a) **(b)** **(c)**

Figure 4.5 Schematic illustrations of the sharing of octahedra in different types of 1D perovskite structures. **(a)** The ⟨100⟩-type, **(b)** the ⟨011⟩-type and **(c)** the ABX_3-type1D perovskites.

The 1D ⟨100⟩-type perovskite structure contains corner-sharing octahedra (see Figure 1.11 (a)), however, the corner-sharing is only present in one direction, leading to a structural formula A_3BX_5. The ⟨011⟩-type 1D perovskite structure, shown in Figure 1.11 (b) also has corner-sharing octahedra, however, they differ in connection compared to the ⟨100⟩-type, though having the same structural formula of A_3BX_5. Finally, the ABX_3-type 1D perovskite contains face-sharing octahedra, as shown in Figure 1.11 (c). In these structures, cations surround the 1D inorganic polymers, to form the full perovskite structure.

The ABX_3-type perovskite is named as such since it has the structural formula of ABX_3, similar to that of 3D perovskites. These 1D perovskites are often referred to as *hexagonal perovskites*, which could be confusing since they may crystallise in other phases than the hexagonal phase, such as the trigonal phase. Hence the terminology adopted here (1D ABX_3-type).[17]

The 1D ABX_3-type perovskites (or any dimensionally reduced perovskite structure) form when the A-cation is too large to be accommodated in the 3D BX_6-framework. In this 1D structure, 1D inorganic polymers of BX_6 octahedra are surrounded by isolated A-cations. Because different modes of sharing of the octahedra are possible for the 1D ABX_3-type perovskite (for example, combinations of face- and corner-sharing), a unique nomenclature for these structures have been developed as described earlier.[16]

As two examples of the 1D ABX_3-type case, firstly consider a 1D 4H-ABX_3-type perovskite structure containing both face- and corner-sharing octahedra, as illustrated in Figure 4.6 (a), with the number 4 indicating the number of octahedral repeat units in the 1D polymer. Likewise, the halide-bridged polymer chain in the 1D 2H-ABX_3-type perovskite exhibits two octahedral repeat units in the polymer, as shown in Figure 4.6 (b). The A-cations surround the inorganic BX-polymers, however, are not shown in Figure 4.6.

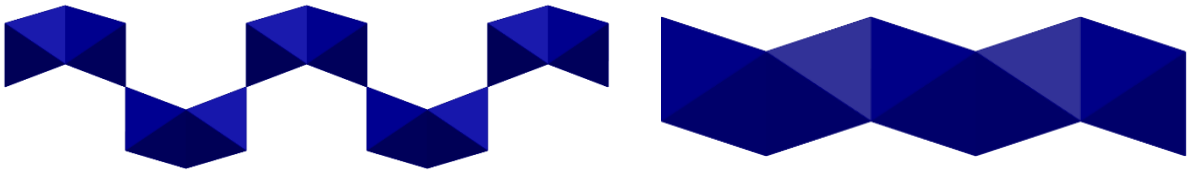

(a) **(b)**

Figure 4.6 Schematic polyhedral representations of the octahedra of **(a)** a 1D 4H-ABX_3-type perovskite and **(b)** the 1D 2H-ABX_3-type perovskite.

Now that the structures of perovskites have been described, one might ask whether the dimensionality or phases of perovskites consisting of specific combinations of A-, B- and X-ions may be predicted. The following section sheds light on this question.

4.1.3 Predicting Perovskites' Dimensionality

In the 3D perovskite structure, the A-site cation must fit in the voids of an empty BX_6-framework, which places some geometric restrictions on the combinations of A-, B- and X-ions that will lead to a 3D structure. In the field of perovskites, typically, two parameters may be employed to surmise if a structure will be 3D or not for a given combination of A-cation and BX, namely the **Goldschmidt Tolerance Factor**[18] and the **Octahedral Factor**[19]. The **Goldschmidt tolerance factor** (t) can be calculated as per Equation (**4.1**):

$$t = \frac{r_A + r_B}{\sqrt{2}\,(r_B + r_X)} \tag{4.1}$$

When the tolerance factor lies in the range $0.71 < t < 1.05$, a 3D perovskite structure is expected. This range does allow for some flexibility. If the tolerance factor lies in the range $0.89 < t < 1$, the cubic 3D phase is expected, whereas when $0.78 \leq t \leq 0.89$, the more distorted phases such as orthorhombic, rhombohedral or trigonal phases are expected.[19,20] Finally, when $0.71 < t \leq 0.78$ or $1.00 < t \leq 1.05$, the tetragonal, hexagonal, or A_4BX_3-type perovskite is expected.[21] Values that lie outside this range predict a lower dimensionality perovskite structure.

The second parameter, the octahedral factor (μ), uses the ratio of the B-cation radius to X-anion radius, as given in Equation (4.2), to infer the compatibility of the constituents of the 3D perovskite framework (hence if the B-cation prefers an octahedral arrangement with the suggested X-anion):

$$\mu = \frac{r_B}{r_X} \tag{4.2}$$

The 3D perovskite structure (octahedral coordination of B and X, BX_6) is predicted to be stable in a range of $0.442 \leq \mu \leq 0.895$. Therefore, should a given combination of A, B and X comply with $0.78 < t < 1.05$ and $0.442 \leq \mu \leq 0.895$, then a 3D perovskite structure is predicted.[19]

The primary assumption of these models is that the ions (A, B and X) are hard spheres, which means that when A is an organic cation, this assumption is not strictly correct, and both these factors do not always correctly predict the outcomes. To this end, Bartel *et al*. suggested an improved tolerance factor (symbol τ), which has been shown to correctly predict 92% of 576 materials of the halide and oxide perovskite-types.[22] It has also predicted the existence of 23 314 stable double perovskites and 1034 experimentally verified perovskite materials. Equation (4.3) gives the tolerance factor as derived by Bartel *et al.*,

$$\tau = \frac{r_X}{r_B} - n_A\left[n_A - \frac{\left(\frac{r_A}{r_B}\right)}{\ln\left(\frac{r_A}{r_B}\right)}\right] \tag{4.3}$$

In Equation (4.3) n_A is the oxidation state of the A-site organic cation, and r_i is the radius of the ion i. Then by definition, $r_A > r_B$ leading to the criteria that when $\tau < 4.18$, a 3D perovskite structure is predicted.[22] One important note is that these *models* are exactly that, models that suggest viable routes for perovskite research. Therefore, they are not *strict guidelines* but rather are used as helpful suggestions when designing perovskite materials.

4.1.4 Perovskite Solar Cells (PSCs)

Between 2005 and 2009, Miyasaka and Teshima worked on the concept of using perovskite materials in solar cells.[7–9] Methylammonium lead iodide ($MAPbI_3$) was initially used as a nanocrystalline perovskite absorbing layer in a dye-sensitised solar cell.[9] Efficiencies of close to 3.8% were reported in the first peer-reviewed publication on perovskite solar cells.[7–9] This inspired a whole new field of research focussing on perovskite solar cells (PSCs), where the move was made from dyes as sensitisers to thin-films of perovskite materials as sensitisers, and the thin-film PSCs is the preferred type to this day.

The best photovoltaic silicon technologies (crystalline and amorphous) currently available can achieve efficiencies of around 25.8%.[23] Recently, a tandem solar cell device, designed by the venture company Oxford PV™, that combines a $MAPbI_3$ thin-film and a traditional silicon thin-film, achieved a certified efficiency of 27.3% under laboratory conditions.[24] The focus has shifted to tandem cells because there is a *theoretical performance limit* for a single layer device (with a band gap of 1.1 eV), as described by the **Shockley–Queisser limit**, which is around 33%, assuming a PCE of 30% should be achievable experimentally.[25] The difference between the theoretical and experimental values are due to unavoidable radiative losses.[25] However, tandem devices, containing more than one sensitiser layer, have much higher predicted theoretical performances, with the performance increasing as the number of layers increases.[26]

4.1.5 The Issue of Lead and the Future of PSCs

The primary barrier to PSC manufacturing at a large scale has been that the best performing cells contain a toxic component, namely lead. Lead is viewed by the **world health organisation (WHO)** as one of the ten most poisonous metals, and so its presence causes many difficulties for commercialisation of PSCs.[27] Moreover, the toxic dose of lead for human consumption is around 15 $\mu g \cdot L^{-1}$ in water and 0.15 $\mu g \cdot L^{-1}$ in air.[28] This is much less than the 0.4 g estimated lead content of a 300 nm thick, 1 m^2 lead-containing PSC.[29]

Hybrid halide perovskites are notoriously sensitive to light, heat and moisture, and so degradation is of real concern, especially since this can lead to lead leakage into the environment.[30] Though several research groups have suggested that encapsulation could solve the leakage problem, the ideal solution would be to remove lead entirely.[31] Therefore, the research focus has shifted towards *lead-free* perovskite structures for use in solar cell devices. Alternative metals include, but are by no means limited to, Group 14 elements such as Sn^{2+} and Ge^{2+}, alkaline earth metals such as Be^{2+}, Mg^{2+}, Ca^{2+}, Sr^{2+}, and Ba^{2+}, transition metals such as V^{2+}, Mn^{2+}, Fe^{2+}, Co^{2+}, Ni^{2+}, Pd^{2+}, Cu^{2+}, Zn^{2+}, Cd^{2+}, and Hg^{2+}, lanthanides such as Eu^{2+}, Tm^{2+}, and Yb^{2+}, and *p*-block elements such as Ga^{2+} and In^{2+}.[32] These alternatives combine a divalent metal ion (B^{2+}) and a monovalent organic cation (A^+, like MA^+).

However, *switching* these valences (using B^+ and A^{2+}), therefore, using non-toxic group 1 metals[33] (the alkali metals, including Li^+, Na^+, K^+, Rb^+ and Cs^+), with a divalent organic dication, is a new and unexplored option for perovskites, providing the starting point of this study.

4.2 Literature Survey

Of interest in the current study are organic-inorganic hybrid structures formed through the combination of dabconium dications and monovalent alkali metal ions and halide ions, with an eye on their application in PSCs. To identify which structures falling into this category have already been published, a literature search was conducted. This study will investigate outstanding members of the series and measure the band gaps and fluorescence properties of these materials to identify potential applications. However, before considering the literature, the naming scheme of these structures employed in this study is explained.

4.2.1 Naming Scheme

The protonation of both nitrogen atoms of a 1,4-diazabicyclo[2.2.2]octane molecule results in the formation of a "dabconium" dication (+2 charge, see Scheme 4.1), which will be called dabconium or the dabconium dication in this study. The current chapter discusses the structures obtained through combining these dabconium dications and metal halides consisting of monovalent alkali metal ions and halide ions.

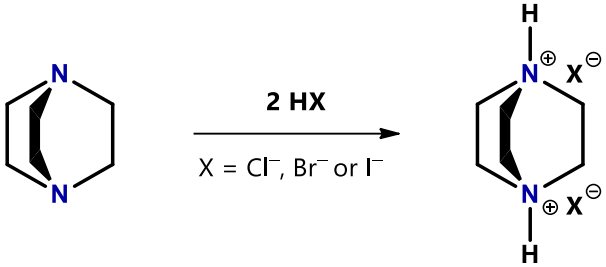

Scheme 4.1 The protonation of 1,4-diazabicyclo[2.2.2]octane using HX (X = Cl^-, Br^- or I^-) to form the dabconium dication.

Compounds, and their corresponding structures will be referred to according to an abbreviation based on their composition, **D-BX$_n$**, with **D** indicating that the cation is dabconium, **B** representing the metal ion, **X** indicating the halide anion, and ***n*** showing the ratio of halide ions to metal ions in the molecular formula. For example, the abbreviation **D-NaCl$_3$** indicates the compound or structure resulting from the combination of dabconium dications and anionic species comprised of Na^+ and Cl^- ions. This naming scheme is adapted to describe polymorphic compounds by the addition of a number in brackets at the end of the abbreviation, e.g., **D-KBr$_3$(1), D-KBr$_3$(2)** etc., which indicates two different structure types for the combination of dabconium and KBr, while having the same molecular formula, **D-KBr$_3$**. This nomenclature applies to different phases or dimensionalities of the same combination, that are polymorphs.

4.2.2 Literature Survey: Dabconium-Containing Alkali Metal Halide Perovskites

A search of the Cambridge Structural Database (CSD (2021, Version 5.42, update May 2021)[34]) indicated that several structures consisting of dabconium dications, and metal-halide anions comprised of monovalent alkali metal ions (Na^+, K^+, Rb^+, Cs^+) and halide anions have been reported in the literature.

Two 1D structures have been reported. The 1D ABX_3-type perovskite structure consisting of dabconium and a KCl-based anion has been reported twice, with the CSD refcodes DOTHOK[35] (**D-KCl$_3$)** and DOTHOK01[36] (**D-KCl$_3$)**. The two structures were determined at 100 K and 120 K, respectively, with the structure remaining in its trigonal phase at both temperatures (space group $R\bar{3}c$). The combination of dabconium and a RbI-based anion also results in the formation of a 1D ABX_3-type perovskite structure, with CSD refcode HEJHOW[37] (**D-RbI$_3$**), with the structure determined to be in a hexagonal phase (space group $P\bar{6}2c$) at room temperature (293 K).

Four 3D perovskite structures have been reported in the literature for the combination of dabconium and a range of monovalent alkali metal ions and halide ions. The perovskite structure obtained from the combination of dabconium and a KBr-based anion (CSD refcode: FIZYIZ,[38] **D-KBr$_3$(2)**) was determined at 300 K to be in the trigonal phase (space group $P3_121$). In addition, three different structures have been reported for the combination of dabconium and a RbCl-based anion (CSD refcodes: GUYNEU[36] (**D-RbCl$_3$(1)**), GUYNEU01[37] (**D-RbCl$_3$(2)**) and GUYNEU02[37] (**D-RbCl$_3$(3)**), with the structures representing two trigonal phases (space groups $P3_221$ and $P3_121$) at 120 K and 293 K and a cubic phase (space group $Pm\bar{3}m$) at 458 K. Furthermore, two 3D structures have been reported containing dabconium dications and a RbBr-based anion (CSD refcodes: HEJGUB (**D-RbBr$_3$(1)**) and HEJGUB01 (**D-RbBr$_3$(2)**)),[37] with the structures representing the trigonal (space group $P3_221$) and cubic (space group $Pm\bar{3}m$) phases of the compound determined at 293 K and 353 K, respectively. Lastly, a monoclinic 3D perovskite structure (space group $C2/c$) was reported to form for the combination of dabconium and a CsCl-based anion as determined at 120 K (CSD refcode: GUYNIY[36] (**D-CsCl$_3$**)).

The literature shows a tendency of the family of structures (dabconium in combination with alkali metal halide anions) to form perovskite structures, either of the 3D or 1D type, however, not all the structures in this family have been reported, and those that have been reported, were determined at different temperatures. Furthermore, no properties of these materials have been reported. Therefore, this study will contribute to the gap in the structural knowledge of this family of compounds by determining the outstanding structures and re-determining the reported structures at a similar temperature. In addition, the

study will also focus on specific properties of the family. Before moving on, it is helpful to consider the different tolerance factors of these combinations to provide some degree of predictability regarding the expected structures.

4.2.3 The Dimensionality of D-BX$_n$ Structures

Table 4.1 summarises the predicted dimensionality of the structures containing a dabconium dication and an alkali metal halide anion reported in the literature, as well as for the outstanding members of the series not yet reported. B and X represent monovalent alkali metal ions and halide ions, respectively. The ionic radius of the dabconium dication was taken as 339 pm, as per the determination using Density Functional Theory Calculations reported in the literature.[39] The Shannon ionic radii[40] of the metal ions were used, where the radii are as follows for VI-coordination: Li^+ = 76 pm, Na^+ = 102 pm, K^+ = 138 pm, Rb^+ = 152 pm and Cs^+ = 167 pm and halides Cl^- = 181 pm, Br^- = 196 pm and I^- = 220 pm. The calculated values for the Goldschmidt Tolerance Factor[18] (t), Bartel's Tolerance Factor[22] (τ) and the Octahedral Factor[19] (μ) are listed in Table 4.1 for the different combinations.

Table 4.1 Prediction of the dimensionality of the structures formed by the combination of dabconium and BX-anions. The Goldschmidt Tolerance Factor[18] (t), Bartel's Tolerance Factor[22] (τ) and the Octahedral Factor[19] (μ) are listed. Values that meet the criteria for a 3D dimensionality are coloured in dark blue, and those that infer a lower dimensionality are shaded in red. The structures reported in the literature are listed, and their dimensionality indicated.

Metal Ion (B)	Halide Ion (X)								
	Cl^-			Br^-			I^-		
	t	τ	μ	t	τ	μ	t	τ	μ
Li^+	1.14	4.35	0.42	1.08	4.55	0.39	0.99	4.86	0.35
	No structure reported			No structure reported			No structure reported		
Na^+	1.10	3.31	0.56	1.05	3.46	0.52	0.97	3.69	0.46
	No structure reported			No structure reported			No structure reported		
K^+	1.06	2.78	0.76	1.01	2.89	0.70	0.94	3.06	0.63
	1D ABX_3-type perovskite (DOTHOK,[35] DOTHOK01[36])			3D perovskite (FIZYIZ[38])			No structure reported		
Rb^+	1.04	2.75	0.84	1.00	2.85	0.78	0.93	3.01	0.69
	3D perovskite (GUYNEU,[36] GUYNEU01,[37] GUYNEU02[37])			3D perovskite (HEJGUB,[37] HEJGUB01[37])			1D ABX_3-type perovskite (HEJHOW[37])		
Cs^+	1.03	2.82	0.92	0.99	2.91	0.85	0.92	3.05	0.76
	3D perovskite (GUYNIY[36])			No structure reported			No structure reported		

Considering the Goldschmidt Tolerance Factor with the octahedral factor first, the values listed in Table 4.1 indicate that if dabconium is combined with LiCl, NaCl, KCl, CsCl, LiBr, or LiI-anions, the resultant structure is unlikely to be of the 3D perovskite type. This is because either the A-site is not large enough (indicated by *t*) or that octahedral connection is impossible (indicated by μ). Bartel's Tolerance Factor agrees with these predictions on combinations containing Li^+. Therefore, it is highly improbable that LiX-based anions with dabconium would result in 3D perovskite structures.

Furthermore, Bartel's Tolerance Factor disagrees with the Goldschmidt Tolerance Factor on combinations containing either NaCl- or KCl-based anions, suggesting the possibility of a 3D dimensionality. Since the structure of the combination of dabconium and KCl-based anions has been reported in the literature (DOTHOK[35] and DOTHOK01[36]), and is of the 1D ABX_3-type, the Goldschmidt Tolerance Factor correctly predicts the dimensionality.

In addition, the octahedral factor suggests that the combination of CsCl-based anions and dabconium is unlikely to form a 3D perovskite structure, since Cs^+-ions might have difficulty coordinating in an octahedral fashion with Cl^--ions. However, this value narrowly misses out on the criterion (0.92 versus 0.895). Goldschmidt's and Bartel's Tolerance Factors agree on a 3D dimensionality, and this is what is found experimentally when considering structure GUYNIY.[36]

Finally, it is predicted by all parameters listed in Table 4.1 that dabconium, when combined with RbCl-, NaBr-, KBr-, RbBr-, CsBr-, NaI-, KI-, RbI- or CsI-based anions, could result in 3D perovskites. This is also strongly supported by the literature survey, which showed that the combinations that contain KBr-, RbCl- or RbBr-based anions all lead to 3D perovskites (structures FIZYIZ,[38] GUYNEU,[36] GUYNEU01,[37] GUYNEU02,[37] HEJGUB[37] and HEJGUB01,[37] respectively). Only the combination with RbI-anions is predicted incorrectly by all three parameters as a 3D perovskite structure, however, a 1D ABX_3-type perovskite structure was reported in the literature (HEJHOW[37]).

It can be deduced that the Goldschmidt Tolerance Factor, the octahedral factor as well as Bartel's Tolerance Factor, when used in combination with each other, are often successful in predicting the formation of a 3D perovskite structure, when considering structures reported in the literature. Considering the values in Table 4.1, these factors predict that a number of the structures that have not yet been reported in the literature may also be of the 3D perovskite-type. Determination of these outstanding structures is one of the aims of the current investigation.

In summary, the literature study found that the combination of dabconium and alkali metal halides leads to either a 1D or 3D structural dimensionality. Therefore, the structural characteristics of these two structural types will be discussed in the following sections and structures obtained in this study will be compared to the literature structures listed earlier to identify structural trends and possible crystal engineering routes.

4.2.4 Aspects of This Study

In the current investigation dabconium cations were combined with the alkali metal halide portions NaCl, NaBr, NaI, KCl, KBr, KI, CsCl, CsBr or CsI in an organic:inorganic molar ratio of 1:1, to form hybrid materials. Due to the tolerance factors' prediction that the combination of dabconium with Li-halide salts is not expected to yield 3D perovskite structures, the Li^+-members of the series were not investigated. In addition, Rb-halide salts are prohibitively expensive, and these members of the series were not included in this study, however, these structures have been reported in the literature.[36,37]

In total eleven compounds were prepared synthetically, and all were characterised by powder X-ray diffraction (PXRD). In addition, eleven single-crystal X-ray structures were determined, eight of which are novel and have not been reported in the literature. To allow for the identification of structural trends between structures determined at the same temperature, all the structures reported in the literature, containing NaX-, KX- or CsX-based anions, were also re-determined at 150 K. The results obtained are categorised according to structural types, and are discussed in different sections below, with each section focussing on a structural type.

For all the structures, single-crystal X-ray diffraction data were collected at 150 K. To determine whether a phase transition occurs on cooling, the calculated powder patterns (PXRD patterns) of the single-crystal structures determined at 150 K were compared to the powder patterns of the bulk samples measured at room temperature. To this end, none of the structures described here underwent phase transitions, as evident from the matching of the powder patterns shown in Appendix D. In addition, the purity of the bulk samples was also determined by matching of the experimental and calculated powder X-ray diffraction patterns. For more information on the powder patterns of the specific samples, see Appendix D.

Since the perovskite solar cell sensitiser material is to be used at room temperature in a solar cell, the proof that no solid-state phase transitions occur between 150 K and room temperature is of the utmost importance. As mentioned before, evidence of this is provided by the PXRD results given in Appendix D. Therefore, it is assumed that the crystal structures at room temperature will show the same structural trends as the crystal structures determined at low-temperature in this study, since no phase transitions are observed, and it would only be cumbersome to include the room temperature SCXRD structures in the discussion.

That said, it is expected that small structural changes associated with the contraction of the structure due to cooling may slightly alter some geometric parameters of the structures, such as B–X–B angles, bond lengths etc. However, these differences would be quite small. They should have no bearing on the identification of any general structural trends.

Furthermore, the band gaps of the materials were measured using diffuse reflectance spectroscopy (DRS) and their fluorescence spectra were obtained employing fluorescence spectroscopy, and these results are described later.

The structural results of the 1D perovskites obtained in this study will be discussed next, followed by the structural results of the 3D perovskite materials. An overall comparison of the structures will then be made to identify structural trends across the 1D and 3D family of compounds. Lastly, the DRS and fluorescence spectroscopy results will be discussed.

4.3 1D Perovskite Structures: Crystallographic Results and Discussion

This section will cover the crystal structures obtained in this study that combine the dabconium dication and BX-based anions to form 1D ABX_3-type perovskite structures, also known in the literature as hexagonal perovskite structures.[17] A total of five structures of this type have been determined in this study, four of which are novel.

The crystallographic parameters of the low-temperature 1D ABX_3-type structures obtained in this study are listed in Table 4.2. Furthermore, selected bond lengths, metal-metal distances, angles, hydrogen bonding parameters and structural descriptors are listed in Table 4.3 for both structures obtained in this study and those described in the literature, which falls into the category of 1D ABX_3-type perovskite structures. The literature structure **D-RbI$_3$**[37] is included in both Table 4.2 and Table 4.3 since no Rb-containing compounds were investigated in the current study, however, its inclusion will be useful in the identification of structural trends later. Furthermore, the structure **D-KCl$_3$**[35,36] has been reported previously (determined at 100 K and 120 K), however, in this study, it has been re-determined at 150 K and proved phase-stable up to 293 K. The data collected for the structure **D-KCl$_3$** in this study is reported and subsequently used in the trend analysis.

Table 4.2 Crystallographic parameters for the 1D ABX_3-type dabconium-containing perovskite structures.

Structure Abbreviation	**D-NaCl$_3$**	**D-NaBr$_3$**	**D-KCl$_3$**
Name	*catena*-[bis(1,4-diazoniabicyclo[2.2.2]octane-1,4-diium) nonakis(μ_2-chloro)-tri-sodium]	*catena*-[bis(1,4-diazoniabicyclo[2.2.2]octane-1,4-diium) nonakis(μ_2-bromo)-tri-sodium]	*catena*-[bis(1,4-diazoniabicyclo[2.2.2]octane-1,4-diium) nonakis(μ_2-chloro)-tri-potassium]
Empirical formula	$3n(C_6H_{14}N_2)^{2+}\cdot n[Na_3Cl_9]^{2-}$	$3n(C_6H_{14}N_2)^{2+}\cdot n[Na_3Br_9]^{2-}$	$3n(C_6H_{14}N_2)^{2+}\cdot n[K_3Cl_9]^{2-}$
Formula weight (g·mol^{-1})	243.53	376.88	259.64
Crystal system	Trigonal	Trigonal	Trigonal
Space group	$R\bar{3}c$	$R\bar{3}c$	$R\bar{3}c$
Temperature (K)	150(2)	150(2)	150(2)
Wavelength (Å)	1.54184	1.54184	0.71073
***a* (Å)**	15.87470(10)	16.3508(2)	16.0388(2)
***b* (Å)**	15.87470(10)	16.3508(2)	16.0388(2)
***c* (Å)**	21.1921(2)	21.9979(2)	22.2094(4)
***α* (°)**	90	90	90
***β* (°)**	90	90	90
***γ* (°)**	120	120	120
Volume (Å^3)	4625.04(7)	5093.19(13)	4947.79(15)
Z	18	18	18
Density calculated (g·cm^{-3})	1.574	2.212	1.569
Absorption coefficient (mm^{-1})	8.077	13.230	1.164
***F*(000)**	2268	3240	2412
Crystal size (mm^3)	0.09×0.05×0.03	0.15×0.19×0.21	0.06×0.06×0.10
Reflections collected	29780	10907	23980
Unique Reflections / R_{int}	1061 / 0.0452	1230 / 0.0251	1613 / 0.0162
Completeness	1.000	1.000	1.000
Parameters	61	56	60
Goodness-of-fit F^2	1.034	1.204	1.157
Final R indices [I>2σ(I)] (R_1 / wR_2)	0.0226 / 0.0777	0.0208 / 0.0532	0.0159 / 0.0422
R indices (all data) (R_1 / wR_2)	0.0230 / 0.0781	0.0209 / 0.0532	0.0164 / 0.0424

Table 4.2 (Continued) Crystallographic parameters for the 1D ABX_3-type dabconium-containing perovskite structures.

Structure Abbreviation	**D-KBr_3(1)**	**D-RbI_3[37]**	**D-CsI_3**
Name	*catena*-[bis(1,4-diazoniabicyclo[2.2.2]octane-1,4-diium) nonakis(μ_2-bromo)-tri-potassium]	*catena*-[1,4-diazabicyclo[2.2.2]octane-1,4-diium tris(μ_2-iodo)-rubidium]	*catena*-[1,4-diazabicyclo[2.2.2]octane-1,4-diium tris(μ_2-iodo)-caesium]
Empirical formula	$3n(C_6H_{14}N_2)^{2+}\cdot n[K_3Br_9]^{2-}$	$n(C_6H_{14}N_2)^{2+}\cdot n[RbI_3]^{2-}$	$n(C_6H_{14}N_2)^{2+}\cdot n[CsI_3]^{2-}$
Formula weight (g·mol^{-1})	392.99	580.36	627.80
Crystal system	Trigonal	Hexagonal	Hexagonal
Space group	$R\bar{3}c$	$P\bar{6}2c$	$P6_3/mmc$
Temperature (K)	150(2)	293(2)	150(2)
Wavelength (Å)	0.71073	0.71073	0.71073
a (Å)	16.5223(3)	9.821(2)	10.0382(2)
b (Å)	16.5223(3)	9.821(2)	10.0382(2)
c (Å)	23.0126(6)	8.2067(16)	7.9849(2)
α (°)	90	90	90
β (°)	90	90	90
γ (°)	120	120	120
Volume (Å^3)	5440.5(2)	685.5(3)	696.81(3)
Z	18	2	2
Density calculated (g·cm^{-3})	2.159	2.812	2.992
Absorption coefficient (mm^{-1})	10.312	10.330	9.267
F(000)	3384	520	556
Crystal size (mm^3)	0.13×0.16×0.16	0.20×0.12×0.10	0.17×0.23×0.43
Reflections collected	15695	4516	7018
Unique Reflections / R_{int}	1916 / 0.0711	565/ 0.1006	456/ 0.0554
Completeness	1.000	0.985	1.000
Parameters	56	23	16
Goodness-of-fit F^2	1.084	1.052	1.305
Final R indices [I>2σ(I)], (R_1 / wR_2)	0.0225 / 0.0544	0.0279 / 0.0609	0.0319 / 0.0804
R indices (all data), (R_1 / wR_2)	0.0249 / 0.0550	0.0284 / 0.0611	0.0330 / 0.0806

Table 4.3 Selected bond lengths, angles, hydrogen bonding parameters and structural descriptors for the 1D ABX_3-type dabconium-containing perovskite structures.

Structure Abbreviation	**D-$NaCl_3$**		**D-$NaBr_3$**		**D-KCl_3**		**D-KBr_3(1)**		**D-RbI_3**[37]	**D-CsI_3**
Organic Cation (A)	Dabconium		Dabconium		Dabconium		Dabconium		Dabconium	Dabconium
Metal Ion (B)	Na^+		Na^+		K^+		K^+		Rb^+	Cs^+
Halide Ion (X)	Cl^-		Br^-		Cl^-		Br^-		I^-	I^-
Structure Type	1D ABX_3-type		1D ABX_3-type		1D ABX_3-type		1D ABX_3-type		1D ABX_3-type	1D ABX_3-type
Temperature (K)	150(2)		150(2)		150(2)		150(2)		293(2)	150(2)
	Na1	**Na2**	**Na1**	**Na2**	**K1**	**K2**	**K1**	**K2**		
B–X (Å)	2.8813(6)	2.8389(3)	3.0310(9)	2.9814(2)	3.1297(3)	3.08170(19)	3.2784(4)	3.22379(17)	3.6698(8)	3.7807(4)
	2.9861(6)		3.1236(10)		3.2143(3)		3.3532(4)			
	Na1	**Na2**	**Na1**	**Na2**	**K1**	**K2**	**K1**	**K2**		
	83.51(2)	88.925(10)	84.51(3)	89.571(6)	86.371(8)	88.907(5)	87.137(13)	88.398(5)	83.133(19)	85.307(5)
	88.04(2)	91.074(10)	88.44(3)	90.426(6)	87.782(4)	91.093(5)	87.636(4)	91.599(5)	93.760(19)	94.693(5)
X–B–X (°)	89.590(7)	180	89.318(5)	180	89.017(7)	180.0	89.348(13)	180	91.786(13)	180
	99.256(7)		98.052(5)		97.224(4)		96.197(4)		172.585(19)	
	172.248(13)		173.071(18)		172.932(4)		173.652(5)			
B–X–B (°)	73.28(3)		72.72(5)		71.913(10)		71.390(9)		67.982(19)	63.741(8)
	75.761(15)		74.63(2)		72.279(6)		71.447(18)			
	Na1···Na2	**Na2···Na2**	**Na1···Na2**	**Na2···Na2**	**K1···K2**	**K2···K2**	**K1···K2**	**K2···K2**		
B···B (Å)	3.4390(17)	3.5785(9)	3.594(3)	3.7026(15)	3.6753(6)	3.7147(3)	3.8284(12)	3.8389(6)	4.1033(8)	3.9924(1)
N–H^+···$^-$X–B (D···A) (Å)	3.0180(12)		3.1733(19)		3.0256(7)		3.1852(15)		3.256	3.773(6)

4.3.1 1D ABX_3-Type Perovskite Unit Cell

The 1D ABX_3-type perovskite structures obtained in the study were of the 2H-ABX_3 structure type, as shown in Figure 4.6 (b). Four of these perovskite structures were found to be isostructural, namely the structures **D-$NaCl_3$**, **D-$NaBr_3$**, **D-KCl_3** and **D-KBr_3(1)**, all crystallising in the trigonal space group $R\bar{3}c$. The crystal structure of **D-KCl_3** has been reported previously[36] (CSD refcode: DOTHOK[35] (determined at 100 K) and DOTHOK01[36] (determined at 120 K)). In this study the structure has been re-determined at 150 K and the compound was found to have the same structure at this temperature as DOTHOK and DOTHOK01.

The crystal structure **D-CsI_3** also forms a 2H-structure, however, this structure is not isostructural to the rest and crystallises in the hexagonal space group $P6_3/mmc$. Moreover, **D-CsI_3** was found to be the only reported structure of its type in the CSD since no other 1D ABX_3-type structures containing Cs–I bonds have been published before. Additionally, the literature structure **D-RbI_3** crystallises in the hexagonal space group $P\bar{6}2c$, which means that this structure is also not isostructural to the others described here.[37]

All the 1D ABX_3-type perovskite structures consist of 1D polymeric halide-bridged polymers, consisting of face-sharing octahedra, that are surrounded by dabconium dications. Figure 4.7 illustrates the packing diagrams of the crystal structures **D-$NaCl_3$**, **D-$NaBr_3$**, **D-KCl_3**, **D-KBr_3(1),** and **D-CsI_3** obtained from the combination of dabconium with BX-based anions (where B and X are given in Figure 4.7) as viewed down the *c*-axis, along the direction of the 1D face-sharing polymer. The isostructurality of structures **D-$NaCl_3$**, **D-$NaBr_3$**, **D-KCl_3**, and **D-KBr_3(1)** is evident from a consideration of their packing diagrams, as illustrated in Figure 4.7 (a) through (d). Additionally, it can be seen in Figure 4.7 (e) and (f) that the 1D perovskite structures comprised of dabconium and RbI-based anions (**D-RbI_3**), as well as CsI-based anions (**D-CsI_3**), exhibit different packing of dications and anionic 1D polymers compared to the isostructural structures.

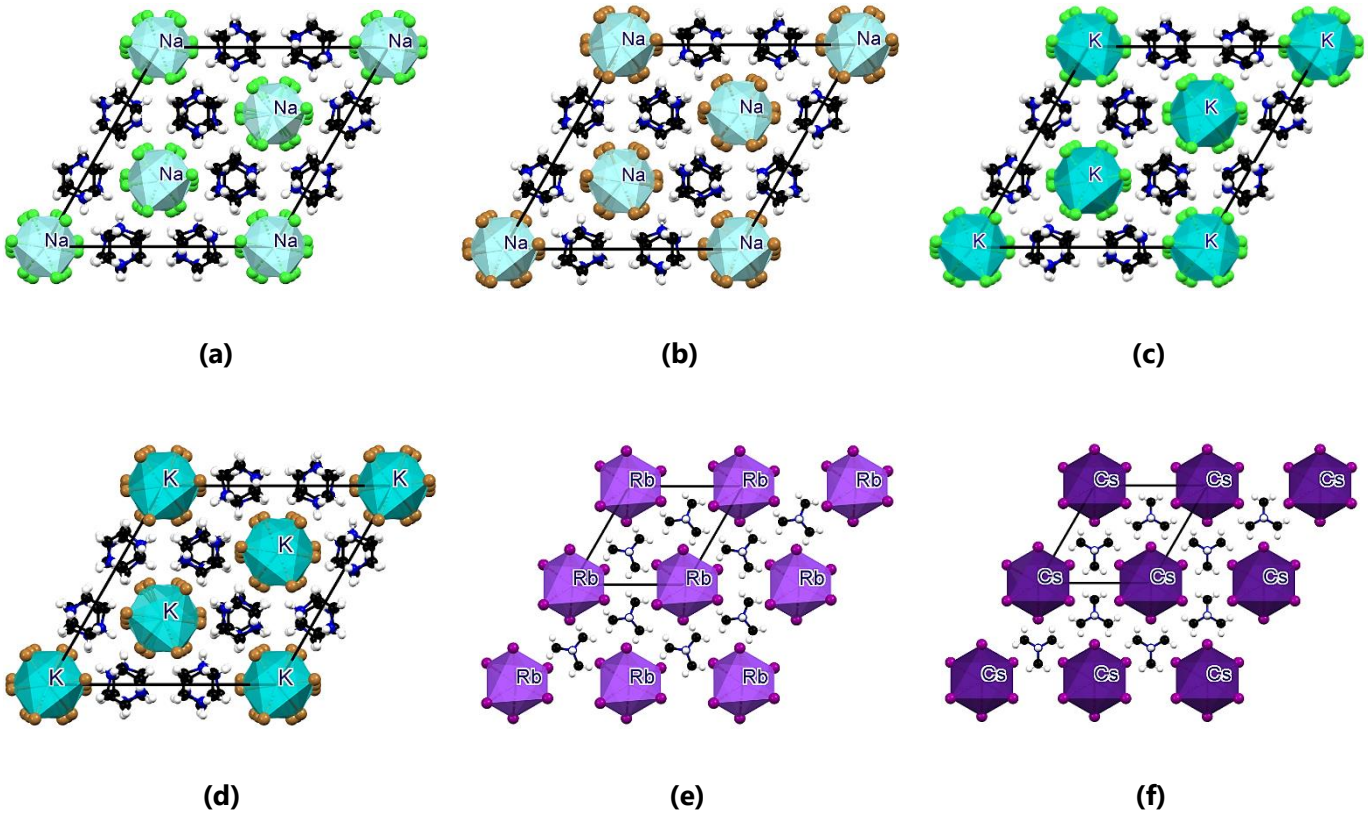

Figure 4.7 View of the unit cell down the *c*-axis of structures **(a) D-$NaCl_3$**, **(b) D-$NaBr_3$**, **(c) D-KCl_3**, **(d) D-KBr_3(1)** and four unit cells shown for **(e) D-RbI_3**[37] and **(f) D-CsI_3** to illustrate the packing. Chloride ions are shown in green, bromide ions in bronze and iodide ions in purple. Unit cells are shown in black.

The structures in this section are referred to as 1D ABX_3-type perovskite structures due to the presence of a halide-tri-bridged anionic polymer extending in the *c*-direction. In a broad definition, the structures form part of the 1D perovskite structural family, as has been previously referred to for **D-KCl$_3$**.[35,36] Six rows of dabconium dications pack around each of the 1D polymers, extending in the *c*-direction. The packing allows for the formation of a three-dimensional hydrogen bonding network, as described later in this section. Furthermore, it was found in this study that the combination of dabconium with KBr leads to two different structure types, one being a 1D ABX_3-type perovskite structure (**D-KBr$_3$(1)**) and the other a 3D perovskite structure (**D-KBr$_3$(2)**). Since these compounds both have the chemical formula **D-KBr$_3$**, they are polymorphs.[41] In this section, only the 1D perovskite structure **D-KBr$_3$(1)** will be discussed, while **D-KBr$_3$(2)** is described in the literature and later in the 3D perovskite section.

4.3.2 Asymmetric Unit and Symmetry Operations

The structures **D-NaCl$_3$**, **D-NaBr$_3$**, **D-KCl$_3$** and **D-KBr$_3$(1)** will be discussed together and comparatively with structure **D-CsI$_3$**. Furthermore, the structure **D-RbI$_3$** will not be discussed in detail since it has already been described in the literature.[37] That said, the structure **D-RbI$_3$** will be included in the structural comparison.

The asymmetric units of the structures **D-NaCl$_3$**, **D-NaBr$_3$**, **D-KCl$_3$** and **D-KBr$_3$(1)** are all similar to the asymmetric unit of structure **D-NaCl$_3$**, which is shown in Figure 4.8 (a). These asymmetric units consist of half a dabconium dication moiety and a $[B_2X_2]^-$ anion, with the anion containing two crystallographically independent metal ions. Two crystallographically different halide ions bridge the metal ions, with repetition of the inorganic part of the asymmetric unit forming a face-shared, halide-tri-bridged polymer. This polymer is formed by the symmetry operations of first a three-fold and subsequently a two-fold rotation axis, as shown in Figure 4.9 (a). In addition, the second half of the dabconium dication is formed by a two-fold rotation axis, as illustrated in Figure 4.9 (b). Moreover, three two-fold screw axes, all at 60° to one another, lying in the *ab*-plane, yields the entire 1D ABX_3-type perovskite structure.

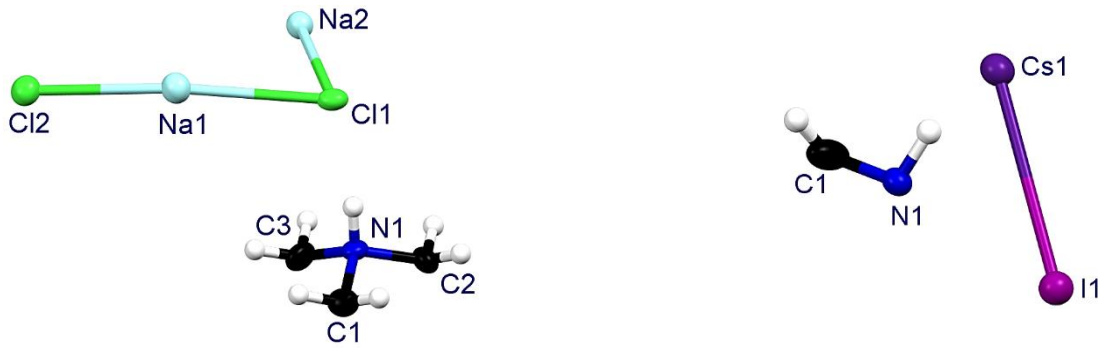

(a) **(b)**

Figure 4.8 Asymmetric units of structure **(a) D-NaCl$_3$**, which is representative of the asymmetric units of **D-NaBr$_3$**, **D-KCl$_3$** and **D-KBr$_3$(1)** and **(b) D-CsI$_3$**.

The asymmetric unit of structure **D-CsI$_3$** is shown in Figure 4.8 (b) and consists of only an H–C–N–H portion of the dabconium dication and a Cs–I moiety. The Cs–I moiety combines with three symmetry operations (Figure 4.9 (c)), which includes a three-fold rotation axis, followed by a six-fold roto-inversion axis and finally a two-fold rotation axis, to form a symmetrical face-shared, halide-tri-bridged polymer. In structure **D-CsI$_3$**, the N–H bond of the H–C–N–H moiety of the dication lies on a three-fold rotation axis, which in combination with a two-fold rotation axis, three mirror planes and a six-fold roto-inversion axis, forms the dabconium dication, as illustrated in Figure 4.9 (d). In addition to these symmetry operators, three two-fold screw axes, all at 60° to one another, lying in the *ab*-plane, combined with a six-fold rotation axis in the *c*-direction, forms the 1D ABX_3-type perovskite structure.

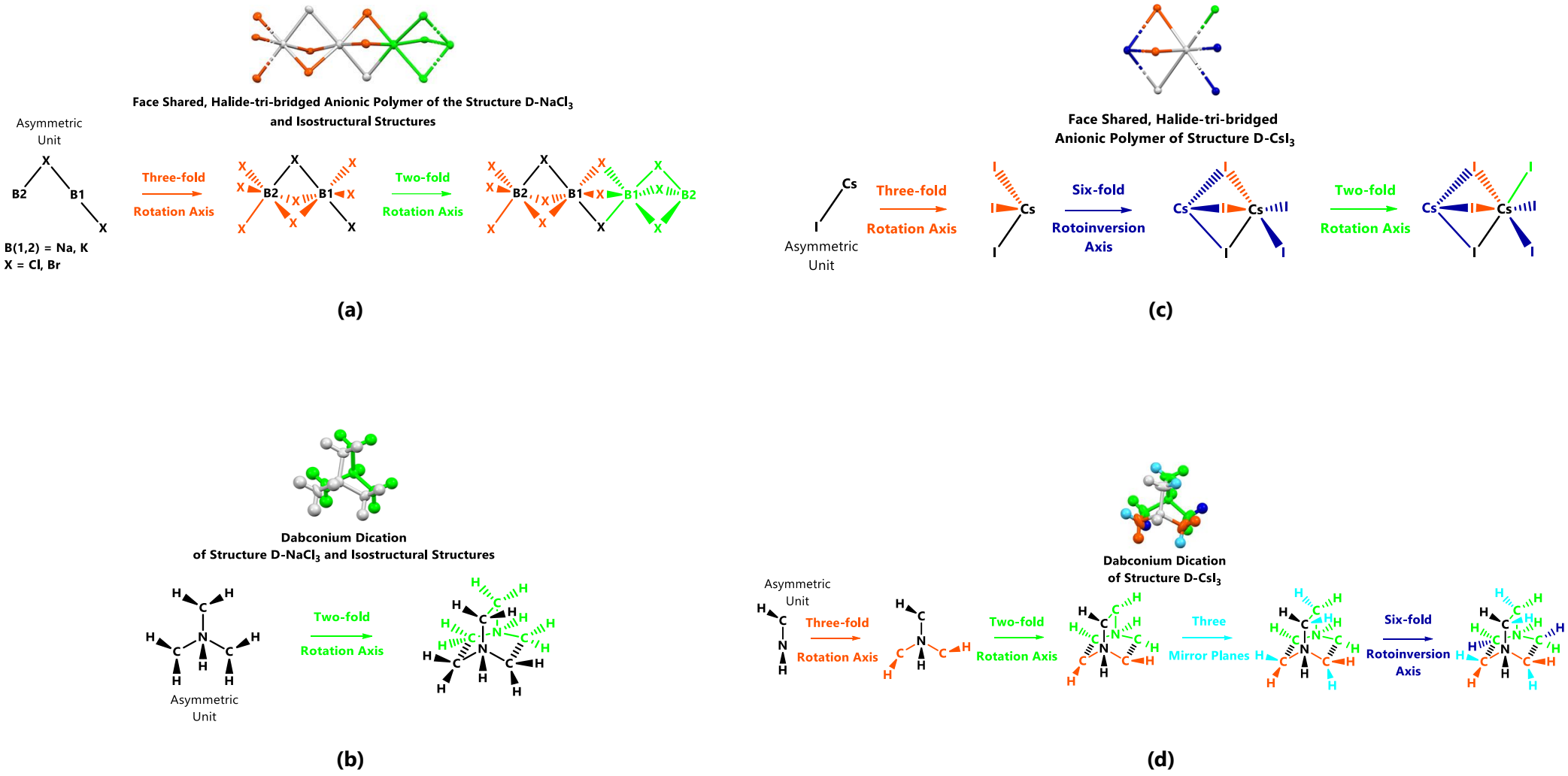

Figure 4.9 Line structures illustrating, using colour, how symmetry operations lead to the formation of **(a)** the face shared, halide-tri-bridged anionic polymer, **(b)** the dabconium dication of structure **D-NaCl$_3$** and its isostructural structures (**D-NaBr$_3$**, **D-KCl$_3$** and **D-KBr$_3$(1)**), **(c)** the face shared, halide-tri-bridged anionic polymer and **(d)** the dabconium dication of structure **D-CsI$_3$**. Asymmetric units are shown in black in the line structures.

Returning to the discussion of the inorganic polymer of structure **D-NaCl$_3$**, which represents all the structures in the series, repetition of the $[B_2X_2]^-$ species along a three-fold rotation axis results in the formation of a one-dimensional, face-shared, halide-tri-bridged polymer along the *c*-direction, as illustrated in Figure 4.10 (a) and (b). In the polymer, the metal ion sequence is such that two Na1 metal ions are followed by one Na2 metal ion. Thus, the metal ion sequence displayed is Na1···Na1···Na2···Na1···Na1···Na2 etc., as illustrated in Figure 4.10 (a). This sequence determines the different distances (B···B and B–X) in the halide-tri-bridged polymer chain, and leads to two distinctly different coordination octahedra, one for each crystallographically independent metal ion, Na1 and Na2, as indicated with colour in Figure 4.10 (b). The red and blue coloured octahedra in Figure 4.10 (b) are mirror images of one another and are the same, but different to the octahedron coloured in yellow. The yellow octahedra have the metal ion Na2 as the central ion, whereas the red and blue octahedra have the Na1 metal ions as the octahedral centre. Cl–Na2–Cl angles have values of 180°, 88.74(2)° and 91.26(2)°, which are much closer to a perfect octahedral arrangement (angles of 180° and 90°) than the Cl–Na1–Cl angles which exhibit values of 171.972(14)°, 83.25(3)°, 88.08(3)°, 89.57(2)° and 99.51(2)°. This means that the geometry of the octahedron containing metal ion Na2 is closer to the ideal octahedral geometry than that of the octahedron containing metal ion Na1.

The ideal B–X–B angle for face-sharing octahedra has been reported as 70.5 °, with relatively little structural flexibility possible in face-shared systems, compared to corner- and edge-shared polyhedral structures.[41] In structure **D-NaCl$_3$**, the Na1–Cl2–Na1 angle has a value of 73.23(4)°, while the Na1–Cl1–Na2 angle equals 76.06(3)°. The B–X–B angles of the rest of the structures in the isostructural family are listed in Table 4.3.

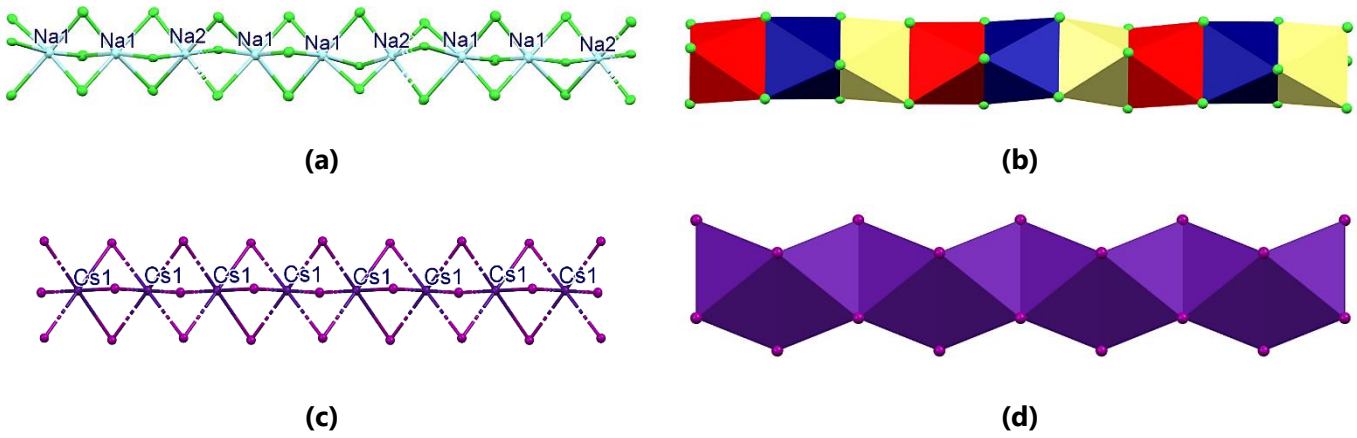

Figure 4.10 (a) The face-shared, halide-tri-bridged polymer formed in the structure **D-NaCl$_3$** with chlorine ions shown in green (also representative of the anionic polymer formed in structures **D-NaBr$_3$**, **D-KCl$_3$** and **D-KBr$_3$(1)**). **(b)** Polyhedral view of the polymer formed in structure **D-NaCl$_3$** (also representative of the anionic polymer formed in the structures **D-NaBr$_3$**, **D-KCl$_3$** and **D-KBr$_3$(1)**). **(c)** The face-shared, halide-tri-bridged polymer formed in structure **D-CsI$_3$** with iodide ions shown in light purple. **(d)** Polyhedral view of the polymer formed in the structure **D-CsI$_3$**.

Furthermore, for the **D-CsI$_3$** structure, a similar 1D face-shared, halide-tri-bridged polymer is formed along the *c*-direction by a three-fold rotation axis on which the Cs^+-ion lies (shown in Figure 4.10 (c) and (d)). Due to the compound crystallising in the hexagonal space group $P6_3/mmc$, in this polymeric chain, only one metal ion is repeated, namely atom Cs1. This in turn implies that only one Cs–I bond length is observed in the structure, with a value of 3.798(6) Å. Additionally, the Cs···Cs distance of 4.0332(5) Å is constant in the halide-bridged polymer. This is markedly different from the other polymeric chain structures discussed here (**D-NaCl$_3$** etc.), which exhibit several B–X bond lengths. In the polymer chain of **D-CsI$_3$**, the octahedra comprising the chain are all the same. The three I–Cs–I angles that make up the octahedra are 180.0°, 94.426(9)° and 85.573(9)°, respectively, values which are closer to the ideal octahedral arrangement than the trigonal phase 1D ABX_3-type perovskite structures in the isostructural series discussed previously. The Cs–I–Cs angle is equal to 64.136°(13). The structure **D-RbI$_3$** is similar to the structure **D-CsI$_3$** in terms of the features listed here. In this structure the Rb–I bond length is equal to 3.6698(8) Å, the I–Rb–I angles have values of 83.133(19)°, 93.760(19)°, 91.786(13)° and 172.585(19)° respectively, the Rb–I–Rb angle is equal to 67.982(19)°, and the Rb···Rb distance is equal to 4.1033(8) Å. The octahedra in

structure **D-RbI$_3$** are more distorted than the octahedra in structure **D-CsI$_3$**, which can be seen when looking down the polymer, as shown in Figure 4.7 (e) and (f). Detailed analysis of the structural trends will be considered in a later section.

4.3.3 Hydrogen Bonding Networks

A three-dimensional hydrogen bonding network is formed in structure **D-NaCl$_3$** and all its isostructural members of the family, made possible by the relative orientation of both the dabconium dication and the polymeric chains, with the dabconium dications optimally positioned in the structure to form hydrogen bonds to bridging halide ion acceptors on the 1D polymers. The D···H distances of the hydrogen bonds increase when Br^- is the halide present in the structure, compared to when the acceptor is Cl^-. The hydrogen bonds are shown as light blue dotted lines in Figure 4.11 (a), and hydrogen bonding parameters are listed in Table 4.3. Each dabconium dication forms two strong, charge assisted N–H^+···$^-$Cl–Na hydrogen bonding interactions to two different halide-tri-bridged polymers, as shown in Figure 4.11 (b).

The dications, packing in a row in the *c*-direction, alternate in orientation, as illustrated in Figure 4.11 (c). However, each third dication displays the same orientation, which agrees with the previous discussion of the symmetry elements involved in generating the dabconium dications. The dications adopt the specific orientations to position their N–H^+ groups to form strong hydrogen bonding interactions to the bridging halide ions of neighbouring halide-tri-bridged polymers.

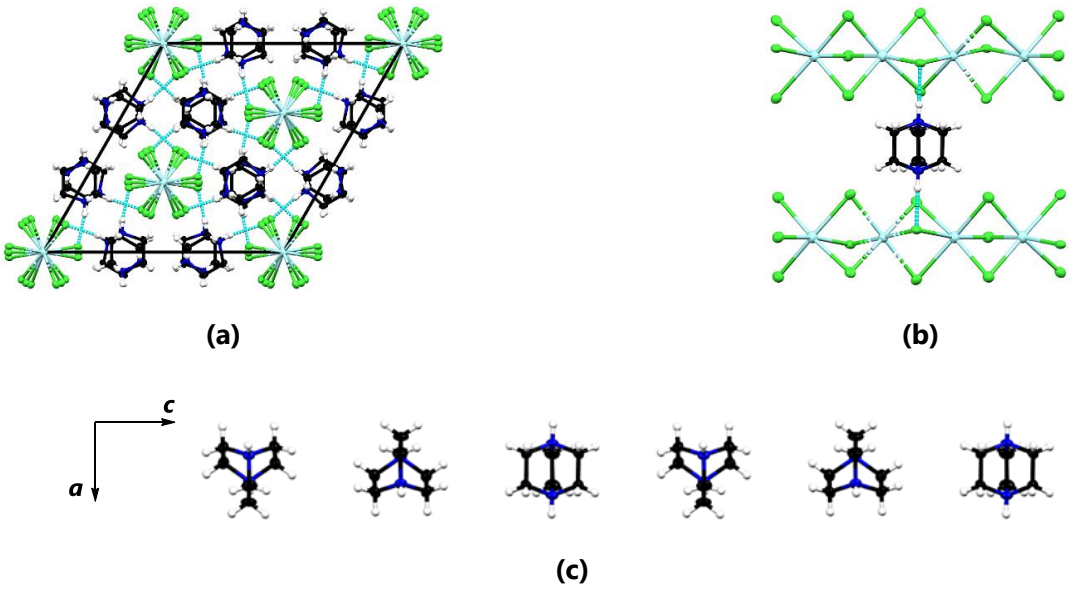

Figure 4.11 (a) Packing diagram of structure **D-NaCl$_3$** viewed down the *c*-axis (unit cell drawn in black). Classical hydrogen bonding interactions are indicated as light blue dotted lines. **(b)** Classical hydrogen bonding interactions showed as light blue dotted lines, linking the dabconium dication with two neighbouring halide-tri-bridged polymers in structure **D-NaCl$_3$**. **(c)** A row of dications viewed down the *b*-direction, showing the alternation in the orientation of the dications in the structure **D-NaCl$_3$** in the *c*-direction. (Note, the structure **D-NaCl$_3$** is also representative of the isostructural structures **D-NaBr$_3$**, **D-KCl$_3$** and **D-KBr$_3$(1)**).

In contrast to structure **D-NaCl$_3$** and its isostructural family members, the dabconium dications in structure **D-CsI$_3$** only have one orientation in a row when viewed down the *c*-axis, as illustrated in Figure 4.12 (a). Each dabconium dication forms two trifurcated hydrogen bonds to six different acceptor atoms on three different neighbouring polymers, as illustrated in Figure 4.12 (b). Thus, each dabconium dication forms six strong, charge assisted N–H^+···$^-$I–Cs hydrogen bonding interactions (with the same length of 3.814(5) Å) to three different halide-tri-bridged polymers, as shown in Figure 4.12 (c). The same trifurcated hydrogen bonds to six different acceptor atoms are also seen in the structure **D-RbI$_3$**, with a length of 3.256 Å, thus shorter than those present in the **D-CsI$_3$** structure (3.773(6) Å). It should also be noted that the cations pack in a slightly different orientation in structures **D-RbI$_3$** and **D-CsI$_3$** which can be seen when considering Figure 4.7 (e) and (f).

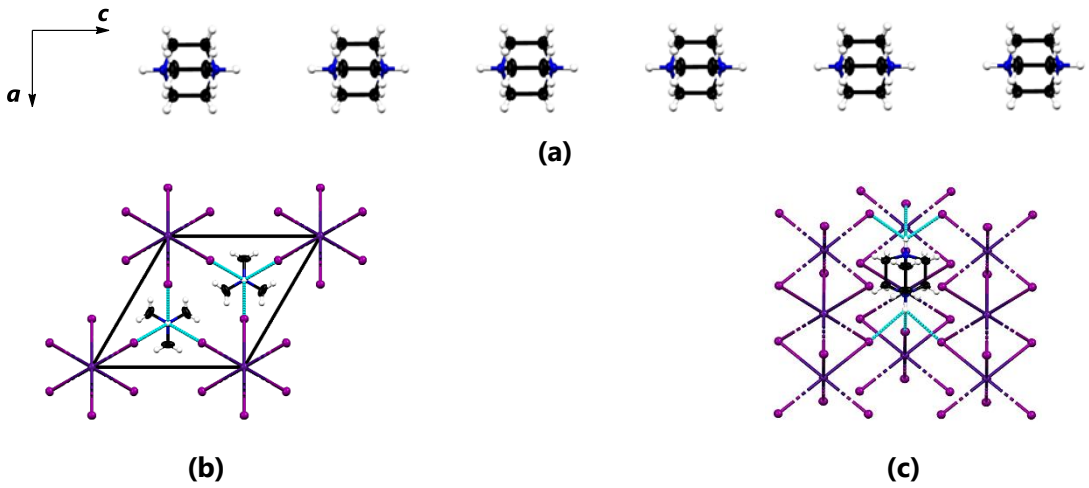

Figure 4.12 (a) A row of dications viewed in the *b*-direction, showing there is only one orientation of dications in structure **D-CsI$_3$**, along the *c*-direction. **(b)** Packing diagram of structure **D-CsI$_3$** viewed down the *c*-axis (unit cell drawn in black). Trifurcated hydrogen bonding interactions are indicated as light blue dotted lines. **(c)** Trifurcated hydrogen bonding interactions in structure **D-CsI$_3$**, viewed down the *a**-axis, showed as light blue dotted lines, linking the dabconium dication with three neighbouring halide-tri-bridged polymers.

4.3.4 Metal···Metal Distances

The 1D ABX_3-type perovskite structures reported here (**D-NaCl$_3$**, **D-NaBr$_3$**, **D-KCl$_3$**, **D-KBr$_3$(1)** and **D-CsI$_3$**) have different metal···metal distances in their halide-bridged polymers, with the distances increasing with increasing metal- and halide-ion size. Specifically, Na···Na distances range between 3.4390(17) Å and 3.7026(15) Å, K···K distances fall between 3.710(2) Å and 3.8389(6) Å and the one Cs···Cs distance is 3.99245(10) Å, with individual distances listed in Table 4.3. In addition, all the metal-ions of these structures lie on the same plane, and hence the B–B–B angles are 180° in each case. However, these B···B distances all lie within the range of other Na–Na (between 2.042 Å and 4.228 Å), K–K (between 0.77 Å and 4.732 Å) and Cs–Cs (between 3.923 Å and 5.41 Å) bond lengths reported in the Cambridge Structural Database (CSD (2021, Version 5.42, update May 2021)[34]).

Thus, considering the distances between the metal ions in the polymers, it appears that bonds or interactions may be formed between the metal ions, which is an interesting and unique feature of these structures. However, to concretely state that they are indeed what is regarded as chemical "bonds", computational analysis should first be conducted to determine if there exists a bond critical point between two successive B-ions. Unfortunately, this falls outside the scope of the current study and therefore this remains only a hypothesis at this stage. For interest's sake, when viewing the face-sharing octahedra of the structures, while the atoms are set to illustrate *space-filling* (see Figure 4.13 (a) and (b)), it shows visually what the hypothesis implies, the metal-ions (Na^+, K^+ and Cs^+) are showed to overlap. The Cs–Cs overlap shown in Figure 4.13 (b) is minimal, however, its distance is less than most reported Cs–Cs bond lengths.

Figure 4.13 The space-filling diagrams of the structures **(a) D-NaCl$_3$** (representative of **D-NaBr$_3$, D-KCl$_3$** and **D-KBr$_3$(1)**) and **(b) D-CsI$_3$**, illustrating the overlap of the metal-ions.

This concludes the discussion on the 1D ABX_3-type perovskite structures. The following section will report on the 3D perovskite structures obtained in this study.

4.4 3D Perovskite Structures: Crystallographic Results and Discussion

A total of six 3D perovskites (two of which have been reported previously) were obtained in this study. These include **D-NaI$_3$**, **D-KBr$_3$(2)**,[42] **D-KI$_3$**, **D-CsCl$_3$**,[36] **D-CsBr$_3$** and a mixed halide structure **D-CsCl$_2$I**. Low temperature (150 K) single-crystal X-ray diffraction data were collected for each of these structures. In addition, the 3D perovskite structures of **D-RbCl$_3$(1)**[36] and **D-RbBr$_3$(1)**[37] have been reported in the literature. These two structures have not been determined in the current study, and will not be discussed in detail, however, reference will be made to them where necessary, and their structural data are given in the relevant tables.

The crystallographic parameters of the low-temperature 3D perovskite structures obtained in this study and those reported in the literature are listed in Table 4.4. Furthermore, selected bond lengths, angles, hydrogen bonding parameters and structural descriptors are listed in Table 4.5 for both structures obtained in this study and those described in the literature, which falls into the category of 3D perovskite structures. The literature structures **D-RbCl$_3$(1)**[36] and **D-RbBr$_3$(1)**[37] are included in both Table 4.4 and Table 4.5, for completeness, since no Rb-containing structures were investigated in the current study, however, their structures will be included in the structural trend analysis The structures **D-KBr$_3$(2)**[42] and **D-CsCl$_3$**[36], previously reported in the literature, were re-determined at 150 K in this study, since the literature structures were determined at 293 K and 120 K respectively.

The discussion of the 3D dabconium containing perovskite structures is split into two main sections: firstly the discussion focusses on the *single halide 3D perovskites* which include structures **D-NaI$_3$**, **D-KBr$_3$(2)**, **D-KI$_3$**, **D-CsCl$_3$** along with **D-CsBr$_3$** and secondly on the *mixed halide 3D perovskite structure* **D-CsCl$_2$I**. Figure 4.14 shows the perovskite building units of the 3D perovskite structures **D-NaI$_3$**, **D-KBr$_3$(2)**, **D-KI$_3$**, **D-RbCl$_3$(1)**, **D-RbBr$_3$(1)**, **D-CsCl$_3$**, **D-CsBr$_3$** and **D-CsCl$_2$I**. This figure illustrates why they are classified as 3D perovskites since they possess the 3D perovskite structural characteristics described earlier.

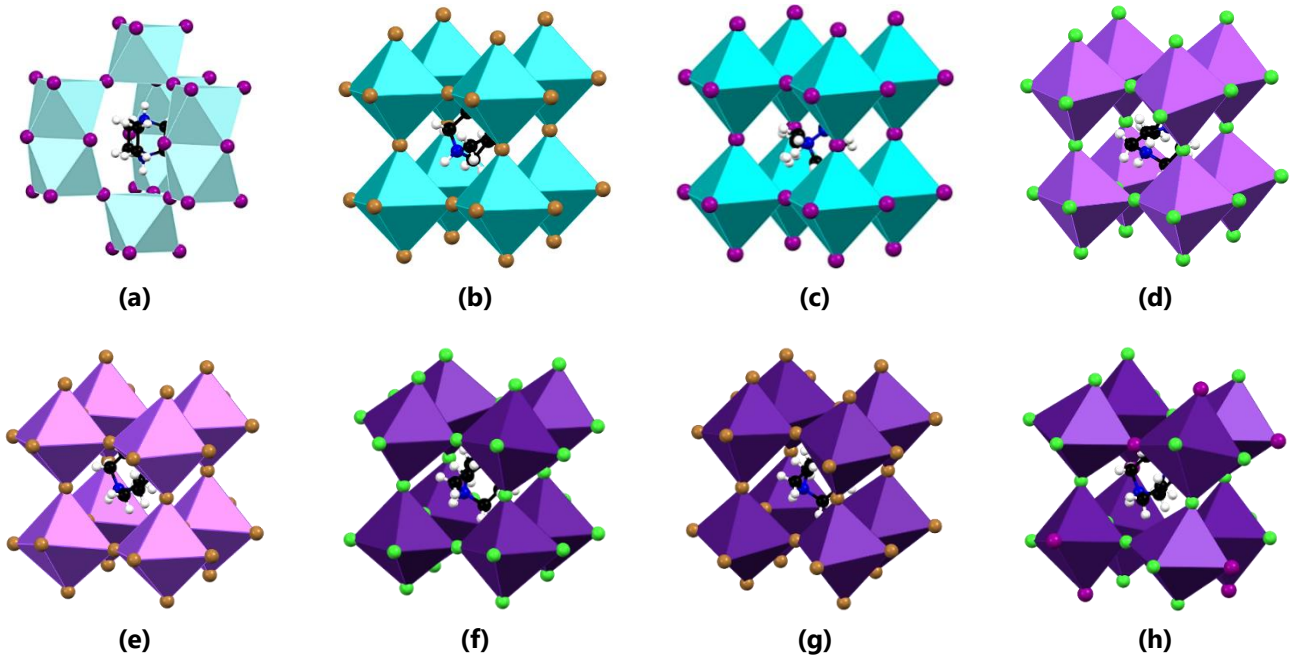

Figure 4.14 Perovskite building blocks of structures **(a) D-NaI$_3$**, **(b) D-KBr$_3$(2)**, **(c) D-KI$_3$**, **(d) D-RbCl$_3$(1)**,[36] **(e) D-RbBr$_3$(1)**,[37] **(f) D-CsCl$_3$**, **(g) D-CsBr$_3$** and **(h) D-CsCl$_2$I** either determined in this study or taken from the literature for the Rb-containing structures.

Table 4.4 Crystallographic parameters of the 3D dabconium-containing perovskite structures.

Structure Abbreviation	**D-NaI$_3$** [a]	**D-KBr$_3$(2)**	**D-KI$_3$**	**D-RbCl$_3$(1)**
Name	*catena*-[tris(1,4-diazabicyclo[2.2.2]octane-1,4-diium) nonakis(μ_2-iodo)-tri-sodium]	*catena*-[bis(1,4-diazabicyclo[2.2.2]octane-1,4-diium) hexakis(μ_2-bromo)-di-potassium]	*catena*-[bis(1,4-diazabicyclo[2.2.2]octane-1,4-diium) hexakis(μ_2-iodo)-di-potassium]	*catena*-[bis(1,4-diazoniabicyclo[2.2.2]octane-1,4-diium) hexakis(μ_2-chloro)-di-rubidium]
Empirical Formula	$3n(C_6H_{14}N_2)^{2+}\cdot n[I_9Na_3]^{6-}$	$2n(C_6H_{14}N_2)^{2+}\cdot n[Br_6K_2]^{4-}$	$2n(C_6H_{14}N_2)^{2+}\cdot n[I_6K_2]^{4-}$	$2n(C_6H_{14}N_2)^{2+}\cdot n[Cl_6Rb_2]^{4-}$
Formula Weight (g·mol^{-1})	1553.48	392.99	538.02	306.01
Crystal System	Hexagonal	Trigonal	Trigonal	Trigonal
Space Group	$P6_3/mmc$	$P3_221$	$R32$	$P3_221$
Temperature (K)	150(2)	150(2)	150(2)	120(2)
Wavelength (Å)	0.71073	0.71073	0.71073	0.71073
***a* (Å)**	9.6913(3)	9.3530(8)	9.720(2)	9.3376(1)
***b* (Å)**	9.6913(3)	9.3530(8)	9.720(2)	9.3376(1)
***c* (Å)**	23.1258(6)	11.4741(7)	12.077(3)	22.3386(5)
***α* (°)**	90	90	90	90
***β* (°)**	90	90	90	90
***γ* (°)**	120	120	120	120
Volume (Å^3)	1881.01(13)	869.26(16)	988.1(5)	1686.77(5)
Z	2	3	3	6
Density Calculated (g·cm^{-3})	2.591	2.252	2.712	1.808
Absorption Coefficient (mm^{-1})	7.465	10.756	7.395	5.069
***F*(000)**	1276	564	738	912
Crystal Size (mm^3)	0.03×0.04×0.05	0.08×0.09×0.10	0.03×0.03×0.06	0.39×0.33×0.21
Reflections Collected	24475	18040	5250	15718
Unique Reflections / R_{int}	853 / 0.1767	1671 / 0.1155	612 / 0.3063	2586 / 0.0544
Completeness	1.000	1.000	1.000	0.997
Parameters	28	40	21	8
Flack Parameter	–	0.48(17)	–0.1(11)	0.009(9)
Goodness-of-fit F^2	1.102	1.508	1.238	1.032
Final R indices [I>2σ(I)], (R_1 / wR_2)	0.1217 / 0.3347	0.2225 / 0.4506	0.2005 / 0.4558	0.0349 / 0.0638
R indices (all data), (R_1 / wR_2)	0.1257 / 0.3385	0.2353 / 0.4905	0.2040 / 0.4597	0.0517 / 0.0680

[a] The name, empirical formula and formula weight listed here were determined from chemical knowledge and not from the reported structure's CIF file, since one of the cations are disordered in the CIF file, hence the name, empirical formula and formula weight are for the non-disordered structure.

Table 4.4 (Continued) Crystallographic parameters for the 3D dabconium-containing perovskite structures.

Structure Abbreviation	D-$RbBr_3$(1)[37]	D-$CsCl_3$	D-$CsBr_3$	D-$CsICl_2$
Name	*catena*-[bis(1,4-diazabicyclo[2.2.2]octane-1,4-diium) hexakis(μ_2-bromo)-di-rubidium]	*catena*-[tetrakis(1,4-diazoniabicyclo[2.2.2]octane-1,4-diium) dodecakis(μ_2-chloro)-tetra-caesium]	*catena*-[1,4-diazabicyclo[2.2.2]octane-1,4-diium tris(μ_2-bromo)-caesium]	*catena*-[1,4-diazabicyclo[2.2.2]octane-1,4-diium di(μ_2-chloro)-(μ_2-iodo)-caesium]
Empirical Formula	$2n(C_6H_{14}N_2)^{2+}\cdot n[Br_6Rb_2]^{4-}$	$4n(C_6H_{14}N_2)^{2+}\cdot n[Cl_{12}Cs_4]^{8-}$	$n(C_6H_{14}N_2)^{2+}\cdot n[Br_3Cs]^{2-}$	$n(C_6H_{14}N_2)^{2+}\cdot n[Cl_2ICs]^{2-}$
Formula Weight (g·mol^{-1})	439.39	1413.81	486.80	444.90
Crystal System	Trigonal	Monoclinic	Orthorhombic	Trigonal
Space Group	$P3_221$	$C2/c$	$Pbcn$	$P3_121$
Temperature (K)	293(2)	150(2)	150(2)	150(2)
Wavelength (Å)	0.71073	0.71073	0.71073	0.71073
***a* (Å)**	9.6444(14)	41.1638(16)	9.8044(2)	9.77000(10)
***b* (Å)**	9.6444(14)	9.48990(10)	9.8273(3)	9.77000(10)
***c* (Å)**	23.254(5)	32.6647(13)	27.3662(7)	11.9653(2)
***α* (°)**	90	90.00	90	90
***β* (°)**	90	131.638(7)	90	90
***γ* (°)**	120	90.00	90	120
Volume (Å^3)	1873.2(7)	9536.4(12)	2636.75(12)	989.11(3)
Z	6	8	8	3
Density Calculated (g·cm^{-3})	2.337	1.969	2.453	2.241
Absorption Coefficient (mm^{-1})	13.522	3.735	11.862	5.515
***F*(000)**	1236	5440	1792	618
Crystal Size (mm^3)	0.22×0.18×0.15	0.10×0.11×0.15	0.08×0.10×0.12	0.11×0.22×0.35
Reflections Collected	12709	135520	19177	31157
Unique Reflections / R_{int}	2875 / 0.0960	15214 / 0.0822	4154 / 0.0444	2095 / 0.0611
Completeness	0.997	0.887	0.964	1.000
Parameters	110	435	111	56
Flack Parameter	0.04(3)	–	–	–0.004(13)
Goodness-of-fit F^2	1.110	0.940	1.276	1.037
Final R indices [I>2σ(I)], (R_1 / wR_2)	0.0652 / 0.1127	0.0304 / 0.0767	0.0598 / 0.0922	0.0173 / 0.0354
R indices (all data), (R_1 / wR_2)	0.1040 / 0.1241	0.0383 / 0.0728	0.0683 / 0.0957	0.0186 / 0.0357

Table 4.5 Selected bond lengths, angles, hydrogen bonding parameters and structural descriptors for the 3D dabconium-containing perovskite structures.

Structure Abbreviation	**D-NaI$_3$** [a]		**D-KBr$_3$(2)**	**D-KI$_3$**	**D-RbCl$_3$(1)**		**D-RbBr$_3$(1)**[37]	
Organic Cation (A)	Dabconium		Dabconium	Dabconium	Dabconium		Dabconium	
Metal Ion (B)	Na^+		K^+	K^+	Rb^+		Rb^+	
Halide Ion (X)	I^-		Br^-	I^-	Cl^-		Br^-	
Structure Type	3D Perovskite (Hexagonal Polytype)		3D Perovskite	3D Perovskite	3D Perovskite		3D Perovskite	
Temperature (K)	150(2)		150(2)	150(2)	120(2)		293(2)	
B–X (Å)	**Na1**	**Na2**			**Rb1**	**Rb2**	**Rb1**	**Rb2**
	3.3335(18)	3.237(11)	3.3162(5)	3.4578(6)	3.2924(7)	3.2894(8)	3.3990(17)	3.3863(13)
		3.433(10)			3.3040(8)	3.3198(8)	3.4070(16)	3.4275(17)
					3.3179(8)	3.2899(8)	3.4374(13)	3.4439(17)
X–B–X (°)	**Na1**	**Na2**			**Rb1**	**Rb2**	**Rb1**	**Rb2**
	89.58(4)	86.6(4)			78.919(19)	82.716(18)	83.26(3)	80.16(3)
	90.42(4)	90.39(3)			83.22(3)	84.68(3)	84.69(5)	84.35(3)
	180	92.5(3)	84.75(11)	86.42(11)	85.01(2)	86.222(18)	86.34(3)	85.07(5)
		175.8(5)	90.061(14)	89.527(13)	89.15(3)	88.140(18)	87.74(3)	88.53(5)
			95.62(13)	94.84(12)	94.441(19)	93.405(19)	93.49(3)	94.51(4)
			172.29(17)	174.01(16)	96.023(18)	97.44(2)	97.16(3)	95.26(3)
					101.322(19)	102.88(3)	102.63(6)	100.83(4)
					163.79(2)	165.32(3)	165.58(6)	164.48(3)
					171.20(3)	170.90(2)	171.03(5)	172.83(6)
B–X–B (°)	75.3(5)	178.5(2)	172.30(17)	174.08(16)	161.35(3)		162.18(5)	
					165.24(3)		165.74(4)	
					172.08(3)		173.03(5)	
N–H$^+$···$^-$X–B (D···A) (Å)	3.813(13)		3.71(3)	3.71(15)	3.034(3)		2.282	
			3.72(3)		3.040(3)		2.244	

[a] The hydrogen bonding data listed for the structure **D-NaI$_3$** could only be determined for the non-disordered cation.

Table 4.5 (Continued) Selected bond lengths, angles, hydrogen bonding parameters and structural descriptors for the 3D dabconium-containing perovskite structures.

Structure Abbreviation	**D-$CsCl_3$**					**D-$CsBr_3$**		**D-$CsICl_2$**	
Organic Cation (A)	Dabconium					Dabconium		Dabconium	
Metal Ion (B)	Cs^+					Cs^+		Cs^+	
Halide Ion (X)	Cl^-					Br^-		I^- and Cl^-	
Structure Type	3D Perovskite					3D Perovskite		3D Perovskite	
Temperature (K)	150(2)					150(2)		150(2)	
	Cs1	**Cs2**	**Cs3**	**Cs4**	**Cs5**	**Cs1**	**Cs2**	**Cl1**	**I1**
	3.3629(5)	3.3323(5)	3.3341(5)	3.3351(5)	3.3444(4)	3.4573(5)	3.4378(5)	3.3828(8)	3.72118(19)
	3.3937(5)	3.3495(5)	3.3393(6)	3.3359(5)	3.4087(5)	3.5009(6)	3.5497(6)	3.4148(7)	
B–X (Å)	3.4161(5)	3.3947(5)	3.4180(5)	3.3886(5)	3.4215(5)	3.5032(6)	3.5610(6)		
		3.3975(6)	3.4252(5)	3.4114(5)					
		3.4184(5)	3.4259(5)	3.4124(5)					
		3.4322(5)	3.4269(5)	3.4359(5)					
	Cs1	**Cs2**	**Cs3**	**Cs4**	**Cs5**	**Cs1**	**Cs2**	**Cl1**	**I1**
	80.656(12)	81.927(13)	78.078(11)	82.305(12)	72.815(17)	79.69(2)	83.311(14)	79.75(3)	96.923(10)
	85.382(14)	82.431(12)	81.574(12)	83.822(12)	80.444(12)	85.729(14)	89.757(13)	95.132(5)	
	88.967(13)	82.955(12)	84.904(14)	84.086(12)	91.617(12)	88.922(15)	89.921(4)	97.67(2)	
	91.031(13)	86.625(13)	86.483(14)	84.591(13)	93.068(12)	89.611(3)	90.078(5)	163.30(3)	
	94.616(14)	89.309(14)	88.294(12)	85.695(14)	93.916(13)	90.963(15)	90.242(13)		
	99.343(12)	89.373(13)	88.913(12)	88.536(12)	96.423(12)	95.504(15)	96.688(14)	**Cl1 & I1**	
	180	91.109(13)	91.368(13)	90.049(12)	99.496(17)	101.11(2)	180	83.273(14)	
X–B–X (°)		91.843(12)	92.410(13)	91.034(14)	166.354(11)	169.24(2)		85.674(14)	
		92.101(12)	93.673(12)	96.113(12)	170.014(18)	171.58(3)		91.662(14)	
		93.471(13)	97.271(13)	97.293(12)				171.413(15)	
		99.357(13)	98.652(13)	97.624(13)					
		100.474(15)	100.887(12)	100.509(15)					
		165.923(12)	163.357(11)	165.047(13)					
		169.011(12)	166.816(12)	166.924(11)					
		172.516(12)	173.478(12)	177.954(11)					
	155.236(15)	158.543(16)	160.943(15)	162.347(19)		154.96(3)		**Cl1**	**I1**
B–X–B (°)	157.464(15)	159.283(15)	161.115(16)	164.333(15)		164.65(3)		159.91(3)	166.102(10)
	157.733(19)	160.572(16)	161.734(15)	167.730(17)		165.89(3)			
N–H^+···$^-$X–B	3.0036(18)	3.0223(17)	3.0246(17)	3.0450(16)		3.194(4)		**Cl1**	
(D···A) (Å)	3.0166(17)	3.0242(16)	3.0373(17)	3.0521(17)		3.224(5)		3.024(3)	

4.4.1 Single Halide 3D Perovskites

The following sections describe the novel 3D single halide perovskite structures (**D-NaI$_3$**, **D-KI$_3$**, and **D-CsBr$_3$**). In addition, the structures **D-KBr$_3$(2)**[42] and **D-CsCl$_3$**[36] which have been reported previously, and re-determined in this study at 150 K, are also described briefly, since they are relevant to this study focussing on dabconium compounds of Na^+, K^+ and Cs^+. Moreover, the structural data listed in Table 4.4 and Table 4.5 are those of the structures determined in this study at 150 K and not from the structures reported in literature.

Structural Discussion of **D-NaI$_3$**

The structure **D-NaI$_3$** is a 3D hexagonal polytype perovskite, which crystallises in the hexagonal space group $P6_3/mmc$. The structure falls in the category of the 6H-type 3D hexagonal polytype perovskites, as illustrated by its NaI_6 framework shown in Figure 4.15 (a) and (b). This organic-inorganic 6H hexagonal halide polytype perovskite is one of only a few of its type, and this structure is associated with the oxide inorganic perovskite $BaTiO_3$.[43]

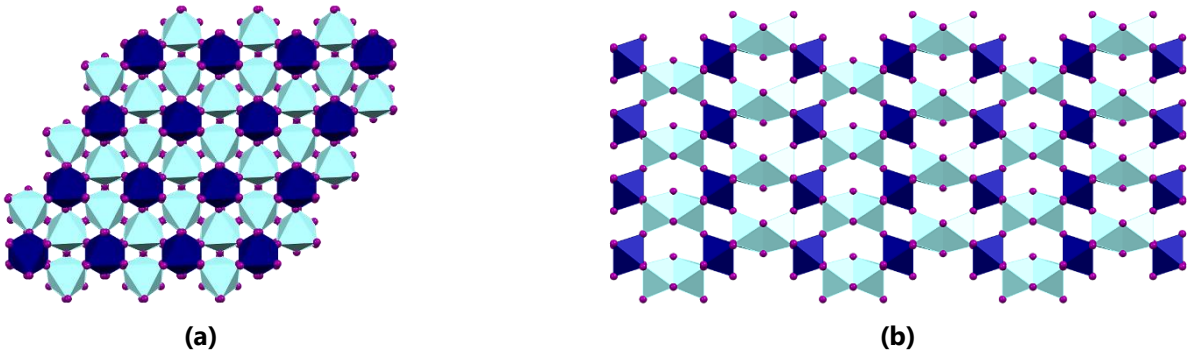

Figure 4.15 The 3×3 expansion of the inorganic framework of **D-NaI$_3$**. **(a)** Viewed down the *c*-direction and **(b)** viewed down the *a*-direction. The two types of octahedra present in the structure, formed around ions Na1 and Na2 respectively, are either present in the cubic (Na1, dark blue) or the hexagonal (Na2, light blue) layers.

The 6H hexagonal polytype is characterised by two different layers of octahedra, one a cubic layer and the second a hexagonal layer, as illustrated with dark and light blue octahedra in Figure 4.15. For the structure **D-NaI$_3$**, the cubic octahedra have Na1-centra, and the octahedra in the hexagonal layers have Na2-centra. Light and dark blue will indicate the two different octahedra (Na1 or Na2, respectively) in this section where necessary, otherwise the octahedra will be coloured light blue. In the hexagonal layer, face-sharing octahedra are present, with hexagonal and cubic layers alternating in the structure, connected *via* corner-sharing of octahedra.

Furthermore, the face-sharing octahedra only possess one B···B distance (4.03(2) Å), similar to the other hexagonal 1D ABX_3-type perovskites (**D-RbI$_3$** and **D-CsI$_3$**) described earlier. This distance lies within the range of Na–Na bond lengths reported in the Cambridge Structural Database (CSD (2021, Version 5.42, update May 2021)[34]), which are between 2.042 Å and 4.228 Å. Therefore, the possibility of Na–Na bonds being present in the structure **D-NaI$_3$** should not be disregarded.

The organic dication is hosted in a supercavity formed by the inorganic framework, specifically a biaugmented tricapped trigonal-prismatic cavity, as illustrated in Figure 4.16. Figure 4.16 (a) and (b) illustrate the Na^+- and I^--ions that form the supercavity, which is more informatively represented by the schematic drawing of the prism in Figure 4.16 (c). Finally, in Figure 4.16 (d), the cavity is "filled" with a dabconium dication, illustrating one of the two types of dabconium dications present in the structure, one of which is disordered, as discussed later. The dabconium dication shown in Figure 4.16 (d) is the cation that does not show disorder, and hence it was possible to refine the complete cation with its hydrogen atoms placed. However, the placement of the hydrogen atoms for the disordered cation was not possible.

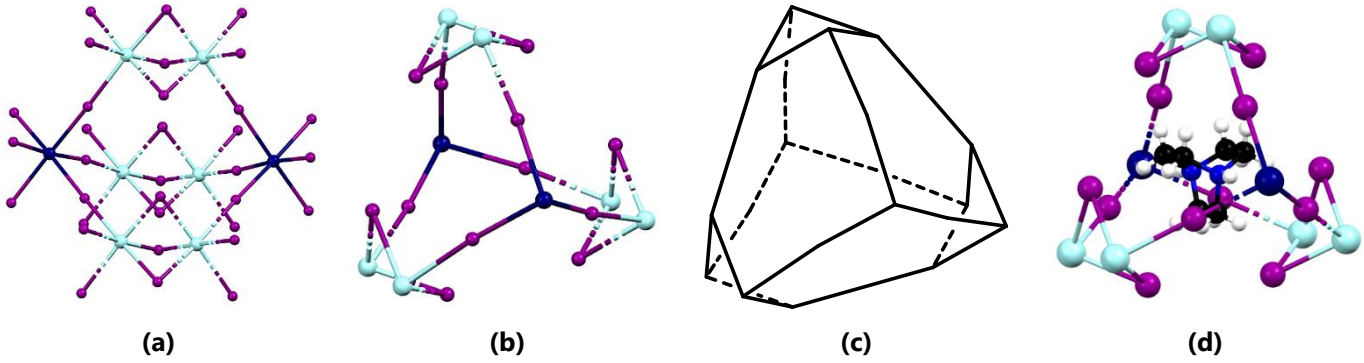

Figure 4.16 The supercavity formed by the inorganic framework of **D-NaI$_3$ (a)** the empty cavity showing only the metal-halide octahedra, **(b)** an illustration of the shape of the cavity with only the Na^+- and I^--ions that form the edges of the biaugmented tricapped trigonal-prism shown and **(c)** a schematic illustration of the prism (dashed lines are drawn "behind" solid lines"). **(d)** The dabconium dication is present in the supercavity.

The asymmetric unit of the structure **D-NaI$_3$** is shown in Figure 4.17 (a). The asymmetric unit consists of a Na1–I2–Na2–I1 moiety and two N–C moieties of two different crystallographically independent dabconium dications.

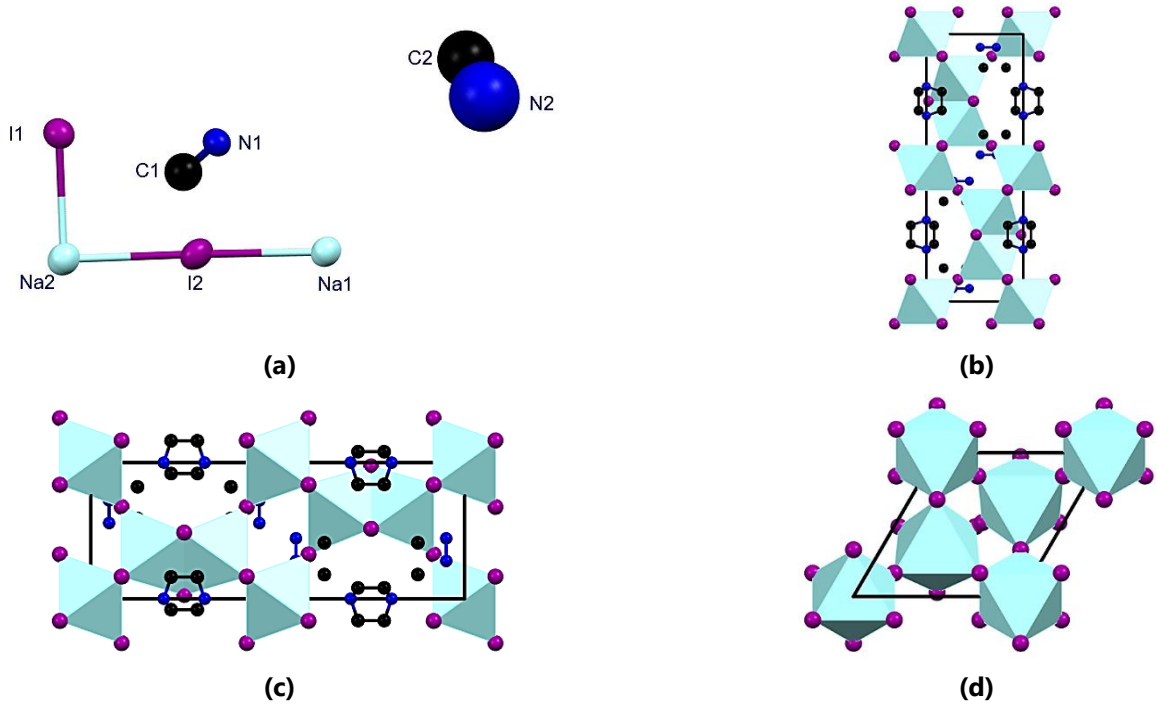

Figure 4.17 (a) The asymmetric unit of **D-NaI$_3$** and the unit cell (shown in black) as viewed down the **(b)** *a*-direction, **(c)** *b*-direction and **(d)** *c*-direction. Hydrogen atoms are omitted for clarity.

The structure is generated from three two-fold screw axes that lie in the *ab*-plane at 120° to one another, in combination with two three-fold rotational axes and four six-fold screw axes, where the latter two types of rotation occur along the *c*-direction, in the unit cell. Furthermore, two proper three-fold rotational axes and two six-fold rotoinversion axes directed in the *c*-direction combine with the aforementioned operations to form the structure. Several inversion centra and mirror or glide planes provide equivalent symmetry operations as the rotational axes, which may also be used to describe the structure. The two N–C moieties in the asymmetric unit each result in a dabconium cation, with one of the cations being ordered, and the second being disordered. Figure 4.17 (b), (c), and (d) show the unit cell of the structure **D-NaI$_3$**. From these three figures, it can be seen that one dabconium dication is disordered.

Furthermore, the octahedra that occupy the cubic sites (those containing Na1-ions, corner-sharing) are less distorted than those that occupy the hexagonal sites (containing Na2-ions, face-sharing). The octahedra containing Na1-ions have a near-ideal octahedral arrangement with I–Na–I angles of 89.58(4)°, 90.42(4)° and 180°, whereas those with Na2-centra are more distorted with I–Na–I angles of 86.6(4)°, 90.39(3)°, 92.5(3)° and 175.8(5)°. This distortion is further seen in the differences in B–X bond lengths, since the Na1–I bonds have only one length of 3.3335(18) Å, whereas the Na2–I bonds have two distinct bond lengths of 3.237(11) Å or 3.433(10) Å.

The ordered dabconium dication forms two trifurcated charge assisted $N–H^{+}\cdots^{-}I–Na1$ hydrogen bonding interactions of length 3.813(13) Å as shown in Figure 4.18 (a). Furthermore, in Figure 4.18 (b), the resulting weak hydrogen bonding interactions are also included and show that each C–H hydrogen atom participates in a bifurcated $C–H\cdots^{-}I–Na$ hydrogen bonding interaction, with these interactions also anchoring the cation in the cavity. In addition, a row of the ordered dabconium dication is shown in Figure 4.18 (c), illustrating that it has two orientations.

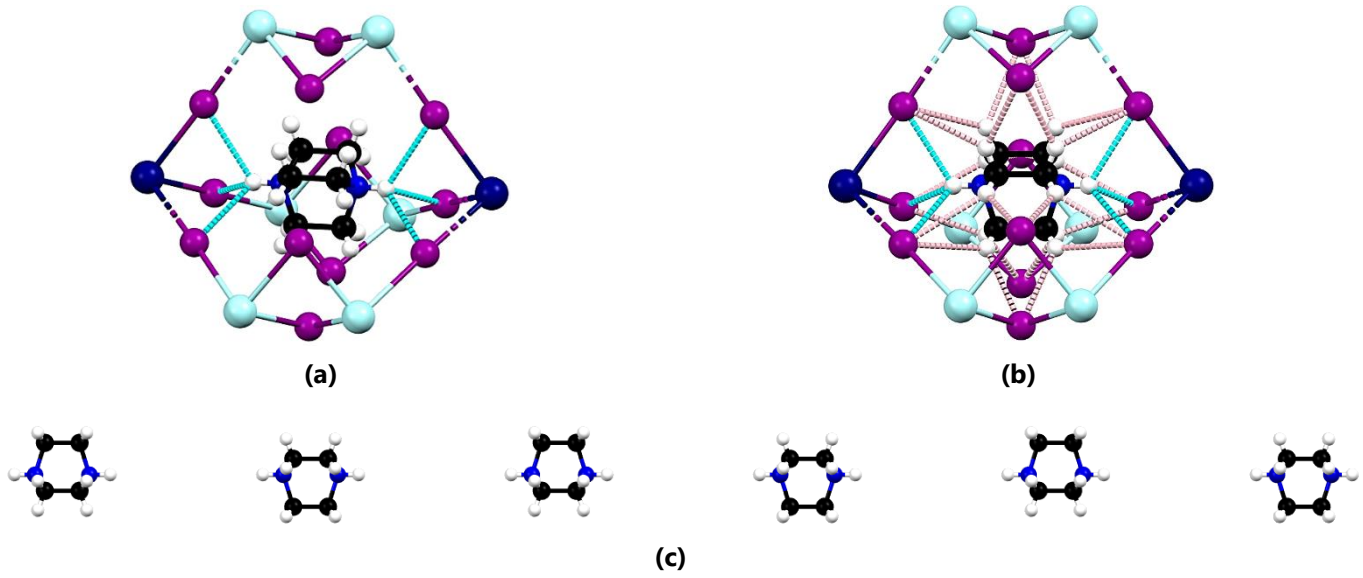

Figure 4.18 (a) The trifurcated charge assisted hydrogen bonding interactions (shown as light blue dashed lines) of the ordered dabconium dication in the structure **D-NaI$_3$**, **(b)** charge assisted (light blue dashed lines) and weak (pink) hydrogen bonding interactions and **(c)** a row of dabconium dications packed down the *c*-direction and viewed down the *b*-direction.

Unfortunately, due to the disordered nature of the second dabconium dication, its hydrogen bonding interactions could not be analysed. This concludes the discussion of the structure **D-NaI$_3$**.

Structural Discussion of **D-KBr$_3$(2)**

The structure **D-KBr$_3$(2)** has been previously reported, as determined at 293 K in the trigonal space group $P3_121$,[42] regrettably the publication is not available in English. The structure re-determined at 150 K in this study shows no difference compared to the room temperature structure and so only a concise description of its main features is given here. Various attempts were made to obtain better quality structural data for this compound, but without success. The structure reported here is of low quality (R_1 = 0.2225), however, the main structural features are evident. The structure reported here crystallises in the chiral trigonal space group $P3_221$ and exhibits the 3D perovskite structure. One important point to note is that the space group $P3_221$ is a member of the pair of enantiomorphic space groups $P3_221$ and $P3_121$, which are both chiral, however, the former contains a left handed three-fold screw axis, and the other a right handed one.[44] This means that the structure obtained in this study at 150 K is an enantiomer of the one reported in the literature, hence the difference in the space group.

The asymmetric unit of the structure contains half a dabconium dication, along with an inorganic moiety (Br1–K1–Br2). The asymmetric unit is shown in Figure 4.19 (a). Repetition of the inorganic portion leads to one type of octahedron. This octahedron is not significantly distorted, as can be seen by considering the Br–K–Br and K–Br–K angles listed in Table 4.5, with Br–K–Br angles equal to 84.75(11)°, 90.061(14)°, 95.62(13)° and 172.29(17)° and K–Br–K angles equal to 172.30(17)°.

The only symmetry elements present in the structure are either rotational or screw axes. Six three-fold screw axes directed down the *c*-direction combines with three two-fold screw axes (at 60° to one another) in the *ab*-plane and a similar arrangement of two-fold rotational axes to generate the unit cell, as shown in Figure 4.19 (b), (c) and (d). In addition, the structure's octahedral tilting may be described by Glazer's notation as belonging to the $a^+b^+c^+$ tilt system.[45,46]

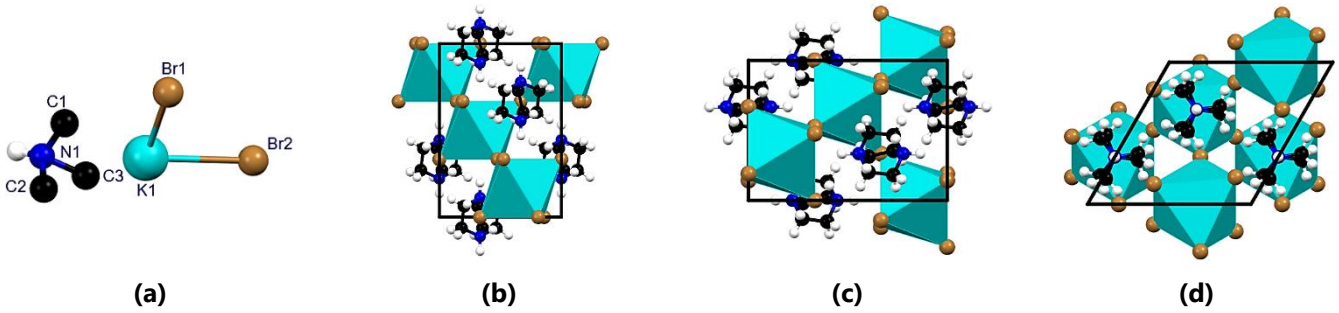

Figure 4.19 (a) The asymmetric unit of **D-KBr$_3$(2)** and the unit cell (shown in black) of the structure **D-KBr$_3$(2)** viewed down the **(b)** *a*-direction, **(c)** *b*-direction and **(d)** *c*-direction.

The structure consists of an inorganic, 3D perovskite framework that forms cavities in which the dabconium cations pack. The chirality of the structure is evident in both the packing of the organic cations and in the inorganic framework. The full dabconium dication is generated *via* a two-fold rotation axis. The dabconium dication packing is regulated by the three-fold screw axis in the *c*-direction. When viewing the packing of the cations along the *c*-direction, the cations pack in a left-handed helical fashion around the three-fold screw axis, as shown in Figure 4.20 (a). As illustrated in Figure 4.20 (b), the inorganic framework forms a left-handed helix around the three-fold screw axis. The helix is left-handed since a clockwise screw motion is always directed towards the observer as may be seen in Figure 4.20 (a) and (b).

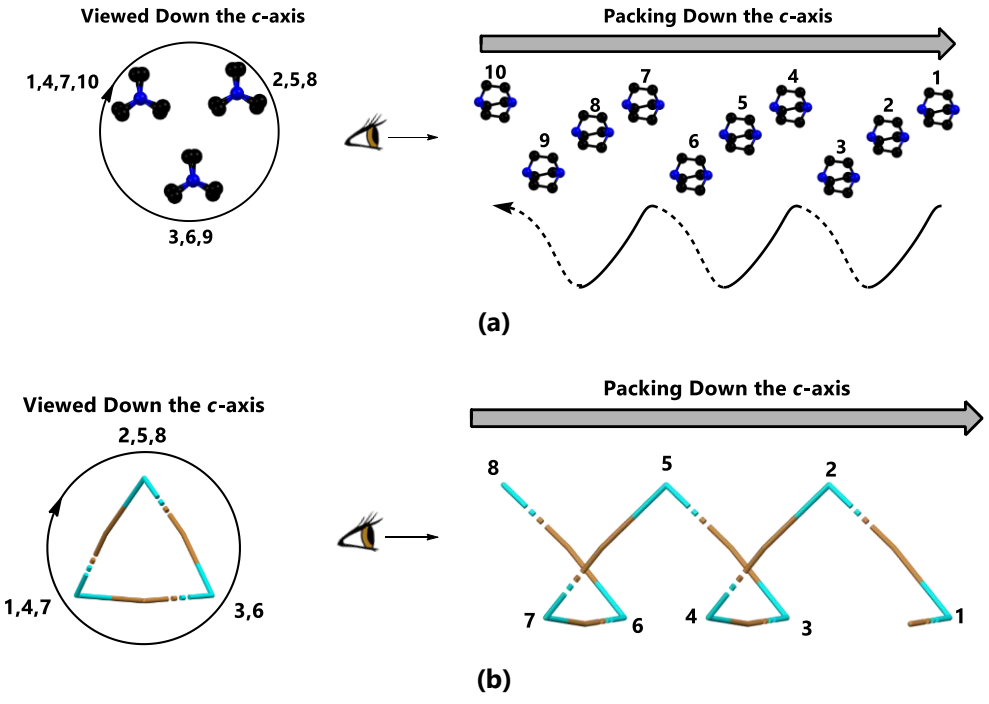

Figure 4.20 The presence of the left-handed helix in the structure **D-KBr$_3$(2)** as illustrated in **(a)** the dication packing and **(b)** the packing of the inorganic framework. Dashed and thick lines in the helix illustrate the differences in depth.

Furthermore, each dabconium dication participates in two bifurcated, charge assisted hydrogen bonding interactions (N–H$^{+}\cdots^{-}$Br(1,2)–K) of length 3.71(3) Å and 3.72(3) Å. Several other weak hydrogen bonding interactions (C–H$\cdots^{-}$Br–K) are also present. These hydrogen bonds anchor the dabconium dications to the cavities formed in the inorganic framework.

On a final note, the structure **D-KBr$_3$(2)** and the 1D ABX_3-type perovskite structure **D-KBr$_3$(1)** are polymorphs. However, the 1D polymorph is formed from crystallisation at room temperature and the 3D polymorph from a higher temperature crystallisation (*ca*. 80 °C), from the same solvent, namely water. Hence, the desired polymorph may be selectively obtained *via* thermodynamic control by careful control of the crystallisation temperature. Moreover, both crystallise in a trigonal space group ($R\bar{3}c$ versus $P3_221$), and with the switch from face-sharing octahedra to corner-sharing octahedral, chirality is introduced in structure **D-KBr$_3$(2)**.

Structural Discussion of **D-KI$_3$**

The structure **D-KI$_3$** is a 3D perovskite structure that crystallises in a trigonal phase, space group *R*32, as shown in Figure 4.21 (a), (b) and (c). The structure does not undergo any phase transitions between 150 K and 293 K, as established by comparison of the powder pattern calculated from its single-crystal structure determined at 150 K and experimental powder pattern measured at 298 K. The space group *R*32 is a chiral, non-enantiogenic space group, which belongs to the Sohncke space groups.

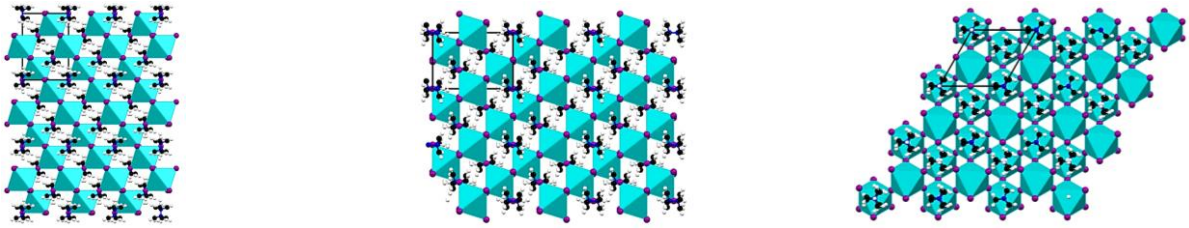

(a) **(b)** **(c)**

Figure 4.21 The 3×3 expansion of the unit cell (shown in black) of **D-KI$_3$** as viewed down the **(a)** *a*-direction, **(b)** *b*-direction and **(c)** *c*-direction.

The asymmetric unit of structure **D-KI$_3$** consists of a H_2C–NH organic moiety and an inorganic K–I moiety (see Figure 4.22 (a)). The entire structure is generated by three two-fold screw axes that lie in the *ab*-plane at 60° to one another and six three-fold screw axes directed in the *c*-direction. This means that only one "type" of KI_6 octahedron is present in the structure. These symmetry operations imply that the dabconium dication has only one orientation down the *c*-, *b*-, *and a*-axes, as shown in Figure 4.22 (b), (c), and (d), however, it also indicates that they pack in a helix formation, indicative of the chirality of the structure.

Furthermore, the tilting of the KI_6 octahedra may be described by Glazer's notation[45,46] as $a^+b^+c^+$. It is evident from Figure 4.21 (a), (b) and (c) that in one direction (the *a*-direction), all the octahedral tilts are in-phase, as well as in the other two directions (the *b*- and *c*-directions).

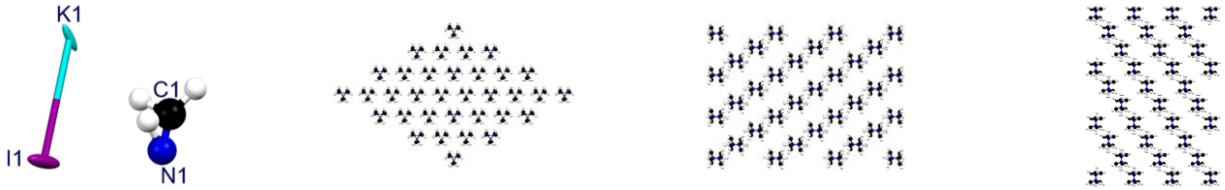

(a) **(b)** **(c)** **(d)**

Figure 4.22 (a) The asymmetric unit of **D-KI$_3$**. The packing of the dabconium dication in the structure **D-KI$_3$** as viewed down the **(b)** *c*-direction, **(c)** *b*-direction and **(d)** *a*-direction.

The chiral nature of the structure may be seen from the presence of right-handed helixes, Figure 4.23 (a) and (b), in the organic and inorganic packing of the structure **D-KI$_3$**.

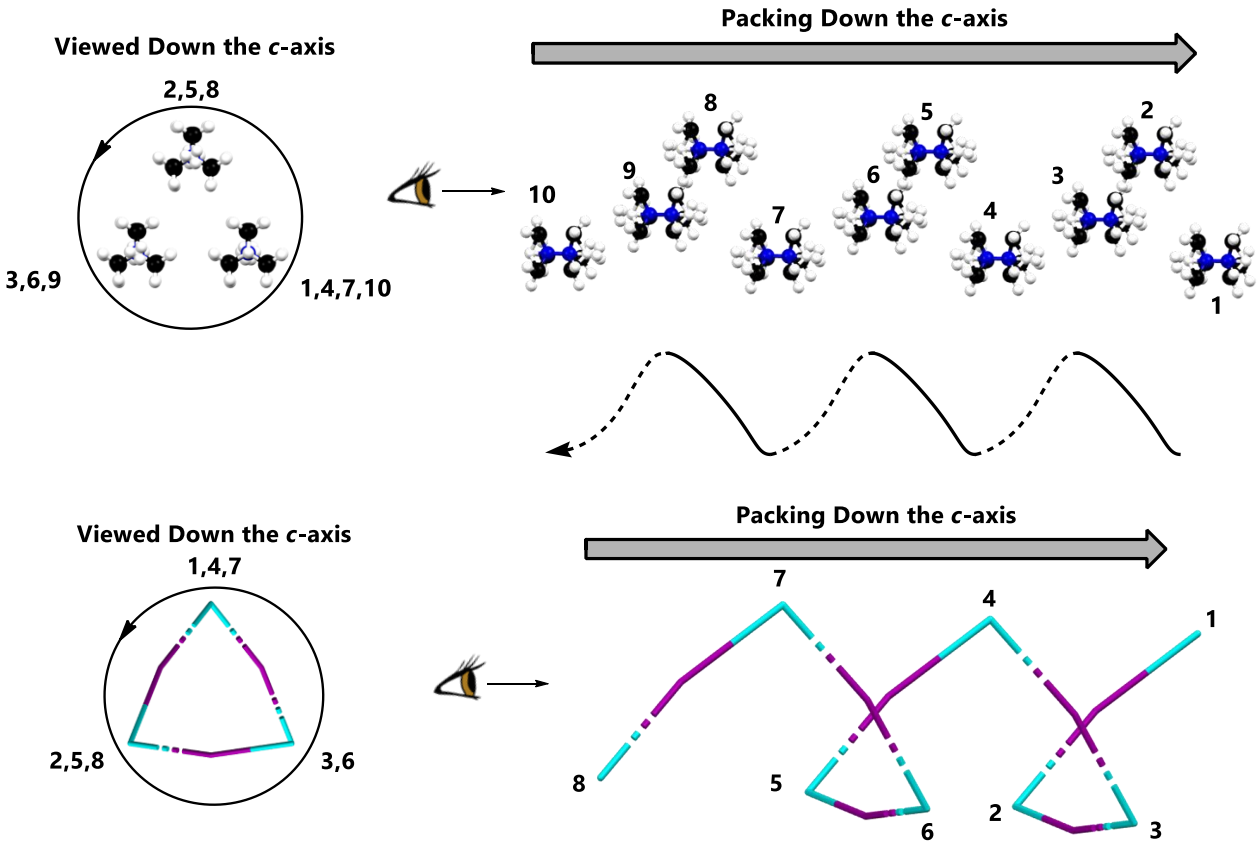

Figure 4.23 The presence of the right-handed helix in the structure **D-KI$_3$** as illustrated in **(a)** the dication packing and **(b)** the packing of the inorganic framework. Dashed and thick lines in the helix illustrate the differences in depth.

In the structure, each dabconium cation packs in a cavity or "box" formed by the inorganic framework, as illustrated in Figure 4.24 (a). In this cage, each dabconium dication participates in two trifurcated, charge assisted hydrogen bonds of the type N–H$^+$···$^-$I–K. These interactions have one length of 3.71(10) Å. Moreover, several bifurcated and single weak hydrogen bonding interactions are also present, as shown in Figure 4.24 (b).

Figure 4.24 KI-cages in the structure **D-KI$_3$** showing **(a)** two charge assisted hydrogen bonding interactions in light blue and **(b)** all hydrogen bonding interactions between the KI-cage and dabconium (charge assisted interactions shown in light blue and weak hydrogen bonding interactions shown in pink).

To allow for the formation of strong N–H$^+$···$^-$I–K hydrogen bonds, some of the iodide hydrogen bonding acceptor ions forming the cage are displaced towards the donor N–H$^+$ groups, resulting in a deviation of the I–K–I bonds from linearity,

and a distortion of the inorganic framework. In total, there are four unique I–K–I angles, as listed in Table 4.5. This concludes the structural analysis of **D-KI$_3$**. The following section will describe the structural features of the structure **D-CsCl$_3$**.

Structural Discussion of **D-CsCl$_3$**

The structure **D-CsCl$_3$** was previously determined at 120 K and reported by Paton *et al.*,[36] however, the structure described here was re-determined at a slightly higher temperature (150 K) in the current study, and the same structure as reported in the literature was obtained. This structure is classified as a 3D monoclinic perovskite since it contains the typical corner-sharing $CsCl_6$ octahedra with the dabconium dication in a 12-coordinate position.

Furthermore, the structure crystallises in the monoclinic phase with the space group *C*2/*c*. Most notably upon first examination is the unusually large unit cell, with a volume of 9536.4(12) Å^3. The asymmetric unit (shown in Figure 4.25 (a)) contains five crystallographically independent caesium ions (three on general positions), twelve chloride ions, along with four unique dabconium dications. To illustrate what has been described here, consider the unit cell as viewed down the three crystallographic directions as shown in Figure 4.25 (b), (c) and (d), further emphasising the complex structure. In addition, according to the notation developed by Glazer, the structure **D-CsCl$_3$** belongs to the $a^+b^+c^-$ tilt system.

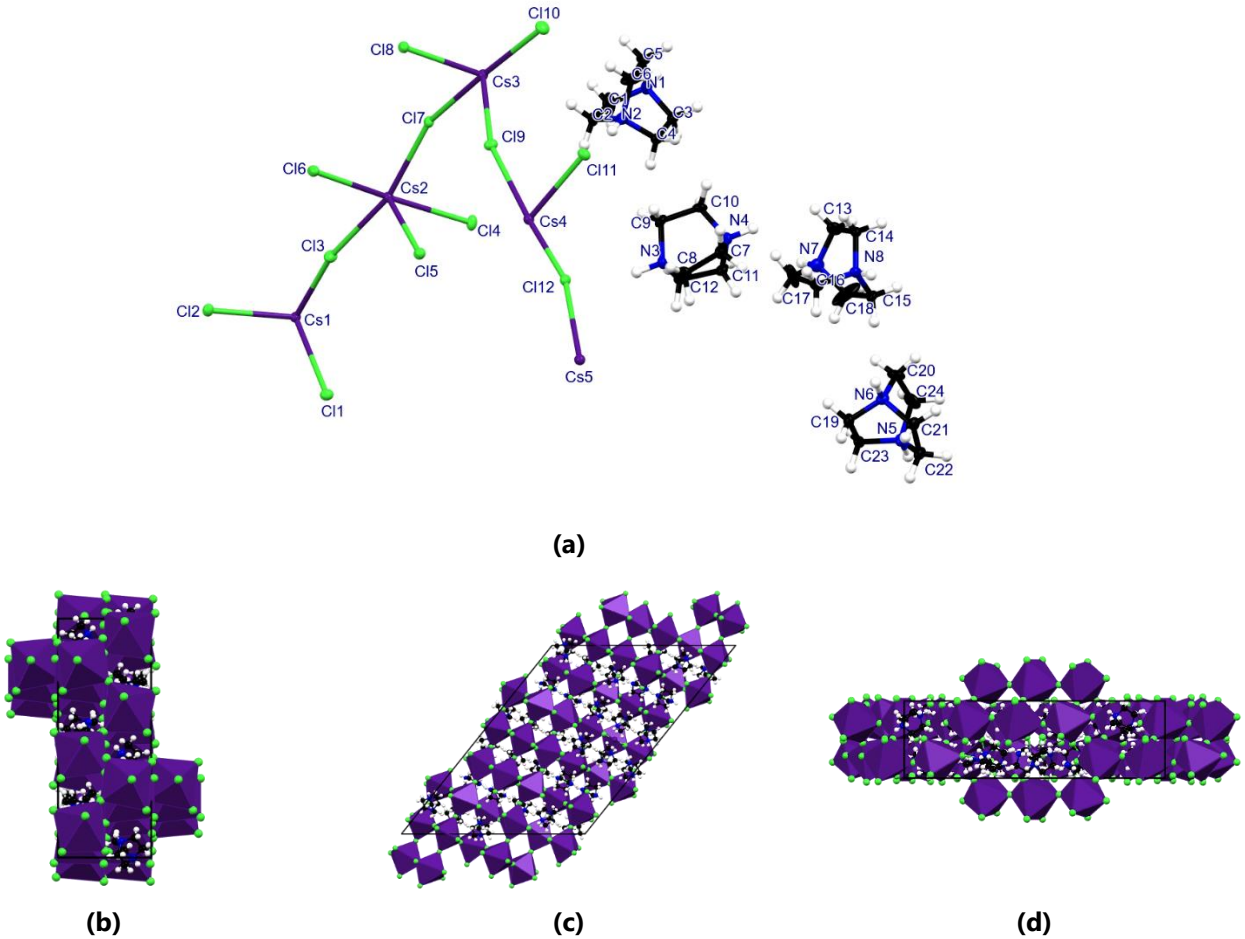

Figure 4.25 (a) The asymmetric unit of structure **D-CsCl$_3$**. The unit cell (shown in black) of **D-CsCl$_3$** as viewed down the **(b)** *a*-direction, **(c)** *b*-direction and **(d)** the *c*-direction.

The major differences between the structure reported by Paton *et al.*[36] and the one reported here are the values of the *c*-cell length and the β-angle. In the literature structure, determined at 120 K, the *c*-axis length is reported as 31.2121(4) Å, whereas the structure determined at 150 K in this study has a *c*-axis length of 32.6647(13) Å. This indicates contraction of the structure along the *c*-direction on cooling. Furthermore, the β-angle in Paton's structure is 128.4835(9)° versus the β-angle of

131.638(7)° reported here. Despite these differences, the same structural features are observed, and the structures can be considered to be the same. Moreover, the differences are ascribed to the two different temperatures at which the structures were determined (120 K versus 150 K), which illustrate that the structure most significantly expands or compresses in the *c*-direction upon heating or cooling since the *a* and *b* unit cell dimensions do not differ significantly between the two temperatures.

In the space group, five glide planes, in the *ac*-plane, equally spaced in the unit cell down the *b*-direction, combines with several inversion centres, five two-fold rotational axes down the *b*-direction and five two-fold screw axes directed in the *b*-direction. Repetition of the asymmetric unit gives the 3D perovskite structure, comprising an inorganic framework consisting of cages or cavities that contain the organic dabconium cations.

In addition, since the structure consists of five distinguishable caesium ions, five different octahedra are present in the structure, shown in Figure 4.26 (a) through (e). Of these, on average, the least distorted octahedron is that containing Cs1 as central ion, with the next least distorted being the octahedron of ion Cs5, while the octahedra surrounding ions Cs2, Cs3 and Cs4 are all equally distorted. The number of unique X–B–X angles found in the octahedra is used as a measure of the distortion. For example, for the octahedron $Cs1Cl_6$, there are seven unique angles, and for $Cs5Cl_6$, there are nine, whereas for $Cs2Cl_6$, $Cs3Cl_6$ and $Cs4Cl_6$, there are 15 unique angles, as listed in Table 4.5. As a result of the different Cs–Cl bond lengths, Cl–Cs–Cl angles and Cs–Cl–Cs angles, as listed in Table 4.5, four unique inorganic cages are formed in the structure, each containing one of the crystallographically independent cations, as illustrated in Figure 4.27.

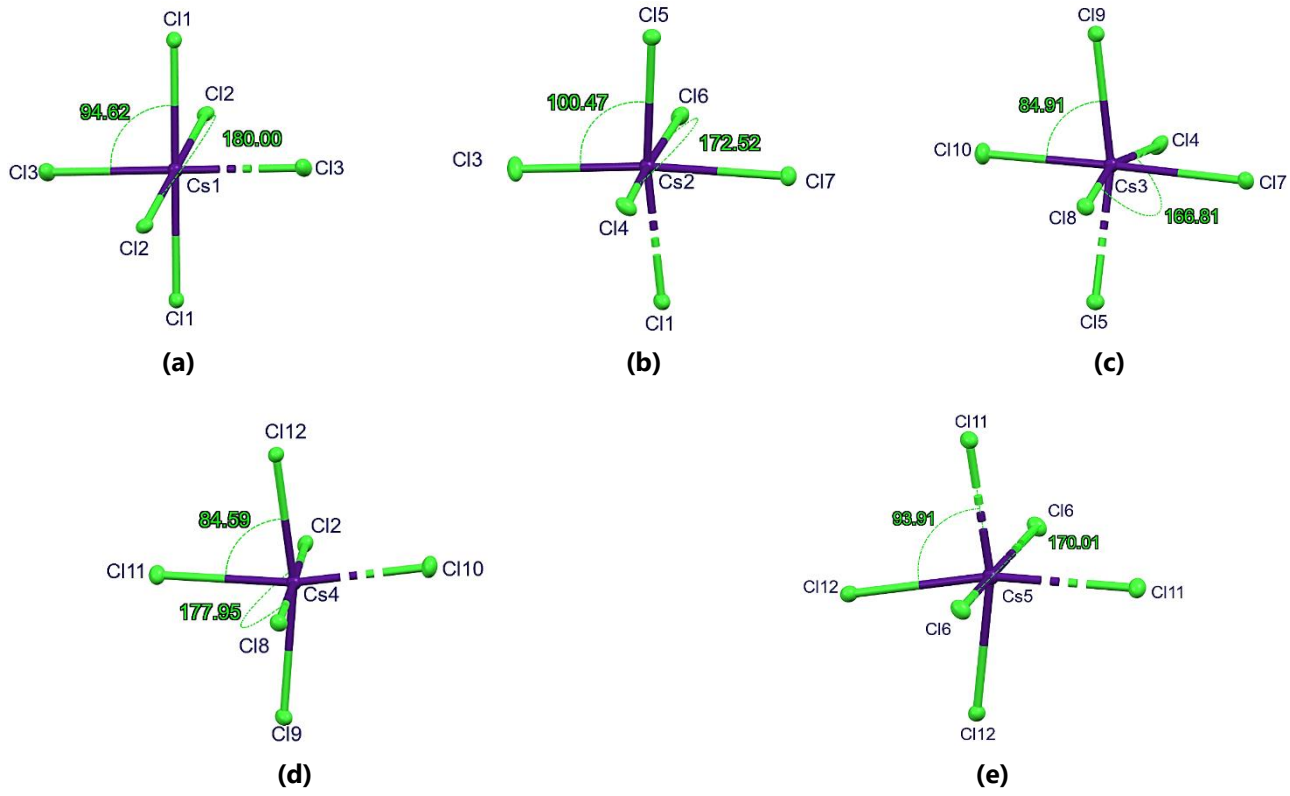

Figure 4.26 The five types of octahedra present in the structure **D-$CsCl_3$**. The octahedra **(a)** $Cs1Cl_6$, **(b)** $Cs2Cl_6$, **(c)** $Cs3Cl_6$, **(d)** $Cs4Cl_6$ and **(e)** $Cs5Cl_6$. Note that measured angles have units of degrees.

Furthermore, each of the four unique dabconium dications forms two charge assisted hydrogen bonding interactions of the type N–$H^+\cdots^-$Cl–Cs, so that eight of the twelve chloride ions are involved in these interactions, as shown in Figure 4.27 (a) and (b). The charge-assisted interactions' lengths range between D···A values of 3.0036(18) Å to 3.021(17) Å, with each interaction having a unique length. Hydrogen bonding parameters are listed in Table 4.5. Weak C–H$\cdots^-$Cl–Cs hydrogen bonds are also present in the structure, as shown in Figure 4.27 (b).

In the four types of cages, the bridging chloride ions involved in hydrogen bonding are displaced towards the N–H$^+$ group of the cation hydrogen bonded to it, resulting in non-linear Cs–Cl–Cs angles, and distortion of the cage and the inorganic framework, as illustrated in Figure 4.27 . In this structure these angles range from 155.26(15)° to 167.730(17)°. The units shown in Figure 4.27 (a) and (b) may be used to build the infinite crystal structure.

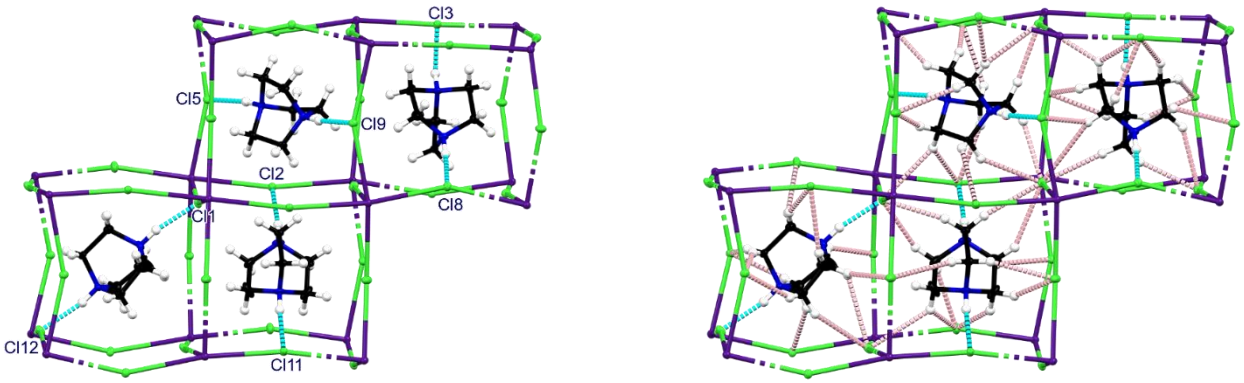

(a) **(b)**

Figure 4.27 The four unique **CsCl** cages that contain the four crystallographically independent dabconium dications in the structure **D-CsCl$_3$**. **(a)** Charge-assisted hydrogen bonding interactions are shown in light blue and (b) charge assisted and weak hydrogen bonding interactions are shown in light blue and pink, respectively.

The final single halide 3D perovskite structure that was obtained in this study is **D-CsBr$_3$** and will be discussed in the final section of this group of structures.

Structural Discussion of **D-CsBr$_3$**

The structure **D-CsBr$_3$** is a 3D perovskite that crystallises in the orthorhombic space group *Pbcn*. The orthorhombic unit cell is shown in Figure 4.28 (a), (b) and (c) as viewed down the *a*-, *b*- and *c*-directions, respectively.

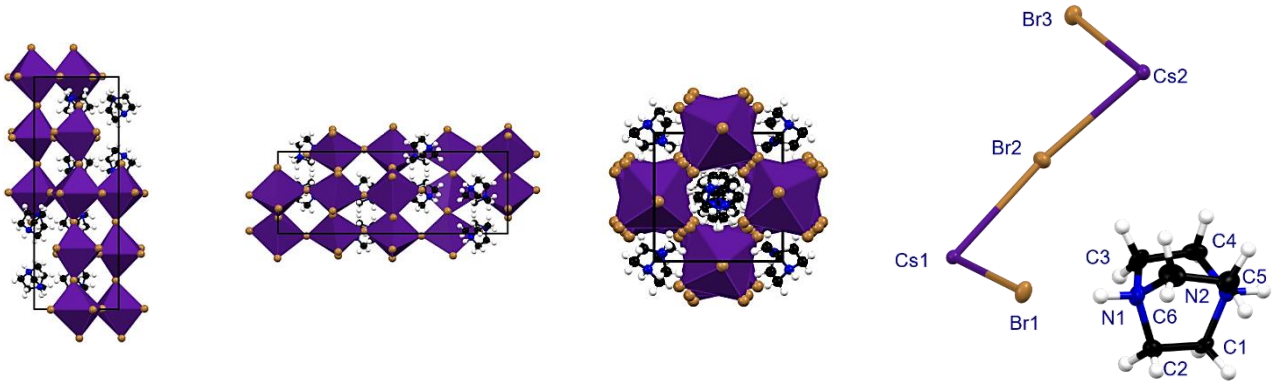

(a) **(b)** **(c)** **(d)**

Figure 4.28 The unit cell (shown in black) of **D-CsBr$_3$** as viewed down the **(a)** *a*-direction, **(b)** *b*-direction and **(c)** *c*-direction. The asymmetric unit of **D-CsBr$_3$** is shown in Figure **(d)**.

The asymmetric unit of the structure **D-CsBr$_3$** (shown in Figure 4.28 (d)) consists of a Br3–Cs2–Br2–Cs1–Br1 moiety and a complete dabconium dication. Four two-fold screw axes in the *c*-direction, six two-fold screw axes in the *a*-direction and six two-fold rotational axes in the *b*-direction in the unit cell led to the formation of 3/8's of the unit cell's constituents. Furthermore, two glide planes in the *a*-direction, three in the *b*-direction and two in the *c*-direction are responsible for another 3/8's of the unit cell. Finally, an inversion centre generates the unit cell's final 2/8th's (or 1/4). These symmetry operators will later be referred to when describing certain structural features. Repetition of the asymmetric unit results in a 3D perovskite structure, with dabconium cations filling cavities formed by the inorganic framework.

In addition, the $CsBr_6$ octahedral tilts (as defined by Glazer's notation[45,46]) belong to the $a^+b^+c^-$ tilt system since the octahedra are tilted in-phase in the *a*- and *b*-directions and out-of-phase in the *c*-direction. Thus, the *c*-direction tilts may initially appear as four distinctly different tilts, however, this is due to two crystallographically different BX_6 octahedra that are present in the inorganic framework, as will be discussed next.

As noted from the asymmetric unit, two crystallographically independent metal ions (Cs1 and Cs2) are present in the structure, along with three different bromide ions (Br1, Br2 and Br3). This leads to a total of six distinct metal–halide (B–X) bond lengths, as listed in Table 4.5. The two different types of octahedra alternate in the BX-framework in the *c*-direction, essentially forming sheets of either $Cs1Br_6$ or $Cs2Br_6$ octahedra. These alternating sheets are shown in Figure 4.29 (a) and (b), illustrating that in the *ab*-plane, "pure" sheets of either $Cs1Br_6$ or $Cs2Br_6$ octahedra occur, whereas the sheets alternate down the *c*-direction. The Cs1-octahedra consist of only Cs1-, Br1- and Br2-ions, whereas the Cs2-octahedra consist of only Cs2-, Br2- and Br3-ions. In the case of the Cs1-octahedra, the Cs1–Br1 bonds have one of two lengths, either 3.5032(6) Å or 3.5009(6) Å and the Cs1–Br2 bonds have one length of 3.4573(5) Å.

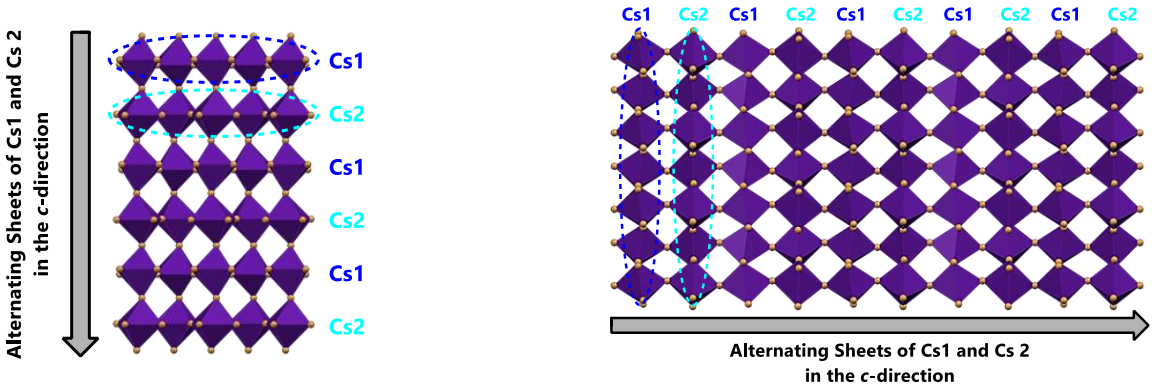

(a) **(b)**

Figure 4.29 The inorganic framework of **D-CsBr₃** as viewed down the **(a)** *a*-direction and **(b)** *b*-direction illustrating the different BX_6 sheets present in the structure.

Similarly, in the Cs2-octahedra, the Cs2–Br2 bonds have one length of 3.4378(5) Å, and the Cs2–Br3 bonds have two lengths, 3.5497(6) Å or 3.5610(6) Å. Structurally this implies the alternation of the two types of octahedral sheets explained earlier. Note that there is only one bridging halide between the two different metal ions (and hence all the sheets), which is Br2. Therefore, all the B–X–B angles must either be Cs1–Br1–Cs1 (164.599(19)°), Cs2–Br3–Cs2 (154.906(18)°) or Cs1–Br2–Cs2 (165.78(2)°), corresponding to the three B–X–B angles measured in the structure. Upon further consideration, it can be seen from the different values of the Br–Cs–Br angles of the Cs1- and Cs2-octahedra that the Cs2-octahedra are significantly less distorted than the Cs1-octahedra, as can be seen in Figure 4.30 (a) and (b).

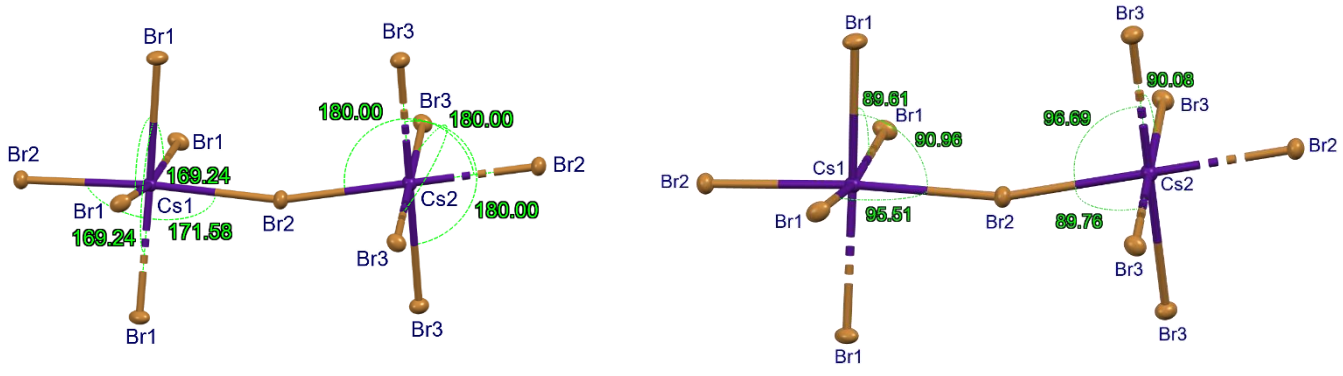

(a) **(b)**

Figure 4.30 Selected X–B–X angles of the two types of octahedra present in the structure **D-CsBr₃**, **(a)** for axially related X–B–X and **(b)** for equatorially related X–B–X angles. Not all angles are shown here, for a complete list, consult Table 4.5. The values of the measured angles are given in units of degrees.

The Br–Cs–Br angles in the Cs2-octahedra are, on average, closer to the ideal values of 90° and 180° of a perfect octahedron, compared to the Cs1-octahedra. This is further confirmed by the data listed in Table 4.5.

Moving on from the inorganic framework and onto the organic sublattice, the packing of the dabconium dications in the **D-CsBr$_3$** structure will be considered. Firstly, viewed down the *a*-direction, the packing of the dabconium dication along the *b*-direction shows alternating orientations for each adjacent dication and four repeated different orientations along the *c*-direction. In a similar vein, as viewed down the *b*-direction, the cations are seen to have alternating orientations along the *a*-direction and four repeating orientations along the *c*-direction. The packing described here is further illustrated in Figure 4.31 (a) and (b).

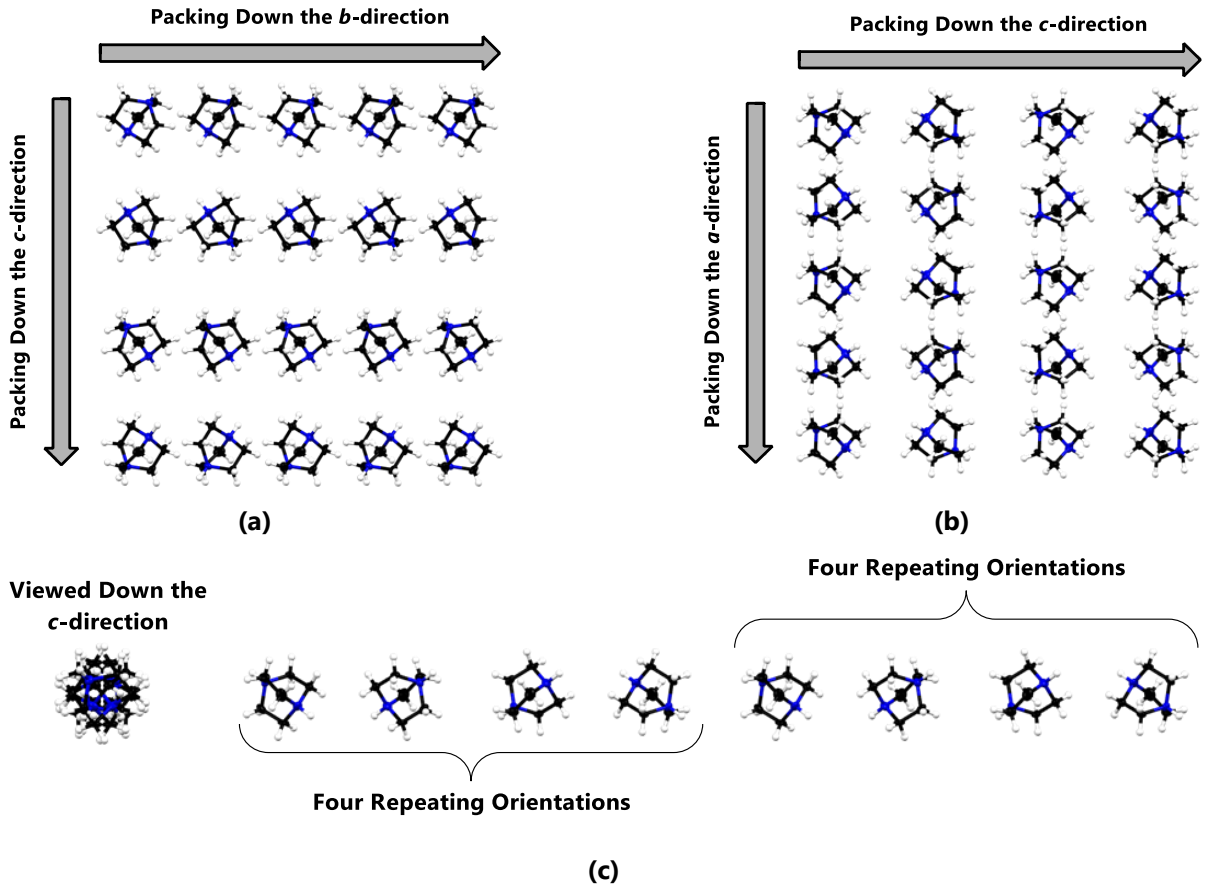

Figure 4.31 The packing of the dabconium dications in the structure **D-CsBr$_3$** as viewed down the **(a)** *a*-direction, **(b)** *b*-direction and **(c)** the packing of the dabconium dication down the *c*-direction.

To better illustrate the packing of the dabconium dication along the *c*-direction, Figure 4.31 (c) shows the packing of a single row of dabconium dications viewed down the *c*-direction and the view of this row of cations along the *b*-direction. This leads to the next feature of the structure **D-CsBr$_3$**, namely, its hydrogen bonding network.

Only two strong charge assisted N–H$^+$···$^-$Br–Cs hydrogen bonds are present for each dabconium dication in the structure **D-CsBr$_3$**. The specific hydrogen bonds are N–H$^+$···$^-$Br1–Cs1 (3.224(5) Å) and N–H$^+$···$^-$Br3–Cs2 (3.194(4) Å). Four different CsBr-cages (see Figure 4.32), each containing one dabconium dication, are present in the structure, and this combination account for all the structural features. Figure 4.32 (a) illustrates only the strong charge assisted hydrogen bonds, whereas Figure 4.32 (b) illustrates the entire hydrogen bonding network, including the weak hydrogen bonds C–H···$^-$Br–Cs, in which the ions Br1, Br2 and Br3 all participate. Moreover, each dabconium dication participates in two bifurcated C–H···$^-$Br–Cs hydrogen bonding interactions, whereas all the charge assisted interactions are only to a single acceptor ion. The B–X–B angles of ions that participate in the N–H$^+$···$^-$Br1–Cs1 hydrogen bonds are significantly more distorted (as described earlier) than those which participate in the N–H$^+$···$^-$Br3–Cs2 hydrogen bonds.

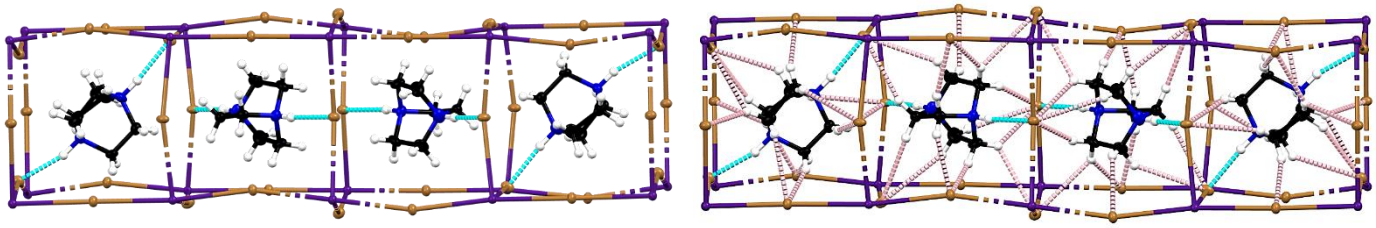

(a) **(b)**

Figure 4.32 The four CsBr-cages present in the structure **D-CsBr$_3$** with **(a)** only charge assisted hydrogen bonds indicated in light blue and **(b)** charge and weak hydrogen bonds indicated in light blue and pink, respectively.

This concludes the single halide 3D perovskite section, and now the discussion will shift to the mixed halide 3D perovskite obtained in this study.

4.4.2 Mixed Halide 3D Perovskite

This section discusses a dabconium-containing 3D perovskite structure containing more than one type of halide ion. In mixed halide systems, one organic cation (A) and one metal ion (B) are used with a combination of two or more halide ions (namely Cl^- and Br^-, Cl^- and I^- or Br^- and I^- or a combination of all three). In this study, only one such structure was obtained from the combination of dabconium, caesium, chloride, and iodide. This combination produced a mixed halide 3D perovskite structure, referred to as **D-CsCl$_2$I**, which is discussed next.

Structural Discussion of **D-CsCl$_2$I**

A 3D perovskite structure was obtained through the combination of CsI, 1,4-diazabicyclo[2.2.2]octane and HCl. The structure obtained is a mixed halide structure and will be denoted **D-CsCl$_2$I**, with the ratio of chloride to iodide ions in the structure equal to 2:1. The polyhedral view of the structure down each of the crystallographic axes is shown in Figure 4.33 (a), (b) and (c), respectively. Selected structural parameters are listed in Table 4.4, and geometric parameters are listed in Table 4.5. In addition, structure **D-CsCl$_2$I** did not exhibit a solid-state phase transition on cooling from RT to LT (as confirmed by PXRD analysis). Hence, the RT and LT structures are the same, with minor changes associated with the contraction of the structure due to cooling. A general discussion on the crystal structure determined at 150 K is given.

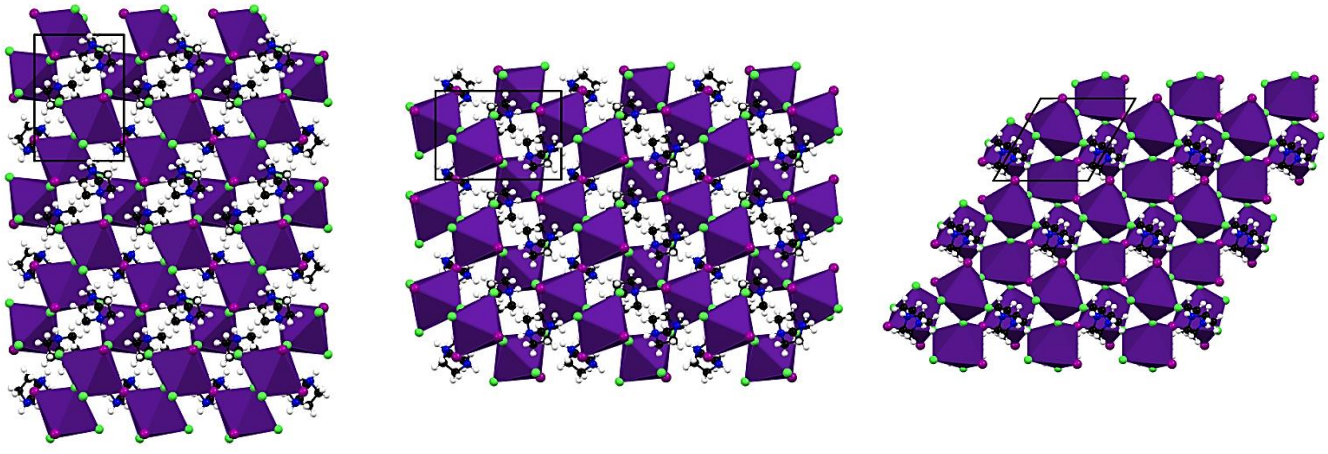

(a) **(b)** **(c)**

Figure 4.33 The 3×3 packing view of the structure **D-CsCl$_2$I** as viewed down the **(a)** *a*-direction, **(b)** *b*-direction and **(c)** *c*-direction. The unit cell is drawn in black.

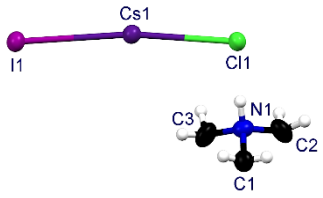

Figure 4.34 The asymmetric unit of the mixed halide structure **D-$CsCl_2I$**.

Structure **D-$CsCl_2I$** crystallises in the chiral trigonal space group $P3_121$, which contains a right-handed three-fold screw axis as symmetry element. The structures **D-KBr_3(2)**,[38] **D-$RbCl_3$(1)**[36] and **D-$RbBr_3$(1)**[37], crystallising in the enantiomorphic space groups $P3_121$ or $P3_221$ are related to structure **D-$CsCl_2I$**, but not isostructural to it. In Figure 4.34, the asymmetric unit of structure **D-$CsCl_2I$** is shown. This asymmetric unit consists of half a dabconium dication (an $NH(CH_2)(CH_2)(CH_2)$ moiety) and a Cl–Cs–I moiety. The complete structure is generated *via* three different types of symmetry operations. A two-fold rotation axis completes the dabconium dication and the combination of a two-fold rotation axis and a three-fold screw axis generates the B–X framework from the Cl–Cs–I moiety and subsequently also leads to three differently orientated dabconium dications in the structure, as discussed later.

In the structure, a 3D perovskite inorganic framework, comprised of Cs^+-, Cl^-- and I^--ions, is formed, with the ratio of Cl^-- to I^--ions equal to 2:1. The dabconium cations pack in cavities created by the inorganic framework. The chirality of the structure is evident in both the packing of the cations and the inorganic framework. The cations pack to form a right-handed helix around the three-fold screw axis, as illustrated in Figure 4.35 (a), and portions of the inorganic framework forms right-handed helices, with one type of helix comprised of Cs^+-ions and Cl^--ions and the other of Cs^+-ions and I^--ions, as illustrated in Figure 4.35 (b) and (c), respectively.

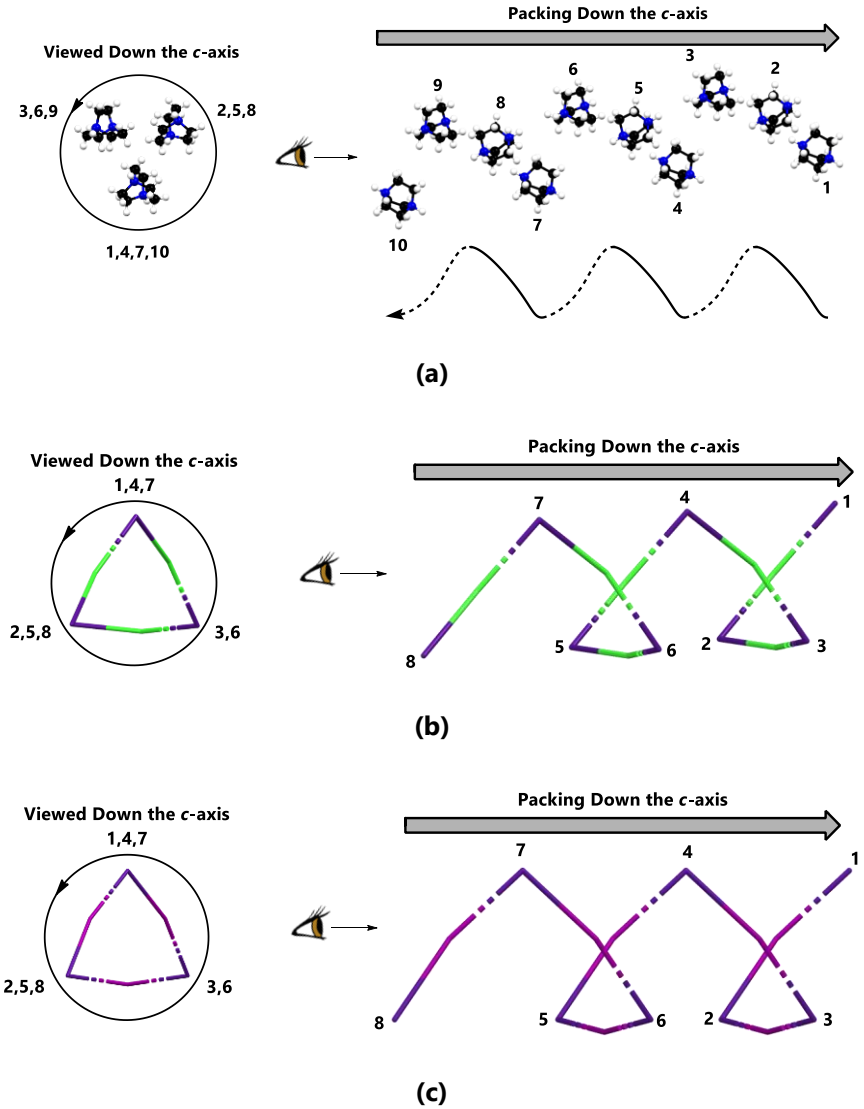

Figure 4.35 The right-handed helixes present in the structure **D-$CsCl_2I$**. **(a)** The helix comprised of the dabconium dications, **(b)** the helix comprised of Cs^+-ions and Cl^--ions and **(c)** the helix comprised of Cs^+-ions and I^--ions. Dashed and thick lines in the helix illustrate the differences in depth.

Considering the inorganic framework, the framework as viewed down the *a*-, *b*- and *c*-directions (Figure 4.36 (a), (b) and (c)) does not clearly show how the 3D perovskite cages come to be. Rather, the three inorganic sheets comprised of Cs^+-, Cl^-- and I^--ions that lie parallel to the $(30\bar{3})$, (033) and $(1\bar{1}1)$ Miller planes, as illustrated in Figure 4.36 (d), (e) and (f), respectively, combine to form the framework, and the sheets are all exactly the same. Hence, they pack roughly perpendicular to each other to form the 3D inorganic framework. Also, since the spacing between adjacent sheets for two of the sheets is a third of the spacing between the third sheet type, the resultant box is rectangular, and not cubic as expected in the ideal perovskite structure.

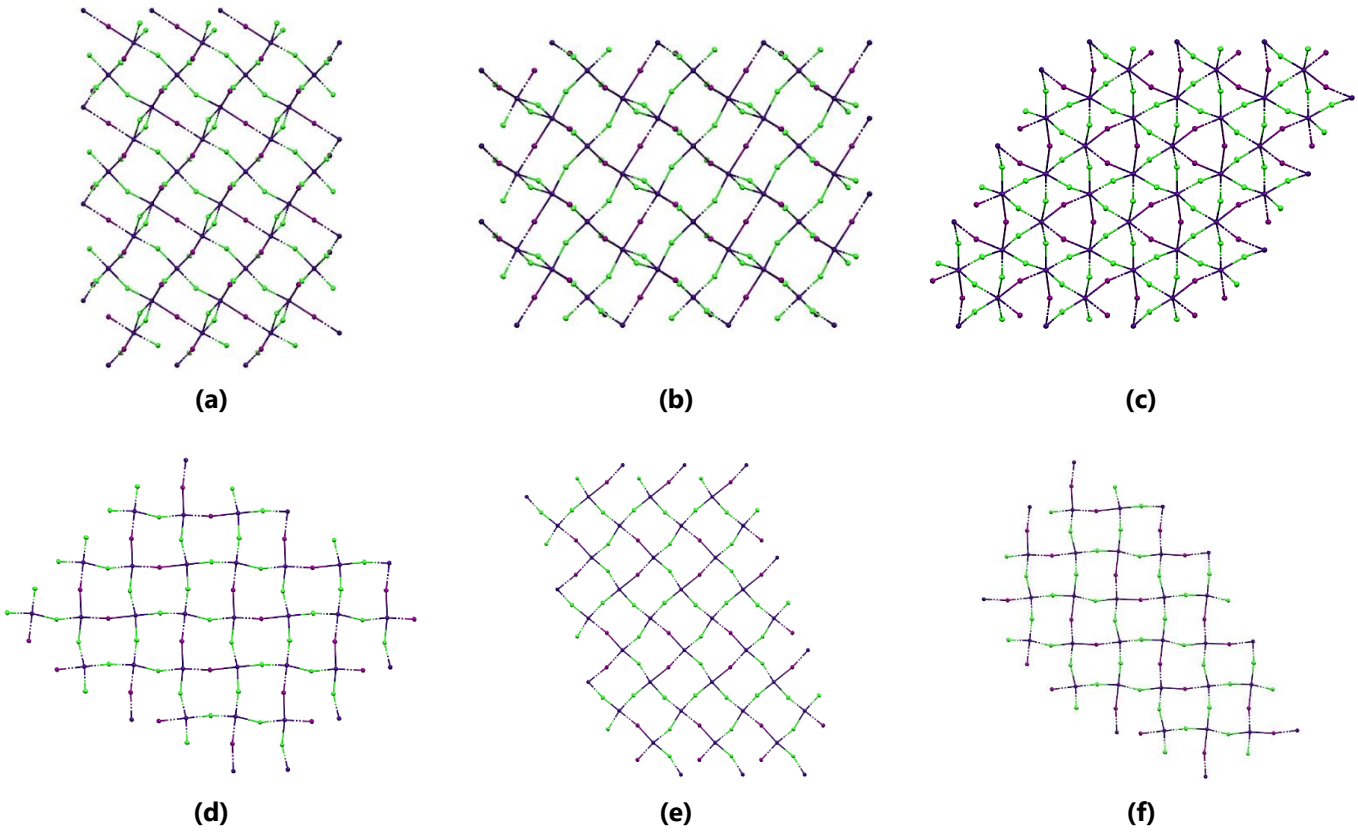

Figure 4.36 The inorganic framework packing as viewed in **(a)** the *a*-direction, **(b)** the *b*-direction and **(c)** the *c*-direction. Inorganic sheets of the structure **D-CsCl$_2$I** parallel to **(d)** the $(30\bar{3})$, **(e)** the (033) and **(f)** the $(1\bar{1}1)$ Miller planes. All sheets are viewed perpendicular to their Miller plane.

The crystal structure of structure **D-CsCl$_2$I** can be viewed as the repeat of dabconium dications occupying the body centre position of an inorganic cage consisting of Cs^+-, Cl^-- and I^--ions (BX_{12} framework), as shown in Figure 4.37. At first glance, Figure 4.37 seems to show three different types of inorganic "boxes" corresponding to the three different orientations of organic dication, however, the ions comprising the boxes, and dimensions of each of the boxes (the bond lengths, angles etc.) are the same, hence only one type of "box" is present, but the boxes are orientated differently relative to each other. Therefore, three distinct orientations of BX_{12} boxes are observed. Each box consists of four Cs^+-ions, one on each corner, eight bridging chloride ions and four bridging iodide ions.

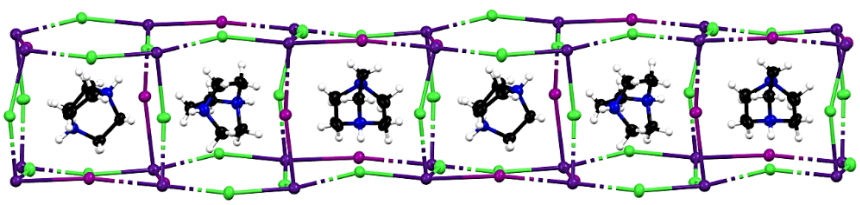

Figure 4.37 A view showing the dabconium dication occupying the body-centre position of the BX_{12} framework, with six subsequent cages shown.

Each dication forms two strong, charge assisted N–H^{+}···$^{-}$Cl–Cs hydrogen bonds to two different chloride ligands, diagonally across the "box", as illustrated in Figure 4.38 (a), with hydrogen bonding parameters listed in Table 4.5. Only bridging chloride ligands act as hydrogen bond acceptors, with no bridging iodide ligands involved in hydrogen bonding. This can be ascribed to the higher electronegativity of the chloride ion compared to the iodide anion, which means that N–H^{+}···$^{-}$Cl–Cs hydrogen bonds are stronger than N–H^{+}···$^{-}$I–Cs hydrogen bonds. Thus, in this structure the strongest type of hydrogen bond is preferred.

As a result of the formation of the hydrogen bond, the Cs–Cl–Cs angle involving the acceptor chloride ion deviates from 180°, with a value of 159.91(3)°, resulting in the chloride ion being displaced towards the N–H^{+} hydrogen bonding group, as can be seen in Figure 4.38 (a). This means that the hydrogen bonding interactions distort the metal halide framework since this specific angle deviates from linearity and differs from the mean Cs–X–Cs angle of 163.006(3)°. The Cs–I–Cs angle is closer to 180°, with a value of 161.102(3)° since the bridging iodide ion is not involved in hydrogen bonding. In addition, weak C–H···$^{-}$X–Cs hydrogen bonds are also present in the structure, as illustrated in Figure 4.38 (b). Both the strong and weak hydrogen bonds anchor the cation in the inorganic box.

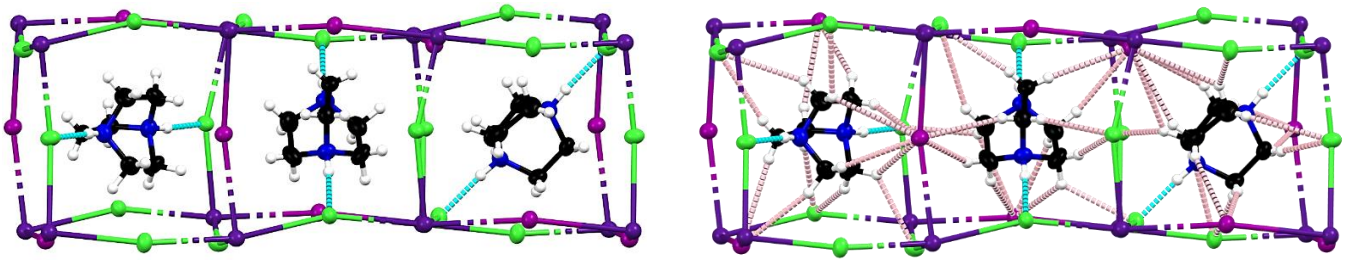

(a) **(b)**

Figure 4.38 (a) Illustration of the charge assisted N–H^{+}···$^{-}$Cl–Cs hydrogen bonds present in the structure **D-CsCl$_2$I** and **(b)** all observed hydrogen bonds (charge assisted and weak). Charge assisted hydrogen bonds are indicated with blue dotted lines and weak hydrogen bonds with pink dotted lines.

The question may now be asked why it was decided to prepare this specific mixed halide compound, and no other mixed halide compounds. The specific combination of Cs^{+}-, Cl^{-}- and I^{-}-ions was selected by applying the principles of crystal engineering, as such the structure **D-CsCl$_2$I** is an example of *crystal engineering*. When considering the Dabconium-Caesium single halide structural family, the perovskite structural dimensionality is 3D for the structures **D-CsCl$_3$** and **D-CsBr$_3$**, however, for **D-CsI$_3$**, a 1D ABX$_3$-type perovskite structure is observed, which means that the change from the bromide to the iodide analogue represents a tipping point in terms of structural dimensionality in this family. The question was asked if a 3D perovskite structure containing iodide ions could be prepared, though the inclusion of other halide ions. By the addition of chloride ions to the components used to prepare the 1D ABX$_3$-type perovskite **D-CsI$_3$**, the structural dimensionality of the compound obtained, structure **D-CsCl$_2$I,** changed to 3D as shown in Scheme 4.2. This means that a degree of control over structural dimensionality may be achieved by mixing halide ions and through selection of the correct combination of halide ions.

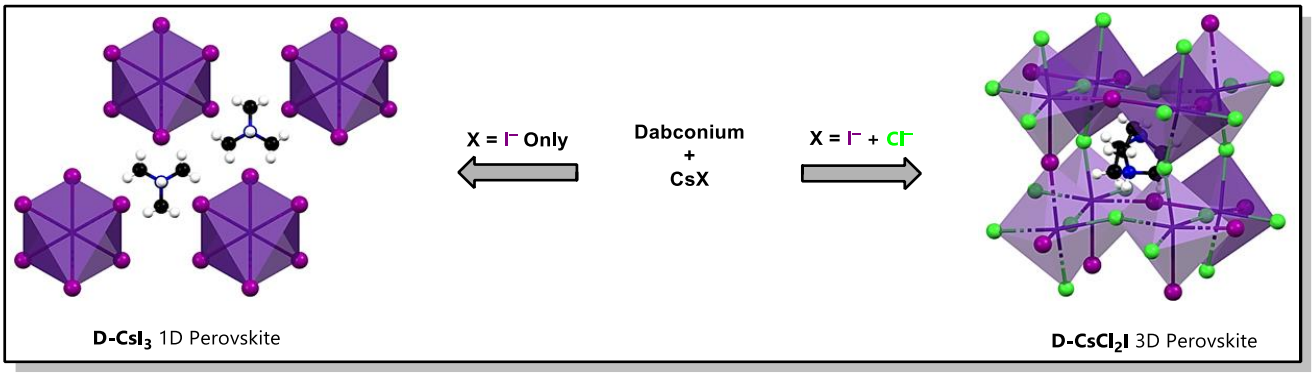

Scheme 4.2 Example of how the precursor mixture constituents govern the dimensionality of the perovskite structure from 1D to 3D, resulting in either the structure **D-CsI$_3$** or **D-CsCl$_2$I**.

This concludes the analysis of the structural features of the 3D perovskite family. Next, a comparison of the structures described here and in the literature is given.

4.5 Structural Comparison and Discussion

This section will endeavour to compare the dabconium containing alkali metal halide perovskite structures studied here, including the rubidium containing literature structures. The structural information and data used are listed in Table 4.2 through Table 4.5. Two important aspects should be noted. The first being that the structures **D-RbBr$_3$(1)**[37] and **D-RbI$_3$**[37] reported in the literature were determined at room temperature and are compared here to low-temperature (150 K) structures. Furthermore, the literature structure **D-RbCl$_3$**[36] was determined at 120 K, and will be included in the structural comparison.

The structural comparison is divided into three sections. The first two sections consider the 1D ABX_3-type and 3D perovskite structures respectively. In the final section, comparisons over the entire family of dabconium containing alkali metal halide perovskites, thus 1D and 3D, are made.

4.5.1 Comparison of 1D ABX_3-type Perovskite Structures

The fact that several structures containing the same organic dication but a range of metal and halide ions crystallise as 1D ABX_3-type perovskite structures allow for the identification of structural trends in this family of compounds. Firstly, the distortion of the octahedron in the 1D polymer will be considered. The distortion in an octahedron (MX_6) can be calculated using different parameters, including B–X bond lengths, B–X–B angles or B···B distances, and then evaluating their range (spread of the values) as shown in Equation (4.4)

$$\Delta P = \frac{1}{N}\sum_{n=1}^{N}\left[\frac{P_n - P_{\text{avg}}}{P_{\text{avg}}}\right]^2 \tag{4.4}$$

where P_{avg} is the average parameter value and P_n indicates the individual parameter values. The calculated value ΔP indicates the spread in the values, hence if $\Delta P = 0$, then there is no spread in the P_n values.

In Table 4.6, the spread of the structural parameters B–X (Δd), B···B (ΔB···B) and B–X–B (ΔB–X–B) are listed with the sum of the ionic radii of the B- and X-constituents of the different 1D ABX_3-type perovskite structures. The distortion of the octahedra of the low-temperature structures is discussed here. However, since no phase transitions were observed between the low-temperature (150 K) and room temperature powder patterns, the same trends should hold for the structures at room temperature. In the last two columns of Table 4.6, the terms "Equatorial" and "Axial" are used. These terms do not refer to the traditional axial and equatorial positions. Instead, the term "equatorial angles" refers to angles that are approximately 90° and "axial angles" refers to angles close to 180°, since the assignment of axial and equatorial ligands in the octahedra would be arbitrary. The so-called "Average Spread" parameter is defined as the average value of the five different individual spread values.

Two types of octahedra are present in the structures isostructural to **D-NaCl$_3$** (see Figure 4.10 (a) and (b)), with the noticeable trend, from consideration of the X–B–X angles of both sets of octahedra (listed in Table 4.2), that the octahedra approach the ideal octahedral geometry with an increase in halide ion radius (Cl^- to Br^-) and increasing metal ion radius (Na^+ to K^+). This observed trend can be explained by looking at the B···B distances and B–X bond lengths. With an increase in halide ion size or metal ion size, the B···B distances and B–X bond lengths increase, allowing for a more symmetrical arrangement of the ions, allowing the octahedral in the 1D face-sharing polymer to tend towards the ideal conformation.

In terms of the B···B distances in the structure **D-NaCl$_3$** and its isostructural counterparts, the B1···B1 distances are shorter than the B1···B2 distances, and as the metal ion radius is increased (Na^+ to K^+), the B···B distances start to converge (i.e., the difference between them decreases). This allows for the octahedra of the two different metal ions to become similar in geometry and approach the ideal octahedral geometry.

A similar trend appears in the B–X bond lengths. Three different B–X bond lengths are found in each of the structures isostructural to **D-NaCl$_3$** and in **D-NaCl$_3$** itself. The B–X bond lengths increase with increasing halide ion radius (from Cl^- to Br^-) and increasing metal ion radius (Na^+ to K^+). Also, the difference between the three bond lengths for each structure becomes smaller as halide and metal ion radii are increased.

Table 4.6 Spread of structural parameters obtained for the 1D ABX_3-type dabconium-containing perovskite structures. The average spread refers to the average of the five calculated spread value's average.

Structure	B^++X^- Ionic Radii (pm)	Δ*d* (Å)	Δ(B···B) (Å)	Δ(B–X–B) (°)	Δ(X–B–X) (°)		Average Spread
					Equatorial	Axial	
D-NaCl$_3$	283	4.5×10^{-4}	4.0×10^{-4}	2.8×10^{-4}	2.8×10^{-3}	4.8×10^{-4}	8.7×10^{-4}
D-NaBr$_3$	298	3.7×10^{-4}	2.2×10^{-4}	1.7×10^{-4}	2.0×10^{-3}	3.9×10^{-4}	6.3×10^{-4}
D-KCl$_3$	319	2.6×10^{-4}	5.2×10^{-6}	1.39×10^{-6}	1.5×10^{-3}	4.2×10^{-4}	4.3×10^{-4}
D-KBr$_3$(1)	334	2.6×10^{-4}	1.9×10^{-6}	1.59×10^{-7}	1.2×10^{-3}	3.2×10^{-4}	3.5×10^{-4}
D-RbI$_3$	372	0	0	0	1.3×10^{-3}	0	2.7×10^{-4}
D-CsI$_3$	387	0	0	0	9.1×10^{-4}	0	1.8×10^{-4}

The values in Table 4.6 shows that with a combination of larger metal and halide ions (i.e., a larger sum of ionic radii), a smaller degree of distortion from the ideal octahedral geometry, or spread in the structural parameters, is observed. Meaning that the "average spread" listed in column eight grows smaller with increasing $B^+ + X^-$ ionic radii. This agrees with the fact that **D-CsI$_3$** crystallises in the ideal space group (hexagonal $P6_3/mmc$) for 1D ABX_3-type perovskites since it shows almost no variation in its structural parameters, bar one, and that the calculated average spread is small (1.8×10^{-4}).[47]

Furthermore, considering all the structures crystallising in the space group $R\bar{3}c$, the structures **D-NaCl$_3$**, **D-NaBr$_3$**, **D-KCl$_3$**, and **D-KBr$_3$(1)** show less distortion in their inorganic framework with the combination of larger metal and halide ions. In addition, the structures **D-RbI$_3$** and **D-CsI$_3$**, both containing larger metal ions and large iodide anions, are more symmetric than the other 1D ABX_3-type perovskite structures, also confirmed by their phases (trigonal versus hexagonal) and space groups ($R\bar{3}c$ versus $P\bar{6}2c$ versus $P6_3/mmc$). The space group $R\bar{3}c$, in which the structures **D-NaCl$_3$**, **D-NaBr$_3$**, **D-KCl$_3$** and **D-KBr$_3$(1)** crystallise, is of lower symmetry than space group $P\bar{6}2c$ in which structure **D-RbI$_3$** crystallises, which, in turn, is again of lower symmetry than space group $P6_3/mmc$, exhibited by structure **D-CsI$_3$**. Thus, the larger the metal and halide ion (indicated in column 2 of Table 4.6), the higher the symmetry of the 1D ABX_3-type perovskite structure formed. Moreover, the space group $P6_3/mmc$ is seen as the ideal and, therefore, the most symmetrical space group for 1D ABX_3-type perovskite structures,[47] meaning that structure **D-CsI$_3$** represents the ideal 1D ABX_3-type perovskite structure.

Continuing the comparison between the higher symmetry structures **D-RbI$_3$** and **D-CsI$_3$**, it is evident that only one axial bond angle is present in either structure. This angle has a value of 172.585(19)° in structure **D-RbI$_3$** and 180.0° in structure **D-CsI$_3$**, indicating an ideal geometry in the latter. Additionally, the distortion from the ideal octahedral geometry noted in Table 4.6 for the equatorial angles is less in the case of the structure **D-CsI$_3$** than for the structure **D-RbI$_3$**. These observations imply that the octahedra in structure **D-CsI$_3$** are less distorted and closer to the ideal octahedral arrangement than the octahedra in structure **D-RbI$_3$**, or in fact, any of the 1D ABX_3-type perovskite structures reported in this chapter.

The correlation between the average spread of the values and the sum of the ionic radii of the B- and X-ions listed in Table 4.6, may be plotted, as shown in Figure 4.39 (a) and (b). The cubed polynomial fit suggests that an x = 180 pm would result

in an average spread of zero. In contrast, the power fit suggests that a near-infinite summed ionic radii would lead to a perfectly symmetrical structure. Considering this with chemical knowledge, one soon realises that the combination of the ionic radii of Cs^+ and I^- is nearly as large a combination as chemically possible using elements on the Standard Elements of the Periodic Table, hence this is why **D-CsI$_3$** is most likely the closest to the ideal structure possible for the 1D ABX$_3$-type perovskite structures. This is unless one ventures into the Lanthanide and Actinide series, which has been done occasionally in the literature.

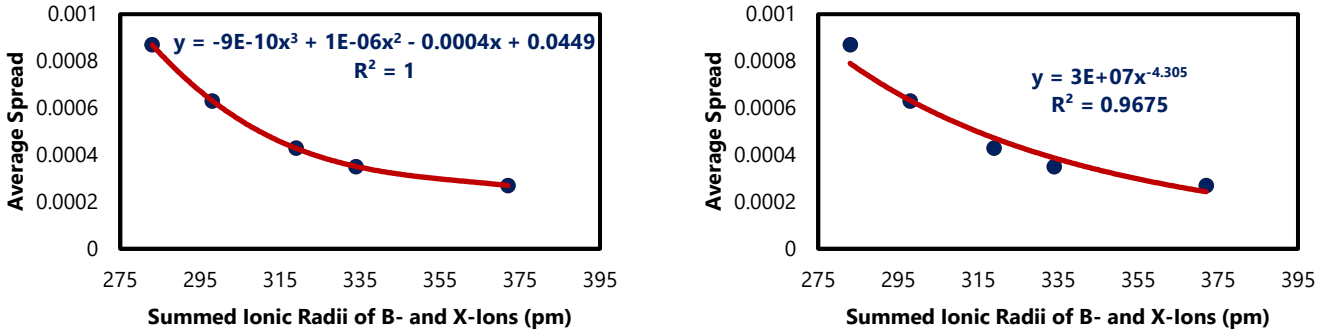

(a) **(b)**

Figure 4.39 Plots of the average spread listed in Table 4.6 for the 1D ABX$_3$-type perovskite structures against the sum of their B- and X-ions' ionic radii, with **(a)** a cubed polynomial fit and **(b)** a power fit.

This then concludes the comparison of the 1D ABX$_3$-type perovskite structures, and the focus will now shift to comparison of the 3D perovskite structures obtained in this study.

4.5.2 Comparison of 3D Perovskite Structures

Several 3D perovskite structures were obtained in this study for the combination of the dabconium dication and an alkali metal halide anion. They crystallise in a range of phases and space groups, making direct structural comparison difficult. However, the inorganic frameworks of the 3D structures will be compared using the same spread of values (calculated as per Equation (4.4)) as for the 1D ABX$_3$-type structures (see Section 4.5.1). To this end, consider Table 4.7, which lists the spread of the structural parameters of the 3D perovskites determined in the literature and this study. The parameters listed are as follows: B–X (Δd), B···B (ΔB···B) and B–X–B (ΔB–X–B) along with the crystal structure's phase and space group. In addition, the literature structures **D-RbCl$_3$(1)** and **D-RbBr$_3$(1)** are also included, though determined at different temperatures than the rest of the structures (120 K and 293 K, respectively).

The structure **D-NaI$_3$** possesses both face- and corner-sharing octahedra. Hence, a comparison of its B–X–B angles in the face- and corner-sharing octahedra would not give a *true* picture of its distortion and therefore is left as "N/A" in the table. Since most of the 3D perovskites crystallise in different phases and different space groups, they have different unit cell dimensions and are not isostructural, hence it is not possible to easily identify trends as was done for the 1D ABX$_3$-type perovskites.

That said, Table 4.7 shows one interesting overall trend: all the structures, though not comparable in a direct sense, have a similar average spread of values, all of the magnitude of approximately 10^{-3}. Furthermore, the spread in their parameters does not differ significantly, with an exception here and there. This shows that all these dabconium containing 3D perovskite structures are quite unsymmetric and possess significant distortions in their inorganic frameworks. Although, most notably, the structure **D-CsCl$_3$** is by far one of the more complex structures, its average spread and calculated parameter spread is comparable to most of the other "more symmetrical" structures. Moreover, the structures **D-RbBr$_3$(1)** and **D-CsCl$_3$** have the same summed ionic radii (348 pm) and average spread.

Table 4.7 Spread of structural parameters obtained for the 3D dabconium-containing perovskite structures. The average spread refers to the average of the five calculated spread value's average.

Structure	$B^+ + X^-$ Ionic Radii (pm)	Δ*d* (Å)	Δ(B–X–B) (°)	Δ(X–B–X) (°)		Average Spread	Phase	Space Group
				Equatorial	Axial			
D-NaI$_3$	322	5.8×10^{-4}	N/A	4.5×10^{-4}	1.4×10^{-4}	3.9×10^{-4}	Hexagonal	$P6_3/mmc$
D-KBr$_3$(2)	334	0	0	2.4×10^{-3}	0	6.1×10^{-4}	Trigonal	$P3_121$
D-KI$_3$	358	0	0	1.5×10^{-3}	0	3.7×10^{-4}	Trigonal	$R32$
D-RbCl$_3$(1)	333	1.5×10^{-5}	7.1×10^{-4}	6.2×10^{-3}	3.9×10^{-4}	1.8×10^{-3}	Trigonal	$P3_221$
D-RbBr$_3$(1)	348	3.7×10^{-5}	7.3×10^{-4}	5.6×10^{-3}	4.4×10^{-4}	1.7×10^{-3}	Trigonal	$P3_221$
D-CsCl$_3$	348	1.2×10^{-4}	4.0×10^{-4}	5.4×10^{-3}	8.7×10^{-4}	1.7×10^{-3}	Monoclinic	$C2/c$
D-CsBr$_3$	363	1.6×10^{-4}	9.1×10^{-4}	3.5×10^{-3}	7.1×10^{-4}	1.3×10^{-3}	Orthorhombic	$Pbcn$
D-CsCl$_2$I [a]	361	1.9×10^{-3}	3.6×10^{-4}	4.8×10^{-3}	5.9×10^{-4}	1.9×10^{-3}	Trigonal	$P3_121$

[a] The sum of the radii of **D-CsCl$_2$I** was taken as $r_{Sum} = r_{Cs^+} + \frac{2}{3}r_{Cl^-} + \frac{1}{3}r_{I^-}$

However, if one considers the range of the sum of the ionic radii (column two of Table 4.7), it is seen that the minimum sum is 322 pm and the maximum sum is 363 pm, which is not an extensive range. Therefore, since the cation is not varied between these structures and as there is not much difference in the B^+ and X^- ionic radii, it makes sense that the distortion in these structures should not vary widely.

To gain further insights into the structural trends, it is necessary to compare the 3D and 1D ABX_3-type perovskites with one another. This is what the next section will cover.

4.5.3 Overall Comparison of Structures

It was noted in Section 4.5.2 that for the 3D perovskites, the sum of the B^+ and X^- ionic radii ranged between 322 pm and 363 pm. However, the whole picture becomes apparent once this is compared to the same range of the 1D ABX_3-type structures (283 pm to 387 pm). Moreover, the structure **D-KBr$_3$** has two dimensional polymorphs, the 1D trigonal ABX_3-type perovskite **D-KBr$_3$(1)** (obtained in this study) and the 3D trigonal perovskite **D-KBr$_3$(2)** (reported previously[42] and re-determined in this study), which may be selectively formed by either allowing crystallisation at room temperature or heating the reaction mixture, respectively.

Therefore, the structure **D-KBr$_3$** is the so-called "pure tipping-point" of the structural series with a summed B^+ and X^- ionic radii of 334 pm (or possibly the value of 333 pm of **D-RbCl$_3$**, however, there is no real difference between 334 pm and 333 pm). It is the *pure* tipping point since **D-NaI$_3$** is also a 3D perovskite, with a lower summed ionic radii of 322 pm. However, it is of the hexagonal polytype and hence exhibits a combination of face- and corner-sharing octahedra, whereas **D-KBr$_3$(2)** is the 3D perovskite with the lowest combined summed radii with only corner-sharing octahedra. Furthermore, **D-CsBr$_3$** is the 3D perovskite with the highest summed ionic radii of 363 pm, illustrating a "cut-off" point in the radii, lower than **D-RbI$_3$** (373 pm) and also **D-CsI$_3$** (387 pm), where the latter two form the 1D ABX_3-type perovskite again. At this stage, a schematic illustration might be of aid. Therefore consider Scheme 4.3. This scheme illustrates the structural trends as a function of the different summed radii of the B- and X-ions.

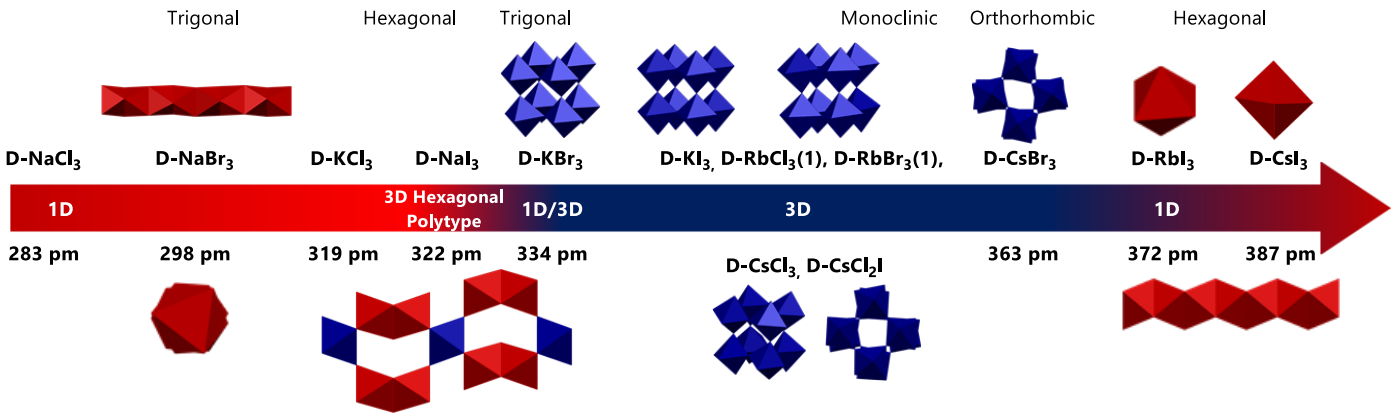

Scheme 4.3 Schematic illustration of the evolution of the perovskite structure dimensionality between 1D and 3D dabconium containing structures. The colours in the arrow change as a gradient from red (indicating 1D ABX_3-type structures) to dark blue (indicating 3D perovskite structures).

Below the empirically determined value of 322 pm for the sum of ionic radii, only 1D ABX_3-type perovskites are obtained. These 1D ABX_3-type perovskites exhibit only face-sharing octahedra, and then at 322 pm, the structure **D-NaI$_3$** is obtained, a 3D hexagonal polytype perovskite which exhibits a mixture of face- and corner-sharing octahedra. Thereafter, the tipping-point (334 pm) is reached with **D-KBr$_3$** where both the 1D ABX_3-type perovskite or pure corner-sharing 3D perovskite may be obtained depending on the reaction conditions, where these reaction conditions suggest that the 3D polymorph is more stable since it is the thermodynamic product. Then between the range of 334 pm and 363 pm, several 3D perovskite phases are obtained, after which at about 373 pm, the structure reverts back to that of a 1D ABX_3-type perovskite which is, however, now most symmetrically in the hexagonal phase, as described earlier.

This empirical relationship allows for crystal engineering since a direct correlation may be made between the summed ionic radii of the B- and X-ions and the resultant structure dimensionality. Hence, any combination of B^+- and X^--ions for which the summed B^+ and X^- ionic radii lie between approximately 330 pm and 365 pm may be combined with dabconium to form a 3D perovskite structure.

For example, the structure **D-CsCl$_2$I** is a prime example of crystal engineering. It has a summed ionic radii of 361 pm, lying in the range expected to deliver a pure corner-sharing 3D perovskite. Taking the example of **D-CsCl$_2$I** a step further, it is seen that **D-CsCl$_3$** is a monoclinic 3D perovskite and that **D-CsI$_3$** is a 1D ABX_3-type perovskite in the hexagonal phase. **D-CsCl$_2$I** is a chiral trigonal perovskite, hence a bit less symmetrical than **D-CsI$_3$**, but more so than **D-CsCl$_3$** and with the added property of being chiral.

The predictability of the structural family now allows for different mixed halide, mixed metal or mixed halide and metal structures to be predicted, much like the tolerance factors described earlier try to achieve. Before moving on, a brief look back at what the Goldschmidt and other tolerance factors predicted and how they match what was obtained in this study, is relevant.

4.5.4 Evaluating the Success of the Predictions using Tolerance Factors

Table 4.8 gives a complete summary of the dimensionalities of the experimental single-crystal structures obtained for the combination of dabconium and BX, where B is a monovalent alkali metal ion and X is a halide ion. The structures listed here are either obtained from the literature or the current study. In addition, values of the Goldschmidt Tolerance Factor (t), Bartel's Tolerance Factor (τ) and the Octahedral Factor (μ) are also listed.

Firstly, it is important to recall what the different factors' values imply. The Goldschmidt Tolerance Factor[18] needs to lie between 0.71 and 1.05 for a 3D dimensionality, the octahedral factor[19] needs to be between 0.442 and 0.895 to allow for octahedral coordination between B and X, and Bartel's Tolerance Factor[22] should be less than 4.18 for a 3D dimensionality.

From Table 4.8, the success of the predictions of the three factors is as follows. The Goldschmidt Tolerance Factor predicted 9/12 (75% accuracy) of the structures correctly. Bartel's Tolerance Factor predicted 7/12 (58% accuracy) of the structures correctly, and the Octahedral Factor correctly predicted an octahedral geometry for 11/12 (92% accuracy) structures.

To understand why the tolerance factors failed more so than the Octahedral Factor, the geometry of the dabconium dication must be considered. The Goldschmidt Tolerance Factor[18] and Bartel's Tolerance Factor model[22] considers the A-site cation as a rigid hard sphere. Figure 4.40 (a) shows the dabconium dication as a rigid sphere with a radius of 3.39 Å as determined by Density Functional Theory calculations based on its electronic geometry.[39] However, in Figure 4.40 (b), the real dimensions of a dabconium dication as determined by SCXRD shows a significant difference in geometrical shape and the values compared to the spherical approximation.

Table 4.8 Summary of the dimensionalities of the structures obtained from the combination of dabconium with BX reported in the literature and determined in this study along with the three prediction factors. Red indicates a lower dimensionality than 3D (1D for the purposes of these findings), and dark blue indicates a 3D dimensionality. Obtained dimensionalities are listed above the values of the three prediction factors. Thus, when a factor is shaded in red, it predicts a lower dimensionality, and if blue, it predicts a 3D dimensionality.

Metal Ion (B)	Halide Ion (X)		
	Cl^-	Br^-	I^-
Na^+	1D t = 1.10 τ = 3.31 μ = 0.56	1D t = 1.05 τ = 3.46 μ = 0.52	3D t = 0.97 τ = 3.69 μ = 0.46
K^+	1D t = 1.06 τ = 2.78 μ = 0.76	1D 3D t = 1.01 τ = 2.89 μ = 0.70	3D t = 0.94 τ = 3.06 μ = 0.63
Rb^+	3D t = 1.04 τ = 2.75 μ = 0.84	3D t = 1.00 τ = 2.85 μ = 0.78	1D t = 0.93 τ = 3.01 μ = 0.69
Cs^+	3D t = 1.03 τ =2.82 μ = 0.92	3D t = 0.99 τ = 2.91 μ = 0.85	1D t = 0.94 τ = 3.05 μ = 0.76

Figure 4.40 (b) shows that the largest radius of the dabconium dication is 4.254/2 = 2.127 Å, whereas the spherical model uses a value of 3.39 Å. Furthermore, since the shape is by no means spherical (tending towards ellipsoidal), it shows that it is not the failure of the models, however, more the fact that dabconium is not spherical (rather leaning towards an ellipsoid) and hence the models cannot be expected to predict the dimensionalities of structures correctly. This is a clear gap in the field of perovskites, since the hard sphere models would work well for inorganic perovskites, however hybrid perovskites are still not being correctly predicted. Bartel's Tolerance Factor is on the right track, however, for now, one has to be satisfied with the empirically determined trends described earlier.

On the other hand, the Octahedral Factor only predicts whether an octahedral arrangement is possible for a given BX-combination and is independent of the A-site cation. Therefore, it may be used without modification, and may in general be used as a guideline for the inorganic framework's potential to form the perovskite-inorganic lattice.

Moreover, since each organic cation considered would differ in shape, it is the author's opinion that no such *rigid* model would be 100% successful. Hence, every organic cation would have to be analysed and considered individually, and then geometrically similar molecules may have a model developed for the prediction of their structures. The Goldschmidt Tolerance or Bartel's Tolerance Factors may be derived for different systems before each study to provide additional information.

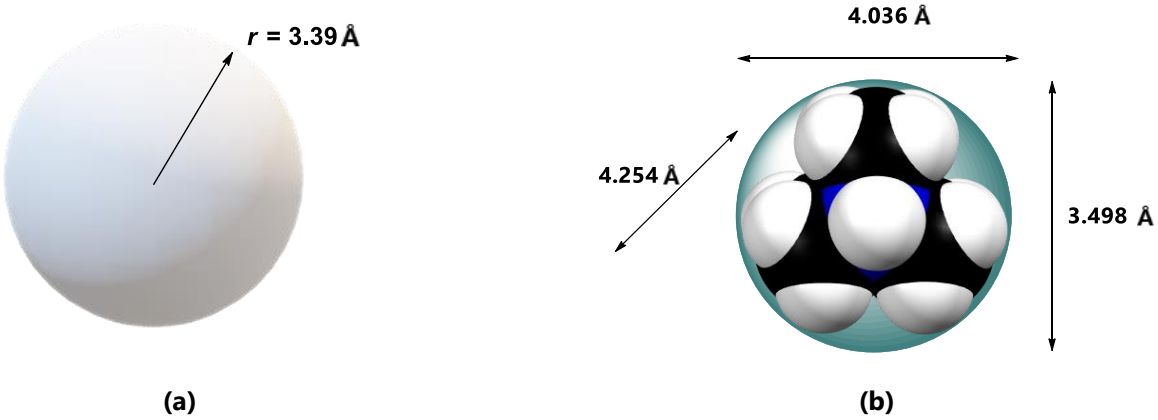

Figure 4.40 The geometrical shape of dabconium. **(a)** The spherical model with radius 3.39 Å and **(b)** the real geometry of a dabconium dication as experimentally obtained in this study.

This concludes the structural trends discussion, and now the results of the property measurements of the dabconium-containing alkali metal halide perovskites will be discussed.

4.6 Material Property Measurement Results

This section presents the measured properties of the dabconium-containing alkali metal halide perovskites described in this chapter. Diffuse reflectance spectroscopy was employed to measure the absorbance of the materials in question. Subsequently, the absorbance data were employed to study the solid-state fluorescence of the same samples.

All samples analysed for material properties were pure according to their powder patterns (Appendix D), except for **D-NaI$_3$, D-KI$_3$**, and **D-CsCl$_2$I**, however, the patterns of these three compounds showed that the perovskite material formed in the large majority to the impurities and hence rationalises why they were included in the property measurements.

4.6.1 Optical Properties

According to the Kubelka-Munk theory, the reflectance data of an infinitely thick specimen can be converted to absorbance data by use of the Kubelka-Munk remission function $\left(F(R_\infty)\right)$, as follows[48–50]

$$F(R_\infty) = \frac{K}{S} = \frac{(1-R_\infty)^2}{2R_\infty} \tag{4.5}$$

where $R_\infty = \frac{R_{\text{sample}}}{R_{\text{standard}}} = \frac{\%R}{100}$ is related to the percentage reflectance of the material, while K and S are the absorption and scattering coefficients, respectively.[48] Furthermore, the Tauc method assumes that the absorbance, and hence the energy-dependent absorbance coefficient (α) of the crystalline material may be expressed as shown in Equation (4.6)

$$(\alpha \cdot h\nu)^{\frac{1}{\gamma}} = B\left(h\nu - E_g\right) \tag{4.6}$$

where h is the Planck constant, ν is the photon's frequency, E_g is the band gap energy, and B is a constant. If the transition is *direct*, then $\gamma = 0.5$, and if the transition is *indirect*, then $\gamma = 2$.[51]. Therefore, by combining Equation (4.6) with the expression for and $F(R_\infty)$, the result is Equation (4.7)

$$(F(R_\infty) \cdot h\nu)^{\frac{1}{\gamma}} = B\left(h\nu - E_g\right) \tag{4.7}$$

Hence, by plotting $(F(R_\infty)\cdot h\nu)^{1/\gamma}$ against $h\nu$, the band gap (E_g) can be determined by extrapolating the linear part of the function and determining its intersection with the x-axis. γ is taken as 0.5 for all dabconium containing materials since they all exhibit only one absorption edge and hence possess direct band gaps. The DRS data collected for the dabconium-containing materials were processed, and the lines of best fit of the linear parts were determined.

Table 4.9 provides a summary of the band gap values of the materials studied in this chapter. Notably, the DRS technique only possesses an accuracy of ±0.5 eV, and hence the values reported here need to be regarded with this error margin in mind.[49] A correlation (R^2) factor of 0.98 or higher was used as a guideline to determine what the range of the linear part was.

Table 4.9 Summary of the optical band gaps of dabconium-containing alkali metal halide perovskite materials. The equations of the lines of best fit of the linear parts of the Kubelka-Munk plots and their correlation factors (R^2) are given with the optical band gaps read-off from the equations.

Material	Line of Best Fit	(R^2)	Band Gap (±0.5 eV)	Dimensionality	Phase
D-NaCl$_3$	$y = 0.3578x - 1.4290$	0.99	3.99	1D	Trigonal
D-NaBr$_3$	$y = 1.8989x - 10.1173$	0.99	5.33	1D	Trigonal
D-NaI$_3$	$y = 1.3108x - 5.6446$	0.98	4.31	3D	Hexagonal
D-KCl$_3$	$y = 0.2718x - 0.9295$	0.99	3.42	1D	Trigonal
D-KBr$_3$(1)	$y = 1.3558x - 7.1795$	0.98	5.30	1D	Trigonal
D-KBr$_3$(2)	$y = 1.0154x - 5.0787$	0.98	5.00	3D	Trigonal
D-KI$_3$	$y = 1.4867x - 6.6837$	0.98	4.50	3D	Trigonal
D-CsCl$_3$	$y = 0.7558x - 3.8300$	0.99	~5.10 [a]	3D	Monoclinic
D-CsBr$_3$	$y = 1.2587x - 6.6228$	0.98	5.26	3D	Orthorhombic
D-CsI$_3$	$y = 1.6814x - 7.7633$	0.98	4.63	1D	Hexagonal
D-CsCl$_2$I	$y = 0.9751x - 4.4257$	0.99	4.54	3D	Trigonal

[a] This value is reported as ~ since the absorbance plateau could not be measured due to instrumental limitations. Therefore, the true value is expected in that region, but there remains some uncertainty at this stage.

The processed spectra are shown in Figure 4.41, with the original spectra included in Appendix A. The following section will identify the trends present in Table 4.9 and suggest possible reasons for the observed trends.

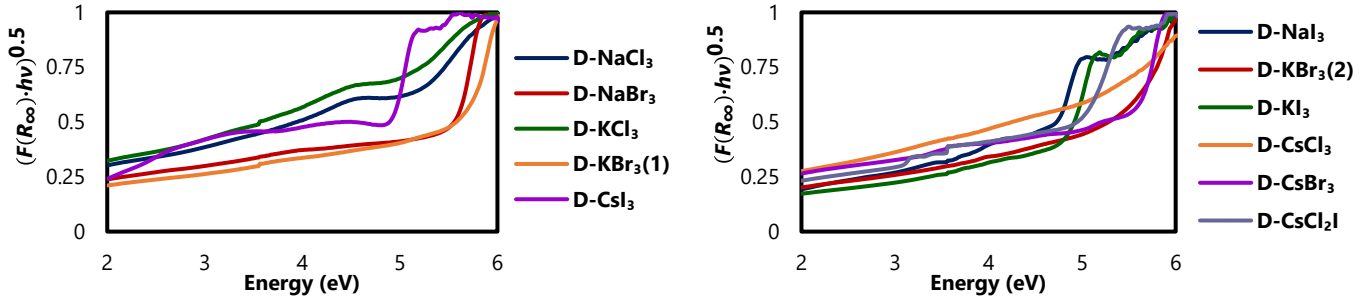

(a) **(b)**

Figure 4.41 Processed and normalised DRS spectra of the dabconium-containing perovskite materials. The line of best fit of each spectrum is given in Table 4.9. The individual spectra are colour coded for each material as listed in the legend. **(a)** The 1D ABX_3-type perovskite materials and **(b)** the 3D perovskite materials. The instrument changes from a deuterium lamp to a wolfram lamp at 350 nm, which leads to a jump-discontinuity in the spectra.

Comparison of Optical Band Gaps

The band gaps obtained for the dabconium-containing perovskites with alkali metal halide anions lie in the range of 3.42 to 5.33 eV. The first important observation from Table 4.9 is that there is no *clear* trend since the compounds form structures with different dimensionalities and, subsequently, multiple phases with different space groups in each phase. However, the four isostructural materials (**D-NaCl$_3$**, **D-NaBr$_3$**, **D-KCl$_3$**[35,36] and **D-KBr$_3$(1)**), all being 1D ABX_3-type trigonal perovskites, may be compared directly. The band gap values for **D-KX$_3$** structures are generally lower than that of the comparable **D-NaX$_3$** structure, for X = Cl^-, Br^-, even though only slightly in the Br^- case. Also, upon substituting Cl^- for Br^- in **D-BX$_3$**, an increase in the band gap is seen for the 1D ABX_3-type trigonal materials. Unfortunately, the only other structure of the 1D ABX_3-type is **D-CsI$_3$**, and since it is not isostructural to the other 1D ABX_3-type structures, no comment can be made regarding these differences.

Furthermore, both **D-NaI$_3$** and **D-CsI$_3$** crystallise in the hexagonal phase, with the former being a 3D perovskite and the latter a 1D ABX_3-type perovskite. The 1D ABX_3-type hexagonal perovskite has a larger band gap (4.63 eV) compared to the 3D hexagonal perovskite (4.30 eV), which may be ascribed to the smaller percentage of face-sharing octahedra in the 3D case versus the 1D case. Another 1D versus 3D comparison may be made between **D-KBr$_3$(1)** and **D-KBr$_3$(2)**[38]. The 3D material has a narrower band gap compared to the 1D material, of 5.00 eV versus 5.30 eV. Again, this narrowing of the band gap in the 3D case may be an effect of having face-sharing octahedra versus corner-sharing octahedra, where, in the corner-sharing case, better orbital overlap between B- and X-ions is possible.

One speculative trend is that of the halide effect in the 3D case. In considering **D-KBr$_3$(2)**[38] and **D-KI$_3$**, it is seen that the Br-analogue has a wider band gap (5.30 eV) compared to the I-case (5.00 eV). In addition, **D-CsCl$_3$**[36] and **D-CsBr$_3$** may be compared, where again both are 3D, but the Cl-analogue has a wider band gap (>5.30 eV) than the Br-containing compound (5.26 eV). Thus, it appears as if, in the 3D case, the chloride-analogues have larger band gaps than the bromide-containing compounds, which, in turn have larger band gaps than the iodide-analogues. In addition, the band gap of the material **D-CsCl$_2$I** is narrower than that of the other Cs-containing materials **D-CsCl$_3$**, **D-CsBr$_3$** or **D-CsI$_3$**, correlating with the effects of the 3D structural dimensionality ($3D_{Band\ Gap} < 1D_{Band\ Gap}$) and that I^--containing perovskite should have a narrower band gap than Br^-- or Cl^--containing perovskite materials.

Since the band gap values reported for the dabconium-containing perovskite are significantly wider than the ideal band gap required for sensitiser materials in PSC devices (1.1 eV suggested by the Shockley–Queisser Theory[25]), perhaps other applications may be better suited to them. Perovskite materials may be used in a range of applications as reported in the literature.[52] To this end, since the absorption edge of these materials have been determined through DRS, the solid-state fluorescence spectra of these materials can easily be studied. This will provide the fluorescence emission properties of these materials with associated absorbance and hence may indicate potential applications.

4.6.2 Solid-State Fluorescence Spectroscopy

It has been reported in the literature that the pure alkali halides exhibit fluorescence spectra when excited by UV-radiation.[53,54] Based on these results, it was decided to investigate whether hybrid perovskites containing alkali metal halides show fluorescence.

From the DRS analysis, the excitation wavelengths of each material may be inferred. This excitation wavelength may then be used to study the solid-state fluorescence spectra of these dabconium-containing perovskites. The following section is divided into two parts. Firstly, the solid-state fluorescence spectra of the 1D ABX_3-type perovskites are discussed and secondly, the fluorescence of the 3D perovskites are discussed.

1D ABX_3-Type Perovskites Solid-State Fluorescence

Five 1D ABX_3-type perovskite materials (**D-$NaCl_3$**, **D-$NaBr_3$**, **D-KCl_3**, **D-KBr_3(1)** and **D-CsI_3**) were obtained in this study, and their solid-state fluorescence properties were studied. Each of these materials were excited at a specific wavelength as determined by DRS, leading to the emission of a singlet at a higher wavelength, as listed in Table 4.10. The solid-state fluorescence spectra of the ABX_3-type dabconium-containing perovskite materials obtained in this study are shown in Figure 4.42. The spectral data were normalised between 0 and 1.

Table 4.10 Summary of the solid-state fluorescence data obtained for the 1D ABX_3-type dabconium-containing perovskites.

Material	Excitation Radiation		Emission Peak	
	Wavelength (nm)	Energy (eV)	Wavelength (nm)	Energy (eV)
D-$NaCl_3$	300	4.13	600	2.07
D-$NaBr_3$	233	5.32	472	2.63
D-KCl_3	363	3.42	–	–
D-KBr_3(1)	234	5.30	473	2.63
D-CsI_3	268	4.63	542	2.29
Blank	260	4.77	520	2.38

The emission spectra all resulted in a doubling of the excitation wavelength, as for example, with **D-$NaCl_3$** it is seen that the excitation wavelength is 300 nm, and the emission peak is at 600 nm. However, this observed peak is not due to fluorescence from the compound, but rather since the instrumentation uses a monochromator as wavelength selector, this *doubling of the wavelength* represents the second order Rayleigh peak, and hence, none of the compounds were found to exhibit solid-state fluorescence at room temperature.[55]

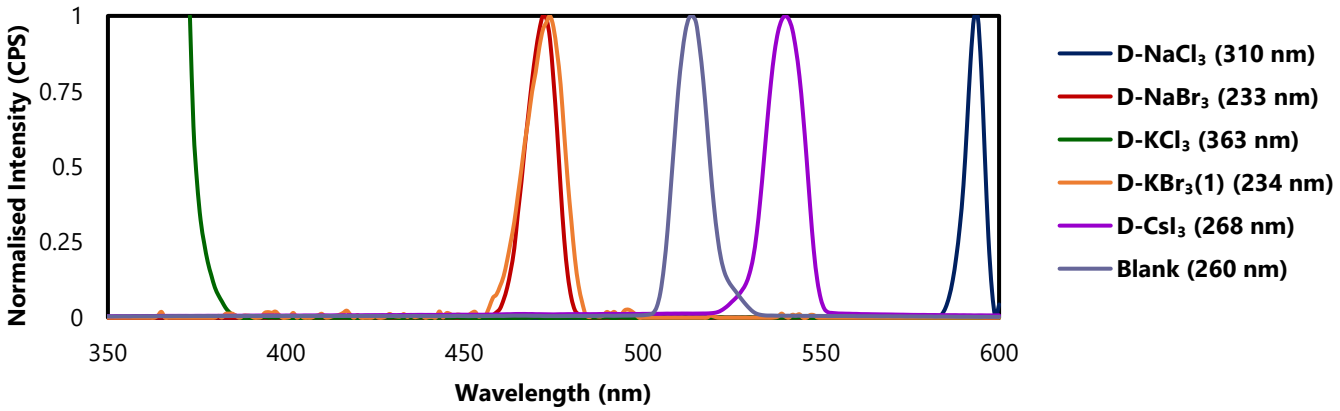

Figure 4.42 The solid-state fluorescence spectra of the 1D ABX_3-type dabconium-containing perovskite materials obtained in this study. The individual spectrum of each material shown in different colours as per the legend, with the excitation wavelength given in brackets, including a spectrum for a blank sample. All of the peaks were assigned as second order Rayleigh peaks.

Furthermore, a peak at the doubling of the excitation wavelength is observed in a blank sample as well. Therefore, since there are no peaks present between the excitation wavelength (also known as the first order Rayleigh peak[55]) and the second order Rayleigh peak, it may be concluded that the 1D ABX_3-type perovskite do not exhibit solid-state fluorescence at room temperature. Moreover, this is clearly seen for **D-KCl_3**, which has an excitation wavelength of 363 nm. Since the instrumentation is limited to a maximum observable wavelength of 600 nm, its second Rayleigh peak (726 nm) could not be

observed, however, only the tail of its first Rayleigh peak is observed and no fluorescence afterwards. Therefore, it cements the fact that the 1D ABX_3-type perovskite do not fluoresce at room temperature.

3D Perovskites Solid-State Fluorescence

Similarly, as was done for the 1D ABX_3-type perovskites, the solid-state fluorescence of the 3D dabconium-containing perovskites were also studied. Table 4.11 lists the results of the solid-state fluorescence for the 3D perovskite materials, and the normalised fluorescence spectra are illustrated in Figure 4.43.

Table 4.11 Summary of the solid-state fluorescence data obtained for the 3D dabconium-containing perovskites.

Material	Excitation Radiation		Emission Peak	
	Wavelength (nm)	Energy (eV)	Wavelength (nm)	Energy (eV)
D-NaI_3	289	4.29	577 & 584	2.15 & 2.12
D-KBr_3(2)	248	5.00	490 & 502	2.53 & 2.47
D-KI_3	276	4.49	545 & 563	2.27 & 2.20
D-$CsCl_3$	252	4.92	495 & 511	2.50 & 2.43
D-$CsBr_3$	236	5.25	468 & 478	2.65 & 2.59
D-$CsCl_2I$	266	4.66	496 & 507	2.49 & 2.45

Similarly, as was seen for the 1D ABX_3-type perovskites, the 3D perovskites also did not exhibit any solid-state fluorescence at room temperature. Again, a peak was observed at double the excitation wavelength, and hence the spectra only illustrate the second order Rayleigh peak. In this case the second Rayleigh peak appears as a doublet, which is due the instrumental limit being reached.[55] Therefore, none of the dabconium-containing materials exhibited photoluminescent properties.

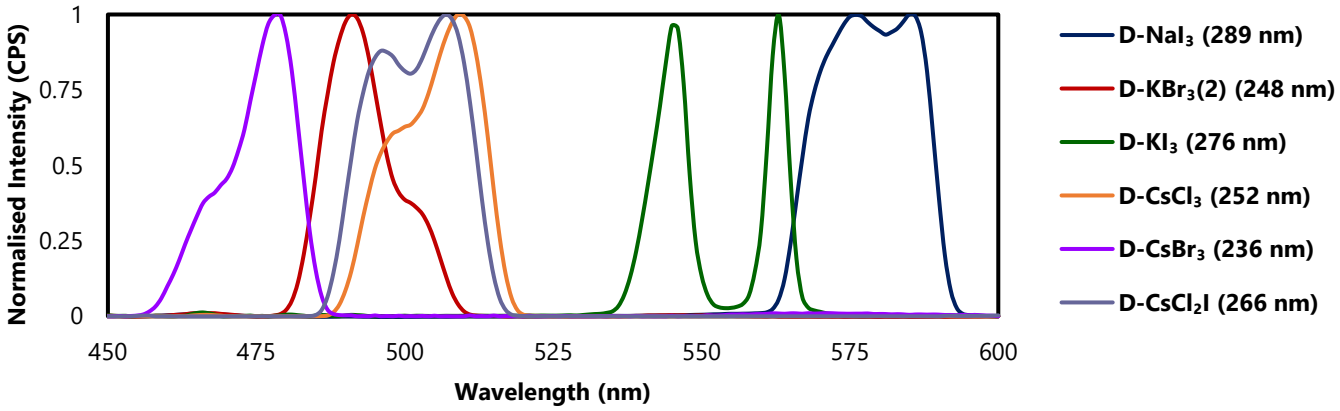

Figure 4.43 The solid-state fluorescence spectra of the 3D dabconium-containing perovskite materials obtained in this study. The individual spectrum of each material shown in different colours as per the legend, with the excitation wavelength given in brackets.

Fluorescence studies of pure alkali halides indicated that these compounds show no or very weak fluorescence at room temperature and that significant fluorescent emission is only observed when the compounds are cooled down to very low temperatures, in the order of 5 K.[53,54,56] The fact that the fluorescence measurements in this study were carried out at room temperature, may explain the absence of fluorescence, and it may be possible that the compounds will fluoresce at much lower temperatures. However, since the available fluorescence spectrometer used in this study could only perform measurements at room temperature, this hypothesis could not be tested.

4.7 Summary and Conclusions

Each combination in the series of dabconium and BX, where B is a monovalent alkali metal ion (Na^+, K^+, Rb^+ or Cs^+) and X a halide ion (Cl^-, Br^- or I^-), lead to perovskites of the general molecular formula ABX_3. Moreover, though the same molecular formulae were seen, two different structural dimensionalities (1D and 3D) were obtained, dividing the structures into categories of either 3D perovskites or 1D ABX_3-type perovskites. In addition, one 3D mixed hybrid halide perovskite was obtained. The information regarding the dimensionality of the different structures is summarised in Figure 4.44.

The 1D ABX_3-type structures, all containing only face-sharing octahedra, crystallised in either a trigonal or hexagonal phase, depending on the value of the sum of the ionic radii of the B- and X-ions, where values in the range of 283 pm to 334 pm result in trigonal phases and values above 372 pm give hexagonal phases. The hexagonal phases were determined to be more symmetrical, and in general, the symmetry increased with an increasing sum of ionic radii. Moreover, in each of the five structures, the metal-metal distances fell within the accepted metal-metal bond lengths reported previously for Na–Na, K–K and Cs–Cs bonds.

The 3D perovskite structures obtained crystallised in either monoclinic, trigonal, or hexagonal phases, which contributed to the structural variety and contributed to knowledge in the field of metal halide perovskites. Pure 3D corner-sharing perovskites were obtained when the sum of the B- and X-ion's radii was between 334 pm and 363 pm, whereas one 3D hexagonal polytype structure was obtained when the sum of the radii was 322 pm. This structure represents the tipping point where face-sharing octahedra are replaced with corner-sharing octahedra and allowed for the identification of the range of combinations where the 3D corner-sharing perovskites may be obtained. This led to the engineering of one mixed halide 3D perovskite using a combination of dabconium, caesium, chloride, and iodide ions, by considering the optimal combinations of B- and X-ions matching the radii of the constituents so that they fall in the 3D range. When the chloride to iodide ratio is optimised to 2:1, the sum of the ionic radii is 361 pm, falling within the range that produces 3D perovskites and confirming the empirically determined range. It should be noted that the combination of dabconium dications and KBr-based anions can result in two different polymorphs, both of the formula ABX_3, with the one structure being a 1D ABX_3 perovskite and the other a 3D perovskite. This structure also represents a tipping point in the series.

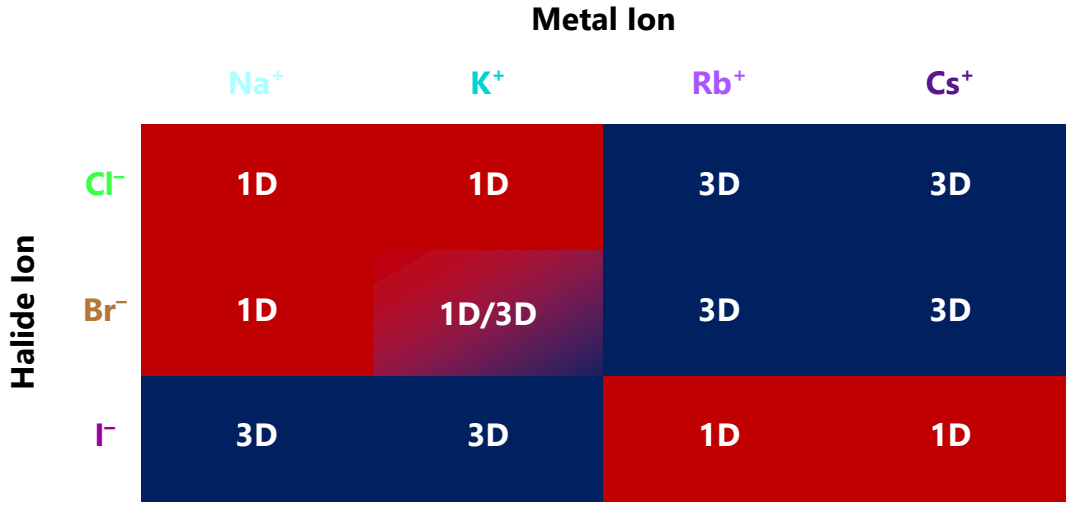

Figure 4.44 A matrix indicating the dimensionality of the dabconium-containing alkali metal single halide structures obtained in this study and those reported in the literature.

Furthermore, the band gaps of the eleven compounds obtained in this study were determined using diffuse reflectance spectroscopy. The band gap values revealed that the structures all possess wide band gaps (>3.0 eV), making them non-ideal as sensitisers in solar cell applications, though with most still falling in the category of semi-conductors (<5.0 eV). Trends in the band gap values were difficult to establish because of the variety in structures and dimensionalities displayed by the

compounds. However, the values suggest that a 3D structure results in a narrower band gap than a 1D structure. With increasing halide ionic radius, a narrower band gap is obtained in the 3D case, and the opposite is true for the 1D case.

Employing solid-state fluorescence spectroscopy, it was determined that these materials do not exhibit any solid-state fluorescence at room temperature. However, because they possess quite wide band gaps, they could possibly possess white-light emission properties, through electroluminescence (i.e., when a material emits radiation on application of a current). Moreover, with white-light, blue light is also obtained. Blue-light emitters are most sought after for their application in LEDs, and in fact the 2014 Nobel Prize was awarded for the discovery of blue-light LED emitters.[57] Therefore this potential application of these materials may be further explored, but falls outside the scope of the current study.

Future work could also include synthesising more mixed halide or mixed metal species in the structural family, vindicated by the success seen with the mixed halide structure obtained in this study. However, numerous possibilities remain within the 334 pm to 363 pm range, and there are options for further application of these materials. The perovskite family class has provided a playground for scientists from all disciplines to join and is yet to show that it is running out of potential. Hence, the future shines bright for perovskite-related research.

4.8 Experimental Methods

This section will describe the methods used in this study to synthesise the materials investigated. General information regarding the characterisation (SCXRD and PXRD) and property measurements (DRS and solid-state fluorescence) is given.

4.8.1 Synthetic Methods

All reagents and solvents (except distilled water) used were reagent grade purchased from Sigma Aldrich™ and were used without further purification or modification. Distilled water was obtained from the in-house distillation facility. **Specific information:** NaCl (≥99%), NaBr (≥99%), NaI (≥99%), KCl (≥99%), KBr (≥99%), KI (≥99%), CsCl (≥99%), CsBr (≥99%), CsI (≥99%), 1,4-diazabicyclo[2.2.2]octane (99%), HCl (37% solution), HBr (48% weight) and HI (57% weight, stabilised solution).

No attempts were made to optimise the yields of the reactions.

Preparation of D-$NaCl_3$. In a 100 ml beaker, 1.0079 g 1,4-diazabicyclo[2.2.2]octane was dissolved in 20 ml distilled water. To this solution, 3.1 ml 11.6 M HCl was added. Thereafter, 0.5050 g NaCl was dissolved in 10 ml distilled water and added to the acidic solution. The resultant solution was left at room temperature, open to the atmosphere, for the solvent to evaporate. After 10 days, 0.8437 g of colourless crystals were collected after washing with acetone. Theoretical yield = 2.1046 g, therefore an experimental yield of 40.0% was obtained.

Preparation of D-$NaBr_3$. To a 100 ml beaker, 1.0153 g 1,4-diazabicyclo[2.2.2]octane was added and subsequently dissolved in 20 ml distilled water, to which 4.0 ml 8.89 M HBr was added. In a separate container, 0.8933 g NaBr was dissolved in 10 ml distilled water and subsequently added to the former solution. The solvent was allowed to evaporate at room temperature, open to the atmosphere, and after 12 days, 1.8461 g of colourless crystals were obtained after washing with acetone. Theoretical yield = 3.2721 g, therefore an experimental yield of 56.4% was obtained.

Preparation of D-KCl_3. 1.0060 g 1,4-diazabicyclo[2.2.2]octane was dissolved in 20 ml distilled water in a 100 ml beaker. To this, 3.2 ml 11.6 M HCl and a solution of 0.6451 g KCl in 10 ml distilled water were added. The final solution was left at room temperature, and allowed to evaporate for 10 days, after which 1.9175 g colourless crystals were harvested and washed with acetone. Theoretical yield = 2.2466 g, therefore an experimental yield of 85.4% was obtained.

Preparation of D-KBr_3(1). In a 250 ml beaker, a solution of 2.0826 g 1,4-diazabicyclo[2.2.2]octane, 45 ml distilled water, and 9 ml 8.89 M HBr was prepared. To this solution, 2.1467 g KBr dissolved in 15 ml water was added. The resultant solution was left for 20 days at room temperature, open to the atmosphere, after which time 5.8023 g colourless single crystals were collected and washed with acetone. Theoretical yield = 7.0893 g, therefore an experimental yield of 81.8% was obtained.

Preparation of D-KBr_3(2). A solution of 2.0007 g 1,4-diazabicyclo[2.2.2]octane along with 2.1225 g KBr, 9 ml 8.89 M HBr in 30 ml distilled water was prepared in a 100 ml glass beaker. The solution was subsequently placed on a hot plate and heated to 90 °C until all the solvent had evaporated. Finally, 6.6743 g of a white powder was obtained, and it was washed with acetone, and its purity was verified using PXRD (see appendix D). Theoretical yield = 7.006 g, therefore an experimental yield of 95.3% yield was obtained. Single crystals of the compound could be obtained from the powder.

Preparation of D-KI_3. In a 100 ml glass beaker, a solution of 30 ml water, 1.5075 g 1,4-diazabicyclo[2.2.2]octane, 1.3442 g KI and 5 ml 7.57 M HI was prepared. The solvent was evaporated on a hot plate at 90 °C. Small colourless crystals were obtained and washed with acetone, with a mass of 4.7263 g obtained. The purity of the sample was studied using PXRD analysis (see Appendix D), showing a small amount of impurities present in the sample. Theoretical yield = 6.8790 g, therefore a crude yield of 68.7% was obtained.

Preparation of D-$CsCl_3$. A 100 ml beaker was charged with 1.5086 g 1,4-diazabicyclo[2.2.2]octane and 20 ml distilled water. To this, 10 ml 11.6 M HCl was added, along with a solution of 2.2630 g CsCl in 20 ml distilled water. Colourless crystals (2.8467g) were collected after evaporation at room temperature for 16 days and subsequently washed with acetone. Theoretical yield = 19.0130 g, therefore an experimental yield of 15.0% was obtained.

Preparation of D-$CsBr_3$. A solution of 40 ml distilled water and 2.0017 g 1,4-diazabicyclo[2.2.2]octane was prepared in a 250 ml glass beaker. Subsequently, 4 ml 8.89 M HBr was added, along with a solution of 3.8058 g CsBr in 20 ml distilled water. After the solution was allowed to evaporate for 20 days at room temperature, 4.5339 g colourless crystals were obtained and thereafter washed with acetone. Theoretical yield = 8.6960 g, therefore an experimental yield of 52.1% was obtained.

Preparation of D-CsI_3. 20 ml distilled water was used to dissolve 0.2178 g 1,4-diazabicyclo[2.2.2]octane in a 100 ml glass beaker. To this, 0.5 ml of a 7.57 M HI solution was added. Following the addition of 0.4640 g CsI in 5 ml distilled water, the resultant solution was left to evaporate at room temperature for seven days. Colourless crystals to the mass of 0.7753 g were collected and washed with acetone. Theoretical yield = 1.1213 g, therefore an experimental yield of 69.1% was obtained.

Preparation of D-$CsCl_2I$. 1,4-diazabicyclo[2.2.2]octane to the mass of 0.2171 g was dissolved in 20 ml distilled water in a 100 ml glass beaker. Following this, 1.2 ml 11.6 M HCl was added and subsequently a solution of 0.4660 g CsI in 5 ml distilled water. The resultant mixture was left to evaporate at room temperature for six days. Finally, 0.6597 g colourless crystals were obtained and washed with acetone. Theoretical yield = 0.7981 g, therefore a crude experimental yield of 82.7% was obtained. PXRD analysis showed a small amount of inpurities present in the sample.

Preparation of D-NaI_3 Single Crystals. To a 10 ml glass vial, 7.5 ml 7.57 M HI, 0.1510 g 1,4-diazabicyclo[2.2.2]octane and 0.2136 g NaI were added. The vial was sealed with a plastic cap and Parafilm and submerged in an oil bath heated to 110 °C. The vial was left in the heated oil bath until all the solid particles had dissolved. Finally, the vial was removed from the oil and left to cool down to room temperature while remaining sealed. Small colourless crystals (0.6823 g) were harvested from the mother liquor. Theoretical yield = 1.9651 g, therefore an experimental yield of 34.7% yield was obtained.

Preparation of D-NaI_3 Bulk Powder. A solution of 30 ml distilled water, 1.5038 g 1,4-diazabicyclo[2.2.2]octane, 5 ml 7.57 M HI and 2.0250 g NaI were added to a 100 ml glass beaker. Thereafter, the solvent was left to evaporate on a hot plate at 90 °C. As a result, 6.3153 g of white powder was obtained and subsequently washed with acetone. PXRD studies showed the purity of the bulk sample (some impurity present, see Appendix D). Theoretical yield = 19.6194 g, therefore a crude experimental yield of 32.1% yield was obtained.

Preparation of D-$NaCl_3$ Bulk Powder. To a 100 ml glass beaker, 2.0005 g 1,4-diazabicyclo[2.2.2]octane, 7 ml 11.6 M HCl, 1.0418 g NaCl and 30 ml distilled water were added. The solution was placed on a hot plate and heated to 90 °C and left until all solvent had evaporated. The resultant white powder (3.8604 g) was washed with acetone and confirmed to be pure **D-$NaCl_3$** using PXRD (see Appendix D). Small single crystals could be obtained from the powder. Theoretical yield = 4.3429 g, therefore an experimental yield of 88.9% yield was obtained.

4.8.2 Characterisation Methods

Powder X-Ray Diffraction

Powder XRD patterns for all bulk materials were collected at room temperature using a Bruker D2 Phaser instrument and Cu radiation (λ = 1.54 Å), with the sample sprinkled on a low background silicon sample holder. A typical powder pattern was collected between 5° and 45° 2θ with a step size of 0.05° and a time interval of between 1 and 3 seconds per step. The X-ray tube was powered at 300 W with 10 mA and 30 kV. To ensure phase purity, and exclude phase transitions, experimental room temperature (*ca*. 298 K) powder patterns were matched against powder patterns calculated from low-temperature (150 K) single-crystal structures.

Single-Crystal X-Ray Diffraction

For all novel single-crystal structures reported, data were collected on either a Rigaku XtaLAB Synergy R single-crystal diffractometer, with a HyPix detector, equipped with a rotating anode source providing Cu or Mo radiation or a Bruker D8 Venture single-crystal diffractometer, with a Photon 100 CMOS detector and an Iμs source providing Cu or Mo radiation was employed. Data were collected at 150 K, with cooling was achieved using an Oxford Cryogenics Cryostat. Structures were solved by direct methods in Shelxt and refined using ShelXL (SHELXT 2018/2, SHELXL2018/3).[58] Hydrogen atoms were placed as observed in the difference map, where possible, otherwise they were placed geometrically using a riding model.

4.8.3 Property Measurement Methods

Diffuse Reflectance Spectroscopy

DRS data were collected using a Cary 500 UV-vis-NIR spectrophotometer with praying mantis DRS attachment. Samples were prepared as a bulk powder for analysis. The reflectance of samples was measured between 200 nm to 800 nm at room temperature. The instrument changes from a deuterium lamp to a wolfram lamp at 350 nm, which leads to a jump-discontinuity in the recorded spectra. DRS data were processed using Kubelka-Munk theory.

Solid-State Fluorescence Spectroscopy

Solid-state fluorescence spectra were measured under ambient conditions employing a Horiba Fluoromax-4 spectrofluorometer, fitted with a Xenon lamp light source and a photomultiplier detector. All data were measured at room temperature. A plane-grating Czery-Turner spectrometer with a wavelength range of 200 to 950 nm was used as the optical system. A front entrance and exit slit of 5.00 nm bandpass was used for both excitation and emission spectra. All samples were prepared by grinding them with a mortar and pestle, whereafter they were sandwiched between two glass microscope slides, secured with tape, and measured at a 45° geometry. The excitation wavelengths employed for each material were determined from their DRS spectra.

4.9 References for Chapter 4

1. Kieslich, G.; Sun, S.; Cheetham, A. K. *Chemical Science* **2014**, *5* (12), 4712–4715. https://doi.org/10.1039/c4sc02211d.
2. Megaw, H. *Nature* **1945**, *155* (3938), 484–485. https://doi.org/10.1038/155484b0.
3. Møller, C. *Nature* **1957**, *180* (4593), 981–982. https://doi.org/10.1038/180981a0.
4. National Renewable Energy Laboratory: Best Research-Cell Efficiency Chart https://www.nrel.gov/pv/cell-efficiency.html (accessed Feb 20, 2021).
5. Zhao, X. G.; Yang, D.; Ren, J. C.; Sun, Y.; Xiao, Z.; Zhang, L. *Joule* **2018**, *2* (9), 1662–1673. https://doi.org/10.1016/j.joule.2018.06.017.
6. Weber, D. *Zeitschrift für Naturforschung B* **1978**, *33* (12), 1443–1445. https://doi.org/https://doi.org/10.1515/znb-1978-1214.
7. Ikeda, N.; Teshima, K.; Miyasaka, T. *Chemical Communications* **2006**, *1* (16), 1733–1735. https://doi.org/10.1039/b516417f.
8. Kojima, A. *ECS Meeting Abstracts* **2008**, *MA2008-02* (2), 27. https://doi.org/10.1149/ma2008-02/1/27.
9. Kojima, A.; Teshima, K.; Shirai, Y.; Miyasaka, T. *Journal of the American Chemical Society* **2009**, *131* (17), 6050–6051. https://doi.org/10.1021/ja809598r.
10. Xiao, Z.; Song, Z.; Yan, Y. *Advanced Materials* **2019**, *31* (47), 1–22. https://doi.org/10.1002/adma.201803792.
11. Gollino, L.; Pauporté, T. *Solar Energy* **2021**, *5* (3), 2000616. https://doi.org/10.1002/solr.202000616.
12. Gebhardt, J.; Rappe, A. M. *Advanced Materials* **2019**, *31* (47), 1–15. https://doi.org/10.1002/adma.201802697.
13. Xiao, Z.; Meng, W.; Wang, J.; Mitzi, D. B.; Yan, Y. *Materials Horizons* **2017**, *4* (2), 206–216. https://doi.org/10.1039/c6mh00519e.
14. Li, W.; Wang, Z.; Deschler, F.; Gao, S.; Friend, R. H.; Cheetham, A. K. *Nature Reviews Materials* **2017**, *2* (3), 1–18. https://doi.org/10.1038/natrevmats.2016.99.
15. Stoumpos, C. C.; Mao, L.; Malliakas, C. D.; Kanatzidis, M. G. *Inorganic Chemistry* **2017**, *56* (1), 56–73. https://doi.org/10.1021/acs.inorgchem.6b02764.
16. Katz, L.; Ward, R. *Inorganic Chemistry* **1964**, *3* (2), 205–211. https://doi.org/10.1021/ic50012a013.
17. Lander, J. J. *Acta Crystallographica* **1951**, *4* (2), 148–156. https://doi.org/10.1107/S0365110X51000441.
18. Goldschmidt, V. M. *Naturwissenschaften* **1926**, *14* (May), 477–485. https://doi.org/10.1007/BF01507527.
19. Chonghea Li, X. L.; Weizhong Ding, L. F.; Yonghui Gao, Z. G. *Acta Crystallographica Section B* **2008**, *64* (6), 702–707. https://doi.org/10.1107/S0108768108032734.
20. Ava, T. T.; Al Mamun, A.; Marsillac, S.; Namkoong, G. *Applied Sciences (Switzerland)* **2019**, *9* (1), 188. https://doi.org/10.3390/app9010188.
21. Yang, W. F.; Igbari, F.; Lou, Y. H.; Wang, Z. K.; Liao, L. S. *Advanced Energy Materials* **2020**, *10* (13), 1–30. https://doi.org/10.1002/aenm.201902584.
22. Bartel, C. J.; Sutton, C.; Goldsmith, B. R.; Ouyang, R.; Musgrave, C. B.; Ghiringhelli, L. M.; Scheffler, M. *Science Advances* **2018**, *2* (5), 1–10. https://doi.org/DOI: 10.1126/sciadv.aav0693.
23. Jeon, N. J.; Na, H.; Jung, E. H.; Yang, T. Y.; Lee, Y. G.; Kim, G.; Shin, H. W.; Il Seok, S.; Lee, J.; Seo, J. *Nature Energy* **2018**, *3* (8), 682–689. https://doi.org/10.1038/s41560-018-0200-6.
24. Cousins, S. Solar eclipse: Oxford firm develops world's most efficient PV cell https://www.ribaj.com/products/oxford-firm-develops-world-s-most-efficient-solar-cell (accessed Jun 11, 2021).
25. Shockley, W.; Queisser, H. J. *Journal of Applied Physics* **1961**, *32* (3), 510–519. https://doi.org/10.1063/1.1736034.
26. Rühle, S. *Solar Energy* **2016**, *130* (June), 139–147. https://doi.org/10.1016/j.solener.2016.02.015.
27. WHO. World Health Organisation https://www.who.int/news-room/fact-sheets/detail/lead-poisoning-and-health.
28. Babayigit, A.; Ethirajan, A.; Muller, M.; Conings, B. *Nature Materials* **2016**, *15* (3), 247–251. https://doi.org/10.1038/nmat4572.
29. Turkevych, I.; Kazaoui, S.; Ito, E.; Urano, T.; Yamada, K.; Tomiyasu, H.; Yamagishi, H.; Kondo, M.; Aramaki, S. *ChemSusChem* **2017**, *10* (19), 3754–3759. https://doi.org/10.1002/cssc.201700980.
30. Ortiz-Cervantes, C.; Carmona-Monroy, P.; Solis-Ibarra, D. *ChemSusChem* **2019**, *12* (8), 1560–1575. https://doi.org/10.1002/cssc.201802992.
31. Jena, A. K.; Kulkarni, A.; Miyasaka, T. *Chemical Reviews* **2019**, *119* (5), 3036–3103. https://doi.org/10.1021/acs.chemrev.8b00539.
32. Hoefler, S. F.; Trimmel, G.; Rath, T. *Monatshefte fur Chemie* **2017**, *148* (5), 795–826. https://doi.org/10.1007/s00706-017-1933-9.
33. Murphy, C.; Cardello, A. V; Brand, J. G. *Physiology & Behavior* **1981**, *26* (6), 1083–1095. https://doi.org/https://doi.org/10.1016/0031-9384(81)90213-4.
34. Groom, C. R.; Bruno, I. J.; Lightfoot, M. P.; Ward, S. C. The Cambridge Structural Database. https://doi.org/DOI: 10.1107/S2052520616003954.
35. Thétiot, F.; Sasaki, I.; Duhayon, C.; Sutter, J. P. *Journal of Chemical Crystallography* **2009**, *39* (3), 225–227. https://doi.org/10.1007/s10870-008-9511-y.
36. Paton, L. A.; Harrison, W. T. A. *Angewandte Chemie* **2010**, *49* (42), 7684–7687. https://doi.org/10.1002/anie.201003541.
37. Zhang, W. Y.; Tang, Y. Y.; Li, P. F.; Shi, P. P.; Liao, W. Q.; Fu, D. W.; Ye, H. Y.; Zhang, Y.; Xiong, R. G. *Journal of the American Chemical Society* **2017**, *139* (31), 10897–10902. https://doi.org/10.1021/jacs.7b06013.
38. Muhammad azeem, Hong Zhang, Li-Jun Ji, Li-Yuan Dong, Pei-Xiang Lu, Wei Li, J. H. *CSD Private Communication* **2020**.
39. Shi, C.; Yu, H.; Wang, Q.; Ye, L.; Gong, Z.; Ma, J.; Jiang, J.; Hua, M.; Shuai, C.; Zhang, Y.; Ye, H. *Angewandte Chemie* **2020**, *132* (1), 173–177. https://doi.org/10.1002/ange.201908945.
40. Shannon, R. D. *Acta Crystallographica Section A* **1976**, *32* (1), 751–767. https://doi.org/10.1023/A:1018927109487.
41. Muller, U. In *Inorganic Structural Chemistry*; John Wiley & Sons Ltd., 2006; pp 166–180.

42. Azeem, M.; Hong, Z.; Li-Jun, J.; Li-Yuan, D.; Pei-Xiang, L.; Wei, L. *Chinese Journal of Structural Chemistry* **2020**, *39* (1), 174–181. https://doi.org/10.14102/j.cnki.0254-5861.2011-2366.

43. Burbank, R. D.; Evans, H. T. *Acta Crystallographica* **1948**, *1* (6), 330–336. https://doi.org/https://doi.org/10.1107/S0365110X48000867.

44. Tanaka, Y.; Kojima, T.; Takata, Y.; Chainani, A.; Lovesey, S. W.; Knight, K. S.; Takeuchi, T.; Oura, M.; Senba, Y.; Ohashi, H.; Shin, S. *Physical Review B* **2010**, *81* (14), 144104. https://doi.org/10.1103/PhysRevB.81.144104.

45. Glazer, A. M. *Acta Crystallographica Section B* **1972**, *28* (11), 3384–3392. https://doi.org/10.1107/s0567740872007976.

46. Glazer, A. M. *Acta Crystallographica Section A* **1975**, *31* (6), 756–762. https://doi.org/10.1107/S0567739475001635.

47. Søndenå, R.; Stølen, S.; Ravindran, P.; Grande, T.; Allan, N. L. *Physical Review B - Condensed Matter and Materials Physics* **2007**, *75* (18), 184105. https://doi.org/10.1103/PhysRevB.75.184105.

48. López, R.; Gómez, R. *Journal of Sol-Gel Science and Technology* **2012**, *61* (1), 1–7. https://doi.org/10.1007/s10971-011-2582-9.

49. Nowak, M.; Kauch, B.; Szperlich, P. *Review of Scientific Instruments* **2009**, *80* (4), 21–24. https://doi.org/10.1063/1.3103603.

50. Kubelka, P.; Franz, M. *Technical Physics* **1931**, *19* (12), 593–601.

51. Pankove, J. I.; Kiewit, D. A. *Journal of The Electrochemical Society* **1975**, *119* (5), 156. https://doi.org/10.1149/1.2404256.

52. Li, J.; Duan, J.; Yang, X.; Duan, Y.; Yang, P.; Tang, Q. *Nano Energy* **2021**, *80* (October), 105526. https://doi.org/10.1016/j.nanoen.2020.105526.

53. Pooley, D.; Runciman, W. A. *Journal of Physics C: Solid State Physics* **1970**, *3* (8), 1815–1824. https://doi.org/10.1088/0022-3719/3/8/022.

54. Chen, C. H.; McCann, M. P. *Chemical Physics Letters* **1986**, *126* (1), 54–57. https://doi.org/10.1016/0009-2614(86)85115-6.

55. Perkowitz, S. *Optical Characterization of Semiconductors: Infrared, Raman, and Photoluminescence Spectroscopy*; Elsevier, 2012.

56. Symmons, H. F. *Journal of Physics C: Solid State Physics* **1971**, *4* (14), 1945–1957. https://doi.org/10.1088/0022-3719/4/14/009.

57. Tan, Z.; Li, J.; Zhang, C.; Li, Z.; Hu, Q.; Xiao, Z.; Kamiya, T.; Hosono, H.; Niu, G.; Lifshitz, E.; Cheng, Y.; Tang, J. *Advanced Functional Materials*. 2018, p 1801131. https://doi.org/10.1002/adfm.201801131.

58. Sheldrick, G. *Acta Crystallographica Section C* **2015**, *71* (1), 3–8. https://doi.org/10.1107/S2053229614024218.

CHAPTER 5

Results: Piperazinium-Containing Hybrid Halide Perovskites

Chapter 5 is the second results chapter of this study. The crystal structures resulting from the combination of BX-based anions, where B is a monovalent alkali metal ion (Na^+, K^+ or Cs^+) and X is either Cl^-, Br^- or I^- with the piperazinium dication (doubly protonated piperazine) are discussed here. 1D and 3D perovskite structures and one organic-inorganic hybrid structure, not falling in the perovskite category, were obtained for these combinations. In addition, the band gaps and solid-state fluorescence spectra of selected piperazinium-containing 3D perovskites were measured and are reported here.

5.1 Introduction

Over recent years, materials exhibiting the perovskite structure have received much attention from the research community due to their extraordinary electronic properties and structural tuneability.[1–3] The general perovskite formula is ABX_3, where A and B are cations and X an anion, that are combined in a specific ratio that maintains charge neutrality and is schematically depicted in Figure 5.1 (a). The perovskite structure is built from an inorganic BX_6-framework and A-site cations which are located within the framework.

The perovskite mineral was discovered by Gustav Rose in the Ural mountains and named after another mineralogist, Lev Perovski, in the early 1800s.[4] More interestingly, the first perovskite crystals were grown in a lab by Well's in 1892.[5] The first report on the crystal structure (albeit not single crystals) was published in 1945 by an Irish crystallographer, Helen Megaw, who determined the perovskite structural features.[6] Further on, in 1957, Møller determined that this so-called perovskite material had photoelectric properties. Still, at the time, the realisation of what these compounds would amount to nearly 50 years later as a result of these photoelectric properties, did not dawn upon him.[7]

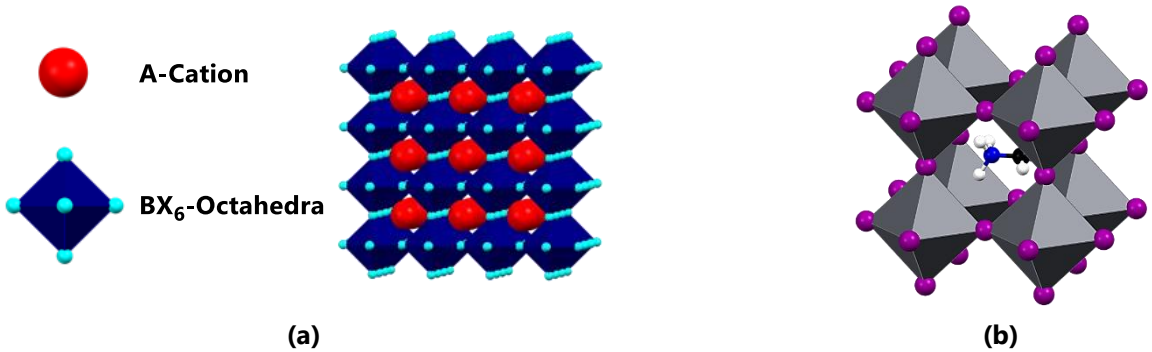

Figure 5.1 The perovskite structure is shown in **(a)** schematically, where the constituents are indicated in the figure and **(b)** a theoretical crystal structure of the cubic 3D perovskite structure of $MAPbI_3$.

In the late 2000s, Miyasaka and Teshima studied organic-inorganic materials as dyes in dye sensitised solar cells, and specifically worked with a hybrid perovskite called methylammonium lead iodide, because of its black colour and hence high visible light absorption.[8–10] The structure consisted of A = $CH_3NH_3^+$, B = Pb^{2+} and X = I^-, and will be abbreviated as $MAPbI_3$, where MA denotes $CH_3NH_3^+$, methylammonium. This specific perovskite, $MAPbI_3$ (methylammonium lead iodide), was first

characterised using powder diffraction methods by Weber in 1978.[11] However, its realisation in optoelectronics came with the work done by Miyasaka and Teshima.[8–10]

The $MAPbI_3$ structure is what is called a 3D perovskite structure that crystallises in different phases depending on the temperature at which the structure is determined, since it may undergo several solid-state phase transitions with a change in temperature.[12] In Figure 5.1 (b), the cubic 3D perovskite phase of $MAPbI_3$ is shown. The lower symmetry phases, such as trigonal, tetragonal, orthorhombic, monoclinic, or triclinic, are associated with the octahedra distorting. Octahedral distortion is characterised by the B–X–B and X–B–X angles deviating from 90° and 180°. For the cubic phase shown in Figure 5.1 (b), these angles are 90° or 180°, and hence the cubic phase is the most symmetrical phase, and the rest are less symmetrical. There exists another class of 3D perovskites called *hexagonal polytypes*, however, they are not applicable here and will not be discussed further.

The 3D perovskite structure may be dimensionally reduced in certain directions to obtain so-called *lower-dimensional* perovskite structures (quasi-3D, 2D, 1D and 0D). One perovskite structure of specific importance in this study is called the 1D ⟨100⟩-type perovskite structure. 2D perovskite structures result from the cutting of the 3D perovskite structure in the ⟨100⟩ set of directions. Then subsequently the resultant 2D ⟨100⟩-type perovskite structure is cut along the {010} set of planes, which finally leads to the 1D ⟨100⟩-type perovskite structure. This 1D structure is characterised by a 1D chain of corner-sharing octahedra extending in one crystallographic direction, shown in Figure 5.2 (a) and the crystal structure of a compound exhibiting this structure $((F_{10}I_6Rb_6Sn_5)_n)$[13] is shown in (b).

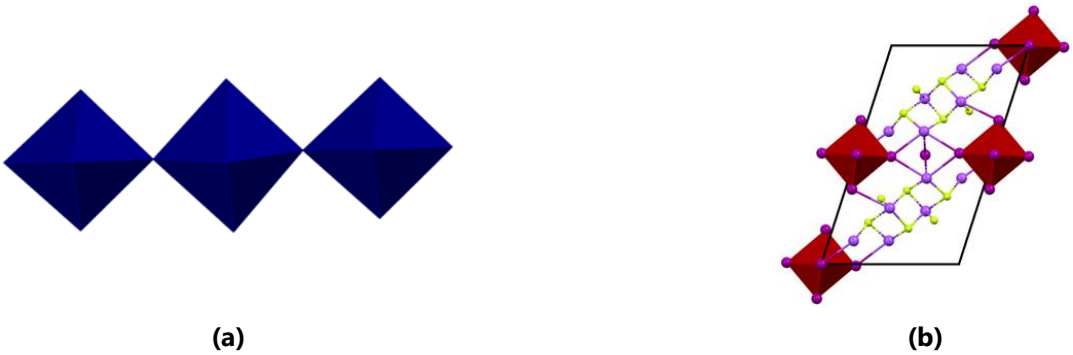

(a) **(b)**

Figure 5.2 The 1D ⟨100⟩-type perovskite structure. **(a)** The octahedra of the 1D ⟨100⟩-type perovskite structure and **(b)** the unit cell (shown in black) for a compound exhibiting the 1D ⟨100⟩-type perovskite crystal structure obtained from literature (ICSD Refcode: 242226) viewed down the *b*-direction along the direction of the octahedral chain.[13]

With the required theory described for the perovskite structure, the following section will place this study into perspective by starting with a literature survey.

5.2 Literature Survey

This study will focus on the perovskite structures that are obtained from the combination of piperazinium dications (defined in the following section) and alkali metal halides. Firstly, information on the organic dication used and the naming scheme employed in this study will be provided.

5.2.1 Naming Scheme

The protonation of both nitrogen atoms of a piperazine molecule results in the formation of a "piperazinium" (piperazine-1,4-diium) dication (+2 charge), which will be referred to as a piperazinium dication in the current chapter. Scheme 5.1 illustrates

the formation of the piperazinium dication from piperazine. The present chapter focuses on structures, band gaps and solid-state fluorescence spectra of compounds obtained by combining these piperazinium cations and metal halide-anions consisting of the monovalent alkali metal ions Na^+, K^+, Rb^+ or Cs^+ and halide ions Cl^-, Br^- or I^-. Rubidium containing structures are reported as obtained from the literature since no rubidium containing materials were synthesised in this study, and hence are considered only in the structural comparison section.

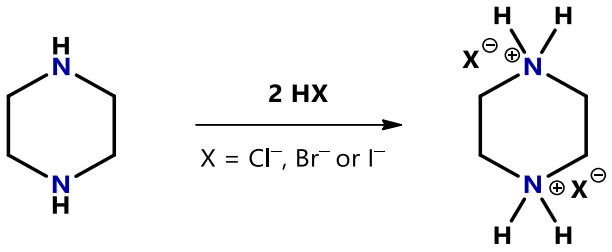

Scheme 5.1 The protonation of piperazine (1,4-diazacyclohexane) using HX (X = Cl^-, Br^- or I^-) to form the diprotonated piperazinium dication.

Structures will be referred to according to the abbreviation of their structural formulas of **P-BX$_n$**. **P** indicates that the dication is piperazinium, with **B** indicating the metal ion, **X** indicating the halide anion, and ***n*** referring to the number of halide ions in the molecular structure. For example, the abbreviation **P-NaCl$_3$** refers to the structure resulting from the combination of piperazine dications and anionic species comprised of NaCl.

5.2.2 Literature Survey: Piperazinium-Containing Alkali Metal Halide Perovskites

A search of the Cambridge Structural Database (CSD (2020, Version 5.42, update May 2021)[14]) indicated that nine structures consisting of the piperazinium dication or monocation and anions comprising monovalent alkali metal ions (Li^+, Na^+, K^+, Rb^+ or Cs^+) and halide anions (Cl^-, Br^- or I^-) have been reported in the literature.

Only one 1D perovskite structure has been reported previously for the combination of piperazinium and monovalent alkali metal halides. The combination of a NaI-based anions and piperazinium results in a 1D ⟨100⟩-type perovskite with CSD refcode: MEXNIP[15] (**P$_3$-NaI$_5$**, space group $P2_1/c$), and crystallises with water molecules and isolated iodide anions as part of the structure. The structure was determined at room temperature (293 K).

Furthermore, a total of six 3D perovskite structures have been reported for the combination of the piperazinium dication with a monovalent alkali metal ion and halide ion. The combination of this dication with a NaI-based anion results in a monoclinic 3D perovskite structure determined at room temperature (293 K), with CSD refcode: MEXMAG[15] (**P-NaI$_3$**, space group $C2/c$). Moreover, at 120 K combinations of the piperazinium dication with a KCl-based anion (refcode: GUYMIX,[16] **P-KCl$_3$**), a KBr-based anion (refcode: MOMLEI,[17] **P-KBr$_3$**), a RbCl-based anion (refcode: GUYMOD,[16] **P-RbCl$_3$**), a RbBr-based anion (refcode: MOMSEP,[17] **P-RbBr$_3$**) and a CsCl-based anion (refcode: GUYMUJ,[16] **P-CsCl$_3$**) all resulted in 3D orthorhombic perovskite structures (space group *Pbcm*) containing isolated water molecules in the structures.

It is interesting to note that the combination of piperazinium dications and NaI-based anions result in either a 1D ⟨100⟩-type perovskite (MEXNIP,[15] **P$_3$-NaI$_5$**) or a 3D perovskite (MEXMAG,[15] **P-NaI$_3$**) structure.

Finally, two 2D organic-inorganic hybrid structures, in an orthorhombic phase (space group *Pbcm*) were reported for the combination of the piperazinium dication with a RbBr-anionic species (**P-Rb$_3$Br$_4$**) and a CsBr-anionic species (**P-Cs$_3$Br$_4$**), with refcodes VONDEK[18] and VONDAG[18] (both determined from data recorded at 93 K) respectively. However, in these structures the cation is mono-protonated. This means that the combination of a RbBr-anionic species and protonated piperazine forms hybrid structures of two different dimensionalities at approximately the same temperature, one being a 3D

perovskite structure containing piperazinium dications (MOMSEP,[17] **P-RbBr$_3$**), while the other (VONDEK,[18] **P-Rb$_3$Br$_4$**), is not classified as a perovskite structure, and has a mono-protonated cation.

The literature survey shows a tendency of the family of structures (piperazinium in combination with alkali metal halide-based anions) to form 3D perovskite structures, however, the perovskite structures that have been reported, were determined at different temperatures. Therefore, in this study the structures will be re-determined at the 150 K. Furthermore, no properties of these materials have been reported. In addition, the study will also focus on the determination of the band gaps and fluorescence spectra of the compounds in the family.

In total five compounds were prepared synthetically, and all were characterised by powder X-ray diffraction (PXRD). In addition, five single-crystal X-ray structures were determined, one of which is new and have not been reported in the literature.

To determine whether a phase transition occurs on cooling, the calculated powder patterns (PXRD patterns) of the single-crystal structures were compared to the powder patterns of the bulk samples measured at room temperature. None of the structures described here underwent phase transitions, as evident from the powder patterns shown in Appendix D. In addition, the purity of the bulk samples used for property measurements was also determined by matching of the experimental and calculated powder X-ray diffraction patterns.

Since a perovskite solar cell is expected to function at room temperature, it is imperative to correlate the band gap values of the different perovskite materials with their crystal structures determined at the same temperature as which the band gaps are measured, and at the temperature at which the device will be used, i.e., room temperature. Thus, the fact that no solid-state phase transitions occur between 150 K and room temperature is important. It is assumed that the crystal structures at room temperature will show the same structural trends as the crystal structures determined at low-temperature in this study, and only small structural changes due to contraction of the structure on cooling are expected. These changes should not affect any general structural trends observed.

The following sections will discuss the findings of this study. The combinations studied here lead to either 1D or 3D perovskite structures, where the 3D perovskite structures were isostructural. One miscellaneous structure was also obtained and is described separately. The available literature is discussed in conjunction with the findings of this study to aid in the identification of structural trends in the families of compounds.

5.3 Perovskite Structures: Crystallographic Results and Discussion

One new 3D perovskite crystal structure combining piperazinium dications with alkali metal halide-anions was determined in the current study. Seven perovskite structures have been reported in the literature for the studied combination, and five of these structures were re-determined at 150 K. The Rb-containing compounds were not included in this study due to the cost of Rb-halide salts. Four compounds were found to exhibit 3D orthorhombic perovskite structures and were isostructural to one another, where the combination of piperazinium and a KI-anionic species delivered a novel structure. The other three structures are the same as those reported in the literature, but determined at a different temperature.

One compound exhibited a 1D perovskite structure, where piperazinium in combination with NaI formed a 1D ⟨100⟩-type perovskite structure and has been reported previously.[15] The combination of piperazinium and NaI also results in a 3D perovskite structure which was not obtained in this study, however, it has been reported in the literature.[15]

This section will be divided into three subsections, with the first section focussing on the 1D perovskite compound, and the second on 3D perovskites. The third section will describe the non-perovskite (miscellaneous) structure also obtained in this study.

Crystallographic parameters of the structures obtained in this study are listed in Table 5.1. Furthermore, selected structural parameters are listed in Table 5.2 for both structures obtained in this study and those described in the literature, which falls into the category of 3D perovskite structures. For example, the literature structures **P-RbCl$_3$**[16] and **P-RbBr$_3$**[17] are included

in Table 5.1 and Table 5.2 for completeness since no Rb-containing structures were investigated in this study. It is also important to note that the structures **P-KCl$_3$**,[16] **P-KBr$_3$**,[17] and **P-CsCl$_3$**[16] have already been described in the literature. However, to allow for the comparison of structures, their structures must be determined at the same temperatures. Therefore, the non-rubidium-containing structures were re-determined in this study at 150 K, and the structures described here are those obtained in this study.

5.3.1 1D Piperazinium-Containing Perovskite Structures

Only one 1D perovskite structure of the ⟨100⟩-type was obtained in this study, and it has been reported previously.[15] This is the structure **P$_3$-NaI$_5$** crystallising in the monoclinic phase with space group $P2_1/c$. Its unit cell is shown in Figure 5.3 (a), (b) and (c), illustrating that the structure crystallises with water molecules and isolated I^--ions in the lattice. The asymmetric unit is also shown in Figure 5.3 (d).

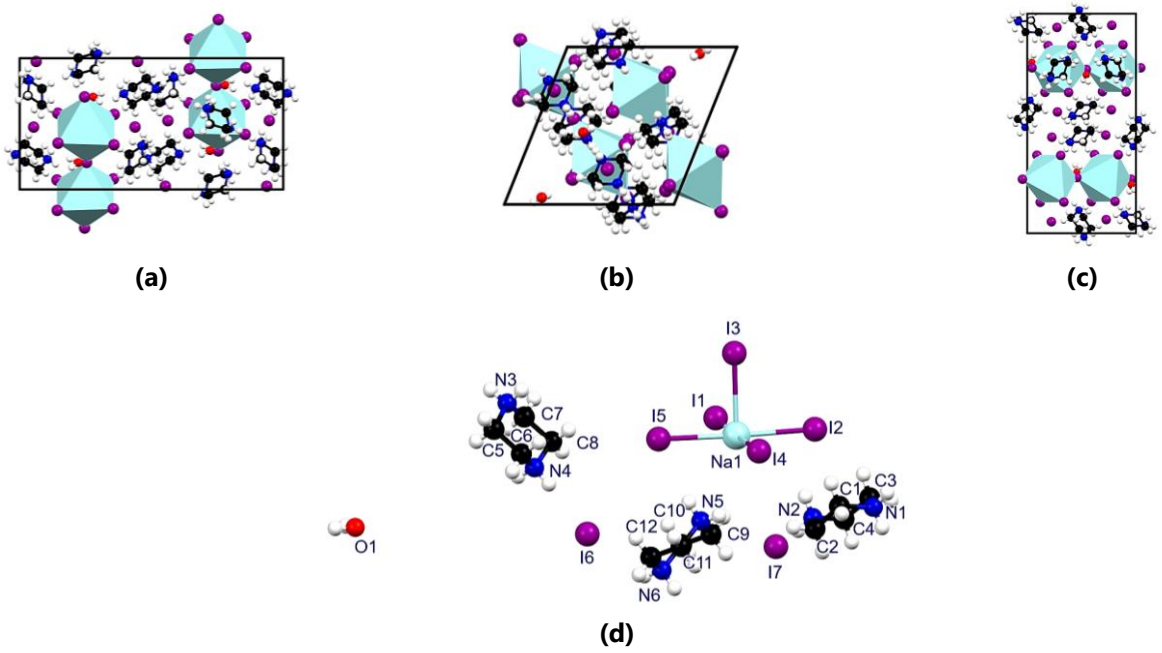

Figure 5.3 The unit cell (shown in black) for the structure **P$_3$-NaI$_5$** as viewed down the **(a)** *a*-direction, **(b)** *b*-direction and **(c)** *c*-direction. **(d)** The asymmetric unit of the structure **P$_3$-NaI$_5$**.

The asymmetric unit of **P$_3$-NaI$_5$** contains three distinct piperazinium dications, a water molecule, two distinct I^--ions and a NaI_5 square pyramidal moiety. Two glide planes in the *ac*-plane combine with 27 rotoinversion axes (distributed throughout the unit cell) and four two-fold screw axes directed along the *b*-direction in the unit cell, form the entire structure.

With only one type of Na-ion present in the structure, the 1D corner-sharing chain of octahedra consists of only one type of NaI_6 octahedron. The octahedra alternate in the inorganic polymer as either slightly tilting upward or tilting downward, illustrated in Figure 5.4 (a) and (b). The I3-ions are the only bridging halides in the structure, with all the other halide ions being terminal or crystallising as separate ions.

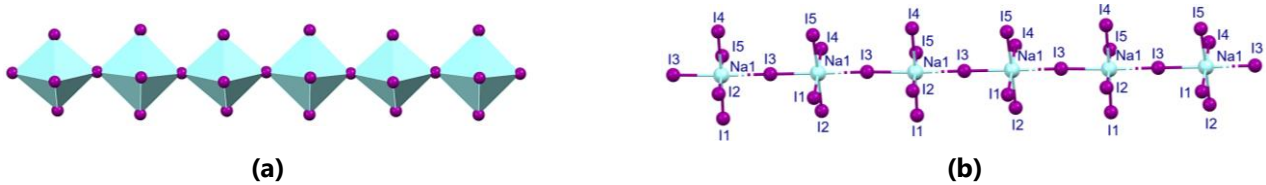

Figure 5.4 (a) The 1D inorganic corner-sharing polymer and **(b)** the illustration of which halide ions participate in which bonding modes in the inorganic polymer.

Furthermore, from Figure 5.4 (b), it is evident that the I3–Na1–I3–Na1⋯ chain continues indefinitely, however, the slight tilting up and down mentioned before is due to I4 swopping with I5 and I1 swopping with I2 in adjacent octahedra.

One interesting aspect of this structure is its hydrogen bonding network, which includes four different types of hydrogen bonding interactions (see Figure 5.5) that also involve the water molecules and isolated iodide ions. Firstly, the piperazinium N–H's act as donors to the oxygen atoms of the water molecules (light blue interactions in Figure 5.5). Secondly, the hydrogen atoms of the water molecules act as donors to the iodide ions in the inorganic chain (pink interactions in Figure 5.5). Thirdly, the piperazinium N–H's act as donors to the iodide ions in the inorganic chain (light green interactions in Figure 5.5). Finally, the piperazinium N–H's also act as the donors to the free iodide ions present in the structure (light grey interactions in Figure 5.5). These interactions are best illustrated by considering the asymmetric unit's hydrogen bonding interactions, as shown in Figure 5.5 (a).

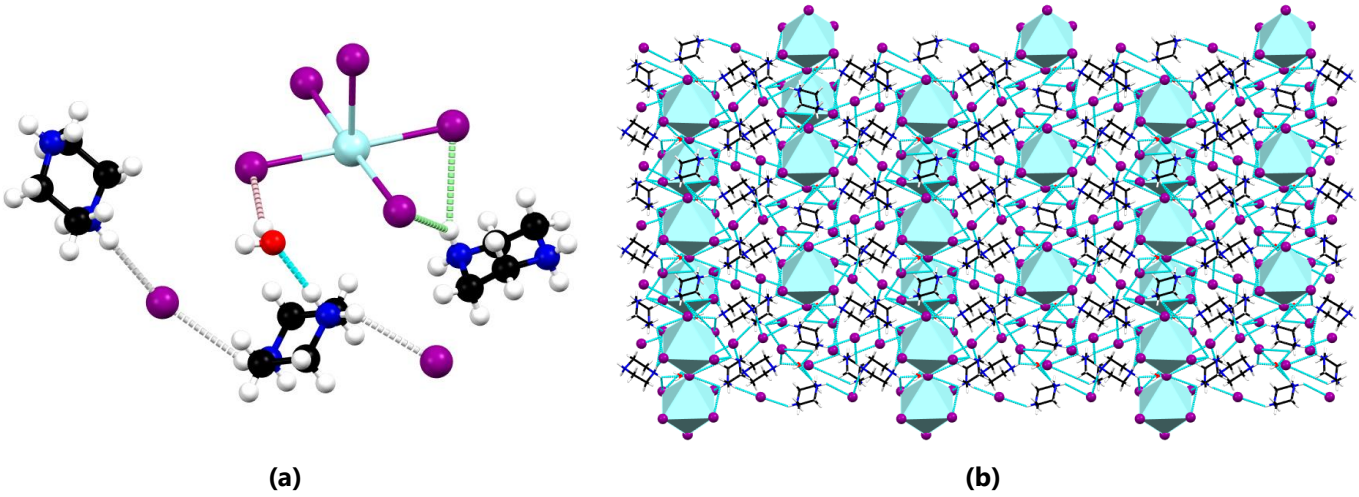

Figure 5.5 (a) The four different hydrogen bonding interactions present in the structure **P_3-NaI_5**. The colours of hydrogen bonds are as defined in the text. **(b)** The 3D hydrogen bonding network (viewed down the *a*-axis) that forms in the structure (all interactions are shown in light blue).

These four hydrogen bonding interactions result in a 3D supramolecular hydrogen bonding network, as illustrated in Figure 5.5 (b). However, for a deeper analysis, the literature regarding this structure may be consulted.[15]

An important note is that this 1D ⟨100⟩-type structure is not the only structure that results from the combination of piperazinium cations and NaI-anions since a 3D perovskite structure has been reported in the literature for this combination. Because it was not obtained in this study, it will not be described here. Its data, however, are listed in Table 5.1 and Table 5.2, yet it is still interesting to know that different structures may be formed from the same constituents. This 3D structure will also be included in the structural comparison.

5.3.2 3D Piperazinium-Containing Perovskite Structures

The combinations of piperazine with KCl, KBr, KI, RbCl, RbBr and CsCl all form 3D perovskite structures which crystallise in the orthorhombic space group *Pbcm*. Since they are all isostructural, they will be discussed together and compared in a later section. Seeing that the structures all crystallise in the orthorhombic crystal system, they are distorted in comparison to the ideal cubic 3D perovskite structure, which crystallises in the $Pm\bar{3}m$ space group.

Table 5.1 Crystallographic parameters for the 1D ⟨100⟩-type and 3D piperazinium-containing perovskite structures.

Structure Abbreviation	**P_3-NaI_5**	**P-NaI_3**[15]	**P-KCl_3**	**P-KBr_3**
Name	*catena*-[tris(piperazine-1,4-diium) (μ_2-iodo)-tetraiodo-sodium diiodide monohydrate]	*catena*-[piperazine-1,4-diium tris(μ_2-iodo)-sodium]	*catena*-[piperazine-1,4-diium tris(μ_2-chloro)-potassium monohydrate]	*catena*-[piperazine-1,4-diium tris(μ_2-bromo)-potassium monohydrate]
Empirical formula	$3n(C_4H_{12}N_2)^{2+}{\cdot}n[I_5Na]^{4-}{\cdot}n(H_2O){\cdot}2n(I)^-$	$n(C_4H_{12}N_2)^{2+}{\cdot}n[I_3Na_2]^-$	$n(C_4H_{12}N_2)^{2+}{\cdot}n[Cl_3K]^{2-}{\cdot}n(H_2O)$	$n(C_4H_{12}N_2)^{2+}{\cdot}n[Br_3K]^{2-}{\cdot}n(H_2O)$
Formula weight (g·mol^{-1})	1193.77	491.85	251.62	384.97
Temperature (K)	150(2)	293	150(2)	150(2)
Wavelength (Å)	1.54184	0.71073	0.71073	0.71073
Crystal system	Monoclinic	Monoclinic	Orthorhombic	Orthorhombic
Space group	$P2_1/n$	$C2/c$	$Pbcm$	$Pbcm$
***a* (Å)**	12.08840(10)	9.842(6)	6.4225(2)	6.6351(2)
***b* (Å)**	22.8522(2)	9.309(6)	12.7451(3)	13.1899(5)
***c* (Å)**	12.10460(10)	12.538(8)	12.7360(3)	13.0852(5)
***α* (°)**	90	90	90	90
***β* (°)**	112.1750(10)	93.450(9)	90	90
***γ* (°)**	90	90	90	90
Volume (Å^3)	3096.53(5)	1146.639	1042.51(5)	1145.17(7)
Z	4	4	4	4
Density calculated (g·cm^{-3})	2.561	2.849	1.603	2.233
Absorption coefficient (mm^{-1})	55.350	8.163	1.234	10.890
***F*(000)**	2168	880	520	736
Crystal size (mm^3)	0.05×0.05×0.07	0.20×0.28×0.38	0.07×0.07×0.13	0.14×0.17×0.18
Reflections collected	34721	3288	22135	7372
Unique Reflections / R_{int}	6444 / 0.0536	1311 / 0.0826	1581 / 0.0328	1548 / 0.0570
Completeness	0.992	0.949	1.000	1.000
Parameters	107	48	66	64
Goodness-of-fit F^2	1.155	1.031	0.857	1.043
Final R indices [I>2σ(I)] (R_1 / wR_2)	0.0958 / 0.2510	0.0575 / 0.0575	0.0211 / 0.0549	0.0373 / 0.1010
R indices (all data) (R_1 / wR_2)	0.0976 / 0.2519	0.0620 / 0.1652	0.0239 / 0.0573	0.0424 / 0.1040

Table 5.1 (Continued) Crystallographic parameters for the 1D ⟨100⟩-type and 3D piperazinium-containing perovskite structures.

Structure Abbreviation	**P-KI$_3$**	**P-RbCl$_3$**[16]	**P-RbBr$_3$**[17]	**P-CsCl$_3$**
Name	*catena*-[piperazine-1,4-diium tris(μ_2-iodo)-potassium monohydrate]	*catena*-[piperazine-1,4-diium tris(μ_2-chloro)-rubidium monohydrate]	*catena*-[piperazine-1,4-diium tris(μ_2-bromo)-rubidium monohydrate]	*catena*-[piperazine-1,4-diium tris(μ_2-bromo)-caesium monohydrate]
Empirical formula	$n(C_4H_{12}N_2)^{2+}{\cdot}n[I_3K]^{2-}{\cdot}n(H_2O)$	$n(C_4H_{12}N_2)^{2+}{\cdot}n[Cl_3Rb]^{2-}{\cdot}n(H_2O)$	$n(C_4H_{12}N_2)^{2+}{\cdot}n[Br_3Rb]^{2-}{\cdot}n(H_2O)$	$n(C_4H_{12}N_2)^{2+}{\cdot}n[Cl_3Cs]^{2-}{\cdot}n(H_2O)$
Formula weight (g·mol^{-1})	525.97	297.99	431.37	345.43
Temperature (K)	150(2)	120(2)	120(2)	150(2)
Wavelength (Å)	0.71073	0.71073	0.71073	0.71073
Crystal system	Orthorhombic	Orthorhombic	Orthorhombic	Orthorhombic
Space group	*Pbcm*	*Pbcm*	*Pbcm*	*Pbcm*
***a* (Å)**	7.0004(2)	6.49270(10)	6.7697(19)	6.6415(2)
***b* (Å)**	13.9506(5)	12.8190(3)	13.414(4)	13.1536(3)
***c* (Å)**	13.6079(5)	12.8837(3)	13.241(4)	12.9042(3)
***α* (°)**	90	90	90	90
***β* (°)**	90	90	90	90
***γ* (°)**	90	90	90	90
Volume (Å^3)	1328.94(8)	1072.31(4)	1202.4(6)	1127.31(5)
Z	4	4	4	4
Density calculated (g·cm^{-3})	2.629	1.846	2.383	2.035
Absorption coefficient (mm^{-1})	7.334	5.320	14.047	3.953
***F*(000)**	952	592	808	664
Crystal size (mm^3)	0.09×0.10×0.13	0.03×0.04×0.30	0.09×0.26×0.34	0.20×0.23×0.25
Reflections collected	7951	10637	10380	13268
Unique Reflections / R_{int}	1415 / 0.0368	1099 / 0.0401	1247 / 0.1037	1634 / 0.0312
Completeness	0.999	0.999	1.000	1.000
Parameters	67	58	58	67
Goodness-of-fit F^2	0.873	1.069	1.154	0.931
Final R indices [I>2σ(I)] (R_1 / wR_2)	0.0175 / 0.0433	0.0185 / 0.0432	0.0444 / 0.0805	0.0167 / 0.0391
R indices (all data) (R_1 / wR_2)	0.0194 / 0.0446	0.0216 / 0.0447	0.0673 / 0.0865	0.0182 / 0.0399

Table 5.2 Selected bond lengths, angles, hydrogen bonding parameters and structural descriptors for the 1D ⟨100⟩-type and 3D piperazinium-containing perovskite structures.

Structure Abbreviation	**P_3-NaI_5**	**P-NaI_3**[15]	**P-KCl_3**	**P-KBr_3**
Organic Cation (A)	Piperazinium	Piperazinium	Piperazinium	Piperazinium
Metal Ion (B)	Na^+	Na^+	K^+	K^+
Halide ion (X)	I^-	I^-	Cl^-	Br^-
Structure Type	1D ⟨100⟩-type Perovskite	3D Perovskite	3D Perovskite	3D Perovskite
Temperature (K)	150(2)	293	150(2)	150(2)
B–X (Å)	3.134(8) 3.168(8) 3.359(8) 3.391(8) 3.401(8) 3.549(8)	3.156(2) 3.325(5) 3.479(5)	3.1651(4) 3.1901(4) 3.2123(4) 3.21523(9) 3.2445(4)	3.2860(11) 3.2963(12) 3.3011(2) 3.3134(11) 3.3524(12)
X–B–X (°)	83.02(19) 86.19(19) 87.7(2) 88.2(2) 88.6(2) 89.0(2) 92.1(2) 92.6(2) 94.0(2) 95.0(2) 174.9(3) 175.8(3) 177.7(3)	84.40(9) 86.15(18) 87.06(9) 87.29(5) 88.41(8) 100.45(19) 166.6(3) 169.12(12)	82.344(7) 83.880(11) 86.916(5) 89.092(11) 91.808(11) 92.968(5) 95.220(11) 97.316(7) 164.015(14) 172.972(17) 179.100(10)	82.75(2) 84.29(3) 86.69(2) 88.38(3) 91.58(3) 93.31(2) 95.75(3) 96.86(2) 164.59(4) 172.67(5) 179.96(4)
B–X–B (°)	175.34(12)	169.12(12) 180	164.998(15) 172.973(17) 175.628(11)	165.86(4) 172.67(5) 175.809(16)
N–H^+···$^-$X–B (Å)	3.427(15) 3.548(15) 3.612(15) 3.720(14) 3.463(16) 3.576(16) 3.705(14) 3.739(15) 3.493(14) 3.580(14) 3.711(13) 3.823(14)	3.628(9) 3.628(10) 3.746(8)	3.1789(8)	3.330(3)
O–H···$^-$X–B (Å)	3.464(13) 3.484(13)	–	3.0477(10) 3.0680(11)	3.191(4) 3.205(4)
N–H^+···$^-$O–H_2 (Å)	2.87(2) 2.88(2)	–	2.805(2)	2.834(3)

Table 5.2 (Continued) Selected bond lengths, angles, hydrogen bonding parameters and structural descriptors for the 1D ⟨100⟩-type and 3D piperazinium-containing perovskite structures.

Structure Abbreviation	**P-KI$_3$**	**P-RbCl$_3$**[16]	**P-RbBr$_3$**[17]	**P-CsCl$_3$**
Organic Cation (A)	Piperazinium	Piperazinium	Piperazinium	Piperazinium
Metal Ion (B)	K^+	Rb^+	Rb^+	Cs^+
Halide Ion (X)	I^-	Cl^-	Br^-	Cl^-
Structure Type	3D Perovskite	3D Perovskite	3D Perovskite	3D Perovskite
Temperature (K)	150(2)	120(2)	120(2)	150(2)
B–X (Å)	3.43354(19)	3.1967(6)	3.3506(19)	3.2879(5)
	3.4761(10)	3.2182(6)	3.3583(10)	3.2964(5)
	3.4882(11)	3.2307(6)	3.3613(19)	3.3033(6)
	3.4909(11)	3.26767(13)	3.3673(15)	3.33190(17)
	3.5391(10)	3.2790(6)	3.4222(15)	3.3695(6)
X–B–X (°)	82.894(17)	80.688(11)	80.79(2)	75.901(11)
	85.40(2)	82.848(16)	83.26(3)	80.635(16)
	86.302(18)	86.162(4)	85.892(17)	84.528(3)
	87.14(2)	88.862(16)	88.00(3)	88.253(17)
	91.24(2)	92.857(16)	92.48(3)	94.523(3)
	93.890(18)	93.570(4)	94.034(18)	95.329(16)
	96.23(3)	95.433(16)	96.26(3)	95.783(17)
	96.636(17)	98.819(11)	98.63(2)	103.188(11)
	164.45(3)	160.59(2)	160.59(4)	151.04(2)
	172.54(4)	171.71(2)	171.26(5)	168.89(3)
	178.37(3)	178.281(8)	179.52(3)	175.964(5)
B–X–B (°)	166.22(3)	161.82(2)	162.11(4)	152.57(2)
	172.54(4)	171.71(2)	171.26(5)	168.89(3)
	176.570(8)	175.64(2)	175.67(3)	176.308(19)
N–H$^+$···$^-$X–B (Å)	3.583(2)	3.1765(14)	3.364(5)	3.1756(14)
O–H···$^-$X–B (Å)	3.404(3)	3.0529(17)	3.253(7)	3.1018(17)
	3.435(3)	3.0899(18)	3.241(6)	3.107(2)
N–H$^+$···$^-$O–H$_2$ (Å)	2.870(2)	2.8345(17)	2.864(6)	2.8571(16)

Asymmetric Unit and Symmetry Operations

The asymmetric units of the isostructural structures **P-KCl$_3$**, **P-KBr$_3$**, **P-KI$_3$**, **P-RbCl$_3$**, **P-RbBr$_3$** and **P-CsCl$_3$** are all similar, with the same symmetry operations leading to the formation of the structures. Figure 5.6 shows the asymmetric unit of structure **P-CsCl$_3$**, which is representative of the rest of the structures in the isostructural series. The asymmetric unit of **P-CsCl$_3$** consist of half a piperazinium dication, which comprises an NH_2–CH_2–CH_2 moiety. Additionally, one water molecule (H_2O) and an $[BX_3]^{2-}$ anion is present, with the three halide ions coordinated to the metal ion. However, all three halide (X) ions, the metal (B) ion and the oxygen atom present in the asymmetric unit, are positioned on point-group elements of the space group *Pbcm*, and hence lie on special positions. Therefore, each of these ions and atom only contributes "half an ion or atom". So, the effective charge of the anion is only –1, which balances with the +1 from the halved piperazinium dication. Four symmetry operations are required to generate the full crystal structure from the asymmetric unit. First, an inversion centre generates the second half of the piperazinium dication. Finally, two two-fold screw axes lying in the *ac*-plane (one in the *a*-direction and the other in the *c*-direction, i.e., they are 90° to one another) and a mirror plane in the *bc*-plane (through Cl3–Cs1–Cl2) generates the inorganic framework, which consists of corner-sharing BX_6 octahedra.

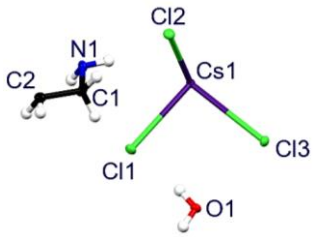

Figure 5.6 The asymmetric unit of the structure **P-CsCl$_3$**, which is representative of the structures **P-KCl$_3$**, **P-KBr$_3$**, **P-KI$_3$**, **P-RbCl$_3$** and **P-RbBr$_3$**.

Unit Cell Description and Isostructurality

These isostructural structures all crystallise in the orthorhombic crystal system with space group *Pbcm*, having similar unit cell parameters and display a similar packing of ions in the unit cell, as illustrated in Figure 5.7 (a), (b) and (c) for the structure **P-CsCl$_3$**, which is representative of the rest of the isostructural structures. Each unit cell is comprised of four of the asymmetric units described in the previous section.

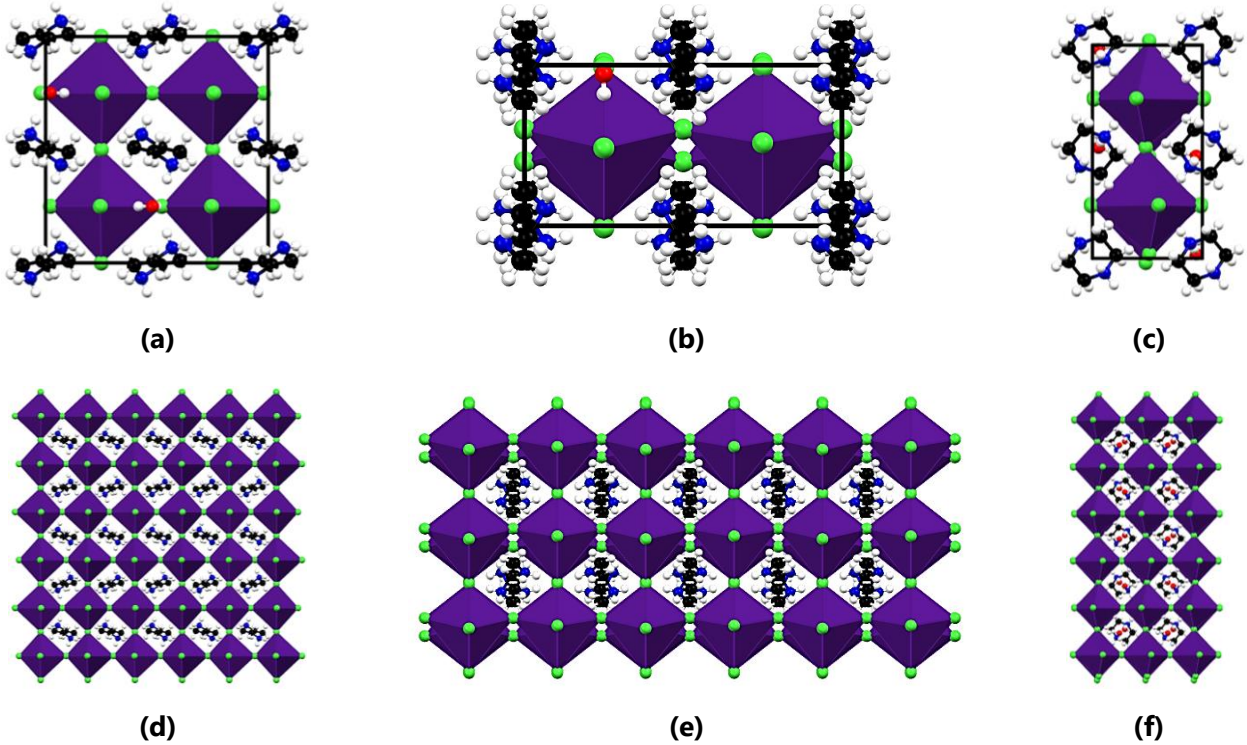

Figure 5.7 The unit cell of structure **P-CsCl$_3$** as viewed down the **(a)** *a*-direction **(b)** *b*-direction and **(c)** *c*-direction. A 3×3 expansion of the unit cell of structure **P-CsCl$_3$** as viewed down the **(d)** *a*-direction **(e)** *b*-direction and **(f)** *c*-direction. The structure **P-CsCl$_3$** is representative of the structures **P-KCl$_3$**, **P-KBr$_3$**, **P-KI$_3$**, **P-RbCl$_3$** and **P-RbBr$_3$**.

The structures all contain corner-sharing octahedra (BX_6 with B = K^+, Rb^+ or Cs^+ and X = Cl^-, Br^- or I^-), which enclose a piperazinium dication in a metal halide cage (inorganic cage). The inorganic cage with central organic cation can be seen as an $a\times2b\times2c$ supercell, which contains two halves of a water molecule (i.e., one water molecule in total) in the *ab*-plane, as illustrated by the red atoms in Figure 5.7. This packing motif is extended in the three crystallographic directions (*a*, *b*, and *c*) as shown in Figure 5.7 (d), (e) and (f), respectively, forming the 3D perovskite structure in its orthorhombic phase.

Figure 5.8 shows $a\times2b\times2c$ supercells for the structures obtained in this study and the literature structures **P-RbCl$_3$** and **P-RbBr$_3$**. This supercell is otherwise known as a perovskite building block since the entire perovskite structure may be built from it. It is evident that the piperazinium dication adopts a stable chair conformation and occupies the central position in the inorganic framework cage. The water molecules occupy square sites (in a B_4X_4 plane) in the *ab*-plane (between four BX_6 octahedra), or more precisely, they pack in the {110} set of Miller planes.

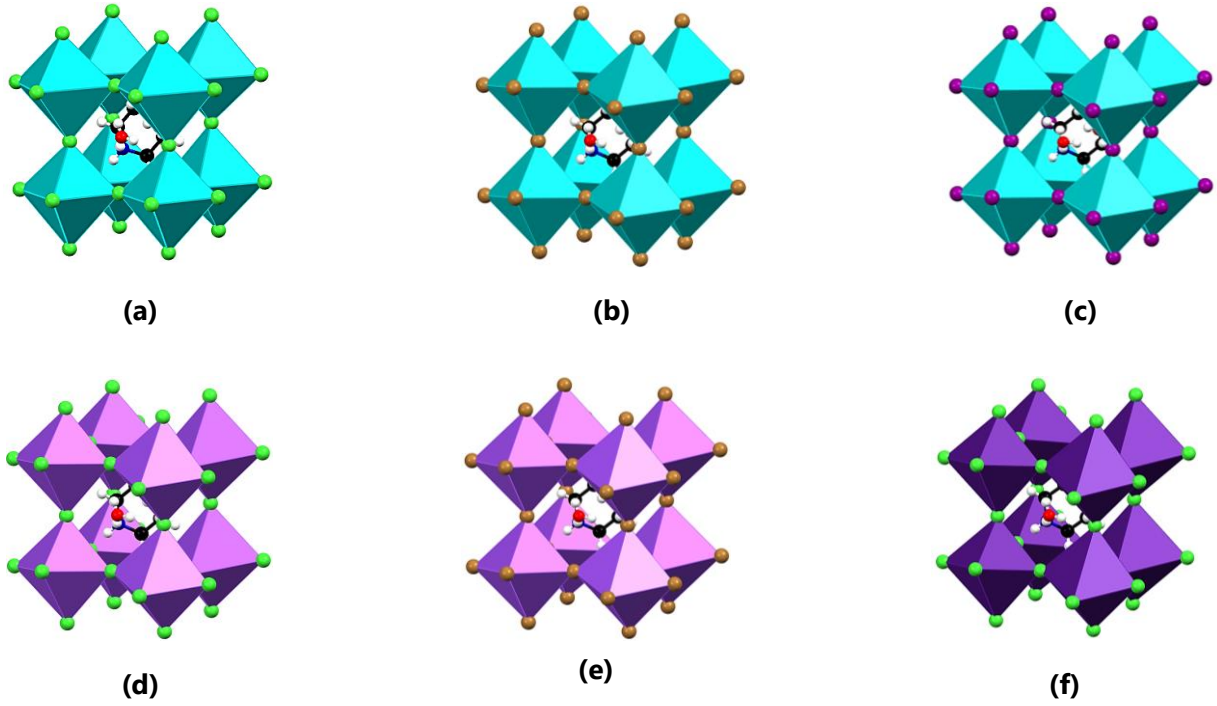

Figure 5.8 Super cell depiction ($a\times2b\times2c$) of structure **(a) P-KCl$_3$**, **(b) P-KBr$_3$**, **(c) P-KI$_3$**, **(d) P-RbCl$_3$**, **(e) P-RbBr$_3$** and **(f) P-CsCl$_3$**.

As shown in Figure 5.8, each piperazinium dication and the associated water molecules are contained in a "box" or "cage" formed by the inorganic framework. The species accommodated in the "box" should be of a specific size to result in a stable 3D perovskite structure. If the species to be fitted inside the box are too large or too small, a 3D perovskite structure cannot be formed.

What is unique in the current series of structures, is the incorporation of water molecules in the piperazinium-containing structures. This is observed for all the piperazinium-containing perovskite structures determined in the present study, as well as the structures reported in the literature, except for the 3D perovskite structure **P-NaI$_3$** (CSD refcode MEXMAG).[15] Since water is typically used as a solvent in this study, water molecules are always available during crystallisation, however, when considering the results reported in Chapter 4, which focused on the dabconium-containing structures, the results showed that no water molecules were included in the dabconium-containing structures, even though water molecules were available.

The incorporation of water molecules in the piperazinium-containing structures can be explained by considering the size of the piperazinium dication compared to the dabconium dication. With a comparative absence of a CH_2-CH_2 moiety, the size and shape of the piperazinium dication are significantly different from that of the dabconium dication. The dabconium dication is approximately spherical in shape, whereas the piperazinium dication is smaller and approximately disc-shaped (when in its chair conformation). The shape and size of the piperazinium dications are therefore not optimal to fit into the "cage" of the

3D perovskite structure since it is too small, especially when the ionic radius of the metal ion is larger (according to the tolerance factor). As a result, water molecules are included in the structure to fill the additional space in the cage. Even though a 3D perovskite structure of a piperazinium-containing 3D perovskite without water molecules in the structure has been reported in the literature, namely structure **P-NaI$_3$** (MEXMAG),[15] the formation of this anhydrous structure is probably the result of the small radius of the Na^+-ion and as a result a smaller inorganic "cage". This will be described in more detail in the structural comparison section.

Octahedral Tilt Angles

Glazer[19,20] developed a system by which the tilting of octahedra in perovskite structures can be described using three descriptors. According to the octahedral tilt description developed by Glazer, the structures **P-KCl$_3$**, **P-KBr$_3$**, **P-KI$_3$**, **P-RbCl$_3$**, **P-RbBr$_3$**, and **P-CsCl$_3$** have polyhedra belonging to the $a^+b^-c^+$ category.[19,20] This classification implies that the inorganic frameworks of the structures are severely distorted (or that the octahedra are *tilted*) since three unique non-uniform tilts are observed in the three crystallographic directions (see Figure 5.9). Figure 5.9 (a) shows the in-phase tilt (subsequent octahedra are tilted either all to the right or left) as observed in the *a*-direction, while Figure 5.9 (b) shows the out of phase tilts (subsequent octahedra are tilted one up and the next down) observed in the *b*-direction. Finally, Figure 5.9 (c) shows the in-phase tilt (subsequent octahedra are either all tilted to the left or right) observed in the *c*-direction. However, special mention should be made of the tilt in the *b*-direction, as it is by far the most excessive tilt of the three. This aspect is further highlighted in the section focussing on hydrogen bonding.

Considering that the ideal cubic perovskite structure would have ideal octahedral arrangements for its BX_6 octahedra, a measure of the distortion of a structure can be obtained from an investigation of the BX_6 octahedra geometries (i.e., how close to 90° and 180° the X–B–X angles are), and the deviation of these geometries from the ideal octahedral geometry. The X–B–X angles indicate the degree of distortion in an octahedron, with X–B–X angles that differ significantly from 90° and 180°, indicating a highly distorted structure.

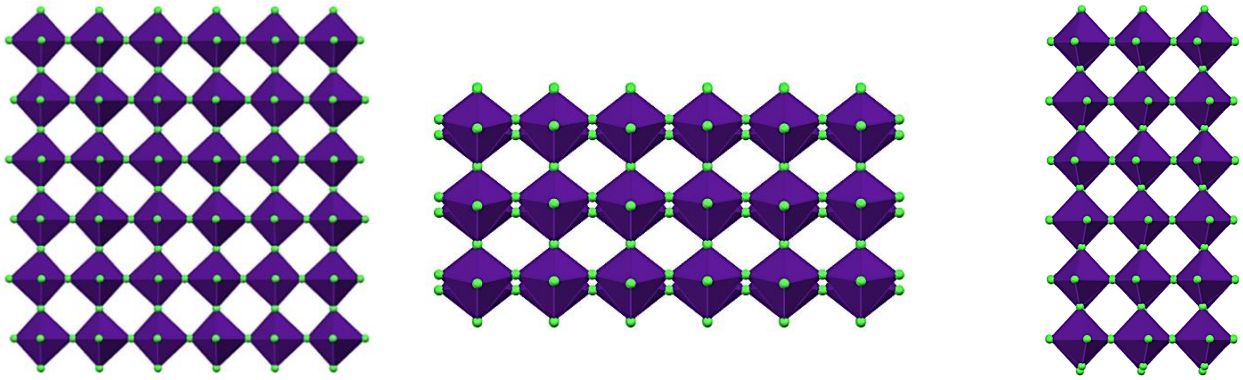

(a) **(b)** **(c)**

Figure 5.9 The inorganic octahedra of structure **P-CsCl$_3$** as viewed down the **(a)** *a*-axis, **(b)** *b*-axis and **(c)** *c*-axis, indicating the assignment of the $a^+b^-c^+$ tilt system. The structure **P-CsCl$_3$** is representative of the structures **P-KCl$_3$, P-KBr$_3$, P-KI$_3$, P-RbCl$_3$** and **P-RbBr$_3$**.

Firstly, the three structures, **P-KCl$_3$**, **P-KBr$_3$** and **P-KI$_3$**, will be considered. Here the trend in X–B–X angles is subtle, however, still present, as can be seen from the values listed in Table 5.2. As the ionic radius of the halide ion increases (from Cl^- to Br^- to I^-), the X–B–X angles all tend towards 90° and 180°.

The rubidium containing structures (structures **P-RbCl$_3$** and **P-RbBr$_3$**) show a similar trend with increasing ionic radius of the halide ion as the potassium group, approaching a more perfectly arranged octahedral framework in structure **P-RbBr$_3$**, with the X–B–X angles closer to the ideal arrangement than in structure **P-RbCl$_3$**.

When considering all six isostructural structures, **P-KCl$_3$**, **P-KBr$_3$**, **P-KI$_3$**, **P-RbCl$_3$**, **P-RbBr$_3$** and **P-CsCl$_3$**, a general trend in X–B–X angles is not as clear. That said, as can be seen from the values in Table 5.2, structure **P-KI$_3$** has, for each unique X–B–X angle, values closest to the ideal values of 90° and 180°. Hence, structure **P-KI$_3$** exhibits the least amount of octahedral tilting of the six isostructural structures, with the structure **P-KBr$_3$** showing the second least amount of tilting. This same trend as observed for the X–B–X angles can be seen in the B–X–B angles, where the structure with B–X–B angles closest to 180° is structure **P-KI$_3$**, which further implies that it is the least tilted structured described here. Structure **P-CsCl$_3$** has X–B–X angles deviating the most from the ideal values, thus displaying the most distortion in the inorganic framework.

Dication Packing

As stated earlier, the piperazinium dication occupies the central position in the inorganic cage whilst adopting a chair conformation. Furthermore, as illustrated in Figure 5.10 (a) and (b), cations in neighbouring rows alternate in orientation. Figure 5.10 (c) and (d) shows two neighbouring rows of cations viewed down the *a*- and *c*-axes, indicating the alternation in orientation.

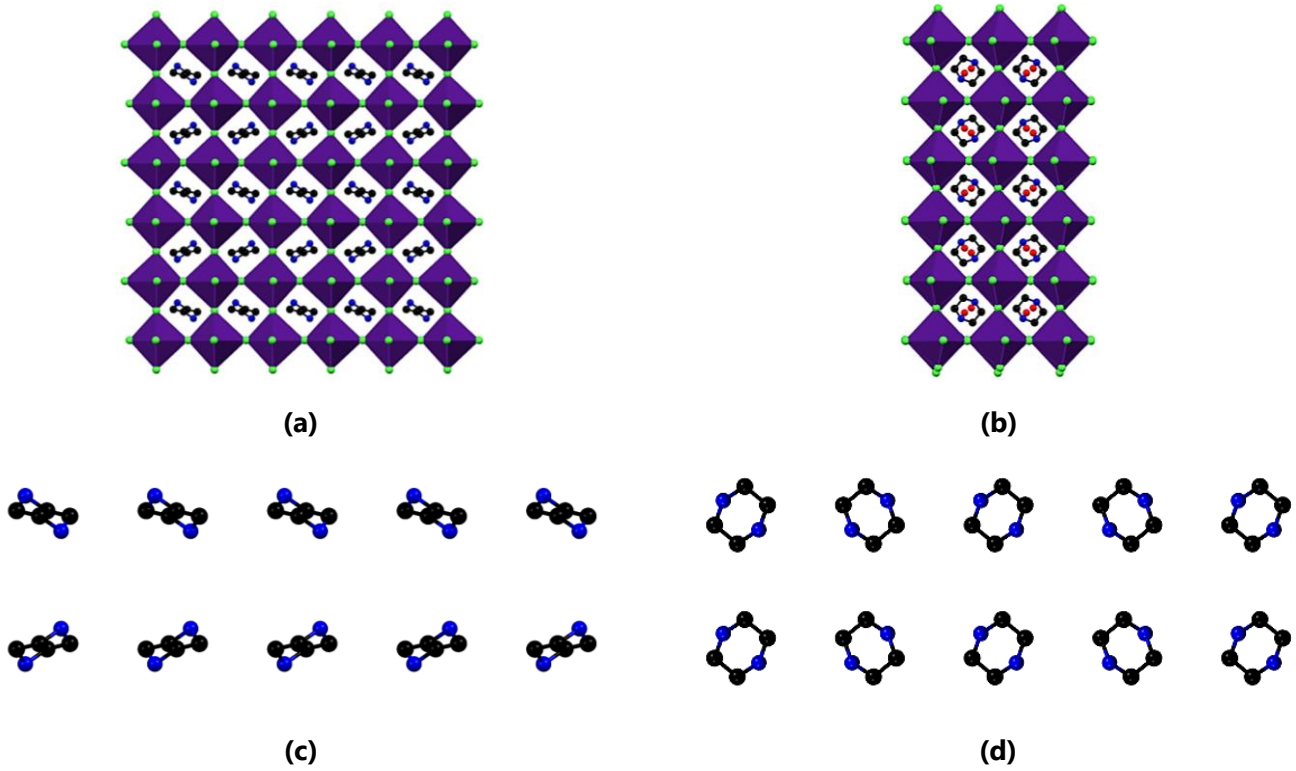

Figure 5.10 A 3×3 expansion of the unit cell of structure **P-CsCl$_3$** as viewed down the **(a)** *a*-axis and **(b)** the *c*-axis. Two rows of cations present in the structure **P-CsCl$_3$** packed in the *b*-direction as viewed down the **(c)** *a*-axis and **(d)** the *c*-axis. The structure **P-CsCl$_3$** is representative of the structures **P-KCl$_3$**, **P-KBr$_3$**, **P-KI$_3$** and **P-RbCl$_3$**. Hydrogen atoms were omitted for clarity.

In combination with the different orientations of the organic dication, hydrogen bonds lead to differing B–X–B angles, distorting the structure, as discussed below.

Hydrogen Bonding Networks

Strong, charge assisted hydrogen bonding interactions are present in the isostructural structures, and these interactions play an important role in the cohesion of the structure. Hydrogen bonding parameters are listed in Table 5.2. Each piperazinium dication participates in four hydrogen bonding interactions, with two hydrogen bonds anchoring the dication to two bridging halides in the inorganic cage, one on each side of the dication. At the same time, two hydrogen bonds occur from each dication to the oxygen atoms of two different water molecules, one on each side of the dication. Each water molecule participates in three hydrogen bonding interactions in total, with each water molecule accepting a hydrogen bond from a dication and forming two hydrogen bonds to two different bridging halide ions in the inorganic framework. Note that the bridging halide ions accepting hydrogen bonds from the dication, and the water molecules are not the same halide ions in the framework, as illustrated in Figure 5.11.

Figure 5.11 shows the hydrogen bonding interactions present in the structure of **P-CsCl$_3$**. Three different types of hydrogen bonds are present in the structure of **P-CsCl$_3$** and its isostructural family, namely, two N–H$^+$···$^-$Cl–Cs, two N–H$^+$···O and four O–H···$^-$Cl–Cs hydrogen bonding interactions, per unit cell. Considering Figure 5.11 (a) and (b), it is evident that the piperazinium dication adopts a position and orientation in the inorganic framework that is the optimal orientation for the formation of the described hydrogen bonds.

Furthermore, the formation of hydrogen bonding interactions in the structures results in the distortion of the inorganic framework. This distortion is evident when considering the B–X–B angles in the structures, with B–X–B angles listed in Table 5.2. However, considering Figure 5.11 (c), (d) and (e), there are different degrees of distortion in B–X–B angles, and only the X–B–X angles where the bridging halide ion is a hydrogen bonding acceptor from the N–H$^+$ group of the cation , are distorted significantly from linearity. The B–X–B angles involving the halide ions that accept hydrogen bonds from water molecules are not significantly distorted. In the view down the *b*-axis (Figure 5.11 (d)), it can be seen that there is a distortion of the B–X–B angles when the bridging halide ion accepts a hydrogen bond from the cation, to position the halide ion in an ideal position for the formation of the hydrogen bond, whereas, in the views down the *a*- and *c*-axes (Figure 5.11 (c) and (e) respectively), the B–X–B angles tend to be less distorted (closer to the ideal 180° and 90°), as they accept hydrogen bonds from the water molecules. Thus, the hydrogen bonds formed by the water molecules distort the B–X–B angles to a lesser degree than the hydrogen bonds involving the cations, with B–X–B bonds involving the water molecules ranging from 168.82(3)° to 176.570(8)°, whereas the B–X–B bonds involving the cations lie in the range of 153.04(3)° to 164.998(15)°.

This can be explained by the positioning of the species involved in hydrogen bonding in the structures. As described previously, the water molecules act as "space fillers" in the structure, due to the smaller size of the piperazinium dication, with one water molecule packing on each "flat side" of the piperazinium dication. The shape of this "water-cation" unit that packs inside an "inorganic box" is illustrated in Figure 5.11 (f), (g) and (h), and it is evident that this unit does not have a spherical shape. Instead, the unit has protrusions where the water molecules are, allowing these molecules to be closer to the inorganic framework, thus requiring less distortion of the B–X–B angles to form hydrogen bonds, compared to hydrogen bonds formed from the cations to the inorganic framework.

Moreover, a correlation is observed between the length of the hydrogen bond and the degree of distortion of the B–X–B angles. For the structures **P-KCl$_3$**, **P-KBr$_3$** and **P-KI$_3$**, there is an increase in hydrogen bond length and an increase in B+X ionic radii as the size of the halide ion increases, with the B–X–B angles tending more towards 180° and 90° as the size of the halide ion increases. Thus, the smaller the sum of the ionic radii, and the smaller the halide ion, the larger the deviation of B–X–B angles from linearity when the bridging halide ion accepts a hydrogen bond from the cation, in the isostructural series.

However, comparing the structure **P-RbCl$_3$** to structure **P-RbBr$_3$** and subsequently to structure **P-CsCl$_3$**, the distortion again becomes more pronounced (see Table 5.2 for specific values). Hence its seems that the least amount of distortion is present in the structure **P-KI$_3$**. Simply put, the structure of **P-KI$_3$** requires the least amount of distortion of the inorganic framework to accommodate the dications and water molecules and to allow for hydrogen bond formation of all the structures in this family. This will be further expanded on in the structural comparison section.

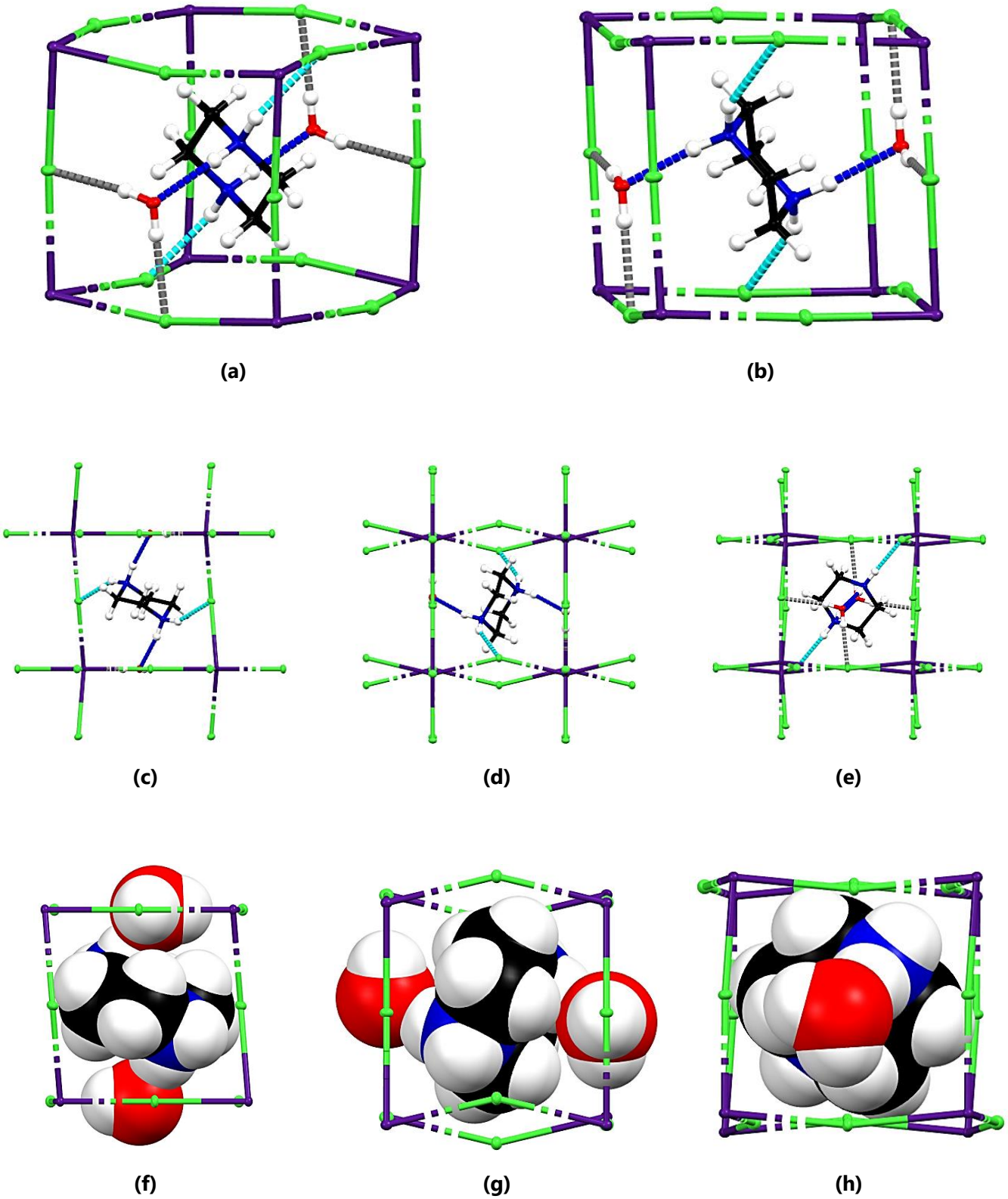

Figure 5.11 Hydrogen bonding network of structure **P-CsCl$_3$**. Three different types of hydrogen bonds are present where N–H$^+$···O hydrogen bonds are shown as blue dotted lines, while N–H$^+$···$^-$Cl–Cs hydrogen bonds are shown as light blue (cyan) dotted lines and O–H···$^-$Cl–Cs hydrogen bonds are shown as grey dotted lines. Figures **(a)** and **(b)** show two different orientations of the piperazinium dication in an inorganic cage with hydrogen bonds indicated while Figures **(c)**, **(d)** and **(e)** show the caged organic dication and Figures **(f)**, **(g)** and **(h)** show space filled visualisation of the same cages as viewed down the *a*-, *b*- and *c*-directions, respectively. The structure **P-CsCl$_3$** is representative of the structures **P-KCl$_3$**, **P-KBr$_3$**, **P-KI$_3$** and **P-RbCl$_3$**.

5.4 Miscellaneous Structure: Results and Discussion

In this study, the perovskite structures formed from the alkali metal halides NaX, KX and CsX are of interest. The results obtain show that only combinations of piperazinium with NaI-, KCl-, KBr-, KI- and CsCl-based anions resulted in perovskite structures. That said, the combinations of piperazinium with NaCl, NaBr, CsBr and CsI were all tested, yet always resulted in mixtures of piperazinium salts containing water and the inorganic metal salt, as shown by the PXRD patterns in Appendix D.

Nevertheless, one structure that was neither an organic or inorganic salt was obtained from one of the reactions that yielded mostly a mixture of the metal halide salt and piperazinium salt. The unique and interesting nature of the structure warrants its inclusion and discussion here, even though it is not a perovskite structure. In an attempt to combine piperazinium and NaBr, the structure shown in Figure 5.12 (a), containing unique trigonal bipyramidal coordinated Na-ions was obtained. This structure is coded **P-NaBr$_2$**. It should be noted that, as illustrated in Figure 5.12 (c), the powder pattern calculated from structure **P-NaBr$_2$** does not match the powder pattern obtained for the bulk sample, meaning that the crystal structure reported here is not representative of the bulk sample.

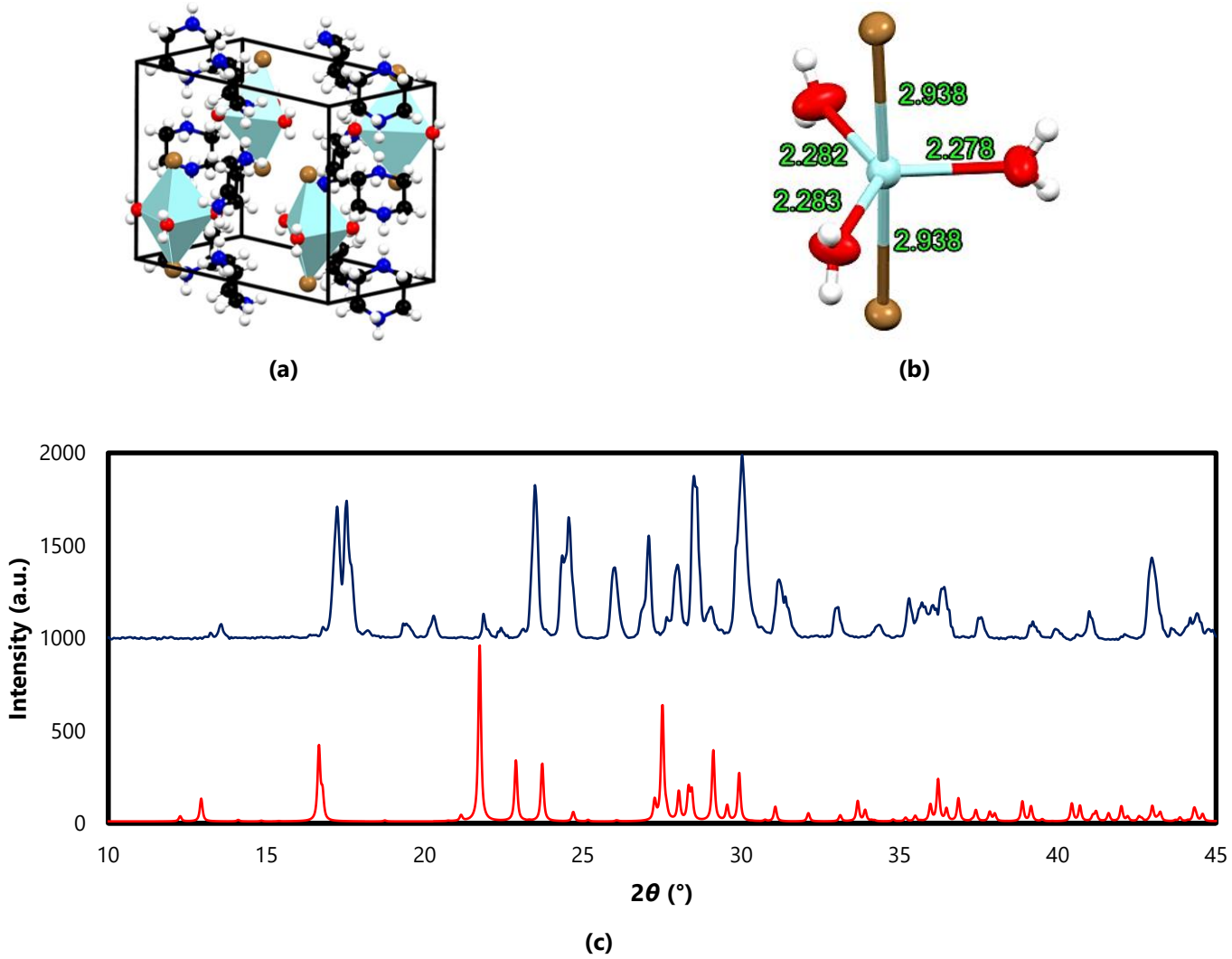

Figure 5.12 The crystal structure obtained from the combination of piperazinium and NaBr. **(a)** The unit cell viewed in an arbitrary direction and **(b)** the trigonal bipyramidal coordinated Na^+-ion. **(c)** The powder pattern of the bulk sample (blue) compared to the calculated pattern (red) of the structure **P-NaBr$_2$**. Distances indicated in (b) have units of Å.

The asymmetric unit of the structure comprises half a piperazinium cation and half a $NaBr_2(OH_2)_3^-$-anion, with the oxygen atoms and Na^+-ion lying on a mirror plane. The structure contains singly protonated piperazine cations and isolated, trigonal

bipyramidally coordinated $NaBr_2(OH_2)_3^-$-anions and crystallises in the orthorhombic space group *Pnma*. To account for charge neutrality, each hydrogen atom of an N–H group was modelled with an occupancy of 0.5, hence on average mono-protonated piperazine is present in the structure. Furthermore, the powder pattern (shown in Figure 5.12 (c)) shows that the structure crystallises in the far minority compared to the bulk sample, and hence no further analysis was conducted on it.

A search of the CSD (CSD (2020, Version 5.42, update May 2021)[14]) was carried out find structures containing isolated anions of the type $BX_2(H_2O)_3^-$, thus anions similar to the anion present in structure **P-NaBr$_2$**, and no hits were found, indicating the uniqueness of this structure. Thus, structure **P-NaBr$_2$** contains anion of the type $BX_2(H_2O)_3^{n-}$ that has never been reported previously, for any metal ion or halide ion. Structures containing octahedral anions of the type $BX_2(H_2O)_4^{n-}$, $BX_2(H_2O)_4^{n-}$ or $BX_3(H_2O)_3^{n-}$, where *n* indicates the charge of the anion, are much more common in the CSD, with a search indicating 30 structures containing anions of the first type $BX_2(H_2O)_4^{n-}$, 54 structures containing anions of the second type and 21 structures containing anions of the type $BX_3(H_2O)_3^{n-}$. Trigonal bipyramidal anions of the type $BX_3(H_2O)_2^{n-}$, $BX_2(H_2O)_4^{n-}$ or $BX_4(H_2O)^{n-}$ are quite rare, but have been reported, with 9 structures containing the anion type $BX_3(H_2O)_2^{n-}$ found in the CSD, 2 containing the anion type $BX(H_2O)_4^{n-}$ and 4 structures containing the $BX_4(H_2O)^{n-}$ type. The purpose of the CSD searches was to investigate the ubiquity or not of structures containing these types of anions, hence the details of the specific structures are not important.

Another interesting feature of structure **P-NaBr$_2$** is the complex hydrogen bonding network formed by the cationic and anionic species. $N–H^+\cdots{}^-X–B$, $N–H^+\cdots O$ and $O–H\cdots{}^-X–B$ charge assisted hydrogen bonds are present in the structure. The anions form a 2D hydrogen bonded sheet, as illustrated in Figure 5.13 (a), with neighbouring anionic sheets connected by hydrogen bonds between anions and from the cations, as shown in Figure 5.13 (b), two form a 3D hydrogen bonded network.

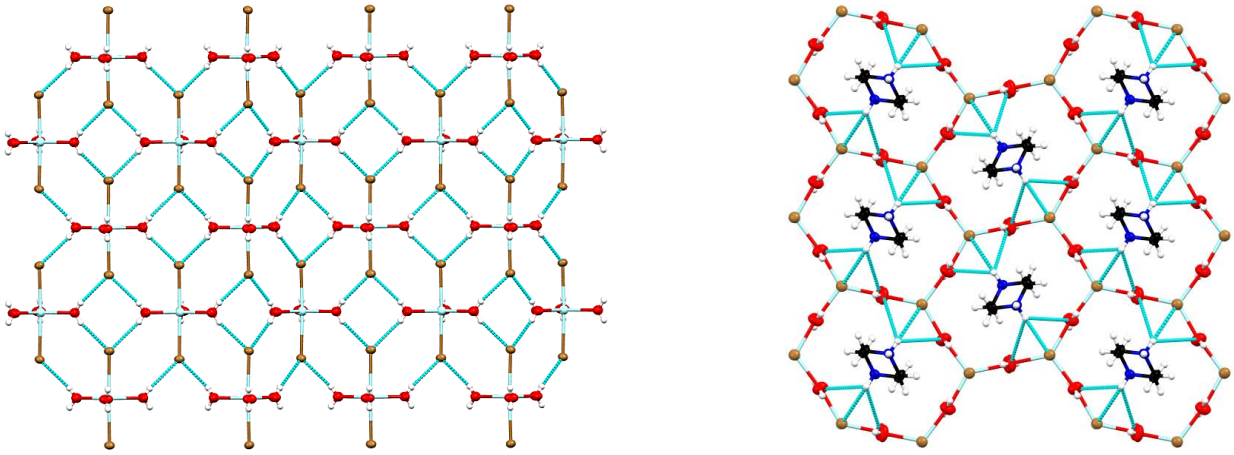

(a) **(b)**

Figure 5.13 (a) The 2D hydrogen bonded sheet and **(b)** the 3D hydrogen bonded network of the structure **P-NaBr$_2$**. Hydrogen bonding interactions are indicated as blue dashed lined.

The discussion will now move to the structural comparison of the perovskite structures obtained in this study and those reported in the literature for structures comprised of piperazinium dications and alkali metal halide anions.

5.5 Structural Comparison and Discussion

In this section, the eight perovskite structures described in this chapter will be compared to identify structural trends. Since six of the eight structures are isostructural, they will enjoy the most attention in the discussion.

5.5.1 Comparison of Inorganic Frameworks

The distortion in an octahedron (BX_6) can be calculated using different parameters, such as B–X bond lengths, B–X–B angles, B···B distances etc., and then evaluating their range (spread of the data) as shown in Equation (5.1)

$$\Delta P = \frac{1}{N}\sum_{n=1}^{N}\left[\frac{P_n - P_{\text{avg}}}{P_{\text{avg}}}\right]^2 \tag{5.1}$$

where P_{avg} is the average parameter value and P_n are the individual parameter values.

Table 5.3 lists the spread of different structural parameters B–X (Δd), B···B (ΔB···B) and B–X–B (ΔB–X–B) of the octahedra, with the sum of the ionic radii of the B and X constituents of the structures. The structures determined at 150 K (where available) were analysed. Only for structure **P-NaI$_3$**, the room temperature data had to be used since the room temperature structure is published in the literature, and the structure was not re-determined in this study. In the last two columns of Table 5.3, the terms "Equatorial" and "Axial" are used. These angles do not refer to the traditional axial and equatorial positions, but rather equatorial angles refer to angles that are close to 90°, and axial angles refer to angles that are close to 180° since the assignment of axial and equatorial ligands in the octahedra would be arbitrary. The "Average Spread" parameter is the average of the four separate spread parameters. Also, Δd refers to the spread in B–X bond lengths.

Table 5.3 Spread of structural parameters and other structural information for piperazinium-containing perovskite structures.

Structure	B+X Ionic Radii (pm)	Δ*d* (Å)	Δ(B–X–B) (°)	Δ(X–B–X) (°)		Average Spread	Contains Water?	Phase	Space Group
				Equatorial	Axial				
P$_3$-NaI$_5$	322	1.4×10^{-3}	0	1.1×10^{-3}	8.2×10^{-6}	6.3×10^{-4}	Yes	Monoclinic	$P2_1/n$
P-NaI$_3$	322	1.6×10^{-3}	9.7×10^{-4}	3.5×10^{-3}	5.6×10^{-5}	1.2×10^{-3}	No	Monoclinic	$C2/c$
P-KCl$_3$	319	6.9×10^{-5}	7.0×10^{-4}	3.1×10^{-3}	1.3×10^{-3}	1.3×10^{-3}	Yes	Orthorhombic	*Pbcm*
P-KBr$_3$	334	4.8×10^{-5}	5.9×10^{-4}	1.7×10^{-3}	1.3×10^{-3}	9.2×10^{-4}	Yes	Orthorhombic	*Pbcm*
P-KI$_3$	358	9.4×10^{-5}	6.2×10^{-4}	3.0×10^{-3}	1.1×10^{-3}	1.2×10^{-3}	Yes	Orthorhombic	*Pbcm*
P-RbCl$_3$	333	9.0×10^{-5}	1.2×10^{-3}	4.4×10^{-3}	1.8×10^{-3}	1.9×10^{-3}	Yes	Orthorhombic	*Pbcm*
P-RbBr$_3$	348	5.8×10^{-5}	1.1×10^{-3}	4.4×10^{-3}	2.1×10^{-3}	1.9×10^{-3}	Yes	Orthorhombic	*Pbcm*
P-CsCl$_3$	348	4.2×10^{-4}	3.4×10^{-3}	8.8×10^{-3}	3.8×10^{-3}	4.1×10^{-3}	Yes	Orthorhombic	*Pbcm*

From Table 5.3, it is apparent that the 1D ⟨100⟩-type structure **P$_3$-NaI$_5$** is the structure with the least distorted octahedra. This makes a lot of sense since it is basically an endless chain of octahedra connected with one bridging halide, and so there should be a minor amount of distortion. Unfortunately, this structure is the only 1D structure, so it is difficult to directly compare it to the 3D perovskites, except for **P-NaI$_3$**, which results from the same combination of ions. However, comparatively, the 1D structure is less distorted since its average spread, as well as the spread of all the individual parameters, is the smaller of the two.

Moving on to the isostructural orthorhombic series, the three structures, **P-KCl$_3$**, **P-KBr$_3$** and **P-KI$_3$**, are in an overall sense the least distorted structures obtained in this family, in terms of their inorganic framework, with the smallest overall spread found in structure **P-KBr$_3$**. However, in these structures the inorganic framework is still highly distorted. The ideal octahedral arrangement with X–B–X angles of 90° and 180° for octahedra is not observed for any of the orthorhombic structures. In all the structures the octahedra differ quite dramatically from this ideal configuration, with the departure from ideality increasing in moving from **P-RbCl$_3$** to **P-RbBr$_3$** and finally to **P-CsCl$_3$**.

In addition, from the values in the table, it is noticeable that the **P-NaI$_3$** structure does not contain water, yet its summed ionic radii of B^+ and X^- is larger than **P-KCl$_3$**, which does crystallise with water. This suggests that there must be additional driving forces behind the incorporation of water in these structures, other than the non-spherical shape of the piperazinium cation. Perhaps the increased number of possible hydrogen bonding interactions when water is introduced versus when it is not could be a reason.

However, to test this idea, consider the substitution of piperazinium with 1-methyl piperazinium (abbreviated MP). Three related structures containing this cation have been reported in the literature, namely VONCEJ[21] (**MP-KBr$_3$**), VONCIN[21] (**MP-RbBr$_3$**) and VONCOT[21] (**MP-CsBr$_3$**). All the structures also contain water molecules. In structures that contain 1-methyl piperazinium that have been reported in the literature, the presence of the water molecule is seen on the side of the cation where the methyl group is not, and the inorganic framework has to bend to accommodate the methyl group. Thus, the methyl group occupies the space of one of the water molecules in the piperazinium hydrate structures, as can be seen by comparing the portions of the structures shown in Figure 5.14 (a), (b), (c), and (d). This does suggest that perhaps that both size and shape effects, and hydrogen bonding drive the inclusion of water in the piperazinium-containing structures.

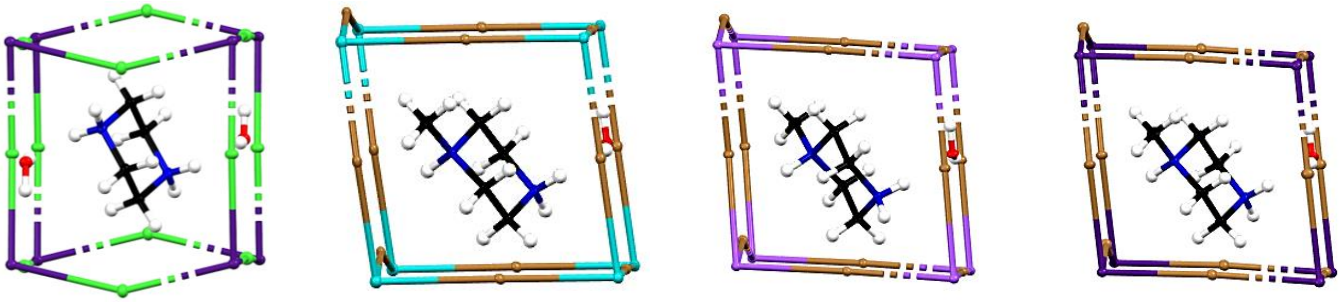

(a) **(b)** **(c)** **(d)**

Figure 5.14 The inorganic "cages" of **(a) P-CsCl$_3$**, **(b)** VONCEJ[21] (**MP-KBr$_3$**), **(c)** VONCIN[21] (**MP-RbBr$_3$**)and **(d)** VONCOT[21] (**MP-CsBr$_3$**).

This concludes the structural comparison section. The next section will assess the accuracy of the prediction of the Goldschmidt Tolerance Factor, the Octahedral Factor, and Bartel's Tolerance Factor.

5.5.2 Evaluation of Tolerance Factor Predictability

Perovskite structures can exist in either a 0D, 1D, 2D or 3D dimensionality. Three parameters may be employed to surmise if certain combinations of BX and the piperazinium dication will lead to a 3D dimensionality or not, namely the Goldschmidt Tolerance Factor,[22] the Octahedral Factor,[23] and Bartel's Tolerance Factor[24] as described next. The Goldschmidt tolerance factor (t) was calculated as per Equation (5.2):

$$t = \frac{r_A + r_B}{\sqrt{2}\,(r_B + r_X)} \tag{5.2}$$

where t is an indication of whether the A-cation (r_A) can *fit* into the 3D perovskite framework, relative to the radii of the B-cation (r_B) and X-anion (r_X). Moreover, in the range of $0.71 < t < 1.05$, a 3D perovskite structure is expected. Furthermore, the octahedral factor may be calculated using Equation (5.3):

$$\mu = \frac{r_B}{r_X} \tag{5.3}$$

The 3D perovskite structure is predicted to be stable in a range of $0.442 \leq \mu \leq 0.895$. Finally, the Tolerance Factor described by Bartel *et al.*[24] is given in Equation (5.4), where n_A is the oxidation state of the A-site organic cation, and r_i is the radius of the ion *i*.

$$\tau = \frac{r_X}{r_B} - n_A \left[n_A - \frac{\left(\frac{r_A}{r_B}\right)}{\ln\left(\frac{r_A}{r_B}\right)} \right] \tag{5.4}$$

By definition $r_A > r_B$ and so when $\tau < 4.18$, a 3D perovskite structure is predicted. Table 5.4 lists the values of the different factors, and indicates if a 3D structure can be expected for the possible combinations of the piperazinium dication and BX, with B = Na^+, K^+, Cs^+ or Rb^+ and X = Cl^-, Br^- or I^-, based on the values of the Goldschmidt Tolerance factor (t),[22] the Octahedral Factor (μ)[23] and Bartel's Tolerance Factor (τ)[24]. The Shannon ionic radii[25] of the metal and halide ions were used in these calculations. The following values were used: Na^+ = 102 pm, K^+ = 138 pm, Rb^+ = 152 pm and Cs^+ = 167 pm and halides Cl^- = 181 pm, Br^- = 196 pm and I^- = 220 pm. Additionally, the piperazinium dication radius was taken as 322 pm, as per Density Function Theory calculation results reported in the literature.[26]

From Table 5.4, it is evident that only for the combination of NaCl and piperazinium, the Goldschmidt Tolerance Factor predicts a lower dimensionality and that the Octahedral Factor predicts a possible issue with the octahedral coordination for CsCl. However, further, all three parameters predict a 3D dimensionality for the remaining combinations, and in most cases, this was also found to be the case experimentally. That said, the piperazinium dication rarely crystallised without a water molecule present, and hence these calculations are technically not completely correct, assuming the cation is only piperazinium. It should actually be an H_2O–Pip^{2+} adduct. Though, to derive a model for this is outside the scope of this study. Despite this possible complication, the prediction of structural dimensionality by the different factors is accurate in almost all of the cases where experimental structures are available.

Table 5.4 Prediction and experimental results of the perovskite structures for the combination of the piperazinium dication and BX as per the different factors listed in the text. Red illustrates a lower dimensionality than 3D and dark blue indicates a 3D dimensionality.

Metal Ion (B)	Halide Ion (X)		
	Cl^-	Br^-	I^-
Na^+	?	Possibly 0D	1D / 3D
	t = 1.06 τ = 3.27 μ = 0.56	t = 1.01 τ = 3.41 μ = 0.52	t = 0.93 τ = 3.65 μ = 0.46
K^+	3D	3D	3D
	t = 1.02 τ = 2.82 μ = 0.76	t = 0.97 τ = 2.93 μ = 0.70	t = 0.91 τ = 3.10 μ = 0.63
Rb^+	3D	3D	?
	t = 1.01 τ = 2.83 μ = 0.84	t = 0.96 τ = 2.93 μ = 0.78	t = 0.90 τ = 3.09 μ = 0.69
Cs^+	3D	?	?
	t = 0.99 τ =2.96 μ = 0.92	t = 0.95 τ = 3.05 μ = 0.85	t = 0.89 τ = 3.19 μ = 0.76

Nevertheless, the piperazinium cation is far from a spherical molecule as assumed when using the 322 pm radius, and it adopts an almost flat disc-like shape as shown in Figure 5.15 (a). However, the adduct is more ellipsoidal (which is already more spherical than a disc), as shown in Figure 5.15 (b), and hence might be why the 3D dimensionality is encountered so often for this series, but with the requirement of water to be present, since the adduct has a good fit in the inorganic cavity.

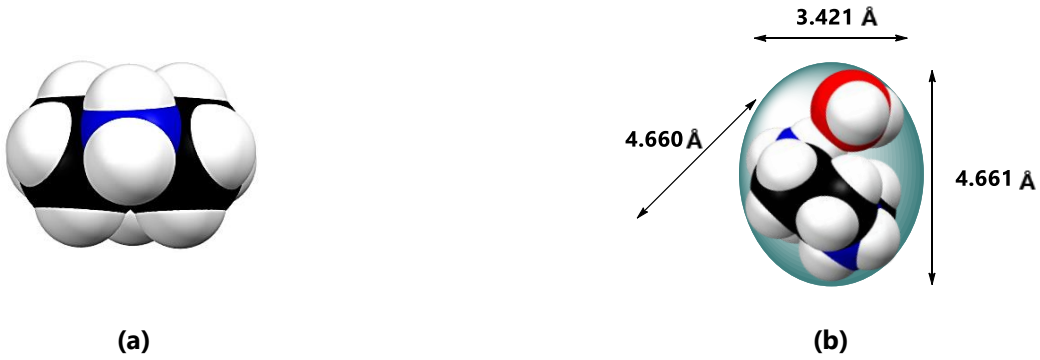

Figure 5.15 (a) The space fill representation of a piperazinium dication as determined by SCXRD and **(b)** the "real" shape of an H_2O–Pip^{2+} adduct.

5.6 Material Property Measurement Results

This section discusses the results of the optical band gap measurements and fluorescence spectra of the materials synthesised in this study. The optical band gaps were determined using diffuse reflectance spectroscopy. Subsequently, this absorption information was used in solid-state fluorescence studies to determine the emission properties of the materials. All samples analysed were showed to be pure from impurities by PXRD analysis (see Appendix D).

5.6.1 Determination of the Optical Band Gap

Using diffuse reflectance spectroscopy, the optical band gaps of the materials **P_3-NaI_5**, **P-KCl_3**, **P-KBr_3**, **P-KI_3** and **P-$CsCl_3$** were determined. The **Kubelka-Munk theory**,[27] which employs the **Tauc method**[28], along with a method developed by Davis and Mot, is employed to analyse the reflectance data.[29,30] The Tauc method assumes that the absorbance, and hence the energy-dependent absorbance coefficient (α) of the crystalline material may be expressed as shown in Equation (5.5)

$$(\alpha \cdot h\nu)^{\frac{1}{\gamma}} = B\left(h\nu - E_g\right) \tag{5.5}$$

where h is the Planck constant, ν is the photon's frequency, E_g is the band gap energy, and B is a constant. If the transition is *direct*, then $\gamma = 0.5$, and if the transition is *indirect*, then $\gamma = 2$.[31] The Kubelka-Munk function shown in Equation (5.6) is employed to process the reflectance data to absorbance data.[27,32,33] According to the theory, an infinitely thick specimen will have a Kubelka-Munk remission function $\left(F(R_\infty)\right)$, also known as an absorption function as follows

$$F(R_\infty) = \frac{K}{S} = \frac{(1 - R_\infty)^2}{2R_\infty} \tag{5.6}$$

where $R_\infty = \frac{R_{sample}}{R_{standard}} = \frac{\%R}{100}$ is related to the percentage reflectance of the material, while K and S are the absorption and scattering coefficients, respectively.[32] The α coefficient in Equation (5.5) is replaced by $F(R_\infty)$ from Equation(5.6). Therefore, yielding Equation (5.7)

$$(F(R_\infty) \cdot h\nu)^{\frac{1}{\gamma}} = B\left(h\nu - E_g\right) \tag{5.7}$$

Thus, by plotting $(F(R_\infty) \cdot h\nu)^{1/\gamma}$ against $h\nu$, the band gap (E_g) can be determined. The DRS data collected for the piperazinium-containing materials were processed, and the lines of best fit of the linear parts were only accepted once a correlation (R^2) factor of 0.98 or higher was obtained. These materials were modelled as indirect band gap materials (i.e., have two transitions)

since the majority of them showed two absorption edges, therefore, $\gamma = 2$. The processed spectra are shown in Figure 4.41, with the original spectra included in Appendix A.

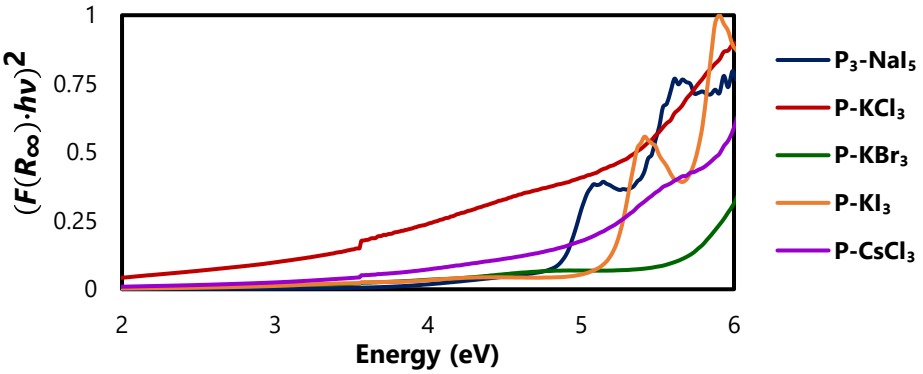

Figure 5.16 Processed and normalised DRS spectra of the piperazinium-containing perovskite materials. The line of best fit of each spectrum is given in Table 4.9. The individual spectra are colour coded for each material as listed in the legend. The instrument changes from a deuterium lamp to a wolfram lamp at 350 nm, which leads to a jump-discontinuity in the spectra.

Table 4.9 summarises the band gap values of the piperazinium-containing materials studied. Notably, the DRS technique only possesses an accuracy of ±0.5 eV.[33]

Table 5.5 Summary of the optical band gaps of piperazinium-containing alkali metal halide perovskite materials. The equations of the lines of best fit of the linear parts of the Kubelka-Munk plots and their correlation factors (R^2) are given with the optical band gaps read-off from the equations. "–" indicates that the second absorption edge was not reached.

Material	Line of Best Fit	(R^2)	Band Gap (±0.5 eV)	Dimensionality	Phase
P_3-NaI_5	$y = 2.6570x - 12.7623$	0.98	4.80	1D	Monoclinic
	$y = 2.9035x - 14.8818$	0.98	5.13		
P-KCl_3	$y = 2.8443x - 13.0687$	0.99	4.59	3D	Orthorhombic
	–	–	–		
P-KBr_3	$y = 1.1119x - 6.6311$	0.99	5.96	3D	Orthorhombic
	–	–	–		
P-KI_3	$y = 2.2354x - 11.5454$	0.99	5.16	3D	Orthorhombic
	$y = 3.0484x - 17.0795$	0.98	5.60		
P-$CsCl_3$	$y = 6.7505x - 30.0828$	0.99	4.57	3D	Orthorhombic
	$y = 3.2634x - 18.4934$	0.98	5.67		

Comparisons of the Optical Band Gaps

The first important piece of information evident from Table 4.9 is that **P_3-NaI_5**, **P-KI_3** and **P-$CsCl_3$** have two absorption edges, implying that they are indirect band gap materials since the one transition (that of lower energy) is phonon-assisted. The other (that of higher energy) is a direct transition.[34] Furthermore, **P_3-NaI_5** is also competing with **P-KCl_3** and **P-$CsCl_3$** to be the material with the narrowest band gap, with measured values of 4.80 eV, 4.59 eV and 4.57 eV respectively. However, due to the ± 0.5 eV uncertainty associated with the DRS technique, it cannot be said with any certainty which is the lower band gap material.[33] Therefore, it can only be said that they have similar band gaps.

Furthermore, the isostructural materials **P-KCl_3**, **P-KBr_3**, **P-KI_3** and **P-$CsCl_3$** may be directly compared. Only the first absorption edge was seen in the DRS spectra of **P-KCl_3** and **P-KBr_3**, however, it cannot be said with certainty at this point if

the two absorption edges seen correspond to the lowest or highest energy band transitions. It is evident that in the potassium series (**P-KCl$_3$**, **P-KBr$_3$**, **P-KI$_3$**), the bromide-containing material has the widest band gap, and the chloride-containing material has the narrowest. Furthermore, with increasing metal ionic radius, hence a reduction in ionisation energy for K^+ versus Cs^+, it is seen that that band gap of **P-CsCl$_3$** is comparable to that measured for **K-Cl$_3$**, which is not expected since usually, the band gap should decrease with such a substitution.[35] In addition, since these structures are isostructural, two absorption edges are expected for **P-KI$_3$** and **P-CsCl$_3$**, and these compounds are probably indirect band gap materials, however, their spectra do not show the second absorption edge since it lies outside of the measuring range of the instrument.

These band gap values are quite large, and hence these materials would not make the best sensitisers for PSCs. However, now that the absorption edges of the materials have been determined, this information may be used to monitor their emission properties through solid-state fluorescence. Subsequent applications may then be considered.

5.6.2 Solid-State Fluorescence Spectroscopy

Pure alkali halides have been shown to exhibit fluorescence when excited by UV-radiation.[36,37] Therefore it was decided to investigate whether hybrid perovskites containing alkali metal halides show fluorescence. The DRS analysis has provided the absorbance data required to study the excitation and subsequent emission properties of these piperazinium-containing perovskite materials. The fluorescence results of all of the compounds will be described together. Table 5.6 summarises the findings of the solid-state fluorescence spectroscopy study of the piperazinium-containing perovskites studied.

Table 5.6 Summary of the solid-state fluorescence data obtained for all the piperazinium-containing perovskites.

Material	Excitation Radiation		Emission Peak	
	Wavelength (nm)	Energy (eV)	Wavelength (nm)	Energy (eV)
P$_3$-NaI$_5$	243	5.10	491	2.53
	258	4.81	521	2.38
P-KCl$_3$	220	5.64	300 – 600	4.13 – 2.07
	275	4.51	555	2.23
P-KBr$_3$	208	5.96	300 – 600	4.13 – 2.07
	237	5.23	479	2.59
P-KI$_3$	215	5.77	300 – 600	4.13 – 2.07
	240	5.17	486	2.55
P-CsCl$_3$	219	5.66	300 – 600	4.13 – 2.07
	272	4.56	549	2.26
Blank	230	5.39	300 – 600	4.13 – 2.07
	260	4.77	520	2.38

Since the piperazinium-containing perovskites were found to be indirect band gap materials, they possess two absorption wavelengths as described by the DRS analysis earlier and as listed in Table 5.6. This subsequently implies that two separate emission profiles should be observed in the fluorescence spectrum. For the 1D ⟨100⟩-type material (**P$_3$-NaI$_5$**), two clear emission peaks were observed, as shown in Figure 5.17 (a). The two excitation wavelengths used, 243 nm and 258 nm, each corresponded to single emission peaks at 492 nm and 521 nm, respectively. However, the emission wavelengths are essentially double that of the excitation wavelengths, hence, the observed emission peaks are in reality the second order Rayleigh peaks and not the fluorescence peaks of the compound. This is confirmed when the spectrum of a blank sample is compared to the spectra of the compounds. The blank sample was excited at 260 nm and presents an emission profile at 520 nm, which confirms that the two emission profiles seen for **P$_3$-NaI$_5$** are only the second order Rayleigh peaks. Therefore, the material **P$_3$-NaI$_5$** does not fluoresce.

Furthermore, the 3D piperazinium-containing perovskites were also taken as indirect band gap materials and were subsequently excited at two different wavelengths, as determined and guided by the DRS analysis. Again, as was observed for the **P_3-NaI_5** compound, the second order Rayleigh peaks are observed as shown in Figure 5.17 (b) and (c).

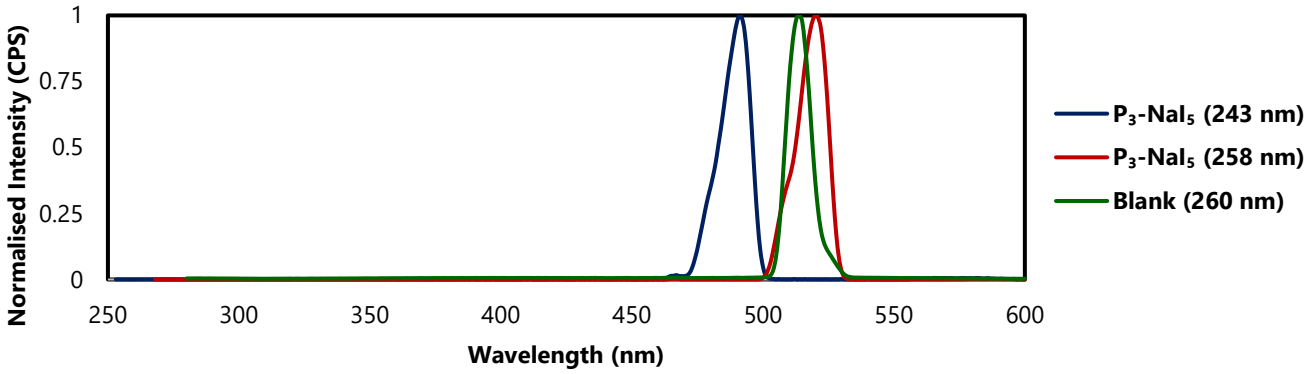

(a)

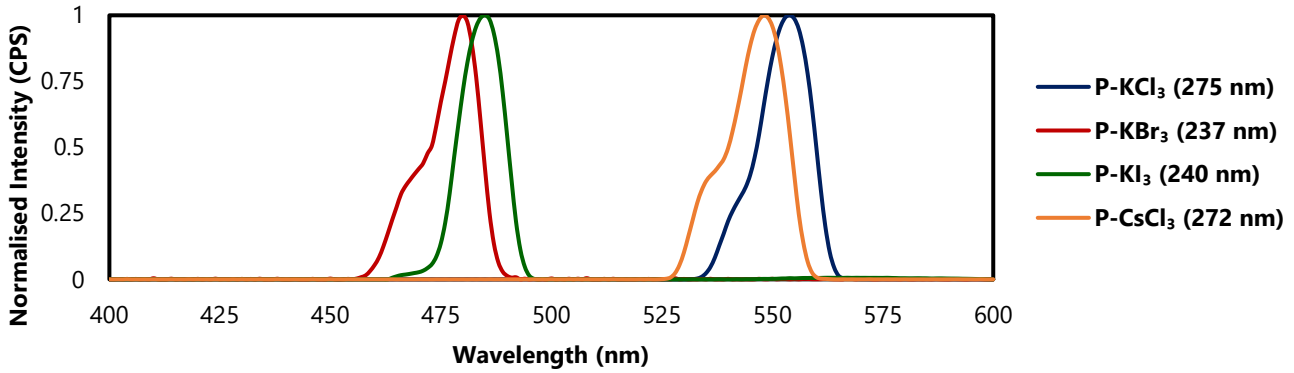

(b)

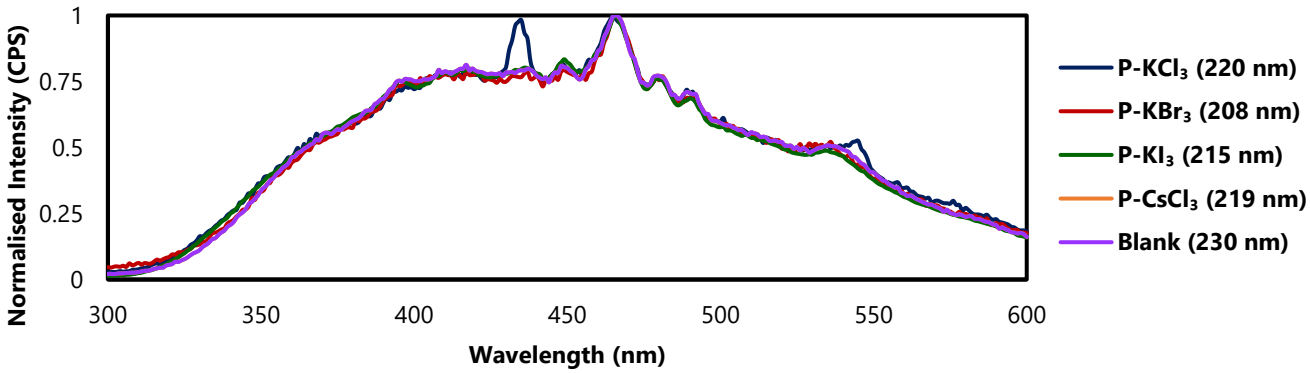

(c)

Figure 5.17 (a) The solid-state fluorescence spectra of the 1D ⟨100⟩-type piperazinium-containing perovskite material **P_3-NaI_5** obtained in this study. The two peaks correspond to the two absorption wavelengths shown with colour in the legend and with the corresponding excitation wavelength given in brackets. Figures **(b)** and **(c)** show the solid-state fluorescence spectra of the 3D piperazinium-containing perovskite materials obtained in this study for the lower energy and higher energy excitation wavelengths respectively. A blank sample is included in Figures **(a)** and **(c)**.

Though it might seem that the higher energy excitation of the 3D compounds results in some fluorescence, it is clear from the spectrum of the blank (excited at 230 nm) that the observed spectra originate from other materials used in the analysis, such as the glass slides etc., and not from the compounds. Therefore, it is concluded that none of the piperazinium-containing perovskite compounds exhibited solid-state fluorescence at room temperature.

Previous studies of the fluorescence properties of pure alkali metal halides indicated that their room temperature fluorescence is weak compared to that observed at *ca.* 5 K.[36–38] Therefore, since the fluorescence in this study was measured at room temperature, it could explain why no fluorescence was observed. However, the fluorescence spectrometer used in this study could only perform measurements at room temperature, hence it could not be established whether fluorescence might be observed at a lower temperature.

5.7 Summary and Conclusions

The structures resulting from a combination of piperazine-1,4-diium, or piperazinium for short, in combination with alkali metal halides (NaX, KX, and CsX, where X = Cl^-, Br^- or I^-) were studied crystallographically using both single-crystal and powder X-ray diffraction techniques. Only structures containing piperazinium, and NaI, KCl, KBr, KI or CsCl produced perovskite structures, and all except that with KI have been reported previously. These perovskite structures were either of the 1D dimensionality (called 1D ⟨100⟩-type perovskite) or 3D dimensionality.

None of the synthesised materials exhibited solid-state phase transitions between 150 K and *ca.* 298 K (room temperature), as illustrated by PXRD in Appendix D. Furthermore, property measurements were conducted on bulk samples of the studied materials. These included optical band gap determinations through diffuse reflectance spectroscopy and solid-state fluorescence spectroscopy.

The materials were found to possess band gaps unsuitable for PSC application and were found to lack any solid-state fluorescence properties at room temperature. However, due to their wide band gaps (> 3.00 eV) they may be considered in electroluminescence applications such as LEDs, for example. A few of the materials possess band gaps close to, or in the region of insulators (> 5.0 eV) and hence could find application as electrical insulators.

5.8 Experimental Methods

The methods used to synthesise single crystals and bulk powder samples for the materials studied are outlined here. In addition, the characterisation methods (single-crystal and powder X-ray diffraction) and the property measurement methods (DRS and solid-state fluorescence) are described.

5.8.1 Synthetic Methods

All reagents and solvents (except distilled water) used were reagent grade, purchased from Sigma Aldrich™ and were used without further purification or modification. Distilled water was obtained from the in-house distillation facility. Specifically: NaCl (≥99%), NaBr (≥99%), NaI (≥99%), KCl (≥99%), KCl (≥99%), KBr (≥99%), KI (≥99%), CsCl (≥99%), CsBr (≥99%), CsI (≥99%), piperazine (99%), HCl (37% solution), HBr (48% wt.) and HI (57% weight, stabilised solution).

No attempts were made to optimise the yields of the reactions.

Preparation of P_3-NaI_5 Single crystals and Bulk Powder. In a 100 ml beaker, 2.0000 g piperazine was dissolved in 35 ml distilled water, to which 13 ml 57% HI solution were added. The mixture was sonicated to dissolve all the solid. A slightly yellow tinted solution resulted. Thereafter, 3.4850 g NaI was added to the solution and dissolved. The light-yellow solution

was placed on a hot plate at 90 °C and was left until all the solvent had evaporated. A white powder and colourless crystals were obtained, and were washed with several aliquots of acetone, and the product was shown to be pure by PXRD analysis. A mass of 8.3300 g was obtained. The theoretical yield is 13.8585 g, hence a yield of 60.1% was obtained for the synthesis.

Preparation of P-KCl_3 Single crystals. A solution of 0.9933 g piperazine, 25 ml distilled water, and 2.0 ml 48% weight solution of HBr was prepared in a 100 ml beaker. 0.8315 g KCl were dissolved in 5 ml distilled water and added to the first mixture. The solution was left at room temperature, open to the atmosphere, to evaporate. Crystals were grown over the period of 21 days and resulted in large colourless crystals. The resultant crystals were washed with acetone and established to be pure by PXRD studies. 2.7713 g of these crystals were obtained, translating to a yield of 98.8%. These crystals were ground into powders for property determinations.

Preparation of P-KBr_3 Single crystals. 2.0357 g piperazine was dissolved in 25 ml distilled water, to which 6.0 ml 48% wt. HBr solution was added in a 100 ml beaker. Separately, 2.7114 g KBr was dissolved in 15 ml distilled water and added to the acidic mixture. The solution was left at room temperature, open to the atmosphere, to evaporate. After 20 days, 7.6502 g of large colourless single crystals, some of which had dimensions of centimetres, were washed with acetone. The purity of the sample was confirmed by PXRD analysis. Since the theoretical yield was 8.7560 g, an experimental yield of 87.4% was obtained. Due to the large mass of crystals obtained, these crystals were ground up and used as the powder samples required for property analysis.

Preparation of P-KI_3 Single crystals. 1.0182 g of piperazine were solvated in 25 ml distilled water, to which 3.1 ml of 57% wt. solution of HI and 1.9752 g KI were added, all in a 100 ml beaker. The solution was left open to the atmosphere, at room temperature, to evaporate for 15 days, after which large colourless crystals were obtained. These crystals were removed from the powder and washed with acetone. 4.2696 g of product was obtained, which resulted in a yield of 68.8%.

Preparation of P-$CsCl_3$ Single crystals. A mixture of 15 ml 37% HCl solution, 1.5089 g of piperazine, and 2.9252 g CsCl was prepared in a 250 ml beaker with the addition of 20 ml distilled water. The solution was left at room temperature to evaporate for 11 days. Thereafter, 4.5810 g of colourless crystals were obtained after washing with acetone. This is a crude yield of 76.3%. However, upon PXRD analysis, it was seen that the powder pattern was not completely clean. Hence why it is stated as a crude yield. Pure **P-$CsCl_3$** was prepared as per the following paragraph.

Preparation of P-$CsCl_3$ Bulk Powder. 2.0017 g of piperazine were dissolved in 35 ml distilled water, to which 9 ml of 37% HCl solution were added in a 250 ml beaker. Separately, 3.9209 g of CsCl was dissolved in 10 ml distilled water and added to the aforementioned mixture. The beaker was heated to approximately 90 °C and left until all the solvent had evaporated. A white powder was obtained and washed with acetone. 7.1005 g of product were obtained, and its purity was confirmed with PXRD (Appendix D). The resultant yield was 88.5%.

5.8.2 Characterisation Methods

Powder X-Ray Diffraction

A Bruker D2 Phaser instrument with Cu radiation (λ = 1.54 Å), with the sample sprinkled on a low background silicon sample holder, was employed to measure the X-ray powder patterns of all materials at room temperature. Generally, patterns were collected between 5° and 45° 2θ with a step size of 0.05°. A counting time of between 1 and 3 seconds per step was used for each measurement. A 300 W lamp with a maximum current of 10 mA and a potential of 30 kV was employed. The powder patterns collected at room temperature were matched with the calculated patterns obtained from the low-temperature (150 K) single-crystal data to ensure phase purity and that no solid-state phase transitions occurred on cooling.

Single-Crystal X-Ray Diffraction

For all single-crystal X-ray diffraction data recorded, either a Rigaku XtaLAB Synergy R diffractometer, with a HyPix detector, equipped with a rotating anode source providing Cu or Mo radiation or a Bruker D8 Venture diffractometer, with a Photon 100 CMOS detector and an Iμs source providing Cu or Mo radiation was employed. Furthermore, to collect data at 150 K, cooling was achieved using an Oxford Cryogenics Cryostat. Subsequently, structures were solved using direct methods in Shelxt and refined in ShelXL (SHELXT 2018/2, SHELXL2018/3).[39] Hydrogen atoms were placed as observed in the difference map, where possible, otherwise they were placed geometrically using a riding model.

5.8.3 Property Determination Methods

Diffuse Reflectance Spectroscopy

DRS data were collected using a Cary 500 UV-vis-NIR spectrophotometer with praying mantis DRS attachment. Samples were prepared in powder form. The reflectance of samples was measured between 200 nm to 800 nm at room temperature. A jump-discontinuity is present in the recorded spectra since the instrument changes from a deuterium lamp to a wolfram lamp at 350 nm. DRS data were processed using Kubelka-Munk theory as explained in the main body of work.[27,32,33]

Solid-State Fluorescence Spectroscopy

A Horiba Fluoromax-4 spectrofluorometer, fitted with a Xenon lamp light source and a photomultiplier detector, was employed to collect solid-state fluorescence data under ambient conditions at room temperature. The optical system uses a plane-grating Czery-Turner spectrometer, with possible wavelengths ranging between 200 nm and 950 nm. A front entrance and exit slit of 5.00 nm bandpass was used for both excitation and emission spectra. Ground samples of the piperazinium-containing perovskite compounds were sandwiched between two glass microscope slides and measured at a 45° geometry. The band gap, as determined by the DRS studies, provided the excitation wavelengths of the materials.

5.9 References for Chapter 5

1. Wang, M.; Wang, W.; Ma, B.; Shen, W.; Liu, L.; Cao, K.; Chen, S.; Huang, W. *Nano-Micro Letters* **2021**, *62* (13), 1–36. https://doi.org/https://doi.org/10.1007/s40820-020-00578-z.
2. Gollino, L.; Pauporté, T. *Solar Energy* **2021**, *5* (3), 2000616. https://doi.org/10.1002/solr.202000616.
3. Li, J.; Duan, J.; Yang, X.; Duan, Y.; Yang, P.; Tang, Q. *Nano Energy* **2021**, *80* (October), 105526. https://doi.org/10.1016/j.nanoen.2020.105526.
4. Webminiral. Perovskite Mineral Data http://webmineral.com/data/Perovskite.shtml#.X9ENF9hLiMo (accessed Jul 20, 2020).
5. Wells, H. L. *Zeitschrift für anorganische Chemie* **1893**, *3* (1), 195–210. https://doi.org/https://doi.org/10.1002/zaac.18930030124.
6. Megaw, H. *Nature* **1945**, *155* (3938), 484–485. https://doi.org/10.1038/155484b0.
7. Møller, C. *Nature* **1957**, *180* (4593), 981–982. https://doi.org/10.1038/180981a0.
8. Ikeda, N.; Teshima, K.; Miyasaka, T. *Chemical Communications* **2006**, *1* (16), 1733–1735. https://doi.org/10.1039/b516417f.
9. Kojima, A. *ECS Meeting Abstracts* **2008**, *MA2008-02* (2), 27. https://doi.org/10.1149/ma2008-02/1/27.
10. Kojima, A.; Teshima, K.; Shirai, Y.; Miyasaka, T. *Journal of the American Chemical Society* **2009**, *131* (17), 6050–6051. https://doi.org/10.1021/ja809598r.
11. Weber, D. *Zeitschrift für Naturforschung B* **1978**, *33* (12), 1443–1445. https://doi.org/https://doi.org/10.1515/znb-1978-1214.
12. Leijtens, T.; Eperon, G. E.; Noel, N. K.; Habisreutinger, S. N.; Petrozza, A.; Snaith, H. J. *Advanced Energy Materials* **2015**, *5* (20), 1–23. https://doi.org/10.1002/aenm.201500963.
13. Stoumpos, C. C.; Mao, L.; Malliakas, C. D.; Kanatzidis, M. G. *Inorganic Chemistry* **2017**, *56* (1), 56–73. https://doi.org/10.1021/acs.inorgchem.6b02764.
14. Groom, C. R.; Bruno, I. J.; Lightfoot, M. P.; Ward, S. C. The Cambridge Structural Database. https://doi.org/DOI: 10.1107/S2052520616003954.
15. Chen, X. G.; Gao, J. X.; Hua, X. N.; Liao, W. Q. *Acta Crystallographica Section C: Structural Chemistry* **2018**, *74* (6), 728–733. https://doi.org/10.1107/S2053229618006885.
16. Paton, L. A.; Harrison, W. T. A. *Angewandte Chemie* **2010**, *49* (42), 7684–7687. https://doi.org/10.1002/anie.201003541.
17. Harrison, W. T. A. *CSD Private Communication* **2019**.
18. Rickaby, K. A.; Slawin, A. M. Z.; Harrison, W. T. A. *Acta Crystallographica Section E: Crystallographic Communications* **2019**, *75* (8), 1249–1252. https://doi.org/10.1107/S2056989019010375.
19. Glazer, A. M. *Acta Crystallographica Section B* **1972**, *28* (11), 3384–3392. https://doi.org/10.1107/s0567740872007976.
20. Glazer, A. M. *Acta Crystallographica Section A* **1975**, *31* (6), 756–762. https://doi.org/10.1107/S0567739475001635.
21. Ferrandin, S.; Slawin, A. M. Z.; Harrison, W. T. A. *Acta Crystallographica Section E* **2019**, *75* (8), 1243–1248. https://doi.org/https://doi.org/10.1107/S2056989019010338.
22. Goldschmidt, V. M. *Naturwissenschaften* **1926**, *14* (May), 477–485. https://doi.org/10.1007/BF01507527.
23. Chonghea Li, X. L.; Weizhong Ding, L. F.; Yonghui Gao, Z. G. *Acta Crystallographica Section B* **2008**, *64* (6), 702–707. https://doi.org/10.1107/S0108768108032734.
24. Bartel, C. J.; Sutton, C.; Goldsmith, B. R.; Ouyang, R.; Musgrave, C. B.; Ghiringhelli, L. M.; Scheffler, M. *Science Advances* **2018**, *2* (5), 1–10. https://doi.org/DOI: 10.1126/sciadv.aav0693.
25. Shannon, R. D. *Acta Crystallographica Section A* **1976**, *32* (1), 751–767. https://doi.org/10.1023/A:1018927109487.
26. Shi, C.; Yu, H.; Wang, Q.; Ye, L.; Gong, Z.; Ma, J.; Jiang, J.; Hua, M.; Shuai, C.; Zhang, Y.; Ye, H. *Angewandte Chemie* **2020**, *132* (1), 173–177. https://doi.org/10.1002/ange.201908945.
27. Kubelka, P.; Franz, M. *Technical Physics* **1931**, *19* (12), 593–601.
28. Tauc, J.; Menth, A. *Journal of Non-Crystalline Solids* **1972**, *8* (10), 569–585. https://doi.org/10.1016/0022-3093(72)90194-9.
29. Davis, E.; Mott, N. *Philosophical Magazine* **1970**, *22* (179), 0903−0922. https://doi.org/https://doi.org/10.1080/14786437008221061.
30. Davis, E.; Mott, N. *Electronic Processes in Non-Crystalline Materials*; Oxford University Press, 2012.
31. Pankove, J. I.; Kiewit, D. A. *Journal of The Electrochemical Society* **1975**, *119* (5), 156. https://doi.org/10.1149/1.2404256.
32. López, R.; Gómez, R. *Journal of Sol-Gel Science and Technology* **2012**, *61* (1), 1–7. https://doi.org/10.1007/s10971-011-2582-9.
33. Nowak, M.; Kauch, B.; Szperlich, P. *Review of Scientific Instruments* **2009**, *80* (4), 21–24. https://doi.org/10.1063/1.3103603.
34. Hook, R. J.; Hall, H. E. *Solid State Physics*, Second Ed.; John Wiley & Sons Ltd., 1991.
35. Wilson, J. N.; Frost, J. M.; Wallace, S. K.; Walsh, A. *APL Materials* **2019**, *7* (1), 1811.01832. https://doi.org/10.1063/1.5079633.
36. Pooley, D.; Runciman, W. A. *Journal of Physics C: Solid State Physics* **1970**, *3* (8), 1815–1824. https://doi.org/10.1088/0022-3719/3/8/022.
37. Chen, C. H.; McCann, M. P. *Chemical Physics Letters* **1986**, *126* (1), 54–57. https://doi.org/10.1016/0009-2614(86)85115-6.
38. Symmons, H. F. *Journal of Physics C: Solid State Physics* **1971**, *4* (14), 1945–1957. https://doi.org/10.1088/0022-3719/4/14/009.
39. Sheldrick, G. *Acta Crystallographica Section C* **2015**, *71* (1), 3–8. https://doi.org/10.1107/S2053229614024218.

CHAPTER 6

Results: Perovskite Solar Cells

The band gaps of the compounds reported in Chapters 4 and 5 are wide, indicating that the compounds do not have potential to be used as sensitisers in PSCs. However, the materials are expected to absorb in the UV-range of the electromagnetic spectrum, based on the band gap values. Since UV-radiation forms part of the solar spectrum, the materials are still expected to absorb radiation when exposed to solar radiation. Based on this assumption, it was decided to test the performance of two of the materials in prototype solar cell devices.

Therefore, as an extension of the current study and to gain experience in the fabrication of perovskite solar cells, prototype perovskite solar cells based on two of the materials obtained in this study were constructed, and their performance compared to that of a benchmark perovskite solar cell. This chapter provides an overview of the fabrication method used to build prototype perovskite solar cells in this study. In addition, a summary of all the prototype devices fabricated in this study is given, along with their characterisation.

6.1 Introduction

The PSC device architecture of choice for lead-containing PSC devices is the p-i-n architecture. For lead-free devices, the inverted planar (n-i-p) architecture is employed.[1] However, in this study, only the p-i-n architecture will be employed and tested for a reference $MAPbI_3$-based device[2] and a device based on one of the perovskite materials prepared and characterised in this study, namely **D-$CsBr_3$**. Figure 6.1 illustrates the device architecture used in this study.[2]

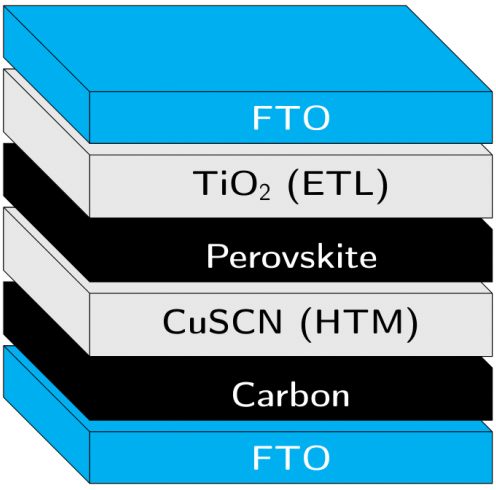

Figure 6.1 PSC device architecture used in this study, as outlined in the literature.[2] The colours used are not representative of the colours of the different layers. FTO, TiO_2 and CuSCN are all colourless materials.

As shown in Figure 6.1, a thin-film of TiO_2 is used as the electron transport layer, copper thiocyanate (CuSCN) as the hole transport layer and carbon as an electrode contact.[2] FTO (fluorine-tin doped oxide) glass is used as additional electric contacts.[2]

6.2 PSC Device Architecture

The PSC device construction method followed in this study is based on the method reported by Patwardhan *et al.*,[2] and the device is fabricated in six (6) steps, as illustrated in the diagrams in Figure 6.2 (a) and (b). Each of these steps will now be discussed in detail.

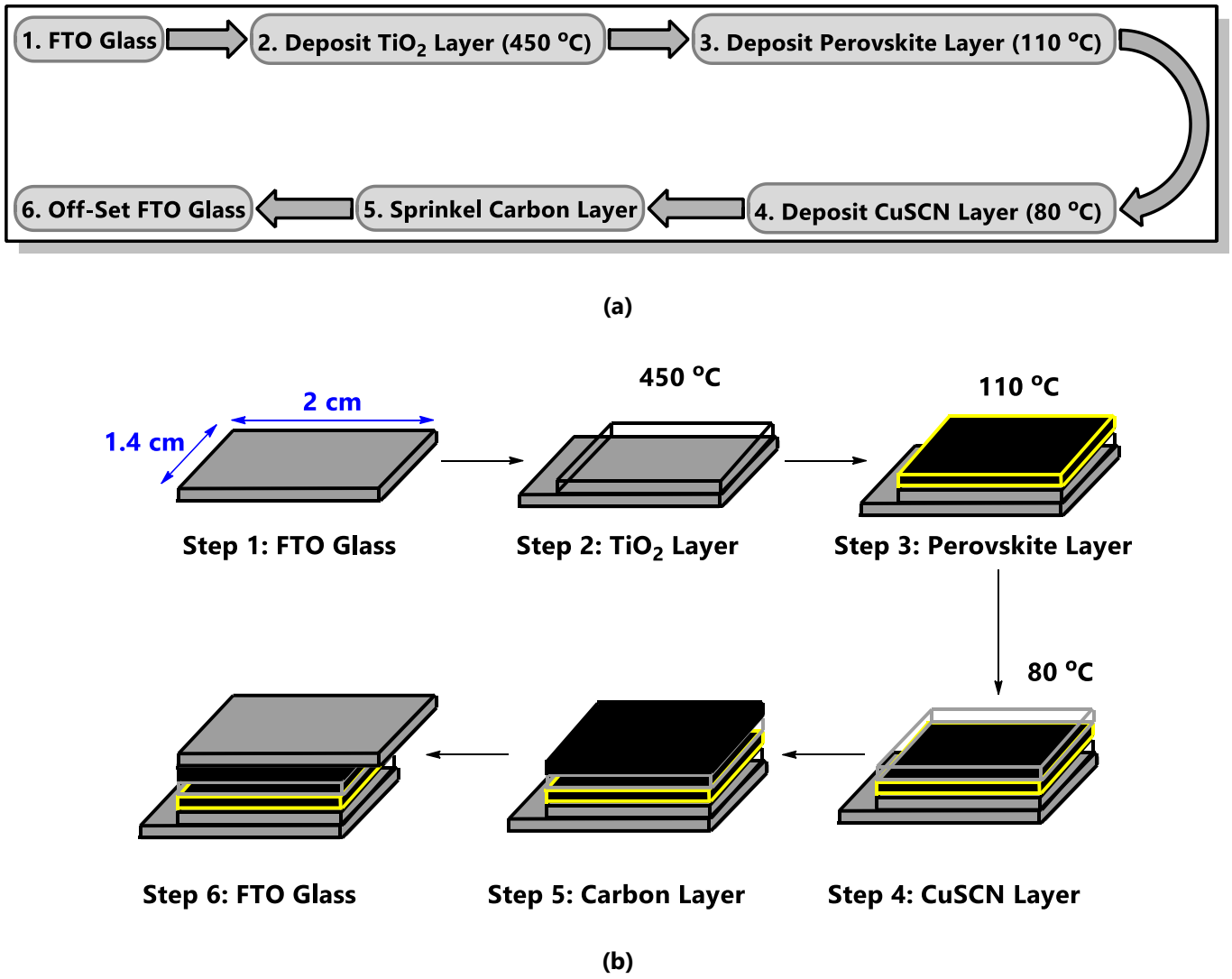

Figure 6.2 (a) A flow diagram of the steps in PSC device fabrication as outlined in the literature and **(b)** a schematic illustration of the device fabrication process. Adapted from Patwardhan *et al.*[2]

6.2.1 Device Fabrication and Layer Characterisation

Step One. An FTO glass plate purchased from Sigma Aldrich is cut to size (1.4 cm by 2 cm), and both sides of the glass are tested with a multimeter to determine which side is conductive. The conductive side (coated side) has low resistance, while the uncoated side has no resistance, as shown in Figure 6.3 (a) and (b), respectively. Furthermore, the non-conductive (non-coated) side is smooth compared to the rougher surface of the conductive (coated) side.

(a) (b)

Figure 6.3 Measurement of the resistance of the FTO glass plate using a multimeter. Figure **(a)** shows that the conductive side has a slight resistance value of 19.6 Ω, whereas, in Figure **(b)**, the non-conductive side gives no measurement at all.

Step Two. The FTO glass plate is placed on the benchtop with the conductive side facing upward. A quarter of the slide is covered with Scotch tape, securing the glass plate to the work surface, as shown in Figure 6.4 (a) and (b). One drop op TiO_2 precursor mixture prepared using 0.2 M titanium isopropoxide + 0.1 M HCl in ethanol,[3] is spread over the FTO slide's surface using a clean pipette. The pipette is rolled over the surface multiple times to ensure even coverage of the slide. The tape is removed, and the slide is placed in an oven or on a hot plate at 450 °C for 20 minutes. The slide is removed from the oven or hot plate and allowed to cool down to room temperature.[2] The TiO_2 layer formed on the slide was characterised using powder X-ray diffraction, and Figure 6.4 (c) shows a match between the experimental and theoretical (anatase TiO_2) powder patterns, while the powder pattern of the FTO slide (SnO_2, cassiterite, 91.56%) is also observed, because the TiO_2 layer (8.44%) is quite thin.

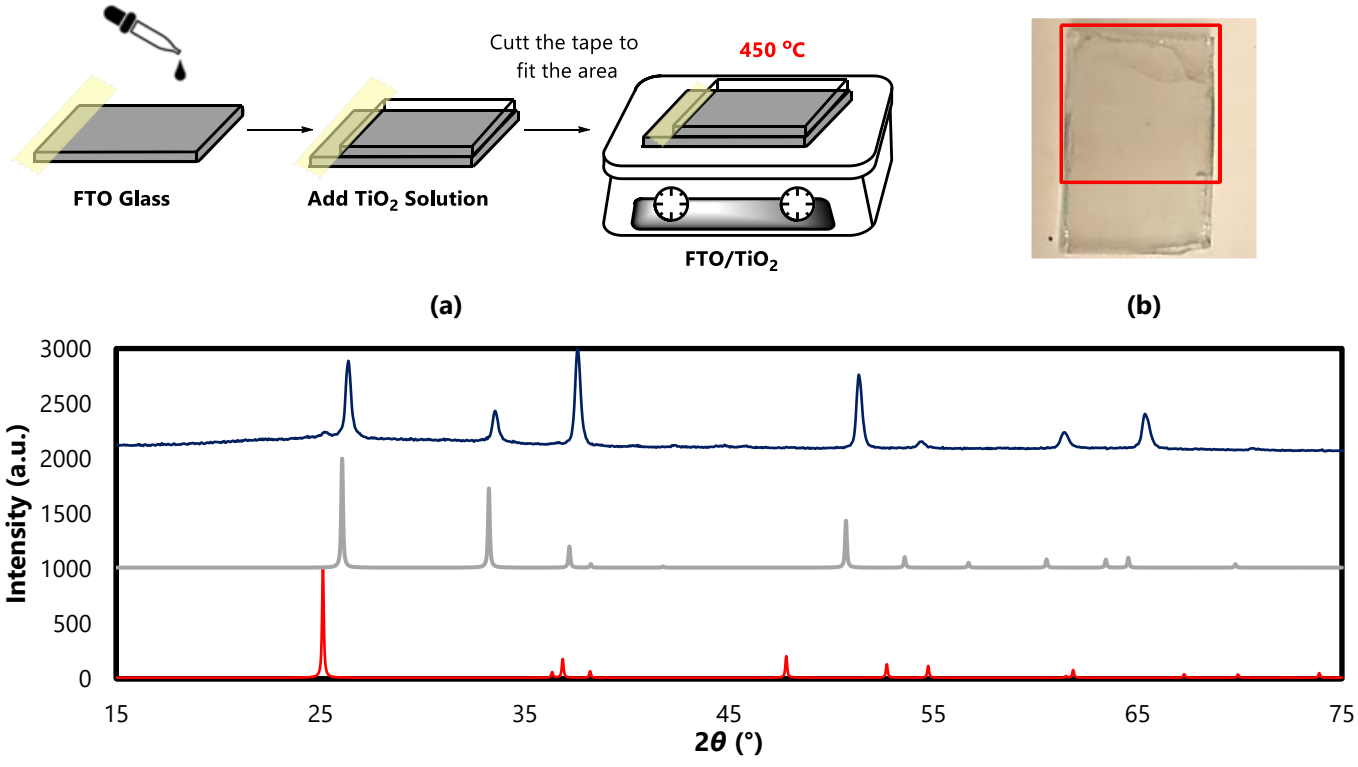

Figure 6.4 The procedure to form the TiO_2 layer on the FTO glass pate, shown schematically in Figure **(a)** and Figure **(b)** a photo of the TiO_2 layer formed on the FTO slide. Figure **(c)** shows the powder X-ray diffraction pattern of the TiO_2 thin-film on the FTO slide (blue) compared with the theoretical powder patterns of anatase (red) and cassiterite (grey). Figure (a) was adapted from Patwardhan *et al.*[2]

Step Three. The FTO slide is placed with the TiO_2 film facing upwards. The uncovered section of the FTO slide is covered with *heat resistant tape*, as illustrated in Figure 6.5 (a), and one drop of the perovskite solution ((1.5 M AX and 0.5 M MX_2 in a solvent of choice) is spread over the uncovered area. A smooth and even coverage should be achieved. Excess tape is removed using a razor blade or scalpel, with the piece of the tape on the slide left intact. The plate is placed on a hot plate and heated to approximately 110 °C, or in the range of 90 °C to 120 °C, depending on the boiling point of the solvent used. When a homogenous colour change is noted, as expected with regards to the colour of the specific perovskite, for example, a change from yellow to black in the case of $MAPbI_3$, as shown in Figure 6.5 (b), the slide is left on the hot plate for a further 10 minutes. When a characteristic colour change is not present (as in the case for **D-$CsBr_3$**), the layer is characterised using PXRD.

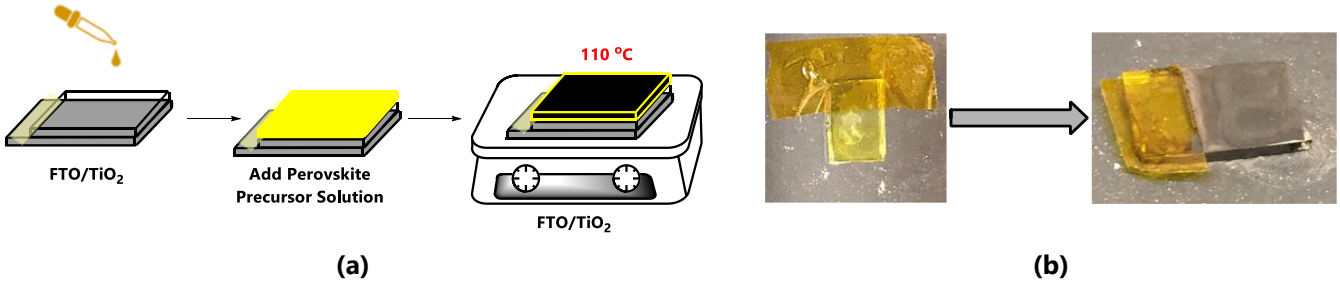

Figure 6.5 (a) A schematic illustration of the deposition of the perovskite layer onto the TiO_2 layer and **(b)** the physical colour change observed for the $MAPbI_3$ perovskite film on heating. Figure (a) was adapted from Patwardhan *et al.*[2]

Step Four. The temperature of the hot plate is lowered to 80 °C, and one drop of CuSCN precursor solution (0.05 M CuSCN in dipropyl sulfide)[4–6] is spread over the perovskite film. The FTO slide is left on the hot plate at 80 °C for 15 minutes, whereafter the slide is removed from the heat and left to cool, as illustrated in Figure 6.6. A powder pattern of this film was obtained and showed that new peaks emerged, signifying that a new layer has formed on top of the perovskite layer.

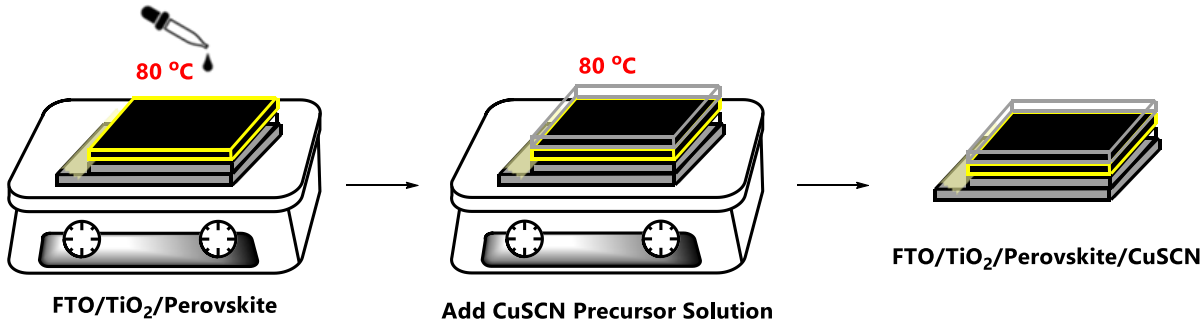

Figure 6.6 A schematic illustration of the deposition of the CuSCN film onto the FTO/TiO_2/perovskite film, where ¼ of the FTO slide is still covered with heat resistant tape. Adapted from Patwardhan *et al.*[2]

Step Five. The heat resistant tape is removed from the FTO slide. A small amount of carbon powder is sprinkled over the FTO/TiO_2/perovskite/CuSCN films. Thereafter, a second FTO slide of the same size as the first is placed with its conductive side down onto the carbon layer, in a laterally shifted position (see Figure 6.7 (a)). The second slide is gently moved over the carbon powder to create a uniform layer of carbon particles.[2] However, this should be done carefully or may be skipped, since this might damage the other layers of the device. Lastly, two binder clips are used to clip the two FTO slides together see Figure 6.7 (b)), allowing for the connection of electrical contacts and the formation of a circuit.

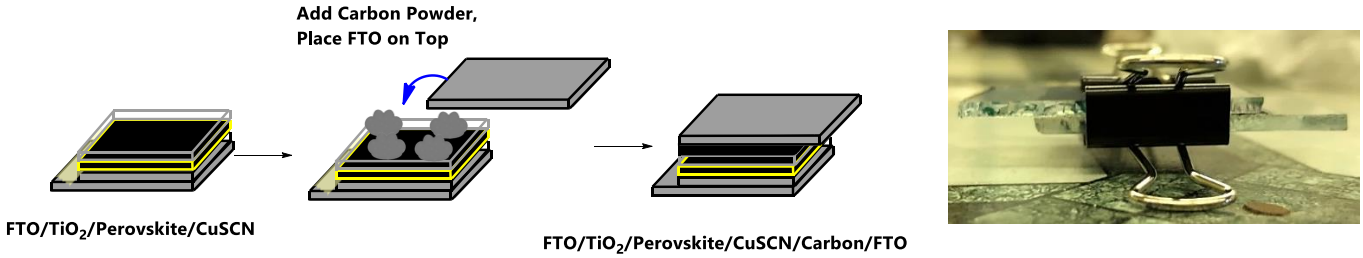

Figure 6.7 (a) The addition of the carbon powder sprinkled over the FTO/TiO_2/perovskite/CuSCN film and the placement of the second FTO plate. **(b)** A photograph of the PSC device illustrating the offset FTO plates. The carbon powder is illustrated in light grey for clarity, however, it is as black as indicated in the final film. Figure (a) was adapted from Patwardhan *et al.*[2]

Four prototype PSC devices were constructed in the current study using the method described above. The first device contained $MAPbI_3$ as perovskite material and is considered to be the benchmark device. Furthermore, two prototype devices containing the 3D perovskite material **D-$CsBr_3$** (band gap of 5.26 eV) were fabricated and characterised in the current study. The first of these prototypes used the **D-$CsBr_3$** material as the sensitiser, and the second used it as the electron transporting layer (ETL) in an $MAPbI_3$-based device. In addition, the fourth and final device used the 1D ABX_3-type material **D-$NaBr_3$** (band gap of 5.33 eV) as an ETL in an $MAPbI_3$-device. The two devices which employ the perovskite as ETLs are discussed later.

After constructing the benchmark PSC device based on $MAPbI_3$ and the **D-$CsBr_3$**-based device, they were characterised, as outlined in the following section. All other devices described later were characterised using the same method.

6.2.2 Electrical Characterisation of the $MAPbI_3$- and D-$CsBr_3$-based PSC Devices

Two leads with alligator clips from a multimeter are connected to the exposed sides of the FTO slides (one to each side) to form a circuit. The device is then placed in full sunlight. First, the multimeter is set to its mV setting and the voltage across the device is measured with sun exposure and when the device is covered, as shown in Figure 6.8 (a) and (b). A distinct drop in voltage was observed on covering the device compared to when it is fully exposed to the sun. A maximum voltage measurement of 5.1 mV was obtained with sun exposure, and this value changed to 1.4 mV on covering the $MAPbI_3$-based device. Voltage measurements of 0.6 mV (uncovered) and 0.1 mV (covered) were measured for the **D-$CsBr_3$**-based device.

Secondly, the multimeter was set to the μA setting, and the current through the device was measured, again with sun exposure and covered, illustrated in Figure 6.8 (c) and (d). The current measurement dropped from 3.0 μA to 0.5 μA when exposed to the sun and covered for the $MAPbI_3$-based device (a maximum of 3.0 μA was measured). The current measurements for the **D-$CsBr_3$**-based device were 0.3 μA and 0.1 μA for uncovered and covered measurements, respectively. These basic tests revealed that the prototype PSCs generate electric current and that the method used in this study is a viable method for the fabrication of perovskite solar cells. Even though the current and voltage measured for the solar cell constructed from **D-$CsBr_3$** is significantly lower than that measured for solar cell based on the benchmark compound $MAPbI_3$, it was illustrated that the **D-$CsBr_3$**-based device still produces as small current and voltage, illustrating that it does absorb a portion of the solar spectrum, and does generate an electric current.

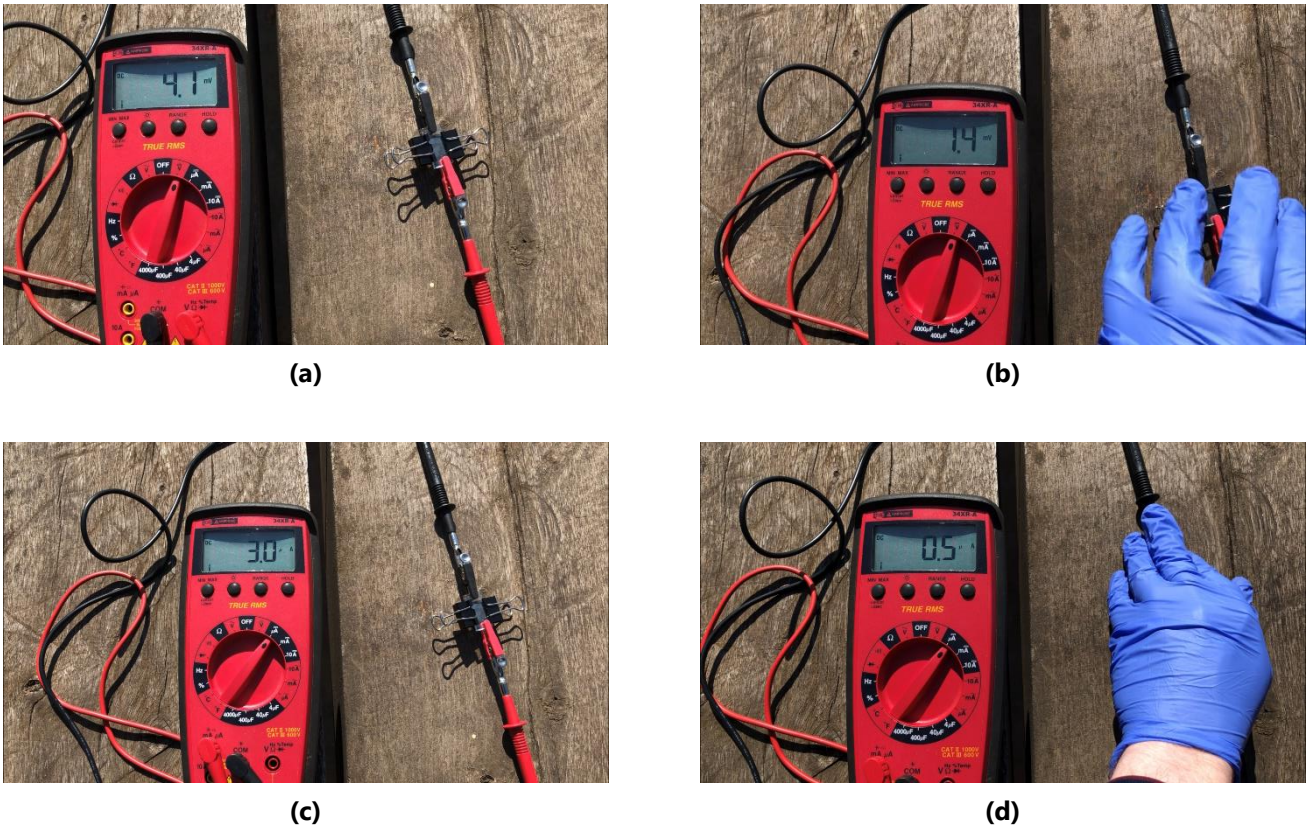

Figure 6.8 Current and voltage measurements of the FTO/TiO_2/$MAPbI_3$/CuSCN/Carbon/FTO cell. Figures **(a)** and **(b)** show the cell's voltage measurement when exposed to sunlight and when it is covered. Figures **(c)** and **(d)** show the cell's current measurement when exposed to sunlight and when it is covered.

6.3 PSC Devices: Results and Discussion

In this study, the perovskite materials **D-$CsBr_3$** (3D perovskite) and **D-$NaBr_3$** (1D ABX_3-type perovskite) were considered in some role in a PSC device. Firstly, as the absorber layer (sensitiser, only **D-$CsBr_3$** tested) described in the previous section, however, this approach did not deliver significant current, and voltage results due to the wide band gap of the perovskite material used. Secondly, both **D-$CsBr_3$** and **D-$NaBr_3$** were used as the ETL of the device, thereby replacing the TiO_2 layer of the $MAPbI_3$-based device described in the method above. This substitution was made since the ETL requires a wide band gap material, making **D-$CsBr_3$** and **D-$NaBr_3$** potential ETLs in solar cells.

Hence, in these devices where the perovskite materials from the current study were used as ETL, the absorber layer used was the benchmark $MAPbI_3$ perovskite.

6.3.1 PSCs with Perovskites from this study as Sensitisers

The perovskite material **D-$CsBr_3$** was tested as the sensitiser layer a prototype PSC device fabricated as outlined in Section 6.2. The $MAPbI_3$-based device was used as a reference device and was discussed in Section 6.2. Both these devices (benchmark and prototype) were based on the architecture FTO/TiO_2/Perovskite/CuSCN/Carbon/FTO.

The formation of the TiO_2 (see Section 6.2) and perovskite layers on the FTO plates were confirmed using PXRD. However, the $MAPbI_3$ film's formation was confirmed by the colour change (yellow to black), as shown in Figure 6.5 (b). The powder

pattern of the **D-CsBr$_3$** film with its calculated pattern is shown in Figure 6.9. The peak positions are a perfect match, and the relative peak heights only differ due to the preferred orientation of the perovskite film on the FTO plate.

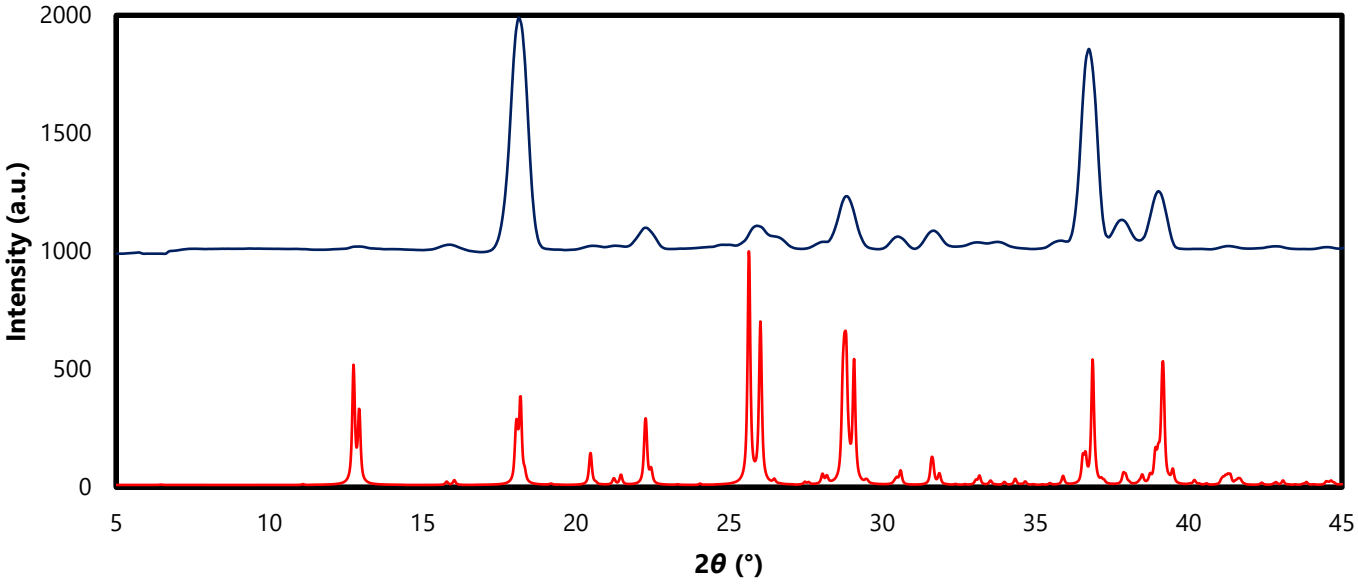

Figure 6.9 The calculated (red) and experimental (blue) powder pattern of **D-CsBr$_3$** as characterisation of the perovskite layer for the device FTO/TiO_2/**D-CsBr$_3$**/CuSCN/Carbon/FTO.

However, due to the extremely wide band gap value of **D-CsBr$_3$**, the device was found to perform poorly and only achieved a maximum current of 0.3 μA and a maximum voltage of 0.6 mV. This is not unexpected since the band gap of **D-CsBr$_3$** is 5.26 eV and is much too wide for use as an absorber layer for the solar spectrum. However, this test aimed to acquire the skills of PSC device fabrication, which was successfully achieved. Therefore, it was decided that no additional materials from this study would be utilised as the sensitiser layer since similar results are expected for all of the materials obtained, due to their wide band gaps.

6.3.2 PSCs with Perovskite as the ETL

Since all the perovskite materials investigated in this study were found to have wide band gaps, their appearance is colourless and opaque, making them unsuitable as sensitiser materials. However, a wide band gap is precisely what is required of an ETL (wide band gap and colourless – no visible light interference). Hence, two different structural types (1D ABX_3 type and 3D perovskite) of the materials investigated in this study were tested as ETLs with $MAPbI_3$ as the absorber layer.

The perovskite materials chosen were **D-NaBr$_3$** (1D ABX_3-type perovskite) and **D-CsBr$_3$** (3D perovskite) to establish the effects of material dimensionality on the viability of the device. Therefore, the device architectures of the two devices fabricated were FTO/**D-NaBr$_3$**/$MAPbI_3$/CuSCN/Carbon/FTO (called the **D-NaBr$_3$** ETL device) and FTO/**D-CsBr$_3$**/$MAPbI_3$/CuSCN/Carbon/FTO (called the **D-CsBr$_3$** ETL device).

The fabrication process was the same as outlined in Section 6.2, except for the deposition of the ETL layer.[2] The perovskite precursor solutions (0.5 M **D-NaBr$_3$** and 0.5 M **D-CsBr$_3$**) were prepared in water. The precursor solution was dripped onto the FTO slide's conductive side and annealed on a hot plate at 120 °C. Thereafter, the deposition of the $MAPbI_3$ layer, the CuSCN layer, and carbon powder were carried out. The characterisation of the perovskite ETL layers was done using PXRD with the powder patterns shown in Figure 6.10 (a) and (b). In both cases, the match between the calculated (red) and experimental (blue) powder patterns is good, with slight differences in intensity due to the preferred orientation of the perovskite films on the FTO slides.

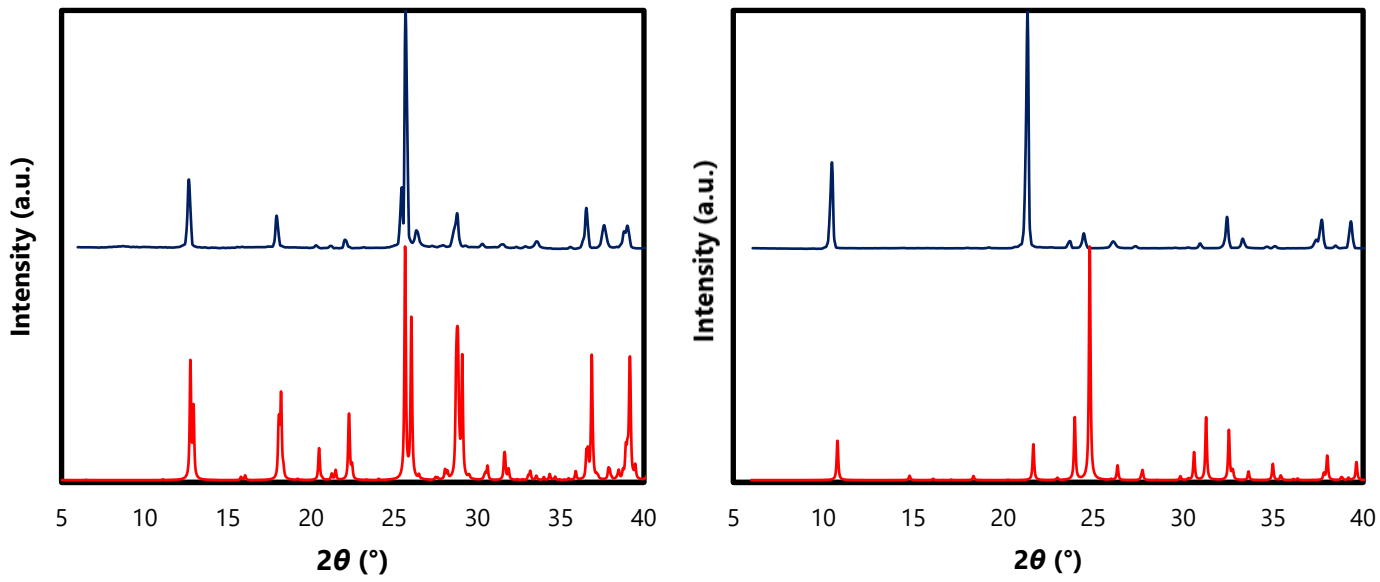

Figure 6.10 The theoretical (red) and experimental (blue) powder pattern of **(a) D-CsBr$_3$** as characterisation of the perovskite layer for the device FTO/**D-CsBr$_3$**/MAPbI$_3$/CuSCN/Carbon/FTO and **(b) D-NaBr$_3$** as characterisation of the perovskite layer for the device FTO/**D-NaBr$_3$**/MAPbI$_3$/CuSCN/Carbon/FTO.

The **D-NaBr$_3$** ETL device showed a maximum current measurement of 0.2 μA and a maximum voltage measurement of 4.5 mV outperforming the **D-CsBr$_3$** ETL device, which did not register any measurements (see Figure 6.11 (a) and (b)). These low or absent voltages may be explained by damage to the perovskite ETL layer during deposition of the MAPbI$_3$ layer. The solvent used to prepare the MAPbI$_3$ precursor solution is DMF, and hence it partially dissolves the top layer of the perovskite ETL layer when deposited on top of this layer. In the case of **D-NaBr$_3$**, the dissolution was less than for **D-CsBr$_3$** stemming from the higher solubility of 3D perovskite in polar solvents compared to lower-dimensional perovskites. That said, this *proof of concept* does not include the optimisation of solvents used, hence investigating possible solutions to this fall outside the scope of the current study.

Figure 6.11 (a) The maximum current measurement and **(b)** the maximum voltage measurement of the PSC device FTO/**D-NaBr$_3$**/MAPbI$_3$/CuSCN/Carbon/FTO.

Major positives of using these materials as ETLs include the ease of fabrication since no organic solvents are required, the requirement of 120 °C for the ETL deposition step compared to 450 °C required for the deposition of TiO_2 and hence improved energy efficiency. Therefore, this is an excellent avenue for future work since using the materials investigated in this study as ETLs show potential.

6.4 Conclusions

The PSC devices fabricated in this study performed as well as could be expected from the method used. The band gap alignment of the different layers was not optimised to allow for optimal electron-hole conduction, and the deposition techniques used were not the most technical. However, for this study, they were sufficient since they showed that the perovskite materials synthesised could be applied to optoelectronic devices, albeit as the ETL in PSCs rather than the sensitising layer.

It would not only be of academic interest to further optimise these devices and address the challenges discussed in this chapter experienced with the fabrication of these devices. Creating a so-called "all perovskite" device would allow for perovskite optoelectronic fabrication to become cheaper, safer, greener, and more straightforward. This is further discussed in the future work chapter.

6.5 Experimental Section

The general procedure to producing a perovskite solar cell was outlined in this chapter, however, reference was made to the use of several precursor solutions and characterisation techniques. This section serves as the general *experimental section* for this chapter.

6.5.1 Preparation of Precursor Solutions

All materials used were obtained commercially from Sigma Aldrich and used without further purification. Specific details are as follows: HCl (37% solution, reagent grade), titanium(iv)isopropoxide (97% solution), acetone (99%), diethyl ether (anhydrous, 99%), ethanol (96%), copper(I)thiocyanate (99%), dipropyl sulfide (97%), fluorine doped tin oxide coated glass slide, methylammine (40% wt. solution in H_2O), HI (57% weight, stabilised solution), lead(II)iodide (99%), *N*,*N*'-dimethylformamide (99.8%).

Preparation of the TiO_2 Precursor Solution. A solution of 0.5 ml (37% solution) HCl, 3 ml titanium(iv)isopropoxide and 50 ml ethanol was prepared in a 100 ml beaker and left to stir at room temperature for 25 minutes. Thereafter the solution was stored in an airtight container at room temperature.

Preparation of the CuSCN Precursor Solution. 12 mg of CuSCN was mixed with 2 ml dipropyl sulfide (DPS) in a small vial. The resultant mixture was left to stir at room temperature for 24 hours, until a colourless solution was obtained.

Preparation of the 0.5 M $MAPbI_3$ Precursor Solution. 3.55 ml of the 40% wt. solution in H_2O methyl amine was placed in a 100 ml beaker to which 5.1 ml 57% HI solution was added slowly and dropwise. After allowing the solvent to evaporate at 80 °C, a white powder was collected. This powder was washed with subsequent aliquots of diethyl ether and acetone to afford 2.4938 g of methylammonium iodide (MAI). Next, 0.4189 g PbI_2 and 0.7193 g MAI were dissolved in 3 ml DMF and stirred at 80 °C for 15 minutes, until a yellow transparent solution resulted, which is the $MAPbI_3$ precursor solution.

Preparation of 0.5 M D-$CsBr_3$ Precursor Solution. To a large vial, 2.4322 g of **D-$CsBr_3$** was dissolved in 10 ml water, which afforded an approximately 0.5 M precursor solution of **D-$CsBr_3$**.

Preparation of 0.5 M D-$NaBr_3$ Precursor Solution. 1.8324 g of **D-$NaBr_3$** was dissolved in 10 ml water in a large vial to afford an approximate concentration of 0.5 M for the precursor solution of **D-$NaBr_3$**.

6.5.2 Characterisation Methods

Powder X-Ray Diffraction

Powder X-ray diffraction methods were used to characterise the layers of the PSC devices studied in this chapter. The patterns were collected at room temperature using a Bruker D2 Phaser instrument and Cu radiation (λ = 1.54 Å), while the covered FTO slide was used as the "sample holder". Patterns were collected between 5° and 75° 2θ with a step size of 0.05° and a time interval of between 1 and 3 seconds per step, depending on the layer being characterised. For perovskite layers, 5° and 45° 2θ was used and for the TiO_2 layers 5° and 75° 2θ was used. The X-ray tube was powered at 300 W with 10 mA and 30 kV.

Electrical Characterisation

An Amprobe 37XR-A TRMS Digital Multimeter was employed to study the electrical response of the solar cells to solar radiation and to further obtain information required in the fabrication process, such as the testing for conductivity of the FTO slides.

6.6 References for Chapter 6

1. Jena, A. K.; Kulkarni, A.; Miyasaka, T. *Chemical Reviews* **2019**, *119* (5), 3036–3103. https://doi.org/10.1021/acs.chemrev.8b00539.

2. Patwardhan, S.; Cao, D. H.; Hatch, S.; Farha, O. K.; Hupp, J. T.; Kanatzidis, M. G.; Schatz, G. C. *The Journal of Physical Chemistry Letters* **2015**, *6* (2), 251–255. https://doi.org/10.1021/jz502648y.

3. Ball, J. M.; Lee, M. M.; Hey, A.; Snaith, H. J. *Energy & Environmental Science* **2013**, *6* (6), 1739–1743. https://doi.org/10.1039/C3EE40810H.

4. Hodes, G.; Cahen, D.; Chung, I.; Lee, B.; He, J.; Chang, R. P. H.; Kanatzidis, M. G. *Accounts of Chemical Research* **2012**, *45* (5), 705–713. https://doi.org/10.1021/ar200219h.

5. Pellet, N.; Gao, P.; Gregori, G.; Yang, T.-Y.; Nazeeruddin, M. K.; Maier, J.; Grätzel, M. *Angewandte Chemie* **2014**, *126* (12), 3215–3221. https://doi.org/10.1002/ange.201309361.

6. Chavhan, S.; Miguel, O.; Grande, H.-J.; Gonzalez-Pedro, V.; Sánchez, R. S.; Barea, E. M.; Mora-Seró, I.; Tena-Zaera, R. *Journal of Materials Chemistry A* **2014**, *2* (32), 12754–12760. https://doi.org/10.1039/C4TA01310G.

CHAPTER 7

Conclusions and Future Work

The first part of this chapter will highlight the conclusions drawn from the results obtained in the current study, specifically those of Chapter 4, Chapter 5, and Chapter 6. Structural trends and band gap trends can now be identified across the dabconium- and piperazinium-containing families since in-depth analyses of trends within the individual structural families have already been completed in the respective results chapters. The second part of this chapter focuses on future work emanating from the current study. Perovskite materials have a wide range of properties and hence potential applications. Therefore, once a family of these structures has been established as synthetically viable, a plethora of research possibilities can be pursued. The possible avenues for further research to follow from this study are described in this chapter. The three main future research avenues include synthetic modification of the composition, property determinations, and the consideration of potential applications.

7.1 Conclusions

This study contributes to the structural and materials science knowledge of alkaline metal halide hybrid perovskites and their potential application as sensitisers or as electron transport layers (ETLs) in solar cells. The structures of these compounds differ from the *traditional* perovskite materials (B^{2+} or B^{3+} materials with monovalent A-site cations) reported in the literature since they are lead-free and combine monovalent alkali metal halide metal halides (B^{+} and X^{-}) with divalent organic cations (A^{2+}). In addition, they can be prepared in aqueous solution, negating the need for toxic organic solvents. Nine novel structures and additional structural data (low-temperature, 150 K data) on seven of the structures were obtained, contributory to the small body of work currently available in the literature on these types of materials. However, the family of materials obtained did not fit the requirements of the proposed applications because of their wide band gap, though most of them possess a 3D structural dimensionality. However, due to their wide band gaps they may be used as ETLs in solar cells.

7.1.1 Structural Trends

Generally, the dabconium alkaline metal halide hybrid perovskites possessed either 1D or 3D structural dimensionalities. The 3D structures typically crystallised in either hexagonal, trigonal, or monoclinic phases, whereas the 1D structures crystallised in either the trigonal or hexagonal phase. A trend between structure dimensionality and the increasing sum of ionic inorganic constituent radii ($r_{B^+}+r_{X^-}$) was noted. Below a sum of radii of 322 pm, the pure 1D ABX_3-type perovskite structure (with face-sharing octahedra in the trigonal phase) was observed. At 322 pm, a hexagonal 3D polytype (mixture of face- and corner-sharing octahedra) perovskite was obtained. Further on, at approximately in the range between 330 pm and 363 pm, the pure 3D perovskite structure was obtained. Thereafter, at sums of ionic radii larger than 363 pm, 1D ABX_3 perovskites in the hexagonal phase were observed.

For the piperazinium-containing alkaline metal halide perovskites, again 1D or 3D dimensionalities were obtained. However, in this case, the organic cation crystallised alongside water molecules in the structures (for both dimensionalities), and all the obtained 3D structures were isostructural (orthorhombic phase with space group *Pbcm*). Furthermore, one 3D structure without water was reported in the literature, however, this structure could not be reproduced in the current study.

Hence, in a structural sense, it is best to visualise the dimensionalities obtained as per Figure 7.1. From this summary, it is evident that the dabconium series is more inclined to form structures of different dimensionalities, based on the sum of ionic

radii, nevertheless, they all form perovskite structures. In contrast, the piperazinium series seem to either form a 3D perovskite structure, with the structures being isostructural, or the product obtained consists of a mixture of organic and inorganic halide salts (see Appendix D). It is also evident that part of the piperazinium series lies undiscovered. Numerous attempts were made in this study to prepare these outstanding compounds, however, the reactions yielded only a mixture of the metal salt and organic salt, and no perovskite or hybrid materials were obtained.

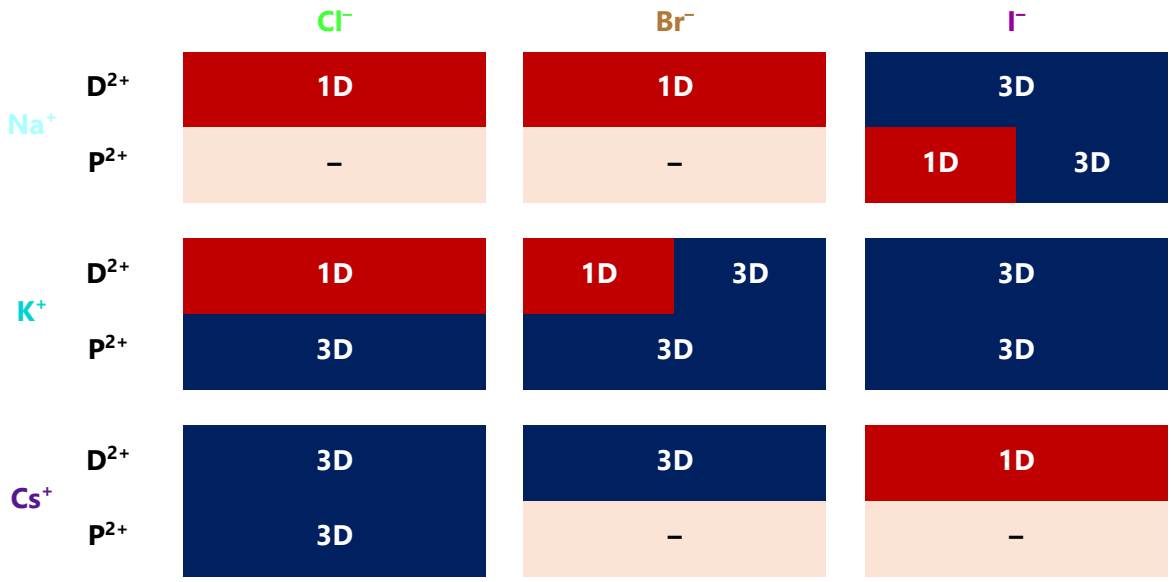

Figure 7.1 Summary of the dimensionality of perovskite structures obtained from the combination of dabconium or piperazinium with alkali metal halides. Metal and halide ions have their usual meaning, and D^{2+} = dabconium and P^{2+} = piperazinium. The labels are ordered down rows and in columns.

Also, the piperazinium series seems to reach its tipping point in going from a 1D to a 3D structure, at a smaller sum of ionic radii (NaI, 322 pm) than dabconium (KBr, 334 pm). This is because the piperazinium dication crystallises with two water molecules, making it a comparatively "larger cation" than dabconium (see Figure 7.2), meaning that the unit becomes too large to be accommodated in a 3D framework at a smaller sum of the ionic radii, causing a change to a 1D structure. The dabconium dication is almost spherical in shape, whereas the piperazinium-water adduct is slightly more ellipsoidal. The piperazinium-water adduct has a larger volume (~311.3 $Å^3$) than that of the approximately spherical shape of dabconium (~251.6 $Å^3$), as illustrated in Figure 7.2. This larger volume explains the earlier transition from 3D to 1D than in the dabconium series.

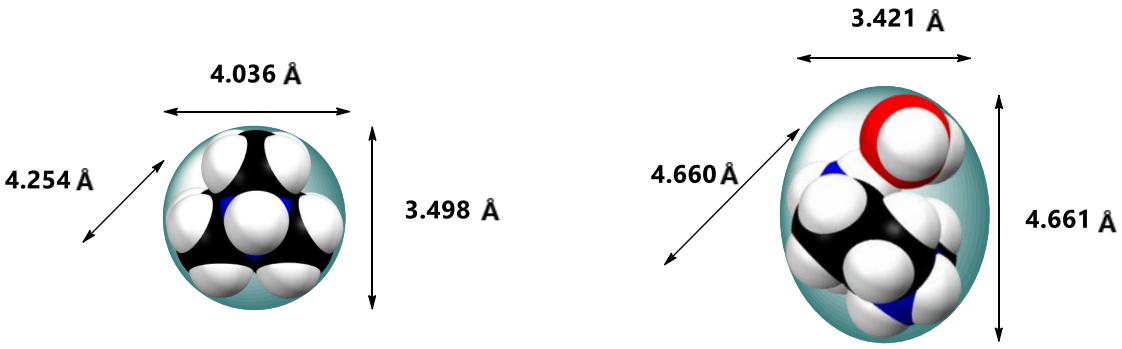

Figure 7.2 Comparison of the 3D shapes and dimensions of dabconium and piperazinium (as the water adduct as found in this study) dications.

With the structural comparison completed, the following section compares the properties measured for the materials in the two families.

7.1.2 Property Trends

Band Gap Trends

The band gaps of the materials investigated fall within the range of 3.42 eV to 5.96 eV. Materials with band gaps smaller than 5.0 eV are classified as semi-conductors while those with wider band gaps are considered insulators.[1]

In the dabconium-containing family, the compounds **D-KCl$_3$** (1D), **D-NaCl$_3$** (1D), **D-NaI$_3$** (3D), **D-KI$_3$** (3D), **D-CsI$_3$** (1D) and **D-CsCl$_2$I** (3D) have band gaps smaller than this cut-off value, and fall in the semi-conductor category, with the smallest band gap of 3.42 eV observed for **D-KCl$_3$**. The rest of the compounds in this family, **D-KBr$_3$(2)** (3D), **D-CsCl$_3$** (3D), **D-CsBr$_3$** (3D), **D-KBr$_3$(1)** (1D) and **D-NaBr$_3$** (1D) are considered to be electrical insulators, with the largest band gap of 5.33 eV displayed by **D-NaBr$_3$**.

The compounds containing the piperazinium cation display both a direct and an indirect band gap, with values ranging from 4.57 eV to 5.96 eV. For two of the compounds only one of the band gaps could be determined due to instrumental limitations. The smallest indirect band gap of 4.80 eV is observed for the 1D compound **P$_3$-NaI$_5$**, with **P-KBr$_3$** (3D) displaying the largest indirect band gap of 5.96 eV. The compounds **P$_3$-NaI$_5$** (1D), **P-KCl$_3$** (3D) and **P-CsCl$_3$** (3D) have indirect band gaps in the semi-conductor range, but the rest of the measured band gaps all fall in the insulator range.

It is of interest to compare the band gaps of the hybrid perovskites determined in this study with those of the pure alkali metal halides. The band gaps of the pure alkali metal halides are typically much wider than those of the compounds in the current study as listed in Table 7.1. Hence, the formation of a hybrid halide structure generally results in reduction of the band gap compared to that of the pure alkali metal halide. There are, however, two exceptions to this trend, with the compounds **D-CsBr$_3$** and **D-CsI$_3$** exhibiting wider band gaps than the pure halide salts CsBr and CsI.

Table 7.1 Comparison of the optical band gaps of pure alkali metal halides with those in the dabconium-containing and piperazinium-containing perovskite materials obtained in this study.

Alkali Metal Halide	Pure Band Gap (eV)	Dabconium-Containing Band Gap (eV)	Piperazinium-Containing Band Gap (eV)
NaCl	8.75[2]	3.99	–
NaBr	7.10[2]	5.33	–
NaI	5.49[2]	4.31	4.80 / 5.13
KCl	8.40[3]	3.42	4.59
KBr	7.50[1]	5.30 / 5.00	5.96
KI	5.80[1]	4.50	5.16
CsCl	8.32[3]	5.10	4.57 / 5.67
CsBr	4.76[4]	5.26	–
CsI	3.87[4]	4.63	–

Because the compounds studied here, specifically the compounds in the dabconium series, crystallised in several dimensionalities and different phases in those dimensionalities, only broad trends may be suggested. Generally, for compounds crystallising in more symmetrical phases, for example, hexagonal being more symmetrical than trigonal, a lower band gap value is observed. Also, compounds with different dimensionalities comprised of the same components show that the 3D structure has a lower band gap than the 1D structure, for example, when considering **D-KBr$_3$(1)** (1D, 5.30 eV) versus **D-KBr$_3$(2)** (3D, 5.00 eV).

The compounds with band gaps falling in the semi-conductor range have potential applications in light emitting diodes (LED's), photocatalysis, photovoltaic devices (as shown in Chapter 6) and semi-conductor lasers.[5,6]

Wide band gap materials are especially sought after in LED applications since the wider the band gap, the shorter the wavelength of emission. This means that desired blue emission can be obtained, which is difficult to obtain using semi-conductors with narrower band gaps since they emit in the green-red spectral region.[5,6] Electrical insulators also have applications in all electronic technology. Electrical insulators prohibit the flow of current and hence are used in high-voltage circuit boards and most household electronics, to limit the loss of electrical energy and limit the threat from electrical fires.[7]

It is known that the A-site cation's only influence on the band gap of perovskite materials is through the distortion which it causes in the BX-framework, as explained in Chapter 1. Hence, this is why no significant differences in band gap between the piperazinium- or dabconium-containing alkali metal halide materials are observed. However, for all the materials studied, the band gaps are quite wide (> 3.0 eV), and further theoretical (computational) investigation might explain why this is the case. However, this falls outside the scope of the current study.

Solid-State Fluorescence Trends

Based on the solid-state fluorescence measurements done in this study, it was found that the compounds do not undergo fluorescence when excited at a wavelength equal to that of their band gaps as determined by DRS spectroscopy, at room temperature.

7.2 Future Work

The future work emanating from this study may be divided into three groups, namely, synthetic modification, property investigations and applications. These will be subsequently discussed in this order.

7.2.1 Synthetic Modification

The materials studied here mainly focussed on single halide, single metal, and single organic cation perovskites, comprising alkali metal halides mixed with either dabconium or piperazinium organic cations. Only one instance of a mixed halide hybrid perovskite was investigated (**D-$CsCl_2I$**). This mixture resulted in an interesting chiral crystal structure and showed the viability of crystal engineering in the dabconium series of structures.

Therefore, the first avenue of future work would be investigating compounds of this type containing mixtures of halides, or metal ions or organic cations, and even further, the mixtures of those mixtures, thus considering a range of permutations. As explained in Chapter 2, the mixing of either the A-, B- or X-ions in hybrid halide perovskites typically leads to increased stability and improved properties of the materials.

Many of the structures studied here were isostructural (for example, **D-$NaCl_3$**, **D-$NaBr_3$**, **D-KCl_3** and **D-KBr_3**, as well as **P-KCl_3**, **P-KBr_3**, **P-KI_3** and **P-$CsCl_3$**). Hence, it is plausible that these structures can *easily* form solid solutions of several different halide or metal ions. Moreover, since the piperazinium-containing perovskites prefer to crystallise with water incorporated in the crystal structure, it could be possible that mixing of piperazinium and dabconium cations in a perovskite structure, results in a material that crystallises without water. Thus, all these crystal engineering routes that can be pursued allow for a vast scope of research options in the field of study of these materials.

In addition, the available literature on alkali metal halide perovskites is limited, and hence further investigation of these systems still presents an opportunity for exploration.

7.2.2 Property Investigations

The properties investigated in this study included the absorption and photoluminescence behaviour of the materials prepared. However, no additional material properties (for example, thermal stability, mechanical stability, stress behaviour, electroluminescence etc.) were studied. While preparing the materials for property measurements, it was noted that these materials possess an unusual hardness and high melting points. In addition, they typically grow good quality macroscopic single crystals from aqueous medium (see Appendix C for examples of crystals obtained in this study) and increase in crystallinity as their temperature is raised. These serendipitously noted properties might make the materials suitable for specific applications and warrant additional investigation.

Specific proposed techniques for further property investigation include thermogravimetric analysis (TGA), differential scanning calorimetry (DSC), hot stage microscopy and testing for electroluminescence. These techniques will give great insights into the stability, phase-stability, and emission properties of these materials and hence their potential use in applications.

7.2.3 Potential Applications

The band gaps of the materials indicate that they are either semi-conductors or insulators. Semi-conductor materials have potential applications in various optoelectronics (LEDs, photovoltaics etc.), and insulators mostly as insulating materials in electronics.[5–7]

Furthermore, in the preliminary observations regarding material stability, these semiconductors and insulators have shown to be remarkably stable towards moisture and high-temperature conditions (as determined by hot stage microscopy). This inherent stability votes well for their potential application in optoelectronic technology, suggesting that they are robust and stable enough to function under the strenuous conditions applicable to the various fields of optoelectronics.

Returning to Lead for Sensitisers

A 3D structural dimensionality does not necessarily translate to a 3D electronic dimensionality. A high electronic dimensionality is sought after when it comes to semiconducting materials.[8] The level of connectivity of the orbitals that comprise the valence band maximum and the conduction band minimum of a structure, are what defines its electronic dimensionality. The electronic dimensionality explains a structure's electronic properties and hence the application of the material to optoelectronics like solar cells.

Many explanations regarding the performance of materials in photovoltaic applications, specifically that of perovskites, are done using their structural dimensionalities rather than the electronic dimensionality since it is easier to determine the structural dimensionality experimentally. However, this does not negate the structural dimensionality as a valid argument since when the structural dimensionality decreases, a similar decrease in electronic dimensionality is usually seen.

To this end, consider Figure 7.3 (a), where the ions $Cs,^{+}$ Pb^{2+} and I^{-} are used to form $CsPbI_3$, Cs_2PbI_4, Cs_3PbI_5, and Cs_4PbI_6, which have structural dimensionalities of 3D, 2D, 1D and 0D, respectively.[8] The calculated band gaps for these structures increase with decreasing electronic and structural dimensionality, with calculated band gaps of 1.48 eV, 1.90 eV, 2.80 eV, and 3.44 eV for the 3D, 2D, 1D, and 0D structures, respectively (see Figure 7.3 (b)).

Firstly, consider the 2D band diagram (second from the left, Figure 7.3 (b)). Though the band edges are quite dispersive parallel to the layers, they become nearly flat perpendicular to the layers, implying that charge carriers will have high effective masses and will most likely not make the transition between layers. In addition, they exhibit strong anisotropy in their optical absorption perpendicular to the layers (see Figure 7.3 (c)). Therefore, when a 2D absorber layer is used in a PSC, the layers should be parallel to the substructure to ensure optimal carrier generation, transport, and collection.

Secondly, for the 1D and 0D structures (in Figure 7.3 (b), the final two), the band edges are much too localised, and hence the band gaps of these materials are too wide for single-junction photovoltaic applications. Therefore, one should look for a 3D structural dimensionality when considering any applications to PSCs.

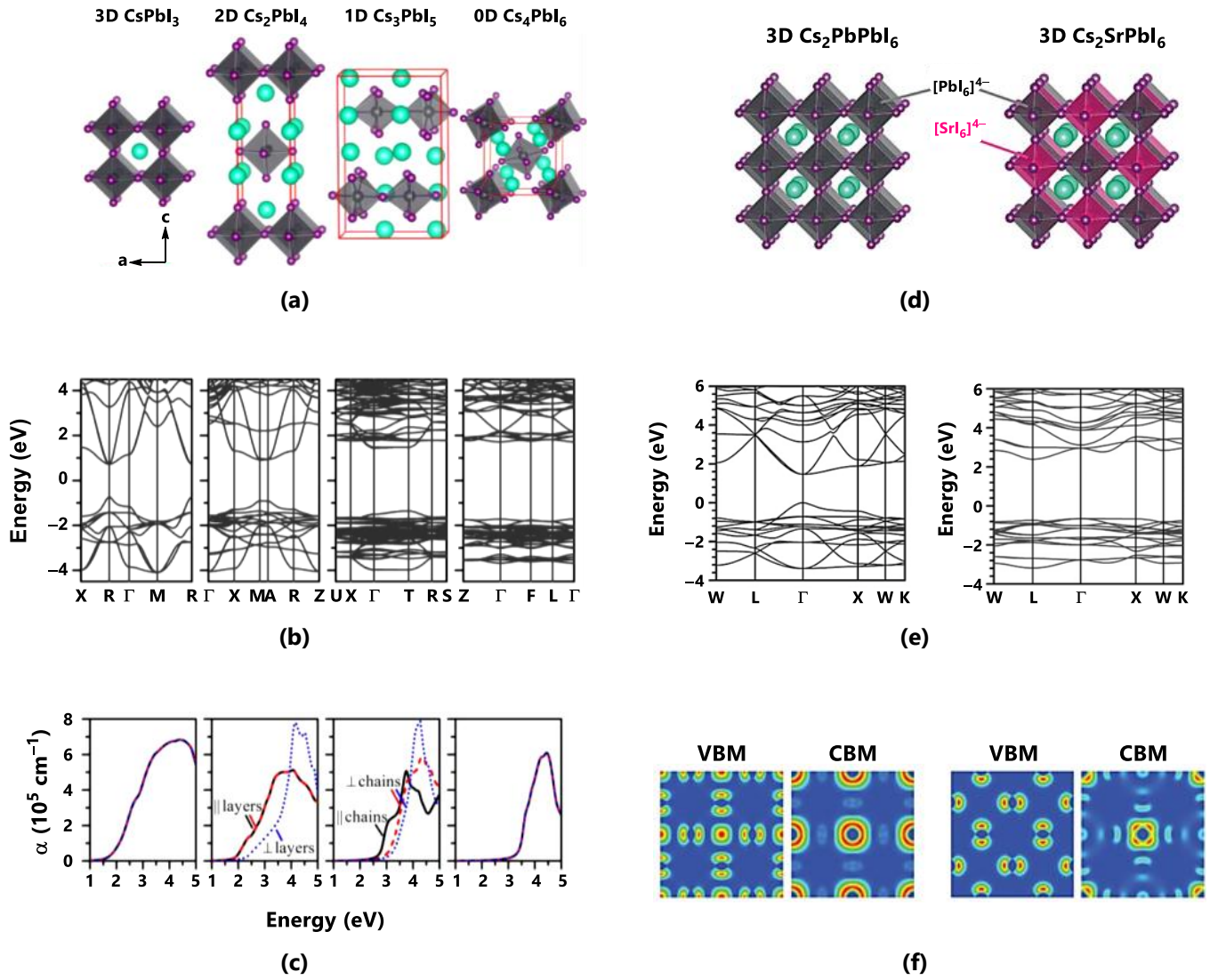

Figure 7.3 For the hypothetical model systems: $CsPbI_3$, Cs_2PbI_4, Cs_3PbI_5, and Cs_4PbI_6 **(a)** the unit cells (shown in orange) of the crystal structures, **(b)** the band structures, and **(c)** the optical absorption coefficient as a function of excitation energy (eV). For $Cs_2Pb_2I_6$ and Cs_2SrPbI_6 **(d)** the crystal structures, **(e)** the band structures, and **(f)** the valence band maximum (VBM) and conduction band minimum (CBM) charge density maps on the (100) plane. Adapted and reproduced with permission.[8] Copyright 2017, The Royal Society of Chemistry.

Nevertheless, a 3D structural dimensionality does not automatically guarantee a high electronic dimensionality, as indicated by the results obtained in this study. It is purely a prerequisite since a lower structural dimensionality will not provide a high electronic dimensionality. For example, consider the 3D perovskite, $CsPbI_3$ (may be written as Cs_2PbPbI_6 in double perovskite notation) and double perovskite 3D Cs_2SrPbI_6. Both have 3D structural dimensionalities, as shown in Figure 7.3 (d), however, unlike $CsPbI_3$, 3D Cs_2SrPbI_6 exhibits localised band edges which lead to an indirect band gap of 3.05 eV (Figure 7.3 (e)), which is similar to that of 0D Cs_4PbI_6. The reason behind this wide band gap is that, even though the $[SrI_6]^{4-}$ octahedra allow for the 3D structural dimensionality, the orbitals of the strontium metal ion do not form part of the band edges due to its high ionicity, as shown in Figure 7.3 (f) on the right. This means that the 3D Cs_2SrPbI_6 has a 0D electronic dimensionality, making it less than ideal for photovoltaic applications.

This final point on high ionicity gives a possible reason why the band gaps that were obtained for the alkali metal hybrid halide materials of this study were so wide. Alkali metal ions have comparatively high ionicity with alkali earth metal ions, hence, it may logically follow, taking Sr^{2+} as an example, that the materials prepared in this study, also possess a 0D electronic dimensionality.[9] However, this must be verified with the assistance of computational methods and is definitely an avenue that should be investigated as future work.

With all these facts in mind, the general statement that a qualifying absorber for PSC application should be structurally 3D is a good starting point. This allows for the best chance to obtain a high electronic dimensional structure, and hence researchers should focus on obtaining 3D structures as a first port of call. However, it does seem that the inclusion of lead in some manner is the best way forward in the field of perovskite optoelectronics, and even more so for their application in solar cells. Therefore, a prudent practice in any future work would be to try and combine the work of this study with lead in some manner (as conceptually explained with the materials of this study as ETLs).

Therefore, to conclude, the field of perovskites and their applications present a nearly never-ending road of possibilities. So, even though much work has been done in this field over the past 12 years, there still exists a whole *undiscovered country* of perovskites.

7.3 References for Chapter 7

1. West, A. R. *Solid State Chemistry and Its Application*, Second Ed.; Wiley, 2014.
2. Messaoudi, I. S.; Zaoui, A.; Ferhat, M. *physica status solidi (b)* **2015**, *252* (3), 490–495. https://doi.org/10.1002/pssb.201451268.
3. de Boer, P. K.; de Groot, R. A. *American Journal of Physics* **1999**, *67* (5), 443–445. https://doi.org/10.1119/1.19282.
4. Jain, A.; Ong, S. P.; Hautier, G.; Chen, W.; Richards, W. D.; Dacek, S.; Cholia, S.; Gunter, D.; Skinner, D.; Ceder, G.; Persson, K. *APL Materials* **2013**, *1* (1), 011002. https://doi.org/10.1063/1.4812323.
5. Fujita, S. *Japanese Journal of Applied Physics* **2015**, *54* (3), 30101. https://doi.org/10.7567/jjap.54.030101.
6. Shinde, S. L.; Senapati, S.; Nanda, K. K. *Advances in Natural Sciences: Nanoscience and Nanotechnology* **2014**, *6* (1), 15002. https://doi.org/10.1088/2043-6262/6/1/015002.
7. Smets, A. H. M.; Jäger, K.; Isabella, O.; Swaaij, R. A.; Zeman, M. *Solar Energy: The Physics and Engineering of Photovoltaic Conversion, Technologies and Systems*, First Ed.; UIT Cambridge, 2015.
8. Xiao, Z.; Meng, W.; Wang, J.; Mitzi, D. B.; Yan, Y. *Materials Horizons* **2017**, *4* (2), 206–216. https://doi.org/10.1039/c6mh00519e.
9. Luo, H.; Dai, S.; Bonnesen, P. V. *Analytical Chemistry* **2004**, *76* (10), 2773–2779. https://doi.org/10.1021/ac035473d.

APPENDIX A

Optical Band Gap Determination

In this Appendix, an example is given of how the optical band gap of a crystalline solid may be obtained using DRS data and the Tauc plot method. The specific sample considered in the example is **P-KI$_3$**, an indirect band gap material.

A.1 DRS Analysis of Perovskite Materials

A.1.1 The First (Indirect) Optical Band Gap of P-KI$_3$

The raw data obtained from the diffuse reflectance spectrometer has a percentage reflectance associated with a given radiation wavelength, as provided in columns 1 and 2 of Table A.1. The percentage reflectance is then converted to a fraction of 1 so that the parameters K and S may be calculated using the formula as indicated in columns 4 and 5 of Table A.1. Following this, the value of the Kubelka-Munk remission function, $F(R_\infty)$, is calculated using the K and S values as shown in column 6 of Table A.1. Finally, the photon energy is calculated from the wavelength of the radiation $\left(E = \frac{hc}{\lambda}\right.$, to be used as the x-axis variable$\left.\right)$ and $(F(R_\infty)\cdot h\nu)^2$ is calculated as the y-axis variable (the Planck constant was taken as $h = 6.626 \times 10^{-34}$ J·s and the speed of light as $c = 2.99792458 \times 10^{8}$ m·s^{-1}).

Table A.1 An extract of the raw and processed diffuse reflectance spectroscopic data for the sample **P-KI$_3$** as per the Tauc plot method outlined in Chapter 3 for an indirect transition.

Wavelength (λ, nm)	%R	R	K / $(1-R)^2$	S / $2R$	$F(R_\infty) = \frac{K}{S}$	Photon Energy $\left(\frac{hc}{\lambda}\right.$, eV$\left.\right)$	$(F(R_\infty)\cdot h\nu)^2$
800	30.85185	0.308518	0.478147	0.617037	0.774908	1.550000	1.442658107
799	30.83225	0.308323	0.478418	0.616645	0.77584	1.551940	1.449752424
798	30.84493	0.308449	0.478242	0.616899	0.775237	1.553885	1.451129892
797	30.83591	0.308359	0.478367	0.616718	0.775665	1.555834	1.456383066
796	30.83245	0.308325	0.478415	0.616649	0.77583	1.557789	1.460665246
⋮	⋮	⋮	⋮	⋮	⋮	⋮	⋮

The Tauc plot requires columns 7 and 8 of Table A.1 to be used as the x- and y-axes values, respectively. Once these two variables are plotted against one another, the result obtained is shown in Figure A.1 (a). In this specific example, two linear regions are identified. The first transition occurs as a phonon-assisted transition (photon + phonon) and the second from a photon-only transition. Therefore, the first (lower energy) transition corresponds to the indirect optical band gap and the linear region where the tangent line will be calculated from. The tangent line is then drawn to the linear region of the Tauc plot, as illustrated in Figure A.1 (b) in red. The equation of this line is determined by regression analysis to be as shown in Equation (A.1)

$$y = 2575.5x - 13302 \tag{A.1}$$

with a coefficient of determination of $R^2 = 0.9864$. For all the structures investigated in this study, the set of data used as the *linear region of the Tauc plot* had to have a coefficient of determination of above 0.98 (meaning $R^2 \geq 0.98$), for the region to be considered as linear.

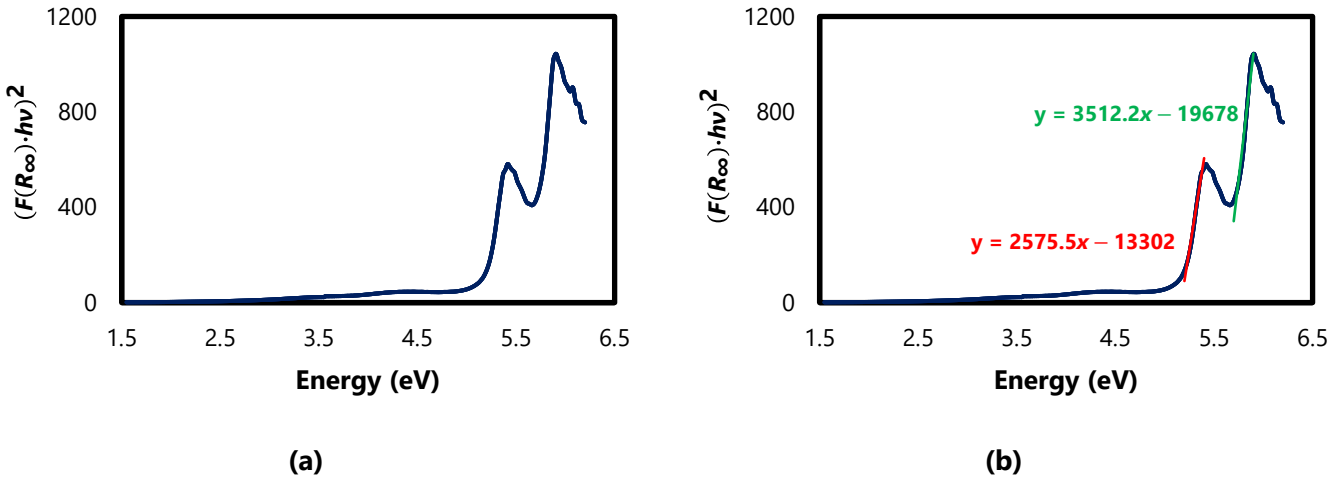

Figure A.1 The Tauc plot method. **(a)** The Tauc plot of **P-KI$_3$** assuming an indirect optical band gap and **(b)** an illustration of how the optical band gap is determined from the Tauc plot.

Therefore, by solving for x in Equation (A.1) and setting $y = 0$, the intercept of the tangential line with the x-axis is obtained as 5.16, and hence the indirect optical band gap of the sample **P-KI$_3$** is 5.16 eV.

A.1.2 The Second (Direct) Optical Band Gap of P-KI$_3$

All the calculated parameters for the direct transition are the same as for the indirect transition, except now the second absorption edge is considered as shown in in Figure A.1 (b) in green. Similar to the method described in the previous section, the line of best fit is obtained for a direct transition (second transition), as shown in Equation (A.2)

$$y = 3512.2x - 19678 \tag{A.2}$$

Therefore, setting $y = 0$ and solving for x, the direct band gap of **P-KI$_3$** is 5.60 eV. Finally, in Figure A.2 the raw reflectance data of the DRS analysis is given for all the materials obtained in this study.

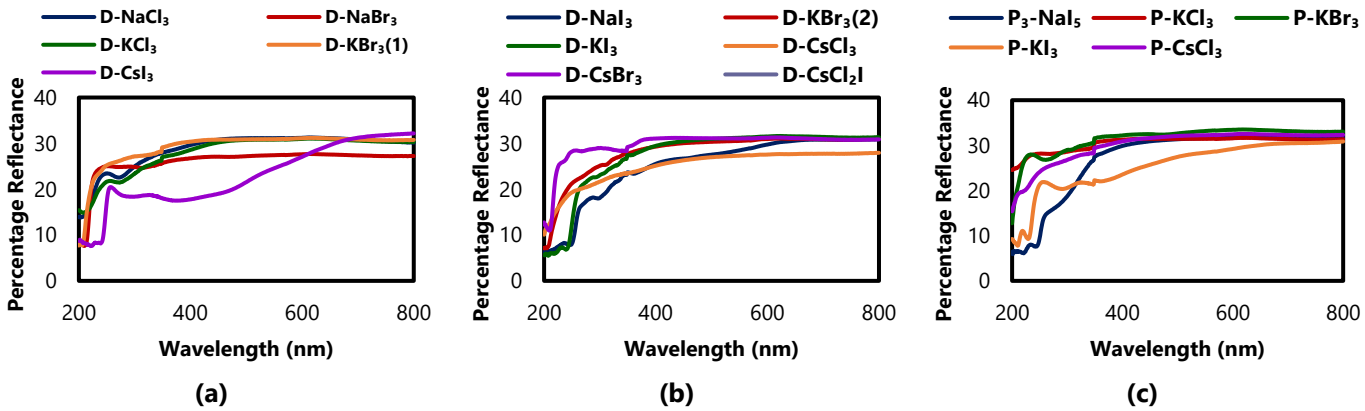

Figure A.2 The raw reflectance data obtained from the DRS analysis plotted against radiation wavelength for **(a)** the 1D ABX_3-type dabconium-containing perovskite materials, **(b)** the 3D dabconium-containing perovskite materials and **(c)** all the piperazinium-containing perovskite materials.

APPENDIX B

Miscellaneous Crystal Structures

Appendix B provides an overview of the organic salt structures obtained during the study. A short description of each structure is given, and its crystallographic properties and physical appearance are shown.

B.1 Miscellaneous Dabconium Salts

Three dabconium salts were obtained during the course of this study, shown in Figure B.1 (a), (b) and (c). These salts contained some combination of bromide ions, dibromide or triiodide ions, and the crystallised compounds obtained from several slow cooling experiments "failed" to produce perovskite materials during crystallisation attempts, instead forming the halide salts. These structures are mentioned here since few literature reports detailing these types of structures are available. However, the structures will not be discussed in detail.

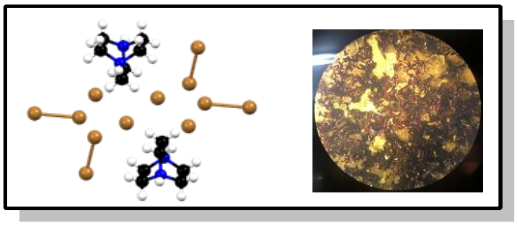

(a)

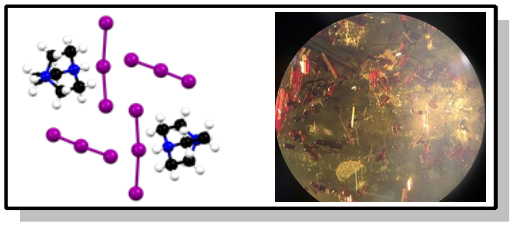

(b)

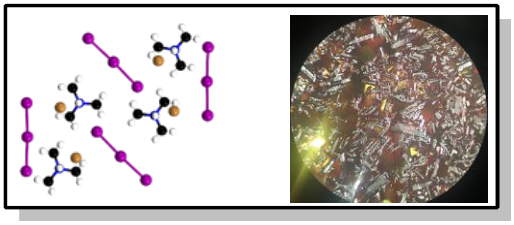

(c)

Figure B.1 The contents of the unit cells and physical appearance of **(a)** dabconium crystallised with Br_2 and Br^--ions, **(b)** dabconium crystallised with I_3^--ions and **(c)** dabconium crystallised with Br^--ions and I_3^--ions.

The structures that contain only bromide or iodide (those shown in Figure B.1 (a) and (b)) crystallise in the monoclinic space group $P2_1/m$. In contrast, the other structure (Figure B.1 (c)), which contains Br^-- and I_3^--ions, crystallises in the orthorhombic space group *Pnma*.

Furthermore, each of these materials is dark red, almost black when examined under the microscope. This suggests a narrow band gap and good light absorption properties. Though no further analysis were conducted on these materials, they might be good candidates for organic dye sensitised solar cells because of these properties.

Finally, several other halide salts containing either dabconium or piperazinium were also obtained. These structures typically included a piperazinium or dabconium dication crystallised with a halide ion (Cl^-, Br^- or I^-), and sometimes a water molecule. However, these structures are fully described in the literature, and hence will not be discussed here.

APPENDIX C

Physical Appearance of Crystals

In this Appendix, photos of crystals employed in crystal structure analysis are shown. These are representative of the crystals that were analysed to obtain the crystal structures described in the main body of work, however, may not be the exact same crystal used in the SCXRD analysis. One common feature of all the perovskite materials obtained in this study is that they are all colourless.

C.1 Dabconium-Containing Crystals

The combination of the dabconium dication with an alkali metal-based anions lead to the formation of either 1D ABX_3-type or 3D perovskite structures. The following two sections will link the physical crystal with its crystal structure.

C.1.1 1D ABX_3-Type Structures

Four combinations lead to the formation of isostructural 1D trigonal structures, namely **D-$NaCl_3$**, **D-$NaBr_3$**, **D-KCl_3** and **D-KBr_3(1)**, and another combination, that of CsI and dabconium, lead to the 1D hexagonal structure **D-CsI_3**. These five structures are shown with the physical appearance of their crystals next to them in Figure C.1. All crystals were colourless.

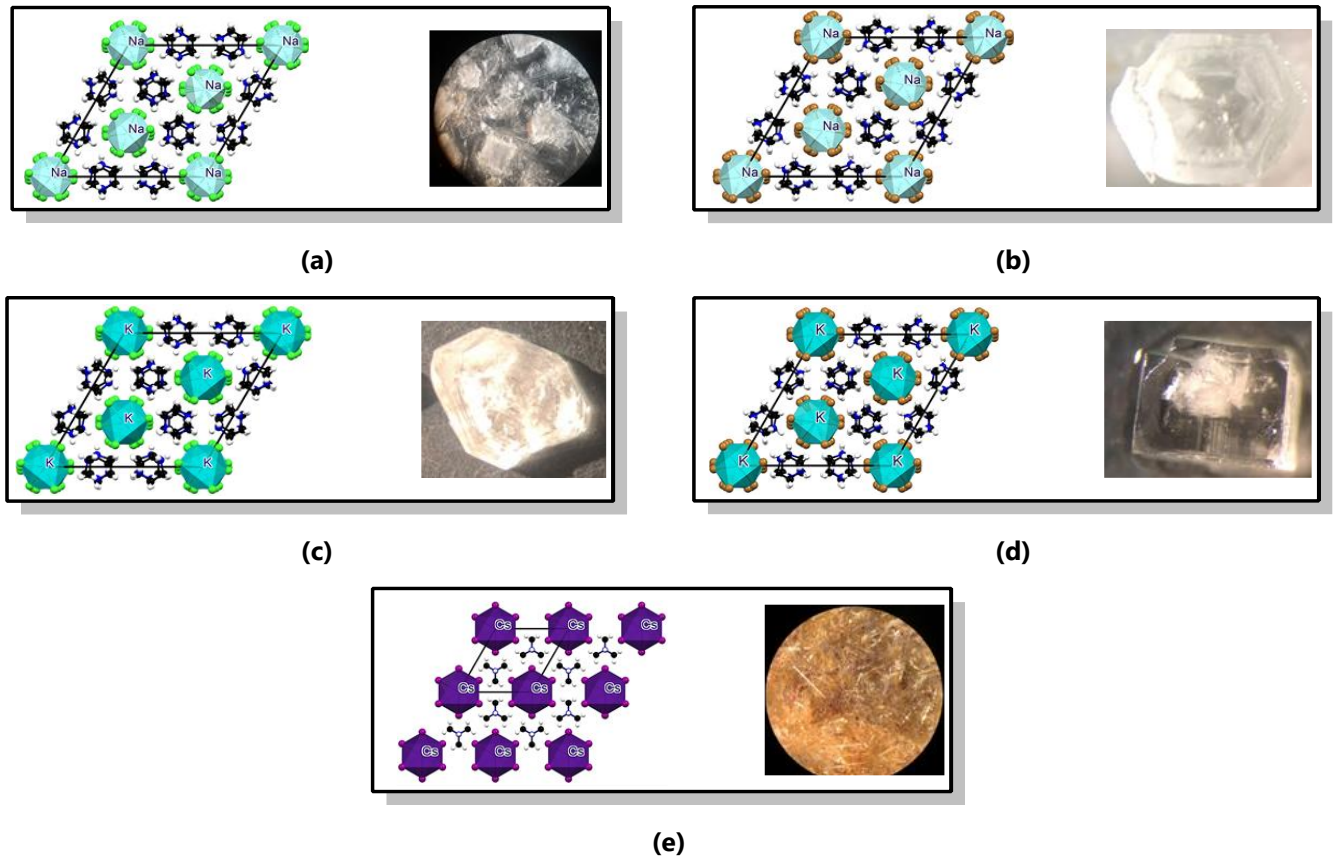

Figure C.1 1D ABX_3-type dabconium-containing structures (shown on the left) with the physical appearances of their crystals (on the right). **(a) D-$NaCl_3$**, **(b) D-$NaBr_3$**, **(c) D-KCl_3**, **(d) D-KBr_3(1)** and **(e) D-CsI_3**.

C.1.2 3D Structures

Six 3D perovskite structures were obtained, namely, the hexagonal **D-NaI$_3$**, the trigonal **D-KBr$_3$(2)**, the trigonal **D-KI$_3$**, the monoclinic **D-CsCl$_3$**, the orthorhombic **D-CsBr$_3$** and the trigonal mixed halide perovskite structure **D-CsCl$_2$I**. These structures and the appearance of their crystals are all shown in Figure C.2. All crystals were colourless. In some cases, the light shone on the crystal was yellow, or the crystal was photographed in oil, hence it appears to have a yellow colour.

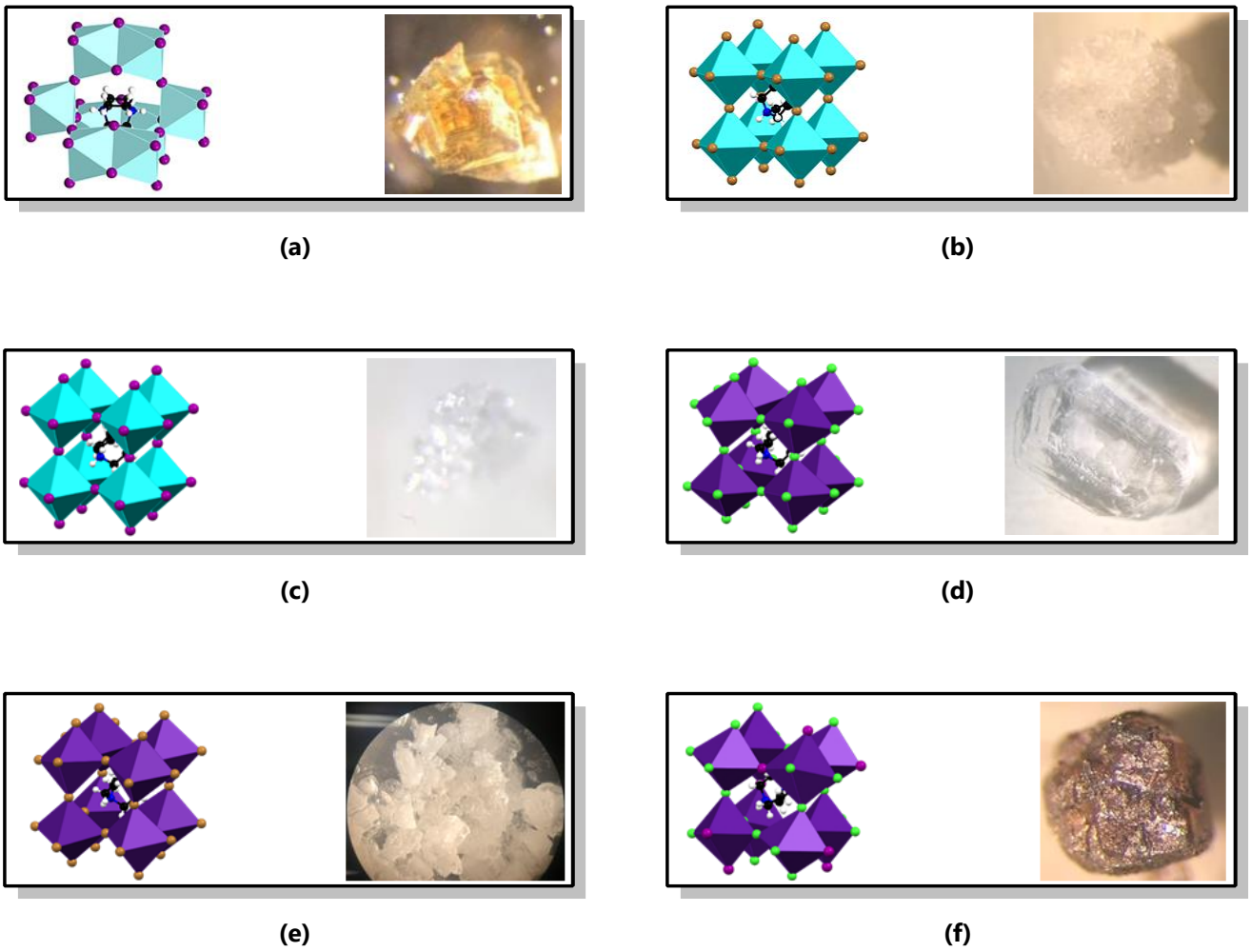

Figure C.2 3D dabconium-containing structures (shown on the left) with the physical appearances of their crystals (on the right). **(a) D-NaI$_3$**, **(b) D-KBr$_3$(2)**, **(c) D-KI$_3$**, **(d) D-CsCl$_3$**, **(e) D-CsBr$_3$** and **(f) D-CsCl$_2$I**.

C.2 Piperazinium-Containing Crystals

Four combinations of piperazinium with alkali metal halides formed isostructural orthorhombic crystal structures **P-KCl$_3$**, **P-KBr$_3$**, **P-KI$_3$** and **P-CsCl$_3$**. These structures crystallised with an isolated water molecule in its asymmetric unit, as shown with the physical appearances of the crystals in Figure C.3 (a) through (d). Furthermore, a monoclinic 1D ⟨100⟩-type perovskite structure, **P$_3$-NaI$_5$**, was also obtained and is shown alongside one of its physical appearances in Figure C.3 (e).

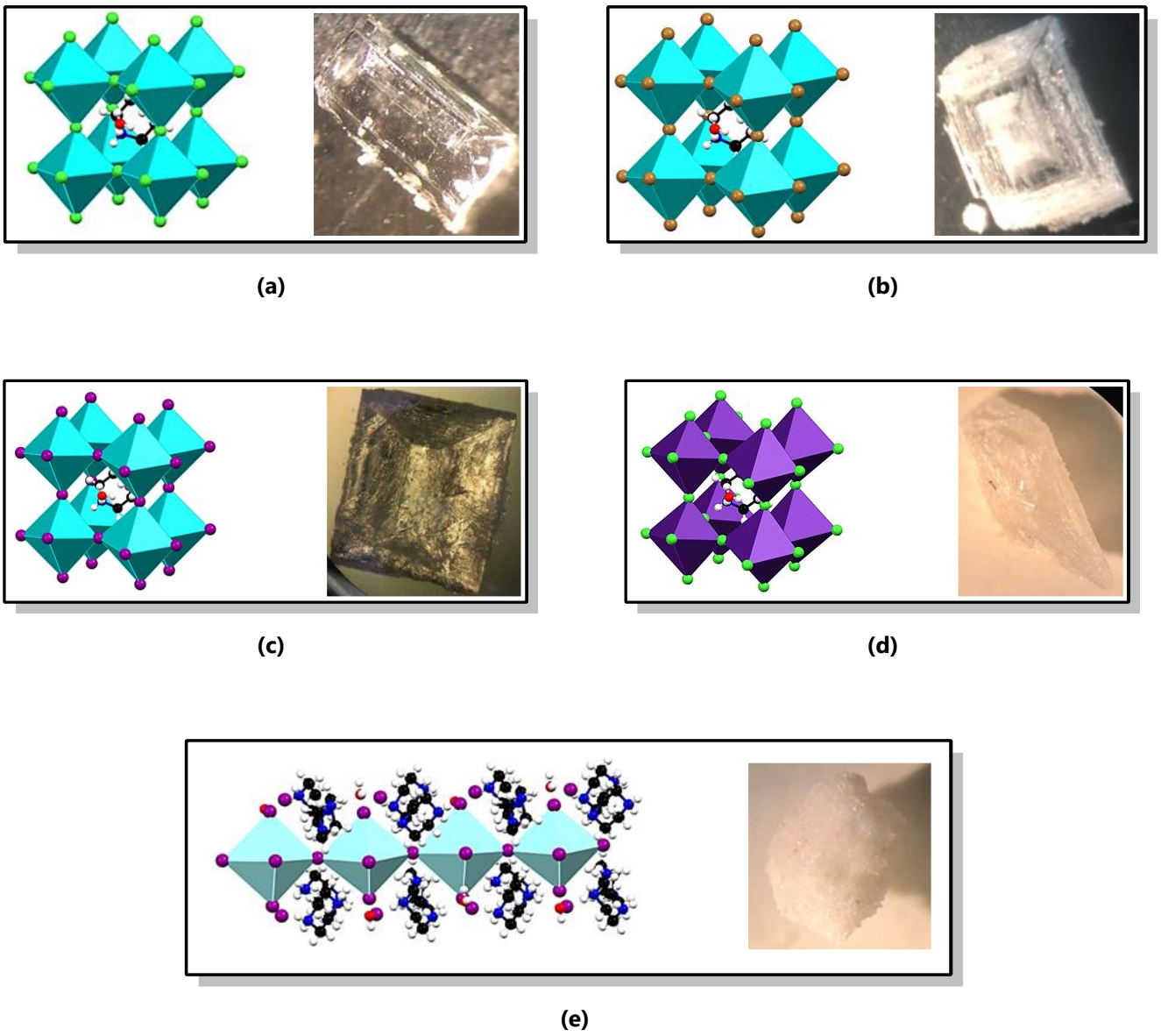

Figure C.3 3D orthorhombic piperazinium-containing structures (shown on the left) with the physical appearances of their crystals (on the right). **(a) P-KCl$_3$**, **(b) P-KBr$_3$**, **(c) P-KI$_3$** and **(d) P-CsCl$_3$**. The monoclinic 1D ⟨100⟩-type perovskite structure **P$_3$-NaI$_5$** and one of its crystals is shown in Figure **(e)**.

APPENDIX D

Powder X-Ray Diffraction Data

In this appendix the powder X-ray diffraction (PXRD) data of all the compounds synthesised in this study are reported. PXRD is a technique employed to prove that the structure of the bulk sample corresponds to the structure determined by single-crystal X-ray diffraction. Only pure bulk samples could be employed for property measurements.

D.1 Dabconium-Containing Perovskites

For all the dabconium-containing perovskites (1D ABX_3-type and 3D) PXRD analysis were done to ensure the purity of the compounds, and exclude temperature induced phase transitions, by matching the experimental powder patterns of the bulk samples determined at room temperature to the powder patterns calculated from the low-temperature SCXRD structures. The PXRD data were collected for 2θ values between 5° and 45°, however, the first peak for most of the compounds only appears after 10°, hence the patterns shown in Figure D.1 through Figure D.11 are plotted for 2θ values 10° to 45° 2θ, with the exception of **D-CsI_3** and **D-$CsCl_2I$** where there are peaks present before 10° 2θ. In all the figures, the calculated powder patterns are shown in red, and the experimental powder patterns in blue.

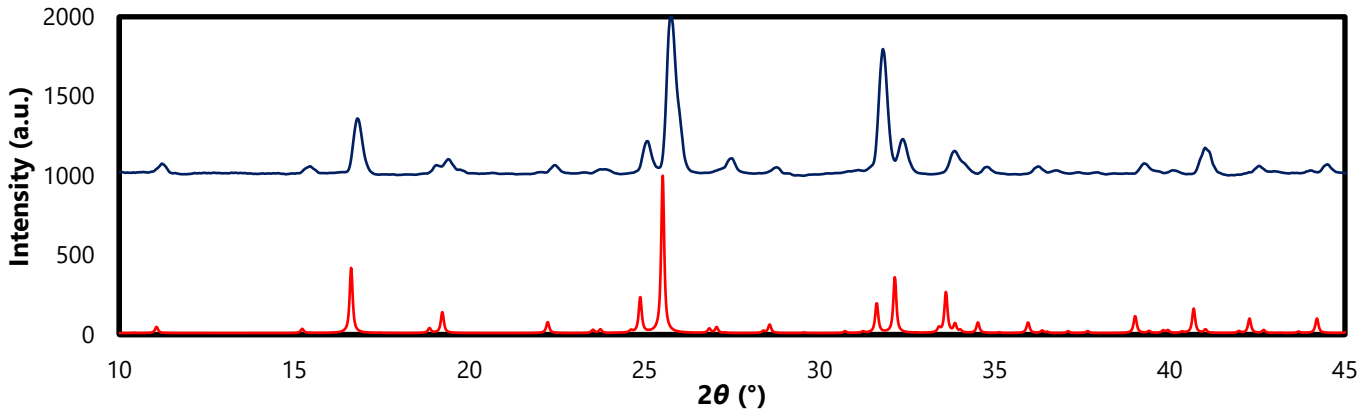

Figure D.1 The calculated (shown in red) and experimental (shown in blue) powder patterns for the combination of 1,4-diazabicyclo[2.2.2]octane with NaCl and HCl in a 1:1:4 ratio, which lead to the formation of the compound **D-$NaCl_3$**.

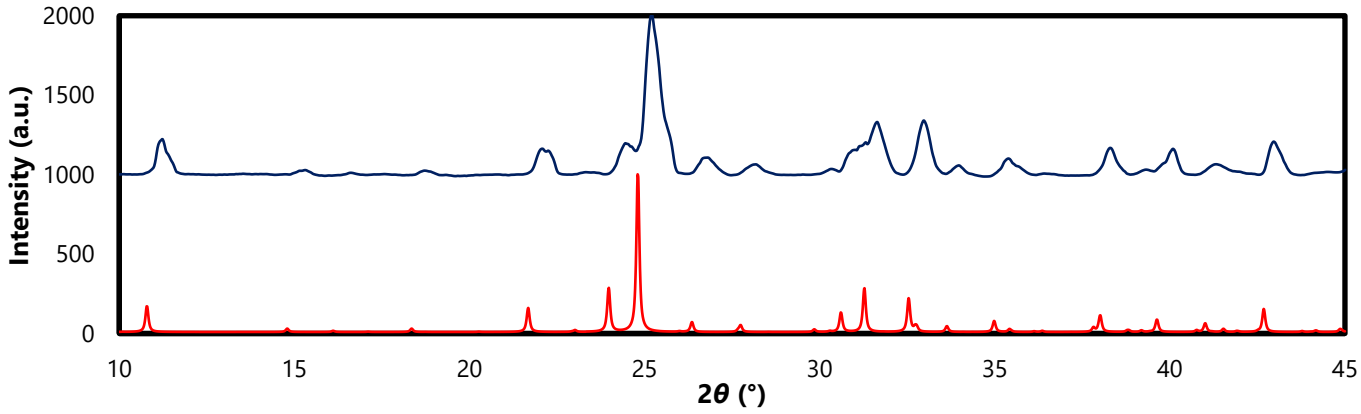

Figure D.2 The calculated (shown in red) and experimental (shown in blue) powder patterns for the combination of 1,4-diazabicyclo[2.2.2]octane with NaBr and HBr in a 1:1:4 ratio, which lead to the formation of the compound **D-$NaBr_3$**.

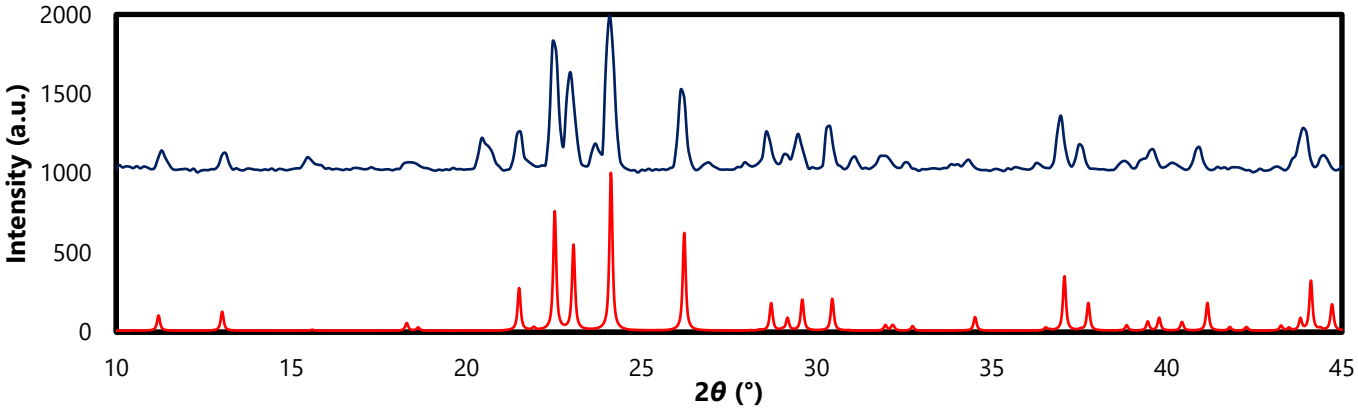

Figure D.3 The calculated (shown in red) and experimental (shown in blue) powder patterns for the combination of 1,4-diazabicyclo[2.2.2]octane with NaI and HI in a 1:1:2.2 ratio, which lead to the formation of the compound **D-NaI$_3$**.

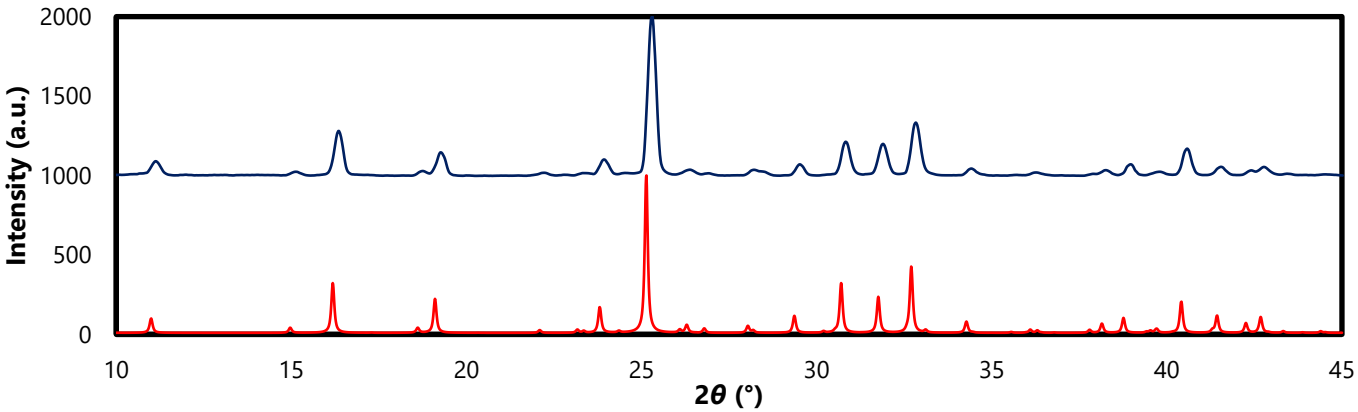

Figure D.4 The calculated (shown in red) and experimental (shown in blue) powder patterns for the combination of 1,4-diazabicyclo[2.2.2]octane with KCl and HCl in a 1:1:4 ratio, which lead to the formation of the compound **D-KCl$_3$**.

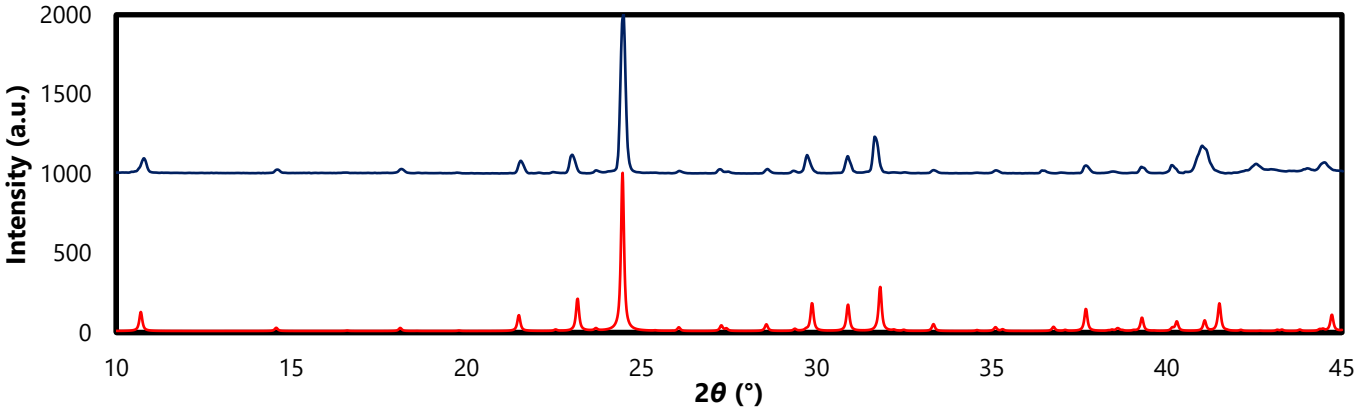

Figure D.5 The calculated (shown in red) and experimental (shown in blue) powder patterns for the combination of 1,4-diazabicyclo[2.2.2]octane with KBr and HBr in a 1:1:4 ratio, which lead to the formation of the compound **D-KBr$_3$(1)**.

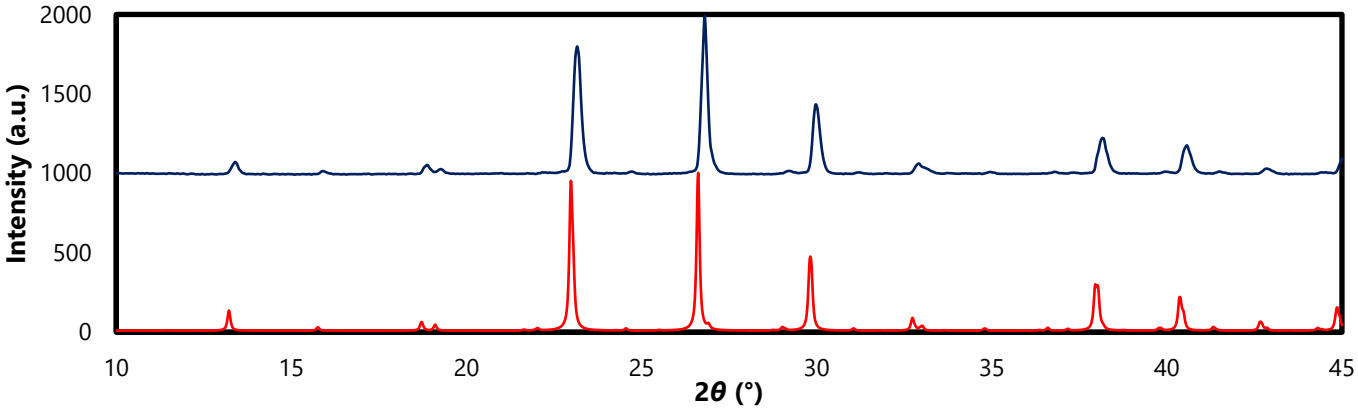

Figure D.6 The calculated (shown in red) and experimental (shown in blue) powder patterns for the combination of 1,4-diazabicyclo[2.2.2]octane with KBr and HBr in a 1:1:2.2 ratio, which lead to the formation of the compound **D-KBr_3(2)**.

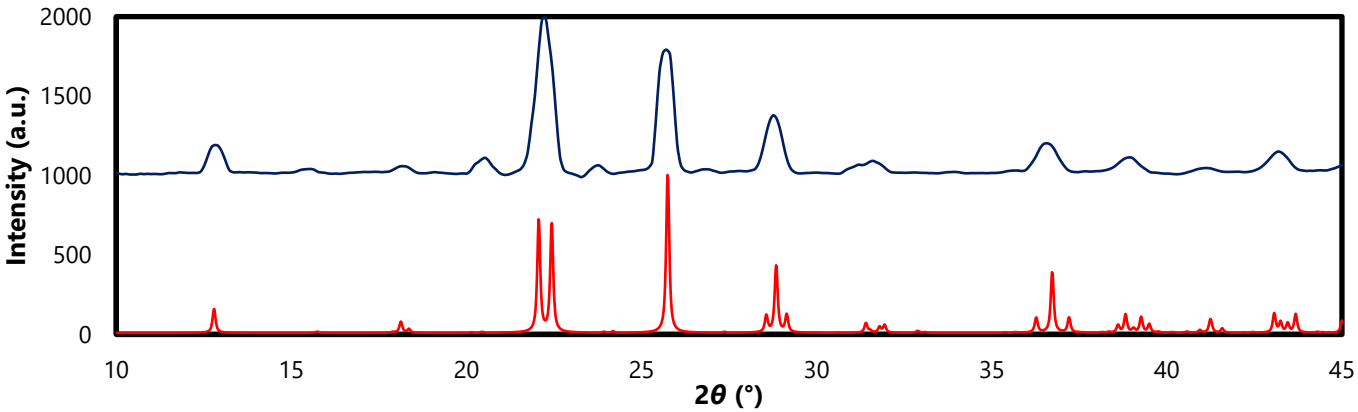

Figure D.7 The calculated (shown in red) and experimental (shown in blue) powder patterns for the combination of 1,4-diazabicyclo[2.2.2]octane with KI and HI in a 1:1:2.2 ratio, which lead to the formation of the compound **D-KI_3**.

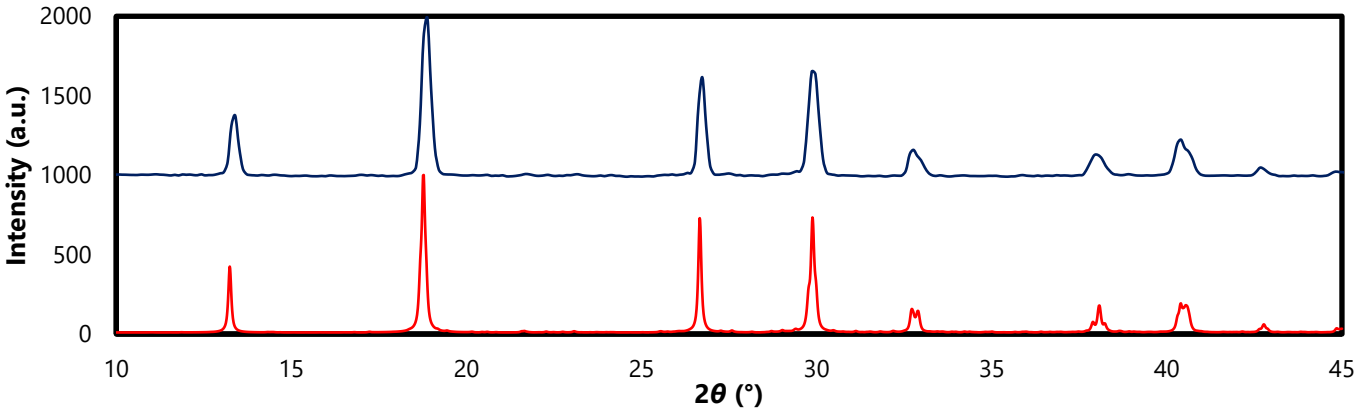

Figure D.8 The calculated (shown in red) and experimental (shown in blue) powder patterns for the combination of 1,4-diazabicyclo[2.2.2]octane with CsCl and HCl in a 1:1:4 ratio, which lead to the formation of the compound **D-$CsCl_3$**.

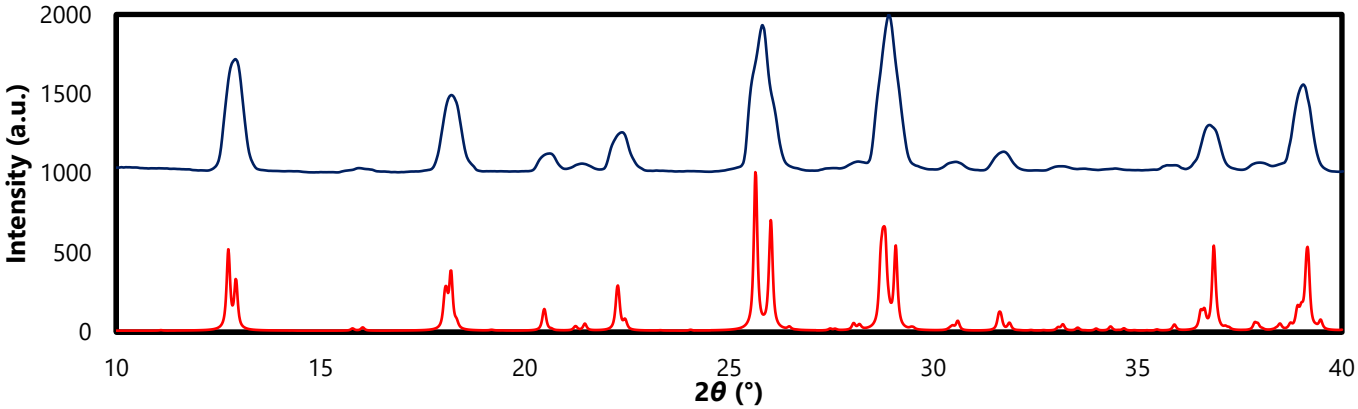

Figure D.9 The calculated (shown in red) and experimental (shown in blue) powder patterns for the combination of 1,4-diazabicyclo[2.2.2]octane with CsBr and HBr in a 1:1:4 ratio, which lead to the formation of the compound **D-CsBr$_3$**.

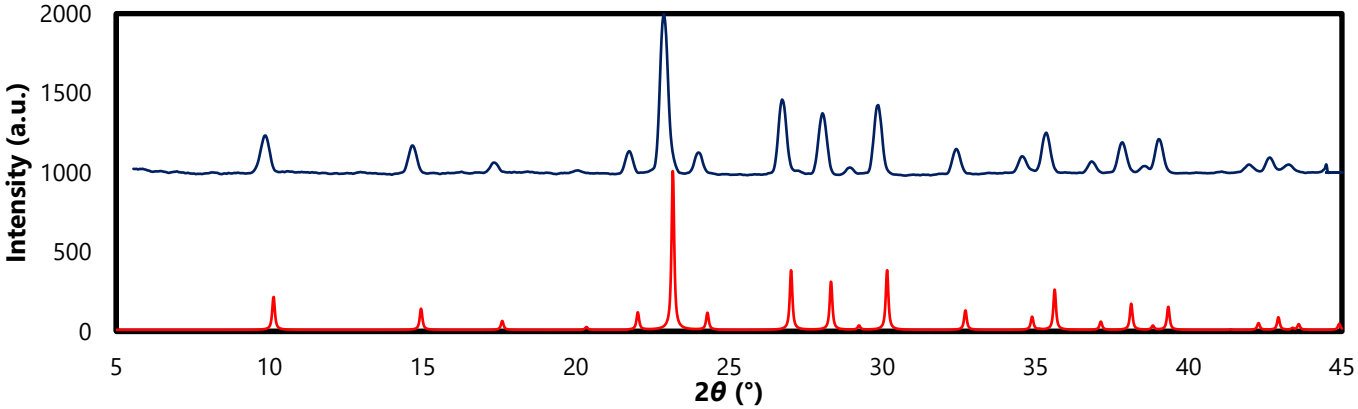

Figure D.10 The calculated (shown in red) and experimental (shown in blue) powder patterns for the combination of 1,4-diazabicyclo[2.2.2]octane with CsI and HI in a 1:1:4 ratio, which lead to the formation of the compound **D-CsI$_3$**.

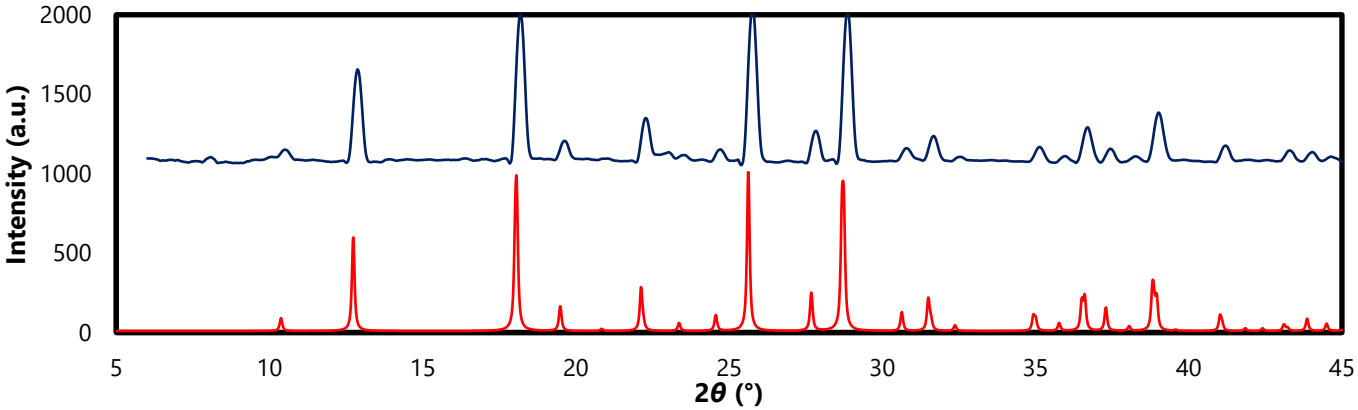

Figure D.11 The calculated (shown in red) and experimental (shown in blue) powder patterns for the combination of 1,4-diazabicyclo[2.2.2]octane with CsI and HCl in a 1:1:8 ratio, which lead to the formation of the compound **D-CsICl$_2$**.

D.2 Piperazinium-Containing Perovskites

For all the piperazinium-containing perovskites (1D ⟨100⟩-type and 3D) PXRD analysis were done to ensure the purity of the compounds and exclude temperature induced phase transitions, by matching the experimental powder patterns of the bulk samples to the powder patterns calculated from their low-temperature SCXRD structures. The PXRD data were collected between 5° and 45° 2θ, however, the first peak for most of the compounds only appears after 10° 2θ, hence the patterns shown in Figure D.12 through Figure D.16 are plotted for 10° to 45° 2θ. In all the figures, the calculated powder patterns are shown in red, and the experimental powder patterns in blue.

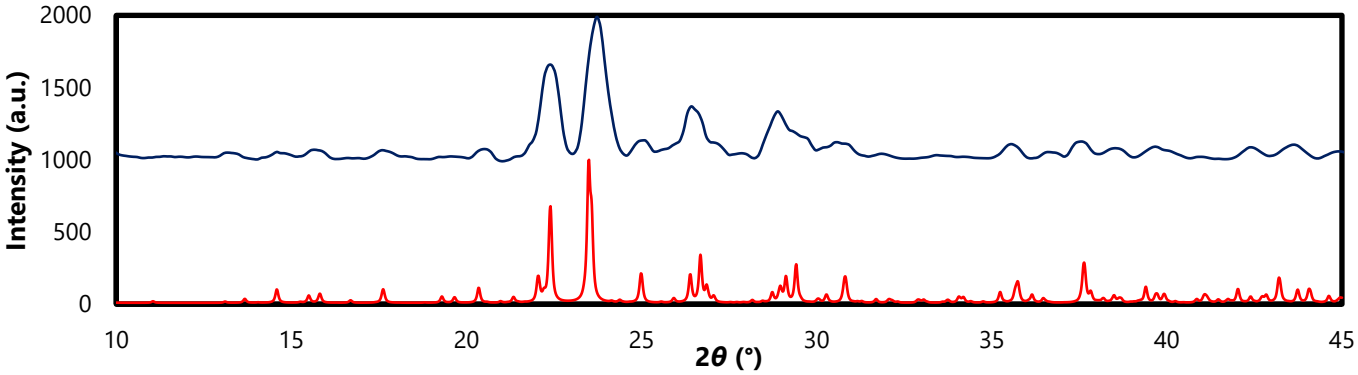

Figure D.12 The calculated (shown in red) and experimental (shown in blue) powder patterns for the combination of piperazine with NaI and HI in a 1:1:2.2 ratio, which lead to the formation of the compound **P_3-NaI_5**.

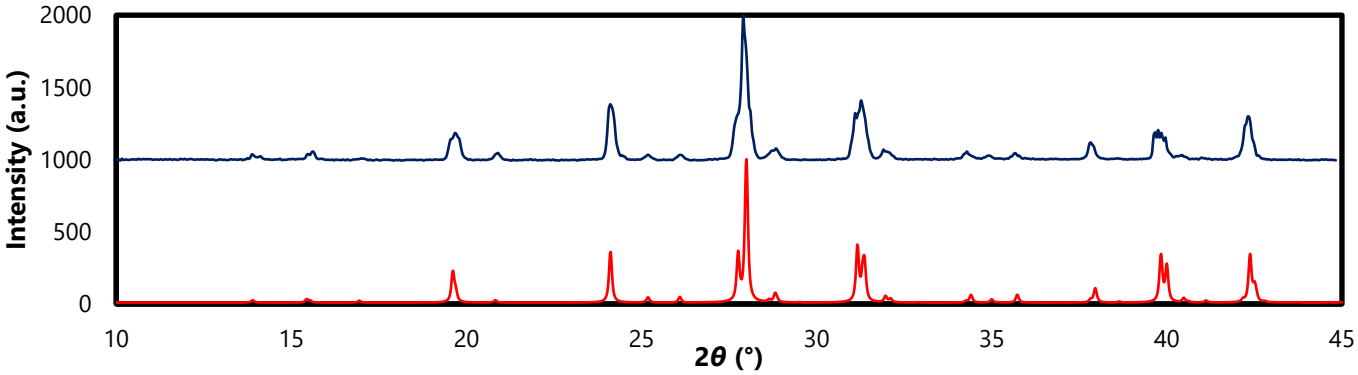

Figure D.13 The calculated (shown in red) and experimental (shown in blue) powder patterns for the combination of piperazine with KCl and HCl in a 1:1:4 ratio, which lead to the formation of the compound **P-KCl_3**.

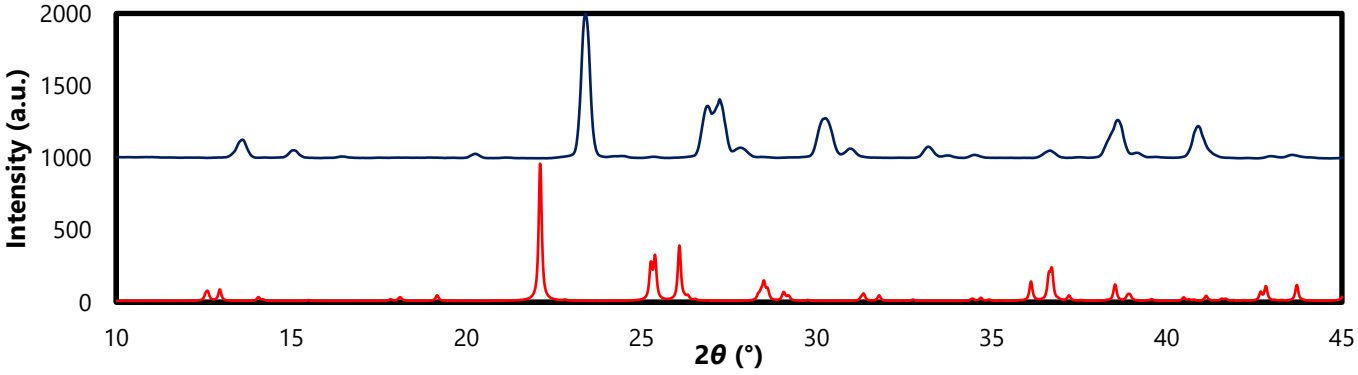

Figure D.14 The calculated (shown in red) and experimental (shown in blue) powder patterns for the combination of piperazine with KBr and HBr in a 1:1:4 ratio, which lead to the formation of the compound **P-KBr_3**.

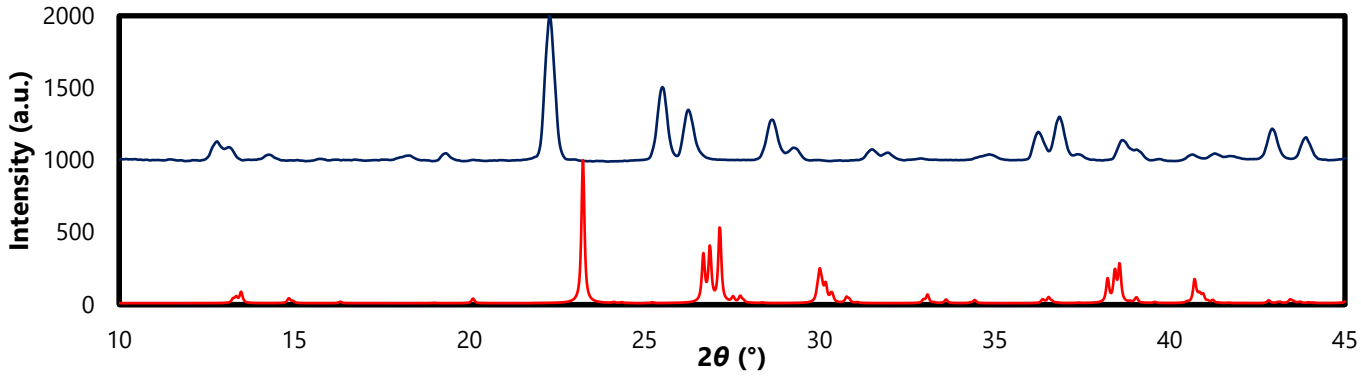

Figure D.15 The calculated (shown in red) and experimental (shown in blue) powder patterns for the combination of piperazine with KI and HI in a 1:1:4 ratio, which lead to the formation of the compound **P-KI$_3$**.

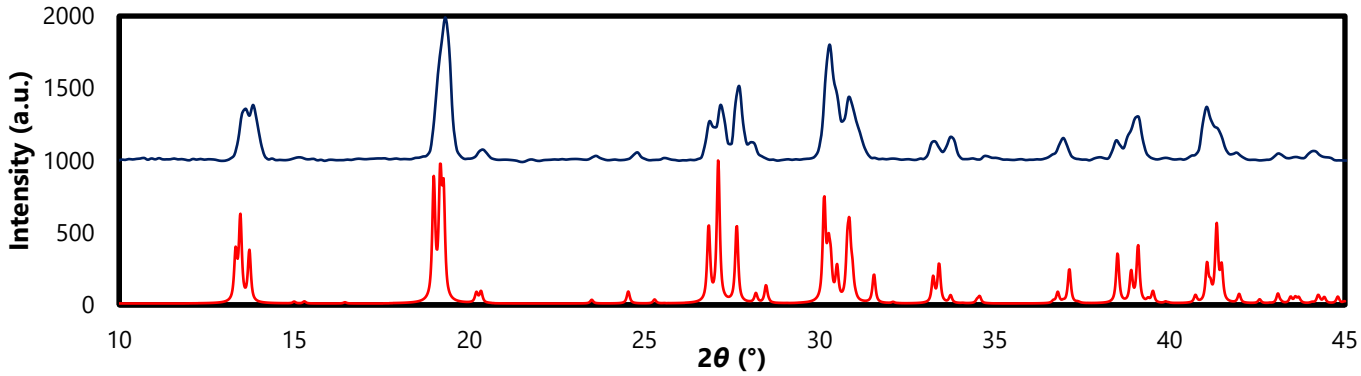

Figure D.16 The calculated (shown in red) and experimental (shown in blue) powder patterns for the combination of piperazine with CsCl and HCl in a 1:1:2.2 ratio, which lead to the formation of the compound **P-CsCl$_3$**.

D.2.1 Other Attempted Synthesis of Piperazinium-Containing Perovskites

The preparation of perovskite or hybrid compounds using the combinations between piperazinium and NaCl, NaBr, CsBr or CsI were attempted several times without success. The materials formed consisted of a mixture of the metal halide salt and the organic halide salt, which was typically hydrated (labelled Pip-X-H_2O, where X is the specific halide). Figure D.17 through Figure D.20 show the PXRD patterns of the resultant mixtures in blue, while the metal salt's pattern is shown in grey and the calculated piperazinium salt's pattern in red. In each instance the experimental pattern is a sum of the patterns of the two salts.

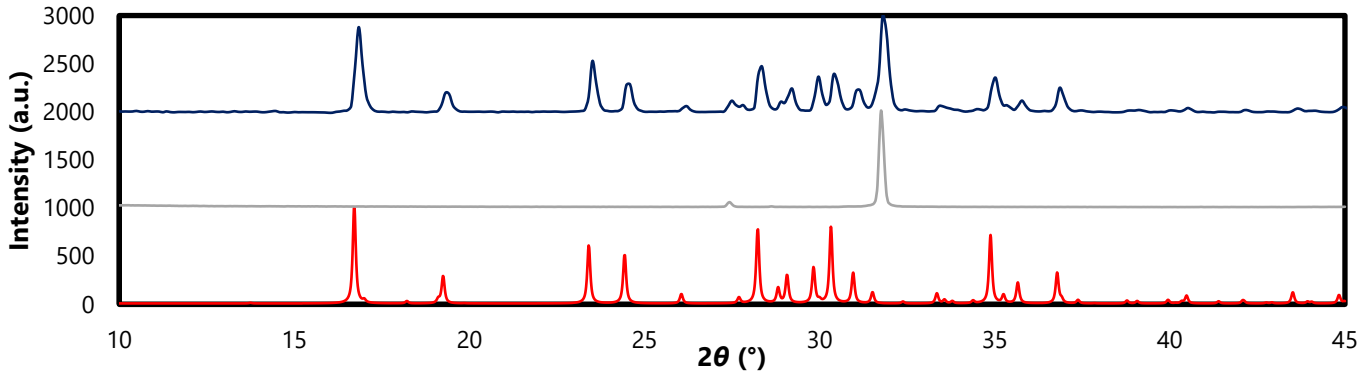

Figure D.17 The experimental (shown in blue) powder pattern for the combination of piperazine with NaCl (pattern shown in grey) and HCl in a 1:1:4 ratio, which lead to a mixture of NaCl and Pip-Cl-H_2O (pattern shown in red).

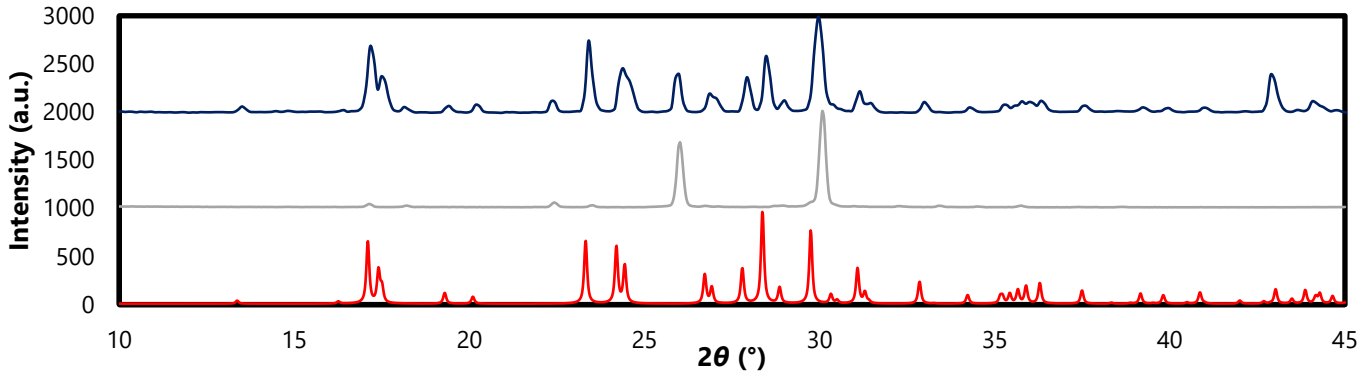

Figure D.18 The experimental (shown in blue) powder pattern for the combination of piperazine with NaBr (pattern shown in grey) and HBr in a 1:1:4 ratio, which lead to a mixture of NaBr and Pip-Br-H_2O (pattern shown in red).

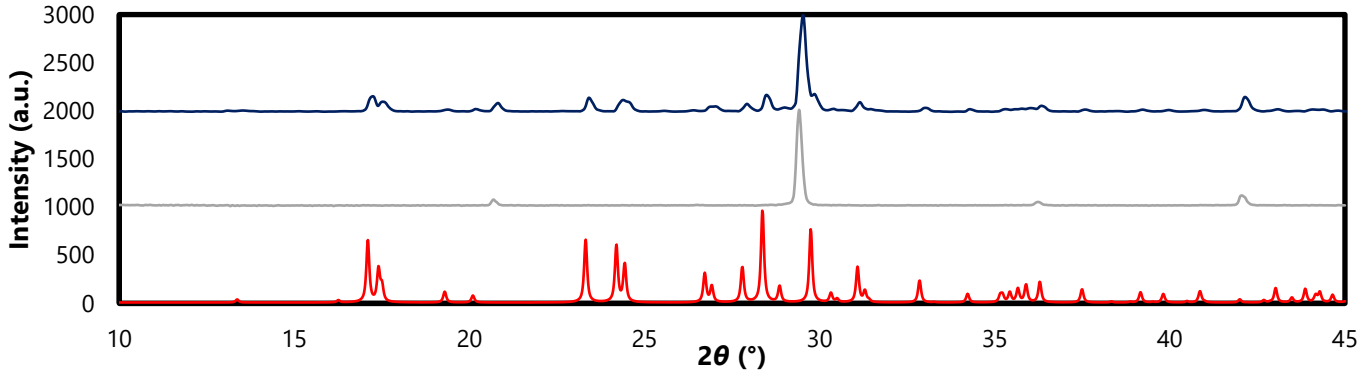

Figure D.19 The experimental (shown in blue) powder pattern for the combination of piperazine with CsBr (pattern shown in grey) and HBr in a 1:1:4 ratio, which lead to a mixture of CsBr and Pip-Br-H_2O (pattern shown in red).

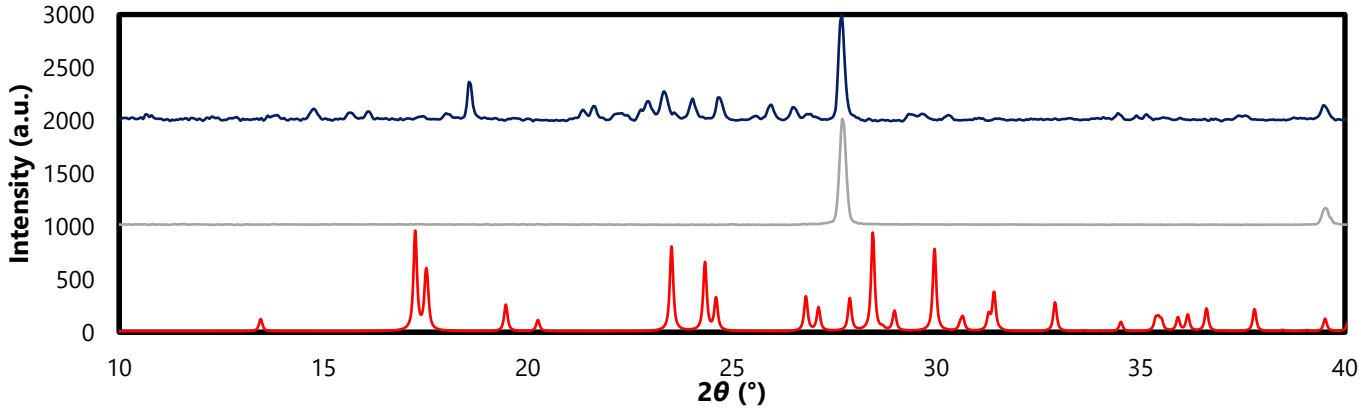

Figure D.20 The experimental (shown in blue) powder pattern for the combination of piperazine with CsI (pattern shown in grey) and HI in a 1:1:4 ratio, which lead to a mixture of CsI and Pip-I-H_2O (pattern shown in red).

APPENDIX E

Crystal Structure Quality

In this, the final appendix of the dissertation, the rationale and brief discussion on the inclusion of the crystal structures of **D-NaI$_3$**, **D-KBr$_3$(2)**, **D-KI$_3$** and **P$_3$-NaI$_5$** is provided. Since these structures formed an integral part in the trend analyses completed earlier, their inclusion was of paramount importance.

E.1 Rationale of Inclusion

The crystal structures of **D-NaI$_3$**, **D-KBr$_3$(2)**, **D-KI$_3$** and **P$_3$-NaI$_5$** were of a relatively poor quality, however, they were included because they form an integral part of the trends discussion in the "Results" chapters, Chapters 4 and 5. Moreover, the obtained structures, though of comparatively inferior quality compared to the other structures obtained in this study, aligned well with the structural trends observed in the dabconium- and piperazinium families. This meant their inclusion was invaluable, to allow for the construction of logical and useful conclusions, as well as aiding in the building of predictive models for crystal engineering, as emphasised in Chapter 4.

Furthermore, since each of these four compounds were obtained using the so-called "Elevated Temperature Evaporation Method", the inferior crystal quality is to be expected. The elevated temperature method accelerates the nucleation of the perovskite materials and hence leads to microcrystalline materials, rather than large single crystals. Additionally, several *other* crystallisation attempts to obtain high quality single crystals failed, resulting in the formation of salts, and hence the only process that lead to formation of the perovskite materials was the "Elevated Temperature Evaporation Method". This left the author with the predicament of choosing inferior single-crystal structure quality over exclusion of the structures. In the end, it was rationalised that the added value of the inclusion of these structures to the overall understanding of the family of structures, should be prioritised, and hence the decision was made to include them.

Importantly, numerous single crystal X-ray diffraction data sets were collected for these perovskite products obtained from the elevated temperature method, and the structures included were the best structures obtained.

As shown in Appendix C, the materials listed here all exhibited crystal morphologies with high mosaicity, suggesting a possible reason for their inferior data sets. This also correlates with what is expected (micro crystallinity) of the crystallisation method, that said, this is purely speculative.

E.2 A- and B-Alerts in CheckCIF Reports

For the structure **D-NaI$_3$**, 10 B-alerts are generated. Three of these may be explained by the use of the "theoretically correct" structure rather than that stated in the CIF file, as explained in Chapter 4.

The structure **D-KBr$_3$(2)** gave three A-alerts and 14 B-alerts. These alerts can be attributed to the low number of unique reflections collected, only 38%, due to the poor quality of the crystal, as a result of the preparation method. Though the A-alerts indicate that the proposed structure does not *fit* the electron density map that well (high R1 and wR2 values), the values obtained here were the best of a series of proposed space groups and crystal systems. Furthermore, the choice in crystal system and space group ($P3_221$) motivated by the close correlation of this structure with its literature structure (an enantiomeric structure), which only suggests the chosen crystal in the data collection was not ideal, as explained earlier.

Considering the structure **D-KI$_3$** (space group *R*32), several A- and B-alerts were generated. In this structure, the inorganic framework could be determined successfully, with the dabconium cation severely disordered. The poor quality of the structure is attributed to the method of preparation of the perovskite resulting in poor quality crystals, and, as a result, poor diffraction data. In addition, the presence of heavy iodide anions in the inorganic framework impacted on the ability to resolve the cation. Several attempts to obtain better quality data were unsuccessful, however, since the inorganic framework could be determined, important structural features could still be identified, which warrants inclusion of the structure. The generated alerts can all be ascribed to the disorder in the cation, and the general poor quality of the data.

Finally, the structure **P$_3$-NaI$_5$** gave two A- and six B-alerts. However, since the obtained structure corresponded to the literature structure, again the inferior quality of the diffraction data is ascribed to the poor crystal quality rather than an incorrect assignment of space group ($P2_1/c$).

AFTERWORD

Like all things, even good things must come to an end. Therefore, this concludes the MSc dissertation of H. J. van der Poll: **The structures and properties of alkali metal halide perovskites containing dabconium or piperazinium**.

Finem perventum est